



Veröffentlichungen der DGK

Ausschuss Geodäsie der Bayerischen Akademie der Wissenschaften

Reihe C

Dissertationen

Heft Nr. 859

Mohammad Omidalizarandi

**Robust Deformation Monitoring of Bridge Structures Using
MEMS Accelerometers and Image-Assisted Total Stations**

München 2020

Verlag der Bayerischen Akademie der Wissenschaften

ISSN 0065-5325

ISBN 978-3-7696-5271-0

Diese Arbeit ist gleichzeitig veröffentlicht in:

Wissenschaftliche Arbeiten der Fachrichtung Geodäsie und Geoinformatik der Universität Hannover

ISSN 0174-1454, Nr. 366, Hannover 2020



Veröffentlichungen der DGK

Ausschuss Geodäsie der Bayerischen Akademie der Wissenschaften

Reihe C

Dissertationen

Heft Nr. 859

Robust Deformation Monitoring of Bridge Structures Using MEMS Accelerometers and Image-Assisted Total Stations

Von der Fakultät für Bauingenieurwesen und Geodäsie
der Gottfried Wilhelm Leibniz Universität Hannover
zur Erlangung des Grades
Doktor-Ingenieur (Dr.-Ing.)
genehmigte Dissertation

Vorgelegt von

Mohammad Omidalizarandi, M.Sc.

Geboren am 03.06.1981 in Teheran, Iran

München 2020

Verlag der Bayerischen Akademie der Wissenschaften

ISSN 0065-5325

ISBN 978-3-7696-5271-0

Diese Arbeit ist gleichzeitig veröffentlicht in:
Wissenschaftliche Arbeiten der Fachrichtung Geodäsie und Geoinformatik der Universität Hannover
ISSN 0174-1454, Nr. 366, Hannover 2020

Adresse der DGK:



Ausschuss Geodäsie der Bayerischen Akademie der Wissenschaften (DGK)

Alfons-Goppel-Straße 11 • D – 80 539 München
Telefon +49 – 331 – 288 1685 • Telefax +49 – 331 – 288 1759
E-Mail post@dgk.badw.de • <http://www.dgk.badw.de>

Prüfungskommission:

Vorsitzender: Univ.-Prof. Dr.-Ing. habil. Christian Heipke

Referent: Univ.-Prof. Dr.-Ing. Ingo Neumann

Korreferenten: Univ.-Prof. Dr.-Ing. habil. Jürgen Müller
Univ.-Prof. Dipl.-Ing. Dr.techn. Werner Lienhart (TU Graz)
Univ.-Prof. Dr.-Ing. Mohammad Ali Sharifi (University of Tehran)

Tag der mündlichen Prüfung: 08.09.2020

© 2020 Bayerische Akademie der Wissenschaften, München

Alle Rechte vorbehalten. Ohne Genehmigung der Herausgeber ist es auch nicht gestattet,
die Veröffentlichung oder Teile daraus auf photomechanischem Wege (Photokopie, Mikrokopie) zu vervielfältigen

Abstract

Today, short- and long-term structural health monitoring (SHM) of bridge structures has received considerable attention. However, permanent, cost-effective, and reliable monitoring are still challenging issues. From a surveying or civil engineer's point of view, vibration-based SHM is often carried out by inspecting the changes in the dynamic responses of bridge structures known as modal parameters, such as eigenfrequencies, eigenforms and modal damping.

The use of cost-effective micro-electro-mechanical-systems (MEMS) accelerometers with a high sampling frequency is becoming more affordable and feasible for the aforementioned monitoring task. Within this dissertation, a three-step scenario is proposed to choose a suitable MEMS accelerometer despite of its purchase price, measurement range and sampling frequency. Firstly, a robust calibration procedure is proposed and implemented to model MEMS related systematic errors such as biases, scale factors, and non-orthogonality angles between the axes. Secondly, a controlled excitation experiment is conducted by using a high-precision shaker. Thirdly, a static test experiment is accomplished over a long period.

Robust, accurate, and automatic estimation of the modal parameters is particularly challenging when vibration measurements are contaminated with a high coloured measurement noise, e.g., due to cost-effective MEMS acceleration data. This is even more challenging when the structure is continuously under imposed forces due to moving vehicles or wind. For this purpose, a robust and automatic vibration analysis procedure the so-called robust time domain modal parameter identification (RT-MPI) approach is proposed and implemented. It is a novel approach in the sense of automatic excitation (e.g. ambient) window selection, automatic and reliable identification of initial eigenfrequencies even closely spaced ones as well as robustly and accurately estimating the modal parameters. To estimate frequencies, damping ratio coefficients, amplitudes, and phase shifts, an observation model consisting of a damped harmonic oscillation (DHO) model, an autoregressive model of coloured measurement noise and a stochastic model in the form of the heavy-tailed family of scaled t-distributions with unknown degree of freedom and scale factor, is employed. The aforementioned three parametric models are jointly adjusted by means of a generalised expectation maximisation (GEM) algorithm. The proposed RT-MPI algorithm is also able to estimate amplitudes in a metric unit and with a high accuracy for the recorded acceleration data by means of double integration of the DHO model. The eigenforms are characterised in a subsequent step, and by using the estimated parameters from the GEM algorithm. In addition, having amplitudes in the metric unit allows to characterise deflection eigenforms in their true scales for selected excitation windows within short time intervals.

The deformation/displacement monitoring by merely using the MEMS accelerometer is challenging, since it suffers from accuracy degradation with time for absolute position/displacement estimates. Therefore, the MEMS accelerometers and an image-assisted total station (IATS) are fused by performing one-dimensional (1D) coordinate update within the Kalman filtering framework. To generate 1D displacement data from the IATS, video frames of a passive target, that is attached to a bridge structure, are captured by means of a telescope camera of the IATS. A passive target centroid detection algorithm is proposed and implemented, which is robust and reliable with respect to poor environmental conditions, such as low lighting, dusty situations, and skewed angle targets. Next, an angular conversion factor of the telescope camera is calibrated, which allows to convert the generated displacement data from pixel to metric unit.

Experiments are performed in four case studies including simulation, controlled excitation and two real applications of a footbridge structure and a synthetic bridge. The estimated modal parameters are compared and validated by their true values as well as their corresponding estimates obtained from reference sensors such as reference accelerometer, geophone, and laser tracker. Additionally, the estimated eigenfrequencies and damping ratio coefficients are compared with a well-known covariance driven stochastic subspace identification (SSI-COV) approach. The results show that the MEMS accelerometers are suitable for identifying all occurring eigenfrequencies of the bridge structures. Moreover, the vibration analysis procedure demonstrates that amplitudes are estimated in submillimetre range accuracy, frequencies with an accuracy of better than 0.1 Hz and damping ratio coefficients with an accuracy of better than 0.1 and 0.2 % for modal and system damping, respectively. The analysis reveals the superiority of the proposed RT-MPI algorithm compared to the SSI-COV algorithm. Finally, a high accurate displacement time series at the level of submillimetre is generated by fusion of the IATS and the MEMS measurements.

Keywords: Vibration analysis, Deformation analysis, Modal parameters, MEMS accelerometer, Image-assisted total station, Robust parameter estimation, Generalised expectation maximisation algorithm, Kalman filter, Bridge monitoring

Zusammenfassung

Heute hat die kurz- und langfristige Überwachung des baulichen Zustands (Structural Health Monitoring, SHM) von Brückenkonstruktionen erhebliche Aufmerksamkeit erhalten. Eine permanente, kosteneffiziente und zuverlässige Überwachung ist jedoch nach wie vor eine große Herausforderung. Aus der Sicht eines Vermessungs- oder Bauingenieurs wird das schwingungsbasierte SHM häufig durchgeführt, indem die Veränderungen in den dynamischen Reaktionen von Brückenkonstruktionen untersucht werden, die als modale Parameter, wie Eigenfrequenzen, Eigenformen und modale Dämpfung, bekannt sind.

Der Einsatz von kostengünstigen MEMS-Beschleunigungsmessern (Micro-Electro-Mechanical-Systems) mit hoher Abtastfrequenz wird für die oben genannte Überwachungsaufgabe immer realistischer und machbar. In dieser Arbeit wird ein dreistufiges Szenario vorgeschlagen, um unter Berücksichtigung des Anschaffungspreises, des Messbereichs und der Abtastfrequenz einen geeigneten MEMS-Beschleunigungsmesser auszuwählen. Erstens wird ein robustes Kalibrierverfahren vorgeschlagen und implementiert, um MEMS-bezogene systematische Fehler wie Offsets, Skalierungsfaktoren und Nichtorthogonalitätswinkel zwischen den Achsen zu modellieren. Zweitens wird ein kontrolliertes Anregungsexperiment unter Verwendung eines hochpräzisen Schwingerregers durchgeführt. Drittens wird ein statisches Testexperiment über einen langen Zeitraum durchgeführt.

Eine robuste, genaue und automatische Schätzung der oben genannten modalen Parameter ist besonders dann eine Herausforderung, wenn Schwingungsmessungen mit einem hohen farbigen Messrauschen, z.B. aufgrund der kostengünstigen MEMS-Beschleunigungsdaten, überlagert sind. Dies ist noch schwieriger, wenn die Struktur unter ständiger Einwirkung von Kräften durch sich bewegende Fahrzeuge oder Wind steht. Zu diesem Zweck wird ein robustes und automatisches Schwingungsanalyseverfahren vorgeschlagen und implementiert, d.h. ein so genannter robuster Ansatz zur Identifizierung modaler Parameter im Zeitbereich (RT-MPI). Es ist ein neuartiger Ansatz im Sinne der automatischen Auswahl des Anregungsfensters (Umgebungsfenster), der automatischen und zuverlässigen Identifizierung der Näherungswerte für die Eigenfrequenzen, selbst wenn diese nahe beieinander liegen, sowie der robusten und genauen Schätzung der modalen Parameter. Zur Schätzung von Frequenzen, Dämpfungsverhältniskoeffizienten, Amplituden und Phasenverschiebungen wird ein Beobachtungsmodell verwendet, das aus einem Modell der gedämpften harmonischen Schwingungen (DHO), einem autoregressiven Modell des farbigen Messrauschens und einem stochastischen Modell in Form der skalierten t-Verteilungen mit unbekanntem Freiheitsgrad und Skalierungsfaktor besteht. Die drei vorgenannten parametrischen Modelle werden gemeinsam mit einem verallgemeinerten Erwartungsmaximierungsalgorithmus (GEM) angepasst. Der vorgeschlagene RT-MPI-Algorithmus ist in der Lage, Amplituden in metrischer Einheit und mit hoher Genauigkeit für die aufgezeichneten Beschleunigungsdaten durch Doppelintegration des DHO-Modells zu schätzen. Die Eigenformen werden in einem nachfolgenden Schritt und unter Verwendung der geschätzten Parameter aus dem GEM-Algorithmus charakterisiert. Darüber hinaus ermöglicht die Angabe der Amplituden in metrischer Einheit die Charakterisierung der Eigenformen in ihren wahren Maßstäben für ein ausgewähltes Anregungsfenster innerhalb eines kurzen Zeitintervalls.

Die Überwachung der Verformung/Verschiebung durch die bloße Verwendung des MEMS-Beschleunigungssensors ist eine Herausforderung, da die Genauigkeit mit der Zeit für absolute Positions-/Verschiebungsschätzungen abnimmt. Daher werden die MEMS-Beschleunigungsmesser

und eine bildgestützte Totalstation (IATS) durch ein eindimensionales (1D) Koordinaten-Update innerhalb des Kalman-Filters verschmolzen. Um 1D-Verschiebungsdaten aus dem IATS zu generieren, werden Videobilder eines passiven Ziels, das an einer Brückenstruktur befestigt ist, mit Hilfe der Teleskopkamera des IATS erfasst. Es wird ein Algorithmus zur Erkennung des passiven Zielschwerpunkts vorgeschlagen und implementiert, der robust und zuverlässig in Bezug auf schlechte Umgebungsbedingungen, wie z.B. schwache Beleuchtung, staubige Situationen und schiefwinklige Ziele, ist. Als nächstes wird ein Winkelumrechnungsfaktor der Teleskopkamera kalibriert, der es erlaubt, die erzeugten Verschiebungsdaten von Pixel in metrische Einheiten umzurechnen.

Die Experimente werden in vier Fallstudien durchgeführt, darunter Simulation, kontrollierte Anregung sowie zwei reale Anwendungen mit einer Fußgängerbrücke und einer synthetischen Brücke. Die geschätzten modalen Parameter werden mit ihren wahren Werten sowie mit den entsprechenden Schätzungen, die von Referenzsensoren wie Referenzbeschleunigungsmesser, Geophon, und Lasertracker erhalten wurden, verglichen und validiert. Zusätzlich werden die geschätzten Eigenfrequenzen und die Dämpfungskoeffizienten mit einem bekannten kovarianzgetriebenen stochastischen Subraumidentifikationsansatz (SSI-COV) verglichen. Die Ergebnisse zeigen, dass die MEMS-Beschleunigungsaufnehmer geeignet sind, alle auftretenden Eigenfrequenzen der Brückenstrukturen zu identifizieren. Darüber hinaus zeigt das Schwingungsanalyseverfahren, dass die Amplituden mit einer Genauigkeit im Submillimeterbereich, die Frequenzen mit einer Genauigkeit von besser als 0,1 Hz und die Dämpfungskoeffizienten mit einer Genauigkeit von besser als 0,1 und 0,2 % für die Modal- bzw. Systemdämpfung geschätzt werden können. Die Analyse zeigt die Überlegenheit des vorgeschlagenen RT-MPI-Algorithmus gegenüber dem SSI-COV-Algorithmus. Schließlich wird durch die Fusion der IATS- und der MEMS-Messungen eine hochgenaue Verschiebungszeitreihe im Submillimeterbereich erzeugt.

Stichworte: Schwingungsanalyse, Deformationsanalyse, modale Parameter, MEMS-Beschleunigungsmesser, bildgestützte Totalstation, robuste Parameterschätzung, Verallgemeinerter Algorithmus zur Erwartungsmaximierung, Kalman-Filter, Brückenüberwachung

Abbreviation

AIC	Akaike Information Criterion
AR	Autoregressive
CUPT	Coordinate Update
DHO	Damped Harmonic Oscillation
df	degree of freedom (t-distribution)
DSLRL	Digital Single-Lens Reflex
ECME	Expectation Conditional Maximisation Either
EM	Expectation Maximisation
EMA	Experimental Modal Analysis
EOPs	External Orientation Parameters
FEM	Finite Element Model
FFT	Fast Fourier Transform
FDD	Frequency Domain Decomposition
FOV	Field Of View
FRF	Frequency Response Function
GEM	Generalised Expectation Maximisation
GHM	Gauss-Helmert Model
GIH	Geodetic Institute Hannover
GMM	Gauss-Markov Model
GNSS	Global Navigation Satellite System
HCT	Hough Circle Transform
IATS	Image-Assisted Total Station
IDS	Institut für Dynamik und Schwingungen
IFMA	Institut für Massivbau
IRF	Impulse Response Function
KF	Kalman Filter
KNN	k-Nearest Neighbour
LSCF	Least-Squares Complex Frequency-domain
LSD	Line Segment Detector
LSSA	Least-squares spectrum analysis

LUH	Leibniz University Hannover
MEMS	Micro-Electro-Mechanical System
ML	Maximum Likelihood
NExT	Natural Excitation Technique
OMA	Operational Modal Analysis
OMAX	OMA with eXogenous inputs
PDF	Probability Density Function
PPS	Pulse Per Second
PSD	Power Spectral Density
PSVC	Portable Shaker Vibration Calibrator
qGMM	quasi-Gauss-Markov Model
RANSAC	RANdom SAmple Consensus
RDT	Random Decrement Technique
RMSE	Root Mean Square Error
RNN	Recurrent Neural Network
RT-MPI	Robust Time Domain Modal Parameter Identification
RTS	Robotic Total Station
SHM	Structural Health Monitoring
SNR	Signal to Noise Ratio
SSI	Stochastic Subspace Identification
TLS	Terrestrial Laser Scanner
UDHO	Undamped Harmonic Oscillation
VAR	Vector-Autoregressive
VCE	Variance Component Estimation
WNT	White Noise Test
ZUPT	Zero Velocity Update
1D	One-Dimensional
2D	Two-Dimensional
3D	Three-Dimensional

List of Figures

1.1	Simulated acceleration data with different damping ratio coefficients.	4
1.2	Exemplary set-up of the MEMS accelerometers and IATS for one-span narrow width bridge structure.	9
1.3	An overview of the research studies.	10
2.1	Scheme of MEMS accelerometers. The master MEMS sensor is located on top and other three slave MEMS sensors are located at the bottom that all are protected by the aluminium housing and connected via wires.	12
2.2	A controlled excitation experiment at the Institute of Dynamics and Vibration Research (IDS), Leibniz University Hannover (LUH), using a shaker to validate the time synchronisation between all three slave MEMS accelerometers (left), the shaker – vibration test system TV 51110 (right) (TIRA Schwingtechnik, 2019)).	14
2.3	AR model coefficients correspond to the ADXL acceleration data recorded from Y and Z axes.	17
2.4	Scheme of the KUKA youBot inside the climate chamber.	18
2.5	Scheme of the entire MEMS acceleration data recorded for fixed positions and for a certain time interval. The acceleration data in the X , Y and Z directions (a_x , a_y and a_z) are illustrated with blue, red and green colours.	19
2.6	MEMS accelerometer calibration parameter - \hat{b}_{gy} [m/s^2].	25
2.7	MEMS accelerometer calibration parameter - \hat{s}_{gy}	25
2.8	MEMS accelerometer calibration parameter - $\hat{\theta}_{yz}$ [$^\circ$].	25
2.9	<i>A posteriori</i> standard deviation of the MEMS acceleration measurements - $\hat{\sigma}_a$ [m/s^2].	26
3.1	An overview of the passive target centroid detection algorithm.	34
3.2	The IATS telescope camera images: image resolution of 320×240 px and $8 \times$ digital zoom for distances of 5 m (left), and 23 m (right).	35
3.3	A scheme of the robust external calibration of the IATS and digital camera by using signalised targets. The correlation model is neglected for simplicity.	39
4.1	An overview of the RT-MPI algorithm.	45
5.1	Fusion of the IATS displacement data and the MEMS acceleration data within the KF framework.	59
5.2	Cross-correlations between the IATS and the laser tracker displacement data (top), and the double integrated adjusted MEMS acceleration data (MEMS displacement data) and the laser tracker data (bottom) within the selected ambient window. . . .	62
5.3	Overlaying of the displacement data obtained from the IATS (red colour), the MEMS displacement data (blue colour) and the laser tracker data (green colour) within the selected ambient window.	62
5.4	The displacements analysis based on the multi-rate KF approach by using the displacement and acceleration measurements: the displacements obtained from the IATS (blue), the predicted displacements (red) and the filtered displacements (green). .	63
6.1	An overview of the experimental studies and their individual goals.	66

6.2	Simulated acceleration data based on the DHO model contaminated with coloured noise (blue solid line), and the DHO model fitted to the simulated acceleration data (red solid line) (The first 20 s).	67
6.3	The estimated coloured noise residuals (red dashed line) and decorrelated residuals (blue solid line) of the simulated acceleration data (The first 20 s).	68
6.4	The DFTs of the simulated acceleration data (black solid line) and their corresponding adjusted data (red solid line) in the amplitude spectrum.	68
6.5	The magnification of the DFTs of the simulated acceleration data (black solid line) and their corresponding adjusted data (red solid line) in the amplitude spectrum, showing two closely spaced frequencies of 5.0 and 5.3 Hz.	69
6.6	Histogram of the estimated white noise residuals (blue colour), fitted normal distribution with $N(\mu = -0.0023, \sigma^2 = (0.2753)^2)$ (green solid colour) and fitted t-distribution with $t(\nu = 4.3662, \sigma^2 = (0.2027)^2)$ (red solid colour).	69
6.7	Histogram of the adjusted weights.	70
6.8	The displacement time series calculated for the simulated acceleration data based on double integration of the DHO model (The first 20 s).	70
6.9	A vibration analysis based on the MEMS and the reference acceleration data as well as the IATS and the laser tracker displacement data sets through the controlled excitation experiment in the laboratory of GIH by using the PSVC 9210D (Omidalizarandi et al., 2018).	73
6.10	Histogram of the white noise residuals estimated for the frequency of 3 Hz, and for (a) the MEMS acceleration data in Z -axis [m/s^2], (b) the PCB reference acceleration data [m/s^2], (c) the IATS displacement data in vertical direction [mm], and (d) the laser tracker displacement data in Z -axis [mm] in a controlled excitation experiment by using the PSVC.	74
6.11	The estimated coloured noise residuals (red dashed line) and the decorrelated residuals (blue solid line) of the vibration measurements corresponding to the frequency of 3 Hz, and for (a) the MEMS acceleration data in Z -axis [m/s^2], (b) the PCB reference acceleration data [m/s^2], (c) the IATS displacement data in vertical direction [mm], and (d) the laser tracker displacement data in Z -axis [mm].	76
6.12	Histogram of the weights estimated for the frequency of 3 Hz, and for (a) the MEMS acceleration data in Z -axis [m/s^2], (b) the PCB reference acceleration data [m/s^2], (c) the IATS displacement data in vertical direction [mm], and (d) the laser tracker displacement data in Z -axis [mm] in a controlled excitation experiment by using the PSVC.	76
6.13	Representation of the frequencies estimated from the IATS displacement data with sampling frequency of 10 Hz through the controlled excitation experiment.	77
6.14	Representation of the frequencies estimated from the laser tracker displacement data with sampling frequency of 200 Hz through the controlled excitation experiment.	77
6.15	Measurement set-up in the Mensa footbridge experiment: The positions of the MEMS and the PCB piezoelectric accelerometers are highlighted by red and blue circles (Herrmann, 2018).	78
6.16	MEMS accelerometers: time series of the acceleration measurements (top) (selected ambient window within the red dashed lines) in which the X - and Y -axes represent time [s] and amplitude [m/s^2]; vertical eigenforms calculated for different eigenfrequencies (bottom). The texts for each eigenform represent estimated phase shifts (blue), eigenfrequencies (black), and amplitudes (red) at specified positions (Omidalizarandi et al., 2020).	80

6.17	3D vertical eigenforms characterised for different eigenfrequencies obtained from the MEMS accelerometers: the first vertical eigenform (4.07 Hz; left) and the second vertical eigenform (13.75 Hz; right). Amplitudes scaled by 200 in Z -axes (Omidalizarandi et al., 2020).	81
6.18	Reference accelerometers: time series of the acceleration measurements (top) (selected ambient window within the red dashed lines) in which X - and Y -axes represent time [s] and amplitude [m/s^2]; vertical eigenforms calculated for different eigenfrequencies (bottom). The texts for each eigenform represent estimated phase shifts (blue), eigenfrequencies (black) and amplitudes (red) at specified positions (Omidalizarandi et al., 2020).	81
6.19	BAM synthetic bridge: time series of (a) the MEMS acceleration measurements [m/s^2] and (b) the geophone velocity measurements [mm/s] (blue solid lines); selected ambient window within the red dashed lines for a duration of 120 s. The blue and orange coloured texts stand for the estimated eigenfrequencies [Hz] and damping ratio coefficients [%], for the first mode at specified positions (Omidalizarandi et al., 2020).	82
A.1	MEMS accelerometer calibration parameters. (a): \hat{b}_{gx} [m/s^2], (b): \hat{b}_{gz} [m/s^2], (c): \hat{s}_{gx} , (d): \hat{s}_{gz} , (e): $\hat{\theta}_{zx}$ [$^\circ$], (f): $\hat{\theta}_{zy}$ [$^\circ$].	91

List of Tables

2.1	Estimated harmonic oscillation parameters obtained from the controlled excitation experiment for the slave MEMS acceleration data with and without applying calibration parameters.	15
2.2	Uncertainties of the estimated harmonic oscillation parameters obtained from the controlled excitation experiment for the slave MEMS acceleration data with and without applying calibration parameters.	16
2.3	Statistics of the estimated unknown parameters in the functional model based on the linear drift, the auto-correlation model based on the AR-univariate process and the stochastic model based on the centred and scaled t-distribution with an unknown df and unknown scale factor for measurements of three cost-effective MEMS accelerometers at a constant temperature	17
6.1	Statistics of the unknown parameters including the DHO model parameters, the correlation model parameters, and the stochastic model parameters, estimated from the RT-MPI algorithm that are compared and validated with the SSI-COV algorithm and their known values for the simulated acceleration data (Omidalizarandi et al., 2020).	71
6.2	Statistics of displacement and vibration analysis for vibration measurements obtained from the PCB reference accelerometer, the MEMS accelerometer, the IATS, and the laser tracker. \hat{f} is the estimated frequency, \hat{A} and \hat{A}_m the estimated amplitudes in $[m/s^2]$ and $[mm]$, respectively, $ \Delta_{\hat{A}_m} $ the absolute deviation of the estimated amplitude in $[mm]$ compared to those from PCB accelerometer, p the AR model order, $\hat{\nu}$ the estimated df, $\hat{\sigma}_\ell$ <i>a posteriori</i> standard deviation of the vibration measurements in their measurements unit, wnt_c the acceptance of the WNT criterion (i.e., yes in case of acceptance, otherwise no), t the length of an excitation window selected and F_s the sampling frequency.	75
6.3	Statistics of the estimated eigenfrequencies $[Hz]$ and damping ratio coefficients $[\%]$ obtained from all three MEMS acceleration data by means of the RT-MPI and SSI-COV algorithms for the Mensa footbridge (Omidalizarandi et al., 2020).	79
6.4	Statistics of frequencies $[Hz]$ and damping ratio coefficients $[\%]$ estimated from the MEMS acceleration data and the geophone velocity data based on the RT-MPI and the SSI-COV algorithms for the BAM synthetic bridge (Omidalizarandi et al., 2020).	83

Contents

Abstract	i
Zusammenfassung	iii
Abbreviation	v
List of Figures	vii
List of Tables	xi
1 Introduction	1
1.1 Structural Health Monitoring of Bridge Structures	1
1.2 Relevant Parameters for a Deformation Process	2
1.2.1 Static deformation parameters	3
1.2.2 Kinematic deformation parameters	3
1.3 Modal Identification Techniques	5
1.4 Related Works	6
1.5 Problem Statements	7
1.6 Research Topics	8
1.7 Outline of the Dissertation	10
2 Suitability Analysis of MEMS Accelerometers for Deformation Monitoring of Bridges	11
2.1 Introduction	11
2.2 Measurement Set-up and Data Acquisition	12
2.3 Suitability Analysis in Selecting Optimal MEMS Accelerometers	13
2.3.1 Controlled excitation experiment	13
2.3.2 Static test experiment	14
2.4 Calibration of MEMS Accelerometers	18
2.4.1 Development of test scenarios for MEMS accelerometers calibration	18
2.4.2 Calibration model of triaxial accelerometers	19
2.4.3 Adjustment of the calibration model with standard Gauss-Helmert model and variance component estimation	20
2.4.4 Adjustment of the calibration model with applied adaptive robust estimation	22
2.4.5 Experimental results of the MEMS accelerometer calibration	24
2.5 Sensor Specifications	26
2.6 Summary	27
3 Potential of Image-Assisted Total Stations for Bridge Monitoring	29
3.1 Introduction	29
3.2 Data Acquisition and Preprocessing	31
3.3 Automatic and Accurate Passive Target Centroid Detection	32
3.4 Conversion of Displacement Time Series from Pixel to Metric Units	33
3.5 External Calibration of Image-Assisted Total Stations and Digital Camera	36
3.6 Sensor Specifications and Measurement Systems	38
3.7 Summary	40

4	Robust Kinematic Deformation Monitoring of Bridge Structures	43
4.1	Introduction	43
4.2	Ambient Window Selection	44
4.3	Identification of Initial Modal Frequencies	46
4.4	Robust Modal Parameter Estimation based on Time Series Analysis	47
4.4.1	Estimation model	48
4.4.2	Robust adjustment procedure	50
4.5	Displacement Analysis based on Double Integration	53
4.6	Characterisation of Eigenforms	53
4.7	Summary	54
5	MEMS-based Bridge Monitoring Supported by Image-Assisted Total Stations	57
5.1	Introduction	57
5.2	Basics of Kalman Filtering for Displacement Analysis	58
5.3	Heterogeneous Data Fusion of Displacement and Acceleration Measurements	61
5.4	Summary	63
6	Experiments and Results	65
6.1	Example based on Simulated Acceleration Data	66
6.2	Example based on Shaker Vibration Calibrator	72
6.3	Example based on a Footbridge	77
6.4	Example based on a Synthetic Bridge	81
6.5	Summary	82
7	Summary, Conclusion and Outlook	85
7.1	Summary and Conclusion	85
7.2	Outlook	88
A	Appendix	91
	List of Publications	93
	Contributions of Authors	95
	Paper 1	99
	Paper 2	125
	Paper 3	145
	Paper 4	177
	Paper 5	207
	Paper 6	219
	Bibliography	231
	Curriculum Vitae	239
	Acknowledgement	241

1 Introduction

1.1 Structural Health Monitoring of Bridge Structures

For more than a decade, short- and long-term structural health monitoring (SHM) of bridge infrastructures has received increasing attention. However, monitoring of such infrastructures in a reliable and cost-effective way is still a challenging issue. According to US Federal Highway Agency statement in 2005, the quality of 28 % of the US bridges, 10 % of the European bridges and an average of 10 % of the Asian bridges are inadequate (Wenzel, 2009a) to be used in daily increasing traffic. Therefore, it highlights the demand for frequent/permanent monitoring, diagnosis and rehabilitation.

The SHM process allows to assess the current health state of the structure, and to detect unsafe conditions, unexpected behaviour or structural damages by means of regular measurements of the structure over time using an array of sensors (Dawson, 1976). An extensive survey of SHM approaches can be found in Doebling et al. (1998). The SHM is commonly conducted based on visual observation, the material properties of structures, and interpretation of structures dynamic characteristics (Alvandi and Cremona, 2006). Such structures related characteristics can be monitored by inspecting the changes in global dynamic behaviour of the structure such as eigenfrequencies, eigenforms and modal damping, which are known as modal parameters.

Permanent monitoring of the bridge structures, in particular, dilapidated, severely damaged or endangered bridges is a challenging issue. The current inspections of the bridge structures in Germany is manifested in the DIN 1076. Accordingly, the civil engineers perform this task as follows: main inspections and tests (at the beginning right after the bridge construction and then every six years), simple inspections and tests (three years after the main inspections and then every six years), surveys (once a year but not regularly) and continuous observations (two times per year). In special cases, such as traffic accidents, flood and heavy storms, specific inspections are carried out (DIN 1076).

Geodetic methods and sensors have gained an increasing reputation in either short- or long-term deformation monitoring of the bridge structures over the last decade. Such techniques and measurements can be considered as complementary information to geological or civil engineering monitoring procedures to pursue several goals, such as (Omidalizarandi et al., 2019c):

- for extensive inspection, assessment, evaluation and rehabilitation of the existing bridges,
- to avoid decommissioning at a very early stage,
- to mitigate a risk and to ensure sufficient safety for the users and the structure itself during operation,
- to reduce repair cost,
- to extend life time,
- to allow life cycle monitoring.

The short- and long-term deformation monitoring of the bridges – from a geodetic point of view – is conducted using a proper measurement system and methodology to reach the aforementioned goals.

The exemplary requirements of such a measurement system for monitoring dynamic behaviour of bridge structures can be considered as follows:

- cost-effectiveness,
- adequate sampling rate,
- appropriate measurement and sensitivity ranges,
- less influence of measurements by environmental factors such as lighting, weather conditions, external obstructions, etc.,
- less need for frequent re-calibration,
- allows identifying deformation parameters of interest.

Depending on the type of deformation monitoring and observed object, the parameters of interest may vary, which are briefly described in the following section.

1.2 Relevant Parameters for a Deformation Process

Deformation monitoring of a bridge is a procedure that involves frequent/permanent measurements to inspect either short-term dynamic behaviour of the bridge structure including eigenfrequencies (i.e. natural frequencies), eigenforms (i.e. mode shapes) and modal damping or long-term deformations and movements. Therefore, unexpected deformations or abnormal dynamic behaviours along with their corresponding influencing factors can be specified at an early stage. The regularity of the monitoring is specified depending on the type of movement which can be a fast movement, e.g., due to the ambient excitation imposed by traffic and wind, or a slow one, e.g., caused by tectonic changes. Moreover, deformation analysis and interpretation of the parameters checked by statistical testing can be carried out as complementary steps and in a post-processing to ensure safety and life-cycle maintenance of the bridge structures.

From a geodetic point of view, the long-term deformation monitoring is carried out by calculating displacements for points/regions of interest at different epochs of time by using measurements of a selected geodetic sensor. Typically, proper choice of the sensor depends on the characteristics of the structure, accessibility, costs, deformation parameters and their corresponding demanded precision and accuracy. The reference points and/or geodetic control network must be established on a stable area out of the deformed region (Caspary, 2000), which enables us to perform a geo-referencing with respect to a global coordinate system. Additionally, the instrument's stability during the measurements must be secured. Ehrhart and Lienhart (2015a), for example, considered the telescope angular tilt reading of image-assisted total stations (IATS) to compensate for minor shakes of the instrument. It is also possible to re-measure the reference points at specified time intervals to obtain a new update information of the sensor position during monitoring.

Deformation models are categorised into four groups (Heunecke et al., 2013):

1. Congruence model,
2. Kinematic model,
3. Static model,
4. Dynamic model.

The first two deformation models are descriptive considering merely the pure description of the deformation while the last two deformation models are casual describing the relationship between the causative effects (loads) and deformations. Kinematic deformation modelling is the main focus of this dissertation due to the following reasons:

- bridge structures are always oscillating with very small excitation amplitudes at a millimetre/submillimetre level,
- no availability of loads information,
- high importance of identification of bridge dynamics behaviours.

The static and kinematic deformation parameters are briefly explained in the following.

1.2.1 Static deformation parameters

Static deformation monitoring of a bridge structure is often carried out by calculating deflections with respect to a reference coordinate system after imposing the loads. Moreover, time is not explicitly modelled. The static deformation monitoring is often accomplished when the bridge structure reaches an equilibrium state. Subsequently, the computed deflection is then compared to a steady situation when there is no influences of the loads. A rigid body movement of the bridge structure induced by, e.g. foundation settlements, creep or tectonics changes, is typically calculated for long-term monitoring. Thus, the static deformation parameters consist of deflection and the rigid body movements. Additionally, cracks caused by means of the induced loads may also be measured and analysed as additional information. As previously stated, stability of the instrument must be ensured during the monitoring procedure to obtain reliable and accurate estimates of the deformation parameters.

1.2.2 Kinematic deformation parameters

As previously mentioned, a kinematic deformation model is a descriptive model where movement (excitation) is a function of time and loads are not modelled. To assess the condition of bridge structures based on this model, the kinematic deformation parameters – which are known as the modal parameters – should be identified. Such parameters include eigenfrequencies, their corresponding eigenforms and damping values. As a preliminary step, vibration measurements are recorded from well-defined discrete points on the structure with a proper sampling frequency, which is specified in advance. In addition, it is also possible to characterise deflection eigenforms in vertical, longitudinal and lateral directions when the structure is moving. The modal parameters are briefly described in the following.

1.2.2.1 Eigenfrequencies and eigenforms

Eigenfrequency is a frequency that an oscillating structure tends to excite even in the absence of external forces. Eigenfrequencies may differ depending on the bridge material (concrete, steel, wood), bridge length, bridge type (suspension, cable stayed, span girder and etc.), and bridge application (roadway, railway, pedestrian). Eigenfrequency is inversely proportional to bridge span, which can be approximately calculated by the following equation, and with $\sigma_f = \pm 0.81$ [Hz] (Cantieni, 1984):

$$f = \frac{100}{L} + 0.6, \quad (1.1)$$

where L is the bridge span in [m] and f is the eigenfrequency in [Hz]. Therefore, the maximum and minimum eigenfrequencies can be calculated with respect to the minimum and maximum bridge spans. According to dynamic load tests on 224 highway bridges performed by the Swiss federal laboratories for materials testing and research (Cantieni, 1984), the fundamental frequency reaches 10 Hz, due to minimum span of 11 m (Meng, 2002). Such a relation between eigenfrequencies and bridge spans is also valid for railway bridges as described by Meng (2002). In addition, according to the dynamic loading test for different railway bridges (Frýba, 1996), the highest fundamental frequency may reach 50 Hz (Meng, 2002). Lämmle (2002) investigated the eigenfrequency changes

depending on the different materials (concrete, steel, wood, and etc.) for footbridge structures. As described by Lämmle (2002) and Hamm (2003), the first vertical eigenfrequency of footbridge structures is approximately between 0.5 and 6 Hz and its average is about 3.18 Hz. However, it is typically close to 2.0 Hz in order to be close to the usual step frequency under walking conditions (Hamm, 2003).

Eigenforms are the vibration forms corresponding to the respective eigenfrequencies (Wenzel, 2009b). The eigenform is often estimated for each identified eigenfrequency at measured points on the structure. The correct positions of the aforementioned points are precalculated in advance, for example, based on a finite element model (FEM) analysis. To reliably determine the vibration behaviour of a structure under an actual load, it is vital to consider higher order eigenfrequencies and their respective eigenforms rather than considering only the first order ones (Wenzel et al., 1999). As described in Wenzel et al. (1999), actual displacement of an oscillating structure is calculated based on the combination of all determined eigenforms.

1.2.2.2 Damping

Damping illustrates the actual degree of exploitation of a real oscillating structure. It is determined based on continuous decay of a vibration signal when it reaches a static equilibrium (Wenzel, 2009b). On one hand, the damping value is increased significantly by behavioural changes, such as transition from elastic to elastoplastic behaviour, e.g., in case of exceeding a maximum load-bearing capacity of the structures (Eibl, 1988). On the other hand, the damping is influenced by the energy content of the vibration signal that causes its amplitude to be changed. Accordingly, the damping values are categorised into two classes of “modal” and “system” damping, which are related to the energy content of the vibration signal. Since resonance often occurs in higher frequencies, it might be adequate to characterise the modal damping for a dominant eigenfrequency (Wenzel, 2009a). The system damping is determined when the energy content of the vibration signal increases due to high loads, such as train passages or heavy traffic (Wenzel, 2009a).

Figure 1.1 shows the time series of acceleration data generated based on a simulation for different damping ratio coefficients (ξ), where ($\xi = 0$) is undamped sinusoidal, ($\xi < 1$) is underdamped, ($\xi = 1$) is critically damped, and ($\xi > 1$) is overdamped. In order to protect the structure against any possible excitation, 1.5 % damping variation is typically allowed (Wenzel, 2009a). However, damping may also vary depending on material and geometry of the structure.

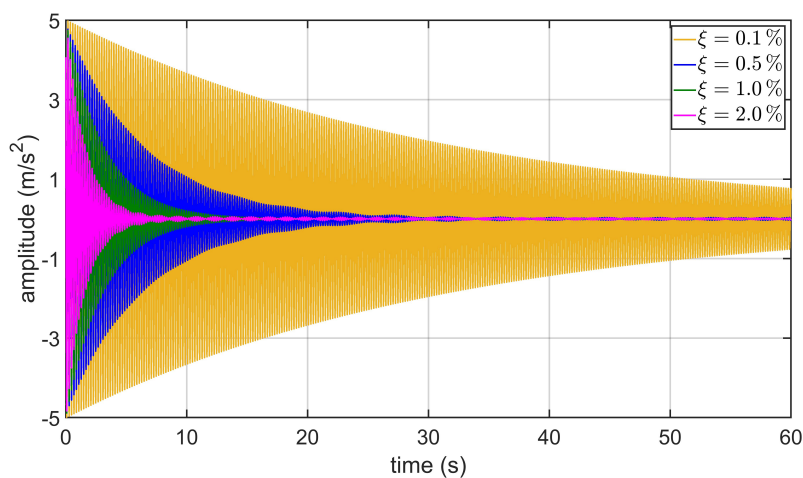


Figure 1.1: Simulated acceleration data with different damping ratio coefficients.

1.3 Modal Identification Techniques

Modal identification techniques are applied to identify the dynamic behaviour of structures. Depending on the availability of input and output data, they are categorised into three groups as follows:

1. Experimental modal analysis (EMA) (Heylen, 1997) using measured forces as input and a vibration response of the structure as output data.
2. Operational modal analysis (OMA) using only the output data.
3. Combined experimental OMA with eXogenous inputs (OMAX) (Guillaume et al., 2006) using an artificial force.

In OMAX approaches, the forces are imposed at the level of operational forces amplitudes or lower. Subsequently the generated excitation is considered as a useful one and not as a noise in the modal identification process (Reynders, 2012).

EMA methods can be carried out based on either the frequency response function (FRF) (Brandt, 2011) in frequency domain or the impulse response function (IRF) in time domain. In these methods, the induced forces to the structure are measured and considered in an estimation procedure. However, such an experiment is not practically suitable to be carried out for large structures, such as bridges. In particular, it is a challenging task to identify the external forces in the case of ambient excitation imposed by wind (Maia et al., 2001). Moreover, it is economically inefficient to generate excitations (Zhang et al., 2012).

In the OMA method, the ambient excitation is of utmost interest, since it reflects the true excitation due to traffic, wind, wave and micro-earthquakes over lifetime of bridge structures (Peeters et al., 2001). The OMA method is advantageous, since there is no need to measure and consider the loads for such excitation. However, the OMA approaches have two drawbacks (Parloo, 2003):

1. estimation of the mode shapes are not correctly scaled and can be varied depending on the amplitude changes,
2. recorded measurements often have poor quality or lower signal to noise ratio (SNR) in the ambient excitation compared to the forced excitation.

OMA can be performed either in frequency domain or in time domain. In frequency domain, the full or half spectra are typically estimated from the measurements and are used as input, e.g. by Peeters et al. (2005a) and Peeters and Van der Auweraer (2005b). In time domain, the measurements are used directly as input. Different OMA approaches are proposed by previous researchers, where the well-known approaches are as follows: natural excitation technique (NExT) (James et al., 1995), stochastic subspace identification (SSI) (Hermans and Van der Auweraer, 1999; Peeters, 2000; Fan et al., 2007; Reynders et al., 2008; Boonyapinyo and Janesupasaeree, 2010), frequency domain decomposition (FDD) (Brincker et al., 2001), random decrement technique (RDT) (Ibrahim, 2001), wavelet (Lardies and Gouttebroze, 2002) and the polyreference (Peeters et al., 2005a; Peeters and Van der Auweraer, 2005b) version of least-squares complex frequency-domain (LSCF) estimates (Guillaume et al., 1998).

In this dissertation, the time domain OMA method is accomplished by using the measurements directly as input while having no information of the induced forces. However, in order to estimate the modal parameters within the adjustment procedure, initial values of frequencies are taken from the frequency domain.

1.4 Related Works

This section is focusing on the previous works, which dealt with geodetic deformation monitoring by considering the static and kinematic deformation behaviours of bridge structures using time series measurements. To monitor and inspect whether short- or long-term movements of bridge structures, different contact- or non-contact-based geodetic measurement techniques were applied by previous researchers. A brief overview of the state of the art are described in the following. Roberts et al. (2004) performed bridge deflection monitoring up to a millimetre accuracy by using a triaxial accelerometer of type Kistler with sampling frequency of 200 Hz and GPS receivers of types Leica CRS1000 and SR530 with a sampling frequency of 10 Hz. The GPS measurements were used in the zero velocity update (ZUPT) and coordinate update (CUPT) to suppress the accumulation drift derived from a single and double integration of the acceleration data over time. A high frequency noise of the acceleration data was detected from a static measurement test which was filtered out based on low-pass or band-pass filters. The spectrum analysis was carried out to identify the main eigenfrequencies. Pakzad et al. (2008) performed vibration monitoring of a suspension road bridge by using a spatially dense wireless sensor network of accelerometers. The sensor network composed of accelerometers of type ADXL202 with sensitivity range of 1 mg at 25 Hz and accelerometers of type Silicon Design 1221 with noise level of approximately 10 μg . The sampling frequency in both accelerometers was set to 1000 Hz and downsampled to 50 Hz by averaging to reduce the noise level. The latter accelerometer was well-suited for capturing ambient excitation with small amplitude at the level of few hundreds of μg . Bürki et al. (2010) conducted kinematic deformation monitoring of a steel bridge using a Leica TCA 2003 equipped with a small CCD camera clipped on a total station (so-called DAEDALUS measurement system). To generate displacement time series, a standard torch as a light emitting target was captured with a sampling frequency of 15 Hz, which was then extracted by means of the blob detection algorithm. Subsequently, a dominant eigenfrequency was detected by using fast Fourier transform (FFT). Liebig et al. (2011) accomplished static deformation monitoring of a motorway bridge structure which was under heavy loads, by using tactile sensor and a terrestrial laser scanner (TLS) of type Zoller+Fröhlich Imager 5006. The combination of both measurement systems also allowed to calibrate a FEM. The TLS were used in a three-dimensional (3D) measurement mode, a two-dimensional (2D) profile measurement mode with a sampling frequency of 12.5 Hz, and one-dimensional (1D) single-point measurement mode with a sampling frequency of 620 Hz. Neitzel et al. (2012) carried out vibration analysis of a bridge structure by using a sensor network of low-cost accelerometers with a sampling frequency of 600 Hz, a TLS of type Zoller+Fröhlich Imager 5003 with a sampling frequency of 7812 Hz (in the single-point measurement mode) and a terrestrial interferometric synthetic aperture radar with a sampling frequency of 200 Hz as a reference sensor for the validation purpose. The TLS measurements were downsampled to 78.12 Hz by averaging over 100 measurements, which allowed detecting small displacements in submillimetre range. To estimate the modal parameters such as first natural frequency and its corresponding damping coefficient, a damped harmonic oscillation (DHO) model was used and solved by the least squares adjustment. Schmitt et al. (2013) carried out deflection and strain analysis of a bridge structure by employing 2D profile measurements of a TLS of type Zoller+Fröhlich Imager 5006 with a sampling frequency of 12.5 Hz. In addition, tactile sensors (strain gauges) were used to obtain strain values with a sampling frequency of 1200 Hz as reference measurements. To obtain accurate estimates of deflections from the 2D profile measurements, B-spline curve approximation was applied in a sense of the least squares adjustment. Next, the nonlinear artificial neuronal networks was applied to directly calculate strain values out of the approximated deflections. The measured strain values were used as train data sets into the neural network. Psimoulis and Stiros (2013) conducted vibration monitoring of a short span railway bridge by using a robotic total station (RTS) with non-constant sampling rate measurements in a range of 5–7 Hz. The least squares spectrum analysis (LSSA) in Pagiatakis (1999) and the Norm-Period code in Pytharouli and Stiros (2008) were employed to estimate the modal parameters for non-equidistant data. In Ehrhart and Lienhart (2015b),

displacement and vibration analysis of a footbridge structure were carried out by using an IATS of type Leica MS50 with a sampling frequency of 10 Hz, an accelerometer of type HBM B12/200 with a sampling frequency of 200 Hz and a RTS of type Leica TS15 with a sampling frequency of 20 Hz. The video frames of a circular target marking attached to the footbridge structure and structural features such as bolts were captured by means of a telescope camera of the IATS to generate displacement time series. For this purpose, the circular target centroids were extracted by means of least squares ellipse fitting with Gauss-Helmert model (GHM). Additionally, the structural features were detected by using template matching, feature matching and optical flow. Schill and Eichhorn (2019) performed deformation monitoring of the bridge structures by using a phase-based profile scanner of type Zoller+Fröhlich Profiler 9012 with a sampling frequency of 50 Hz. Ehrhart (2017b) accomplished static and kinematic deformation monitoring of bridge structures by using the IATSs of types Leica MS60 and MS50. As reported by Ehrhart (2017b), the Leica MS60 allows capturing video frames with a practical sampling frequency of 30 Hz, which is adequate to identify eigenfrequencies of bridge structures in a range of less than 15 Hz considering Nyquist sampling theorem. Moreover, it was demonstrated that image-based angle measurements which are obtained from the IATS are superior to conventional automated angle measurements of RTS to retroreflective prisms and can achieve a better precision at the level of less than 0.1 mgon (1σ).

1.5 Problem Statements

As previously mentioned, frequent/permanent, reliable, and cost-effective short- and long-term monitoring and diagnosis of bridge structures is a challenging issue. Often, civil engineers inspect and monitor the bridge structures by using high-end sensors with extremely high accuracy. However, it may not be economically suitable for permanent monitoring. As a preliminary step, it is crucial to select a proper and cost-effective measurement device, which can be mounted on the bridge structure for a long time. Next, the selected sensor should be calibrated, which allows to obtain reliable data sets. Environmental conditions such as temperature and humidity have an impact on the sensor measurements, which should be considered during the calibration procedure. Furthermore, it is of great importance to select a sensor, which is less influenced by systematic errors. In addition, it should not need frequent re-calibrations.

To estimate modal parameters including eigenfrequencies, damping ratio coefficients, amplitudes and phase shifts, a proper functional model is required to be determined. In addition, the estimation of the modal parameters in a robust, accurate, precise and automatic procedure is also a challenging issue. This is even more challenging in case of cost-effective vibration measurements, which are often contaminated with high coloured measurement noise. Additionally, such measurements are also suspected to numerous outliers of different magnitudes, which are required to be handled. The eigenfrequencies must be identified in an optimal and reliable manner in advance, which are used as initial values within the adjustment procedure. Moreover, to optimally and correctly characterise eigenforms of the bridge structures, the sensor positions need to be known or calculated in advance.

The state-of-the-art approaches mainly focus on estimations of the eigenfrequencies, eigenforms and modal damping. However, the eigenforms are not typically estimated in their true scales. To characterise deflection eigenforms with a high accuracy, and by using acceleration data, the amplitudes are required to be estimated in a metric unit. Furthermore, the estimated damping ratio coefficients are always varied depending on the amount of loads that are imposed on the bridge structures. Subsequently, it is a very complex and demanding task to obtain accurate estimates of the damping ratio coefficients, and in an acceptable range, in either ambient or forced excitation experiments.

At the end, it is of great interest to perform long-term deformation/displacement monitoring of the

bridge structures at millimetre/submillimetre level accuracy. However, it is a challenging issue in case of the acceleration data, since its double integrated data is drifting over time. Therefore, an additional sensor is required to deal with this problem. Finally, a reliable and accurate data fusion is required to be performed to overcome the deficiencies of both measurement systems in short- and long-term displacement and vibration monitoring.

1.6 Research Topics

The main objective of this research is to perform robust kinematic deformation monitoring of bridge structures using micro-electro-mechanical-systems (MEMS) and an IATS. The information obtained from both aforementioned measurement systems are complementary to each other and the strength of one measurement method overcomes the weakness of the other in a short- and long-term displacement and vibration analysis. Multiple MEMS as part of a geo-sensor network are mounted at different positions of a bridge structure, which are precalculated by means of a FEM analysis.

Despite of the purchase price and an adequate sampling frequency of the MEMS sensors, a three-step scenario is proposed to select an optimal one. Firstly, a robust calibration procedure is proposed and implemented to degrade the influence of the MEMS-related systematic errors such as biases, scale factors and non-orthogonality angles between the axes. Therefore, it ensures the reliability of the measurements over a long period. Secondly, a controlled excitation experiment is carried out by using a high-precision shaker to estimate harmonic oscillation parameters, and to compare them with a reference accelerometer. Thirdly, a static test experiment is accomplished by recording 3D acceleration data over a long period. Therefore, it allows to estimate an offset and a drift of the measurements over a long period. Additionally, auto-correlation as well as underlying distributional model parameters are estimated for each axis individually.

A robust modal parameter identification technique in the time domain is proposed and implemented to characterise the dynamic response of the bridge structure robustly, accurately, and automatically (Omidalizarandi et al., 2020). As a preliminary step, an ambient window is selected in an automatic procedure for the recorded measurements under either ambient or forced excitation. Next, a novel cost function is introduced, which enables to optimally and reliably identify eigenfrequencies even closely spaced ones. Then, the aforementioned eigenfrequencies are used as initial values within the adjustment procedure. To estimate the modal parameters including eigenfrequencies, amplitudes, phase shifts, and damping ratio coefficients, an observation model consisting of: (1) a DHO model, (2) an autoregressive (AR) model of the coloured measurement noise and (3) a stochastic model in the form of scaled t-distributions is employed (Omidalizarandi et al., 2020). The aforementioned three parametric models are jointly adjusted by means of a generalised expectation maximisation (GEM) algorithm given in Alkhatib et al. (2017). The eigenforms are characterised in a subsequent step, and by using the aforementioned estimated parameters from the GEM algorithm. The term “robust” in this dissertation means that the proposed approach is outlier-resistant. This is achieved by stochastically modelling the outliers by means of the heavy-tailed scaled t-distribution with unknown degree of freedom and unknown scale factor (Kargoll et al., 2018). Subsequently, an underlying adjustment model of the GEM algorithm allows for self-tuning, robust and maximum likelihood (ML) estimation of the parameters (Alkhatib et al., 2017). A novel double integration using the DHO model is proposed and implemented to convert the acceleration data to displacement data in a metric unit (e.g. in mm). Subsequently, it enables to characterise deflection eigenforms in their true scales, and with a high accuracy (Omidalizarandi et al., 2020). The proposed robust modal parameter identification algorithm is applicable for any type of data sets even those contaminated with high coloured measurement noise.

Besides the MEMS accelerometers, the IATS as a modern geodetic sensor that allows to perform kinematic deformation monitoring. For this purpose, a 1D displacement time series is generated

based on video frames of a passive target captured by an embedded on-axis telescope camera of the IATS. An optimal passive target pattern is selected as a preliminary step, which is utilised for generating displacement time series from the IATS. Such a passive target is beneficial due to being cost-effective as well as easy to mount. Next, a fast, automatic, reliable, and accurate passive target centroid detection approach is proposed and implemented, which has less sensitivity to poor environmental conditions, such as low lighting, dusty situations and skewed angle targets (Omidalizarandi et al., 2019a). The vertical angular conversion factor of the telescope camera of the IATS is calibrated, which is used to convert displacements from pixel [px] unit to metric unit such as millimetre in vertical direction (Omidalizarandi et al., 2018).

Figure 1.2 illustrates an exemplary set-up of the MEMS accelerometers and IATS for one-span narrow width bridge structure. As it can be seen, five MEMS accelerometers can be mounted at the first, second, and third quarters of the bridge structure. However, discussions with civil engineering experts often assists to optimally set-up the sensors. To perform displacement monitoring and analysis in this dissertation, the video frames of the passive target, attached in the vicinity of one the MEMS accelerometers (see Fig. 1.2), is captured by the telescope camera of the IATS located at point S2. Therefore, a high accurate 2D displacement time series is generated in an image plane perpendicular to the viewing direction. The third dimension of the displacement data, with less accuracy, is generated based on slope distance measurements towards the passive target. In this work, the IATS could not be set-up at point S1 due to effects of the bridge vibration. In addition, merely the 1D displacement and acceleration data in the vertical direction have been considered for simplicity. However, the proposed procedure can be fully extended to the 3D displacement and acceleration data.

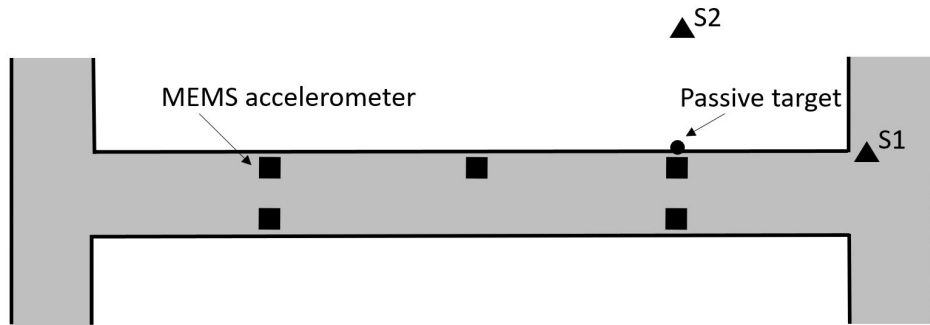


Figure 1.2: Exemplary set-up of the MEMS accelerometers and IATS for one-span narrow width bridge structure.

The state-of-the-art of the IATS with low sampling frequency (e.g. 10 to 20 Hz) has a limitation to detect higher frequencies in the light of Nyquist sampling theorem. To overcome this problem, similar to the works of Omidalizarandi and Neumann (2015); Omidalizarandi et al. (2016, 2019b), a high-resolution digital camera with a higher sampling frequency can be attached on top of the IATS by means of a clamping system. Therefore, the external calibration parameters or the relative orientation of the sensor origins are calculated to relate the data of the sensors to each other. To robustly and accurately estimate the external calibration/orientation parameters (EOPs) between the IATS and the external digital camera, a rigorous bundle adjustment procedure similar to the work of Omidalizarandi et al. (2019b) can be applied. The functional models are determined based on the collinearity equations, the 3D Helmert transformation, and the constraint equation. To estimate the unknown parameters of the aforementioned functional models, three robust adjustment models are developed and implemented, which are as follows (Omidalizarandi et al., 2019b):

1. An expectation maximisation (EM) algorithm to solve a GHM with grouped t-distributed random deviations,

2. An EM algorithm to solve a corresponding quasi-Gauss-Markov model (qGMM) with t-distributed pseudo-misclosures,
3. A classic least-squares procedure to solve the GHM with variance components and outlier removal.

Finally, the long-term kinematic deformation monitoring is conducted by fusing 1D displacement data obtained from the IATS and 1D acceleration data recorded from the MEMS accelerometer with different sampling frequency based on 1D CUPT within the framework of Kalman filter (KF). Such data fusion allows to compensate for the drift of the double integrated MEMS acceleration data over time (Omidalizarandi et al., 2019c). The 1D displacement data generated from the IATS is merely obtained for the passive target that is attached in the vicinity of one of the MEMS accelerometers. Therefore, the relative 1D displacements between other MEMS accelerometers can be calculated based on the amplitudes derived from the double integration of the recorded acceleration data. An overview of the aforementioned research topics is represented in Figure 1.3.

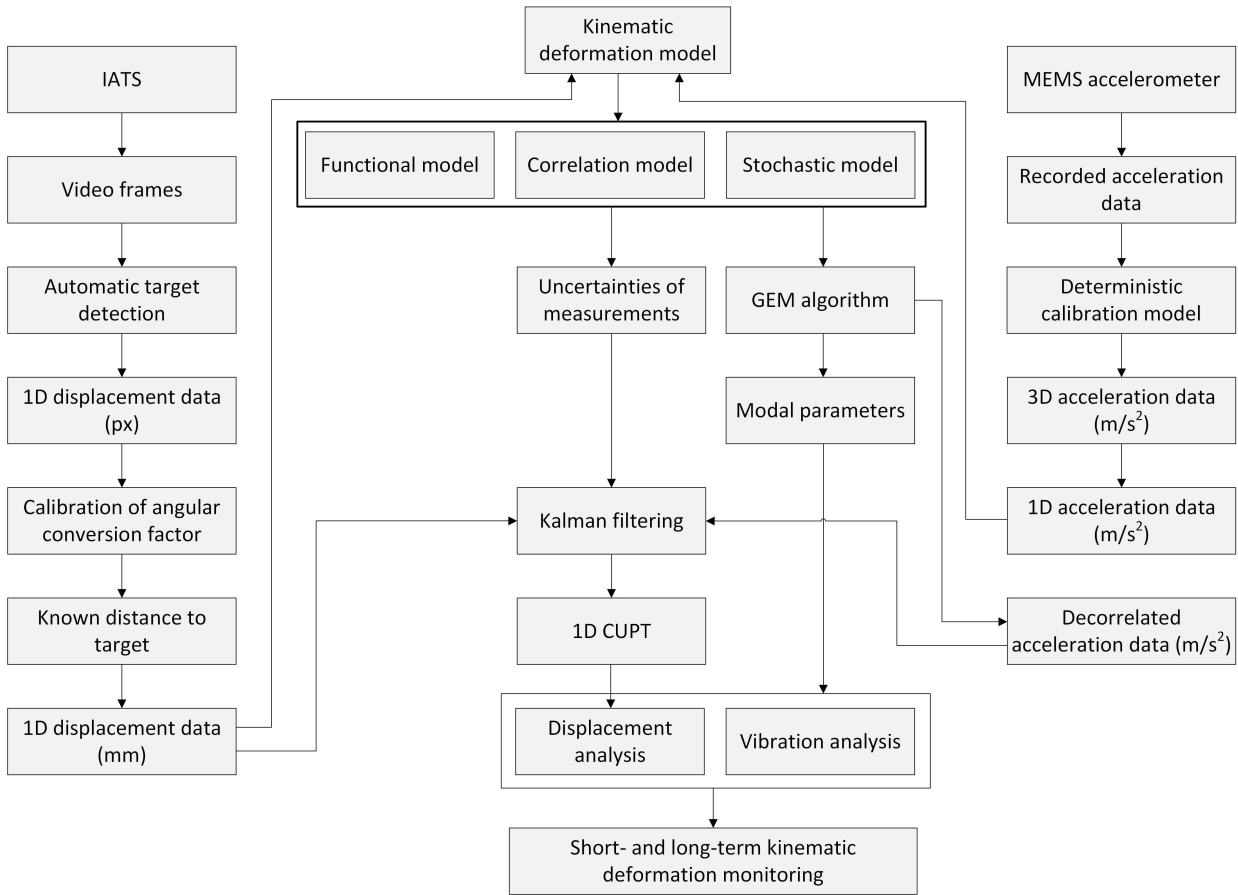


Figure 1.3: An overview of the research studies.

1.7 Outline of the Dissertation

This dissertation is organised in seven chapters as follows: chapter 2 describes the potential of MEMS accelerometers for bridge deformation monitoring. In chapter 3, the potential of IATS for bridge deformation monitoring is discussed. Robust kinematic deformation monitoring of bridge structures is introduced in chapter 4. Chapter 5 presents the MEMS-based bridge monitoring supported by IATS. Results of the experiments for a simulated data, a footbridge, and a synthetic bridge are discussed in chapter 6. Summary, conclusion, and outlook are given in chapter 7.

2 Suitability Analysis of MEMS Accelerometers for Deformation Monitoring of Bridges

2.1 Introduction

The use of cost-effective MEMS sensors for the task of vibration-based SHM of bridge structures is becoming more affordable and feasible. It can be used for frequent/permanent monitoring, which can assist to avoid any deterioration of the bridge structures. Therefore, the repair cost and risk is reduced and lifetime of the bridge structures is ensured. In the following, the MEMS sensor is called MEMS accelerometer due to merely using its acceleration data.

In this dissertation, the MEMS accelerometer is used due to the following reasons:

- being cost-effective,
- possibility to set-up a sufficient number of the MEMS accelerometers at different positions of the bridge structures,
- allowing permanent monitoring by performing measurements with a high sampling frequency, e.g., 100 Hz, at specified time intervals,
- recording acceleration measurements from a three axes accelerometer to identify eigenfrequencies of the bridge structure in longitudinal, lateral and vertical directions,
- feasibility of detecting all eigenfrequencies and eigenforms of the bridge structures,
- possibility of localising potentially damages in parts of the bridge structures by using densely distributed sensors, and based on identified eigenfrequencies and eigenforms.

However, the lateral and the vertical directions are of utmost interests, since wind and driving directions of vehicles are mainly influencing in the lateral and the vertical directions, respectively.

Different MEMS accelerometers with different qualities (i.e., uncertainties of the measurements) and prices are available in the market. Therefore, it is important to select one, which suits well for the purpose of cost-effective kinematic deformation monitoring of bridge structures. In spite of the purchase price and an adequate sampling frequency of the MEMS accelerometer, a three-step scenario is proposed in this chapter to select an optimal one. Firstly, the calibration procedure is carried out using a youBot for fixed positions and for certain time intervals, and over different temperature ranges. Thus, the MEMS related systematic errors are modelled, and their impacts on long-term measurements are degraded. Secondly, a controlled excitation experiment is performed by using a high-precision shaker to compare estimated harmonic oscillation parameters with a reference accelerometer. Thirdly, a static test experiment is conducted to estimate an offset and a drift of the measurements over a long period. In addition, this experiment allows to model auto- and cross-correlations for the 3D acceleration data. However, merely the auto-correlation is considered and the discussion of the cross-correlation model is out of scope of this dissertation.

This chapter is organised as follows: The ongoing section describes the measurement set-up and the data acquisition. Section 2.3 discusses a suitability analysis in selecting optimal triaxial MEMS accelerometers for the purpose of bridge monitoring. The calibration of the MEMS accelerometer is

introduced in section 2.4. This section is subdivided in 5 subsections and provides outlines of test scenarios for the calibration, calibration model of triaxial accelerometers, estimation procedure via two different adjustment models, as well as the experimental results. Section 2.5 outlines specifications of a selected MEMS accelerometer for bridge monitoring. Finally, the summary of this chapter is given in section 2.6.

2.2 Measurement Set-up and Data Acquisition

A geo-sensor network of the cost-effective MEMS accelerometers are mounted at specific positions of a bridge structure, which is precalculated in advance by means of the FEM analysis. Additionally, the FEM analysis can provide the measurement directions. To perform the FEM analysis, a 3D model can be used which is created, for example, by using a 2D plan of the bridge structure (von der Haar, 2017).

For the time being, the geo-sensor network of the MEMS accelerometers comprises a master node and three measuring nodes that are so-called master and slave sensors (see Fig. 2.1). The MEMS are connected via wires and the 3D acceleration data are transmitted via USB to a PC. The measurement starts by triggering the slave sensors from the master sensor via cable. The system is protected by an aluminium housing, which is resistant against temperature, humidity, rain, wind and etc. (Omidalizarandi et al., 2019c).

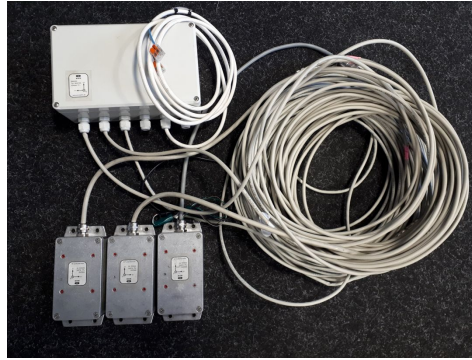


Figure 2.1: Scheme of MEMS accelerometers. The master MEMS sensor is located on top and other three slave MEMS sensors are located at the bottom that all are protected by the aluminium housing and connected via wires.

The master and slave sensors consist of the MEMS accelerometer and a control/storage unit. The MEMS acceleration data is recorded with a specified sampling frequency of 100 Hz. On the one hand, it allows to identify eigenfrequencies of bridge structures in a range of 0.1 to 50 Hz (in the view of Nyquist sampling theorem). On the other hand, it yields less data storage for a long-term deformation monitoring. High eigenfrequencies close to 50 Hz often occur in railway bridges (Meng, 2002; Roberts et al., 2004). However, in case of a bridge structure with higher eigenfrequencies than 50 Hz, a higher sampling frequency can be specified. The acceleration range is set to $\pm 2g$, which is adequate to sense ambient excitation. However, higher ranges such as $\pm 4g/\pm 8g/\pm 16g$ can also be set if it is desired (Omidalizarandi et al., 2019c). The acceleration measurements are stored into the SD memory card in blocks.

A time stamp transmitted by the master node at each memory block is provided by an integrated low-cost global navigation satellite system (GNSS) equipment. Thus, the time synchronisation between the MEMS sensors is carried out based on the GPS time. Currently, the time synchronisation between the MEMS accelerometers is at the level of 0.01 s, which enables to properly characterise eigenforms of bridge structures.

Side-by-side vibration measurements from proper reference sensors are conducted and analysed to get reliable evaluation, assessment, and validation of the aforementioned cost effective measurement system in determination of the modal parameters of bridge structures.

2.3 Suitability Analysis in Selecting Optimal MEMS Accelerometers

A three-step scenario is proposed to select a suitable MEMS accelerometer regardless of the sampling frequency and the purchase price. In the first step, a robust and automatic calibration procedure is developed and implemented to estimate the calibration parameters including three biases, three scale factors, and three non-orthogonality angles between the axes. The acceleration data is recorded over different temperature ranges to have a good realisation of the changes of the calibration parameters. Therefore, in spite of calibrating the MEMS accelerometer data, a proper MEMS accelerometer is selected whose corresponding measurements are less influenced by the aforementioned systematic errors. Additionally, a robust estimation of the calibration parameters over a variety of temperature ranges is carried out, which subsequently enables to perform interpolation at a specified temperature for a later in-situ monitoring. Moreover, it is desired to select a sensor, which has a stability of the calibration parameters over a long period and does not need frequent re-calibrations. Further information regarding the calibration procedure is given in section 2.4.

In the second step, a controlled excitation experiment is carried out by using a high-precision shaker at laboratory environment. The advantages of such experiment are twofold (Omidalizarandi et al., 2019c):

1. the harmonic oscillation parameters including frequency, amplitude, damping ratio coefficient as well as phase shift are estimated and then compared with known vibration parameters. Additionally, it allows to evaluate and compare them with the estimated parameters obtained from either other slave MEMS accelerometers or reference sensors,
2. the time synchronisation between different MEMS accelerometers are compared and validated based on the estimated phase shifts.

The aforementioned controlled excitation experiment is presented in the next subsection. In the third step, a static test experiment is carried out by using 3D acceleration data recorded from three different axes over a long period, e.g., 24 hours. Subsequently, a long-term stability of the measurements is investigated by estimating an offset (intercept) and (linear or quadratic) drift coefficients for all axes. Therefore, it enables us to select a sensor with minimal offset and drift values. Moreover, the (unknown) auto- and cross-correlations as well as the (unknown) distributional characteristics of the acceleration measurements can be investigated by employing a vector-autoregressive (VAR) process with t-distributed errors (Kargoll et al., 2020b). However, the discussion of the VAR process is out of scope of this dissertation and merely the auto-correlation is considered. The readers are referred to Kargoll et al. (2020a,b) for more information regarding the VAR process. The third step of the aforementioned scenario is briefly discussed in subsections 2.3.2. In this dissertation, all aforementioned three-step scenario have been carried out for one type of MEMS accelerometer from Bosch GmbH. However, it is possible to apply them for any types of accelerometers in a selection process.

2.3.1 Controlled excitation experiment

As previously stated, the controlled excitation experiment is conducted by using a high-precision shaker (Fig. 2.2, right) at the laboratory. The shaker is so-called the vibration test system, which is of type TV 51110. It has a frequency range of 2 – 7000 Hz and its maximum displacement peak-peak is 13 mm (see manufacturer's data sheet for details in TIRA Schwingtechnik (2019)). The

slave MEMS accelerometers are mounted on a levelled plate connected to four shakers that include highly accurate reference accelerometers recording the acceleration measurements with a sampling rate of 1024 Hz (see Fig. 2.2, left).

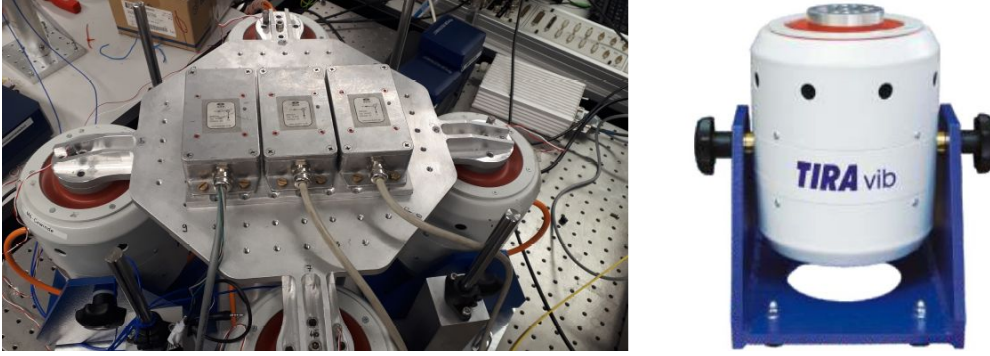


Figure 2.2: A controlled excitation experiment at the Institute of Dynamics and Vibration Research (IDS), Leibniz University Hannover (LUH), using a shaker to validate the time synchronisation between all three slave MEMS accelerometers (left), the shaker – vibration test system TV 51110 (right) (TIRA Schwingtechnik, 2019)).

The experiments are carried out for frequencies of 5, 10 and 20 Hz, and with a duration of 60 s. The estimated harmonic oscillation parameters and their corresponding uncertainties are provided in Tables 2.1 and 2.2 for the three slave MEMS accelerometers used, namely, *IMU_slave_02*, *IMU_slave_03* and *IMU_slave_04* with and without applying the calibration parameters. The estimated parameters comprise the frequency [Hz], the amplitudes in both units of $[m/s^2]$ and $[mm]$, the phase shift $[^\circ]$, the absolute gravity value, and an AR model order for which the estimation procedure is described in chapter 4. The uncertainties of the amplitudes in $[m/s^2]$ and $[mm]$ have been calculated based on error propagation using Equations 4.23 and 4.26, respectively. The comparison of the estimated phase shifts between sensors show the variations up to 5° . Additionally, comparison of the estimated frequencies with their nominal values demonstrate minor and major differences for lower and higher frequencies, respectively. For example, the frequency of 5 and 20 Hz have differences of approximately 0.003 and 0.01 Hz, respectively. Subsequently, it proves higher influence of the time synchronisation on higher frequencies, which is expected. In addition, as can be seen in Table 2.2, better uncertainty estimates are obtained for lower frequencies. Besides, the analyses show the better uncertainty estimates for the sensor *IMU_slave_02* compared to the others. Furthermore, less impact of the calibration parameters on the estimated modal parameters for a short time interval is observable (Omidalizarandi et al., 2019c). As shown in Omidalizarandi et al. (2019c), increasing the length of time series demands for increasing the AR model order to satisfy the white noise acceptance test. The reason lies in the fact that acceleration data recorded for a longer period of time are contaminated with a higher coloured measurement noise, which is due to environmental influences.

2.3.2 Static test experiment

A static test experiment is carried out to estimate offset and (linear or quadratic) drift coefficients over a long period. In addition, the auto-correlation in addition to the distributional characteristics of the acceleration data are investigated for each axis of the MEMS accelerometers individually. For this purpose, 3D acceleration data are recorded from three cost-effective MEMS accelerometers, and for a duration of approximately 24 hours. Two of the aforementioned MEMS accelerometers are of type BNO055 from Bosch GmbH but with different boards. The first one is with Arduino UNO-Board that is so-called NAMS, and the second one is with Tinkerforge-Board that is so-called IMU. The third MEMS accelerometer is of type ADXL345 with Arduino UNO-Board. The readers

Table 2.1: Estimated harmonic oscillation parameters obtained from the controlled excitation experiment for the slave MEMS acceleration data with and without applying calibration parameters.

MEMS Sensor	Calib. status	\hat{f} [Hz]	\hat{A} [m/s ²]	\hat{A} [mm]	$\hat{\varphi}$ [°]	$ g $ [m/s ²]	p
<i>IMU_slave_02</i>	No	5.0028	0.312	0.316	5.49	10.419	9
		10.0056	1.436	0.363	153.26	10.424	6
		20.0112	5.562	0.352	100.92	10.504	10
	Yes	5.0028	0.306	0.310	5.57	9.801	9
		10.0056	1.407	0.356	153.34	9.804	6
		20.0112	5.442	0.344	101.18	9.851	9
<i>IMU_slave_03</i>	No	5.0027	0.352	0.356	5.79	10.420	12
		10.0055	1.589	0.402	152.37	10.424	21
		20.0108	5.940	0.376	102.46	10.527	14
	Yes	5.0027	0.345	0.349	5.86	9.821	12
		10.0055	1.560	0.395	152.43	9.823	21
		20.0108	5.826	0.368	102.64	9.882	14
<i>IMU_slave_04</i>	No	5.0027	0.387	0.391	7.63	10.357	10
		10.0056	1.733	0.438	156.81	10.363	6
		20.0108	6.314	0.399	106.17	10.519	11
	Yes	5.0027	0.383	0.388	7.69	9.814	10
		10.0056	1.716	0.434	156.87	9.816	6
		20.0108	6.249	0.395	106.35	9.866	11

are referred to the data sheets of the aforementioned sensors for details information (Datasheet ADXL345, 2015; Datasheet BNO055, 2016).

The observation model is consisting of (1) a functional model based on a linear drift, (2) an auto-correlation model based on the AR process, and (3) a stochastic model based on the scaled t-distribution. The unknown parameters include an offset, a linear drift coefficient, AR model order and coefficients, scale factor and degree of freedom (df) of the underlying t-distribution. However, an adequate AR model order can be selected based on the either Akaike information criterion (AIC) (Kargoll et al., 2020a) or an acceptance of white noise test (WNT) criterion described by Kargoll et al. (2018). The WNT criterion is investigated by calculating a test statistic based on the maximum cumulated periodogram excess over a cumulated white noise periodogram. Therefore, it is accepted when being smaller than a critical value by considering a predefined significance level (i.e. $\alpha=0.05$). The aforementioned observation model has a structure of a Gauss-Markov model (GMM). Further information regarding the estimation procedure of the AR-univariate algorithm can be found in chapter 4.

The static acceleration measurements ℓ_1, \dots, ℓ_n ($n = 32743, 33300$, and 43107 in case of the NAMS, IMU, and ADXL) are recorded at approximately a constant temperature and with sampling frequencies of 0.38, 0.5 and 0.5 Hz from the aforementioned MEMS accelerometers. Therefore, they

Table 2.2: Uncertainties of the estimated harmonic oscillation parameters obtained from the controlled excitation experiment for the slave MEMS acceleration data with and without applying calibration parameters.

MEMS Sensor	Calib. status	$\hat{\sigma}_f$ [Hz]	$\hat{\sigma}_A$ [m/s ²]	$\hat{\sigma}_A$ [mm]
<i>IMU_slave_02</i>	No	2.65e-07	9.25e-06	9.35e-06
		2.66e-06	5.84e-04	1.48e-04
		2.57e-05	0.0171	0.0011
	Yes	2.58e-07	8.86e-06	8.97e-06
		2.61e-06	5.59e-04	1.41e-04
		2.76e-05	0.0181	0.0011
<i>IMU_slave_03</i>	No	3.06e-07	1.21e-05	1.22e-05
		2.60e-06	6.00e-04	1.62e-04
		4.26e-05	0.0311	0.0019
	Yes	3.01e-07	1.16e-05	1.17e-05
		2.60e-06	6.00e-04	1.55e-04
		4.18e-05	0.0299	0.0018
<i>IMU_slave_04</i>	No	2.20e-07	9.89e-06	1.01e-05
		1.83e-06	4.60e-04	1.16e-04
		5.61e-05	0.0461	0.0029
	Yes	2.20e-07	9.69e-06	9.80e-06
		1.81e-06	4.51e-04	1.14e-04
		5.55e-05	0.0453	0.0029

are modelled based on the linear drift with following equation:

$$\begin{aligned}\ell_t &= \mathbf{f}_t(\boldsymbol{\beta}) + e_t \\ &= c_0 + c_1 x_t + e_t,\end{aligned}\tag{2.1}$$

where $\boldsymbol{\beta}$ are the unknown functional parameters including the offset (c_0) in [m/s²], and the linear drift coefficient (c_1) in [m/s³]. e_t is the random deviation contaminated with the coloured noise, and x_t are equidistant time instances ($t = 1, \dots, n$). In case of quadratic drift of the acceleration data, a quadratic coefficient is added to the Equation 2.1.

Table 2.3 summarises the statistics of the estimated parameters based on the AR-univariate algorithm. The \hat{c}_0 [m/s²] is the estimated offset, \hat{c}_1 is the estimated linear drift coefficient [m/s³], $\hat{\sigma}_l$ is the estimated standard deviation of white noise measurements, p is the AR model order, and wnt_c is the acceptance or rejection of the WNT criterion.

Comparison of the AR model orders for different MEMS accelerometers reveals a higher coloured measurement noise in the ADXL and the IMU acceleration data, particularly in their Y and Z axes, compared to the NAMS accelerometer. This is even higher in the ADXL acceleration data, which can be observed from rejection of the WNT criterion even up to the AR model order 25. Figure 2.3

Table 2.3: Statistics of the estimated unknown parameters in the functional model based on the linear drift, the auto-correlation model based on the AR-univariate process and the stochastic model based on the centred and scaled t-distribution with an unknown df and unknown scale factor for measurements of three cost-effective MEMS accelerometers at a constant temperature

Sensor	Axis	\hat{c}_0 [m/s ²]	\hat{c}_1 [m/s ³]	$\hat{\sigma}_{c_0}$ [m/s ²]	$\hat{\sigma}_{c_1}$ [m/s ³]	$\hat{\sigma}_l$ [m/s ²]	p [-]	wnt _c [-]	$\hat{\nu}$ [-]
NAMS	X	-0.3597	6.81e-09	6.84e-05	1.37e-09	0.0066	1	yes	16.89
	Y	0.2811	-6.12e-08	0.0001	2.91e-09	0.0132	1	yes	120
	Z	-0.1354	6.64e-09	0.0001	3.13e-09	0.0141	1	yes	120
IMU	X	0.1685	-1.39e-07	0.0001	3.35e-09	0.0118	1	yes	120
	Y	-0.0978	3.45e-07	0.0001	3.68e-09	0.0115	7	yes	120
	Z	-0.1316	2.97e-08	0.0004	1.04e-08	0.0360	11	yes	120
ADXL	X	0.0799	-7.96e-10	5.70e-05	1.14e-09	0.0272	1	yes	2.1
	Y	0.2965	2.21e-09	0.0002	5.17e-09	0.0480	25	no	2.95
	Z	-0.4211	7.34e-09	0.0002	4.99e-09	0.1182	25	no	2.1

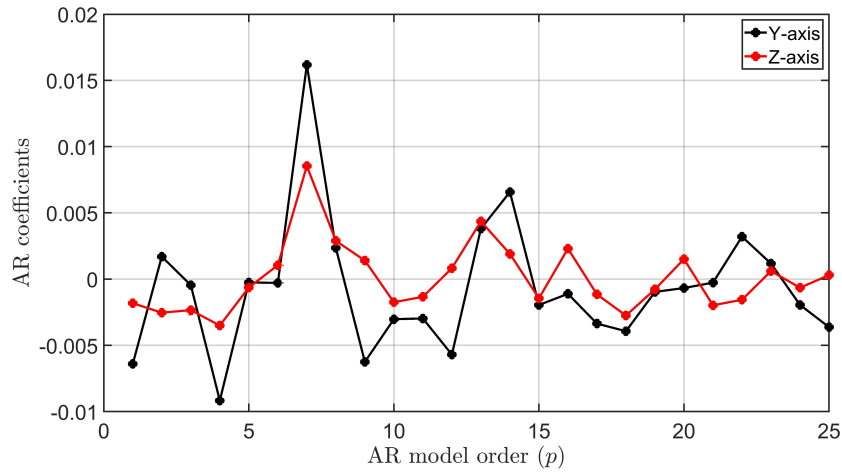


Figure 2.3: AR model coefficients correspond to the ADXL acceleration data recorded from Y and Z axes.

illustrates the AR model coefficients correspond to the acceleration data recorded in Y and Z axes of the ADXL in order to have an impression about size of the AR model coefficients. As it can be seen, the AR model coefficient at order 7 is slightly larger than the others for both Y and Z axes. The analyses reveal a less coloured measurement noise in the X-axis of all aforementioned MEMS accelerometers. In addition, the acceleration data recorded from the X-axis has significantly a better uncertainty of the white noise measurements compared to the Z-axis. Moreover, the IMU acceleration data shows higher estimates of the df of the underlying t-distribution, i.e., rather close approximation of the normal distribution, in all three axes compared to two other sensors. The IMU data shows slightly higher drift at a constant temperature compared to other two accelerometers. However, as it was shown in Kemkes (2016), the IMU data, particularly the measurements recorded from its X-axis, has a better stability of the measurements, i.e., approximately linear behaviour,

over temperature ranges of 8 to 40°C compared to the NAMS acceleration data. Consequently, the IMU is selected as a suitable sensor among two other aforementioned MEMS accelerometers. For this purpose, the estimates of the calibration parameters as well as the long-term stability of the measurements over a variety of temperature ranges, the stochastic model parameters and the auto-correlation model parameters are considered.

2.4 Calibration of MEMS Accelerometers

In this chapter, a robust and computationally efficient calibration procedure is proposed and implemented to obtain reliable acceleration measurements recorded from the MEMS accelerometers. Such a calibration procedure mainly eliminates the MEMS related systematic errors such as biases, scale factors and non-orthogonalities between the axes. The experimental studies and analyses of this research demonstrate that the estimated modal parameters from calibrated acceleration data have minor deviations from those obtained from uncalibrated ones in a short time interval. However, the proposed calibration procedure is more beneficial either for a long-term monitoring, e.g. few minutes or higher, or to enhance the accuracy of the displacements calculated from the double integration.

2.4.1 Development of test scenarios for MEMS accelerometers calibration

A calibration procedure is designed, developed, and implemented based on a common six-position static acceleration tests, cf. Shin and El-Sheimy (2002). A KUKA youBot (see Fig. 2.4) is utilised to automatically perform calibration for fixed positions and for a certain time interval. It is an omnidirectional mobile robot with an arm consisting of 5 axes and 4 wheels. Its weight is 5.3 kg and its minimum and maximum velocities are 0.01 and 0.8 m/s (KUKA youBot, 2012). The MEMS accelerometer is rigidly attached to the arm of the youBot to ensure its stability through the entire experiment.

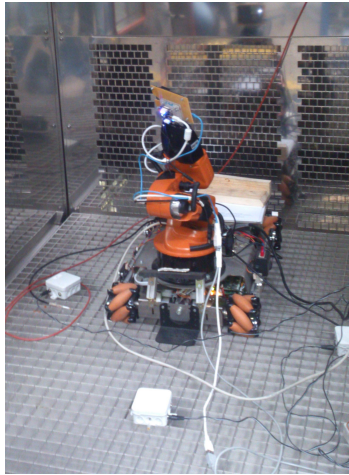


Figure 2.4: Scheme of the KUKA youBot inside the climate chamber.

Figure 2.5 depicts the MEMS acceleration data recorded in all three directions for 20 positions each measured for 5 minutes. As we can see, the positions were defined approximately symmetric to have more reliable and accurate estimates of the calibration parameters. The first and last few seconds of the measurements recorded at each position are discarded due to its transition measurements of the youBot from one position to the other. It could be seen in this figure, that still some transition measurements remain that are approximately connecting two consecutive measurements. Therefore, they are treated as outliers within the calibration estimation procedure.

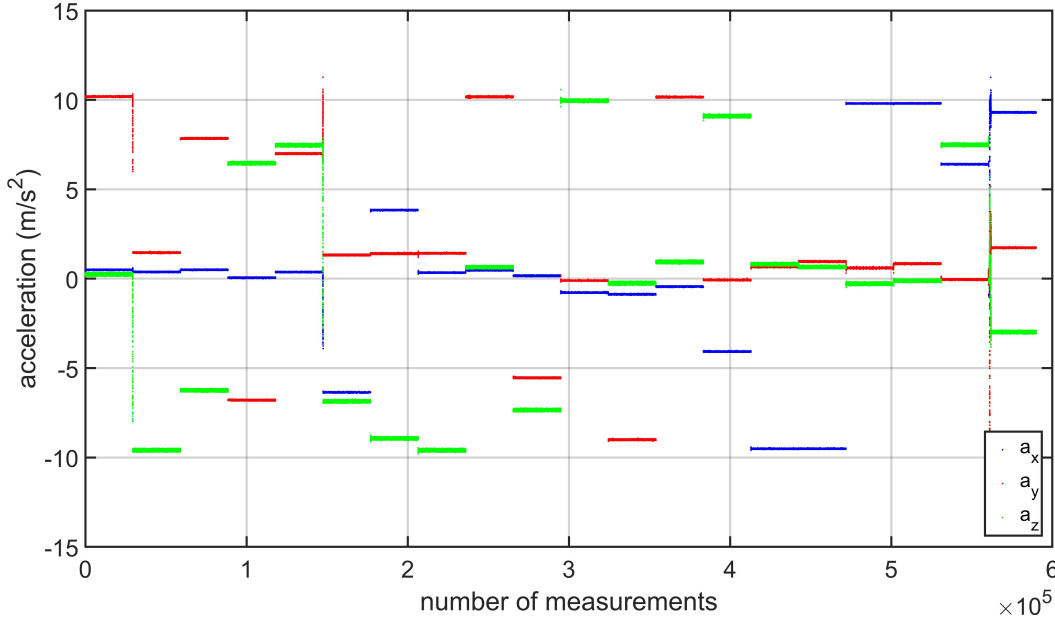


Figure 2.5: Scheme of the entire MEMS acceleration data recorded for fixed positions and for a certain time interval. The acceleration data in the X , Y and Z directions (a_x , a_y and a_z) are illustrated with blue, red and green colours.

Since the performance characteristics of MEMS accelerometers are highly dependent on the environmental conditions such as temperature or humidity variations, the calibration procedure is accomplished in a climate chamber and over different temperature ranges between 10 to 30°C. Therefore, it allows to observe the changes of the calibration parameters. Aforementioned temperature ranges have been selected due to the restrictions of the climate chamber and the youBot in higher or lower temperatures (Omidalizarandi et al., 2019c). Kemkes et al. (2019) compared the variations of humidity and temperature inside the housing box which protects MEMS accelerometer, with its surrounding environment. Thus, its corresponding investigation reveals that the humidity inside the housing box is kept constant despite changes of the humidity outside of the box. By contrast, the temperature inside the housing is adapted to the outside temperature.

2.4.2 Calibration model of triaxial accelerometers

A functional equation for the calibration of triaxial accelerometers is determined based on the work of Shin and El-Sheimy (2002) as follows:

$$\begin{aligned}
 f_g &= \left[\frac{l_{gx} - b_{gx}}{1 + s_{gx}} \right]^2 \\
 &+ \left[\tan \theta_{yz} \left(\frac{l_{gx} - b_{gx}}{1 + s_{gx}} \right) \left(\frac{1}{\cos \theta_{yz}} \right) + \left(\frac{l_{gy} - b_{gy}}{1 + s_{gy}} \right) \right]^2 \\
 &+ \left[\tan \theta_{zx} \tan \theta_{yz} - \frac{\tan \theta_{zy}}{\cos \theta_{zx}} \left(\frac{l_{gx} - b_{gx}}{1 + s_{gx}} \right) + \left(\frac{\tan \theta_{zx}}{\cos \theta_{yz}} \right) \right. \\
 &\times \left. \left(\frac{l_{gy} - b_{gy}}{1 + s_{gy}} \right) + \left(\frac{1}{\cos \theta_{zx} \cos \theta_{zy}} \right) \left(\frac{l_{gz} - b_{gz}}{1 + s_{gz}} \right) \right]^2 - |g|^2 \\
 &= 0,
 \end{aligned} \tag{2.2}$$

where l_{gx} , l_{gy} , and l_{gz} are the acceleration data recorded in all three directions. Unknown calibration parameters include three biases (b_{gx} , b_{gy} , b_{gz}), three scale factors (s_{gx} , s_{gy} , s_{gz}), and three non-orthogonality angles between the axes (θ_{zx} , θ_{zy} , θ_{yz}). The θ_{zx} and θ_{zy} are the non-orthogonalities of the Z -axis with respect to the X and Y axes, and θ_{yz} is the non-orthogonality between X and Y axes. A local gravity value (here $g \approx 9.812623860 \text{ m/s}^2$) is defined as a constraint within the adjustment procedure. Thus, it allows a reliable estimate of the calibration parameters with respect to the reference value. For more information, the readers are referred to Shin and El-Sheimy (2002).

The gravity value can also be calculated based on the Equation 2.3 described by Titterton and Weston (1997) as

$$\begin{aligned} g(0) &= 9.780318(1 + 5.3024 \cdot 10^{-3} \times \sin^2 L - 5.9 \cdot 10^{-6} \times \sin^2 2L), & (\text{m/s}^2) \\ g(h) &= \frac{g(0)}{(1 + \frac{h}{R_0})^2}, & (\text{m/s}^2) \end{aligned} \quad (2.3)$$

where L is the geodetic latitude, h is the orthometric height above sea level, and R_0 is the Earth radius.

2.4.3 Adjustment of the calibration model with standard Gauss-Helmert model and variance component estimation

In this adjustment model, the aforementioned deterministic calibration model (Equation 2.2) is solved in a nonlinear standard GHM based on the principle of weighted least squares. To accurately and reliably obtain the unknown calibration parameters, the proposed approach by Shin and El-Sheimy (2002) is improved by assigning optimal weights to the observations based on the variance component estimation (VCE) in an iterative manner. The proposed adjustment model is not memory and computationally efficient due to an inverse of a large weight matrix within the GHM. Despite of downsampling of the acceleration measurements by 100, its computation is still time consuming.

It is assumed that stochastically independent observation vectors belong to 3 distinct groups with $k \in \{1, 2, 3\}$ that correspond to the acceleration measurements recorded in X , Y , and Z directions. It is further assumed that the stochastic observation vector and its corresponding error vector model follow a normal distribution, which is described by

$$\mathbf{l}_k \sim N(\boldsymbol{\mu}_k, \boldsymbol{\Sigma}_k), \quad \mathbf{e}_k \sim N(\mathbf{0}, \boldsymbol{\Sigma}_k), \quad (2.4)$$

where $\boldsymbol{\Sigma}_k$ is the positive definite variance-covariance matrix of \mathbf{l}_k , $\boldsymbol{\mu}_k$ are the expected values of \mathbf{l}_k and $E(\mathbf{e}_k) = \mathbf{0}$. The condition equation is defined based on Equation 2.14, which is solved by minimising the square sum of the residuals for the downsampled acceleration measurements. For more information concerning the GHM, the readers are referred to Niemeier (2008). An uncertainty of the acceleration measurements recorded from each axis is initially defined based on the standard deviation of the measurements. Therefore, the weight is calculated for each distinct group with

$$\mathbf{P}_k = \sigma_0^2 \boldsymbol{\Sigma}_k^{-1}, \quad (2.5)$$

where σ_0^2 is the unknown theoretical variance of unit weight, which here is considered *a priori* to be 1. Similar to the Algorithm 3 proposed in Omidalizarandi et al. (2019b), the adjustment model is solved in three iterative procedures. In the first iterative procedure, the unknown functional model parameters ($\boldsymbol{\xi}$) are estimated while a convergence criterion, as defined in the following, is fulfilled.

$$d = (\max |\boldsymbol{\xi}^{(s)} - \boldsymbol{\xi}^{(s+1)}|) \leq 10^{-12}, \quad (2.6)$$

where d is the maximum of the absolute differences of the estimated unknown parameters. In the second iterative procedure, the stochastic model is introduced by assigning optimal weights to the observations based on the VCE algorithm, as proposed by Koch (2014a) and applied in Omidalizarandi et al. (2019b). For this purpose, the covariance matrix of the observations is calculated as

$$\Sigma_{ll} = \begin{bmatrix} \Sigma_{xx} & \cdots & 0 \\ \vdots & \Sigma_{yy} & \vdots \\ 0 & \cdots & \Sigma_{zz} \end{bmatrix} = \begin{bmatrix} s_1^2 \mathbf{Q}_{11} & \cdots & 0 \\ \vdots & s_2^2 \mathbf{Q}_{22} & \vdots \\ 0 & \cdots & s_3^2 \mathbf{Q}_{33} \end{bmatrix}, \quad (2.7)$$

where the factors $\{s_1^2, s_2^2, s_3^2\}$ are initialised based on the given *a priori* variances of the observables and \mathbf{Q}_{11} , \mathbf{Q}_{22} and \mathbf{Q}_{33} are the cofactor matrices, which their corresponding variance components (i.e. σ_k^2 for $k \in \{1, 2, 3\}$) are expected to have values close to 1. The VCE procedure proceeds until $\hat{\sigma}_k = [1, 1, 1]'$ is achieved with an adequate estimation accuracy. Thus, the estimated factors, which are *a posteriori* variances of the observables are calculated as

$$\hat{s}_k^2 = \prod_{c=1}^{C-1} (s_k^2)^{(c)} \cdot \prod_{r=1}^{R-1} (\hat{\sigma}_k^2)^{(r)} \quad \text{for } k \in \{1, 2, 3\}, \quad (2.8)$$

where C and R are the maximum numbers of iterations (see Algorithm 3 in Omidalizarandi et al. (2019b)). Next, a global test is accomplished in the third iterative procedure to evaluate the correctness of the analysis (Amiri-Simkooei and Jazaeri, 2013). Thus, the null and alternative hypotheses are defined similar to the works of Teunissen (2006) and Koch (2013a) with

$$H_0 : \sigma_0^2 = \hat{\sigma}_0^2 \quad \text{vs.} \quad H_1 : \sigma_0^2 \neq \hat{\sigma}_0^2. \quad (2.9)$$

The test value is defined by considering the normally distributed observations as proposed by Neitzel (2010) and Amiri-Simkooei and Jazaeri (2013) with

$$T_{\chi^2} = \frac{\hat{\sigma}_0^2}{\sigma_0^2} (m - u), \quad (2.10)$$

where m and u are the numbers of observations and the unknown parameters. Here, a significance level of $\alpha = 0.05$ is considered. Therefore, if $T_{\chi^2} \leq \chi_{(m-u, 1-\alpha)}^2$, the null hypothesis is accepted; otherwise, it is rejected when the assumptions are violated (see Niemeier (2008)). To identify the outliers in the acceleration measurements, the χ^2 test with 95% confidence levels are applied with

$$T_{\chi_g^2} = \frac{\mathbf{e}_g^T \mathbf{P}_g \mathbf{e}_g}{\sigma_0^2}, \quad (2.11)$$

where $T_{\chi_g^2}$ is the χ^2 test value, the \mathbf{e}_g ((1×1) or (3×1) dimensions) and \mathbf{P}_g ((1×1) or (3×3) dimensions) are the residuals and the weight matrix of a few observables. Since performing data snooping proposed by Baarda (1968) for such large number of the measurements is time consuming, the outliers having test values above the calculated limit are reweighted by (Medić et al., 2019):

$$p_g = \frac{1}{\hat{s}_k^2} \cdot \exp \left(-\frac{e_g^2}{(3\hat{s}_k^2)^2} \right), \quad (2.12)$$

where the e_g and p_g account for one element of the \mathbf{e}_g and \mathbf{P}_g . The entire adjustment procedure repeats again to obtain the reliable and accurate estimates of the unknown parameters.

2.4.4 Adjustment of the calibration model with applied adaptive robust estimation

Adjustment of the calibration model is further improved by means of an adaptive robust estimation procedure to obtain more accurate, robust, and reliable calibration parameters. In addition, it is a memory and computationally more efficient approach than the former one. For this purpose, a component-wise vector multiplication is employed throughout the weighting for the entire MEMS acceleration data.

In this model, the unknown calibration parameters are estimated based on an iterative re-weighted least squares adjustment in a nonlinear GHM with t-distributed random deviations, as introduced by Koch (2014a) and extended by Omidalizarandi et al. (2019b). The observables \mathcal{L}_1 , \mathcal{L}_2 and \mathcal{L}_3 (i.e. l_{gx} , l_{gy} , and l_{gz}) are assumed to be stochastically independent and belong to 3 different groups, where each group k consists of n_k observables.

Since the cost-effective MEMS acceleration data are expected to contain numerous outliers, the t-distribution, which has heavier tails than normal distributions is used as outlier distribution in the context of a robust ML estimation (Parzen, 1979; Wiśniewski, 2014). Therefore, lower weights are assigned to the random deviations located in the tails of the probability density function (PDF), yields a robust estimation procedure. A weight matrix is formed based on the locations of the random deviations under the PDF of the scaled centred (Student's) t-distribution with individual unknown location parameter $\mu_{k,i}$, group-dependent unknown scale factor σ_k^2 , and group-dependent unknown df ν_k (Omidalizarandi et al., 2019b). The stochastic observation model is described by

$$\mathcal{L}_{k,i} \stackrel{\text{ind.}}{\sim} t_{\nu_k}(\mu_{k,i}, \sigma_k^2), \quad (2.13)$$

where an observable $\mathcal{L}_{k,i}$ with $k \in \{1, 2, 3\} = \{x, y, z\}$ and $i \in \{1, \dots, n_k\}$ is associated with its corresponding t-distribution depending on the measurement directions in the different axes.

In order to benefit from the large amount of the acceleration data recorded from the calibration procedure and to avoid downsampling of the measurements, the GHM with t-distributed random deviations algorithm proposed by Omidalizarandi et al. (2019b) is extended. The new adjustment model prevents an inverse of quadratic form of the weight matrix within the adjustment procedure, which makes it computationally efficient and fast. The proposed algorithm is described in the following. To begin with the adjustment problem, the condition equation is set-up by

$$\mathbf{h}(\boldsymbol{\xi}, \boldsymbol{\mu}) = \mathbf{0}_{[r \times 1]}, \quad (2.14)$$

where $\boldsymbol{\xi}$ is the $(u \times 1)$ -vector of functional parameters and $\boldsymbol{\mu}$ the $(n \times 1)$ -vector of expected values of \mathcal{L} (i.e. $\boldsymbol{\mu} = \mathbf{l} + \mathbf{e}$). All of the unknown parameters are stacked within the $(u + n + 6)$ -vector

$$\boldsymbol{\theta} = [\boldsymbol{\xi}^T, \boldsymbol{\mu}^T, \sigma_x^2, \sigma_y^2, \sigma_z^2, \nu_x, \nu_y, \nu_z]^T, \quad (2.15)$$

all recorded observations are structured as a vector in a component form within the $(n \times 1)$ -vector

$$\boldsymbol{\ell} = [\boldsymbol{\ell}_x^T, \boldsymbol{\ell}_y^T, \boldsymbol{\ell}_z^T]^T = [\ell_{x,1}, \dots, \ell_{x,n_x}, \ell_{y,1}, \dots, \ell_{y,n_y}, \ell_{z,1}, \dots, \ell_{z,n_z}]^T, \quad (2.16)$$

and the weight matrix is also structured as a vector in a component form

$$\mathbf{P} = [\mathbf{p}_x^T, \mathbf{p}_y^T, \mathbf{p}_z^T]^T = [p_{x,1}, \dots, p_{x,n_x}, p_{y,1}, \dots, p_{y,n_y}, p_{z,1}, \dots, p_{z,n_z}]^T. \quad (2.17)$$

In this adjustment model, instead of calculating the weight for each distinct group, the weight is calculated for each individual observable n_k . Next, the $\mathbf{h}(\boldsymbol{\theta})$ is linearised and thus initialised by using the expansion point $\boldsymbol{\theta}^{[0]} := \boldsymbol{\theta}^{(s)}$ as

$$\begin{aligned}
 \mathbf{h}(\boldsymbol{\theta}) &\approx \mathbf{h}(\boldsymbol{\theta}^{[0]}) + \frac{\partial \mathbf{h}(\boldsymbol{\theta}^{[0]})}{\partial \boldsymbol{\theta}}(\boldsymbol{\theta} - \boldsymbol{\theta}^{[0]}) \\
 &= \mathbf{m} + \frac{\partial \mathbf{h}(\boldsymbol{\theta}^{[0]})}{\partial \boldsymbol{\xi}}(\boldsymbol{\xi} - \boldsymbol{\xi}^{[0]}) + \sum_{k=1}^3 \frac{\partial \mathbf{h}(\boldsymbol{\theta}^{[0]})}{\partial \boldsymbol{\mu}_k}(\boldsymbol{\mu}_k - \boldsymbol{\mu}_k^{[0]}) \\
 &= \mathbf{m} + \mathbf{A}(\boldsymbol{\xi} - \boldsymbol{\xi}^{[0]}) + \sum_{k=1}^3 \mathbf{B}_k(\boldsymbol{\mu}_k - \boldsymbol{\ell}_k + \boldsymbol{\ell}_k - \boldsymbol{\mu}_k^{[0]}) \\
 &= \mathbf{A}\Delta\boldsymbol{\xi} + \sum_{k=1}^3 \mathbf{B}_k(\boldsymbol{\mu}_k - \boldsymbol{\ell}_k) + \mathbf{m} + \sum_{k=1}^3 \mathbf{B}_k(\boldsymbol{\ell}_k - \boldsymbol{\mu}_k^{[0]}) \\
 &= \mathbf{A}\Delta\boldsymbol{\xi} + \sum_{k=1}^3 \mathbf{B}_k(\boldsymbol{\mu}_k - \boldsymbol{\ell}_k) + \mathbf{m}_p,
 \end{aligned} \tag{2.18}$$

where $\mathbf{m} = \mathbf{h}(\boldsymbol{\theta}^{[0]})$ is the vector of misclosures, $\mathbf{A} = \partial \mathbf{h}(\boldsymbol{\theta}^{[0]})/\partial \boldsymbol{\xi}$ is the $(r \times u)$ -matrix of partial derivatives of $\mathbf{h}(\boldsymbol{\theta})$ with respect to $\boldsymbol{\xi}$ initialised at $\boldsymbol{\theta}^{[0]}$, and $\mathbf{B}_k = \partial \mathbf{h}(\boldsymbol{\theta}^{[0]})/\partial \boldsymbol{\mu}_k$ is the $(r \times n_k)$ -matrix of partial derivatives of $\mathbf{h}(\boldsymbol{\theta})$ with respect to $\boldsymbol{\mu}_k$ initialised at $\boldsymbol{\theta}^{[0]}$, $\Delta\boldsymbol{\xi} = \boldsymbol{\xi} - \boldsymbol{\xi}^{[0]}$, and the pseudo-misclosures are:

$$\mathbf{m}_p = \mathbf{m} + \sum_{k=1}^3 \mathbf{B}_k(\boldsymbol{\ell}_k - \boldsymbol{\mu}_k^{[0]}). \tag{2.19}$$

Therefore, the original condition equation is rewritten in the linearised form as

$$\mathbf{A}\Delta\boldsymbol{\xi} + \mathbf{B}\mathbf{e} + \mathbf{m}_p = \mathbf{0}. \tag{2.20}$$

The quadratic matrix \mathbf{B} is stored in a component form composed of three vectors denoted by \mathbf{b}_x , \mathbf{b}_y , and \mathbf{b}_z , which allows to increase the efficiency of the computation. Subsequently, a component-wise vector multiplication \otimes is performed in the second summand of the Equation 2.20 via

$$\sum_{k=1}^3 \mathbf{B}_k(\boldsymbol{\mu}_k - \boldsymbol{\ell}_k) = \mathbf{b}_x \otimes (\boldsymbol{\mu}_x - \boldsymbol{\ell}_x) + \mathbf{b}_y \otimes (\boldsymbol{\mu}_y - \boldsymbol{\ell}_y) + \mathbf{b}_z \otimes (\boldsymbol{\mu}_z - \boldsymbol{\ell}_z). \tag{2.21}$$

The unknown parameters and the expected values of the observables can be calculated through

$$\Delta\boldsymbol{\xi}^{(s+1)} = - \left(\mathbf{A}^T \left(\sum_{k=1}^3 \mathbf{B}_k [\mathbf{P}_k^{(s)}]^{-1} \mathbf{B}_k^T \right)^{-1} \mathbf{A} \right)^{-1} \mathbf{A}^T \left(\sum_{k=1}^3 \mathbf{B}_k [\mathbf{P}_k^{(s)}]^{-1} \mathbf{B}_k^T \right)^{-1} \mathbf{m}_p, \tag{2.22}$$

$$\boldsymbol{\xi}^{(s+1)} = \boldsymbol{\xi}^{(s)} + \Delta\boldsymbol{\xi}^{(s+1)}, \tag{2.23}$$

$$\mathbf{e}_k^{(s+1)} = [\mathbf{P}_k^{(s)}]^{-1} \mathbf{B}_k^T \left(\sum_{k=1}^3 \mathbf{B}_k [\mathbf{P}_k^{(s)}]^{-1} \mathbf{B}_k^T \right)^{-1} \left(-\mathbf{A}\Delta\boldsymbol{\xi}^{(s+1)} - \mathbf{m}_p \right), \tag{2.24}$$

$$\boldsymbol{\mu}_k^{(s+1)} = \boldsymbol{\ell}_k + \mathbf{e}_k^{(s+1)}. \tag{2.25}$$

In the initial step $s = 0$, a uniform weight matrix $\mathbf{P}^{(0)} = \mathbf{I}$ is considered within the solution equations, which is re-weighted in the next iteration steps. Since the weight matrix was stored in the component form, thus $\sum_{k=1}^3 \mathbf{B}_k [\mathbf{P}_k^{(s)}]^{-1} \mathbf{B}_k^T$ can be determined through the component-wise vector multiplication via

$$\mathbf{b}_x \otimes [\mathbf{p}_x^{(s)}]^{-1} \otimes \mathbf{b}_x + \mathbf{b}_y \otimes [\mathbf{p}_y^{(s)}]^{-1} \otimes \mathbf{b}_y + \mathbf{b}_z \otimes [\mathbf{p}_z^{(s)}]^{-1} \otimes \mathbf{b}_z.$$

To obtain an improved solution $\boldsymbol{\theta}^{(s+1)}$ through the aforementioned solution equations, a constrained EM algorithm is employed by maximising the log-likelihood function subject to $\mathbf{h}(\boldsymbol{\theta}) = \mathbf{0}$ (Omidalizarandi et al., 2019b).

The group-dependent unknown scale factors and *a posteriori* variances of the observables for $k \in \{x, y, z\}$ are calculated through

$$(\sigma_k^2)^{(s+1)} = \frac{1}{n_k} \sum_{i=1}^{n_k} p_{k,i}^{(s)} \left(\ell_{k,i} - \mu_{k,i}^{(s+1)} \right)^2. \quad (2.26)$$

$$(s_k^2)^{(s+1)} = (\sigma_k^2)^{(s+1)} \left(\frac{\nu_k^{(s+1)}}{\nu_k^{(s+1)} - 2} \right). \quad (2.27)$$

The dfs ν_x , ν_y , and ν_z are estimated through searching the zeros of (Kargoll et al., 2018)

$$\begin{aligned} 0 = & 1 + \log \nu_k^{(s+1)} - \psi \left(\frac{\nu_k^{(s+1)}}{2} \right) + \psi \left(\frac{\nu_k^{(s+1)} + 1}{2} \right) \\ & - \log \left(\nu_k^{(s+1)} + 1 \right) + \sum_{i=1}^{n_k} \frac{1}{n_k} \left(\log p_{k,i}^{(s+1)} - p_{k,i}^{(s+1)} \right), \end{aligned} \quad (2.28)$$

with variables

$$p_{k,i}^{(s+1)} = \frac{\nu_k^{(s+1)} + 1}{\nu_k^{(s+1)} + \left(\frac{\ell_{k,i} - \mu_{k,i}^{(s+1)}}{\sigma_k^{(s+1)}} \right)^2}, \quad (2.29)$$

where ψ denotes the digamma function. An interval Newton method (Algorithm 6.1 in Hargreaves (2002)) is employed to perform the zero search and to obtain a unique solution within an extremely narrow interval (Omidalizarandi et al., 2019b).

2.4.5 Experimental results of the MEMS accelerometer calibration

In order to have a better realisation of the calibration parameters changes for a MEMS accelerometer, a calibration procedure is conducted in a climate chamber over different temperatures. The 11 experiments are carried out over temperature ranges of 10 to 30°C, started from 10°C, reached to 30°C and then reversed back again to 10°C.

Figures (2.6–2.8) illustrate the exemplary estimates of the calibration parameters computed by the two proposed adjustment models, which are abbreviated to GHM–VCE and GHM–GEM. The remaining estimates of the calibration parameters are provided in Figures A.1(a)–A.1(f) in the Appendix. The accurate, and robust estimates of the unknown calibration parameters are obtained for the biases and the scale factors in both approaches, which have approximately similar values. It can be seen that the estimated calibration parameters in forward and reversed back measurements are nearly hysteresis, which might be due to changes of the temperatures from low to high and inversely. In addition, the shifts between the estimated calibration parameters obtained from both adjustment models are related to the different number of measurements, i.e., the downsampled measurements are used in the GHM–VCE approach. However, such differences are very small and therefore negligible. Furthermore, the GHM–GEM approach is performed in a time efficient manner even for the case of using the entire recorded acceleration measurements.

As we expected, the trend of changes for the estimates of the calibration parameters are clearly visible, particularly for the biases and the scale factors. Subsequently, it allows to correct the

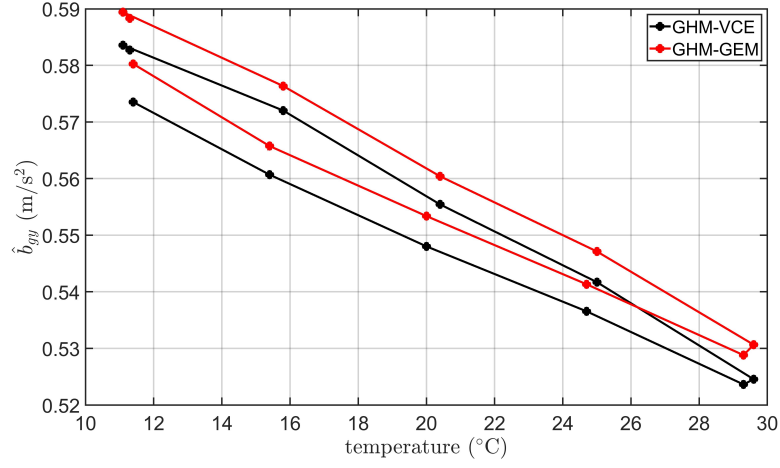


Figure 2.6: MEMS accelerometer calibration parameter - \hat{b}_{gy} [m/s^2].

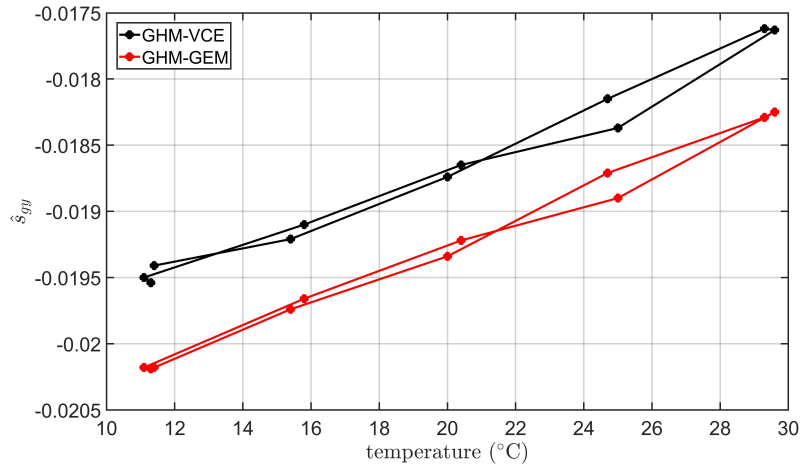


Figure 2.7: MEMS accelerometer calibration parameter - \hat{s}_{gy} .

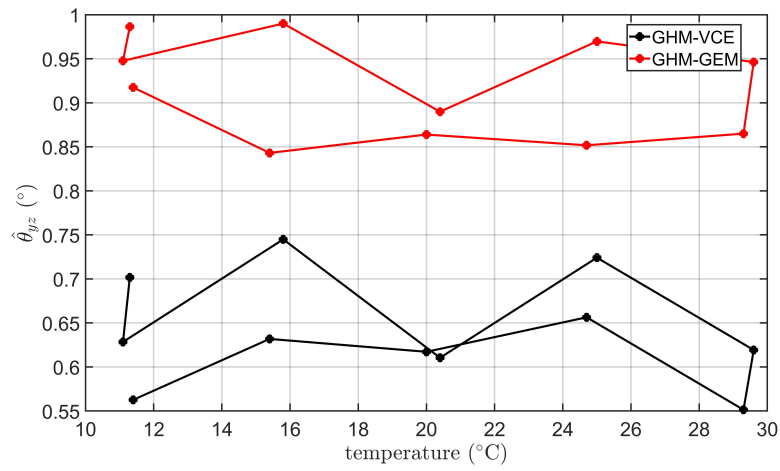


Figure 2.8: MEMS accelerometer calibration parameter - $\hat{\theta}_{yz}$ [$^{\circ}$].

acceleration measurements recorded in-situ environment at a specified temperature by means of a linear interpolation. However, the range of changes for the estimates of the three non-orthogonality angles are quite small and may still linearly be determined. There might be either a mathematical correlation between the unknown parameters or a correlation between the acceleration measurements recorded from the relevant axes. Investigation of such a correlation is out of the focus of this dissertation and can be considered as a future work.

Figure 2.9 depicts the estimates of *a posteriori* standard deviations of the acceleration measurements. As it can be seen, the estimated standard deviations in both adjustment models, and for the measurements recorded in *X* and *Y* directions have approximately similar values. However, a significant difference can be observed for *Z* direction. This can be due to the reason that the acceleration measurements obtained from the *Z* direction are much noisier than the two other axes. In addition, in the second adjustment model, and by downsampling by factor 100, the number of observations has been reduced significantly. Therefore, it is difficult to get the reliable estimates of the corresponding uncertainty.

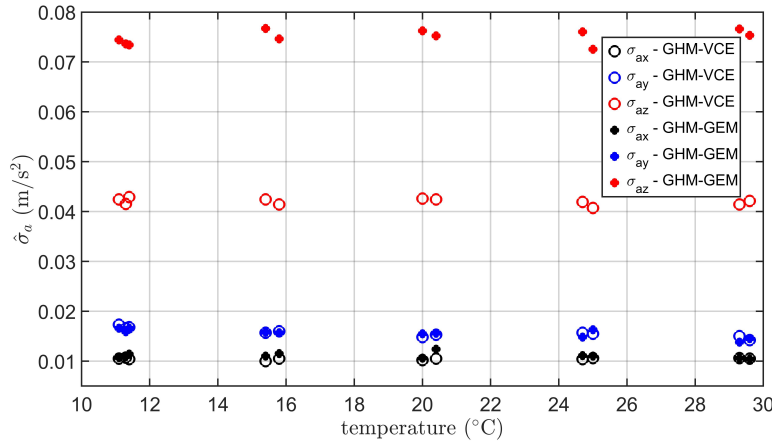


Figure 2.9: *A posteriori* standard deviation of the MEMS acceleration measurements - $\hat{\sigma}_a$ [m/s^2].

2.5 Sensor Specifications

In this study, a cost-effective MEMS sensor, e.g. of type BNO055 from the Bosch company, has been used. The sensor dimension (width \times length \times height) is 40 \times 40 \times 19 mm and its weight is 12 g. It has 9 degrees of freedom comprising a triaxial 14-bit accelerometer, a triaxial magnetometer, and a triaxial 16-bit gyroscope, which outputs acceleration, magnetic field strength, and rotation data, respectively. Additionally, the fused sensors output quaternion, Euler angles, rotation vector, linear acceleration, gravity and independent heading, roll and pitch angles information (see manufacturer's data sheet for details (Datasheet BNO055, 2016)). However, merely the 3D acceleration data have been recorded, which allow monitoring of a bridge structure in longitudinal, lateral, and vertical directions. The maximum sampling frequency of the MEMS accelerometer is 200 Hz. Even though, it is set to 100 Hz in this dissertation, which is minimum 4 times higher than typical eigenfrequencies of a bridge structure in the range of 0.1 to 25 Hz. Acceleration ranges can be defined in the ranges of $\pm 2g/\pm 4g/\pm 8g/\pm 16g$, which is set to $\pm 2g$.

The MEMS accelerometer is factory calibrated and can perform automatic continuous self-calibration during the measurements (Datasheet BNO055, 2016). However, this functionality is turned off to avoid its direct influences on the raw measurements and thus obtaining calibration parameters in a robust and reliable procedure as described in section 2.4.

2.6 Summary

A suitability analysis of the cost-effective MEMS accelerometers used for kinematic deformation monitoring of bridge structures is investigated in this chapter. It is conducted based on the three-step scenario as follows: In the first step, an automatic, robust, and accurate calibration procedure is proposed and implemented to compensate the systematic errors of the MEMS accelerometers including biases, scale factors, and non-orthogonality angles between the axes. Moreover, it allows to enhance the accuracy of displacements derived from double integration of the acceleration measurements over time. In addition, it assists to select an optimal MEMS accelerometer with less impact of the systematic errors.

To perform the calibration, the MEMS accelerometer is attached to the KUKA youBot and placed in a climate chamber, which allows to perform automatic measurements for fixed positions and for certain time intervals over different temperature ranges. The calibration model is solved based on two different adjustment models, namely, GHM–GEM and GHM–VCE. The analysis demonstrates a very close approximation of the parameters from both approaches, in particular for the biases and the scale factors. However, the GHM–GEM approach is computationally more efficient than the GHM–VCE. Furthermore, the entire recorded acceleration measurements are taken into account in the estimation procedure, which leads to better estimates of *a posteriori* standard deviations of the acceleration measurements. The analysis shows a minor impact of the calibration parameters on the estimates of the modal parameters for a short time interval, e.g., a few minutes. However, to perform kinematic deformation monitoring for a longer period of time, e.g., 10 minutes or higher, the calibration parameters are required to be considered.

The second step of the aforementioned scenario is accomplished under a controlled excitation experiment by using a shaker which includes high-end reference accelerometer. Thus, it allows to estimate the harmonic oscillation parameters including frequency, amplitude and phase shift. Additionally, it enables to compare and validate the estimates of the parameters with their known values as well as with those estimation obtained from other MEMS accelerometers or the reference sensor. Moreover, such experiment allows to check for time synchronisation between the MEMS accelerometers based on the estimates of the phase shifts. According to the analyses, the estimated phase shifts between the measurements of different MEMS accelerometers fluctuate up to 5° , i.e., approximately at a level of maximum 0.01 s time delay in our case, that is sufficient to characterise the eigenforms.

In the third step, a static test experiment is conducted to estimate offset and drift coefficients over a long period. In addition, it allows to handle auto-correlation for the 3D acceleration data and to characterise an underlying stochastic distribution model by employing the AR process with t-distributed errors. Therefore, it assists to select a suitable sensor with less AR model order, which accounts for the less auto-correlation. Furthermore, it is also possible to handle cross-correlation by employing the VAR process, which is given in Kargoll et al. (2020b).

To this end, the aforementioned three-step scenario assist us in the selection process to optimally choose the proper MEMS accelerometers for the purpose of the kinematic deformation monitoring of bridge structures. This is performed by selecting the MEMS accelerometers, which their measurements have been less influenced by the systematic errors. Additionally, long-term stability of the measurements with minimal offset and drift values over different temperature ranges are investigated. Moreover, the stochastic model parameters as well as auto-correlation model parameters assist us in such selection process. Besides, it is desired to select a MEMS accelerometer, which has a better uncertainty of the measurements in X and Y directions. It should be noted that the MEMS accelerometers used in this dissertation have the worst uncertainties in Z direction compared to two other axes. Consequently, the MEMS sensors are set-up along their X and Y axes parallel to the vertical and the lateral directions of bridge structures.

3 Potential of Image-Assisted Total Stations for Bridge Monitoring

3.1 Introduction

Alternative to the MEMS accelerometers, geodetic measurement systems can be used for either short- or long-term deformation monitoring of bridge structures. To perform kinematic deformation monitoring, a proper sensor is selected which has a capability to detect maximum excitation amplitudes corresponding to the eigenfrequencies of an oscillating structure. In addition, it should be able to perform measurements with a required sampling frequency (Lienhart et al., 2017).

An IATS as a modern geodetic sensor allows to acquire polar measurements as well as video frames, which are typically captured by either an embedded or external camera. The combination of both aforementioned types of measurements is beneficial, since an accurate metric displacement time series can be generated for sequences of the video frames, which enables to perform displacement and vibration monitoring, cf. Ehrhart and Lienhart (2015a,b). The state-of-the-art IATSs, e.g. Leica Nova MS50/MS60 MultiStations, has a narrow angle on-axis telescope camera with capability of a digital zoom factor (e.g. $8\times$ zoom factor), which is used to magnify captured signalised or non-signalised targets. Subsequently, one can perform displacement analysis at the level of millimetre/submillimetre accuracy.

The IATS is superior to a conventional RTS due to the following reasons (Ehrhart, 2017b):

- no need to set-up retroreflective prisms on the structures,
- reducing costs,
- mitigating labour works,
- allowing to detect both signalised passive targets or non-signalised (e.g. natural, structural) ones by using image/video data,
- allowing to generate displacement time series with a higher accuracy in an image plane perpendicular to the viewing direction,
- higher and more constant sampling frequency, which allows to extract higher eigenfrequencies than those from RTS,
- extracting low and stable eigenfrequencies in long-term deformation monitoring,
- less aliasing effects of vibration signals due to detection of higher frequency ranges.

To perform highly accurate deformation monitoring by means of the IATS, the instrument warm-up effects, proper camera and total station calibrations, mapping parameters (i.e. to relate the image coordinate system to the total station coordinate system), and a suitable image processing algorithm are required (Ehrhart and Lienhart, 2017a; Ehrhart, 2017b). The readers are referred to Ehrhart (2017b) for further detailed explanations concerning the aforementioned procedures.

Lighting condition is a challenging issue in image-based measurement systems such as IATS that makes the measurements even impossible in case of a complete dark condition (Lienhart et al.,

2017), which is not the case in the RTS or conventional total stations. To overcome this problem, Bürki et al. (2010) and Wagner et al. (2013) utilise a light emitting target. However, often such a target needs a power supply as well as an accessibility to the bridge structure. Ehrhart and Lienhart (2015b) uses natural targets as an alternative solution to the passive/active targets. Even though, it still requires light sources at night. Moreover, low lighting increases image noise and thus, depending on the target type and its corresponding detection approach, the resulting accuracy might be affected.

The feasibility of an optimal passive target pattern and its automatic, fast, and accurate centroid detection approach are investigated in Omidalizarandi et al. (2019a). The proposed approach is robust and reliable with respect to poor environmental conditions, such as low lighting, dusty situations, and skewed angle targets.

Omidalizarandi et al. (2018) benefit from the aforementioned passive target centroid detection procedure for the purpose of displacement and vibration monitoring of a footbridge structure in vertical direction. Therefore, a displacements time series is generated in the pixel unit by using video frames that are captured by the telescope camera of the IATS. Afterwards, it is converted to a meaningful metric unit such as millimetre by calibrating a vertical angular conversion factor of the telescope camera in a laboratory environment.

Non-orthogonal viewing direction of part of a monitored bridge structure towards the IATS is also an important factor, which has an impact on the uncertainty of the generated displacement time series. Ehrhart (2017b) proposed an approach to encounter this problem for different set-ups of the IATS. As a simple approach, the 3D point clouds around a target can be acquired, e.g., by means of the scanning functionality of the IATS. Subsequently, the normal vector of a plane is calculated, which is used to project the target to a plane that is orthogonal to the viewing direction.

The state-of-the-art of the IATS, e.g., the Leica MS50 with a practical sampling frequency of 10 Hz, has a limitation to detect higher frequencies due to its low sampling frequency. To overcome this problem, a newer version of the IATS such as the Leica MS60 can be used. Alternatively, a high-resolution digital camera with higher sampling frequency might be attached on top of the IATS by means of a clamping system. Subsequently, EOPs between the fused sensors can be determined similar to researches of Omidalizarandi and Neumann (2015); Omidalizarandi et al. (2016). For this purpose, the TLS measurements should be replaced by the IATS measurements. To estimate the EOPs between the IATS and the external digital camera, the space resection in photogrammetry by using the collinearity condition equations, the 3D Helmert transformation, and the constraint equation are solved within a GHM and GMM adjustment. The observables comprise the measurements of signalised target points, which need to be acquired by means of the IATS, a high resolution digital camera, and a laser tracker for the validation purpose. Furthermore, Omidalizarandi et al. (2019b) have proposed three adjustment models to estimate the EOPs robustly and accurately.

Such a sensor fusion technique allows to perform long-term congruence deformation monitoring in addition to its capability in kinematic deformation monitoring. However, merely using state-of-the-art wide angle full-frame digital single-lens reflex (DSLR) camera, e.g., Nikon D750, for detecting such a small displacement, i.e., submillimetre range, is not possible. It is due to the fact that such a camera has a larger field of view (FOV) and covers a larger area of an oscillating object with less resolution. Therefore, a telescopic lens could be attached to the aforementioned DSLR camera to decrease the FOV and also to increase the resolution.

In case of the IATS, a short-term kinematic deformation monitoring is carried out by identifying the modal parameters based on generated displacement time series. For this purpose, Omidalizarandi et al. (2018) employed an observation model consisting of an undamped harmonic oscillation (UDHO) model in terms of a sum of sinusoids, an auto-correlation model in terms of the AR process, and a stochastic model in the form of the heavy-tailed family of scaled t-distributions.

Next, the aforementioned three parametric models are jointly adjusted by means of the GEM algorithm. Kargoll et al. (2019) and Omidalizarandi et al. (2020) extended the aforementioned observation model by considering the DHO model instead of the UDHO model. Therefore, it allows to estimate the damping ratio coefficient as an additional unknown parameter within the adjustment procedure. The readers are referred to chapter 4 for further information.

The generated displacement time series from the IATS can also be used for the long-term deformation monitoring despite of its application in short-term kinematic deformation monitoring. For this purpose, an absolute deformation time series can be generated by comparing an actual video frame with an initial one that is captured at the beginning of a measurement campaign. However, target detection through a proper image processing algorithm, stability of the instrument during the monitoring, influences of weather conditions such as air temperature and humidity as well as frequent measurements of control points play important roles on the accuracy of long-term deformation monitoring.

To perform long-term kinematic deformation monitoring, the recorded acceleration data by the MEMS accelerometer may be fused with the generated displacement data based on video frames of the passive target captured by the IATS. The passive target can be attached in the vicinity of one of the MEMS accelerometers for an efficient and a reliable data fusion. The aforementioned data fusion seems to be vital, since the computed absolute position changes by double integrating the MEMS acceleration data drift very fast (typically already in a few seconds). Therefore, the CUPT is accomplished within the framework of the KF to solve the aforementioned data fusion.

3.2 Data Acquisition and Preprocessing

The state-of-the-art IATS comprises a robotic total station functionality and an imaging sensor. Additionally, 3D laser scanning and GNSS connectivity might also be included, e.g., the IATS of type Leica MS50. Further details description of the IATS can be found in Wagner et al. (2014).

The IATS measurements consist of the polar measurements such as horizontal directions, vertical angles, and distance measurements in addition to the video streams that are captured by an embedded or external attached camera. Additionally, having embedded on-axis telescope camera with capabilities of an optical magnification as well as the **camera zoom factor** functionality allows to perform displacement monitoring in a submillimetre range (Ehrhart and Lienhart, 2015a; Omidalizarandi et al., 2018). Furthermore, the IATS benefits from the motorised axes of rotations, which can be utilised for automatic and autonomous measurements of specified active targets (i.e. retroreflective prism targets) or passive targets (i.e. signalised or non-signalised targets) at different time epochs.

In order to utilise the IATS for displacement and vibration analysis of the bridge structures, as a preliminary step, the displacement time series is generated in the following steps:

1. initial pointing to a passive target that is attached to the bridge structure and reading the polar measurements,
2. reading the polar measurements in particular slope distance measurements that is needed for the conversion from pixel to metric unit,
3. turning on the autofocus of the telescope camera of the IATS to capture sharp images,
4. reducing FOV by $8\times$ digital zoom,
5. capturing the video frames of the passive target at different time epochs,
6. calculating the relative displacements by subtracting the target centroids that are extracted from the sequences of the video frames,

7. calculating the angular conversion factor of the telescope camera,
8. conversion from pixel unit to metric unit.

Such a measurement system is advantageous over other vision-based measurement systems, since it allows to obtain displacements in metric unit without the need for an additional measurement system.

To generate displacement time series for the purpose of short-term kinematic deformation monitoring, the extracted passive target centroids are always averaged over a certain period of time to define the equilibrium position. Therefore, the displacement time series is calculated as follows:

$$\delta_{y_i} = \alpha S(y_i - \bar{y}), \quad (3.1)$$

where y_i is the target centroid that is extracted at epoch i [px], \bar{y} is the average of the extracted target centroid within a certain period of time [px], S is the slope distance [mm], and α is the angular conversion factor ["/px]. Further explanations regarding the target centroid extraction as well as calibration of the angular conversion factor of the telescope camera of the IATS are provided in the following sections.

In order to benefit from an individual functionality of the IATS, the GeoCOM interface (Leica Geosystems, 2014) is used in the Python programming language (Omidalizarandi et al., 2018). Moreover, the stability over time for either short- or long-term deformation monitoring can be controlled by measuring the tilt of the IATS in the horizontal and vertical directions similar to the research of Ehrhart and Lienhart (2015b). For a more precise conversion, the instrument's axes errors, vertical index error, and collimation error can also be considered.

3.3 Automatic and Accurate Passive Target Centroid Detection

An optimal passive target composes of a circular border with four intersected lines and its centroid detection algorithm is proposed by Omidalizarandi et al. (2019a). The proposed target centroid detection approach is proved to be an accurate, robust, reliable, and fast under poor environmental conditions such as low lighting, dusty environment, and skewed angle targets. In addition, in case of poor initial sighting to the target or an incomplete viewing target pattern, the proposed approach is still able to reliably localise the target. The aforementioned passive target design is cheap regarding its manufacturing costs, which allows to attach several of them close to the MEMS accelerometers. Thus, the video frames of the aforementioned passive targets, that are captured by the telescope camera of the IATS, can be used for the purpose of either short- or long-term deformation monitoring.

The manual initial sighting to the passive target is accomplished merely at the first measurement epoch. Afterwards, all subsequent measurements are carried out automatically by means of motorised axes of rotations of the IATS by using the measurement values of the initial pointing similar to researches of Ehrhart and Lienhart (2015a,b).

The passive target centroid detection algorithm proposed by Omidalizarandi et al. (2019a) is briefly explained in the following. For each image frame that is extracted from the captured video streams, the localisation of the passive target is performed by using the Hough circle transform (HCT) (Kaehler and Bradski, 2016). Afterwards, the template matching is carried out to detect the circular target border among all spurious detected circles. Therefore, it allows one to crop the images to a region of interest that contains the passive target. Its advantages are twofold: (1) limiting the search space to extract relevant edge features of the target and (2) speeding up the process (Reiterer and Wagner, 2012). The cropping is performed based on the measurements of the slope distance to the target, object size of the target, and the horizontal and vertical FOVs of the telescope camera

of the IATS as follows:

$$FOV = 2 \cdot \tan^{-1} \left(\frac{D}{2 \cdot S} \right) \quad [\text{rad}], \quad (3.2)$$

$$d_w = \frac{w \cdot FOV}{FOV_h \cdot \left(\frac{\pi}{180} \right)} \quad [\text{px}], \quad (3.3)$$

$$d_h = \frac{h \cdot FOV}{FOV_v \cdot \left(\frac{\pi}{180} \right)} \quad [\text{px}], \quad (3.4)$$

where S is the slope distance [m], D the target size in object space [m], d_w , d_h the target width and height [px], w and h the width and heights of the captured image [px], FOV_h and FOV_v the horizontal and the vertical FOVs, which in case of the IATS, are set to 1.25° and 0.95° , respectively (Omidalizarandi et al., 2019a). It should be noted that the circle detection in a noisy image is challenging. Therefore, the precise manual initial sighting from the previous step assists to reliably recognise the passive target.

The median blur and bilateral filtering are applied to smooth the cropped images by reducing the noise and to preserve the sharp edges. To extract line features of the cropped image, the line segment detector (LSD) (Grompone von Gioi et al., 2012) is applied. It is advantageous compared to the Canny edge detector (Canny, 1986), since there is no need to connect fragmented extracted edges. Additionally, it is only parametrised at the beginning and does not need any further changes in case of either poor lighting conditions or viewing angles (Omidalizarandi et al., 2019a).

In the next step, azimuths of the extracted lines are calculated and sorted in a descending order. Then, the azimuths with maximum bin values are selected based on a histogram of the azimuths in an iterative procedure. In each iteration, the LSD lines with a deviation less than a predefined angle threshold of 15° from the corresponding azimuth bin value are selected. Afterwards, the selected LSD vector lines are converted to LSD raster lines to increase the redundancy. The random sample consensus (RANSAC) (Fischler and Bolles, 1981) line fitting algorithm is then applied to fit the line to the LSD raster lines and to discard spurious lines. To increase the reliability and robustness of the fitted lines, a Huber-robust line fitting (Kaehler and Bradski, 2016) is applied to those LSD raster lines within a predefined buffer width from each side of the fitted RANSAC line. The fitted Huber lines are intersected. Subsequently, the intersected points are clustered by using the k -d tree neighbourhood algorithm and by considering a threshold of 2 pixels. Afterwards, the maximum cluster is selected and a final intersection point is calculated based on the weighted average values of the interested points. Figure 3.1 illustrates an overview of the proposed target centroid detection algorithm. For further information, the readers are referred to Omidalizarandi et al. (2019a).

3.4 Conversion of Displacement Time Series from Pixel to Metric Units

The calculated displacement time series in pixel units is converted to metric units by using calibration parameters of the IATS. The calibration parameters, which are related to its optical measurement system, comprise the internal calibration of the telescope camera of the IATS including focal length, principal point, radial, and tangential distortions. In addition, the corresponding total station related error sources consist of, e.g., zero offset, horizontal collimation error, vertical index error, tilting axis error, and compensator index error.

In this dissertation, the internal calibration of the telescope camera of the IATS is neglected, since it has small effect on the short-term kinematic deformation monitoring due to the relative computation of the displacement time series for the sequence of the video frames (Ehrhart and Lienhart,

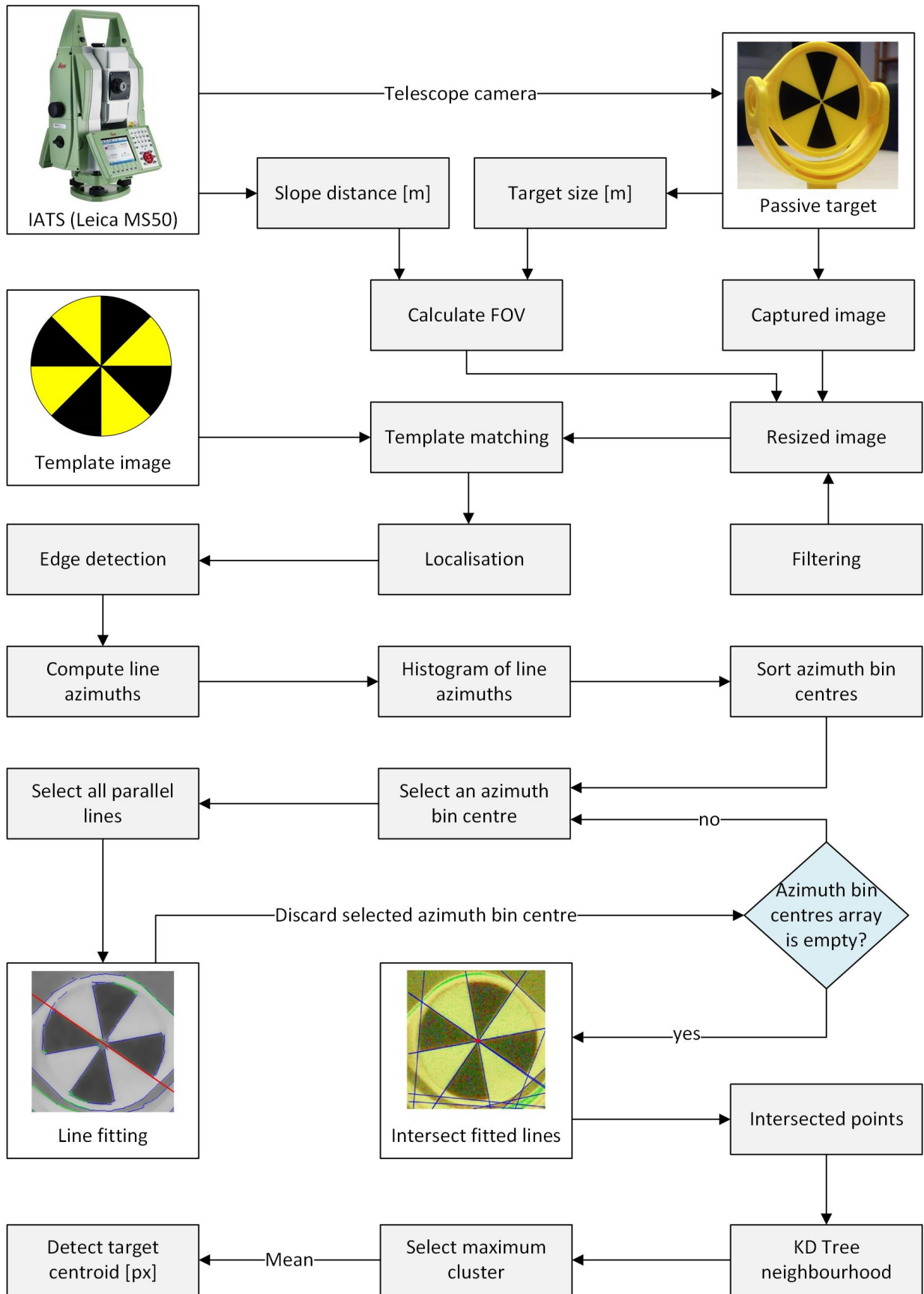


Figure 3.1: An overview of the passive target centroid detection algorithm.

2015a). In addition, reduction of the FOV by $8\times$ digital zoom allows to take a small central portion of the image captured with $1\times$ digital zoom. Subsequently the effect of the aforementioned camera calibration parameters is mitigated (Omidalizarandi et al., 2018). Figure 3.2 illustrates captured images by the telescope camera of the IATS for two different distances. As previously stated, the FOV is reduced by $8\times$ digital zoom and the image resolution is set to 320×240 px. As it can be seen, the target centroid is located approximately close to the centre, which is due to the precise manual initial sighting at the beginning of the measurements. Additionally, the proposed target pattern including redundant line features mitigates the impact of the radial and tangential distortions at centre of the images. Furthermore, the remaining systematic errors are treated as coloured measurement noise, which is separated from white noise through the AR process (Omidalizarandi et al., 2018). Further explanation of the aforementioned AR procedure is described in the next chapter.

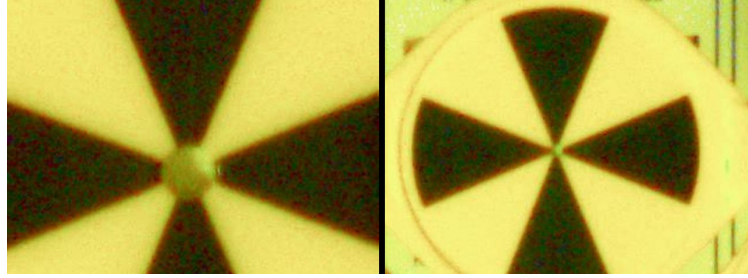


Figure 3.2: The IATS telescope camera images: image resolution of 320×240 px and $8\times$ digital zoom for distances of 5 m (left), and 23 m (right).

A long-term deformation monitoring at the accuracy level of millimetre/submillimetre can be accomplished by using a deformation time series, which is generated from the video frames of the IATS. For this purpose, the internal camera calibration of the IATS can be performed similar to researches of Walser (2004); Ehrhart (2017b); Zhou et al. (2017) to model the corresponding systematic errors and to increase the reliability of the measurements.

The generated displacement time series is converted from pixel to metric units by means of the angular conversion factor of the telescope camera of the IATS, which needs to be calibrated. In this dissertation, since the displacement and vibration analysis is performed in the vertical direction, the vertical angular conversion factor is merely calibrated. To begin with its calibration, a coded target pattern is designed in AutoCAD 2016 software with fixed coded target distances. Since the telescope camera of the IATS has a very small FOV, the aforementioned coded target pattern is plotted in two different paper sizes of A2 and A4 with distances of 0.09 and 0.0335 m. Therefore, it allows to cover more coded targets in the images captured at different distances up to approximately 30 m (Omidalizarandi et al., 2018).

A target centroid of the coded target in the image space is extracted based on the image processing techniques as described in Omidalizarandi et al. (2018). To obtain the 3D object coordinates of the coded targets, multiple images from different viewing angles are captured by using a high-resolution digital camera. Afterwards, the target centroids extracted in the image space are put into the space resection bundle adjustment and solved in an iterative procedure.

The vertical angular conversion factor is computed based on the following equations:

$$psy_i = \frac{\delta_{XYZ_i}}{\delta_{xy_i}} \quad [\text{mm/px}], \quad (3.5)$$

$$psy = \hat{p}_1 \cdot S + \hat{p}_0, \quad (3.6)$$

$$\hat{p}_v = \hat{p}_1 \cdot S + \hat{p}_0, \quad (3.7)$$

$$F\hat{O}V_v = \frac{\hat{p}_v \cdot h}{S} \quad [\text{rad}], \quad (3.8)$$

$$\hat{\alpha}_v = \frac{F\hat{O}V_v}{h} \cdot \frac{180 \cdot 3600}{\pi} \quad ["/\text{px}], \quad (3.9)$$

where δ_{XYZ_i} is the difference between 3D coordinates of the target centroids in [m], δ_{xy_i} is the difference between the target centroids in both x and y directions in [px], psy_i is the pixel size in the y direction at a specified slope distance, \hat{p}_1 and \hat{p}_0 are the estimated coefficients of the first degree polynomial, S is the slope distance in [m], \hat{p}_v is the estimated pixel size value obtained from fitted polynomial at a specified slope distance, $F\hat{O}V_v$ is the estimated vertical FOV in [rad], h is the height of the image in [px] and $\hat{\alpha}_v$ is the estimated vertical angular conversion factor in ["/px]. To fit the first degree polynomial and to evaluate them, for example, *polyfit* and *polyval* MATLAB routines can be used, respectively (Omidalizarandi et al., 2018).

The estimated $\hat{\alpha}_v$ is equal to 1.9583 ["/px], which is a close approximation of 1.9632 ["/px] given in Ehrhart and Lienhart (2015a). Additionally, the estimated $F\hat{O}V_v$ is equal to 1.04442°, which slightly differs from its corresponding value given in the user manual of the sensor (Omidalizarandi et al., 2018).

3.5 External Calibration of Image-Assisted Total Stations and Digital Camera

As previously mentioned, to tackle the low sampling rate problem of the IATS, e.g., Leica MS50, a high-resolution digital camera with higher sampling rate may be attached on top of the IATS similar to the researches of Omidalizarandi and Neumann (2015); Omidalizarandi et al. (2016). Typically, wide angle DSLR cameras are not able to detect such small displacements in submillimetre range due to a larger FOV with considerably less resolution. To overcome this problem, a telescopic lens might be attached to the aforementioned DSLR cameras to decrease the FOV and therefore to increase the resolution.

Additionally, the high-resolution DSLR camera may allow to perform long-term congruence deformation monitoring both in direction of the laser beam of the IATS and perpendicular to that despite of its capability in short-term kinematic deformation monitoring. This can be carried out by extracting points, lines or plane features both from the 3D scanning point clouds and the images captured at different epochs of time. Subsequently, aforementioned data fusion is beneficial, since both measurements are complementary to each other and the weakness of one sensor data is compensated by the strength of another one. However, in case of large incidence angles, the measurements obtained from both sensors do not necessarily enhance the accuracy of deformation monitoring, but increase the precision (Omidalizarandi et al., 2019b). In such a case, multiple images from free set-ups of cameras may additionally be captured. The discussion of congruence deformation monitoring is out of scope of this dissertation and may be conducted in future work.

In the context of sensor fusion, the relative orientation parameters between the sensor origins must be known. For geodetic sensors including embedded cameras, such as the IATS with the telescope or overview cameras, the EOPs are typically known from a calibration procedure in the manufacturing process. By contrast, in case of an externally attached camera, the EOPs are priorly unknown, which should be determined through a proper calibration procedure (Omidalizarandi et al., 2019a).

To determine the EOPs between the high-resolution DSLR camera and a geodetic sensor such as a TLS, Omidalizarandi and Neumann (2015); Omidalizarandi et al. (2016, 2019b) benefit from signalised target points. The observables comprise the 2D coordinates of the signalised target points

acquired from the captured images, their corresponding 3D coordinates measured by the TLS as well as horizontal angle reading of the TLS (Az). Additionally, high accurate 3D coordinates measured by a laser tracker are used for the purpose of validation. For simplicity, the observables are assumed to be independent and therefore the stochastic model is defined as a block diagonal matrix. In addition, the internal camera calibration parameters are calculated in advance from the laboratory calibration to prevent their correlation with the EOPs (Omidalizarandi et al., 2019b).

The deterministic models are defined based on the space resection technique in photogrammetry by using the collinearity condition equations (Eqs. 3.10 and 3.11), the 3D Helmert transformation (Eq. 3.12), and a constraint equation (Eq. 3.13). The unknown parameters consist of the 6 EOPs between the the TLS and the digital camera, i.e., three translations (X_C, Y_C, Z_C) and three orientations (κ, φ, ω), the 7 EOPs between the TLS and the laser tracker, i.e., the scale (λ), the translations (X'_c, Y'_c, Z'_c), and the orientations ($\kappa', \varphi', \omega'$), as well as the target coordinates in the TLS coordinate system ($X_{TLS}, Y_{TLS}, Z_{TLS}$) (Omidalizarandi et al., 2019b). Thus, the mathematical functions are as follows:

$$F_x = x' - f \frac{p}{q}, \quad (3.10)$$

$$F_y = y' - f \frac{s}{q}, \quad (3.11)$$

$$\mathbf{F} = \lambda \mathbf{R}_{\kappa' \varphi' \omega'} \begin{bmatrix} X_{TLS} \\ Y_{TLS} \\ Z_{TLS} \end{bmatrix} + \begin{bmatrix} X'_c \\ Y'_c \\ Z'_c \end{bmatrix} - \begin{bmatrix} X_L \\ Y_L \\ Z_L \end{bmatrix}, \quad (3.12)$$

$$\mathbf{F} = \begin{bmatrix} X \\ Y \\ Z \end{bmatrix} - \begin{bmatrix} X_{TLS} \\ Y_{TLS} \\ Z_{TLS} \end{bmatrix}, \quad (3.13)$$

where (x', y') are rectified target coordinates in the image space according to Brown's equations (Duane, 1971), f is the focal length, (X_L, Y_L, Z_L) are the target coordinates in the laser tracker coordinate system, (X, Y, Z) are the unknown target coordinates in the TLS coordinate system. The rotation matrix ($\mathbf{R}_{\kappa' \varphi' \omega'}$) is the product of the individual rotation matrices which are derived as follows:

$$\mathbf{R}_{\omega'} = \begin{bmatrix} 1 & 0 & 0 \\ 0 & \cos \omega' & \sin \omega' \\ 0 & -\sin \omega' & \cos \omega' \end{bmatrix},$$

$$\mathbf{R}_{\varphi'} = \begin{bmatrix} \cos \varphi' & 0 & -\sin \varphi' \\ 0 & 1 & 0 \\ \sin \varphi' & 0 & \cos \varphi' \end{bmatrix},$$

$$\mathbf{R}_{\kappa'} = \begin{bmatrix} \cos \kappa' & \sin \kappa' & 0 \\ -\sin \kappa' & \cos \kappa' & 0 \\ 0 & 0 & 1 \end{bmatrix}.$$

The (p, s, q) parameters given in Equations 3.10 and 3.11 are calculated by transforming the TLS

target coordinate to the 3D camera coordinate system by means of the following equation:

$$\begin{bmatrix} p \\ s \\ q \end{bmatrix} = \mathbf{R}_{\kappa\varphi\omega} \left(\mathbf{R}_{Az} \begin{bmatrix} X_{TLS} \\ Y_{TLS} \\ Z_{TLS} \end{bmatrix} - \begin{bmatrix} X_c \\ Y_c \\ Z_c \end{bmatrix} \right), \quad (3.14)$$

where the rotation matrix $\mathbf{R}_{\kappa\varphi\omega}$ is set up in analogy to $\mathbf{R}_{\kappa'\varphi'\omega'}$. In addition, the \mathbf{R}_{Az} is the rotation matrix based on the measured Az , which is defined of the same type as $\mathbf{R}_{\kappa'}$.

Omidalizarandi et al. (2019b) proposed three adjustment models to estimate the EOPs between the fused sensors by a rigorous bundle adjustment procedure robustly, and accurately. The developed and implemented adjustment methods are as follows:

1. the EM algorithm to solve the GHM with grouped t-distributed random deviations,
2. the EM algorithm to solve the qGMM with t-distributed pseudo-misclosures,
3. a classical least-squares procedure to solve the GHM including the VCE and outlier removal procedure.

The first adjustment model, which is an extension to Koch (2014b), allows for observation group-specific scale factors and group-specific dfs. The second adjustment model is established by transforming the GHM's condition equations into observation equations of a substitute GMM. Subsequently, instead of downweighting outlying observations individually, all observations which are causing large misclosure values are uniformly downweighted. The third adjustment model takes the form of a classical GHM. Additionally, the VCE is applied to recalculate the covariance matrix of the observations in an iterative manner. The statistical testing such as chi-square or t-student tests are applied to identify outliers and to exclude them (Schneider, 2008).

The non-linear deterministic models are linearised based on the Taylor series expansion. Therefore, a direct linear transformation together with the RANSAC algorithm are applied to estimate the initial values for the collinearity equation. Moreover, the closed-form solution by using unit quaternions is applied to estimate the initial values for the 3D Helmert transformation (Horn, 1987). Figure 3.3 shows a scheme of the proposed algorithm. The readers are referred to Omidalizarandi et al. (2019b) for further information.

3.6 Sensor Specifications and Measurement Systems

Previous sections described a general procedure that could be applied to any type of the IATS. However, in this dissertation, an IATS of type Leica Nova MS50 MultiStation with a practical sampling frequency of 10 Hz is used to perform displacement and vibration analyses. The total station functionalities of the IATS allow to perform polar measurements with following accuracy levels:

- an angular accuracy of 1'' (according to ISO 17123-3),
- an optical-distance measurement accuracy of 1 mm + 1.5 ppm for prism targets from 1.5 to 10000 m (according to ISO 17123-4),
- an optical-distance measurement accuracy of 2 mm + 2 ppm for non-prism targets, e.g., passive targets, from 1.5 to 2000 m.

In addition, the used IATS consists of an overview camera with diagonal FOV of 19.4° and a telescope camera with diagonal FOV of 1.5°. Both the telescope and the overview cameras comprise 5

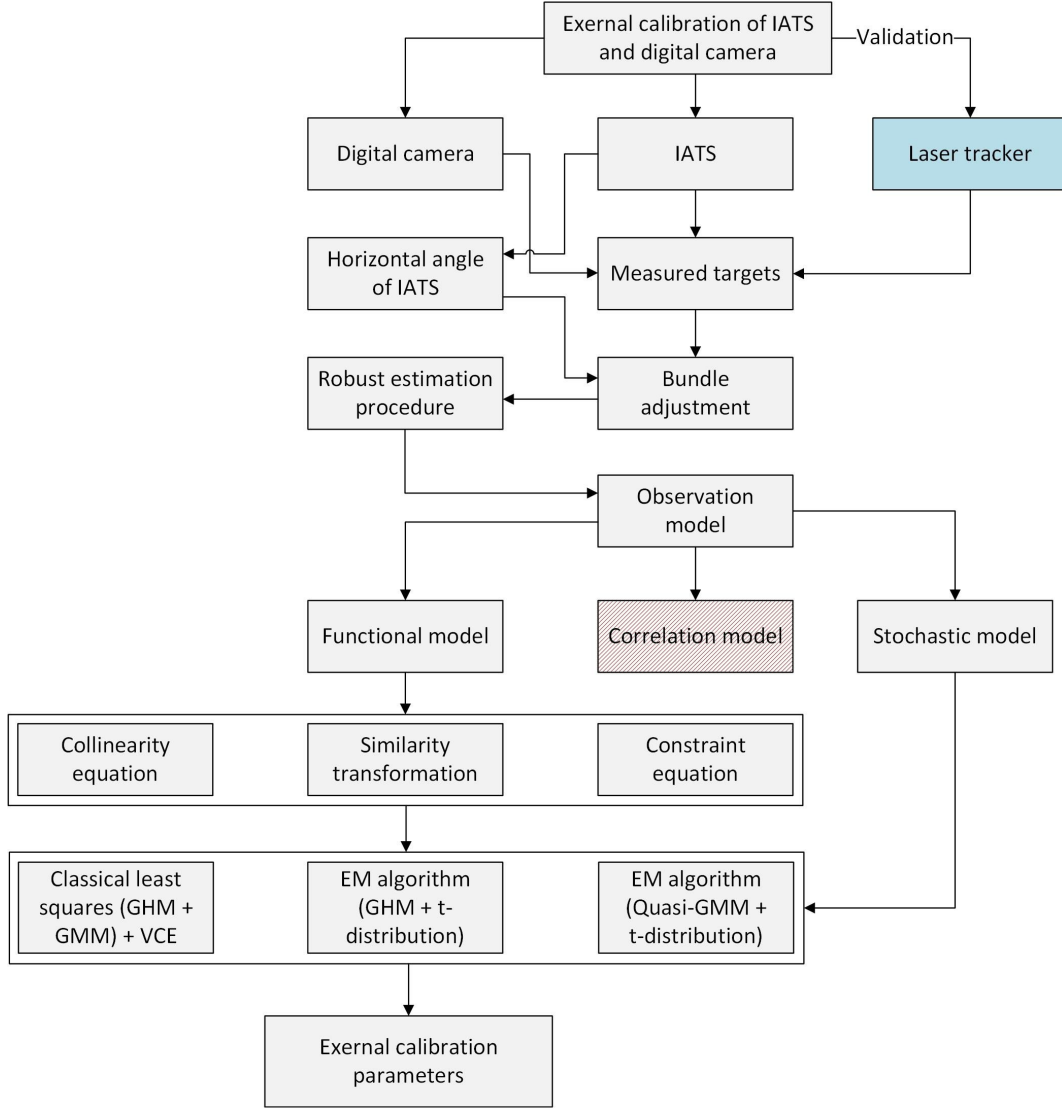


Figure 3.3: A scheme of the robust external calibration of the IATS and digital camera by using signalised targets. The correlation model is neglected for simplicity.

megapixels CMOS sensors. The telescope camera is an on-axis camera with $30\times$ optical magnification of the overview camera, which is located in the optical path of the IATS. The horizontal and vertical FOVs of the telescope camera of the used IATS are 1.3° and 1.0° . The angular resolution (α) of the telescope camera is approximately $1.7''/\text{px}$, which is calculated by dividing the diagonal FOV by the diagonal length, in [px], of an captured image (Leica Geosystems, 2013).

The resolutions of the captured images vary from $320 \times 240 \text{ px}$ to $2560 \times 1920 \text{ px}$. However, the Leica MS50 allows to capture video streams with a resolution of $320 \times 240 \text{ px}$ (Ehrhart and Lienhart, 2015a). The white balance is set to ‘automatic’ and the autofocus is set to ‘on’ to capture sharp images. As previously stated, the FOV is reduced by $8\times$ zoom using the **camera zoom factor** functionality of the GeoCOM interface to increase the resolution. In addition, the reflectorless distance measurements to the passive targets allow to precisely set the telescope’s focus motor position (Ehrhart and Lienhart, 2015a). The entire video acquisition procedure is controlled via our self-developed graphical user interface in the Python programming language (Omidalizarandi et al., 2018).

3.7 Summary

A good feasibility of an IATS for displacement and vibration analysis of bridge structures is shown in this chapter.

The IATS as a modern geodetic sensor benefits from polar measurements as well as two embedded on-axis telescope and overview cameras. The combination of both types of the measurement allows to perform displacement/deformation analysis of bridge structures in submillimetre/millimetre range accuracy.

The IATS is privileged over the MEMS accelerometers in either short- or long-term displacement monitoring. It is due to the reason that absolute position changes derived from double integration of the MEMS acceleration data are drifting fast. However, in short-term displacement monitoring, e.g., a few seconds, it is possible to obtain a higher accurate displacement data from the MEMS acceleration data. It can be achieved by double integration of the DHO model (see section 4.5). Additionally, the MEMS accelerometers are more suitable to perform vibration analysis and to detect all eigenfrequencies, e.g. in a range of 0.1 to 25 Hz that often occur in bridge structures. However, the state-of-the-art IATS, e.g. Leica MS60, allows to identify eigenfrequencies of bridge structures up to 15 Hz (Ehrhart, 2017b) by considering the Nyquist sampling theorem.

The IATS merely allows to perform vibration analysis in only two directions orthogonal to viewing direction. In addition, it is challenging to characterise eigenforms by using one IATS. Therefore, additional IATS or cameras (e.g. DSLR camera) should be utilised. On the contrary, the MEMS accelerometer is cost-effective and therefore numerous of them can be set-up at different positions of bridge structures. Therefore, the acceleration data are recorded in vertical, lateral, and longitudinal directions. Subsequently, the eigenforms can be characterised in all three directions.

Calibration parameters have a great affect on the accuracy of the displacement/absolute deformation time series, which are obtained from the IATS in either short- or long-term deformation monitoring. However, the MEMS acceleration data are recorded directly and there is no need for an additional data conversion. Furthermore, as previously stated, the calibration parameters of the MEMS accelerometers have less impact on the estimated modal parameters in short-term kinematic deformation monitoring. However, they should be considered for long-term deformation monitoring to achieve more accurate and reliable results.

The IATS is a contactless measurement system and therefore it can acquire measurements by being set up away from the bridge structures. The IATS is capable of capturing signalised/non-signalised targets and there is no need to set-up retroreflective prisms on the structures. In addition, it is noteworthy to mention that the IATS is advantageous to a conventional RTS for vibration analysis. It is due to the fact that the IATS has a higher and constant sampling rate, which enables to detect eigenfrequencies in a wider range with a higher accuracy.

A displacement time series is generated by measuring a slope distance to a passive target, and by using sequences of video streams of the passive target, which is captured by an embedded on-axis telescope camera of the IATS with a practical sampling frequency of 10–20 Hz depending on the instrument's type. The passive target is possibly attached in the vicinity of one of the MEMS accelerometers. An absolute deformation time series can be generated by comparing the detected targets that are obtained from actual video frames and an initial one captured at the beginning of measurement campaign. For this purpose, as a preliminary step, the feasibility of a proper passive target pattern consisting of four intersected lines with a circular border as well as its accurate and reliable centroid detection approach is investigated in (Omidalizarandi et al., 2019a). Next, a vertical angular conversion factor is calibrated in a laboratory environment, which allows to convert the generated displacement from pixel to metric units such as millimetre.

A comprehensive observation model consisting of the DHO model, an auto-correlation model in the form of an AR process, and a stochastic model in the form of heavy tailed family of scaled t-distributions with an unknown df and with unknown scale factor are employed and jointly adjusted by means of the GEM algorithm. Therefore, a robust and consistent procedure is proposed and implemented, which allows to robustly, accurately, and reliably perform displacement and vibration analyses of the bridge structures. Readers are referred to chapter 4 for more information.

The overall analyses demonstrate that the IATS, i.e., Leica MS50, is capable to identify eigenfrequencies up to 5 Hz, i.e., in the view of Nyquist sampling theorem. The vibration analyses obtained from both controlled excitation and the bridge structures demonstrate that amplitudes are estimated in submillimetre range accuracy and frequencies with an accuracy of better than 0.1 Hz. However, the damping ratio coefficients could not be detected as accurate as of that obtained from the MEMS acceleration data. This is due to the reason that the amplitudes of an oscillation are lower than the uncertainties of the measurements. In addition, the higher frequencies that are not detected are superimposed on the lower frequencies and therefore can change the magnitudes of the amplitudes (Omidalizarandi et al., 2019c).

To overcome the deficiency of the IATS with a low sampling frequency, a high resolution digital camera, that is equipped with a telescopic lens, can be mounted on top of it. To estimate the EOPs between the fused sensors, a robust sensor fusion approach is proposed and implemented which can be extended and used to other sensor fusion problems by defining a proper functional model. For this purpose, the four non-linear functional models are defined based on the space resection by collinearity equations, the 3D Helmert transformation, and the constraint equation. The aforementioned functional models are then solved in a rigorous bundle adjustment procedure by using the signalised target points. Next, the three different adjustment models are developed and implemented to robustly and high accurately estimate the EOPs between the fused sensors. In addition, the Laser tracker as a highly accurate reference sensor is considered for the purpose of validation.

The IATS and the MEMS accelerometer data sets can be used as complementary information to each other and the weakness of one sensor data is compensated by the strength of another one. Such information is particularly of interest when maximum amplitudes that are derived from an ambient excitation experiment for a bridge structure (e.g. a concrete bridge) are considerably small, i.e., at the level of the coloured measurement noise of the MEMS acceleration data. In addition, the MEMS acceleration data yields accurate estimates of the modal parameters such as eigenfrequencies, amplitudes, and damping ratio coefficients over short time but suffers from accuracy degradation with time for absolute displacements/positions estimates. Therefore, 1D CUPT is carried out by fusing the IATS displacement data and the MEMS acceleration data within the KF framework to encounter this problem (Omidalizarandi et al., 2019c). Further information is presented in chapter 5.

4 Robust Kinematic Deformation Monitoring of Bridge Structures

4.1 Introduction

Kinematic deformation monitoring of an oscillating structure, such as a bridge, plays an important role in characterising the dynamic behaviour of the structure. It further allows to assess the current states of the health of the structure and to avoid its deterioration at an early stage. To perform vibration-based SHM of the bridge structure from a geodetic point of view, the kinematic deformation monitoring is carried out by estimating the modal parameters including eigenfrequencies, eigenforms, and modal damping.

The aforementioned modal parameters, in particular, eigenfrequencies may vary case by case, depending on geometry, material, weight, stress, and strain of a structure (Neitzel et al., 2011). In addition, applied excitations as well as environmental conditions, e.g., temperature and humidity variations, cause changes of the modal parameters (Peeters et al., 2001; Rohrmann et al., 2000). Subsequently, it is a challenging task to recognise deterioration of a structure under such conditions. Typically, statistical hypothesis testing is accomplished to interpret the changes of the estimated modal parameters. However, a large-scale data acquisition, e.g., over a year, and under different loading and environmental conditions are required. Such comprehensive experiments are time consuming, which is out of scope of this dissertation. Therefore, to simplify the task, the focus is more on the estimation of the aforementioned modal parameters, i.e. for a specific temperature.

As a preliminary step, a suitable and cost-effective measurement system is required. It is desirable to choose a sensor which is capable of performing automatic and permanent vibration measurements at specified time intervals and with an adequate sampling frequency. For this purpose, as previously mentioned, a geo-sensor network of MEMS accelerometers are located at predefined positions, which are precalculated from the FEM analysis. Subsequently, the recorded acceleration data are used to identify all eigenfrequencies occurring at the bridge structures (in the view of Nyquist sampling theorem).

Robust, accurate, and automatic estimates of the aforementioned modal parameters is also a challenging task. Particularly, this is even more challenging when the structure is under continued imposition of the forces due to moving vehicles or wind. Thus, to have reliable realisation of the aforementioned modal parameters changes, a robust kinematic deformation monitoring procedure is developed and implemented, which can be extended and used for any type of time series data sets. The proposed approach is so-called robust time domain modal parameter identification (RT-MPI) technique. It can be conducted either in near real-time or in a post-processing to achieve robust and high accurate results.

The RT-MPI algorithm allows to automatically select an excitation (ambient) window. It further allows for an automatic and a reliable identification of initial eigenfrequencies as well as a robust and accurate estimation of eigenfrequencies, damping ratio coefficients and eigenforms of an oscillating structure. The modal parameters including eigenfrequency, damping ratio coefficient, amplitude, and phase shift are jointly estimated by means of the GEM algorithm, and by determining an observation model consisting of: (1) a DHO model, (2) the AR model of coloured measurement noise and (3) a stochastic model in the form of the heavy-tailed family of scaled t-distributions.

The eigenforms are characterised in a subsequent step, and by using the estimated parameters from the GEM algorithm. An overview of the proposed RT-MPI algorithm is sketched in Figure 4.1.

The proposed RT-MPI approach is superior to the state-of-the-art approaches such as data driven stochastic subspace identification (SSI-DATA) (e.g., Boonyapinyo and Janesupasaeree (2010)) or covariance driven stochastic subspace identification method (SSI-COV) (e.g., Magalhaes et al. (2009); Reynders et al. (2008)), due to the following reasons:

- achieve robust, reliable, and accurate estimates of the modal parameters,
- no need to define the system order,
- high accurate estimates of amplitudes in both units of $[m/s^2]$ and $[mm]$,
- being able to characterise a deflection eigenform in its true scale for selected excitation window within a short time interval.

This chapter continues by automatically selecting a proper excitation window for either ambient or forced vibration measurements, which is introduced in section 4.2. Eigenfrequencies are identified in section 4.3, which are used as initial frequency values within the adjustment procedure. Next, the robust estimation procedure is explained in section 4.4. The displacement analysis based on double integration is described in section 4.5. The characterisation of eigenforms is presented in section 4.6. Finally, a summary is given in section 4.7.

4.2 Ambient Window Selection

As a preliminary step, a proper excitation window is selected, which allows to optimally estimate the modal parameters, in particular, damping ratio coefficients (Omidalizarandi et al., 2020). The aforementioned excitation window is a so-called ambient window when it comprises ambient vibration measurements. In an ideal case, the excitation window, that consists of a perfect free vibration decay of a vibration signal, should be selected. However, selection of such an ambient window is often a crucial task, since a bridge structure is mostly under continuous imposition of loads such as moving vehicles or wind. Subsequently, the estimates of the damping ratio coefficients can be significantly influenced depending on the energy contents of the signal and the amplitudes (Wenzel, 2009a).

The ambient window selection procedure is started by detecting the peaks of vibration measurements, e.g., MEMS acceleration data. A minimum peak height value is set to three times standard deviation of the acceleration data. The k-nearest neighbour (KNN) search algorithm is applied within a range of 10 – 15 s to cluster the selected peaks. The aforementioned range is defined due to mitigating the energy contents of the imposed external forces in a few seconds. A peak with maximum value in each cluster is selected as a starting point. Acceleration data within an ambient window with a size of 10 s are selected, which are then input into the estimation procedure to estimate the modal parameters (see sections 4.3 and 4.4 for detailed explanations of initialisation and estimation steps). Next, the ambient window is enlarged incrementally by a defined step size, e.g., 10 s, to meet the next significant peak of a new cluster (see **Algorithm 1** in Omidalizarandi et al. (2020)).

A pattern recognition methodology might be beneficial for detecting undesirable signals caused by e.g., passing trains or electrical sources (Wenzel, 2009a). In addition, as mentioned by Wenzel (2009a), such abnormal signals typically appear with extremely sharp rises having amplitudes significantly greater than a normal signal.

In near real-time processing of our proposed algorithm, it is not necessary to omit either the unwanted signals or the sharply rising peaks. However, in a post-processing step, the starting point

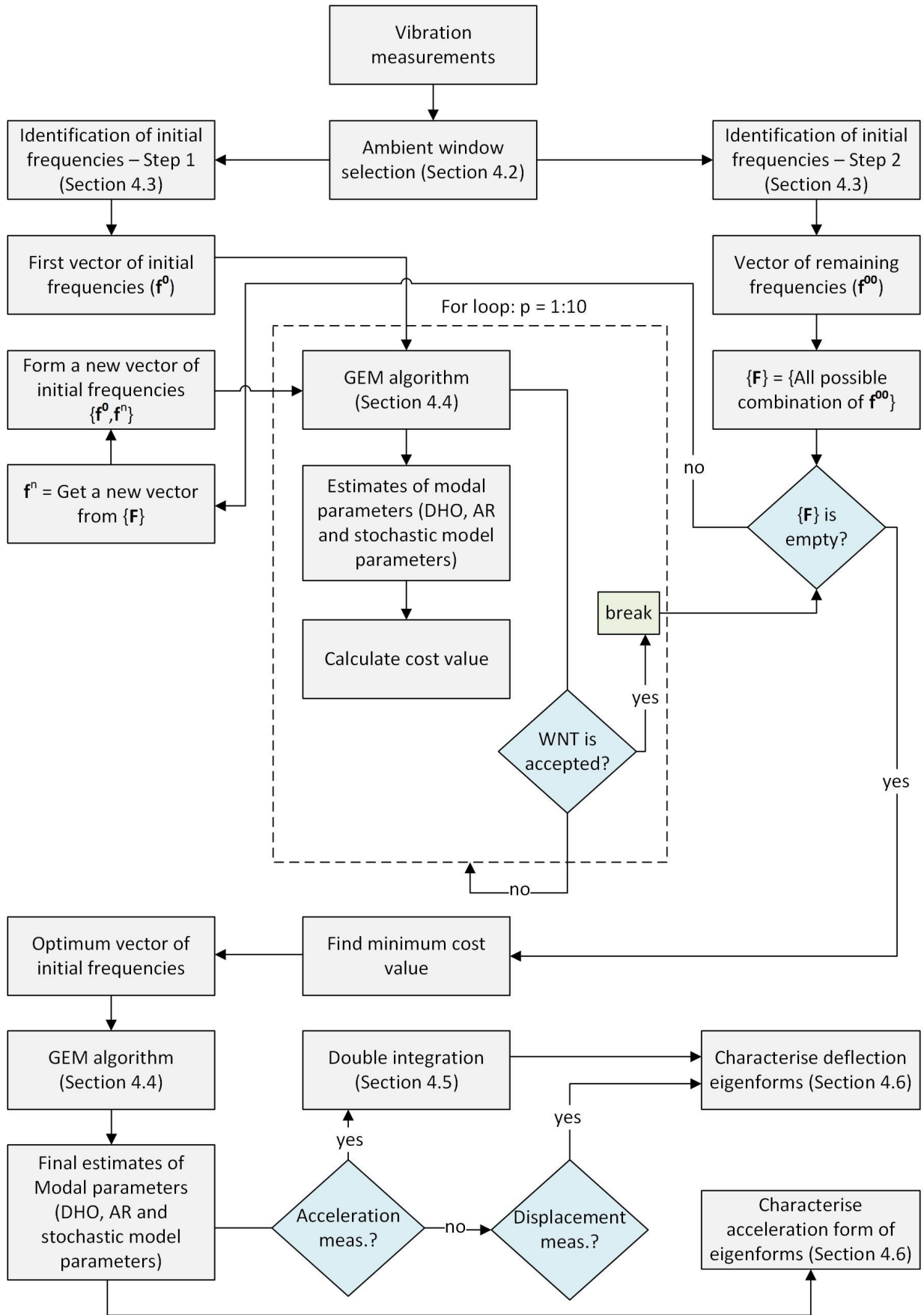


Figure 4.1: An overview of the RT-MPI algorithm.

of the ambient window is moved forward through the peaks within each cluster and thus repeating the estimation procedure. The aforementioned repetitive procedure proceeds till obtaining an acceptance of WNT criterion described by Kargoll et al. (2018). Consequently, it can be interpreted that in case of the acceptance of the WNT criterion, the influence of the unwanted signals caused, i.e., mainly due to the external forces, might have been mitigated with the selected ambient window (Omidalizarandi et al., 2020).

4.3 Identification of Initial Modal Frequencies

Identification of initial eigenfrequencies as approximate values plays an important role in the estimation procedure of the proposed RT-MPI algorithm. Such identification task is even more challenging in case of either closely spaced frequencies or presence of high coloured measurement noise in the vibration measurements (Omidalizarandi et al., 2020).

To deal with the aforementioned problems, the eigenfrequencies determination is performed in two steps and with different parameterisation of the signal subspace dimension and noise power threshold (see **Algorithm 2; Steps 1 and 2** in Omidalizarandi et al. (2020)). The first step allows to extract well-separated eigenfrequencies with dominant amplitudes. By contrast, the second step enables to identify closely spaced frequencies or possibly those frequencies with lower amplitudes.

For this purpose, a pseudospectrum is calculated based on the eigenspace analysis of the correlation matrix of the measurements (ℓ) (Marple, 1987) by using multiple signal classification (MUSIC) algorithm (Jiang and Adeli, 2007; Amezcua-Sanchez and Adeli, 2015). The MUSIC algorithm allows to extract high-resolution frequencies by using the vibration measurements either contaminated with high coloured measurement noise or having low SNR value (Amezcua-Sanchez and Adeli, 2015). In the first and the second parameterisation of the MUSIC algorithm, the signal subspace dimension is set to the integer value of half of a sampling frequency ($F_s/2$) and ($3 \cdot F_s/2$). In addition, an integer length of the FFT is set to 1024 and 4096.

To get rid of spurious frequencies extracted from the MUSIC algorithm and to obtain correct initial values, the two following steps are carried out: firstly, the frequencies are bounded within the determined boundaries. Then, they are replaced with the corresponding frequencies obtained from the DFT, which have maximum amplitudes within the boundaries. Secondly, two upper and lower limits of noise power thresholds are calculated based on the estimates of the power spectral density (PSD) of the vibration measurements, which are used in the first and second MUSIC algorithm parameterisation. The readers are referred to Omidalizarandi et al. (2020) for detailed information regarding the calculation of the noise power thresholds.

The frequencies identified from the first step (see **Algorithm 2; Step 1** in Omidalizarandi et al. (2020)) are input to the robust estimation step, which is described in the following section. Next, a new vector of frequencies, which consists of remaining frequencies, is formed by subtracting the frequencies extracted from the first and second steps. Then, all possible combinations of the remaining frequencies are determined and added to the first vector of the initial frequencies (i.e. frequencies identified from the first step) at each iteration (see **Algorithm 3** in Omidalizarandi et al. (2020)).

Finally, an optimal vector of initial frequencies is selected based on a minimum estimate of cost values, which are calculated with

$$\text{cost}^{(n)} = e^{T_f^{(n)}} + e^{T_\epsilon^{(n)}} + \log_{10}(p^{(n)}) + \text{wnt}_c + \epsilon_A, \quad (4.1)$$

where p is the AR model order, wnt_c the cost value for the WNT criterion (i.e. being 0 or 1 in case of acceptance or rejection of the WNT criterion), ϵ_A the root mean square error (RMSE) of amplitudes of the frequencies identified from the first step (see **Algorithm 2** in Omidalizarandi et al. (2020))

using the amplitude spectrum of the raw measurements and the estimated measurements. In addition, $T_f^{(n)}$ and $T_\xi^{(n)}$ are the mathematical formulations at iteration (n), which are calculated based on the weighted square sum of estimates of the eigenfrequencies and the damping ratio coefficients as follows:

$$\begin{aligned} T_f^{(n)} &= \frac{\hat{\mathbf{f}}^T \hat{\Sigma}_f \hat{\mathbf{f}}}{M}, \\ T_\xi^{(n)} &= \frac{\hat{\boldsymbol{\xi}}^T \hat{\Sigma}_\xi \hat{\boldsymbol{\xi}}}{M}, \end{aligned} \quad (4.2)$$

where $\hat{\mathbf{f}}$ are the estimated eigenfrequencies, $\hat{\boldsymbol{\xi}}$ the estimated damping ratio coefficients, $\hat{\Sigma}_f$ and $\hat{\Sigma}_\xi$ are *a posteriori* covariance matrices of the estimated frequencies and damping ratio coefficients, and M the number of identified eigenfrequencies.

In the aforementioned cost function, the defined $\log_{10}(p)$ function possibly enables us to select a lower AR model order. This is due to the reason that a higher AR model order may absorb those undefined frequencies with lower amplitudes as coloured measurement noise. At the end, the selected initial vector of eigenfrequencies is then input to the adjustment procedure again to achieve the final estimates of the modal parameters (see estimation step in **Algorithm 3** of Omidalizarandi et al. (2020)).

4.4 Robust Modal Parameter Estimation based on Time Series Analysis

The proposed RT-MPI algorithm in this chapter can be considered in the category of the OMA method. It allows to perform displacement and vibration analyses of bridge structures by using only vibration measurements, e.g. MEMS acceleration data, without the necessity to impose external forces. After selecting a proper excitation window as described in section 4.2, the RT-MPI algorithm is carried out in two following steps:

1. identification of initial modal frequencies (see section 4.3),
2. estimation step.

The estimation step is described in this section. The proposed approach allows to automatically, robustly and accurately estimate the modal parameters including eigenfrequencies, amplitudes, phase shifts, and damping ratio coefficients. In addition, there is no necessity to define tuning parameters. However, *a priori* knowledge about the SNR of the measurements is beneficial in the identification of initial modal frequencies in an optimal manner. As previously stated, the eigenforms are characterised in the subsequent step, and by using the estimated parameters from the GEM algorithm.

Previously, Kargoll et al. (2018) proposed a self-tuning robust estimation procedure in the sense of an iterative reweighted least-squares approach. An observation model was defined based on a linear regression time series model with AR model and t-distributed random deviations. Next, an expectation conditional maximisation either (ECME) algorithm was proposed to obtain adaptive robust ML estimation of the parameters. The GEM algorithm given in Alkhatib et al. (2017) is derived from the ECME algorithm, which is proposed by Kargoll et al. (2018). In the GEM algorithm, a univariate and linear regression model is extended to a multivariate and nonlinear regression model. In addition, in the GEM algorithm, the underlying optimisation problem is based on the research of Dempster et al. (1977) in which the maximum expectation of the parameters is approximated within each step of the EM algorithm instead of fully reaching it (Alkhatib et al., 2017).

In this dissertation, as stated before, the 1D version of the GEM algorithm, which is associated with univariate AR process is applied. Therefore, merely 1D vibration measurements recorded from each direction are considered. Omidalizarandi et al. (2018) proposed a robust displacement and vibration analysis procedure by estimating eigenfrequencies, amplitudes, and phase shifts. An observation model consisting of the UDHO model, the AR model and t-distributed random deviations was employed and jointly adjusted by means of the GEM algorithm. Omidalizarandi et al. (2020) extended the research of Omidalizarandi et al. (2018) as follows:

1. changing the functional model from UDHO model to DHO model,
2. additionally estimating the damping ratio coefficients,
3. achieving precise and accurate estimates of the amplitudes in both units of $[m/s^2]$ and $[mm]$,
4. automatically selecting an excitation window,
5. identifying initial eigenfrequencies,
6. characterising the eigenforms.

A brief explanation of the aforementioned robust modal parameter estimation procedure is described in the next subsections.

4.4.1 Estimation model

As previously mentioned, an observation model is defined to obtain robust estimates of the modal parameters for a 1D regression time series. It consists of: (1) a parametric nonlinear DHO model, (2) a parametric auto-correlation model in terms of a univariate, covariance-stationary AR process, and (3) a parametric stochastic model in terms of the independent heavy-tailed scaled t-distribution. The aforementioned parametric models are briefly described in the following.

4.4.1.1 Functional model

To estimate the modal parameters including eigenfrequencies, amplitudes, phase shifts, and damping ratio coefficients, a proper functional model is defined. For this purpose, as stated before, Omidalizarandi et al. (2020) extended the research of Omidalizarandi et al. (2018) by changing the functional model from UDHO model to DHO model, which is introduced in Amezquita-Sanchez and Adeli (2015). Therefore, it allows to additionally estimate the damping ratio coefficients.

The vibration measurements ℓ_1, \dots, ℓ_n , which are obtained at equidistant time instances x_t ($t = 1, \dots, n$), e.g., from accelerometers, video streams of an IATS or other geodetic sensors, can be modelled based on

$$\begin{aligned} \ell_t &= h_t(\boldsymbol{\theta}) + e_t \\ &= \frac{a_0}{2} + \sum_{j=1}^M [a_j \cos(2\pi f_j \sqrt{1 - \xi_j^2} x_t) + b_j \sin(2\pi f_j \sqrt{1 - \xi_j^2} x_t)] \cdot \exp(-2\pi \xi_j f_j x_t) + e_t, \end{aligned} \quad (4.3)$$

where f_1, \dots, f_M are the undamped frequencies, a_0, a_1, \dots, a_M , and b_1, \dots, b_M the Fourier series coefficients and ξ_1, \dots, ξ_M the damping ratio coefficients, which are included in the unknown parameter vector $(\boldsymbol{\theta})$. The $f_{jd} = f_j \sqrt{1 - \xi_j^2}$ corresponds to the damped frequency and e_t is the random deviation contaminated with the coloured noise that is a so-called coloured noise residual. As we can see from Equation 4.3, by setting all the damping ratio coefficients equal to zero, the DHO model is converted to the UDHO model.

The preceding highly non-linear observation equation can be written in the form of

$$\ell_t = \mathbf{A}_t \boldsymbol{\theta} + e_t, \quad (4.4)$$

where \mathbf{A}_t is the design matrix, which is assumed to have full rank. The vibration measurements (ℓ_t) are subtracted from their mean value throughout the entire ambient window selected. However, they are detrended in case of either linear or quadratic drifts. This can be performed either by means of calibration parameters or by replacing the term offset $\frac{a_0}{2}$ in Equation 4.3 by $c_0 + c_1 x_t$ for the linear drift (Omidalizarandi et al., 2019c) or by $c_0 + c_1 x_t + c_2 x_t^2$ in case of quadratic drift.

4.4.1.2 Auto-correlation model

Previously, in the context of time series measurements, e.g., Nassar et al. (2004) benefit from the AR process to model relatively high measurement noise contaminated in gyroscope measurements. In addition, as described by Kuhlmann (2003), measurements with a high sampling frequency are often subject to auto-correlation due to similar time dependent systematic errors between neighbouring measurements. Thus, in this dissertation, to deal with high coloured measurement noise in the vibration measurements, e.g., cost-effective MEMS acceleration data, the AR process given in Kargoll et al. (2018) is applied to 1D vibration measurements to handle the auto-correlation. It is possible to model both auto- and cross-correlations of the 3D vibration measurements (recorded from three different axes) by employing a VAR process and multivariate t-distributed random deviations as proposed by Kargoll et al. (2020a). However, it is out of focus of this dissertation and can be considered in the future research. For simplicity, the random deviations (e_t) are assumed to be autocorrelated through a univariate covariance-stationary AR process by (Kargoll et al., 2018):

$$e_t = \alpha_1 e_{t-1} + \dots + \alpha_p e_{t-p} + u_t, \quad (4.5)$$

where u_t is the white noise variable. In addition, $\boldsymbol{\alpha}^T = [\alpha_1, \dots, \alpha_p]$ are the AR coefficients, which are considered as unknown parameters within the estimation procedure.

4.4.1.3 Stochastic model

In this dissertation, stochastic dependencies between the acceleration data recorded from different axes, have been neglected and shall be analysed in the future. Thus, the white noise components u_1, \dots, u_n are assumed to be stochastically independent and follow the centred and scaled t-distribution $t_\nu(0, \sigma^2)$ with an unknown degree of freedom ν , zero mean and an unknown scale factor σ^2 , that is

$$u_t \stackrel{\text{ind.}}{\sim} t_\nu(0, \sigma^2). \quad (4.6)$$

Such assumption allows to account for the outliers of different magnitudes, heavy-tailed white noise components, and setting the level of precision (Kargoll et al., 2019). In view of the preceding equation, the white noise variable is obtained by:

$$u_t = e_t - \alpha_1 e_{t-1} - \dots - \alpha_p e_{t-p} = \alpha(\mathbf{L})(\ell_t - h_t(\boldsymbol{\theta})), \quad (4.7)$$

where the lag operator $L^j e_t := e_{t-j}$ and the lag polynomial $\alpha(\mathbf{L}) = 1 - \alpha_1 L - \dots - \alpha_p L^p$ are used as convenient notations. For simplicity, the required initial values e_0, e_{-1} , etc., are set to zero. $\alpha(\mathbf{L})$ is considered as a digital filter to decorrelate the random deviations (Kargoll et al., 2018).

4.4.1.4 Log-likelihood function

The aforementioned three parametric models are combined in a joint log-likelihood function, which is defined based on the natural logarithm of the joint PDF of the scaled t-distributed white noise

components (Kargoll et al., 2018) with

$$\log L(\boldsymbol{\theta}, \sigma^2, \boldsymbol{\alpha}, \nu | \boldsymbol{\ell}) = n \log \left[\frac{\Gamma\left(\frac{\nu+1}{2}\right)}{\sqrt{\nu\pi}\sigma\Gamma\left(\frac{\nu}{2}\right)} \right] - \frac{\nu+1}{2} \cdot \sum_{t=1}^n \log \left[1 + \frac{1}{\nu} \left(\frac{\alpha(\mathbf{L})(\ell_t - h_t(\boldsymbol{\theta}))}{\sigma} \right)^2 \right], \quad (4.8)$$

where Γ is the gamma function. The maximisation of the aforementioned joint log-likelihood function enables for robust and ML estimation of the parameters. It further allows self-tuning of the t-distribution model parameters (Kargoll et al., 2018). For this purpose, the unknown parameters of DHO model, AR error model and t-distributed random deviations are defined as unknown parameter vector $\boldsymbol{\Theta}^T = [\boldsymbol{\theta}^T, \boldsymbol{\alpha}^T, \sigma^2, \nu]^T$, which are jointly adjusted by means of 1D version of the GEM algorithm given in Alkhatib et al. (2017). The GEM algorithm is briefly described in the following section.

4.4.2 Robust adjustment procedure

To begin with the estimates of the unknown parameters ($\boldsymbol{\Theta}^T$) based on the GEM algorithm, firstly, the highly nonlinear DHO model (Equation 4.3) is linearised. As the simulation results shown in Kargoll et al. (2019), the GEM algorithm is not sensitive to the initial values compared to the standard least-squares adjustment. It is due to the reason that GEM algorithm benefits from the AR process and the scaled t-distribution for ML estimation of the parameters. However, a proper identification of frequencies are required in advance. Mautz (2001) applied a global optimisation approach to overcome this problem and to perform spectral analysis of a time series with unknown frequencies. In this research, the initial frequencies are identified based on the proposed algorithm described in section 4.3. The initial damping ratio coefficients are set to 0. The AR model order is initially set to 1 and is progressively increased by 1 to reach its maximum predefined value. As stated before, the estimates of the modal parameters obtained from the GEM algorithm enable to calculate the cost value (Equation 4.1) for each vector of initial frequencies and for each AR model order (Omidalizarandi et al., 2020). Such estimation procedure can be considered as global optimisation procedure, which allows to efficiently and reliably obtain globally optimum estimates of the modal parameters.

The GEM algorithm consists of the expectation step (E-step) and the maximisation step (M-step) (Alkhatib et al., 2017). In the E-step, the weights are calculated at each iteration step of this algorithm, which are used to downweight outliers and to estimate the parameters in the M-step. The observation weight at iteration step i ($w_t^{(i)}$) is calculated by using initial or estimated parameter values $\boldsymbol{\theta}^{(i)}$, $\boldsymbol{\alpha}^{(i)}$, $\sigma^{(i)}$ and $\nu^{(i)}$ with (Alkhatib et al., 2017)

$$w_t^{(i)} = \frac{\nu^{(i)} + 1}{\nu^{(i)} + \left(u_t^{(i)} / \sigma^{(i)} \right)^2}. \quad (4.9)$$

The calculated weights are the diagonal elements of the weight matrix $\mathbf{W}^{(i)}$, which is used within the subsequent M-step. Initially, the weight matrix is set to the unit matrix $\mathbf{W}^{(0)} = \mathbf{I}_n$. Furthermore, the scale factor is set to the identity value $\sigma^{(i)} = 1$ and the degree of freedom is set to $\nu^{(0)} = 30$. In addition, the AR process coefficients are set to zero ($\boldsymbol{\alpha}^{(0)} = \mathbf{0}_{[p \times 1]}$). Such initial assumptions account for approximately standard normal and uncorrelated random deviations.

The M-step is accomplished by estimating the unknown parameter vector consisting of four parameter groups $\boldsymbol{\Theta}^{(i)} = [\boldsymbol{\theta}^{(i)}, \boldsymbol{\alpha}^{(i)}, \sigma^{(i)}, \nu^{(i)}]$ individually. First, the parameters $\boldsymbol{\theta}$ of the nonlinear DHO model are estimated by solving the linearised normal equations

$$\Delta \boldsymbol{\theta}^{(i+1)} = \left(\frac{1}{(\sigma^2)^{(i)}} \cdot (\overline{\mathbf{A}}^{(i)})^T \mathbf{W}^{(i)} \overline{\mathbf{A}}^{(i)} \right)^{-1} \frac{1}{(\sigma^2)^{(i)}} \cdot (\overline{\mathbf{A}}^{(i)})^T \mathbf{W}^{(i)} \Delta \boldsymbol{\ell}^{(i)}, \quad (4.10)$$

where $\overline{\Delta \ell}_t^{(i)} := \alpha^{(i)}(\mathbf{L})\Delta \ell_t$ is the decorrelated filtered reduced observation calculated from reduced observations $\Delta \ell_t^{(i)} = \ell_t - h_t(\boldsymbol{\theta}^{(i)})$, and $\overline{\mathbf{A}}_{t,k}^{(i)} := \alpha^{(i)}(\mathbf{L})\mathbf{A}_{t,k}$ are the decorrelated filtered Jacobi matrix components calculated from Jacobi matrix components $\mathbf{A}_{t,k}^{(i)} = \frac{\partial h_t(\boldsymbol{\theta}^{(i)})}{\partial \theta_k}$.

The Jacobi matrix $\mathbf{A}_{t,k}^{(i)}$ is defined based on the partial derivatives of DHO model (4.3) with respect to the unknown parameters, that read

$$\frac{\partial h_t(\boldsymbol{\theta}^{(i)})}{\partial a_0} = \frac{1}{2}, \quad (4.11)$$

$$\frac{\partial h_t(\boldsymbol{\theta}^{(i)})}{\partial a_j} = \cos(2\pi f_j^{(i)} \sqrt{1 - (\xi_j^2)^{(i)} x_t}), \quad (4.12)$$

$$\frac{\partial h_t(\boldsymbol{\theta}^{(i)})}{\partial b_j} = \sin(2\pi f_j^{(i)} \sqrt{1 - (\xi_j^2)^{(i)} x_t}), \quad (4.13)$$

$$\begin{aligned} \frac{\partial h_t(\boldsymbol{\theta}^{(i)})}{\partial \xi_j} = & \exp(-2\pi f_j^{(i)} \xi_j^{(i)} x_t) \cdot (-2\pi f_j^{(i)} \xi_j^{(i)} \sqrt{1 - (\xi_j^2)^{(i)} x_t}) \cdot \dots \\ & \left[b_j^{(i)} \cos(2\pi f_j^{(i)} \sqrt{1 - (\xi_j^2)^{(i)} x_t}) - a_j^{(i)} \sin(2\pi f_j^{(i)} \sqrt{1 - (\xi_j^2)^{(i)} x_t}) \right] + \dots \\ & \exp(-2\pi f_j^{(i)} \xi_j^{(i)} x_t) \cdot (-2\pi f_j^{(i)} x_t) \cdot \dots \\ & \left[b_j^{(i)} \sin(2\pi f_j^{(i)} \sqrt{1 - (\xi_j^2)^{(i)} x_t}) + a_j^{(i)} \cos(2\pi f_j^{(i)} \sqrt{1 - (\xi_j^2)^{(i)} x_t}) \right], \end{aligned} \quad (4.14)$$

$$\begin{aligned} \frac{\partial h_t(\boldsymbol{\theta}^{(i)})}{\partial f_j} = & \exp(-2\pi f_j^{(i)} \xi_j^{(i)} x_t) \cdot (2\pi \sqrt{1 - (\xi_j^2)^{(i)} x_t}) \cdot \dots \\ & \left[b_j^{(i)} \cos(2\pi f_j^{(i)} \sqrt{1 - (\xi_j^2)^{(i)} x_t}) - a_j^{(i)} \sin(2\pi f_j^{(i)} \sqrt{1 - (\xi_j^2)^{(i)} x_t}) \right] + \dots \\ & \exp(-2\pi f_j^{(i)} \xi_j^{(i)} x_t) \cdot (-2\pi \xi_j^{(i)} x_t) \cdot \dots \\ & \left[b_j^{(i)} \sin(2\pi f_j^{(i)} \sqrt{1 - (\xi_j^2)^{(i)} x_t}) + a_j^{(i)} \cos(2\pi f_j^{(i)} \sqrt{1 - (\xi_j^2)^{(i)} x_t}) \right]. \end{aligned} \quad (4.15)$$

A Gauss-Newton step with step size $\gamma \in (0, 1]$ is calculated (Equation 4.16), which assists for a better convergence of the GEM algorithm.

$$\boldsymbol{\theta}^{(i+1)} = \boldsymbol{\theta}^{(i)} + \gamma \boldsymbol{\Delta} \boldsymbol{\theta}^{(i+1)}, \quad (4.16)$$

Next, the estimates of the coloured noise residuals is computed with $e_t^{(i+1)} = \ell_t - h_t(\boldsymbol{\theta}^{(i+1)})$. Thus, it allows to assemble the matrix $\mathbf{E}^{(i+1)}$ with (Alkhatib et al., 2017)

$$\mathbf{E}^{(i+1)} = \begin{bmatrix} e_0^{(i+1)} & \dots & e_{1-p}^{(i+1)} \\ \vdots & & \vdots \\ e_{n-1}^{(i+1)} & \dots & e_{n-p}^{(i+1)} \end{bmatrix}. \quad (4.17)$$

The solution of the normal equations with respect to the AR coefficients is calculated based on (Alkhatib et al., 2017)

$$\boldsymbol{\alpha}^{(i+1)} = \left((\mathbf{E}^{(i+1)})^T \mathbf{W}^{(i)} \mathbf{E}^{(i+1)} \right)^{-1} (\mathbf{E}^{(i+1)})^T \mathbf{W}^{(i)} \mathbf{e}^{(i+1)}. \quad (4.18)$$

The estimated AR process is necessary to be invertible. For this purpose, all roots (i.e., possibly complex valued roots) of $\alpha^{(i+1)}(z) = 0$ are checked to be located within the unit circle. Otherwise, all roots with a magnitude larger than 1 are mirrored into the unit circle (Porat, 1994; Kargoll et al., 2018).

The estimated AR coefficients are used to filter the coloured noise residuals and, thus, to estimate the white noise residuals result through (Alkhatib et al., 2017)

$$u_t^{(i+1)} = \alpha^{(i+1)}(\mathbf{L})e_t^{(i+1)}. \quad (4.19)$$

The scale factor is calculated by dividing the weighted sum of squared white noise residuals by the number of observations as (Alkhatib et al., 2017)

$$(\sigma^2)^{(i+1)} = \frac{1}{n} \sum_{t=1}^n w_t^{(i)} \left(u_t^{(i+1)}\right)^2. \quad (4.20)$$

Finally, a zero search of the Equation 4.21 is carried out to estimate the degree of freedom of the underlying t-distribution (Alkhatib et al., 2017).

$$0 = \log \nu^{(i+1)} + 1 - \psi\left(\frac{\nu^{(i+1)}}{2}\right) + \psi\left(\frac{\nu^{(i+1)} + 1}{2}\right) - \log(\nu^{(i+1)} + 1) + \frac{1}{n} \sum_{t=1}^n \left(\log w_t^{(i+1)} - w_t^{(i+1)}\right), \quad (4.21)$$

where ψ is the digamma function and the weights $w_t^{(i+1)}$ are computed by substituting $u_t^{(i+1)}$, $\sigma^{(i)}$ and $\nu^{(i)}$ into the Equation 4.9. The readers are referred to Alkhatib et al. (2017) for detailed explanations regarding derivation and implementation of the GEM algorithm.

As proposed by Kargoll et al. (2017), the zero search based on the interval Newton method (see Algorithm 6.1 in Hargreaves (2002) for details) is applied by using *INTLAB* library (Rump, 1999). Thus, it allows to reliably estimate the ν of the t-distribution¹. However, the aforementioned zero search based algorithm is not computationally efficient and, thus, it is mainly suitable for the post-processing step. In near real-time processing, the ν can be estimated based on the standard MATLAB routine *fzero* to speed up the procedure. However, the estimates of the ν is not reliable enough and its estimates are rather close approximations of the normal distribution with higher degree of freedom. Therefore, to get fast and reliable estimate of the ν , standard MATLAB routine *mle* can be used. The analysis demonstrates that the estimates of ν derived from the *mle* is very close to that one derived from the *INTLAB* library. Consequently, the new estimates of the ν obtained from the *mle* is put into the GEM algorithm again to get reliable and robust estimates of the parameters.

A cosine form of the Equation 4.3 without considering the damping ratio coefficient (Equation 4.22) is used to compute amplitudes and phase shifts.

$$a_j \cos(2\pi f_j x_t) + b_j \sin(2\pi f_j x_t) = A_j \cos(2\pi f_j x_t + \phi_j). \quad (4.22)$$

Therefore, the amplitudes and the phase shifts² are calculated by

$$A_j = \sqrt{a_j^2 + b_j^2}, \quad (4.23)$$

¹The *INTLAB* library version 10 has been used.

²To estimate the phase shifts, the MATLAB routine *atan2* is applied to calculate a four-quadrant inverse tangent by using the estimated Fourier coefficients.

$$\phi_j = \tan^{-1}\left(\frac{-b_j}{a_j}\right). \quad (4.24)$$

4.5 Displacement Analysis based on Double Integration

To derive amplitudes in a metric unit, e.g., millimetre, the DHO model (Equation 4.3) is double integrated without considering the term of the offset, that is

$$\begin{aligned} d_t &= H_t(\boldsymbol{\theta}) + e_t \\ &= \sum_{j=1}^M \left[\left[\exp(-2\pi f_j x_t \xi_j) \cdot \cos(2\pi f_j x_t \sqrt{1 - \xi_j^2}) \cdot (2a_j \xi_j^2 - a_j + 2b_j \xi_j \sqrt{1 - \xi_j^2}) \right] / (4f_j^2 \pi^2) - \right. \\ &\quad \left. \left[\exp(-2\pi f_j x_t \xi_j) \cdot \sin(2\pi f_j x_t \sqrt{1 - \xi_j^2}) \cdot (b_j - 2b_j \xi_j^2 + 2a_j \xi_j \sqrt{1 - \xi_j^2}) \right] / (4f_j^2 \pi^2) \right] + e_t, \end{aligned} \quad (4.25)$$

where a_1, \dots, a_M , and b_1, \dots, b_M are the Fourier coefficients, f_1, \dots, f_M the eigenfrequencies and ξ_1, \dots, ξ_M the damping ratio coefficients, which are the estimates of the modal parameters obtained from the estimation procedure (see section 4.4). Next, the calculated displacements ($\mathbf{d} = \sum_{t=1}^n d_t$) are considered as observables, which are put into the GEM algorithm by considering the DHO model as a functional model. Using the new estimates of the modal parameters, the amplitude (Am_j) is calculated for each eigenfrequency in the unit of $[m]$ based on the Equation 4.23.

For the purpose of validation, the amplitudes are calculated by (Omidalizarandi et al., 2018)

$$Acm_j = \frac{A_j}{(2 \cdot \pi \cdot f_j)^2}, \quad (4.26)$$

where f_j is the estimated eigenfrequency in $[Hz]$, A_j is the estimated amplitude in $[m/s^2]$ and Acm_j is the expected and calculated amplitude in $[m]$. Theoretically, the Acm_j is equal to Am_j for each eigenfrequency. However, in reality, there is a slight and negligible difference between them, which is due to the uncertainty of the estimated parameters.

4.6 Characterisation of Eigenforms

As a preliminary step, to correctly characterise the eigenforms, it is required that MEMS accelerometers are located at certain positions, which are precalculated from the FEM analysis. Then, the 1D acceleration data are recorded for a duration of, e.g., 10 minutes at each sensor position. Next, the acceleration data are put into the GEM algorithm to estimate the modal parameters. The UDHO model described by Kargoll et al. (2018) and Omidalizarandi et al. (2018) is used as a functional model. This is due to the reason that the estimates of the damping ratio coefficients, as one of the unknown parameter in the DHO model, is a very challenging issue for long-term measurements.

The amplitudes and phase shifts are computed based on the Equations 4.23 and 4.24. The estimated phase shifts are then used to identify the sign of the amplitudes. For example, the sign of the amplitude is changed when the phase shift difference is approximately 180° . Having amplitude values and their corrected signs, depending on the eigenform orders, the polynomials of meaningful degree are estimated based on either regression or least-squares adjustment. It should be noted that the prior knowledge about eigenfrequencies and their corresponding eigenforms can be provided by the FEM analysis in advance. However, it is also possible to characterise the eigenforms without any knowledge about their orders. In this case, the B-spline curve approximation similar to the research of Bureick et al. (2016) could be applied.

The aforementioned estimates of the eigenforms do not yield true scales. To overcome this prob-

lem, the DHO model is fitted to a selected excitation window within a short time interval, e.g. few minutes. Therefore, it enables to estimate amplitudes in metric units by means of the double integration of the DHO model. Subsequently, it allows to characterise deflection mode shapes with true scales for the selected excitation window.

The aforementioned eigenform characterisation procedure is beneficial, since it delivers reasonable results even in case of using a low number of sensors. In addition, its connection to the proposed robust modal parameter estimation procedure allows to robustly and accurately characterise the eigenforms in their true scales.

4.7 Summary

A novel robust time domain modal parameter identification technique is proposed and implemented in this chapter, which can be used for any type of vibration measurements in the form of time series. The proposed vibration analysis procedure allows to automatically select an excitation (e.g. ambient) window and to identify initial eigenfrequencies, automatically and reliably. It further allows to estimate the modal parameters including eigenfrequencies, eigenforms, and damping ratio coefficients robustly and accurately. Moreover, it enables to perform double integration of the acceleration data and to obtain amplitudes in metric units with a high accuracy. Having amplitude estimations in metric units for a selected ambient window, e.g., in a range of few minutes, allows to characterise deflection eigenforms in their true scales with a high accuracy.

In order to estimate the modal parameters, initial eigenfrequencies are required to be identified in advance. For this purpose, the identification is performed in two steps and with different parameterisation of the noise power threshold and the signal subspace dimension. In the first step, the well-separated initial eigenfrequencies are extracted, which are above a noise power threshold. Next, all possible combinations of the remaining frequencies, identified from the second step, are added to the initial eigenfrequencies identified from the first step. Subsequently, a new vector of initial frequencies is formed at each iteration.

To begin with the estimation procedure, the observation model consisting of the parametric DHO model, the parametric auto-correlation model in the form of an AR process, and the parametric stochastic model in terms of heavy tailed family of scaled t-distributions with an unknown df and scale factor is employed, which is jointly adjusted by means of the GEM algorithm. Consequently, a self-tuning, robust, and ML estimation of the parameters is obtained. The aforementioned estimation procedure is repeated for each vector of initial eigenfrequencies and for each AR model order to calculate the cost value. A high AR model order may absorb those undefined frequencies with low amplitudes. Thus, the maximum AR model is set to 10, which yields fast convergence of the algorithm. However, in case of high systematic errors of sensor measurements, the AR model order is increased to a higher value. An optimal vector of initial frequencies that is associated with the minimum cost value is selected. To obtain final estimates of the modal parameters, the estimation step is carried out again by using the optimal vector of initial frequencies selected from the previous step.

The excitation window selection, the identification of initial frequencies and the estimation step are complementary to each other in the proposed RT-MPI algorithm. In addition, they ensure robust and accurate estimation of the modal parameters. The improper selection of an excitation window has a direct influence on the estimates of the amplitudes and damping ratio coefficients. In addition, the aforementioned two steps in identification of the initial frequencies allow to identify both well-separated and closely spaced frequencies. It should be mentioned that well-defined selection of the initial eigenfrequencies can lead to fast and efficient convergence of the adjustment procedure. The calculated noise power threshold enables to get rid of spurious frequencies. The inadequate choice of the AR model order may absorb those undefined frequencies with low amplitudes. The

minimum value of the defined cost function allows to optimally and reliably identify the initial frequencies. The proposed robust estimation procedure is particularly of great importance when vibration measurements are contaminated with a high coloured measurement noise, e.g., cost effective MEMS acceleration data. Therefore, it allows to handle the auto-correlation and to account for the outliers of different magnitudes and heavy-tailed white noise components. The zero search based on the *INTLAB* enables to reliably estimate the df of the t-distribution. However, it is not computationally efficient and mainly suitable for a post-processing step. Subsequently, the *fzero* and the *mle* MATLAB routines can be used alternatively to speed up the procedure in near real-time processing. However, the *mle* MATLAB routine yields more reliable results compared to the *fzero* which is due to reliable estimation of the df of the underlying t-distribution. The numerical results of the proposed RT-MPI algorithm for different experimental case studies are presented and discussed in chapter 6.

5 MEMS-based Bridge Monitoring Supported by Image-Assisted Total Stations

5.1 Introduction

Permanent, cost-effective, and reliable monitoring of dilapidated, severely damaged or endangered bridges is challenging. As stated before, only high end geodetic sensors such as IATS are often not economically sustainable for such permanent monitoring tasks. Besides, the selected geodetic sensor should be able to perform measurements with an adequate required sampling frequency. Furthermore, number of directions corresponding to bridge motions of interest, measurement range, demanding accuracy, installation requirements, measurement duration, storage, data transmission, time synchronisation of measurements, cost, etc. should be considered.

To perform short- and long-term deformation/displacement monitoring of bridge structures, the fusion of cost-effective MEMS accelerometers and an IATS is beneficial due to the following reasons:

- providing complementary frequency bands by detecting lower frequency ranges from the IATS displacement data and upper frequency ranges from the MEMS acceleration data (Xu et al., 2019),
- achieving a high accurate estimates of the displacement time series with a wider frequency bandwidth as well as a higher resolution (Xu et al., 2019),
- increasing the redundancy,
- compensating a drift of absolute position/displacement estimates derived from the double integration of the MEMS acceleration data by using the IATS displacement data,
- using estimated displacement data to assess the bridge structure conditions under different loads as well as performing model calibration (Xu et al., 2019).

Previous researchers such as Hong et al. (2013); Park et al. (2018) integrated acceleration and displacement data by superimposing double integrated acceleration measurements and displacement measurements, which yields displacements with an optimal coverage of frequency bands. Smyth and Wu (2007); Xu et al. (2017, 2019) applied the KF approach by using the equations of motion to solve state space model parameters consisting of displacements and velocities.

In this chapter, the feasibility of fusing cost-effective MEMS accelerometers and an IATS for generating high accurate displacement time series is investigated. On one hand, the IATS is often used to acquire polar measurements of a measured object, which can be then converted to the 3D Cartesian coordinates. However, to perform displacement analysis in a submillimetre range, such 3D coordinates are not practically appropriate. On the other hand, as stated before, the displacement analysis by merely using the MEMS accelerometer is challenging, since it suffers from accuracy degradation with time for absolute position/displacement estimates.

To overcome the aforementioned problem, a high accurate 1D displacement time series is generated from the IATS by capturing video frames of a passive target – introduced in section 3.3 – that is attached to a bridge structure. The passive target centroid detection algorithm proposed by Omidalizarandi et al. (2019a) – described in section 3.3 – is applied to extract the target centroids

with high accuracy. Further explanations regarding conversion of the displacement time series from pixel to metric unit is given in Omidalizarandi et al. (2018), which is briefly described in section 3.4. In this dissertation, merely 1D displacement time series have been generated. However, it is also possible to generate 3D displacement time series as described by Ehrhart (2017b). In this case, as previously mentioned in section 1.6, a 2D displacement time series is generated from the measurements of an image plane, which is perpendicular to a viewing direction. The third dimension of the aforementioned displacement time series is obtained based on the slope distance measurements towards a target or structural features.

To this end, the displacements and acceleration measurements are obtained, which are often auto-correlated. As described by Kuhlmann (2003), the white measurement and process noise are required to be considered within the KF approach. For this purpose, Kuhlmann (2003) modified the KF algorithm by considering a shaping filter, which allows to tackle coloured measurement noise contaminated with GPS measurements used for deformation analysis. In this dissertation, the decorrelation of the coloured measurement noise is carried out based on the AR process as part of the GEM algorithm – described in chapter 4 – for selected excitation window. Therefore, it enables to robustly and accurately estimate the uncertainties of the white noise measurements used in the KF algorithm. Additionally, the estimated modal parameters from the acceleration data are used to generate double integrated acceleration data (see section 4.5), which is then synchronised with the displacement measurements of the IATS based on the cross-correlation.

Finally, to fuse the 1D MEMS acceleration data with the 1D displacement data obtained from the IATS, Omidalizarandi et al. (2019c) performed 1D CUPT within the KF approach, which avoids drifting of the MEMS-related displacements over a longer period of time. An overview of the proposed approach within the multi-rate KF framework is sketched in Figure 5.1, which is briefly described in this chapter. The proposed data fusion approach is not the main focus of this dissertation and it is an initial idea that needs to be improved in the future work.

This chapter is organised as follows: The ongoing section introduces the basics of the KF approach for displacement analysis. Section 5.3 presents the heterogeneous data fusion of displacement and acceleration measurements. At the end, the summary is given in Section 5.4.

5.2 Basics of Kalman Filtering for Displacement Analysis

The KF is a recursive optimal filter, which is accomplished in three steps of initialisation, prediction, and filtering. Therefore, an optimum estimate of the state vector parameters is obtained recursively based on a weighted average of a predicted state vector and a new observation vector (Gelb, 1974). The aforementioned weighting is carried out by considering a covariance matrix of the process noise and a covariance matrix of the observations. Xu et al. (2017) applied ML estimation to specify the uncertainties of the measurements and the process noise. In this dissertation, the uncertainties of the measurements including acceleration and displacement data are determined based on the GEM algorithm described in chapter 4.

The fusion process typically starts by describing differential equations. In this chapter, the description of the data fusion process directly starts with a standard solution approach based on the classical discrete KF framework, for simplicity. To begin with the KF estimation, the state vector y^k at epoch k is described as

$$\mathbf{y}^k = \begin{bmatrix} d^k \\ v^k \\ a^k \end{bmatrix}, \quad (5.1)$$

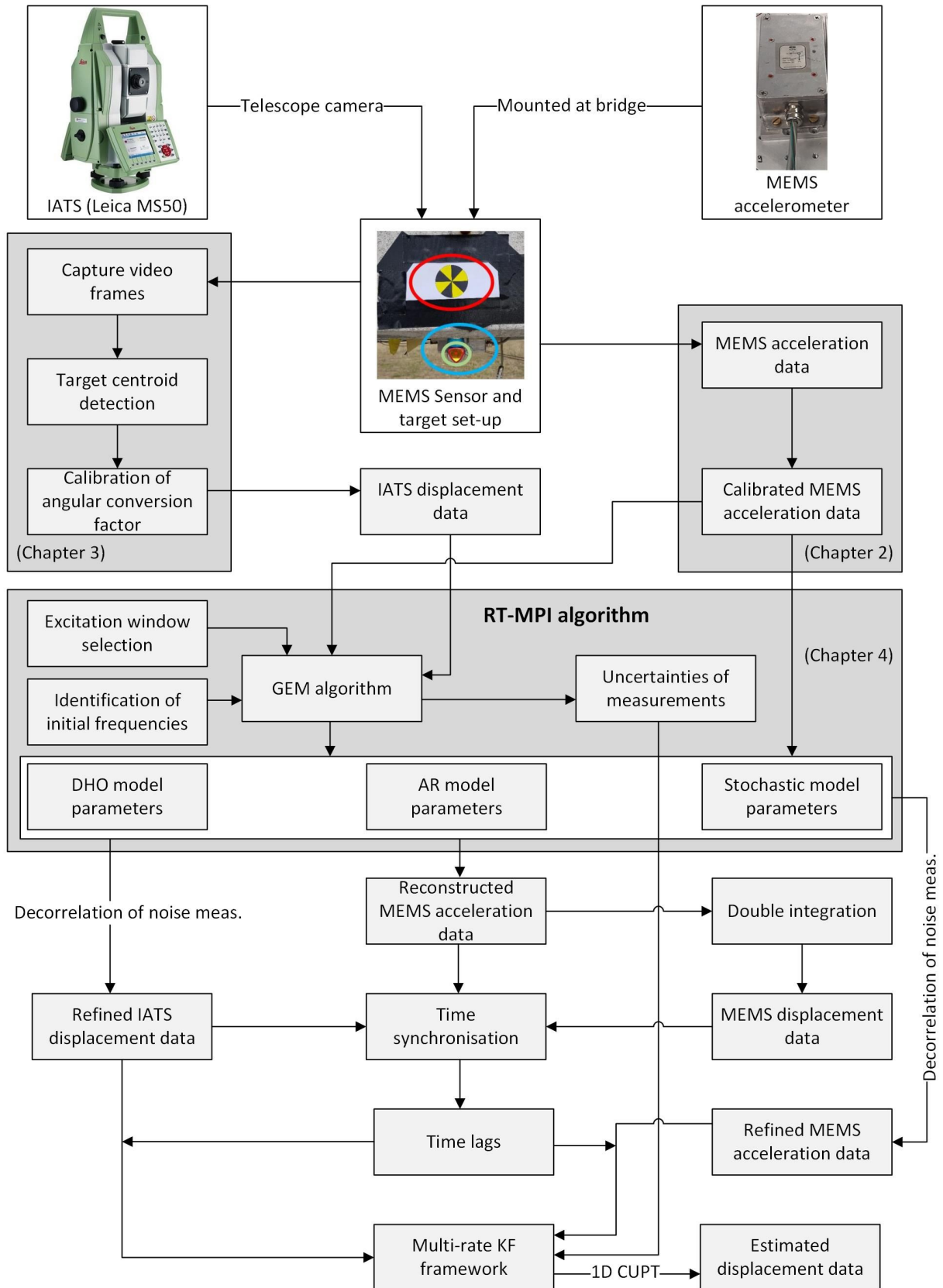


Figure 5.1: Fusion of the IATS displacement data and the MEMS acceleration data within the KF framework.

where d^k , v^k , and a^k are the displacements, the velocities, and the accelerations at the epoch k . However, Smyth and Wu (2007) considered the measured acceleration as an input and the displacement as an observed output. Subsequently, the state vector was merely described based on the displacements and velocities. As previously stated, further investigations, comparisons and possibly improvements of the proposed data fusion shall be performed in the future work.

The predicted state vector ($\bar{\mathbf{y}}^{k+1}$) at epoch $k+1$ is computed based on the linear system equation as

$$\bar{\mathbf{y}}^{k+1} = \mathbf{\Phi}^k \cdot \hat{\mathbf{y}}^k + \mathbf{G}^k \cdot \mathbf{w}^k + \mathbf{L}^k \cdot \mathbf{u}^k, \quad (5.2)$$

where $\mathbf{\Phi}^k$ is the transition matrix calculated from the equations of motion with respect to the state vector parameters, $\hat{\mathbf{y}}$ is the updated state vector at epoch k , \mathbf{G}^k and \mathbf{w}^k are the matrix and vector of disturbing variables or noises. \mathbf{L}^k and \mathbf{u}^k are the matrix and vector of acting forces. In this dissertation, the influence of acting forces is neglected for simplification. The prediction step allows to compensate the displacement data gaps derived by different sampling frequencies of the acceleration and displacement measurements. Alternatively, the IATS displacement data with a lower sampling frequency can be resampled based on a reconstructed displacement data by using the estimated DHO model parameters (see Figure 5.1).

The observation model is determined by

$$\begin{aligned} \ell^{k+1} &= \mathbf{A}^{k+1} \hat{\mathbf{y}}^{k+1} + \mathbf{e}^{k+1}, \\ \begin{bmatrix} d^{k+1} \\ a^{k+1} \end{bmatrix} &= \begin{bmatrix} 1 & 0 & 0 \\ 0 & 0 & 1 \end{bmatrix} \begin{bmatrix} d^{k+1} \\ v^{k+1} \\ a^{k+1} \end{bmatrix} + \mathbf{e}^{k+1}, \end{aligned} \quad (5.3)$$

where ℓ is the observation vector, \mathbf{A} the design matrix and \mathbf{e} the vector of residuals. The transition matrix is then derived by integration with respect to the state vector parameters, that is

$$\mathbf{\Phi}^k = \begin{bmatrix} 1 & \Delta t & \frac{1}{2} \Delta t^2 \\ 0 & 1 & \Delta t \\ 0 & 0 & 1 \end{bmatrix}, \quad (5.4)$$

where Δt is the sampling interval. The covariance matrix of the process noise is defined based on Wiener-sequence acceleration (Bar-Shalom et al., 2004) with

$$\mathbf{\Sigma}_{ww} = \begin{bmatrix} \frac{1}{20} \Delta t^5 & \frac{1}{8} \Delta t^4 & \frac{1}{6} \Delta t^3 \\ \frac{1}{8} \Delta t^4 & \frac{1}{3} \Delta t^3 & \frac{1}{2} \Delta t^2 \\ \frac{1}{6} \Delta t^3 & \frac{1}{2} \Delta t^2 & \Delta t \end{bmatrix} \tilde{q}, \quad (5.5)$$

where \tilde{q} is the ratio between the system noise and observation noise. The covariance matrix of the observations is given by

$$\mathbf{\Sigma}_u = \begin{bmatrix} \sigma_d^2 & 0 \\ 0 & \sigma_a^2 \end{bmatrix}, \quad (5.6)$$

where σ_d and σ_a are the *a priori* standard deviations of the displacements and the accelerations, which are set to 0.0001 m and 0.013 m/s², respectively. A correlation between the displacement and acceleration data is neglected due to their independent measurements. As stated before, the aforementioned *a priori* standard deviations are obtained from the estimation procedure described

in chapter 4. The similar numerical results can be found in subsection 2.3.2 and chapter 6. For further detailed formulations concerning the KF steps, please refer to Kalman (1961); Gelb (1974); Omidalizarandi and Zhou (2013).

5.3 Heterogeneous Data Fusion of Displacement and Acceleration Measurements

A 1D displacement data, with a sampling frequency of 10 Hz, obtained from an IATS, e.g., Leica MS50, is integrated with an acceleration data, with a sampling frequency of 100 Hz, recorded from a MEMS accelerometer in the vertical direction to generate high accurate displacement time series. As previously stated, the coloured measurement noise of the aforementioned measurements are decorrelated based on the AR process, as part of the GEM algorithm, to handle the autocorrelation. Next, 1D CUPT is performed within the KF framework based on the equations of motion, which subsequently allows to optimally estimate state vector parameters including displacements, velocities and accelerations (see section 5.2). Therefore, the displacement drift derived from double integration of the acceleration data is minimised by using the IATS displacement data within the filtering step of the KF algorithm (Omidalizarandi et al., 2019c).

In order to fuse different sensors with different measurements and sampling frequencies, a time synchronisation is required in advance. Ideally, a very precise time synchronisation should be accomplished at the hardware level, e.g., by using GPS pulse per second (PPS) signals and a micro-controller. However, in this dissertation, the time synchronisation between displacement and acceleration measurements is carried out based on the cross-correlation (Ferrari et al., 2016). This is a challenging task, since the measurements of different sensors might have different units. To overcome this problem in this research, the MEMS acceleration data is double integrated within a selected excitation window. Next, the displacement time series obtained from the MEMS accelerometers and the IATS are resampled to a sampling frequency of a reference sensor, i.e., a laser tracker, with a sampling frequency of 1000 Hz. In case of not availability of the reference sensor, the resampling can be performed to a sampling frequency of the acceleration data similar to the work of Park et al. (2018). Next, the cross-correlations between the IATS and MEMS displacement data are calculated with respect to the laser tracker (Figure 5.2). The calculated time lags account for maximum values of occurred cross-correlations (Omidalizarandi et al., 2019c).

Figure 5.2 illustrates the cross-correlations between the IATS and the MEMS displacement data with respect to the laser tracker displacement data in which their maximum cross-correlation values are 0.74 and 0.82, respectively. Theoretically, it is expected to achieve a better cross-correlation between the IATS and the laser tracker data. However, the proposed double integration approach (see section 4.5) deduces a high accurate MEMS displacement data with a wider frequency bandwidth as well as a higher resolution, which yields slightly higher maximum cross-correlation values. To have a better realisation of the generated displacement data and the accuracy of the time synchronisation, the generated IATS and the MEMS displacement data are overlaid with the laser tracker data after performing the time synchronisation (see Figure 5.3) (Omidalizarandi et al., 2019c). As it can be seen from this figure, the peaks of the aforementioned displacement data sets are properly fitted together. In addition, peaks of the MEMS displacement data are slightly closer to the peaks of the laser tracker compared to the IATS data, which reveals the extraction of higher eigenfrequencies from the MEMS displacement data. The slightly jagged laser tracker data are at the level of the corresponding uncertainty of the measurements, which is very small.

Two alternative solutions are proposed and implemented to fuse displacement and acceleration data with different sampling frequencies within the KF framework. In the first solution, multi-rate KF similar to the work of Smyth and Wu (2007) and Ferrari et al. (2016) is applied. Therefore, innovation and design matrices are adaptively updated to be compatible with the sampling frequencies

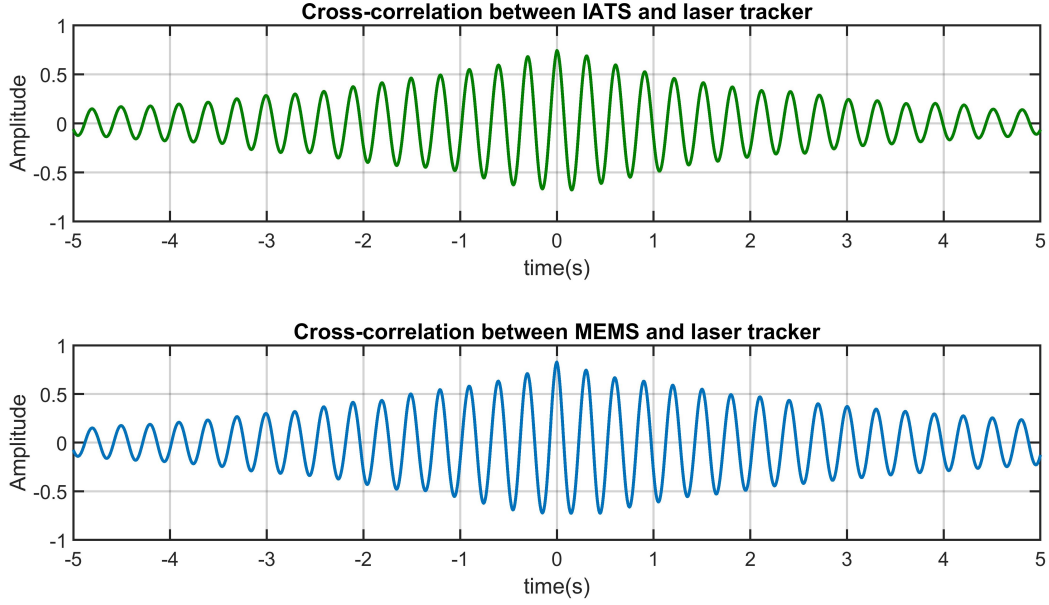


Figure 5.2: Cross-correlations between the IATS and the laser tracker displacement data (top), and the double integrated adjusted MEMS acceleration data (MEMS displacement data) and the laser tracker data (bottom) within the selected ambient window.

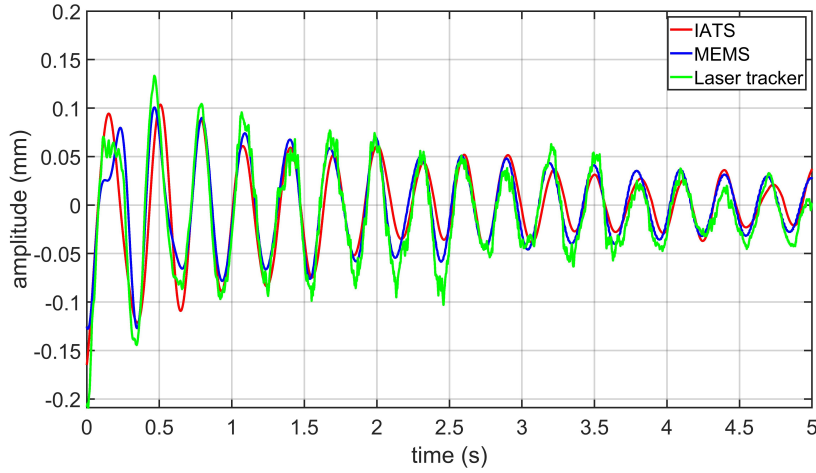


Figure 5.3: Overlaying of the displacement data obtained from the IATS (red colour), the MEMS displacement data (blue colour) and the laser tracker data (green colour) within the selected ambient window.

of the measurements (Figure 5.4). In the second solution, the displacement data are resampled to the sampling frequency of the acceleration data. Each of the aforementioned approaches has its own advantages and disadvantages. In the multi-rate KF, different types of measurements are fused with their own sampling frequencies. In addition, it allows considering the measurements with their estimated uncertainties obtained from the estimation procedure. However, it is a challenging task when the IATS displacement data are not available. By contrast, the resampling KF enables us to consider more displacement data sets than the raw displacement observations (Omidalizarandi et al., 2019c). However, it is vital to accurately and reliably estimate the DHO model parameters, since the resampled displacement data is directly influenced by the estimated DHO

model parameters. The pattern recognition techniques may assist to predict the displacement data for different loads, which shall be considered in the future work.

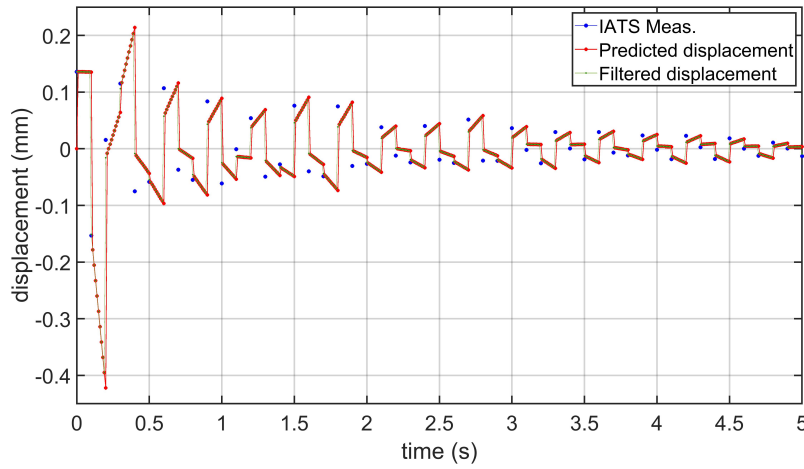


Figure 5.4: The displacements analysis based on the multi-rate KF approach by using the displacement and acceleration measurements: the displacements obtained from the IATS (blue), the predicted displacements (red) and the filtered displacements (green).

5.4 Summary

In this chapter, the good feasibility of MEMS accelerometers supported by an IATS for short- and long-term displacement monitoring of bridge structure is demonstrated. For this purpose, the IATS displacement data and the MEMS acceleration data are fused within the KF framework.

Such a sensor fusion is beneficial due to good and complementary coverage of lower and upper frequency ranges by means of the IATS and MEMS displacement data. Subsequently, a high accurate displacement time series at a submillimetre range is generated, which has a higher resolution as well as a wider frequency bandwidth.

A time synchronisation at the level of approximately 0.01 – 0.02 s is carried out, as a preliminary step, based on cross-correlation of the displacements time series of the aforementioned sensors with a reference sensor. MEMS displacement data is generated by double integration of the MEMS acceleration data within a selected excitation window and by using the DHO model parameters estimated from the GEM algorithm. Furthermore, the aforementioned estimation procedure allows to decorrelate the high coloured measurement noise contaminated with the acceleration data. Subsequently, *a posteriori* standard deviations of the white noise measurements of the displacement and the acceleration data are estimated, which are used within the KF algorithm.

The 1D CUPT within the multi-rate KF framework is carried out to compensate a displacement drift of the MEMS accelerometers by using the IATS displacement data in vertical direction. Alternatively, the resampling KF is performed by resampling the IATS displacement data to the sampling frequency of the acceleration data. The resampling of the displacement data based on their estimated modal parameters greatly improves the results by increasing the number of the IATS displacements data. However, its estimation is directly influenced by the estimated DHO model parameters. By contrast, the multi-rate KF allows to perform aforementioned data fusion by using different types of measurements with their own sampling frequencies.

6 Experiments and Results

Experiments are carried out in four case studies including simulation, controlled excitation and two real applications of a footbridge structure and a synthetic laboratory bridge. In the first case study, a simulated acceleration data is generated, which is then employed and solved by the proposed RT-MPI algorithm (Omidalizarandi et al., 2020). Therefore, the analysis of the simulated data allows to compare and validate the estimated DHO parameters, i.e., eigenfrequencies, damping ratio coefficients, amplitudes, and phase shifts, with their true values. In addition, the estimated parameters are compared with the well-known SSI-COV algorithm which was implemented in MATLAB by Cheynet (2020). In the simulation experiment, it is expected to reach the highest accuracy of the estimates of the aforementioned parameters due to generating a free vibration decay of a signal. However, true measurements are contaminated with coloured measurements noise and outliers to assess the robustness of the proposed algorithm. Subsequently, the frequencies are estimated at the accuracy level of third to fourth decimals, the damping ratio coefficients are estimated at the accuracy level of second to third decimals, the amplitudes (depending on amplitudes of low and high frequencies) in $[m/s^2]$ are estimated at the accuracy level of second to third decimals, the amplitudes in $[mm]$ are estimated at the accuracy level of second to fourth decimals, and the phase shifts are estimated at an average accuracy level of approximately 1.0° . The analysis of this experiment is mainly inspired from the research of Omidalizarandi et al. (2020) with a minor extension, which is related to the estimates of df by means of the *mle* MATLAB routine. Subsequently, despite of speeding up the process, it yields correct estimates of the df . In addition, some complementary results are also provided. To this end, the analysis of the simulation experiment proves the proposed RT-MPI algorithm theoretically and numerically. In addition, it is demonstrated that the robustness and accuracy of the proposed algorithm is much more than expected and needed for real application of bridge structures, and thereof, is fully satisfactory.

In the controlled excitation experiment, the aforementioned DHO parameters are estimated for MEMS acceleration data as well as IATS displacement data. Subsequently, the estimated parameters are compared and validated with their corresponding known values. Additionally, it gives an idea about the auto-correlation and stochastic models of the vibration measurements. Moreover, the estimated uncertainties of the measurements from this experiment could also be used in 1D CUPT within the KF approach. Using high accurate reference sensors such as a laser tracker enables us to validate the estimated amplitudes in $[mm]$. Moreover, such experiments allow to check the accuracy of time synchronisation between different MEMS accelerometers. The analysis of this case study is mainly inspired from the research of Omidalizarandi et al. (2018). However, it is extended by adding the analysis of the MEMS accelerometers. Furthermore, the analysis is improved by the recent version of the RT-MPI algorithm.

In the third case study, a vibration analysis is carried out for a footbridge structure, and by using the MEMS and PCB piezoelectric (PCB piezotronics, 2019) reference accelerometers. Therefore, the modal parameters including eigenfrequencies, damping ratio coefficients, and eigenforms could be identified for both aforementioned sensors what allows to perform a validation. As a preliminary step, the FEM analysis is performed, which allows to place the sensors in their optimal positions. In addition, it provides us the foreknowledge about possible eigenfrequencies and eigenforms. The analysis of this case study reveals that the MEMS accelerometers are suitable for identifying all occurring eigenfrequencies of the bridge structures. Moreover, the vibration analysis procedure demonstrates that amplitudes are estimated in submillimetre range accuracy, frequencies with an

accuracy of better than 0.1 Hz and damping ratio coefficients with an accuracy of better than 0.1 and 0.2% for modal and system damping, respectively. Additionally, the estimated eigenfrequencies and modal damping are compared with the SSI-COV approach. The results demonstrate the superiority of the proposed RT-MPI algorithm compared to the SSI-COV algorithm. The reason lies in the fact the proposed RT-MPI algorithm does not restrict to a free vibration decay of vibration measurements, and thus, can provide the accurate and robust results for the entire time series. This is achieved by performing the estimation at each selected excitation (e.g. ambient) window. Subsequently, median values of all estimated eigenfrequencies and damping ratio coefficients yield reliable and accurate results. The aforementioned accuracy of the estimated parameters could even be improved by performing the measurements at different time intervals over a day or a week. Therefore, the influence of imposed loads such as moving vehicles and wind could be mitigated. It should be mentioned that the influence of the temperature and humidity on the estimated modal parameters are neglected, since it is required extensive experiments over a month or a year which was out of the timeline of this dissertation.

The fourth case study is conducted for a synthetic laboratory bridge, which is oscillated by imposing a load by a modal hammer. The measurements are performed by using MEMS accelerometers, an IATS, a laser tracker, and a geophone. The analysis of this experiment is inspired from the research of Omidiazarandi et al. (2020). The results show that the frequencies are estimated at the accuracy level of third decimals, and the damping ratio coefficients are estimated at the accuracy of second to third decimals. Consequently, it demonstrates the high accuracy and robustness of the proposed RT-MPI algorithm. In addition, the MEMS and the IATS measurements are fused in this experiment, which subsequently enables to generate a high accurate displacement time series at the level of submillimetre by performing 1D CUPT within the KF framework. An overview of the aforementioned experimental studies is represented in Figure 6.1.

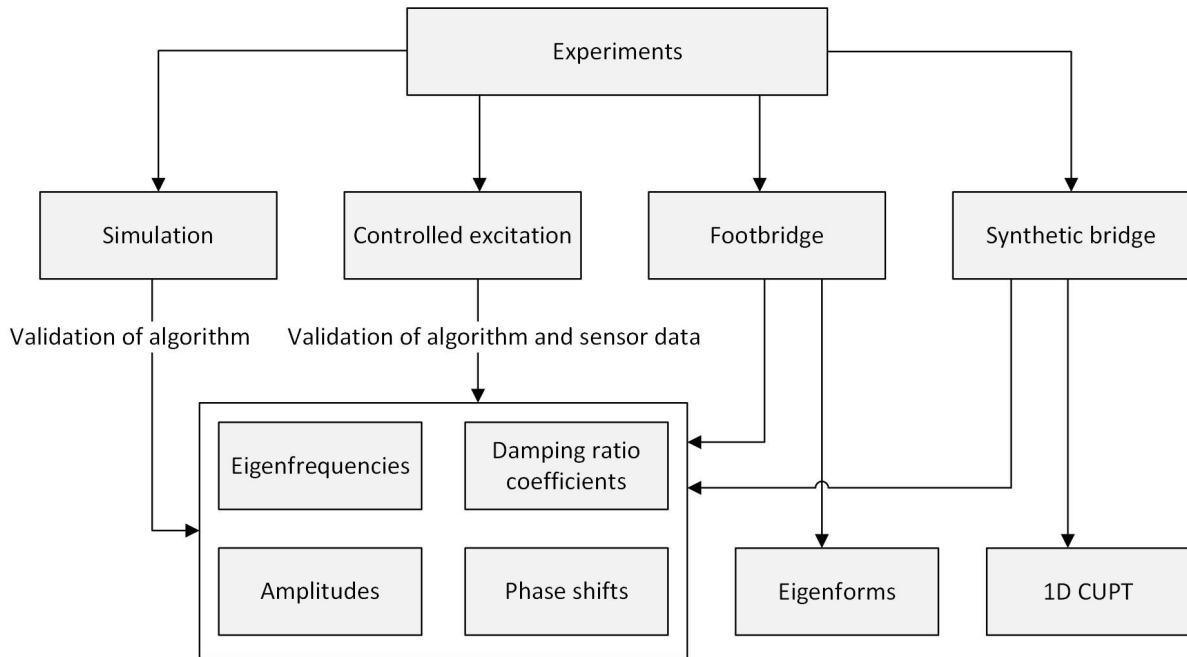


Figure 6.1: An overview of the experimental studies and their individual goals.

6.1 Example based on Simulated Acceleration Data

In the simulation experiment, a true observation vector is defined based on the DHO model with a sampling frequency of 100 Hz, which spanned 100 s of the acceleration data. The parameter val-

ues of the DHO model (Equation 4.3) are set to $a_0 = 0 \text{ [m/s}^2\text{]}$, $a_j = (4.0, 2.0, 2.0, 8.0) \text{ [m/s}^2\text{]}$, $b_j = (-3.0, 3.0, 3.0, 7.0) \text{ [m/s}^2\text{]}$, $f_j = (5.0, 5.3, 15.0, 35.0) \text{ [Hz]}$, $\xi_j = (0.5, 0.8, 0.8, 0.5) \text{ [%]}$ (for $j \in [1, 2, 3, 4]$). The white noise vector is generated under the t-distribution assumption (see Equation 4.6) with parameter values $\sigma^2 = 0.04$ and $\nu = 4.0$ and with the same length of the simulated acceleration data. Next, the white noise vector is turned into the coloured noise vector by considering an AR(1) process with the AR model coefficient value $\alpha_1 = 0.4$. The generated coloured noise vector is then added to the true observation vector to generate the noisy and auto-correlated acceleration data (Figure 6.2).

The unknown parameters consist of the functional model parameters (Equation 4.3), i.e., Fourier coefficients, frequencies, and damping ratio coefficients, the parameters of the correlation model (Equation 4.5), i.e., the AR model coefficients and the parameters of the stochastic model (Equation 4.6), i.e., the unknown df and the unknown scale factor, which are adjusted by means of the GEM algorithm (see section 4.4). The amplitudes and phase shifts are calculated by considering the cosine form of the Equation 4.3 without damping ratio coefficients (Equation 4.22) and based on the Equations 4.23 – 4.24, respectively. As stated before, the initial frequencies are required to be identified in advance (see section 4.3). The overview of the proposed RT-MPI algorithm can be seen from Figure 4.1. The first 20 s of the simulated acceleration data and their corresponding adjusted data are illustrated in Figure 6.2. In addition, Figure 6.3 shows the estimated coloured noise residuals and decorrelated residuals of the simulated acceleration data. Such results are derived from the filtering (Equation 4.7) of the former residuals by means of the inverted estimated AR model.

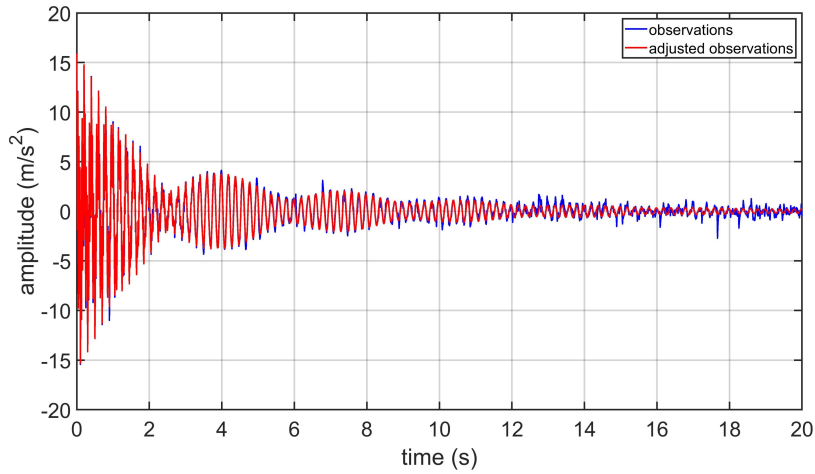


Figure 6.2: Simulated acceleration data based on the DHO model contaminated with coloured noise (blue solid line), and the DHO model fitted to the simulated acceleration data (red solid line) (The first 20 s).

Figure 6.4 depicts the DFTs of both simulated acceleration data and their corresponding adjusted data in the amplitude spectrum. As it can be seen, all eigenfrequencies are identified even two closely spaced frequencies of 5.0 and 5.3 Hz. Figure 6.5 illustrates the magnification of the aforementioned closely spaced frequencies. The amplitudes of the dominant peaks, which correspond to all eigenfrequencies, in both DFT results are very close to each other, which yields a minimum RMSE value (see Equation 4.1). Subsequently, it demonstrates an optimal and reliable identification of the eigenfrequencies as well as a robust and accurate estimation of the modal parameters.

Figure 6.6 shows histogram of the estimated white noise residuals, a fitted normal distribution with parameter values $N(\mu = -0.0023, \sigma^2 = (0.2753)^2)$ as well as fitted t-distribution with parameter

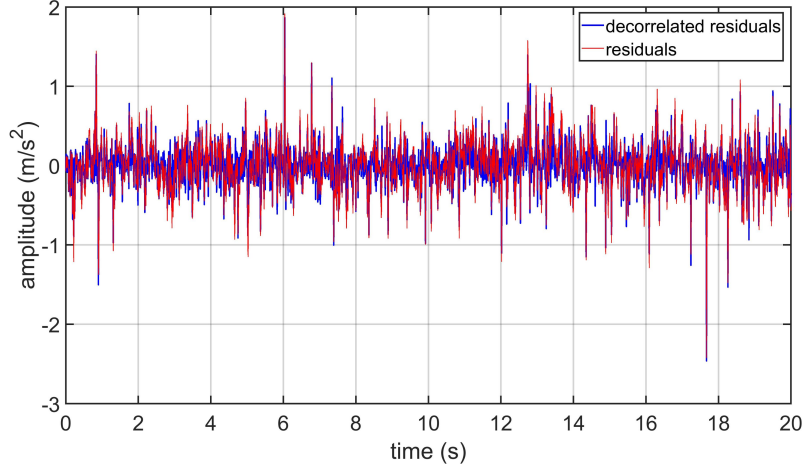


Figure 6.3: The estimated coloured noise residuals (red dashed line) and decorrelated residuals (blue solid line) of the simulated acceleration data (The first 20 s).

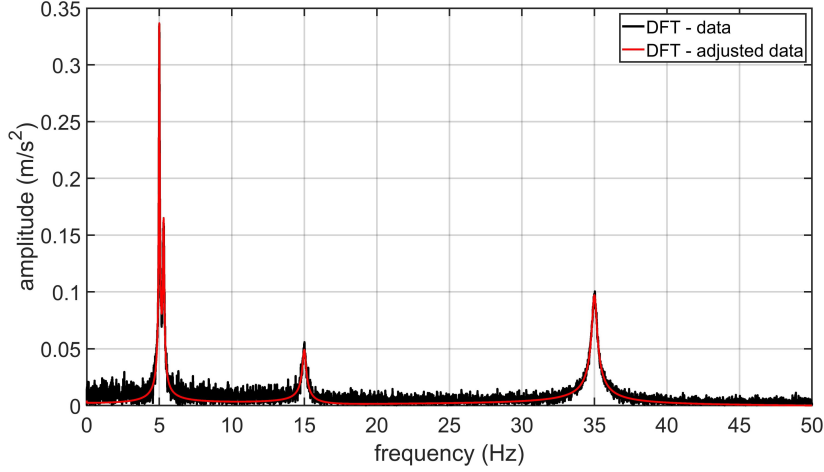


Figure 6.4: The DFTs of the simulated acceleration data (black solid line) and their corresponding adjusted data (red solid line) in the amplitude spectrum.

values $t(\nu = 4.3662, \sigma^2 = (0.2027)^2)$. As it can be seen, the t-distribution is nicely fitted to the white noise residuals, which is narrower than the normal distribution. Figure 6.7 depicts the histogram of the adjusted weights. As described by Koch (2013b); Kargoll et al. (2018); Kargoll et al. (2020a), the adjusted weights increase relatively smooth from lower to higher values in which outliers are located in the tails of t-distribution, and thus, having lower weights.

To estimate amplitudes in metric unit, e.g., millimetre, Omidalizarandi et al. (2020) proposed two different methods of double integration by using the DHO model and the equations of motion, which are briefly described in section 4.5. Figure 6.8 represents the first 20 s of displacement time series for the simulated acceleration data, which is generated based on double integration of the DHO model. It is worth mentioning that the aforementioned double integration approach is capable of reconstructing highly accurate displacement time series while there is a robust and accurate estimate of the DHO model parameters available from the estimation procedure. An optimal and proper selection of an excitation (ambient) window highly affects the accuracy of the estimated amplitudes obtained from double integration. For furthermore information in this regard, please

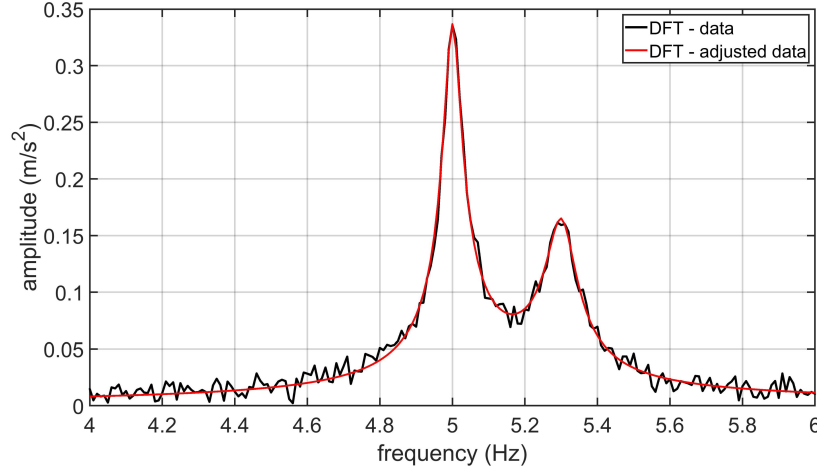


Figure 6.5: The magnification of the DFTs of the simulated acceleration data (black solid line) and their corresponding adjusted data (red solid line) in the amplitude spectrum, showing two closely spaced frequencies of 5.0 and 5.3 Hz.

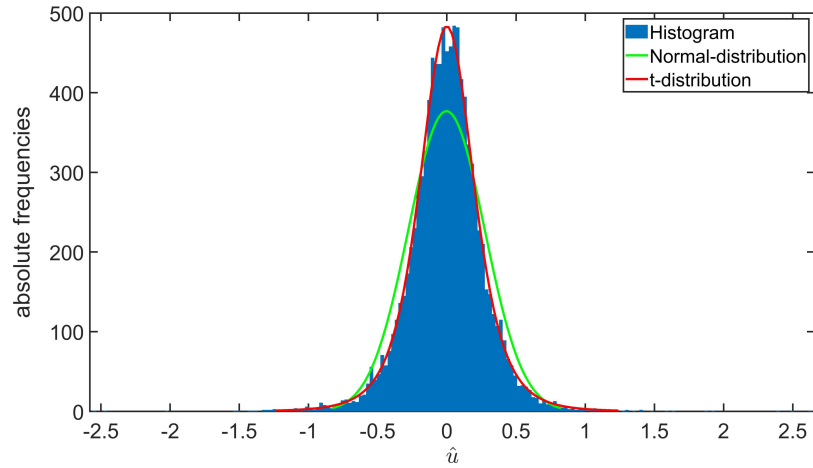


Figure 6.6: Histogram of the estimated white noise residuals (blue colour), fitted normal distribution with $N(\mu = -0.0023, \sigma^2 = (0.2753)^2)$ (green solid colour) and fitted t-distribution with $t(\nu = 4.3662, \sigma^2 = (0.2027)^2)$ (red solid colour).

refer to the chapter 4.

Table 6.1 represents the statistics of the estimated unknown parameters including the DHO model parameters, the correlation model parameter, and the stochastic model parameters by the proposed RT-MPI algorithm (Omidalizarandi et al., 2020). In addition, the DHO model parameters are compared with the SSI-COV algorithm implemented in MATLAB by Cheynet (2020). However, the aforementioned SSI-COV algorithm cannot estimate correlation and stochastic model parameters. In order to use the SSI-COV algorithm, two slightly different time series are generated based on two different white noise vectors, which are then used to calculate the cross covariance of the different data sets. The SSI-COV algorithm is applied by tuning the parameters similar to the work of Cheynet et al. (2017) as follows: (1) the time lag of a correlation function is set to 6.4 cycles of a lower frequency (Magalhaes et al., 2009), i.e., here $6.4 \cdot 5 = 32$, (2) the minimum and maximum values of modal orders are set to 2 and 30, respectively, (3) the eigenfrequency variation is set to $1 \cdot 10^{-2}$, (4) the modal damping coefficient variation is set to $3 \cdot 10^{-2}$, (5) the minimum MAC

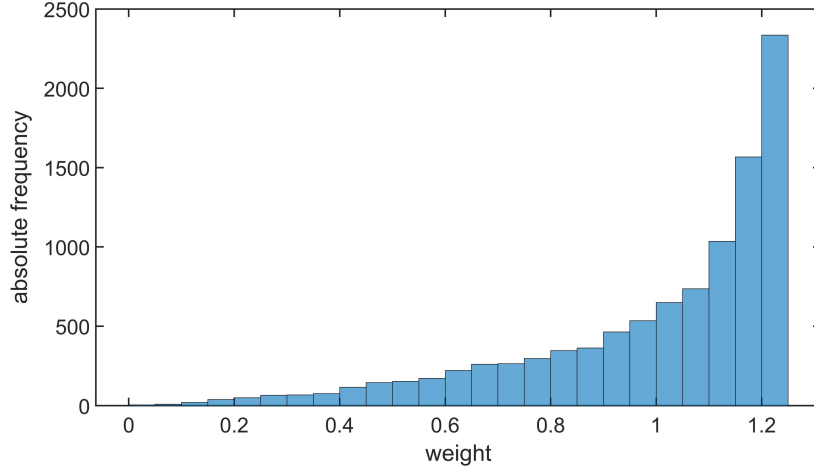


Figure 6.7: Histogram of the adjusted weights.

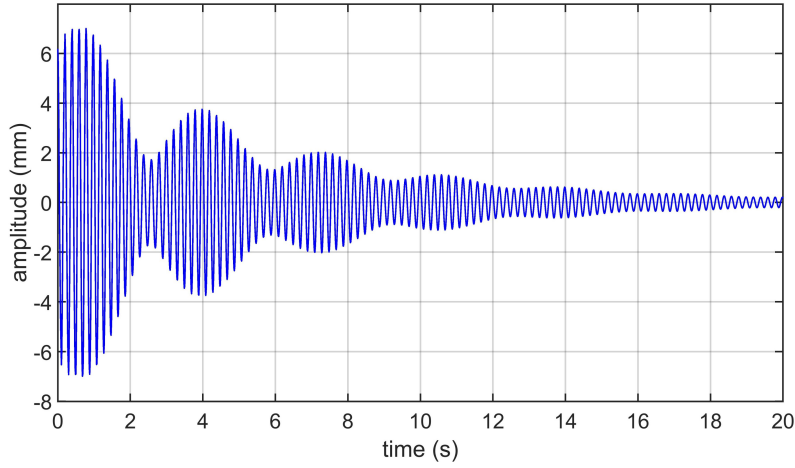


Figure 6.8: The displacement time series calculated for the simulated acceleration data based on double integration of the DHO model (The first 20 s).

variation between eigenforms is set to $5 \cdot 10^{-3}$, and (6) the distance between two modes is set to $2 \cdot 10^{-2}$ (Omidalizarandi et al., 2020).

In the proposed RT-MPI algorithm, the unknown parameters are estimated for three cases where the ν is obtained by applying *INTLAB*, *fzero*, and *mle*. As it can be seen, the estimated frequencies from the aforementioned three variants of the RT-MPI algorithm are very close to each other in which their differences are at the level of third to fourth decimals. The percentage errors for two lower frequencies (i.e., 5 and 5.3 Hz), and for two higher ones (i.e., 15 and 35 Hz), are 0.0191 and 0.0005 % in case of the *INTLAB*, 0.0283 and 0.0085 % in case of the *fzero*, 0.0191 and 0.0005 % in case of the *mle*, and 0.0194 and 0.0053 % in case of the SSI-COV algorithm, respectively. The percentage error of the estimated damping ratio coefficients with their nominal values reveal the average values of 1.02, 1.87, and 1.03 % for the first to third variants of the RT-MPI algorithm, respectively, which is about 1.44 % in case of the SSI-COV algorithm. To this end, the frequencies and damping ratio coefficients are estimated high accurately in both RT-MPI (all variants) and the SSI-COV algorithms. Regarding the estimates of the amplitudes in $[\text{m/s}^2]$ in the RT-MPI algorithm, the average percentage errors of 0.9, 1.19, and 0.9 % are calculated for the first to third

Table 6.1: Statistics of the unknown parameters including the DHO model parameters, the correlation model parameters, and the stochastic model parameters, estimated from the RT-MPI algorithm that are compared and validated with the SSI-COV algorithm and their known values for the simulated acceleration data (Omidalizarandi et al., 2020).

Parameters	f [Hz]	A [m/s ²]	A_{DHO} [mm]	A_{MOTION} [mm]	ξ [%]	ϕ [°]	α_1 [-]	ν [-]	σ^2 [-]
Simulated data	5.0000	5.0000	5.0661	5.0661	0.5000	36.8699	0.5000	4.0000	0.0400
	5.3000	3.6056	3.2514	3.2514	0.8000	-56.3099			
	15.0000	3.6056	0.4059	0.4059	0.8000	-56.3099			
	35.0000	10.6301	0.2198	0.2198	0.5000	-41.1859			
RT-MPI (ν determined by <i>INTLAB</i>)	4.9996	5.1110	5.1792	5.1539	0.5141	37.7709	0.4939	4.3662	0.0411
	5.3016	3.6282	3.2697	3.2494	0.7976	-58.1599			
	15.0001	3.5848	0.4036	0.3798	0.8053	-56.8767			
	34.9999	10.6103	0.2194	0.1452	0.5015	-41.2764			
RT-MPI (ν determined by <i>fzero</i>)	4.9999	5.1322	5.2003	5.1745	0.5153	37.2764	0.4991	10000	0.0757
	5.3029	3.5597	3.2064	3.1862	0.7731	-59.4356			
	14.9978	3.5773	0.4028	0.3789	0.7942	-56.1857			
	34.9992	10.6376	0.2199	0.1452	0.5016	-41.3963			
RT-MPI (ν determined by <i>mle</i>)	4.9996	5.1112	5.1795	5.1538	0.5142	37.7676	0.4939	4.4274	0.0413
	5.3016	3.6278	3.2693	3.2474	0.7974	-58.1643			
	15.0001	3.5846	0.4035	0.3712	0.8052	-56.8707			
	34.9999	10.6104	0.2194	0.1399	0.5015	-41.2769			
SSI-COV	5.0010	-	-	-	0.4900	36.8331	-	-	-
	5.3010	-	-	-	0.8100	55.7620			
	15.0012	-	-	-	0.7800	56.5484			
	34.9991	-	-	-	0.5000	56.9214			

variants. Subsequently, it shows that the first and third variants achieve highly accurate estimates of the amplitudes in [m/s²], which are slightly better than the second variant. In addition, double integration by using the DHO model achieves considerably accurate estimates of the amplitudes in [mm] compared to the second method which is using the equations of motion. The percentage errors of the estimated amplitudes in [mm] based on the DHO model are 0.88, 1.21, and 0.89 % for the first to third variants. In case of the equation of motion, the percentage errors of the estimated amplitudes in [mm] are 10.54, 11.18, and 11.79 % for the first to third variants, which have significant differences with their nominal values. It should be mentioned that the current version of the SSI-COV algorithm does not derive the amplitudes. The percentage errors of the estimated phase shifts show average levels of 1.74, 1.85, and 1.74 % for the first to third variants of the RT-MPI algorithm. However, the estimated phase shifts from the SSI-COV algorithm are significantly different, which are therefore not comparable with their nominal values as well as the RT-MPI algorithm. The percentage errors of the estimated AR(1) model coefficient (α_1) for all three variants of the RT-MPI algorithm are 1.22, 0.18, and 1.22 %, which are very small and negligible. The stochastic model parameters (ν and σ^2) obtained from the first and third variants of the RT-MPI algorithm reveal accurate estimates of the parameters. By contrast, the second variant of the RT-MPI algorithm shows significant differences from its true values in which accounts for a rather close approximation of the normal distribution with the higher df. However, the SSI-COV algorithm does not calculate the AR and stochastic model parameters (Omidalizarandi et al., 2020).

The analysis of the simulation study demonstrates and validates the robustness, and high accuracy of the estimated unknown parameters in the first and third variants of the RT-MPI algorithm. However, the first variant is computationally expensive compared to the second and third one.

Subsequently, the first variant is mainly suitable to be applied in a post-processing step. The third variant is slightly slower (i.e., some few seconds) than the second one, which is due to applying the GEM algorithm once more with correct estimates of the df. To get a rough idea of a run time speed of the aforementioned three variants, the analysis of the simulated data with a length of 10000 takes about 10144, 64, and 67 s for the first to third variants. Therefore, it indicates that the first variant is approximately 153 times slower than two other variants. However, the run time speed of the algorithm can be changed depending on size of data sets, a maximum AR model order, and the number of vectors of initial eigenfrequencies. It is worth mentioning that the estimated modal parameters from the second variant of the RT-MPI algorithm do not show significant differences with their nominal values despite of significantly different estimates of the stochastic model parameters. In near real-time processing, it is recommended to apply either the second or the third variants of the RT-MP algorithm. However, the third variant will achieve more robust and accurate results. Moreover, the analysis reveals that the RT-MPI algorithm is superior to the SSI-COV algorithm with no necessity for defining tuning parameters. It might be a good idea to jointly benefit from the SSI-COV and the RT-MPI algorithms in real-time processing, which its further investigation could be part of the future work.

6.2 Example based on Shaker Vibration Calibrator

Controlled excitation experiments are carried out to estimate harmonic oscillation parameters consisting of frequencies, amplitudes, and phase shifts for vibration measurements (ℓ) obtained from either the MEMS acceleration data or the IATS displacement data. Subsequently, the estimated parameters are compared and validated with their corresponding known values. In addition, it gives an idea about the auto-correlation and stochastic models of the vibration measurements. Possibly, time-variability of the AR model (Kargoll et al., 2017) can also be investigated through the GEM algorithm, but it is out of focus of this dissertation.

For this purpose, the controlled excitation experiments are carried out by using shakers in the laboratories of the Geodetic Institute Hannover (GIH), Institute of Concrete Construction (IFMA), and the IDS, LUH. As previously stated, the shaker in the IDS was used for the suitability analysis in selecting optimal MEMS accelerometers (see section 2.3). In this section, the controlled excitation experiment is conducted by using a portable shaker vibration calibrator 9210D (PSVC) (Figure 6.9, left) in the laboratories of IFMA and GIH, due its availability at the time of experiment. Additionally, two high-end reference sensors such as a laser tracker of type AT960-LR (Figure 6.9, right) and a reference accelerometer of type PCB ICP quartz are used for the purpose of validation. The laser tracker is a reference measurement system, which allows to measure 3D point data with a maximum permissible error of $15\mu\text{m} + 6\mu\text{m}/\text{m}$, and maximum sampling frequency of 1000 Hz (Hexagon, 2015). However, in this experiment, its sampling frequency is set to 200.

The aforementioned experiment is accomplished for oscillation frequencies of 2, 3, 4, 10, and 15 Hz with an amplitude of 0.3 m/s^2 , which are set throughout two sensitive dials of PSVC. Each frequency is measured for about seven minutes by means of the MEMS, the IATS, the PCB reference accelerometer, and the laser tracker. However, the higher frequencies of 10 and 15 Hz cannot be detected by the IATS, due to its low practical sampling frequency of 10 Hz (in view of the Nyquist sampling theorem). The PSVC is located at a distance of approximately 5.36 m from the laser tracker and the IATS. The laser tracker measurements are performed by using a Leica red-ring reflector (RRR) 0.5 inch ball (i.e., with a radius of $6.35\text{ mm} \pm 0.0025\text{ mm}$ and an acceptance angle $\leq \pm 30^\circ$), that is mounted on a small platform attached to the PSVC (Figure 6.9, left). The MEMS accelerometer is placed inside the aforementioned platform which records the acceleration data with the sampling frequency of 100 Hz in this research. The PCB reference accelerometer is an internal sensor of the PSVC, which its sampling frequency is set to 200 Hz. An optimal passive target (as proposed by Omidalizarandi et al., 2019a) is rigidly attached to the platform, which is

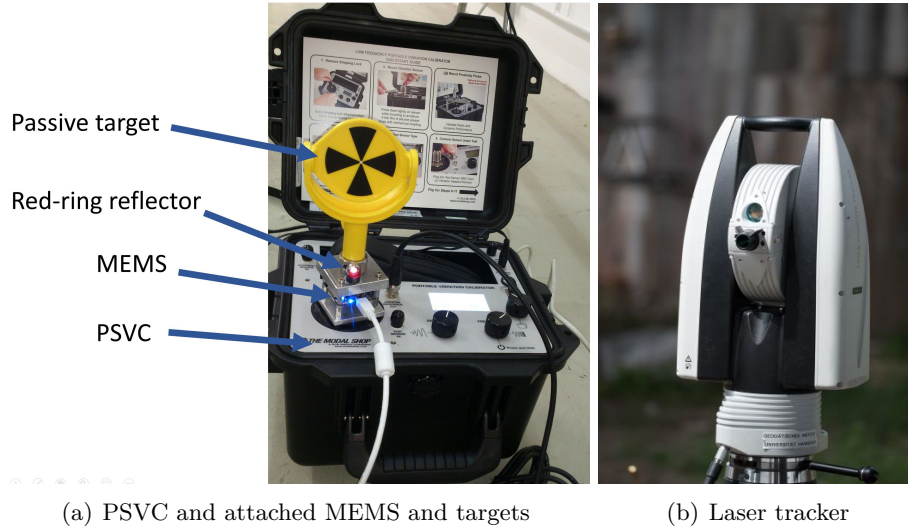


Figure 6.9: A vibration analysis based on the MEMS and the reference acceleration data as well as the IATS and the laser tracker displacement data sets through the controlled excitation experiment in the laboratory of GIH by using the PSVC 9210D (Omidalizarandi et al., 2018).

captured by means of the telescope camera of the IATS with the sampling frequency of 10 Hz. The centroid of the passive target is extracted based on the research of (Omidalizarandi et al., 2019a) to generate a highly accurate displacement data (see section 3.3). Afterwards, the calibrated vertical angular conversion factor is used to convert vertical displacements data from pixel to metric unit (see section 3.4).

In this experiment, it is assumed that vibration measurements have no significant damping. Therefore, an observation model consisting of the UDHO model (i.e. the DHO model (Equation 4.3) by setting the damping ratio coefficients to zero), the AR model, and the scaled t-distribution with an unknown df and an unknown scale factor are employed and jointly adjusted by means of the GEM algorithm (Omidalizarandi et al., 2018). To test whether the damping of observed oscillations from the aforementioned PSVC is significant or not, Kargoll et al. (2019) proposed two bootstrap tests and compared the calculated p-values with the significance level ($\alpha = 0.05$). As a result, it was verified that the vibration measurements recorded from the PSVC have no significant damping. Subsequently, it justifies the right use of the UDHO model within the GEM algorithm in the aforementioned experiment. As described by Kargoll et al. (2019), the proposed bootstrap testing procedure can be used for a factory calibration of the PSVC by testing oscillation-related parameters using the recorded acceleration data. The readers are referred to Kargoll et al. (2019) for further information in this regard.

Table 6.2 summarises the statistics of the displacement and vibration analysis for the aforementioned four sensors, and with an excitation window size of 50 s except for the IATS. The excitation window size of 100 s is selected for the IATS data due to its low sampling frequency. According to the analysis, the percentage errors of the estimated frequencies for the three lower ones (i.e., 2, 3, and 4 Hz), and for the two higher ones (i.e., 10, and 15 Hz) show average levels of 0.0044, and 0.0048 % in case of the PCB, 0.010, and 0.011 % in case of the MEMS, 0.0036, and 0.0028 % in case of the laser tracker, which is about 0.066 % in case of the IATS for the three lower ones. In case of the IATS, the estimated frequencies have relatively larger percentage errors compared to the estimates obtained from other sensors. This is due to the reason that it has significantly lower sampling frequency compared to others. In case of the MEMS, its corresponding percentage error is very small, which is negligible. For the MEMS accelerometer, the amplitudes in $[m/s^2]$ are

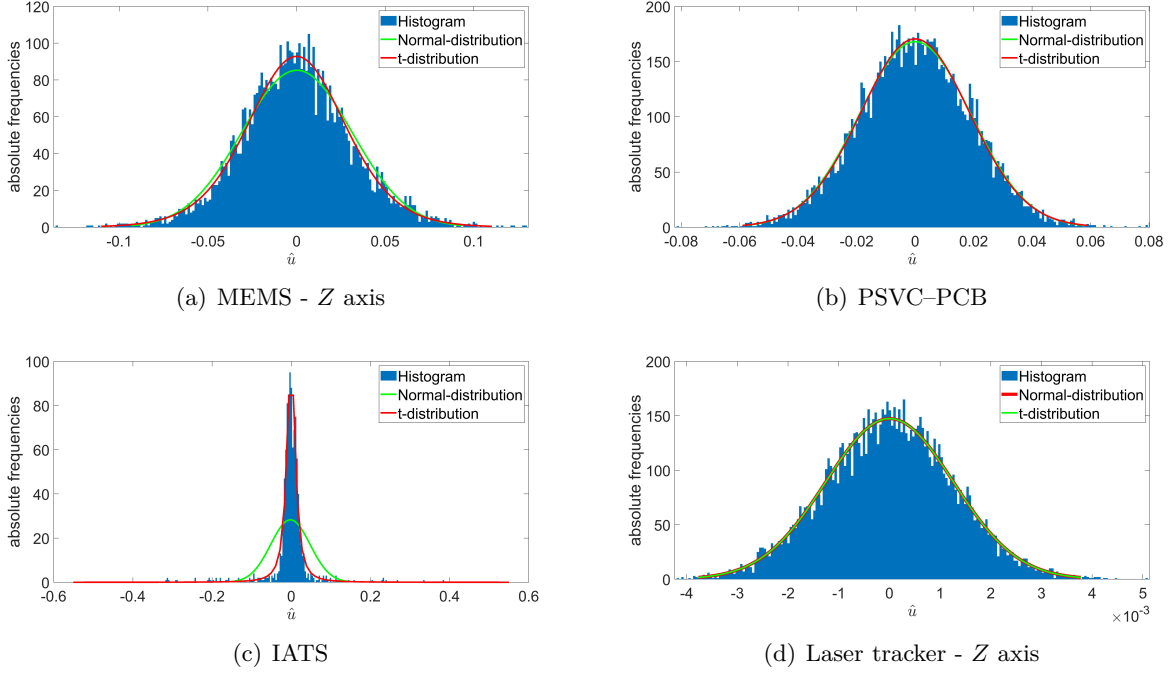


Figure 6.10: Histogram of the white noise residuals estimated for the frequency of 3 Hz, and for (a) the MEMS acceleration data in Z-axis [m/s²], (b) the PCB reference acceleration data [m/s²], (c) the IATS displacement data in vertical direction [mm], and (d) the laser tracker displacement data in Z-axis [mm] in a controlled excitation experiment by using the PSVC.

compared with the reference accelerometer for the three lower, and two higher frequencies. Accordingly, the analysis shows the percentage errors of 3.13, and 2.52 %. The percentage errors of the amplitudes in [mm] for the three lower and the two higher frequencies are about 3.13, and 2.56 % in case of the MEMS, and 0.95, and 3.16 % in case of the laser tracker. In case of the IATS, its corresponding estimate for the three lower frequencies is 8.93 %, which is relatively large compared to others. The analyses demonstrate that the laser tracker delivers slightly better estimates of the amplitudes, which is expected. The estimated amplitude from the IATS is still considerably small and has a maximum deviation of 0.0805 mm for the frequency of 2 Hz. The estimated df of the t-distribution underlies the white noise components in which the low df corresponds to heavy-tailed t-distribution. Concerning the PCB measurements, the estimated df are roughly between 9 and 58. Its corresponding estimates by the laser tracker measurements reveal a closer approximation of normal distribution, particularly for the lower frequencies, compared to the PCB. The estimated df from the MEMS are roughly varied between 6 to 16, where the higher estimates of the df are obtained from the lower frequencies of 2 and 3 Hz. By contrast, the estimated df from IATS measurements are below 2, which indicates unstable estimates of the df. Therefore, it shows a large number of outliers in the measurement noise of the IATS with a heavy-tailed t-distribution. Subsequently, the df for the IATS analysis is set to 3, which is in accordance with the recommendation of the guide to the expression of uncertainty in measurement (ISO, 2008) in which input quantities with statistically determined (i.e., type-A) standard uncertainties affect the output quantities. For better realisation of the aforementioned statements concerning the estimated df, histogram of the white noise residuals estimated for the frequency of 3 Hz, and from all aforementioned sensors are provided in Figure 6.10.

Concerning the estimates of AR model order (p), the laser tracker measurements have the highest estimated AR model orders. This is due to the fact that the laser tracker measurements have a drift, which can be seen in Figure 6.14 with a low frequency of approximately 0.05 Hz. In addition,

Table 6.2: Statistics of displacement and vibration analysis for vibration measurements obtained from the PCB reference accelerometer, the MEMS accelerometer, the IATS, and the laser tracker. \hat{f} is the estimated frequency, \hat{A} and \hat{A}_m the estimated amplitudes in $[m/s^2]$ and $[mm]$, respectively, $|\Delta_{\hat{A}_m}|$ the absolute deviation of the estimated amplitude in $[mm]$ compared to those from PCB accelerometer, p the AR model order, $\hat{\nu}$ the estimated df, $\hat{\sigma}_\ell$ a *posteriori* standard deviation of the vibration measurements in their measurements unit, wnt_c the acceptance of the WNT criterion (i.e., yes in case of acceptance, otherwise no), t the length of an excitation window selected and F_s the sampling frequency.

Sensor	\hat{f} [Hz]	\hat{A} [m/s ²]	\hat{A}_m [mm]	$ \Delta_{\hat{A}_m} $ [mm]	p [-]	$\hat{\nu}$ [-]	$\hat{\sigma}_\ell$ [-]	wnt_c [-]	t [s]	F_s [Hz]
PSVC-PCB [m/s ²]	2.0001	0.2705	1.7126	0.0	7	34.81	0.0206	yes	50	200
	3.0001	0.2911	0.8191	0.0	6	52.15	0.0191	yes		
	4.0002	0.2929	0.4637	0.0	7	9.31	0.0193	yes		
	10.0005	0.2956	0.0749	0.0	1	46.64	0.0179	yes		
	15.0007	0.2954	0.0332	0.0	1	57.24	0.0179	yes		
MEMS [m/s ²] (Z-axis)	2.0002	0.2831	1.7925	0.0799	7	15.26	0.0482	yes	50	100
	3.0003	0.2992	0.8421	0.0230	1	12.08	0.0309	yes		
	4.0004	0.2986	0.4726	0.0089	3	8.67	0.0336	yes		
	10.0011	0.2923	0.0740	0.0009	5	6.88	0.0508	yes		
	15.0016	0.2838	0.0319	0.0013	4	8.46	0.0688	yes		
Laser tracker [mm]	2.0001	-	1.7441	0.0315	36	33.61	0.0014	yes	50	200
	3.0001	-	0.8204	0.0013	13	275.85	0.0013	yes		
	4.0001	-	0.4598	0.0039	26	196.37	0.0012	yes		
	10.0003	-	0.0731	0.0018	20	17.17	0.0012	yes		
	15.0004	-	0.0319	0.0013	30	13.05	0.0010	no		
IATS [mm]	2.0013	-	1.6321	0.0805	1	3.0	0.0492	yes	100	10
	3.0020	-	0.7415	0.0776	1	3.0	0.0262	yes		
	4.0027	-	0.4076	0.0561	1	3.0	0.0196	yes		

it can also be due to a time-variability of the AR model, which is justified by considering the time-variability through the GEM algorithm, and thus, obtaining the WNT acceptance for the frequency of 15 Hz, and with an AR model order 13. The IATS displacement data shows a minimum AR model of 1 compared to the other sensors. However, the AR model order is also influenced by the number of measurements, which can be seen from the analysis of the shaker and for a duration of 5 minutes in the research of Omidalizarandi et al. (2019c). The analysis of IATS provided in this section is improved compared to the research of Omidalizarandi et al. (2018), and by using the recent version of the proposed RT-MPI algorithm.

Figure 6.11 depicts the estimated coloured noise residuals and the decorrelated residuals of the given vibration measurements, which are obtained from the aforementioned four sensors. The fluctuation in the coloured noise residuals of the laser tracker data are mainly due to remaining frequencies of the measurement drifts with small amplitudes. Figure 6.12 illustrates histogram of the adjusted weights. As it can be seen, the adjusted weights estimated from both reference sensors are increased smoother compared to those estimated from the MEMS and the IATS data. However, the adjusted weights obtained from the IATS data do not increase smoothly, which proves the existence of numerous outliers. Figures 6.13 and 6.14 represent the eigenfrequencies estimated for the IATS and the laser tracker data, respectively. As it can be seen, the lowest frequencies of 0.6667 and 0.0527 Hz correspond to the measurements drift in the IATS and the laser tracker data.

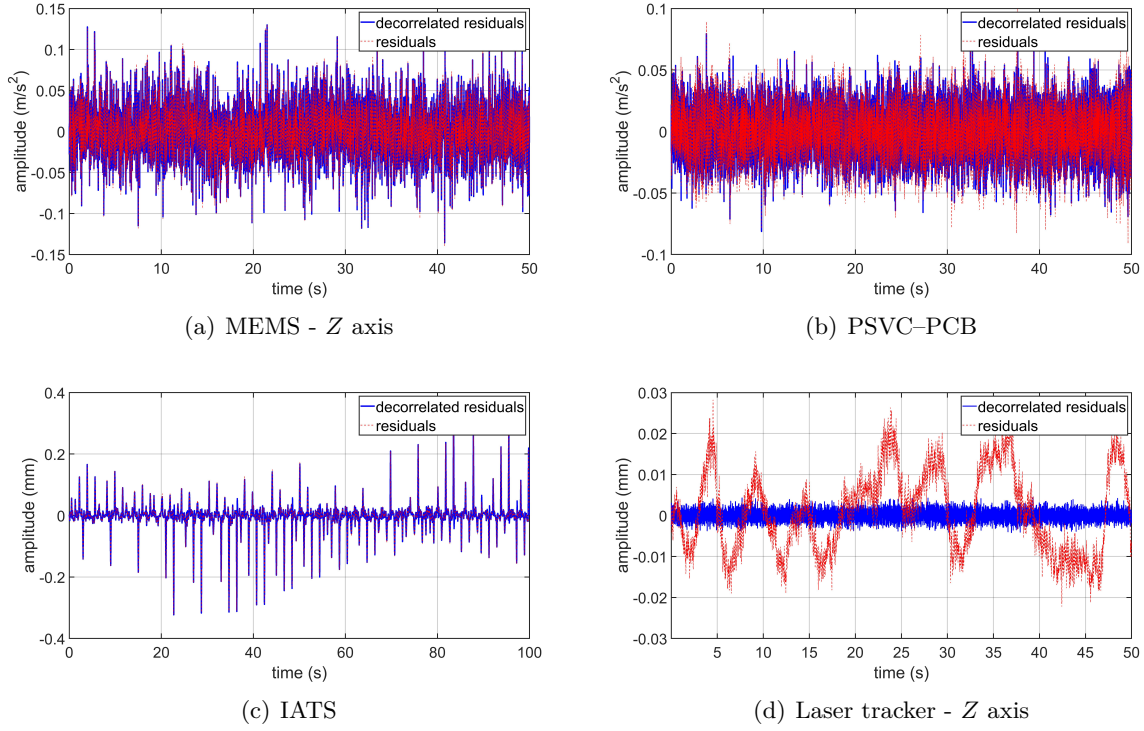


Figure 6.11: The estimated coloured noise residuals (red dashed line) and the decorrelated residuals (blue solid line) of the vibration measurements corresponding to the frequency of 3 Hz, and for (a) the MEMS acceleration data in Z -axis [m/s^2], (b) the PCB reference acceleration data [m/s^2], (c) the IATS displacement data in vertical direction [mm], and (d) the laser tracker displacement data in Z -axis [mm].

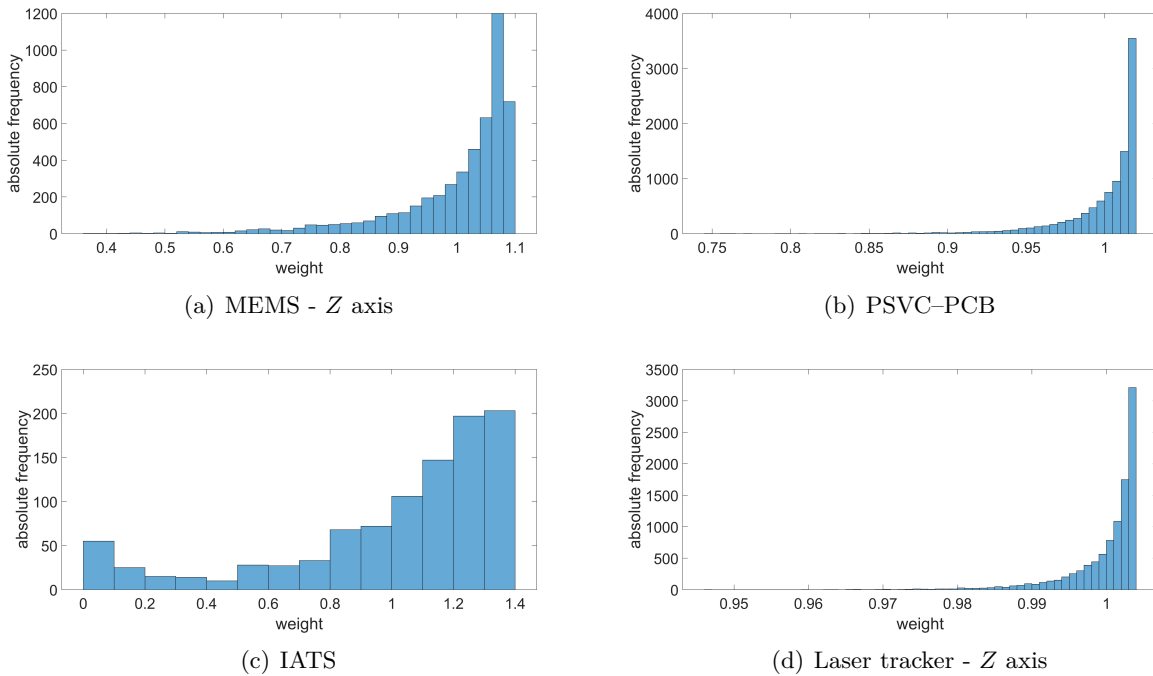


Figure 6.12: Histogram of the weights estimated for the frequency of 3 Hz, and for (a) the MEMS acceleration data in Z -axis [m/s^2], (b) the PCB reference acceleration data [m/s^2], (c) the IATS displacement data in vertical direction [mm], and (d) the laser tracker displacement data in Z -axis [mm] in a controlled excitation experiment by using the PSVC.

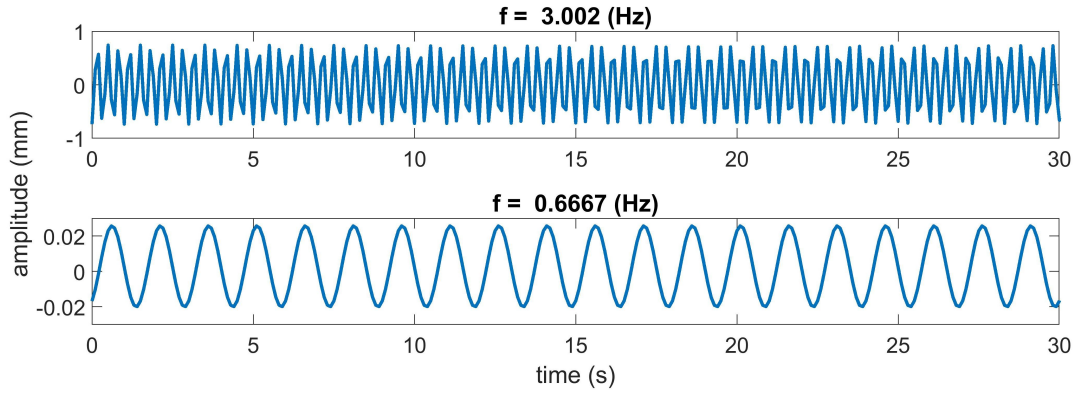


Figure 6.13: Representation of the frequencies estimated from the IATS displacement data with sampling frequency of 10 Hz through the controlled excitation experiment.

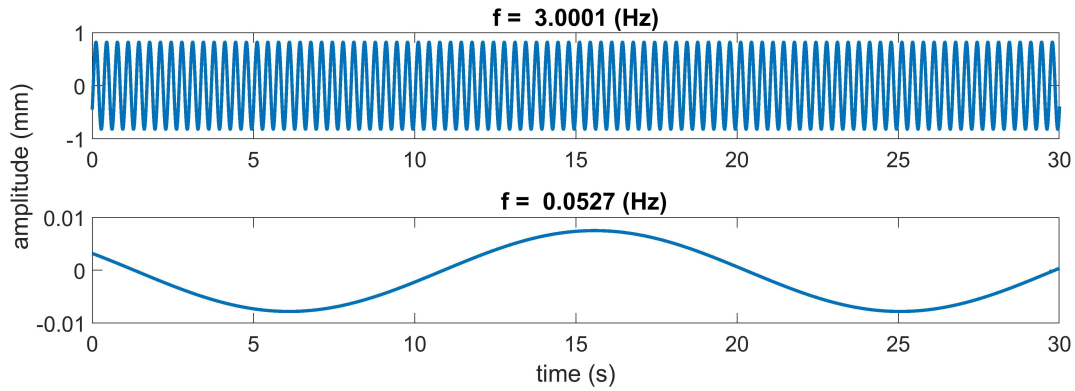


Figure 6.14: Representation of the frequencies estimated from the laser tracker displacement data with sampling frequency of 200 Hz through the controlled excitation experiment.

6.3 Example based on a Footbridge

A vibration analysis of a footbridge structure is performed by using the MEMS and PCB piezoelectric (PCB piezotronics, 2019) reference accelerometers with sampling frequencies of 100 and 2000 Hz. The aforementioned footbridge is the Mensa footbridge, located in Hannover, Germany. It has a length of 27.05 m (23.22 m main span and 3.83 m side span) and a width of 2.42 m (see Fig. 6.15). The reference acceleration data is downsampled to 100 Hz to speed up the processing. In addition to the aforementioned reference accelerometer, the Mensa footbridge is dynamically analysed based on the FEM analysis. For further information regarding the FEM analysis, please refer to Omi-dalizarandi et al. (2020). Subsequently, such a real application of the footbridge structure allows to compare and validate the estimated modal parameters including eigenfrequencies, eigenforms, and damping ratio coefficients with the reference accelerometers as well as the FEM analysis.

The geo-sensor network of the MEMS accelerometers are located at certain positions that are precalculated by means of the FEM analysis. Subsequently, it allows to correctly characterise eigenforms. As previously stated, the MEMS accelerometer is a three axis accelerometer, which is capable of recording vibration measurements in longitudinal (X -axis), lateral (Y -axis), and vertical (Z -axis) directions of bridge structures. By contrast, the reference accelerometer used is a one axis accelerometer in which its multiple set-ups are required to record vibration measurements in all three directions. However, in this research, the eigenforms are merely characterised in vertical direction

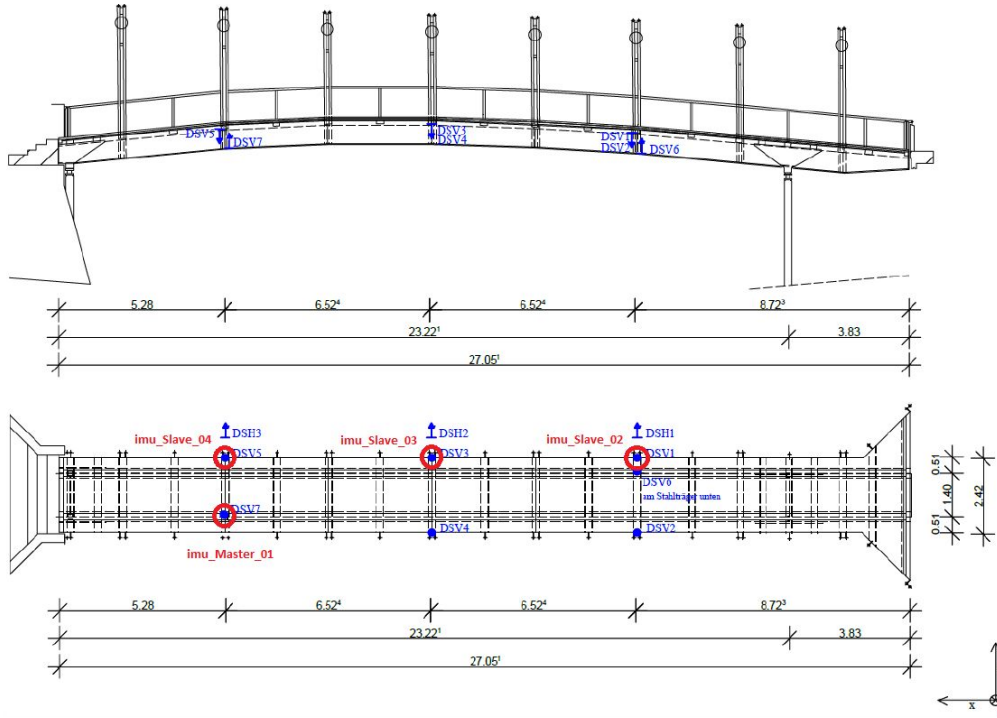


Figure 6.15: Measurement set-up in the Mensa footbridge experiment: The positions of the MEMS and the PCB piezoelectric accelerometers are highlighted by red and blue circles (Herrmann, 2018).

due to the usage of only three MEMS slave sensors, namely, *IMU_Slave_02*, *IMU_Slave_03*, and *IMU_Slave_04* (see Fig. 6.15). The MEMS accelerometer is set-up along its *X*-axis due to having a better uncertainty compared to *Z*-axis. However, the uncertainties of *X* and *Y*-axes are not significantly different from each other. Three reference sensors, namely, DSV1, DSV3, and DSV5 are located near the aforementioned MEMS slave sensors, for the validation purpose (Omidalizarandi et al., 2020).

Typically, the dynamic response of a footbridge is recorded under an ambient excitation imposed by either moving pedestrians (mainly in vertical direction) or wind (mainly in lateral direction). In this research, an additional excitation is induced by impulses from a modal hammer. The modal parameters including eigenfrequencies and damping ratio coefficients are estimated for the vertical and torsion modes, which are provided in the research of Omidalizarandi et al. (2020). According to the aforementioned analysis, the estimates of the damping ratio coefficients are influenced by the amount of loads. However, since the energy contents of external forces are decreased through time, it is expected that the estimates of damping ratio coefficients reach gradually to an equilibrium. Accordingly, it is possible to obtain a unique damping ratio coefficient by calculating a weighted average or a median of the estimated values. Such calculation can also be performed similarly for the eigenfrequencies (Omidalizarandi et al., 2020).

Table 6.3 summarises the statistics of estimated eigenfrequencies [Hz] and damping ratio coefficients [%] obtained from the RT-MPI algorithm. In this chapter, it is merely provided for the first and second vertical modes (i.e., indexed by V) and the fourth torsion mode (i.e., indexed by T). In addition to the aforementioned estimated parameters, the first torsion mode and two other vertical modes are also estimated in Omidalizarandi et al. (2020). The median of estimated parameters is calculated for the entire time series of vibration measurements to obtain the final estimates. The estimated parameters are then compared to the SSI-COV algorithm, which is implemented in MATLAB by Cheynet (2020).

Table 6.3: Statistics of the estimated eigenfrequencies [Hz] and damping ratio coefficients [%] obtained from all three MEMS acceleration data by means of the RT-MPI and SSI-COV algorithms for the Mensa footbridge (Omidalizarandi et al., 2020).

Sensor	Time [s]	Method	f_{V1} [Hz]	ξ_{V1} [%]	f_{V2} [Hz]	ξ_{V2} [%]	f_{T4} [Hz]	ξ_{T4} [%]
MEMS	7.22–357.05	RT-MPI	4.085	0.36	13.764	0.72	26.323	0.66
		SSI-COV	4.084	0.81	13.734	0.47	26.294	0.65
	7.22–57.22	RT-MPI	4.066	0.38	13.801	0.95	26.353	0.72
		SSI-COV	4.073	0.32	13.742	0.73	26.335	0.54
	65.95–115.95	RT-MPI	4.106	0.26	13.781	0.78	26.314	0.58
		SSI-COV	4.100	0.20	13.868	0.19	26.302	0.55
	123.95–173.95	RT-MPI	4.072	0.90	13.766	0.76	26.344	0.65
		SSI-COV	4.072	1.10	13.769	0.60	26.319	0.57
	185.79–235.79	RT-MPI	4.112	0.45	13.769	0.70	26.293	0.62
		SSI-COV	4.088	0.40	13.776	0.51	26.285	0.63
	246.62–296.62	RT-MPI	4.084	0.26	13.763	0.44	26.284	0.67
		SSI-COV	4.087	0.28	13.774	0.32	26.282	0.65
	307.05–357.05	RT-MPI	4.098	0.38	13.762	0.71	26.324	0.68
		SSI-COV	4.095	0.40	13.764	0.49	26.312	0.57
2D plan		FEM	3.642	—	13.294	—	—	—

The comparison of both aforementioned algorithms demonstrates that the RT-MPI algorithm allows to efficiently decrease the influence of loads on the estimated parameters. Particularly, more accurate and reliable results are obtained for the damping ratio coefficients by means of the median of estimates. However, the SSI-COV algorithm does not achieve reasonable results for the estimates of damping ratio coefficients while considering the entire time series at once. As it can be seen from Table 6.3 and for the time interval of 7.22 – 357.05 s, the damping ratio coefficients corresponding to the first and second vertical modes as well as the first torsion mode are not estimated correctly in the SSI-COV algorithm. It can be justified by their comparisons with the estimates obtained from other time intervals. By contrast, both approaches achieve rather close estimates of the parameters in shorter time intervals. However, the SSI-COV algorithm does not achieve reliable results for the damping ratio coefficients corresponding to the second vertical and the first torsion modes. In addition, maximum deviation of the estimated eigenfrequencies in both approaches is approximately 0.03 Hz (Omidalizarandi et al., 2020). Besides, the percentage errors have been calculated with respect to the estimated parameters obtained from the RT-MPI algorithm considering the entire time series (7.22 – 357.5 s). The estimated frequencies and damping ratio coefficients above percentage errors of 1 % and 20 %, respectively, are highlighted in bold. As it can be seen, all the estimated frequencies are below the threshold of 1 %. Some damping ratio coefficients correspond to the first and second vertical eigenfrequencies are above the threshold of 20 %, which is due to the higher imposition of the loads. However, median of the estimated parameters over the entire time series reduce the influence of the loads. It should be noted that the frequencies and damping ratio coefficients have been provided up to third and second decimals, respectively. This is due to the reason that loads and environmental factors affect on the uncertainties of the estimated parameters. However, as previously shown in sections 2.3.1 and 6.2, the MEMS accelerometers can deliver better accuracy, in particular for the frequencies, in controlled excitation experiments.

The estimated parameters obtained from the MEMS and the reference acceleration measurements are compared for the last 60 s of the measurements, and with an incremental step size of 5 s for the validation purpose. The provided analysis in Omidalizarandi et al. (2020) demonstrates that

all eigenfrequencies can be detected precisely for both acceleration measurements. As described by Wenzel (2009a), the modal and system damping could be possibly altered between 0 – 0.1 and 0 – 0.2. Therefore, the median of all estimated damping ratio coefficients for each ambient window selected is within the aforementioned range which is acceptable (Omidalizarandi et al., 2020).

According to the FE simulations which were analysed based on the 3D CAD model created from the 2D plan (Omidalizarandi et al., 2020), the frequencies of 3.642 and 13.294 Hz from the FEM analysis are equivalent to the frequencies of 4.1 and 13.75 Hz. Subsequently, it demonstrates that merely approximate estimates of the eigenfrequencies can be calculated from the FEM analysis and no calculation of the damping ratio coefficients can be provided (Omidalizarandi et al., 2020). However, the FEM calibration may improve the results, which is out of the scope of this dissertation.

To characterise the eigenforms (see Figs. 6.16 – 6.18), the modal parameters including amplitudes, eigenfrequencies, and phase shifts were estimated in advance, and by considering the UDHO model within the GEM algorithm (see chapter 4). For this purpose, the estimation of the aforementioned parameters is accomplished for the entire time series and for each sensor's measurements individually. Comparison of the eigenforms deduced from the MEMS and the reference accelerometers demonstrates the reliability, robustness, and high accuracy of the estimation procedure in the proposed RT-MPI algorithm. As previously stated, it is also possible to characterise the deflection eigenforms with true scales within the selected ambient window, and for a short time interval. In this case, the UDHO model is replaced by the DHO model. Next, the double integration of the DHO model is carried out to obtain highly accurate estimates of the amplitudes. Such deflection eigenforms can also provide the estimates of damping ratio coefficients for the vibration measurements recorded at each sensor node (Omidalizarandi et al., 2020).

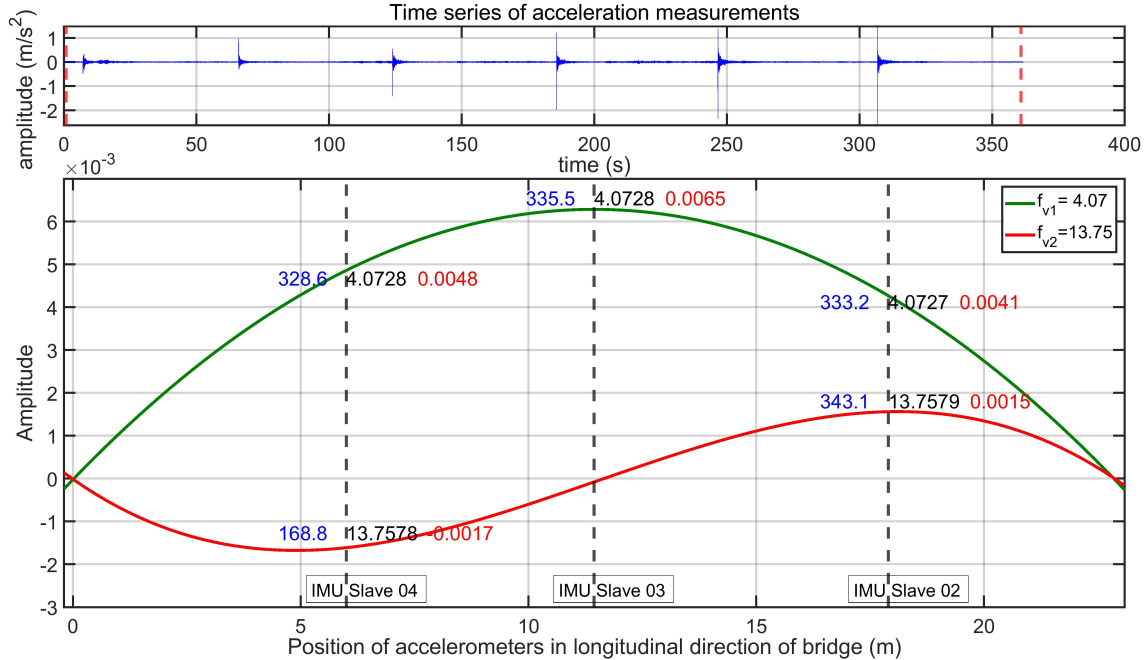


Figure 6.16: MEMS accelerometers: time series of the acceleration measurements (top) (selected ambient window within the red dashed lines) in which the X - and Y -axes represent time [s] and amplitude [m/s²]; vertical eigenforms calculated for different eigenfrequencies (bottom). The texts for each eigenform represent estimated phase shifts (blue), eigenfrequencies (black), and amplitudes (red) at specified positions (Omidalizarandi et al., 2020).

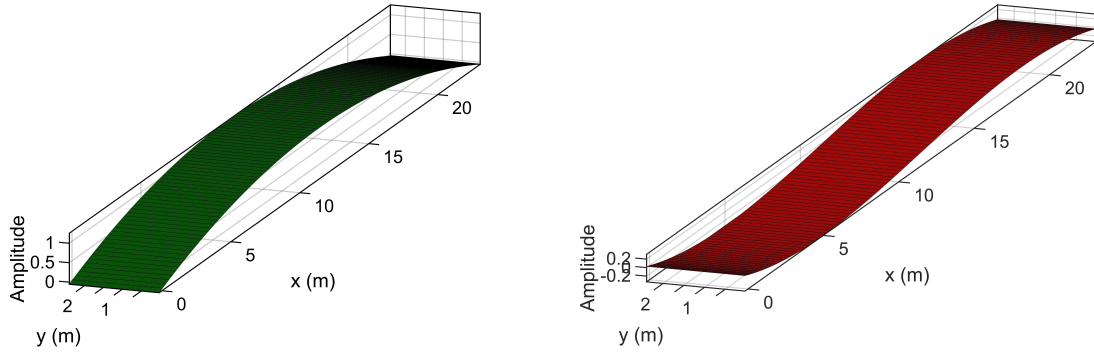


Figure 6.17: 3D vertical eigenforms characterised for different eigenfrequencies obtained from the MEMS accelerometers: the first vertical eigenform (4.07 Hz; left) and the second vertical eigenform (13.75 Hz; right). Amplitudes scaled by 200 in Z-axes (Omidalizarandi et al., 2020).

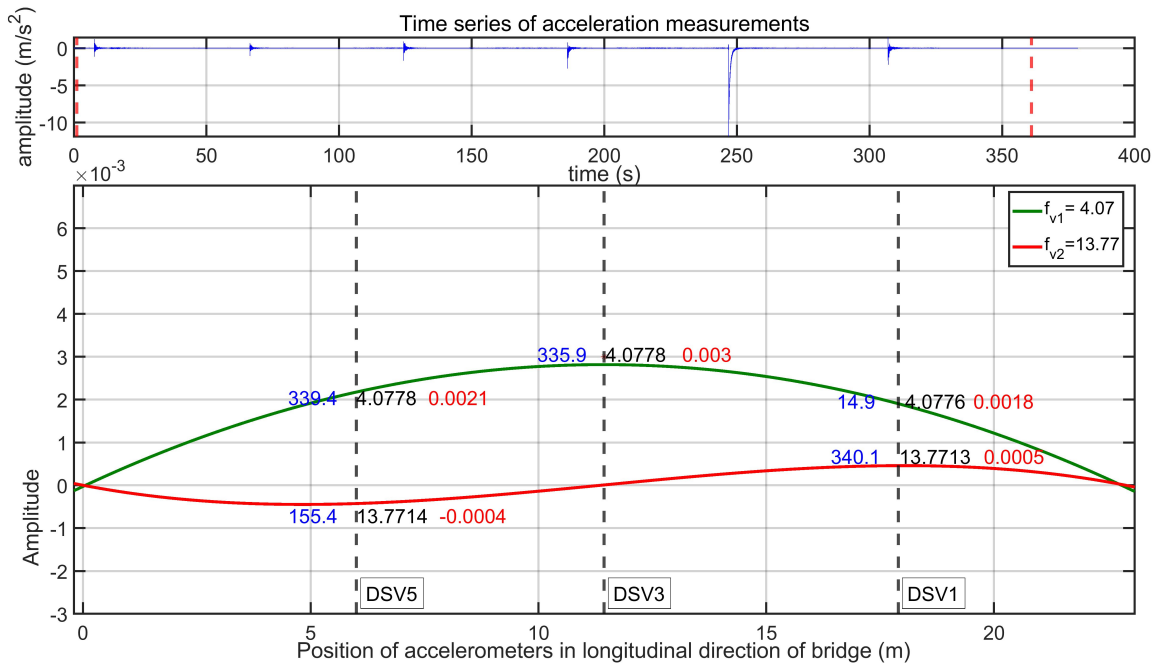


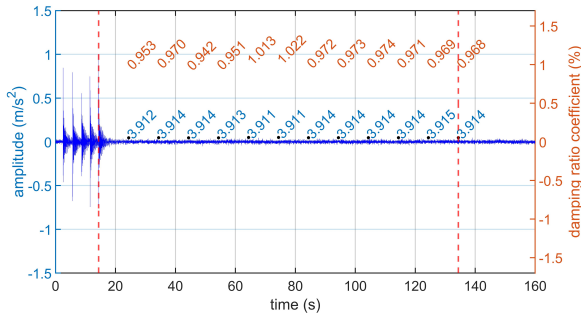
Figure 6.18: Reference accelerometers: time series of the acceleration measurements (top) (selected ambient window within the red dashed lines) in which X - and Y -axes represent time [s] and amplitude [m/s^2]; vertical eigenforms calculated for different eigenfrequencies (bottom). The texts for each eigenform represent estimated phase shifts (blue), eigenfrequencies (black) and amplitudes (red) at specified positions (Omidalizarandi et al., 2020).

6.4 Example based on a Synthetic Bridge

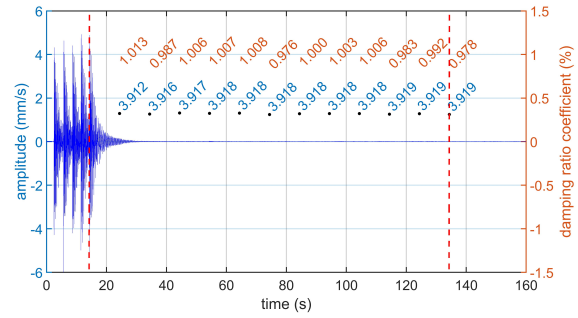
A vibration analysis of a synthetic bridge from the BAM, located approximately 80 km from Berlin, Germany, with a length of 24.0 m, a width of 0.8 m, and a height of 0.3 m is carried out. The aforementioned bridge is a rigid platform without any natural frequencies. Therefore, the modal hammer is used to generate an artificial oscillation. The vibration measurements are recorded by using the MEMS accelerometers, the IATS of type Leica MS50, a geophone, and the laser tracker of type Leica AT960-LR with sampling frequencies of 100 Hz, 10 Hz, 1000 Hz, 1000 Hz, respectively. However, in this research, the focus is on the MEMS acceleration data as well as the geophone velocity data (i.e., reference measurements), which allows to validate the estimated modal parameters including

eigenfrequencies and damping ratio coefficients (Omidalizarandi et al., 2020).

Figure 6.19 illustrates the MEMS acceleration data as well as the geophone velocity data, which are recorded in vertical direction. The MEMS accelerometer is set-up along its Z -axis. The first ambient window, with a length of 10 s, is started from the last peak with a high amplitude which is then enlarged by a step size of 10 s to reach the maximum duration of 120 s. As it can be seen from this figure, the estimated first eigenfrequency and its corresponding damping ratio coefficient are represented for different ambient window sizes. Table 6.4 summarises the statistics of the aforementioned modal parameters estimations by means of the RT-MPI algorithm, and for the measurements of the MEMS and the geophone. In this table, merely the part of analysis of the research of Omidalizarandi et al. (2020) is represented. However, the median values are calculated for the entire analysis. The estimated parameters are then compared with the analysis of the MEMS acceleration data based on the SSI-COV algorithm. Frequencies of 3.91, 6.13, and 15.77 Hz correspond to the 1st – 3rd modes, respectively. The analysis demonstrates robustness, reliability, and highly accurate eigenfrequencies and damping ratio coefficients estimations which are derived from the MEMS acceleration data in the proposed RT-MPI algorithm. The aforementioned estimated parameters are then compared and evaluated with the analysis obtained from the geophone measurements and the SSI-COV algorithm. According to the analysis, the estimated eigenfrequencies deviate about a maximum of 0.01 and 0.04 Hz with respect to the analysis obtained from the geophone measurements and the SSI-COV algorithm. Additionally, deviation of the estimated damping ratio coefficients from both aforementioned approaches is below 0.1 %, which is within the range and is acceptable (Omidalizarandi et al., 2020).



(a) MEMS accelerometer (IMU_Slave_02) measurements



(b) Geophone measurements

Figure 6.19: BAM synthetic bridge: time series of (a) the MEMS acceleration measurements [m/s²] and (b) the geophone velocity measurements [mm/s] (blue solid lines); selected ambient window within the red dashed lines for a duration of 120 s. The blue and orange coloured texts stand for the estimated eigenfrequencies [Hz] and damping ratio coefficients [%], for the first mode at specified positions (Omidalizarandi et al., 2020).

6.5 Summary

In this chapter, a good feasibility of cost-effective MEMS accelerometers for displacement and vibration analysis of bridge structures is demonstrated. The proposed RT-MPI algorithm in this research allows to estimate the modal parameters including eigenfrequencies, eigenforms, damping ratio coefficients, and amplitudes robustly, reliably, and high accurately. The estimates of the amplitudes in metric unit enables to characterise deflection eigenforms in their true scales, and with a high accuracy for a selected excitation window. The time synchronisation between different sensor nodes is an important step, which greatly influences the estimated eigenforms. The FEM analysis assists to position the sensor nodes, which subsequently allows to correctly characterise the eigenforms.

Table 6.4: Statistics of frequencies [Hz] and damping ratio coefficients [%] estimated from the MEMS acceleration data and the geophone velocity data based on the RT-MPI and the SSI-COV algorithms for the BAM synthetic bridge (Omidalizarandi et al., 2020).

Time [s]		24.4	44.4	64.4	84.4	104.4	Median
MEMS RT-MPI	f_1 [Hz]	3.912	3.914	3.911	3.914	3.914	3.914
	ξ_1 [%]	0.95	0.94	1.01	0.97	0.97	0.97
	f_2 [Hz]	6.132	6.129	6.119	6.134	6.136	6.132
	ξ_2 [%]	1.55	1.63	1.59	1.53	1.52	1.54
	f_3 [Hz]	15.774	15.775	15.760	15.783	15.781	15.775
	ξ_3 [%]	0.93	0.90	0.93	0.91	0.92	0.92
Geophone RT-MPI	f_1 [Hz]	3.912	3.917	3.918	3.918	3.918	3.918
	ξ_1 [%]	1.01	1.01	1.01	1.00	1.01	1.00
	f_2 [Hz]	6.135	6.139	6.141	6.136	6.136	6.141
	ξ_2 [%]	1.52	1.52	1.53	1.52	1.54	1.53
	f_3 [Hz]	15.764	15.773	15.777	15.769	15.770	15.772
	ξ_3 [%]	0.95	0.92	0.91	0.92	0.92	0.92
MEMS SSI-COV	f_1 [Hz]	3.920					
	ξ_1 [%]	0.90					
	f_2 [Hz]	6.131					
	ξ_2 [%]	1.48					
	f_3 [Hz]	15.734					
	ξ_3 [%]	0.97					

To estimate the modal parameters including eigenfrequencies, damping ratio coefficients, phase shifts, and amplitudes for a short-term deformation monitoring, the observation model is defined based on the DHO model, the AR model, and stochastic model in form of the scaled t-distributions, which are jointly adjusted by means of GEM algorithm. The combination of the aforementioned three parametric models allow for self-tuning, robust, and ML estimation of the parameters. Additionally, it ensures the efficient convergence of the algorithm. The identification of initial frequencies and a proper selection of an excitation window play important roles, and significantly influencing the final parameter estimates. For a long-term deformation monitoring, the DHO model is replaced by the UDHO model to avoid an influence of damping on characterisation of eigenforms. In the proposed RT-MPI algorithm, the unknown parameters can be estimated for three cases where the df (ν) is obtained by applying the *INTLAB* library as well as *fzero* and *mle* MATLAB routines. Double integration by using the DHO model achieves considerably accurate estimates of the amplitudes in metric unit.

According to the experimental studies, calibration of the MEMS accelerometer has a minor impact on the estimates of modal parameters, particularly on the eigenfrequencies, for a short time interval, e.g., a few minutes. However, it is essential to be considered for long-term vibration measurements, e.g., 10 minutes or more, to compensate for the systematic errors of the MEMS accelerometer including biases, scales, and non-orthogonality angles between the axes.

Experimental studies are carried out based on the simulated acceleration data, the controlled excitation, and two real applications of the footbridge and the synthetic bridge. For real experiments, the MEMS accelerometers with a specified sampling frequency of 100 Hz and the IATS (i.e., using video frames captured by its telescope camera) with a sampling frequency of 10 Hz are used. In addition, the reference sensors such as the laser tracker, the geophone and the reference PCB accelerometers are used for the validation purpose.

Aforementioned experiments allow to estimate the modal parameters including eigenfrequencies, eigenforms, damping ratio coefficients, amplitudes – in $[m/s^2]$ and $[mm]$ – and phase shifts, which are compared and validated with their true values, the reference sensors, the FEM analysis as well as the well-known SSI-COV algorithm. According to the analysis, both RT-MPI (all three variants of estimating df) and SSI-COV algorithms achieve rather similar results for the frequencies and damping ratio coefficients in the simulation experiment. However, the damping ratio coefficients estimates in the SSI-COV algorithm are merely stable and reliable while there is a perfect free vibration decay of a signal. By contrast, the proposed RT-MPI algorithm is able to robustly and accurately estimate damping ratio coefficients even in case of imposed loads at different time intervals in real experiments. This is achieved by calculating the median values of estimated damping ratio coefficients for selected excitation windows. Similarly, a median value is also calculated for estimated eigenfrequencies to obtain a unique value. In the simulation experiments, the estimates of amplitudes by using the RT-MPI algorithm have very small differences to their true values, which is negligible. However, the SSI-COV algorithm could not estimate the amplitudes. The first and third variants of the RT-MPI algorithm achieve robust and highly accurate estimates of the parameters, which are slightly better than the second variant. However, in case of highly noisy vibration measurements, the second variant of the RT-MPI algorithm cannot correctly estimate the ν , which may influence the final parameter estimates. The first variant of the RT-MPI algorithm is computationally expensive and it is suitable for post-processing. The second and third variants of the RT-MPI algorithm are relatively fast, which can be used for near real-time processing. For example, the analysis of the simulated data with length a 10000 data sets shows that the first variant is approximately 153 times slower than two other variants. To this end, the analysis demonstrates superiority of the RT-MPI algorithm compared to the SSI-COV algorithm. In addition, in the simulation experiment, the proposed RT-MPI algorithm is theoretically and numerically proved. Moreover, it is demonstrated that the robustness and accuracy of the proposed RT-MPI algorithm are much more than expected and needed for real application of bridge structures, which is fully satisfactory.

In the controlled excitation experiment, the estimated df of t-distribution for the laser tracker and the PCB acceleration measurements reveal rather close approximation of a normal distribution. This is relatively similar for the MEMS acceleration data, in particular for lower frequencies. By contrast, the estimated df regarding the IATS displacement data with heavy tails show a large number of outliers in the measurement noise of that sensor. This can also be justified based on the histogram of adjusted weights. According to that, the adjusted weights for the reference sensors measurements such as the laser tracker displacement data as well as the PCB acceleration data are increased smoothly, which is almost similar to the MEMS acceleration data. By contrast, adjusted weights obtained from the IATS displacement data do not increase gradually and smoothly, which proves the existence of numerous outliers. In addition, the estimates of AR model order demonstrate relatively high auto-correlation of the noise measurements for cost-effective MEMS accelerometer. However, the AR model order is relatively large for the laser tracker displacement data compared to other sensors data sets. The reason lies in the existence of systematic errors such as the measurements drift over a long period. By considering the time-dependent AR model within the GEM algorithm, particularly for the laser tracker measurements, the AR model order might be decreased.

The overall analysis demonstrates that the proposed RT-MPI algorithm can estimate all eigenfrequencies, their corresponding eigenforms as well as damping ratio coefficients for cost-effective MEMS acceleration data recorded at a bridge structure. The analysis showed a submillimetre accuracy level for amplitudes, considerably better than 0.1 Hz for the eigenfrequencies, and damping ratio coefficients estimates of better than 0.1 and 0.2 % for modal and system damping. Besides, the lower eigenfrequencies (in the view of Nyquist sampling frequency) can also be identified from the IATS displacement data with a high accuracy.

7 Summary, Conclusion and Outlook

7.1 Summary and Conclusion

In this dissertation, a robust kinematic deformation monitoring of bridge structures is performed by using cost-effective MEMS accelerometers and an IATS. Use of cost-effective MEMS accelerometers for permanent monitoring and inspection of the bridge structures is economically plausible. It enables to prevent any deterioration of the structures at the earliest possible stage. Subsequently, the repair cost and risk is reduced and lifetime of the bridge structures is ensured. On the contrary, the IATS is a relatively expensive sensor and its continuous measurements over several months or years is not feasible. The information obtained from both systems are complementary to each other and the strength of one measurement method overcomes the weakness of the other in short- and long-term displacement and vibration monitoring.

The MEMS accelerometers are used to perform vibration analyses and to identify the modal parameters including eigenfrequencies, eigenforms and damping ratio coefficients in longitudinal, lateral and vertical directions of the bridge structures. For this purpose, multiple MEMS as part of a geo-sensor network are mounted at certain positions of a bridge structure, which are precalculated by means of a FEM analysis. Therefore, it allows to correctly characterise the eigenforms. Since absolute position/displacement changes derived from double integration of the MEMS acceleration data are drifting fast, the IATS as an aiding measurement system is used (Omidalizarandi et al., 2019c). However, in short-term displacement monitoring, e.g., a few seconds, it is possible to obtain a high accurate displacement data from the MEMS acceleration data. This is achieved based on double integration of the DHO model, and by using the estimated parameters from the GEM algorithm within a selected excitation window. The data fusion of the MEMS accelerometers and the IATS is carried out within the KF framework, which subsequently allows for a complementary coverage of lower and upper frequency ranges. Therefore, a high accurate displacement time series at a submillimetre range is deduced, which has a higher resolution as well as a wider frequency bandwidth.

Despite of the purchase price and an adequate sampling frequency of the MEMS accelerometers, a three-step scenario is proposed to select an optimal one, which are as follows:

1. A robust calibration procedure is proposed and implemented to estimate MEMS-related systematic errors such as biases, scale factors and non-orthogonality angles between the axes. The calibration is carried out in a climate chamber over different temperature ranges, which subsequently enables us to have a good realisation of the changes of the calibration parameters. Therefore, a MEMS accelerometer with minimal influences of the aforementioned systematic errors can be selected (Omidalizarandi et al., 2020).
2. A controlled excitation experiment is accomplished by using a high-precision shaker. Therefore, it allows to estimate harmonic oscillation parameters, and to compare and validate them with their known values as well as with the analyses obtained from either other MEMS accelerometers or a reference accelerometer. Moreover, it enables to check the time synchronisation accuracy between different MEMS accelerometers (Omidalizarandi et al., 2020).
3. A static test experiment is conducted by recording 3D acceleration data over a long period. Therefore, it allows to estimate an offset and a drift of the measurements. Additionally, the unknown auto-correlation parameters as well as underlying distribution model parameters are

estimated by employing the AR process with t-distributed errors. Moreover, the uncertainties of the measurements are estimated. Subsequently, a less AR model order, a high df of the t-distribution, and better uncertainties of measurements, are considered as important influencing factors in the selection process. At the end, the estimated uncertainties of the measurements assists to optimally set-up the MEMS sensors at bridge structures.

The calibration model of the MEMS accelerometers is solved based on two different adjustment models, namely, GHM–GEM and GHM–VCE. The analysis demonstrates a very close approximation of the parameters from both approaches. However, the GHM–GEM approach is computationally more efficient than the GHM–VCE. The analysis shows a minor impact of the calibration parameters on the estimates of the modal parameters for a short time interval, e.g., a few minutes. However, to perform kinematic deformation monitoring for a longer period of time, e.g., 10 minutes or higher, the calibration parameters are required to be considered.

To generate a high accurate displacement time series from the IATS, as a preliminary step, an optimal passive target pattern is selected, which is cost-effective and easy to mount. A fast, automatic, reliable, and accurate passive target centroid detection approach is proposed and implemented, which has less sensitivity to poor environmental conditions, such as low lightning, dusty situations and skewed angle targets (Omidalizarandi et al., 2019a). Next, a displacement time series is generated based on video frames of the passive target captured by an embedded on-axis telescope camera of the IATS. In addition, a slope distance to the aforementioned passive target is measured. The angular conversion factor of the telescope camera is calibrated, which allows to convert displacements from pixel to metric unit such as millimetres (Omidalizarandi et al., 2018).

The state-of-the-art of the IATS has a limitation to detect higher frequencies due to low sampling frequency (e.g. 10 to 20 Hz). To overcome this problem, a high-resolution digital camera with a higher sampling frequency can be attached on top of the IATS by means of a clamping system. Afterwards, the external calibration parameters are estimated to relate the data of the sensors to each other. To detect such small displacements at the level of submillimetre, the aforementioned digital camera could be equipped with a telescopic lens, which needs an additional calibration procedure. The external calibration parameters between the IATS and an high-resolution digital camera can be estimated robustly and accurately based on a rigorous bundle adjustment procedure similar to the research of Omidalizarandi et al. (2019b). The functional models are determined based on the collinearity equations, the 3D Helmert transformation, and the constraint equation. The constraint equation is defined to estimate target coordinates as unknown parameters within the adjustment procedure. Three different adjustment procedures are developed and implemented to deal with high non-linearities of the functional models, which are as follows (Omidalizarandi et al., 2019b):

1. An EM algorithm to solve a GHM with grouped t-distributed random deviations.
2. An EM algorithm to solve a qGMM with t-distributed pseudo-misclosures.
3. A classical least-squares procedure to solve the GHM with VCE and statistical outlier removal.

The comparison of the aforementioned three adjustment models demonstrates the robust, accurate and precise estimation of the parameters, in particular by the second and third procedure. In addition, the second adjustment model is computationally more efficient than the other two (Omidalizarandi et al., 2019b).

The MEMS acceleration data or the IATS displacement data are often contaminated with a high coloured measurement noise. In addition, they are mostly suspected of having numerous outliers. Therefore, a novel robust time domain modal parameter identification approach the so-called RT-MPI technique is proposed and implemented. It allows to identify dynamic responses of the bridge structures such as eigenfrequencies, eigenforms and damping ratio coefficients in a robust, accurate, precise, cost-effective, efficient, and automatic manner. It further allows to automatically

select an excitation (e.g. ambient) window, and to identify initial eigenfrequencies automatically and reliably. Moreover, it enables to perform double integration of the acceleration data and to obtain amplitudes in metric unit with a high accuracy. Having amplitude estimations in metric unit for a selected ambient window, e.g., in a range of few minutes, allows to characterise deflection eigenforms in their true scales with a high accuracy. The proposed approach can be applied for any type of vibration measurements in the form of time series to perform displacement and vibration analysis.

The aforementioned steps in the proposed RT-MPI algorithm including the excitation window selection, the identification of initial frequencies and the estimation step are complementary to each other, which ensures robust and accurate estimation of the modal parameters. The improper selection of an excitation window directly influences the estimates of amplitudes and damping ratio coefficients. In addition, the proposed approach in identification of the initial frequencies allows to identify both well-separated and closely spaced frequencies (Omidalizarandi et al., 2020).

To begin with the estimation procedure, a comprehensive observation model consisting of a DHO model, an auto-correlation model in the form of an AR process and a stochastic model in the form of the heavy-tailed family of scaled t-distributions is employed. Therefore, it allows to jointly adjust the parameters including eigenfrequencies, Fourier series coefficients, damping ratio coefficients, AR coefficients, df and scale factor of the underlying t-distribution by means of the GEM algorithm. Subsequently, it yields a robust, and ML estimation of the parameters. The amplitudes and phase shifts are calculated based on the Fourier series coefficients and the eigenforms are characterised in a subsequent step, and by using the estimated parameters from the GEM algorithm. Besides, the time synchronisation between different sensor nodes is an important step, which greatly affects the estimates of the eigenforms.

The aforementioned estimation procedure is performed in a repetitive procedure for each vector of initial eigenfrequencies, and for each AR model order to calculate the cost value. An inadequate choice of AR model order may absorb those undefined frequencies with low amplitudes. Thus, the maximum AR model is set to 10, which yields fast convergence of the algorithm. However, in case of high systematic errors of sensor measurements, the AR model order is increased to a higher value. Besides, coloured measurement noise characteristics can also be observed from the estimated AR model order from the static test experiment. An optimal vector of initial frequencies that is associated with the minimum cost value is selected. The estimation step is carried out again by using the optimal vector of initial frequencies selected from the previous step to obtain final estimates of the modal parameters (Omidalizarandi et al., 2020). The aforementioned estimation procedure further assists us to decorrelate the high coloured measurement noise contaminated with the acceleration data. Subsequently, *a posteriori* standard deviations of the white noise measurements of the displacement and the acceleration data are estimated, which are used within the following KF algorithm.

Two alternative approaches of multi-rate and resampling KF algorithms are proposed to perform 1D CUPT, and to compensate a displacement drift of the MEMS accelerometers by using the IATS displacement data (Omidalizarandi et al., 2019c). The resampling approach greatly improves the results by increasing the number of the IATS displacements data. However, its estimation is directly influenced by the estimated DHO model parameters. By contrast, the multi-rate KF allows to perform data fusion with their own sampling frequencies. In both aforementioned approaches, a time synchronisation is performed, as a preliminary step, based on cross-correlation of the IATS and the MEMS displacements time series with a reference sensor.

Experimental studies are carried out based on a simulated acceleration data, controlled excitations, and two real applications of a footbridge and a synthetic bridge. For real experiments, besides the MEMS accelerometers and the IATS, the reference sensors such as a laser tracker, a geophone and

a reference PCB accelerometer are used for the validation purpose. Aforementioned experiments allow to estimate the modal parameters including eigenfrequencies, eigenforms, damping ratio coefficients, amplitudes – in $[m/s^2]$ and $[mm]$ – and phase shifts, which are compared and validated with their true values, the reference sensors, the FEM analysis as well as the well-known SSI-COV algorithm. According to the analysis, both RT-MPI and SSI-COV algorithms achieve rather similar results for the frequencies and damping ratio coefficients in the simulation experiment. However, the damping ratio coefficients estimates in the SSI-COV algorithm are merely stable and reliable while there is a perfect free vibration decay of a signal. By contrast, the proposed RT-MPI algorithm is able to robustly and accurately estimate damping ratio coefficients even in case of fluctuating loads at different time intervals in real experiments. This is achieved by calculating the median values of the estimated damping ratio coefficients for selected excitation windows. Similarly, a median value is also calculated for estimated eigenfrequencies to obtain a unique value. In the simulation experiments, the estimates of amplitudes by using the RT-MPI algorithm have small differences to their true values, which is negligible. However, the SSI-COV algorithm cannot estimate the amplitudes. To this end, the analysis demonstrates superiority of the RT-MPI algorithm compared to the SSI-COV algorithm (Omidalizarandi et al., 2020).

In the simulation experiment, the estimated df of the t-distribution for the laser tracker and the PCB acceleration measurements reveal rather close approximation of a normal distribution. This is relatively similar for the MEMS acceleration data, in particular for lower frequencies. By contrast, the estimated df regarding the IATS displacement data with heavy tails show a large number of outliers in the measurement noise of that sensor. In addition, the estimates of the AR model order demonstrate relatively high auto-correlation of the noise measurements for MEMS accelerometers. However, the AR model order is relatively large for the laser tracker displacement data compared to other sensors data sets. The reason lies in the existence of systematic errors such as measurements drift over a long period. By considering the time-dependent AR model within the GEM algorithm, particularly for the laser tracker measurements, the AR model order might be decreased.

The overall analysis demonstrates that the proposed RT-MPI algorithm can estimate all eigenfrequencies, their corresponding eigenforms as well as damping ratio coefficients by using MEMS acceleration data recorded at a bridge structure. The analysis showed a submillimetre accuracy level for amplitudes, considerably better accuracy than 0.1 Hz for the eigenfrequencies and better accuracy than 0.1 and 0.2 % for damping ratio coefficients in modal and system damping, respectively (Omidalizarandi et al., 2020). In addition, lower eigenfrequencies could also be identified from the IATS displacement data with high accuracy. However, in case of the IATS, the damping ratio coefficients could not be detected as accurate as those obtained from the MEMS acceleration data. This is due to the fact that the amplitudes of the oscillation are lower than the uncertainties of the measurements. In addition, the higher frequencies that are not detected (in the view of Nyquist sampling theorem) are superimposed on the lower frequencies and therefore can change the magnitudes of the amplitudes.

7.2 Outlook

In light of this dissertation, there are still some open questions and recommendations that can be addressed as future research, which are as follows:

1. A fully automated and knowledge-based software could be developed and implemented, which consists of data acquisition, online data preprocessing and processing, data transmission, offline data post-processing, deformation analysis, and an alarming system.
2. The influence of the MEMS-related calibration parameters on the estimated modal parameters for a long period could be investigated.

3. A time synchronisation between sensor nodes could be improved at the hardware level to achieve the highest possible accuracy.
4. A cross-correlation between either 3D acceleration data of a MEMS accelerometer or the acceleration data recorded from other MEMS accelerometers could be handled based on a VAR process. However, in this dissertation, such a cross-correlation is neglected. Therefore, its influence on the estimated modal parameters is required to be investigated.
5. The VAR process could also be used in a selection process of a suitable MEMS accelerometer. In this case, a minimal VAR model order shows a minimum cross-correlation between the 3D-axes of the MEMS accelerometer (Kargoll et al., 2020b).
6. The feasibility of a cost-effective vision-based measurement system with a high sampling frequency in deformation monitoring of a bridge structure could be investigated. In addition, an external high-resolution digital camera equipped with a telescopic lens could be mounted on top of an IATS to improve the deformation analysis over a short-time interval.
7. A convolutional neural network could be applied to localise a passive target for captured images.
8. A model selection problem or a significance test could be applied to improve the identification of initial eigenfrequencies.
9. A global optimisation and an interval search algorithm could be applied to fit DHO models to the selected excitation windows over the entire time series at once. For this purpose, a maximum and a minimum estimate of the eigenfrequencies could be selected as an upper and a lower bounds of interval. This might help to obtain a unique estimates of eigenfrequencies over a long period.
10. A pattern recognition technique based on a recurrent neural network (RNN) could be applied to improve an excitation (e.g. ambient) window selection procedure. In addition, RNN could be applied to predict a dynamic response of a bridge structure over either different temperature ranges or different loads.
11. The proposed 1D CUPT approach in this dissertation can be extended to 3D CUPT to cover all directions of a bridge structure. This can be accomplished by generating 3D displacement time series from an IATS.
12. Exhaustive experimental studies for different bridge structures such as short- and long-span bridges with different materials, and over different temperature ranges can be carried out to have a good realisation of the changes of the modal parameters. Such experiments allow to test estimated eigenfrequencies and damping ratio coefficients against their corresponding estimated values from previous epochs and to verify the structural health of a bridge.

A Appendix

Figures A.1(a)–A.1(f) depict the estimates of the calibration parameters (remaining from chapter 2), which are computed by the GHM–VCE and GHM–GEM.

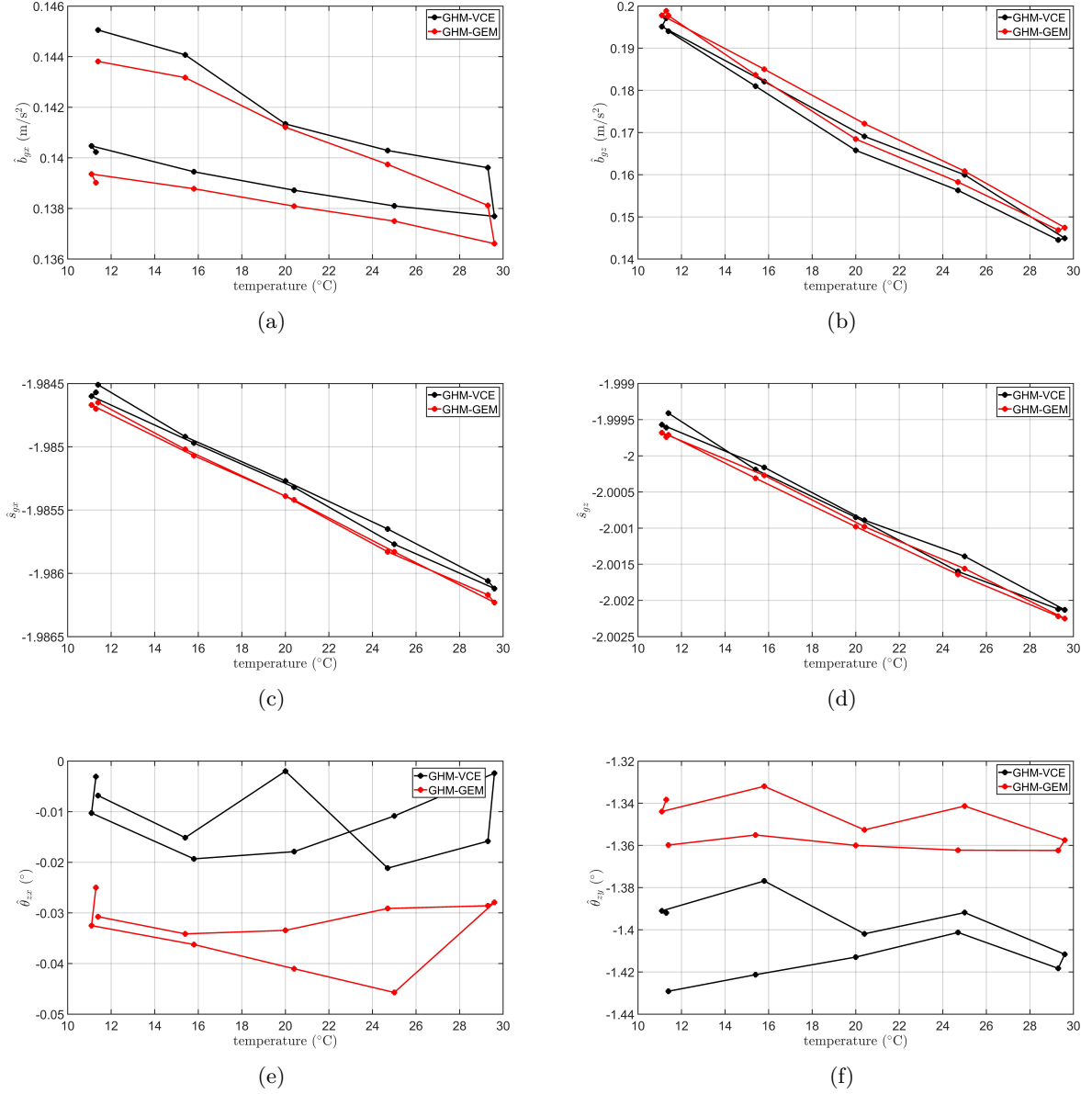


Figure A.1: MEMS accelerometer calibration parameters. (a): \hat{b}_{gx} [m/s^2], (b): \hat{b}_{gz} [m/s^2], (c): \hat{s}_{gx} , (d): \hat{s}_{gz} , (e): $\hat{\theta}_{zx}$ [$^\circ$], (f): $\hat{\theta}_{zy}$ [$^\circ$].

List of Publications

This cumulative dissertation is based on the following six publications which were all subject to a peer-review process.

Peer Reviewed Publications

- Omidalizarandi, M., Kargoll, B., Paffenholz, J.-A. and Neumann, I. (2018). Accurate vision-based displacement and vibration analysis of bridge structures by means of an image-assisted total station. *Advances in Mechanical Engineering*, 10(6). DOI: <https://doi.org/10.1177/1687814018780052>
- Omidalizarandi, M., Paffenholz, J.-A., Neumann, I. (2019a). Automatic and accurate passive target centroid detection for applications in engineering geodesy. *Survey Review*, 51(367), 318–333.
- Omidalizarandi, M., Kargoll, B., Paffenholz, J.-A. and Neumann, I. (2019b). Robust external calibration of terrestrial laser scanner and digital camera for structural monitoring. *Journal of Applied Geodesy*, 13(2), 105–134. DOI: <https://doi.org/10.1515/jag-2018-0038>
- Omidalizarandi, M., Neumann, I., Kemkes, E., Kargoll, B., Diener, D., Rüffer, J., Paffenholz, J.-A. (2019c). MEMS based bridge monitoring supported by image-assisted total station. *The International Archives of Photogrammetry, Remote Sensing and Spatial Information Sciences*, XLII-4/W18, 833–842. DOI: <https://doi.org/10.5194/isprs-archives-XLII-4-W18-833-2019>
- Kargoll, B., Omidalizarandi, M., Paffenholz, J.-A., Neumann, I., Kermarrec, G., Alkhatib, H. (2019). Bootstrap tests for model selection in robust vibration analysis of oscillating structures. In: *Proceedings of the 4th Joint International Symposium on Deformation Monitoring (JISDM)*, Athens.
- Omidalizarand, M., Herrmann, R., Marx, S., Kargoll, B., Paffenholz, J.-A. and Neumann, I. (2020). A validated robust and automatic procedure for vibration analysis of bridge structures using MEMS accelerometers. *Journal of Applied Geodesy*, 14(3), 327–354. DOI: <https://doi.org/10.1515/jag-2020-0010>

Further publications in which the author of this cumulative dissertation was either the first author or co-author are listed as follows:

Peer Reviewed Publications

- Omidalizarandi, M. and Neumann, I. (2015). Comparison of target- and mutual information based calibration of terrestrial laser scanner and digital camera for deformation monitoring. *The International Archives of Photogrammetry, Remote Sensing and Spatial Information Sciences*, 40(1), 559–564.

- Omidalizarandi, M., Paffenholz, J.-A., Stenz, U. and Neumann, I. (2016). Highly accurate extrinsic calibration of terrestrial laser scanner and digital camera for structural monitoring applications. In: Proceedings of the 3rd Joint International Symposium on Deformation Monitoring (JISDM), Vienna [CD-ROM].
- Kargoll, B., Omidalizarandi, M., Alkhatib, H., and Schuh, W. D. (2017). A modified EM algorithm for parameter estimation in linear models with time-dependent autoregressive and t-distributed errors. Proceedings ITISE, 1132–1145.
- Kargoll, B., Omidalizarandi, M., Alkhatib, H. and Schuh, W. D. (2017). Further Results on a Modified EM Algorithm for Parameter Estimation in Linear Models with Time-Dependent Autoregressive and t-Distributed Errors. In International Work-Conference on Time Series Analysis, 323–337, Springer, Cham.
- Yang, H., Omidalizarandi, M., Xu, X., and Neumann, I. (2017). Terrestrial laser scanning technology for deformation monitoring and surface modeling of arch structures. Composite Structures, 169, 173–179. DOI: 10.1016/j.compstruct.2016.10.095.
- Aghayari, S., Saadatseresht, M., Omidalizarandi, M., and Neumann, I. (2017). Geometric calibration of full spherical panoramic Ricoh-Theta camera. ISPRS Annals of the Photogrammetry, Remote Sensing and Spatial Information Sciences IV-1/W1 (2017), 4, 237–245.
- Zhao, X., Kargoll, B., Omidalizarandi, M., Xu, X., and Alkhatib, H. (2018). Model selection for parametric surfaces approximating 3D point clouds for deformation analysis. Remote Sensing, 10(4), 634.
- Kargoll, B., Omidalizarandi, M., Loth, I., Paffenholz, J.-A. and Alkhatib, H. (2018). An iteratively reweighted least-squares approach to adaptive robust adjustment of parameters in linear regression models with autoregressive and t-distributed deviations. Journal of Geodesy, 92(3): 271–297.

Non Reviewed Publications

- Neumann, I., Omidalizarandi, M. (2016). Fusion of TLS and image based measurements for monitoring of natural and artificial objects, In: GeoMonitoring 2016, Braunschweig, Germany.
- Paffenholz, J.-A., Becker, A., Omidalizarandi, M., Busse, V. (2018). Untertägige Verformungsüberwachung diskreter Ankerköpfe mittels Videotachymetrie, In: Busch W. (Hg.): GeoMonitoring 2018. Clausthal-Zellerfeld, Germany, pp. 225–240.
- Kemkes, E., Rüffer, J., Omidalizarandi, M., Diener, D., Paffenholz, J.-A., Neumann, I. (2019). Ein neues Verfahren zum MEMS-basierten Brückenmonitoring-Zielsetzung und Statusbericht, In: Tagungsband Geomonitoring 2019, 215–226. DOI: <https://doi.org/10.15488/4524>

Contributions of authors

Paper 1

Omidalizarandi, M., Paffenholz, J.-A., Neumann, I. (2019a). Automatic and accurate passive target centroid detection for applications in engineering geodesy. Survey Review, 51(367), 318–333.

In this study, an optimal passive target pattern and its robust and high accurate target centroid detection algorithm is proposed. It allows to overcome the restrictions of previously target patterns and their detection approaches in poor environmental conditions such as low lightning, dusty situations and skewed angle targets. The proposed passive target is cheap regarding its manufacturing costs and easy to mount. The detection approach is invariant to scale, rotation and illumination of the target. In addition, it successfully detects target centroids in subpixel even in the case of an incomplete viewing target pattern.

In this paper, Mohammad Omidalizarandi proposed the research idea of the optimal passive target pattern and its target centroid detection algorithm. In addition, he developed and implemented the proposed approach. Prof. Jens-André Paffenholz motivated the study, improved the conception and assisted in performing the experiments. In addition, he provided a GeoCOM interface, which facilitate the data transmission. Mohammad Omidalizarandi performed the analysis, drafted the manuscript and designed the figures and tables. Prof. Jens-André Paffenholz and Prof. Ingo Neumann reviewed the manuscript, and supervised the procedure.

Paper 2

Omidalizarandi, M., Kargoll, B., Paffenholz, J.-A. and Neumann, I. (2018). Accurate vision-based displacement and vibration analysis of bridge structures by means of an image-assisted total station. Advances in Mechanical Engineering, 10(6). DOI: <https://doi.org/10.1177/1687814018780052>

The focus of this research is to perform robust and accurate displacement and vibration analysis of a footbridge structure by means of an IATS. For this purpose, video frames of the proposed passive target pattern are captured by an embedded on-axis telescope camera of the IATS. Next, an angular conversion factor of the telescope camera is calibrated, which allows for an accurate conversion of the derived displacement time series from pixel to metric unit. To estimate eigenfrequencies, amplitudes, and phase shifts, an observation model consisting of a UDHO model, an AR model, and a stochastic model in the form of scaled t-distribution is employed, and jointly adjusted by means of the GEM algorithm. Experiments are carried out in two case studies under a controlled excitation in a laboratory environment, and a real application of the footbridge structure. The conducted controlled excitation allows to compare and validate the aforementioned estimated parameters with their known values as well as with those obtained from reference sensors such as a laser tracker and PCB ICP reference accelerometers. Consequently, it enables us to validate the proposed algorithm and sensor data analysis.

In this paper, Mohammad Omidalizarandi proposed the research idea for robust displacement and vibration analysis by means of the IATS. He developed and implemented the proposed approach. In addition, he performed experiments and their corresponding analyses. Prof. Boris Kargoll provided the MATLAB codes of the GEM algorithm from his previous research. In addition, he contributed to the section “Displacement and vibration analysis” of the manuscript by describing the robust estimation algorithm. Mohammad Omidalizarandi drafted the manuscript and designed the figures

and tables. Prof. Boris Kargoll, Prof. Jens-André Paffenzholz and Prof. Ingo Neumann reviewed the manuscript. Prof. Ingo Neumann motivated the study and supervised the procedure.

Paper 3

Omidalizarandi, M., Kargoll, B., Paffenzholz, J.-A. and Neumann, I. (2019b). Robust external calibration of terrestrial laser scanner and digital camera for structural monitoring. Journal of Applied Geodesy, 13(2), 105–134. DOI: <https://doi.org/10.1515/jag-2018-0038>.

This research work aims to robustly and high accurately estimate EOPs between TLS and high-resolution digital camera. In addition, a laser tracker is included as a highly accurate reference sensor for the purpose of validation. To relate the data of the sensors to each other, the functional models are determined based on the collinearity condition equations, the 3D Helmert transformation, and some constraint equations, which are solved in a rigorous bundle adjustment procedure. The unknown parameters consisting of the 6 EOPs between the TLS and the camera, the 7 EOPs between the TLS and the LT, and the target coordinates in the TLS coordinate system. The aforementioned highly non-linear functional models are adjusted based on three different adjustment models. The first one is an EM algorithm to solve a GHM with grouped t-distributed random deviations. The second one is an EM algorithm to solve a qGMM with t-distributed pseudo-misclosures, and a third one is a classical least-squares procedure to solve the GHM with VCE and statistical outlier removal. The proposed methodology and adjustment models can be similarly performed for the integration of the IATS and digital camera in this dissertation.

In this paper, Mohammad Omidalizarandi proposed the research idea to robustly estimate the EOPs between the sensors. He developed and implemented the aforementioned bundle adjustment procedure as well as the third adjustment model. Prof. Boris Kargoll provided the MATLAB codes for the first and the second adjustment models, which were modified and adopted by Mohammad Omidalizarandi. Mohammad Omidalizarandi performed the experiments and their corresponding analyses, drafted the manuscript and designed the figures and tables. Prof. Boris Kargoll contributed to the sections 4.1 and 4.2 of this manuscript. Prof. Boris Kargoll, Prof. Jens-André Paffenzholz and Prof. Ingo Neumann revised and improved the manuscript. Prof. Ingo Neumann offered suggestions step by step and supervised the procedure.

Paper 4

Omidalizarand, M., Herrmann, R., Marx, S., Kargoll, B., Paffenzholz, J.-A. and Neumann, I. (2020). A validated robust and automatic procedure for vibration analysis of bridge structures using MEMS accelerometers. Journal of Applied Geodesy, 14(3), 327–354. DOI: <https://doi.org/10.1515/jag-2020-0010>

In this research work, a robust and automatic procedure, that is so-called RT-MPI technique, is proposed to perform vibration analysis of bridge structures using cost-effective MEMS accelerometers. For this purpose, a proper excitation window is selected in an automatic manner. Next, initial eigenfrequencies used within the adjustment procedure are identified automatically and reliably by minimising a novel cost function. In addition, it allows to overcome the difficulties in extraction of closely spaced frequencies. To estimate the modal parameters including eigenfrequencies, amplitudes, phase shifts and damping ratio coefficients, an observation model consisting of the DHO model, an AR model a stochastic model in the form of scaled t-distributions, is employed and jointly adjusted by means of GEM algorithm. The eigenforms are characterised in a subsequent step, and with a high accuracy, using aforementioned estimated parameters. Considering the AR process enables us to handle the auto-correlation and to overcome a highly coloured measurement noise contaminating the vibration measurements, e.g., due to cost-effective MEMS acceleration data. Moreover, a double integration of the DHO model enables to estimate amplitudes in metric unit,

and with a high accuracy. Therefore, it allows to characterise deflection eigenforms with their true scales for the selected excitation window within a short time interval. The experiments are carried out for two types of bridge: a footbridge and a synthetic outdoor laboratory bridge. The analyses are compared and validated with high-end reference measurements, the FEM analysis as well as the well known SSI-COV approach. In addition, a simulation experiment is performed to theoretically validate the proposed algorithm by comparing the estimated parameters with their known values. The analysis demonstrates the proposed RT-MPI algorithm is superior to the SSI-COV algorithm with no necessity for defining tuning parameters.

In this paper, Mohammad Omidalizarandi proposed the research idea for robust vibration analysis of bridge structures. He developed and implemented the proposed RT-MPI algorithm. In addition, he extended the functional model of the GEM algorithm from UDHO to DHO model. Mohammad Omidalizarandi and Prof. Jens-André Paffenholz performed the experiments with the assistance of Mrs. Eva Kemkes and Mr. Dmitri Diener. Moreover, Dr. Ralf Herrmann provided the reference sensor measurements of the aforementioned bridge structures. Mohammad Omidalizarandi performed the analyses, drafted the manuscript and designed the figures and tables. The FEM analysis was done by Dr. Christoph von der Haar from the IFMA institute. Dr. Ralf Herrmann contributed to the description of the reference sensor measurements in section 2, vibration analysis based on the FEM analysis in section 5, and the FEM related results in section 6.2 of this manuscript. Dr. Ralf Herrmann, Prof. Boris Kargoll, Prof. Steffen Marx, Prof. Jens-André Paffenholz and Prof. Ingo Neumann reviewed the manuscript. Prof. Ingo Neumann motivated the study and supervised the procedure.

Paper 5

Omidalizarandi, M., Neumann, I., Kemkes, E., Kargoll, B., Diener, D., Rüffer, J., Paffenholz, J.-A. (2019c). MEMS based bridge monitoring supported by image-assisted total station. The International Archives of Photogrammetry, Remote Sensing and Spatial Information Sciences, XLII-4/W18, 833–842. DOI: <https://doi.org/10.5194/isprs-archives-XLII-4-W18-833-2019>.

In this study, the feasibility of a fusion of MEMS accelerometers and an IATS for short- and long-term deformation monitoring of bridge structures is investigated. In order to degrade MEMS related systematic errors, the deterministic calibration parameters are determined for fixed positions using a KUKA youBot in a climate chamber over certain temperature ranges. The measured acceleration data suffers from accuracy degradation for absolute displacement/position estimates with time. To overcome this problem, the IATS displacement data and the MEMS acceleration data are fused based on the 1D CUPT within the KF framework. The coloured measurements noise of the aforementioned data sets are decorrelated based on the AR process as part of the GEM algorithm. Therefore, it allows to robustly and accurately estimate the uncertainties of the white noise measurements used in the KF algorithm. Consequently, the proposed data fusion approach enables to generate a high accurate displacement time series, which can be used for later deformation analysis of bridge structures.

In this paper, Mohammad Omidalizarandi proposed the research idea for the fusion of the MEMS and the IATS for displacement monitoring. He developed and implemented the proposed approach. Mrs. Eva Kemkes, Mr. Dmitri Diener, and Prof. Jens-André Paffenholz performed the experiment of the synthetic bridge. Mohammad Omidalizarandi performed the analyses, drafted the manuscript and designed the figures and tables. Mr. Jürgen Rüffer and Prof. Jens-André Paffenholz contributed to the section 1.1 of this manuscript. Prof. Ingo Neumann, Mrs. Eva Kemkes, Prof. Boris Kargoll, Mr. Jürgen Rüffer, and Prof. Jens-André Paffenholz reviewed the manuscript. Prof. Ingo Neumann and Prof. Jens-André Paffenholz motivated the study and supervised the procedure.

Paper 6

Kargoll, B., Omidalizarandi, M., Paffenzholz, J.-A., Neumann, I., Kermarrec, G., Alkhatib, H. (2019). Bootstrap tests for model selection in robust vibration analysis of oscillating structures. In: Proceedings of the 4th Joint International Symposium on Deformation Monitoring (JISDM), Athens.

In this contribution, two bootstrap testing (likelihood ratio test and Wald test) procedures are proposed to decide whether the oscillation of a structure is damped or not. The bootstrap tests are derived from an observation model consisting of a parametric DHO model, a parametric autocorrelation model in the form of an AR process, and a parametric stochastic model in term of scaled t -distribution with unknown df and scale factor. The aforementioned three parametric models are jointly expressed as a likelihood function, and jointly adjusted by means of the GEM algorithm. The validation of the bootstrap test are carried out by means of the closed-loop Monte Carlo simulation. In addition, the aforementioned tests are also applied to a controlled excitation experiment.

In this paper, Prof. Boris Kargoll and Dr. Hamza Alkhatib proposed the research idea for the bootstrap testing procedure. Prof. Boris Kargoll and Dr. Hamza Alkhatib developed and implemented the bootstrap tests. Mohammad Omidalizarandi extended the functional model. Dr. Hamza Alkhatib performed analyses of the Monte Carlo simulation. Mohammad Omidalizarandi performed the analyses of the controlled excitation experiment. Prof. Boris Kargoll and Dr. Hamza Alkhatib drafted the manuscript. Mohammad Omidalizarandi contributed to the sections III.B, III.C and part of conclusion. Prof. Jens-André Paffenzholz, Prof. Ingo Neumann, Dr. Gaël Kermarrec, and Dr. Alkhatib reviewed and revised the manuscript. Mohammad Omidalizarandi, Dr. Hamza Alkhatib, and Prof. Boris Kargoll motivated the study. Dr. Alkhatib supervised the procedure.

Paper 1

Automatic and accurate passive target centroid detection for applications in engineering geodesy

Mohammad Omidalizarandi*, Jens-André Paffenholz and Ingo Neumann

Geodetic Institute, Leibniz Universität Hannover, Hannover, Germany

*Corresponding author, email zarandi@gih.uni-hannover.de

A novel automatic and accurate passive target centroid detection approach is proposed and developed which has numerous fields of applications, such as in engineering geodesy, photogrammetry, robotics and navigation. It is robust and reliable with respect to poor environmental conditions, such as low lighting, dusty situations and skew angle targets. This research is conducted in two parts. Firstly, an optimal target selection and its accurate automatic and fast centroid detection is performed. Afterwards, two case studies of the proposed approach are presented for automatic target pointing by means of the telescope camera of an image assisted total station (here Leica Nova MS50 MultiStation) and automatic target measurements for a digital camera (here Nikon D750). The results show that a circular target with a line pattern consisting of four intersected lines is an optimal pattern. The accuracy of the proposed method varies depending on the image resolution and distances to the objects. We performed experiments for distances between 1.6 and 28 m for the image assisted total station and achieved sub-millimetre accuracy.

Keywords: Passive target centroid detection, Optimal target pattern, Image assisted total stations, Digital camera, Image processing, Image analysis

Introduction

There is an increasing demand nowadays for automatic, low cost and accurate monitoring of civil engineering structures (e.g. buildings, bridges, dams) or natural objects (e.g. landslides) using state-of-the-art *image assisted total station* (IATS) (Reiterer *et al.* 2009, Bürki *et al.* 2010, Thuro *et al.* 2010, Wagner *et al.* 2013, Wagner *et al.* 2014, Ehrhart and Lienhart 2015a, 2015b, Guillaume *et al.* 2016, Wagner 2016, 2017). Total stations with externally attached cameras or embedded cameras are commonly referred to as IATS.

In the context of sensor fusion, when using a camera in combination with, for example, a total station or a laser scanner, the external calibration parameters (i.e. the relative orientation of the sensor origins) must be known to relate the data of the sensors to each other. For embedded cameras, the external calibration parameters are usually known through the manufacturer's calibration procedure. There is typically no need for the user to determine the external calibration parameters before a measurement task. By contrast, when using an externally attached camera, the external calibration parameters are *a-priori* unknown and have to be determined by an appropriate calibration procedure. In any case, an internal camera calibration should be performed to convert the pixel coordinate system to the metric coordinate system. Walser (2004), Ehrhart and Lienhart

(2016) and Zhou *et al.* (2017) proposed camera calibration approaches to convert pixel coordinates to their corresponding metric coordinates. However, it is also possible to rotate the telescope of an IATS to the detected target by knowing the pixel differences between the initial pointing in the direction of the optical path of the telescope and the precise direction to the detected target's centroid. In this case, the instrument's axial errors, vertical index error, collimation error, in addition to the internal camera calibration parameters need to be obtained and considered to relate pixel coordinates to metric coordinates precisely.

Considering the classical total station part of the IATS, active targets (i.e. retroreflective tape and classical prisms) are measured by the reflector-based distance measurement unit. Passive targets (i.e. marked target locations or arbitrary artificial object surfaces) are determined by the reflectorless distance measurement unit. An IATS benefits from both the images captured by its telescope camera and the precise polar measurements (i.e. horizontal directions, zenith angles and distance measurements). The motorised axes of rotations of the IATS allows for accurate, automatic and autonomous monitoring. Bürki *et al.* (2010) overviewed the advantages and disadvantages of the traditional *automatic target recognition* (ATR) technique that demands an active target (i.e. a classical prism) as follows:

- (1) Mandatory use of a reflector as target, which limits the measurement range.
- (2) Systematic angular measurement errors due to inaccurate ATR zero offset calibration.
- (3) Less applicability for industrial metrology due to the dependency of ATR angular measurements on the reflector.
- (4) Systematic errors due to the varying intensity of the laser emitter and subsequent uneven target illumination.

Passive targets, as a low-cost alternative to the retroreflective tape and classical prisms, have numerous applications in engineering geodesy (e.g. cheap manufacturing costs and accurate target pointing by means of the IATS, self-positioning update of the IATS with respect to the control points), photogrammetry (e.g. automatic camera calibration), robotics and navigation. In addition, in the case of mounting prisms in difficult to access environments, such as rock faces, tunnels and bridges, passive targets seem to be more beneficial as there is no need of removal between measurement campaigns due to their cheap manufacturing costs. Ehrhart and Lienhart (2015a, 2015b) presented a displacement and vibration monitoring of a footbridge structure using the telescope camera of an IATS to measure circular targets rigidly attached to the footbridge structure. The target centres are extracted by least squares ellipse fitting within a Gauss-Helmert model (GHM). In addition, the user interaction and manual pointing by the operator has only to be performed in the first measurement epoch (i.e. to initially point to the targets). Subsequently, the motorisation of the axes of rotations is used to automatically point to the targets based on the measurement values of the initial pointing. This procedure is used for all subsequent epochs.

Automatic target detection can be carried out with different approaches, such as coded target (CT) detection (Zhou *et al.* 2015), ellipse detection (Chow *et al.* 2010, Ehrhart and Lienhart 2015a, Guillaume *et al.* 2016), circle matching (Bürki *et al.* 2010), cross line detection (Reiterer and Wagner 2012, Yi *et al.* 2018), least squares template matching (Grün 1996, Akca 2003, Grün and Akca 2005, Bürki *et al.* 2010, Kregar *et al.* 2013) and centre of mass (Bürki *et al.* 2010). Zhou *et al.* (2015) automatically detected concentric rings of CTs using the open source OpenCV library (Kaehler and Bradski 2016). Subsequently, all calibration parameters at a certain focus position were calculated

by means of CTs and angular readings from a total station. New sets of calibration parameters were computed by cubic polynomial interpolation at different focus positions. The challenges regarding this solution are the need to define some thresholds and constraints to get rid of spurious detected ellipses, the need to restrict the effect of non-perpendicularity of the surface of CTs to the aiming direction and the need for a complete viewing target pattern within the image's field of view (FOV). Subsequently, CTs seem to be the proper choice of targets for camera calibrations, since both the target centroid coordinates and the ID (i.e. target identification number) are obtained simultaneously. Nevertheless, this may not be a good solution for highly accurate monitoring applications, as it is merely dependent on the ellipse detection. In addition, it is also a challenging issue in the case of poor lighting conditions or skewed targets (i.e. targets with bad incidence angles). Yi *et al.* (2018) proposed an automatic approach to detect cross-shaped passive target patterns using the radiometric and geometric information of three-dimensional (3D) point clouds based on discrete Morse theory on the intensity image. Reiterer and Wagner (2012) compared template matching, edge-based and point-based methods. They applied the edge-based technique to a region-of-interest (ROI) which contains the target. The proposed approach is advantageous for extracting relevant edges within the ROI and speeding up the process by reducing the search domain. The disadvantages of the proposed approach are the sensitivity to a change of the lighting conditions and the requirement of a user interaction to set the threshold parameters. They found that the edge-based method is the best-suited detection method compared to template- or point-based methods. The template matching method is based on finding the maximum correlation between a template and the search images using grey values. It is variant with respect to scale, rotation and illumination of the objects. As described by Reiterer and Wagner (2012), the template matching technique can be improved by extracting features along contours and using them in the matching procedure.

The novelty of our approach is twofold: firstly, we propose an optimal passive target pattern which overcomes the restrictions of the formerly proposed target patterns by applicability without special light conditions, low manufacturing costs, subpixel detection accuracy, fast run time speed and ease of mounting. Secondly, the highly accurate detection of its centroid is based on digital image processing techniques and the classical polar measurements of an IATS. The proposed target pattern and its detection approach is robust and reliable in poor environmental conditions, such as low lighting (i.e. no need for active illumination), dusty situations and skew angle targets. Moreover, it is invariant to the scale, rotation and illumination of the targets. It also works well even after a poor initial pointing to the target. In addition, it successfully detects target centroids in the case of an incomplete viewing target pattern. Therefore, the proposed target pattern is cheap regarding its manufacturing costs and its detection approach is fast and accurate, which suits numerous applications, such as deformation monitoring. The focus of this work is on the optimal passive target selection and its accurate, automatic and fast centroid detection. The conversion of pixel coordinates to the corresponding metric coordinates based on camera calibration parameters will be performed in future research.

Sensor Specifications

In our experiments, we used the telescope camera of an IATS (here Leica Nova MS50 MultiStation (MS50)) and a digital single lens reflex (DSLR) camera (here Nikon D750) attached on top of a terrestrial laser scanner (TLS).

The Leica MS50 measures prism targets from 1.5 m to 10000 m with an accuracy of 1 mm + 1.5 ppm and a measurement time of typically 1.5 s. Furthermore, it measures non-prism targets (arbitrary artificial object surfaces) from 1.5 m to 2000 m with an accuracy of 2 mm + 2 ppm and a measurement time of typically 1.5 s. Its laser dot size is about 8 mm x 20 mm at 50 m. The Leica MS50 includes an overview camera with a diagonal FOV of 19.4° and a telescope camera with a FOV of 1.5°. Both cameras have 5-megapixel CMOS sensors (2560 x 1920 px; maximum image size), where the telescope camera has a 30 X optical magnification (Leica Geosystems 2013). The angular resolution (α) of the telescope camera is approximately 1.7"/px, which is computed by division of the diagonal FOV by the diagonal length of the captured image in pixel units. According to Leica Geosystems (2013), the horizontal and vertical FOVs of the telescope camera of the Leica MS50 are 1.3° and 1.0°, respectively. In this research, concerning the use of the telescope camera of the Leica MS50, its autofocus is set to 'on', the image resolution varies from [640 x 480 px] to [2560 x 1920 px] and the white balance is set to 'automatic mode'. Moreover, reflectorless distance measurements to the targets allow one to set the telescope's focus motor position (autofocus) precisely. We used the GeoCOM interface (Leica Geosystems 2014) to get full access to the individual functionality of the Leica MS50. We implemented the GeoCOM interface in the script language Python 3.4 for simplicity, in addition to our proposed target centroid detection algorithm. The Leica MS50 can be controlled via the graphical user interface that we developed, see Figure 1, which allows us to perform the data acquisition and analysis (target centre detection) in an efficient and effective manner.

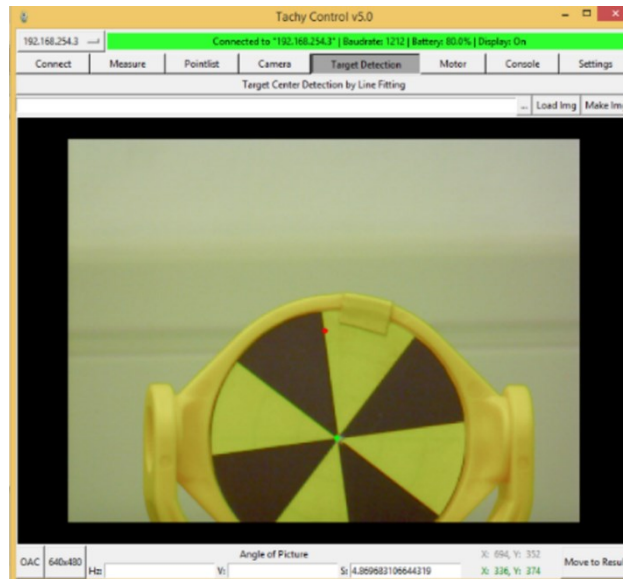


Figure 1. Graphical user interface in script language Python 3.4 to control Leica total stations and run our target centroid detection algorithm.

The full frame DSLR camera (here NIKON D750; 24 megapixel) is used in combination with a laser scanner; it is firmly attached on top of the laser scanner. This sensor fusion allows us to perform displacement analyses of natural and artificial objects in both horizontal and vertical directions perpendicular to the laser beam (Omidalizarandi and Neumann 2015, Omidalizarandi *et al.* 2016). In addition, it benefits from a larger FOV and, subsequently, covers a larger part of the monitored object compared to the embedded cameras of state-of-the-art IATS. The following parameters for the DSLR camera were chosen for our experiments: the image size is set to 'large' with a size of

[6016 x 4016 px]. The focus mode is set to ‘manual’, the autofocus is set to ‘off’, the lens focus is set to ‘infinity’, the exposure is set to ‘aperture-priority auto’, the white balance is set to ‘auto’, the ISO sensitivity is set to ‘100’ and the aperture (f-stop) is set to ‘6.3’ (Nikon 2014).

Data Acquisition and Pre-processing

The research was conducted with different passive target patterns to select the optimal one and, consequently, extract the target centroid automatically and accurately. Two different methodologies are proposed and their advantages and disadvantages are presented and discussed in detail.

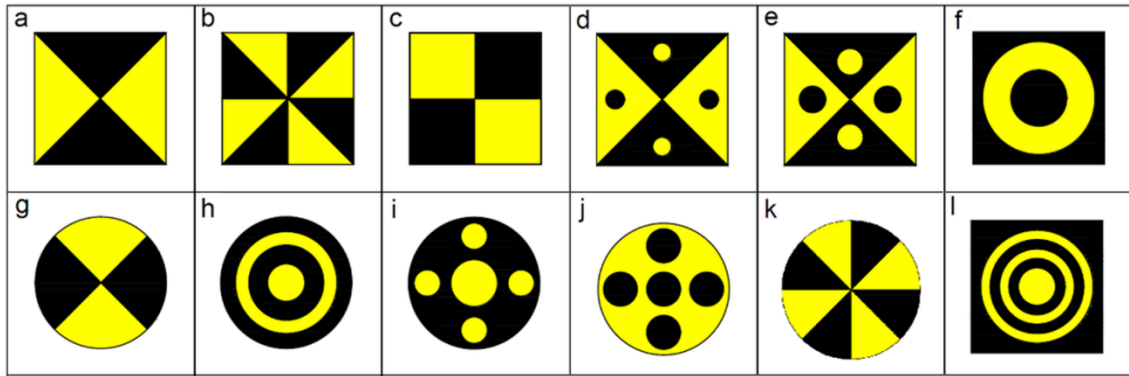


Figure 2. Design of passive target candidates.

The target candidates can be classified based on border shapes or patterns. The targets with rectangular and circular borders are so-called R_b and C_b targets, respectively. Target patterns that include line features, circle features or a combination of them are so-called L_p , C_p or LC_p targets. Figure 2 shows our twelve target candidates: rectangular target with line pattern (R_bL_p target; a, b, c), rectangular target with circle pattern (R_bC_p target; f, l), rectangular target with line and circle pattern (R_bLC_p target; d, e), circular target with line pattern (C_bL_p target; g, k) and circular target with circle pattern (C_bC_p target; h, i, j).

In our research, the R_b and C_b targets have been designed in the software AutoCAD 2016 by Autodesk with a size of 0.07 and 0.06 m, respectively. Targets were captured with the telescope camera of the Leica MS50 at various distances up to a maximum distance of about 28 m. The target size can be adopted to suit the maximum distances to the objects and monitoring applications. Note that the target size in the image space is changing with the distance to the IATS. Figure 3 shows target b, which was captured with the telescope camera of the Leica MS50 at different distances.

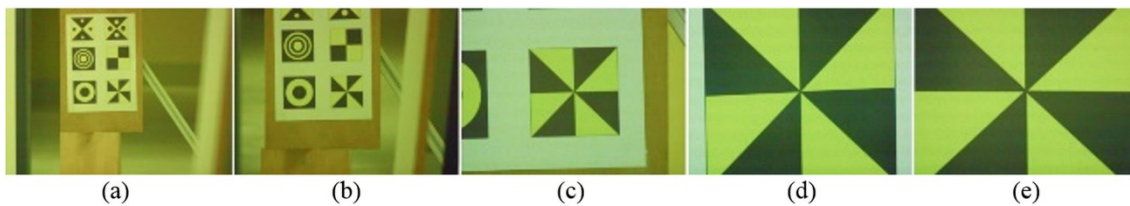


Figure 3. Captured targets at different distances. (a) 28.33, (b) 20.13, (c) 7.28, (d) 3.34 and (e) 1.67 m.

A cropping of the captured images is performed to extract the corresponding target to extract the relevant features within the ROI and to speed up the procedure (Reiterer and Wagner 2012). It is based on the object size of the target, the slope distance, and the horizontal and vertical FOVs of the telescope camera. Based on Eqs. (2) and (3), the change of the horizontal and vertical FOVs to lower values leads to a larger cropped target image, which, subsequently, decreases the cropping sensitivity to skew angle targets and slope distances. Since the telescope camera of the IATS is coaxial with the line of collimation, one has the possibility to initially localise the targets and to crop the corresponding captured images based upon the centre of the target and the computed target width and height in pixel units (Eqs. (2) and (3)). Equation (1) computes the FOVs based on the target size in the object space and the measured slope distance to the target. Afterwards, based on the width and height of the captured image, and the horizontal and vertical FOVs of the telescope camera, the target width and height are computed in pixel units.

$$FOV = 2 \times \tan^{-1}(D/(2 \times S)) \quad [rad] \quad (1)$$

where D = target size in object space [m] and S = slope distance [m].

$$d_w = \frac{w \times FOV}{FOV_h} \quad (2)$$

$$d_h = \frac{h \times FOV}{FOV_v} \quad (3)$$

where d_w = target width [px]; d_h = target height [px];
 w = width of captured image [px]; h = height of captured image [px];
 FOV_h = horizontal FOV [rad]; and FOV_v = vertical FOV [rad].

Line Feature Extraction

Edges in digital images can be extracted based on either the Canny edge detector (Canny 1986) or the line segment detector (LSD) algorithm (Grompone von Gioi *et al.* 2012). The LSD algorithm is preferable for the L_p or C_p target, since the connectivity between the extracted edges is better than in the Canny operator and there is no need for edge linking to connect fragmented extracted edges. The LSD parameters include: sigma of Gaussian filter (here set to 0.75), bound to the quantisation error on the gradient norm (here set to 2.0), the gradient angle tolerance (here set to 22.5°), the minimal density of region points in the rectangle (here set to 0.7), the number of bins (here sets to 1024) and the gradient modulus in the highest bin (here set to 255). The aforementioned thresholding parameters are set for different images with different resolutions and there is no need for further changing of parameters to extract the line features based on the LSD algorithm. Please refer to Grompone von Gioi *et al.* (2012) for more information concerning the LSD algorithm. The Canny operator is a better choice compared to LSD to extract any types of C_p targets due to deriving smoother extracted edges. Figure 4a shows the cropped image of the captured image from the Nikon D750 camera and Figures 4b and 4c show extracted edges by means of the Canny edge detector using the OpenCV library and the LSD, respectively.

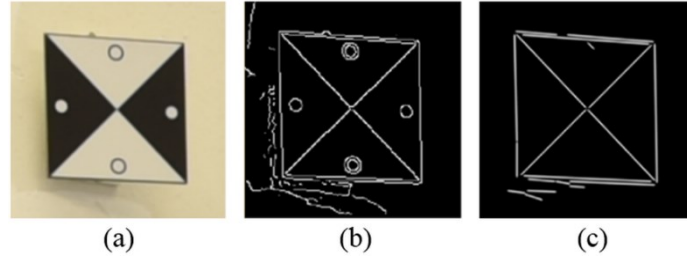


Figure 4. (a) Cropped image, (b) extracted edges by the OpenCV Canny edge detector and (c) extracted edges by the LSD.

Optimal Target Pattern Selection

The optimal target pattern selection is performed for the twelve designed R_b and C_b targets with L_p and C_p patterns (Fig. 2). In C_p targets, after extracting the edges by the Canny edge detector, the next step is to form contours from the extracted edges. In C_p targets, the circle radius in the object space [m] is converted to the image space [px] using Eqs. (1) to (3). This procedure is only valid for targets perpendicular to the laser beam. In the case of skew angle targets, circles are changing to ellipses and the computation of the normal vector of the target planes is needed to estimate the radius more accurately. This leads to additional measurements on the target surface for the computation of the normal vector, which is not cost-efficient and might be a time-consuming task. Thus, among the twelve targets under investigation, L_p targets are better choices than C_p targets due to their accurate and easier target centroid detection, even in the case of bad incidence angles. Therefore, targets d, e, i and j are not suitable, because all four circles must be visible to allow us to compute the centroid by means of averaging over the centres of four circles.

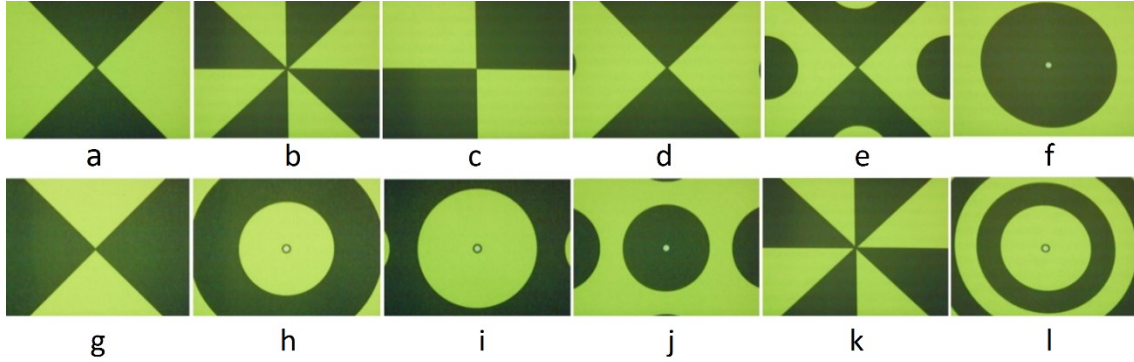


Figure 5. Captured passive targets at a distance of about 1.6 m. Targets patterns a to l from top left side to the bottom right.

As can be seen from Figure 5, parts of the measured targets at a distance of about 1.6 m captured by a Leica MS50, are not visible and, therefore, a target centroid detection of the aforementioned C_p or LC_p targets are more problematic.

It should be noted that the designed targets were optimised for digital image processing using either the captured images from the embedded telescope camera of a Leica MS50 or high-resolution images of external digital cameras. Better results could be obtained for manual pointing by human observers by using circular targets with concentric circles matched to the width of the cross-hairs at different distances.

Targets b and k are chosen for an in-depth evaluation and further experiments due to their numerous intersecting lines and, consequently, an increased redundancy

compared to the other target designs. These two targets will be investigated in more detail in the following section.

Target Centroid Detection

The target centroid detection is performed for targets b and k to select the optimal one. Two different methodologies are presented in more detail: the *longest line-based target centroid detection* (LL-TCD) (see Fig. 11, and Fig. 17 in Appendix A) and the *azimuth-based target centroid detection* (A-TCD) (see Fig. 11, and Fig. 18 in Appendix A).

In both approaches, the cropping of the captured images from the IATS are carried out by considering the horizontal and vertical FOVs equal to 1.25° and 0.95° , respectively (Figs. 6a and 11). The next step is to apply the median blur filtering to reduce the noise and to smooth the cropped images. Thereafter, a bilateral filter, which is non-linear, edge-preserving and noise reducing, is applied to preserve the sharp edges of the image (Figs. 6b and 11). The LSD is then applied to extract the edges of the filtered cropped image from the previous stage (Figs. 6c and 11). Note that the horizontal and vertical FOVs previously mentioned are only appropriate when manual target pointing measurements are close to the centre of the target. Later, the horizontal and the vertical FOVs are set to 0.3° for practical reasons in the structural monitoring applications (due to the significant movements of targets), to cover a greater part of the captured image.

Longest Line-based Target Centroid Detection

The lengths of all extracted edges are computed and sorted in descending order in the *longest line-based target centroid detection* (LL-TCD) approach. The longest line is then selected at the first iteration (Figs. 6d and 11). Next, the longest line selected is extended on both sides to the edges of the image (Fig. 6e). The buffer lines with $d_w/80$ pixels (i.e. the value of 80 pixels has been chosen by trial and error) distance from the extended line are defined, which support the selection of all lines in the same direction and assist the removal of spurious lines which are not within the buffer lines (Fig. 11).

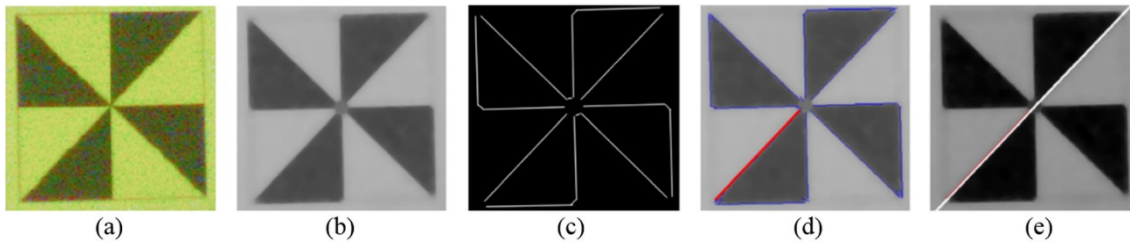


Figure 6. The longest line-based target centroid detection: (a) Cropped image of rectangular target with line pattern, (b) filtered target image with applied median blur and bilateral filtering, (c) edge image with applied LSD algorithm, (d) longest LSD line selection at the first iteration and (e) its extension to other sides.

Afterwards, vector lines are converted to raster lines to increase the redundancy by having more raster points (Fig. 11). Random sample consensus (RANSAC) (Fischler and Bolles 1987) line fitting, Huber robust line fitting or least squares line fitting (with an applied Gauss Helmert model (GHM)) can be applied to fit the line to the extracted edges. The OpenCV Huber line fitting is based on the M-estimator technique and is robust, efficient and fast. It fits the line iteratively using the weighted least squares algorithm. After each iteration, the weights w_i are adjusted based on the inverse of

distance function $\rho(r_i)$ (Eqs. 4), where r_i is the distance between i^{th} point and the corresponding fitted line and C is a threshold (Huber 1981, Kaehler and Bradski 2016).

$$\rho(r) = \begin{cases} \frac{r^2}{2} & \text{if } (r < C) \\ C \cdot \left(r - \frac{C}{2}\right) & \text{otherwise} \end{cases} \quad \text{where } C = 1.345 \quad (4)$$

If the OpenCV Huber line fitting is applied, the accuracy of the fitted line is unknown. Therefore, a GHM-based least squares line fitting approach is implemented to overcome this issue. Global and local tests based upon a χ^2 test with a 95% confidence level are applied. Data snooping is performed to reject large residuals or outliers one by one. In the local test, all points with normalized χ^2 test values above a predefined test value can be rejected at once to speed up the procedure. In the Huber robust M-estimator technique (Huber 1981), measurements are re-weighted based upon the inverse of the distance function. In this case, the observations with large residuals have the lowest weights. According to our experiments, the GHM-based line fitting approach results are slightly different from those of the OpenCV Huber line fitting algorithm. It is possible to compute the standard deviations of the detected target centroids for different distances (e.g. in our experiment, up to 28 m with 13 target measurements at different distances in one set up) and to fit a polynomial curve (i.e. we applied the polyfit function of the software MATLAB 2016a by Mathworks) to approximate the curve parameters. In order to increase the run time speed of the procedure, the OpenCV Huber line fitting is used to fit the line and then the standard deviations of the detected target centroids for each specific distance is estimated based on the curve parameters calculated from the GHM-based line fitting. Figure 7 shows the standard deviations calculated from the GHM line fitting approach in a solid red colour and the fitted polynomial curve (i.e. degree 6) in a dashed black colour. In order to give an impression about the accuracy of the detected target centroids, the approximate pixel size is calculated in metric units for two different image sizes at slope distances of 1, 10, 20 and 30 m (Table 1). The maximum standard deviations, about 6 pixels, appeared at a distance of 1.67 m. As we can see in Figure 7 and Table 1, the pixel size at a distance of 1.67 m for the image sizes of [2560 x 1920 px] and [640 x 480 px] are approximately 0.01 mm and 0.05 mm. Therefore, the maximum standard deviations of the detected target centroids for the image sizes mentioned previously are approximately 0.08 and 0.33 mm, respectively.

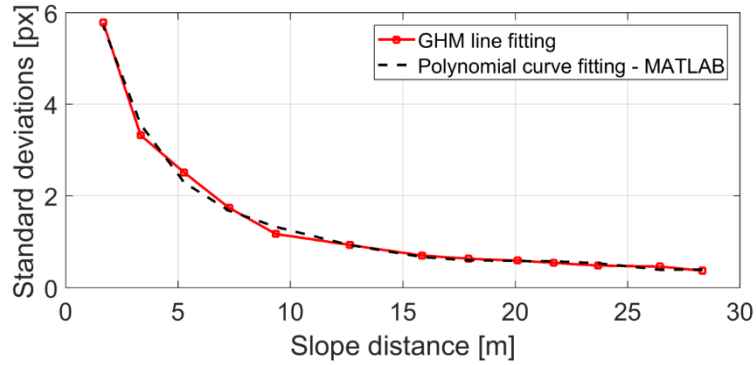


Figure 7. Standard deviations of the Gauss-Helmert model line fitting (solid red), Polynomial curve fitting of degree 6 – MATLAB (dashed black).

Image size [px]	Slope distance [m]	Pixel size [mm]
2560 x 1920	1	0.008
2560 x 1920	10	0.082
2560 x 1920	20	0.164
2560 x 1920	30	0.245
640 x 480	1	0.033
640 x 480	10	0.327
640 x 480	20	0.655
640 x 480	30	0.982

Table 1. Pixel size in metric units for image sizes of [2560 x 1920 px] and [640 x 480 px] at a distance of 1, 10, 20 and 30 m.

The Huber robust line fitting approach is applied to the extracted edges, which are within the buffer lines, to robustly fit the line and get rid of outliers. This procedure proceeds until no extracted edges remain. Small and spurious extracted lines are discarded by thresholding. Consequently, the intersection points of all extracted lines are detected. A k-d tree nearest neighbourhood algorithm is applied to detect the neighbouring intersection points within 2 pixels.

The k-d tree or k-dimensional tree is a space-partitioning data structure which is used to organise points in a space with k dimensions. It is a binary tree which associates each node in the tree with one of the k-dimensions using a hyperplane that is a perpendicular to the corresponding axis. The hyperplane is used to divide the space into the two parts known as left sub-tree and right sub-tree. Therefore, each node is associated to each sub-tree based on smaller or greater values at each root. This procedure proceeds until only one element remains in the last tree (Bentley 1975).

The maximum intersection point cluster closest to the initial pointing point is then selected. At the end, the mean of the maximum cluster selected is computed to derive the final intersection point (Fig. 11).

A drawback of the target pattern b is the high chance of maximum intersection point clusters at the four corners of the targets. To overcome this problem and to detect the target centroids more reliably, circles with a radius of $d_w/8$ pixels around the intersection points detected are defined. All edge lines are then intersected with the defined circle. Afterwards, the azimuth between the detected intersection points of line-line and intersection points of line-circle are computed and subtracted from each other to obtain the inner angles. In targets b and k, for instance, in the ideal case and no skew angles of the target, eight 45° angles between edge lines should be obtained (i.e. $8 \times 45^\circ = 360^\circ$). However, these angles can vary depending on the skew angle of the targets. Thus, a threshold angle of 10° is considered to overcome this problem. The probability of all intersection points of line-line are then calculated based on the multiplication of accepted angles with 12.5% to achieve 100% (i.e. $8 \times 12.5\% = 100\%$) as a maximum possible probability. Next, the mean of the intersection points at maximum probability is computed to achieve the final intersection point. Figures 8a, 8b and 8c show all the lines extracted and the representation of all intersection points of line-circle with corresponding probabilities. The centroid intersection point has the highest probability for selection compared to the other intersection points. However, the probability and reliability of the target centroid detected is decreased by missing some line patterns and by detecting spurious lines due to the noisy image.

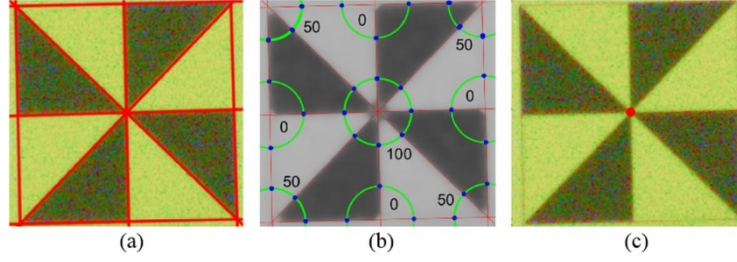


Figure 8. The longest line based target centroid detection: (a) Depiction of all lines extracted, (b) depiction of all intersection points of line-circle with corresponding probabilities and (c) final detected target centroid.

Azimuth-based Target Centroid Detection

In the *azimuth based target centroid detection* (A-TCD) approach, a paper printed target pattern k (Fig. 9) is designed to increase the efficiency and run time speed of the algorithm under different lighting conditions (e.g. normal lighting, very bright: direct lighting, semi-dark: close indirect lighting, dark: far indirect lighting and totally dark: no source of light).



Figure 9. Designed circular target with line pattern: (left) paper printed target and (right) target printed on reflective tape.

In this methodology (see Fig. 11 for pseudo-code of the procedure), firstly, the localisation of the target in each captured image is performed by means of the Hough circle transform (HCT) (Kaehler and Bradski 2016) to detect circular objects. The radius of the circles in the HCT is calculated based on Eqs. (2) and (3), and by considering the horizontal and vertical FOVs of 1.3° and 1.0° , respectively. In order to discard the spurious detected circles, the captured image is cropped in the region of detected circles and converted to a binary image. In addition, the target template image is resized based on the calculated target width and height and converted to a binary image. The histogram of the binary image from circles is compared to that from a target template image and the circle image with the maximum correlation is selected.

In the next step, edge lines are extracted to a selected region of detected circles by means of the LSD. The relevant edges are extracted within the ROI, which also speeds up the process. In the case of a very noisy image, a detection of circles is nearly impossible. Thus, the whole cropped image is considered for further processing. Next, line azimuths are calculated. Based on a histogram of the azimuths, the maximum azimuth is selected. Afterwards, the angles between the LSD lines and the maximum azimuth direction are computed and the lines within a predefined angle threshold, less than 15° here, are accepted. The RANSAC algorithm is applied to fit an optimal line to the selected lines and to remove spurious or false lines, which are nearly parallel to each line pattern (Figs. 10c and 11). Buffer lines with $d_w/80$ pixels from each side are defined and the Huber robust line fitting algorithm is applied to extract lines more accurately. The k-d-

tree neighbourhood is applied to detect the neighbouring intersection points within 2 pixels. Subsequently, the maximum intersection point cluster is selected and the mean of them results in the final intersection point (Fig. 11). The advantage of C_bL_p targets compared to the former ones (R_bL_p) is that their detection by the second methodology is faster and working well even without a good initial pointing. This is due to the fact that the chance of a target centroid detection at the centre cluster is much higher, because of fewer parallel lines at the edges of the designed target pattern. Another difference between the previous two approaches is that applying the RANSAC line fitting in the LL-TCD approach is arbitrary, since the buffer lines are defined along the longest lines iteratively and directions are already known. However, in the A-TCD approach, the RANSAC line fitting needs to be applied to estimate line parameters among all detected parallel lines randomly. Later results prove that the C_bL_p targets seem to be a better solution than the R_bL_p targets.

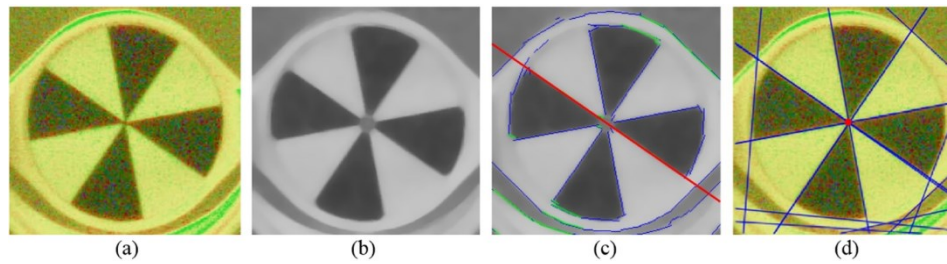


Figure 10. The azimuth-based target centroid detection: (a) Cropped image of circular target with line pattern, (b) filtered target image with applied median blur and bilateral filtering, (c) selected parallel lines within predefined angle threshold in green and fitted line with RANSAC algorithm in red, (d) all extracted lines in blue and final detected target centroid with red.

Algorithm: Target centroid detection using image assisted total stations (Leica MS50)

1. Input:

2. Initial pointing to the passive target with specific size
3. Read slope distance from Leica MS50
4. Capture passive target using telescope camera of Leica MS50
5. Read template image of target (optional)

6. Pre-processing:

7. Calculate target size in pixel units
8. Calculate horizontal and vertical FOVs
9. Crop captured image
10. Median blur filtering
11. Bilateral filtering
12. Edge detection using LSD
13. Template matching (Optional)
14. Detect circles in cropped image using Hough circle transform
15. Create binary image for detected circle regions
16. Resize template image based on the size of cropped image
17. Create binary image of template image
18. Compare histogram of template image and detected circle regions
19. Select circle region with maximum correlation
20. **if** (Template matching)

21.	Detect edges within the selected circle region
22.	else
23.	Use all extracted edges
24.	end if
25.	Target centroid detection:
26.	if (azimuth based target centroid detection approach (A-TCD))
27.	Compute line azimuths
28.	Calculate histogram of line azimuths
29.	Sort azimuth bin centres in descending order
30.	while (azimuth bin centres array is empty?)
31.	Select azimuth bin centre from beginning
32.	Select all parallel lines
33.	Convert line vectors to raster
34.	RANSAC line fitting
35.	Huber line fitting
36.	Discard selected azimuth bin centre
37.	end while
38.	end if
39.	if (longest line based target centroid detection approach (LL-TCD))
40.	Assign code 0 to all lines
41.	Compute line lengths
42.	Discard small and spurious lines
43.	Sort lines based on lengths in descending order
44.	while (all lines have code 1?)
45.	Select longest line with code 0
46.	Select parallel lines within buffer size
47.	Convert line vectors to raster
48.	RANSAC line fitting or Huber line fitting
49.	Assign code 1 to all selected lines within buffer as visited lines
50.	end while
51.	Final processing:
52.	Compute intersection points of all lines
53.	Store intersection points in array
54.	K-d tree neighbourhood
55.	Select neighbouring points within 2 pixels
56.	if (azimuth based target centroid detection approach (A-TCD))
57.	Select cluster with maximum intersection points
58.	Else if (longest line based target centroid detection approach (LL-TCD))
59.	Select cluster with maximum probability
60.	end if
61.	Mean of selected intersection points
62.	Output:
63.	Detect target centroid [px]
64.	Use GeoCOM interface to automatically rotate telescope to the detected point
65.	Detect target centroid [m]

Figure 11. Pseudo-code of the proposed target centroid detection approaches.

Experimental Results

In this research, an optimal target pattern selection and its accurate and automatic centroid detection is presented. The efficiency, reliability, repeatability, separability and accuracy of the proposed method is now evaluated and examined with two sample applications. The first test is performed using the telescope camera of an IATS (here Leica MS50) in the laboratory of the Geodetic Institute Hannover (GIH) of the Leibniz Universität Hannover. The dimensions of the laboratory are approximately 58 m (length) x 2.5 m (width) x 3 m (height). The aim is to select the optimal target pattern among twelve designed targets and detect the target centroid automatically after an initial, rough pointing. The second test is carried out to validate our proposed target centroid detection. It is performed by using a DSLR camera (here Nikon D750 24.3-megapixel) and a terrestrial laser scanner (TLS; here Zoller+Fröhlich Imager 5006) in the 3D laboratory of the GIH (about 6 m (width) x 8.5 m (length) x 5 m (height)). In the second test, the goal is to obtain highly accurate external calibration parameters between the TLS and the DSLR camera.

Case study I – Optimal Target Pattern Selection and Its Accurate Centroid Detection Using Image Assisted Total Stations

In this case study, the rectangular target with a line pattern (R_bL_p) and the circular target with a line pattern (C_bL_p) are examined, evaluated and compared to select the optimal one. Subsequently, the target centroid detection is carried out based on image processing techniques. Table 2 and Figure 12 indicate the applicability of the *longest line based target centroid detection* (LL-TCD) approach for the R_bL_p target (i.e. target b in Fig. 2) at different distances with different line fitting approaches by calculating the absolute deviations between the three line fitting approaches and one precise manual pointing measurement. The results (Fig. 12) show that the three line fitting approaches are very close for distances longer than 5 m. On the other hand, for distances below 5 m, the RANSAC line fitting shows larger deviations (in pixel units) than the two other line fitting methods. The RANSAC line fitting randomly fits the line and is robust regarding the outliers and for selecting true line patterns. However, the final intersection points may change slightly for each run of the algorithm due to its random characteristics. Subsequently, it was found that even by applying the RANSAC algorithm, the detected target centroids are accurate enough and comparable with the two other line fitting approaches in the metric unit. As previously indicated in Table 1 and can be seen in Figure 12, the maximum absolute deviations between the RANSAC line fitting and the one-time manual pointing is about 10 pixels at the distance of 1.67 m, which is approximately equivalent to 0.14 mm for the image size of [2560 x 1920 px]. The probability shown in Table 2 Column 7 proves that the LL-TCD approach can successfully detect the target centroid. In addition, as we can see in Table 2, σ_{xy} [px] shows that standard deviations of the detected target centroid points can be calculated by the law of error propagation for the intersected lines. The standard deviation changes inversely with distance and features better values for targets at longer distances, which is reasonable.

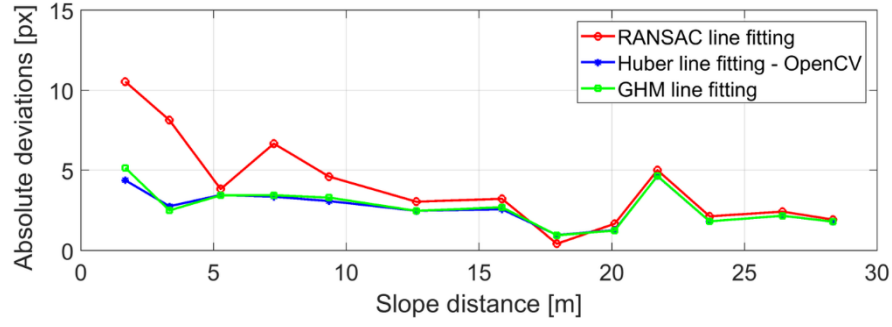


Figure 12. Absolute deviations between line fitting approaches and manual pointing, RANSAC line fitting (red), OpenCV Huber line fitting (blue) and Gauss-Helmert model line fitting (green) in the longest line-based target centroid detection approach.

Image No.	Slope distance(m)	$\Delta d_{\text{RANSAC-Manual}}$ (px)	$\Delta d_{\text{Huber-Manual}}$ (px)	$\Delta d_{\text{GHM-Manual}}$ (px)	σ_{xy} (px)	Probability (%)
1	28.336	1.9290	1.7976	1.7996	0.37	100
2	26.439	2.4211	2.1674	2.1686	0.46	100
3	23.692	2.1308	1.8181	1.8188	0.48	100
4	21.723	5.0085	4.6402	4.6501	0.54	100
5	20.113	1.6662	1.2704	1.2423	0.59	100
6	17.934	0.4296	0.9624	0.9520	0.63	100
7	15.862	3.2253	2.5709	2.6966	0.70	100
8	12.649	3.0417	2.4760	2.4690	0.93	100
9	9.357	4.6096	3.0831	3.2997	1.17	100
10	7.279	6.6705	3.3538	3.4473	1.74	100
11	5.272	3.8300	3.4602	3.4431	2.51	100
12	3.343	8.1340	2.7586	2.4969	3.32	100
13	1.676	10.5392	4.3811	5.1585	5.79	100

Table 2. Statistics of the target pattern b (see Fig. 2) based on the longest line-based target centroid detection approach.

Tables 3 and 4 and Figure 13 represent the applicability of the LL-TCD and the A-TCD approaches for the C_bL_p target (i.e. target k in Fig. 2) in different lighting conditions (i.e. normal, very bright (direct lighting), semi-dark (close indirect lighting), dark (far indirect lighting) and totally dark (no source of light)) with different line fitting approaches. Columns (2) to (6) in Tables 3 and 4 show the slope distances to the target, absolute deviations between the RANSAC-based LL- or A-TCD approaches with one-time manual measurement, absolute deviations between the Huber-based LL- or A-TCD approaches with a single manual measurement, processing times (in seconds) and the different lighting conditions, respectively. Tables 3 and 4 show that the two approaches differ slightly. The run time of the A-TCD approach is, on average, about five times smaller than in the LL-TCD approach (see Tables 3 and 4). The times shown (in seconds) indicate the processing time with the Huber line fitting algorithm. The processing can be even faster by using GPU programming for real-time applications. The two proposed approaches failed in total darkness without a source of light. A repeatability test was performed for target k (see Fig. 2) at image numbers 14 to 18, 19 to 23 and 24 to 30 by a single manual pointing and then applying a target centroid detection algorithm. Furthermore, the probability of 62.5% for image number 30 in the dark lighting condition shows the benefit of having more lines and, thus, more redundancy in the procedure of the target centroid detection. For a better understanding of the results in Tables 3 and 4, note that each pixel at the distance of 28.11 m for the image size of [2560 x 1920 px] equals about 0.23 mm. Therefore, the maximum deviation of about 6 pixels between the LL-TCD and A-TCD approaches with single manual pointings in ‘dark’ lighting

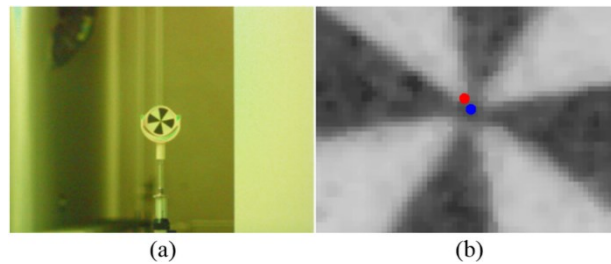
conditions amounts to about 1.38 mm. This demonstrates the limits of human vision when pointing to distant targets (28 m) in poor lighting conditions.

<i>Image No.</i>	<i>Slope distance(m)</i>	$\Delta d_{RANSAC-Manual}$ (px)	$\Delta d_{Huber-Manual}$ (px)	<i>Time (sec.)</i>	<i>Lighting condition</i>	<i>Probability (%)</i>
14	28.119	2.4578	2.3904	37.583	normal	100
15	28.118	0.7700	0.7811	40.932	normal	100
16	28.119	3.2439	3.2896	26.322	normal	100
17	28.119	2.4607	2.4284	22.590	normal	100
18	28.119	0.1930	0.2451	34.623	normal	100
19	28.111	2.0228	1.9919	48.816	normal	100
20	28.110	1.2612	1.2507	43.722	normal	100
21	28.110	0.2016	0.0890	37.168	normal	100
22	28.110	3.1033	3.1502	42.402	normal	100
23	28.110	2.3159	2.3731	35.615	normal	100
24	28.110	4.8719	4.7083	4.8923	dark	100
25	28.111	5.9831	6.0042	14.515	dark	100
26	28.110	2.7642	2.7737	6.9635	dark	100
27	28.110	2.6628	2.3948	11.776	dark	100
28	28.109	2.7977	3.1688	9.3259	dark	100
29	28.109	3.2131	3.2303	6.7233	dark	100
30	28.109	4.6414	2.4050	14.497	dark	62.5
31	19.531	1.6256	1.5527	25.539	very bright	100
32	19.543	-	-	-	totally dark	Failed

Table 3. Statistics of the target pattern k (see Fig. 2) based on the longest line-based target centroid detection approach.

<i>Image Nr.</i>	<i>Slope distance(m)</i>	$\Delta d_{RANSAC-Manual}$ (px)	$\Delta d_{Huber-Manual}$ (px)	<i>Time (sec.)</i>	<i>Lighting condition</i>	<i>Centroid detected?</i>
14	28.119	2.7049	2.4835	4.1680	normal	yes
15	28.118	0.6968	0.6972	4.0233	normal	yes
16	28.119	3.2854	3.2970	4.1100	normal	yes
17	28.119	2.4519	2.4462	4.4490	normal	yes
18	28.119	0.2954	0.2684	4.2359	normal	yes
19	28.111	1.9522	1.9228	4.0063	normal	yes
20	28.110	0.6870	0.6419	4.5735	normal	yes
21	28.110	0.5696	0.6082	4.1813	normal	yes
22	28.110	2.2340	2.1881	4.9542	normal	yes
23	28.110	1.8595	1.8585	4.7490	normal	yes
24	28.110	5.0083	4.8121	4.4399	dark	yes
25	28.111	5.9855	5.8264	4.1196	dark	yes
26	28.110	2.1833	2.0391	5.4152	dark	yes
27	28.110	2.5941	2.5507	4.4269	dark	yes
28	28.109	2.6632	2.7626	4.9119	dark	yes
29	28.109	3.0693	3.0821	4.5334	dark	yes
30	28.109	3.0727	2.7556	4.7361	dark	yes
31	19.531	1.3034	1.1858	4.0632	very bright	yes
32	19.543	-	-	-	totally dark	Failed

Table 4. Statistics of the target pattern k (see Fig. 2) based on the azimuth-based target centroid detection approach.



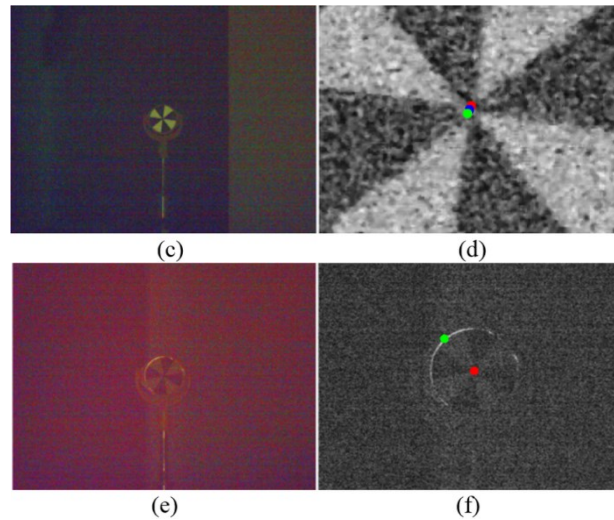


Figure 13. The longest line-based target centroid detection approach; (a, c, e) captured passive targets number 14, 30 and 32 with an image size of 2560 x 1920 px, (b, d, e) manual measurements to the target k at different places (red dot), RANSAC-based detected centroid (green dot), and Huber-based detected centroid (blue dot). [Note: Target 32 (f) failed in detection due to totally dark lighting condition].

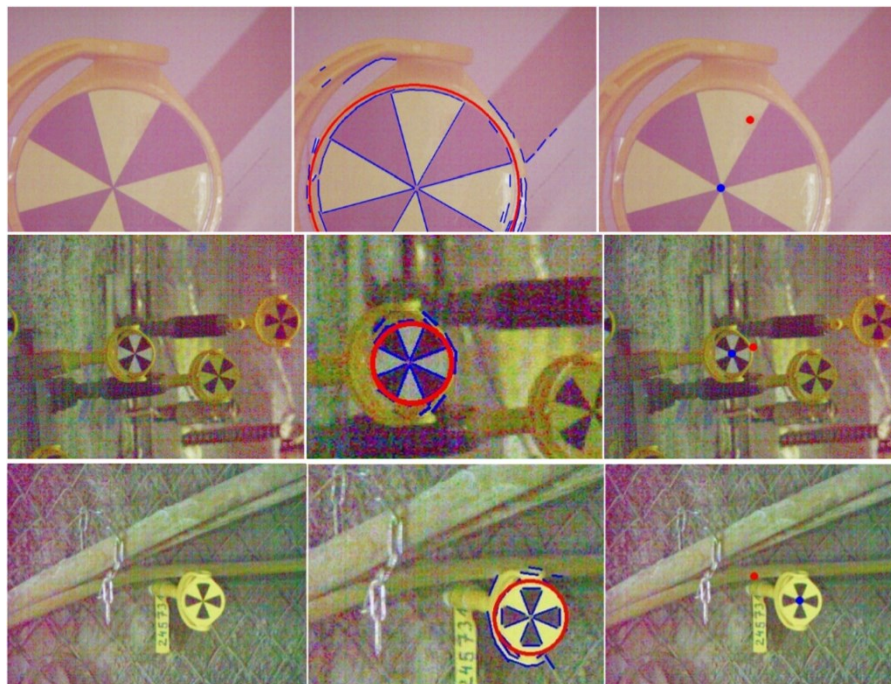


Figure 14. The azimuth-based target centroid detection approach; (left) captured passive targets with image size of 640 x 480 px (middle) cropped image in addition to detected edges (blue colour) and detected Hough circle in red (right), manual measurements to the target k at different places (red dot) and Huber-based detected centroid (blue dot).

Figure 14 shows the applicability of the A-TCD approach and its successful target centroid detection in a semi-dark lighting condition, for imperfect target pattern (top) or when close to artificial objects or other targets (middle) or poor initial pointing (bottom). The captured images with an image size of 640 x 480 px are depicted on the left side. The centre pictures show the cropped images with the detected edges and Hough circles. On

the right side, the measurements performed after intentionally poor initial pointing and the corresponding detected target centroids are shown. As we can see in Figure 14 (top, middle and bottom), localisation assists us to overcome the problem of being close to the artificial objects or even poor initial pointing to perform target centroid detection more reliably, accurately and faster.

We also performed a repeatability test for the captured images of the target pattern k (see Fig. 2) with an image size of 2560 x 1920 px at the fixed orientation and fixed distance of 4.88 m from the Leica MS50. For this purpose, we intentionally pointed to various places of the target (i.e. a radius of 0.03 m) between the centre and border around the target and captured the images. The columns (2) and (3) in Table 5 show the absolute deviations between the Huber-based A-TCD approach with a single manual measurement in pixels and metric units, respectively. The standard deviations of the X, Y and Z coordinates in Table 5 (bottom) prove that we can successfully detect target centroids with a high accuracy even with imprecise initial manual pointing to the target.

<i>Image No</i>	$\Delta d_{\text{Huber-Manual}}$ (px)	$\Delta d_{\text{Huber-Manual}}$ (m)	<i>X_centroid (m)</i>	<i>Y_centroid (m)</i>	<i>Z_centroid (m)</i>
32	1.65	0.0006	1.2545	2.0645	-1.4453
33	89.75	0.0165	1.2545	2.0640	-1.4454
34	85.63	0.0159	1.2545	2.0640	-1.4454
35	68.34	0.0128	1.2545	2.0641	-1.4454
36	44.46	0.0082	1.2546	2.0641	-1.4454
37	66.02	0.0124	1.2546	2.0641	-1.4453
38	82.54	0.01539	1.2546	2.0641	-1.4453
39	156.38	0.02911	1.2546	2.0641	-1.4453
40	163.54	0.03061	1.2545	2.0641	-1.4454
41	119.40	0.02218	1.2546	2.0641	-1.4453
42	114.33	0.02122	1.2545	2.0643	-1.4453
43	166.70	0.03124	1.2546	2.0641	-1.4455
44	213.85	0.04121	1.2546	2.0641	-1.4455
45	139.87	0.02601	1.2544	2.0644	-1.4453
46	141.37	0.02610	1.2545	2.0643	-1.4454
47	167.30	0.03145	1.2545	2.0643	-1.4454
48	166.38	0.03152	1.2546	2.0642	-1.4454
49	162.45	0.03015	1.2546	2.0642	-1.4454
50	239.06	0.04437	1.2545	2.0643	-1.4454
<i>std dev.</i>			0.00006	0.00013	0.00006

Table 5. Statistics of the repeatability test of the target pattern k (see Fig. 2) at a distance of 4.88 m based on the azimuth-based target centroid detection approach.

Case study II – Application in Highly Accurate External Calibration of TLS and DSLR Camera

In this case study, the goal is to validate our target centroid detection approaches. It integrates a DSLR camera with a TLS and calculates the external calibration parameters based upon a rigorous statistical space resection bundle adjustment. Local and global tests are performed to reject large residuals and outliers. Furthermore, a variance component estimation is performed to assign the optimal weights to the observations. Please refer to Omidalizarandi and Neumann (2015) and Omidalizarandi *et al.* (2016) for a detailed discussion in this regard. In our previous research, we calculated the target centroid using the subpixel target mode of the software PhotoModeler 5.2.3 by Eos Systems Company and measured four circles around the target centre. Afterwards, the target centroids were calculated by averaging over the four circle centres (Fig. 15c). Here, we detect the target centroids using the LL-TCD approach and compare its results with those of PhotoModeler. As we can see from Figure 15c, the target pattern features only two lines,

which are fewer than the four lines in our optimal targets (i.e. targets b and k in Fig. 2). However, the results prove that even with only two intersected lines, we can achieve accurate results that are approximately equivalent with the PhotoModeler measurements. The PhotoModeler measurements are sensitive to the image resolution and noise, which both degrade the accuracy and reliability of its target centroid detection. Additionally, Photomodeler always requires manual thresholding and the definition of maximum and minimum diameter size of circles to automatically detect their centroids, which is time-consuming and a challenge.

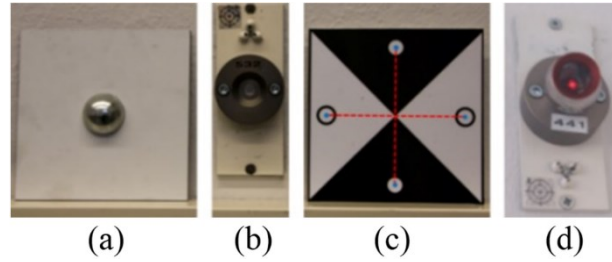


Figure 15. (a) Back of the target, (b) magnetic holder, (c) front of the target with depiction of the detected centroid of circles using the PhotoModeler software, and (d) corner cube reflector mounted on the magnetic holder.

Figure 16 shows the absolute deviations between the target centroids detected with different line fitting approaches and PhotoModeler measurements in pixel units. Table 6 gives the statistics of these absolute deviations. As the table shows, the mean and maximum deviations based on the RANSAC line fitting approach differ slightly from those of the two other line fitting approaches.

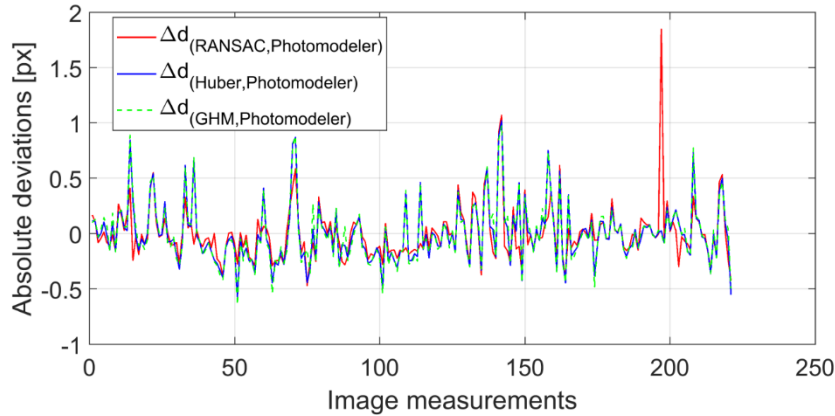


Figure 16. Absolute deviations between the detected target centroids of different line fitting approaches and PhotoModeler measurements (in pixel units).

		Δd_{RANSAC}	Δd_{Huber}	Δd_{GHM}
Mean	[px]	0.0000	0.0000	0.0000
Max	[px]	1.8485	1.0208	0.9768
Std dev.	[px]	0.2506	0.2649	0.2696

Table 6. Statistics of the absolute deviations between the detected target centroids with different line fitting approaches and the PhotoModeler measurements (in pixel units).

Table 7 gives the calculated external calibration parameters between the TLS and the DSLR camera with an applied GHM and variance component estimation. The last column in Table 7 shows the differences between the calculated parameters (i.e. external calibration parameters between the TLS and the DSLR camera plus focal length) from the PhotoModeler measurements and from the detected target centroid based on the LL-TCD approach. There are no significant differences when comparing the results and calculated standard deviations of the two approaches.

6 DOF	Values PhotoModeler (1)	σ PhotoModeler	Values LL-TCD approach (2)	σ LL-TCD approach	Δ (1), (2)
ω (Deg.)	90.4873	0.0028	90.4820	0.0027	0.0053
φ (Deg.)	-9.3086	0.0035	-9.3129	0.0036	0.0043
κ (Deg.)	-0.2303	0.0017	-0.2299	0.0016	-0.0004
X_c (m)	-0.0129	0.0003	-0.0129	0.0003	0.0000
Y_c (m)	0.2147	0.0002	0.2149	0.0002	-0.0002
Z_c (m)	0.0880	0.0005	0.0871	0.0005	0.0009
f (mm)	20.4132	0.0028	20.4155	0.0028	-0.0023

Table 7. External calibration parameters between the TLS and the DSLR camera (6 DOF) plus focal length with applied Gauss-Helmert model based on PhotoModeler image measurements (Omidalizarandi *et al.* 2016) and the longest line-based target centroid detection approach.

Conclusions

In this research, a novel automatic, low-cost and accurate passive target centroid detection approach was proposed, implemented and evaluated. It is robust, reliable and accurate with respect to lighting, dusty environment and skew angle targets. According to our experiments, a circular target with a line pattern (target k in Fig. 2) is a suitable target design and pattern due to the four intersected lines, which increase the redundancy. Moreover, in normal, very bright, semi-dark and dark lighting conditions, paper targets seem to be adequate. There is no need to use reflective targets.

We proposed two methodologies to deal with rectangular and circular targets, namely, *azimuth-based target centroid detection* method and *longest line-based target centroid detection*. In both approaches, cropping the captured images based on the horizontal and vertical FOVs of the cameras, target size in object space as well as slope distance to the target help us to perform a fast, reliable and accurate processing in the region-of-interest. The LSD algorithm is superior to the Canny edge detector and features fewer spurious lines. Three different line fitting methods (i.e. RANSAC, OpenCV Huber and Gauss-Helmert model) were compared and achieved very close and comparable results. The localisation of the targets based on template matching increased the reliability of the results.

The efficiency, reliability, repeatability and accuracy of our proposed approaches were evaluated and examined with two practical tests. In the first test, the *longest line based target centroid detection* and the *azimuth based target centroid detection* methods were compared with single precise manual pointing measurements for the captured images from the telescope camera of the Leica MS50. It shows that our proposed approaches are even better than single manual measurements. Furthermore, our methods allow for an automatic target detection based on precise or imprecise initial pointing coordinates. The experiments were performed at distances between 1.6 and 28 m and demonstrated sub-millimetre accuracy for an image size of 2560 x 1920 px.

In the second test, the PhotoModeler image measurements were compared with the *longest line-based target centroid detection* approach. The results of this test prove that we obtain approximately equivalent results with the two methods.

Outlook

In future work, we will calibrate the vertical angular resolution of the telescope camera of the Leica MS50 to permit a precise conversion of the pixel coordinates to the metric coordinates. The time series of detected target centroids may be used for accurate displacement and vibration analyses of, for example, bridge structures at frequencies less than 5 Hz (in view of the Nyquist sampling theorem). The proposed target pattern and its detection approach is suitable for applications in Engineering Geodesy, such as the monitoring of construction sites with many cheap paper-based targets.

Acknowledgements

The research presented was partly performed in the scope of the collaborative project ‘Spatio-temporal monitoring of bridge structures using low cost sensors’ with ALLSAT GmbH, which was supported by the German Federal Ministry for Economic Affairs and Energy (BMWi) and the Central Innovation Programme for SMEs (Grant ZIM Kooperationsprojekt, ZF4081803DB6).

References

- Akca, D., 2003. Full automatic registration of laser scanner point clouds. *Optical 3-D Measurement Techniques VI Zurich*, September 22–25, 330–337.
- Bürki, B., *et al.*, 2010. DAEDALUS: A versatile usable digital clip-on measuring system for Total Stations. In: Mautz, R., Kunz, M., Ingensand, H., eds., *Proceedings of the 2010 International Conference on Indoor Positioning and Indoor Navigation (IPIN)*. IEEE, 1–10.
- Canny, J., 1986. A computational approach to edge detection. *IEEE Transactions on Pattern Analysis and Machine Intelligence*, (6), 679–698.
- Chow, J., Ebeling, A., and Teskey, B., 2010. Low cost artificial planar target measurement techniques for terrestrial laser scanning. *Proceedings of the FIG Congress 2010: Facing the Challenges–Building the Capacity*.
- Ehrhart, M., and Lienhart, W., 2015a. Image-based dynamic deformation monitoring of civil engineering structures from long ranges. *SPIE/IS&T Electronic Imaging, International Society for Optics and Photonics*, 9405, 94050J. <http://spie.org/Publications/Proceedings/Paper/10.1117/12.2075888>.
- Ehrhart, M., and Lienhart, W., 2015b. Monitoring of civil engineering structures using a state-of-the-art image assisted total station. *Journal of Applied Geodesy*, 9 (3), 174–182.
- Ehrhart, M., and Lienhart, W., 2016. Accurate measurements with image-assisted total stations and their prerequisites. *Journal of Surveying Engineering*, 143 (2), 04016024.
- Fischler, M. A., and Bolles, R. C., 1987. Random sample consensus: a paradigm for model fitting with applications to image analysis and automated cartography. *Readings in computer vision*, 726–740.
- Guillaume, S., *et al.*, 2016. Contribution of the image-assisted theodolite system QDaedalus to geodetic static and dynamic deformation monitoring. *3rd Joint International Symposium on Deformation Monitoring (JISDM)*. [CD-ROM].

- https://www.fig.net/resources/proceedings/2016/2016_03_jisdms_pdf/nonreviewed/JISDM_2016_submission_66.pdf.
- Grompone von Gioi, R., *et al.*, 2012. LSD: a line segment detector. *Image Processing On Line*, 2, 35–55. <http://www.ipol.im/pub/art/2012/gjmr-lsd/article.pdf>
- Grün, A., 1996. Least squares matching: a fundamental measurement algorithm, *Close range photogrammetry and machine Vision*, K. Atkinson, ed., Whittles, 217–255.
- Grün, A., and Akca, D., 2005. Least squares 3D surface and curve matching. *ISPRS Journal of Photogrammetry and Remote Sensing*, 59 (3), 151–174.
- Huber, P. J., 1981. *Robust statistics*. John Wiley, New York.
- Kaehler, A. and Bradski, G., 2016. *Learning OpenCV 3: Computer Vision in C++ with the OpenCV Library*. O'Reilly Media, Inc.
- Kregar, K., Grigillo, D., and Kogoj, D., 2013. High precision target center determination from a point cloud. *ISPRS Annals of the Photogrammetry, Remote Sensing and Spatial Information Sciences*, 1 (2), 139–144. <https://www.isprs-ann-photogramm-remote-sens-spatial-inf-sci.net/II-5-W2/139/2013>.
- Leica Geosystems, 2013. *Leica Nova MS50 White paper*. Leica Geosystems AG, 12 pages.
- Leica Geosystems, 2014. *Leica Nova MS50 GeoCOM Reference Manual*. Version 5.50.
- Nikon, Digital Camera D750, 2014. *User's Manual*.
- Omidalizarandi, M. and Neumann, I., 2015. Comparison of target- and mutual information based calibration of terrestrial laser scanner and digital camera for deformation monitoring, *The International Archives of Photogrammetry, Remote Sensing and Spatial Information Sciences*. 40 (1), 559–564. DOI: 10.5194/isprsarchives-XL-1-W5-559-20. <https://www.int-arch-photogramm-remote-sens-spatial-inf-sci.net/XL-1-W5/559/2015>.
- Omidalizarandi, M., *et al.*, 2016. Highly accurate extrinsic calibration of terrestrial laser scanner and digital camera for structural monitoring applications, *Proceedings of the 3rd Joint International Symposium on Deformation Monitoring (JISDM)*, Vienna, March 30 – April 1, 2016, 8. [CD-ROM]. https://www.fig.net/resources/proceedings/2016/2016_03_jisdms_pdf/reviewed/JISDM_2016_submission_92.pdf.
- Reiterer, A., *et al.*, 2009. A 3D optical deformation measurement system supported by knowledge-based and learning techniques. *Journal of Applied Geodesy*, 3 (1), 1–13.
- Reiterer, A. and Wagner, A., 2012. System consideration of an image assisted total station - evaluation and assessment, *Allgemeine Vermessungsnachrichten (avn)*, 119 (3), 83–94. <https://mediatum.ub.tum.de/doc/1099092/1099092.pdf>.
- Thuro, K., *et al.*, 2010. New landslide monitoring techniques—developments and experiences of the alpEWAS project. *Journal of Applied Geodesy*, 4 (2), 69–90.
- Wagner, A., *et al.*, 2013. Bridge monitoring by means of video-tacheometer – a case study. *Allgemeine Vermessungsnachrichten (avn)*, 120 (8-9), 283–292. <https://mediatum.ub.tum.de/doc/1174927/1174927.pdf>.
- Wagner, A., *et al.*, 2014. Long-range geo-monitoring using image assisted total stations. *Journal of Applied Geodesy*, 8 (3), 223–234.
- Wagner, A., 2016. A new approach for geo-monitoring using modern total stations and RGB+D images. *Measurement*, 82, 64–74.
- Wagner, A., 2017. New geodetic monitoring approaches using image assisted total stations, Thesis (PhD), Technische Universität München, München. <https://mediatum.ub.tum.de/doc/1338051/1338051.pdf>.

- Walser, B., 2004. Development and calibration of an image assisted total station, Thesis (PhD), ETH Zürich, Zürich.
http://www.igp-data.ethz.ch/berichte/Blaue_Berichte_PDF/87.pdf.
- Wendt, A., and Dold, C., 2005. Estimation of interior orientation and eccentricity parameters of a hybrid imaging and laser scanning sensor. *Proceedings of the ISPRS working group*, 5, 1682–1750.
http://www.isprs.org/proceedings/XXXVI/5-8/Paper/PanoWS_Berlin2005_Wendt.pdf
- Yi, C., *et al.*, 2018. Automatic detection of cross-shaped targets for laser scan registration. *IEEE Journal*, 99, 2169–3536, DOI: 10.1109/ACCESS.2018.2799841.
- Zhou, Y., *et al.*, 2015. Close range angles deformation monitoring by telescope camera of total station MS50 using automatic detection of coded targets. *Proceedings of the 2nd Int. Workshop on Civil Engineering and Architecture*, Istanbul, 153–162.
- Zhou Y., *et al.*, 2017. Calibration method for IATS and application in multi-target monitoring using coded targets, *Journal of Applied Geodesy*, 11 (2), 99–106, DOI: 10.1515/jag-2016-0021.

Appendix A: Flowcharts of the proposed target centroid detection approaches

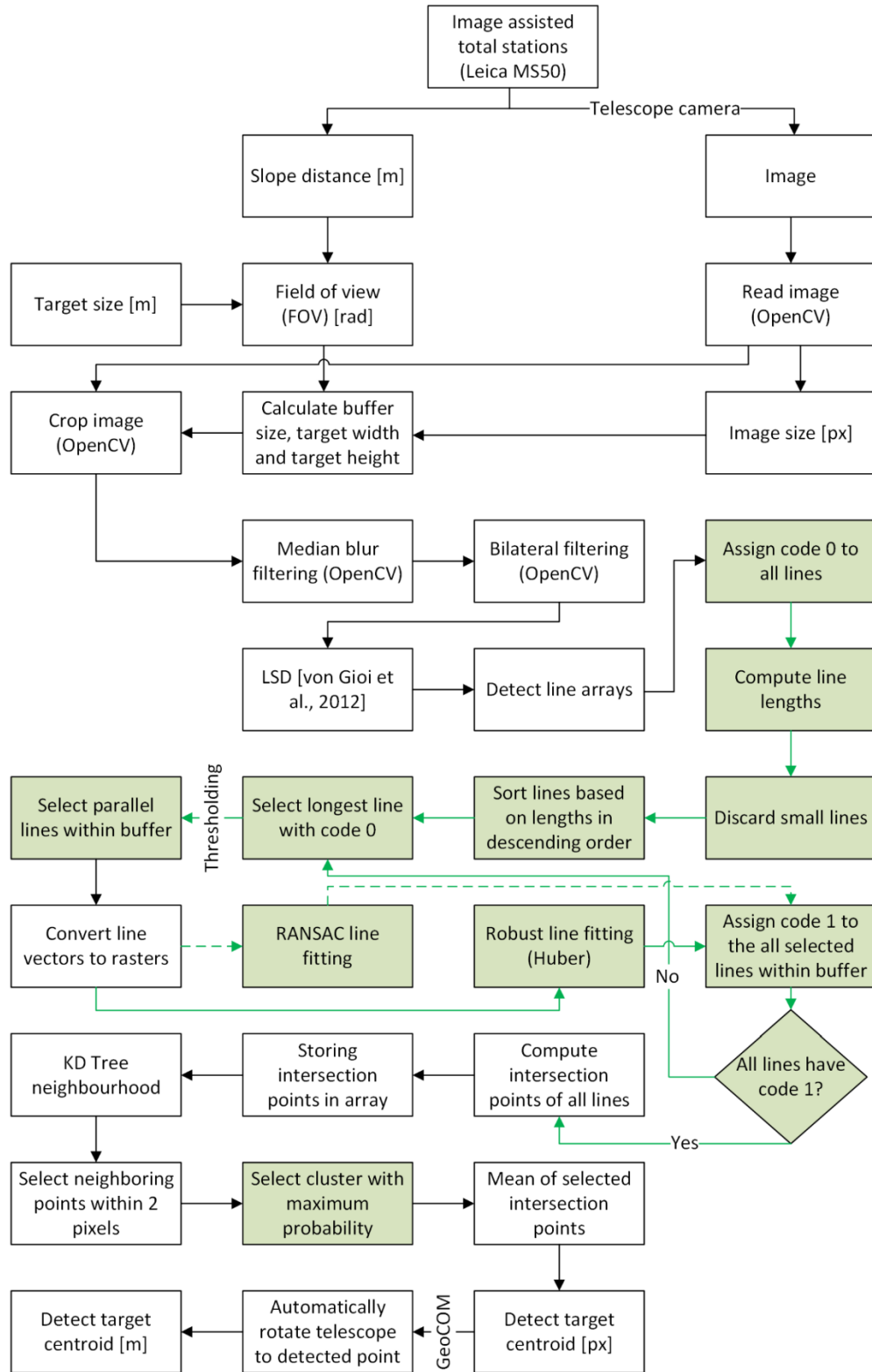


Figure 17. Flowchart of the longest line based target centroid detection (LL-TCD).

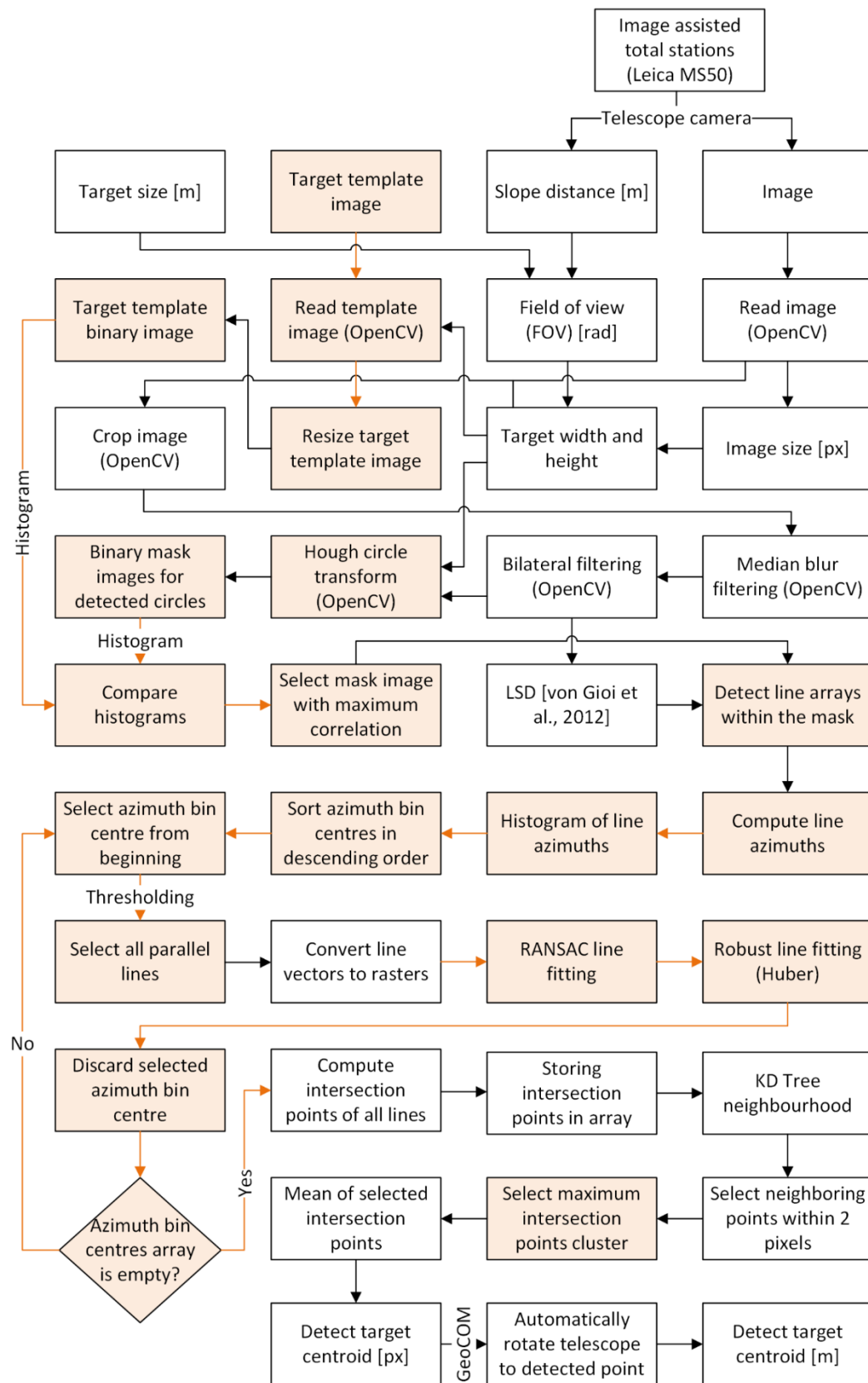


Figure 18. Flowchart of the azimuth based target centroid detection (A-TCD) approach.

Paper 2

Accurate vision-based displacement and vibration analysis of bridge structures by means of an image-assisted total station

Mohammad Omidalizarandi^{}, Boris Kargoll^{},
Jens-André Paffenholtz^{} and Ingo Neumann

Abstract

Today, short- and long-term structural health monitoring of bridge infrastructures and their safe, reliable and cost-effective maintenance have received considerable attention. For this purpose, image-assisted total station (here, Leica Nova MS50 MultiStation) as a modern geodetic measurement system can be utilized for accurate displacement and vibration analysis. The Leica MS50 measurements comprise horizontal angles, vertical angles and distance measurements in addition to the captured images or video streams with practical sampling frequency of 10 Hz using an embedded on-axis telescope camera. Experiments were performed for two case studies under (1) a controlled laboratory environment and (2) a real-world situation observing a footbridge structure using a telescope camera of the Leica MS50. Furthermore, two highly accurate reference measurement systems, namely, a laser tracker Leica AT960-LR and a portable shaker vibration calibrator 9210D in addition to the known natural frequencies of the footbridge structure calculated from the finite element model analysis are used for validation. The feasibility of an optimal passive target pattern and its accurate as well as reliable detection at different epochs of time were investigated as a preliminary step. Subsequently, the vertical angular conversion factor of the telescope camera of the Leica MS50 was calibrated, which allows for an accurate conversion of the derived displacements from the pixel unit to the metric unit. A linear regression model in terms of a sum of sinusoids and an autoregressive model of the coloured measurement noise were employed and solved by means of a generalized expectation maximization algorithm to estimate amplitudes and frequencies with high accuracy. The results show the feasibility of the Leica MS50 for the accurate displacement and vibration analysis of the bridge structure for frequencies less than 5 Hz.

Keywords

Image-assisted total stations, calibration, autoregressive model, generalized expectation maximization, displacement and vibration analysis, footbridge monitoring

Date received: 9 October 2017; accepted: 4 May 2018

Handling Editor: Xiangyang Xu

Introduction

Today, short- and long-term structural health monitoring (SHM) of the bridge infrastructures and their safe, reliable and cost-effective maintenance has received considerable attention. For this purpose, various measurement systems with different levels of accuracies and

Geodetic Institute, Leibniz Universität Hannover, Hannover, Germany

Corresponding author:

Mohammad Omidalizarandi, Geodetic Institute, Leibniz Universität Hannover, Nienburger Straße 1, 30167 Hannover, Germany.
Email: zarandi@gih.uni-hannover.de



Creative Commons CC BY: This article is distributed under the terms of the Creative Commons Attribution 4.0 License

(<http://www.creativecommons.org/licenses/by/4.0/>) which permits any use, reproduction and distribution of the work without further permission provided the original work is attributed as specified on the SAGE and Open Access pages (<https://us.sagepub.com/en-us/nam/open-access-at-sage>).

prices are being widely used depending on the demand. SHM is commonly being conducted based on visual observation, the properties of the material of the structures and the interpretation of the structural characteristics by inspecting the changes in the global behaviour of the structure (e.g. natural frequencies, mode shapes and modal damping).¹ Therefore, SHM is interpreted as a process to detect structure damages or identify their characteristics by the discrete or continuous measurements over time. Furthermore, the dynamic characteristics of a structure, such as frequencies, can change due to the temperature variations or the damages occurring in the structure.² From a surveying engineer's point of view, it is crucial to detect any deterioration of the structures (even small cracks) by frequent measurements. Typically, the geodetic measurement systems, such as total station, robotic total station (RTS), terrestrial laser scanner (TLS), laser tracker (LT), global positioning system (GPS) or other sensors such as digital camera or accelerometer, can be used for displacement and vibration monitoring. The Nyquist theorem must be fulfilled to identify the frequencies of the oscillating structure correctly. Consequently, the proper measurement systems must be used according to the sampling frequency required and the maximum amplitude derived from the oscillation of the structure.³ Bridges (including footbridges or road bridges) generally oscillate in a range of 1.2–10 Hz (or more).⁴ Previous researchers used different geodetic sensors for vibration monitoring of the bridge structures. Psimoulis and Stiros,⁵ for example, used RTS for vibration monitoring of a cable bridge, pedestrian suspension bridge and steel railway bridge for non-constant sampling rate measurements of the RTS in a range of 5–7 Hz and performing spectral analysis based on the Norm-Period code.⁶ Roberts et al.⁷ presented the hybrid configuration of GPS with a sampling frequency of 10 Hz and triaxial accelerometer with sampling frequency of 200 Hz for a bridge deflection monitoring. On one hand, the accelerometer measurements of this hybrid measurement system were beneficial to eliminate the disadvantages of GPS measurements regarding multipath, cycle slips errors and the need for good satellite coverage. On the other hand, GPS measurements were utilized to suppress accumulation drift of the acceleration data over time through velocity and coordinate updates. Neitzel et al.⁸ used the sensor network of the low-cost accelerometers with a sampling frequency up to 600 Hz, the TLS (Zoller + Fröhlich Imager 5003) in a single-point measurement mode with a sampling frequency of 7812 Hz and a terrestrial interferometric synthetic aperture radar (t-InSAR) with a sampling frequency of 200 Hz for vibration analysis of the bridge structure. They defined a functional model based on a damped harmonic oscillation and solved it in the sense of the least square adjustment. The reason for such a

high sampling frequency of the TLS was to detect displacements smaller than 1 mm by averaging the measurements over 100 measurements and to reach a practical sampling frequency of 78.12 Hz. An overview of the TLS-related structural monitoring was given in Vosselman and Maas.⁹

Structural monitoring by means of the vision-based measurement technologies is becoming increasingly popular in the context of civil engineering structures such as buildings, bridges and dams. In particular, an image-assisted total station (IATS), which can be a total station with an integrated external camera, for example, a high-resolution digital camera mounted on top of the scanning system by means of a clamping system, cf. Omidalizarandi et al.,^{10,11} or an internally embedded camera, was employed by Reiterer et al.,¹² Bürki et al.,¹³ Wagner et al.,^{14,15} Ehrhart and Lienhart,^{2,16} Guillaume et al.,¹⁷ Wagner^{18,19} and Lienhart et al.³ Most modern IATS measurement systems have motorized axes of rotation, which allow for an automatic rotation of the telescope to the points previously measured at different epochs of time. The IATS measurements comprise horizontal directions, vertical angles and distance measurements (in a polar coordinate system) in addition to the captured object images or video streams using embedded or externally attached cameras. The internally embedded on-axis telescope camera in addition to the motorized axes of rotations is particularly well-suited to an accurate, automatic and autonomous measurement of structures in static and dynamic monitoring. Subsequently, it enables us to measure both active targets (i.e. retro-reflective prism targets) and passive targets (i.e. signalized or non-signalized targets). Therefore, IATS with an on-axis telescope camera is advantageous over other vision-based measurement systems since the displacements in the image space can be converted directly to the metric unit by means of total station capabilities. In addition, its stability over time can be controlled by measuring its telescope angles and tilt reading³ using GeoCOM interface.²⁰

Ehrhart and Lienhart¹⁶ used the telescope camera of an IATS for the displacement and vibration monitoring of a footbridge structure based on the captured video frames of the circular target marking rigidly attached to the structure. Afterwards, least-squares ellipse fitting based on the Gauss–Helmert model (GHM) was applied to extract the target centres. Ehrhart and Lienhart² and Lienhart et al.³ employed an IATS (Leica MS50 with a sampling frequency of 10 Hz), an RTS (Leica TS15 with a sampling frequency of 20 Hz) and an accelerometer (HBM B12/200 with a sampling frequency of 200 Hz) for vibration analysis of a footbridge structure based on measurements of the circular target markings (i.e. signalized targets) and structural features (like bolts, that is, non-signalized targets) of the bridge.

The choice of a feasible optical target pattern and its accurate, automatic recognition at different epochs of time is the preliminary step in image-based structural monitoring using passive targets. Different target patterns with different detection techniques were previously proposed by several researchers, for instance, least-squares template matching by Gruen,²¹ Akca,²² Gruen and Akca²³ and Bürki et al.,¹³ coded target detection by Zhou et al.,²⁴ ellipse detection by Ehrhart and Lienhart¹⁶ and Guillaume et al.,¹⁷ circle matching by Bürki et al.,¹³ cross-line detection by Reiterer and Wagner²⁵ and centre-of-mass detection by Bürki et al.¹³ Omidalizarandi et al.²⁶ presented an optimal circular target with the line pattern consisting of four intersected lines and proposed a target centroid detection approach, which was shown to be robust, reliable and accurate regarding the lighting condition, dusty environment and skewed angle targets.

After extracting the target centroid, the next step is to accomplish camera calibration to convert the pixel (px) coordinates to more meaningful metric quantities, such as theodolite angle readings (i.e. horizontal and vertical directions^{27–29}). Based on the pixel differences between the initial pointing to the corresponding target of interest and the precisely calculated direction to the detected target centroid, an accurate remeasurement of the centroid of the target is also possible (i.e. taking advantage of the motorized axes of rotation of the IATS). However, the instrument's axes errors, vertical-index error and collimation error can also be considered to perform the conversion from the pixel to the metric coordinates more precisely. In order to capture sharp images with the telescope camera of the IATS, the corresponding targets should be focused by turning on the autofocus capability of the IATS. This, however, leads to changes in the internal camera calibration

parameters. Zhou et al.²⁴ proposed IATS telescope camera calibration based on measurements of the coded targets and their angular reading from the total station at a certain focus positions. Subsequently, new sets of calibration parameters were calculated by means of cubic polynomial interpolation at certain focus positions. In the context of displacement monitoring and for the purpose of converting object movements within the image space from the pixel unit to a proper angular quantity, Ehrhart and Lienhart¹⁶ merely calibrated the vertical angular conversion factor in the temperature-controlled laboratory with a fixed and stable set-up of the total station and the target. The video frames of the circular target marking were captured with a sampling frequency of 10 Hz at a fixed position for different horizontal and vertical rotations of the telescope camera of IATS. In addition, telescope angles were measured with a sampling frequency of 20 Hz to improve the measured reference angles by averaging.

The focus of this research is to perform accurate displacement and vibration analysis for two case studies under (1) a controlled excitation in a laboratory environment and (2) an uncontrolled excitation in a real-world situation observing a footbridge structure using the telescope camera of the Leica MS50 (Figure 1, left) with a sampling frequency of 10 Hz. Furthermore, two highly accurate reference measurement systems, namely, a laser tracker Leica AT960-LR (with a sampling frequency of 200 Hz; Figure 1, middle) and a portable shaker vibration calibrator (PSVC) 9210D (with a sampling frequency of 200 Hz; Figure 1, right) in addition to the known natural frequencies of the footbridge structure calculated from the finite element model (FEM) analysis are used for validation. To perform accurate displacement and vibration analysis, first, the feasibility of the optimal passive target pattern and its



Figure 1. Leica Nova MS50 MultiStation (left), Laser Absolute Tracker AT960-LR (middle) and Portable Shaker Vibration Calibrator 9210D (right).

accurate and reliable detection at different epochs of time are investigated. Subsequently, the vertical angular conversion factor of the telescope camera of the Leica MS50 is calibrated, which allows for an accurate conversion of the derived displacements from the pixel unit to the metric unit. A linear regression model in terms of a sum of sinusoids and an autoregressive (AR) model of the coloured measurement noise is employed to estimate amplitudes and frequencies with high accuracy. The white noise components of the AR process are assumed to independently follow a scaled (Student's) t -distribution to accommodate for outliers. The adjustment of this combined observation model is carried out by means of the generalized expectation maximization (GEM) algorithm described in Alkhatib et al.³⁰ In the first application and under controlled excitation, we compare the oscillation frequency and the amplitude derived from the PSVC time series with the results obtained from the Leica MS50 video frames and the LT. In the second application and under uncontrolled excitation, we compare the oscillation frequency and the amplitude derived from the LT time series with the Leica MS50 video frames of the footbridge structure.

Sensor specifications and measurement systems

We used an IATS (here, Leica Nova MS50 MultiStation; Figure 1, left) for displacement and vibration analysis in our experiments. The Leica MS50 includes the following:

1. Precise three-dimensional (3D) laser scanning;
2. A precise total station with an
 - Angular accuracy of 1" (according to ISO 17123-3);
 - Optical-distance measurement accuracy of 1 mm + 1.5 ppm (according to ISO 17123-4) for prism targets from 1.5 to 10,000 m; as well as
 - Optical-distance measurement accuracy of 2 mm + 2 ppm for non-prism targets (i.e. here passive targets) from 1.5 to 2000 m with a measurement time of 1.5 s;
3. An overview camera with diagonal field of view (FOV) of 19.4°;
4. A telescope camera with diagonal FOV of 1.5°;
5. GNSS connectivity.

Both the overview and the telescope cameras include 5 MP complementary metal-oxide semiconductor (CMOS) sensors in which the telescope camera is an on-axis camera located on the optical path of the Leica MS50 with 30× optical magnification of the overview camera.³¹ In this work, we benefit from the total

station's capabilities in terms of precise distance measurements of the passive targets, in addition to the digital imaging by means of the telescope camera. The angular resolution (α) of the telescope camera is approximately 1.7"/px, which is basically calculated by dividing the diagonal FOV by the diagonal length of the captured image in the pixel unit. To accomplish displacement monitoring more accurately, the angular resolution should be calculated from the calibration procedure in a controlled laboratory environment. According to Leica Geosystems,³¹ the horizontal and vertical FOVs of the telescope camera of the Leica MS50 are 1.3° and 1.0°, respectively. As we calculate the vertical displacement in our experiments, we merely benefit from its vertical angular conversion factor for displacement and vibration monitoring based on the live video stream functionality of the Leica MS50. The nominal sampling rate of the live video stream of the Leica MS50 is 20 Hz.³¹ However, in practice, we could capture the video stream with a sampling frequency of 10 Hz using OpenCV library. In order to get full access to the individual functionality of the Leica MS50 and for ease of use, we made use of the GeoCOM interface,²⁰ which is written in the script language Python 3.4. In addition, the target centroid detection algorithm proposed by Omidiazarandi et al.²⁶ is utilized to extract the target centroid with high accuracy. The resolutions of the captured images vary from 320 × 240 px to 2560 × 1920 px. However, for live video stream, it is only possible to capture video streams with a resolution of 320 × 240 px. Subsequently, the target centroid detection approach should be robust, reliable and accurate and should work well even in the case of a low-resolution image. The autofocus is set to 'on', and the white balance is set to 'automatic' to ensure the capture of sharp images. We performed vibration analysis with an image resolution of 320 × 240 px and 1× zoom (Figure 2, left); however, we achieved meaningless results, since such small displacements were not detectable at all. Therefore, as Ehrhart and Lienhart¹⁶ proposed, we reduced the FOV by 8× zoom using the *camera zoom factor* functionality of the GeoCOM interface (Figure 2, right), which gave us reasonable results.

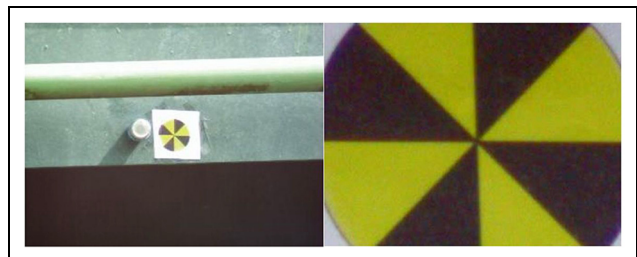


Figure 2. The Leica MS50 telescope camera images: image resolution of 320 × 240 px and 1× zoom (left) and image resolution of 320 × 240 px and 8× zoom (right).

It should be noticed that reflectorless distance measurements to the targets allow us to set the telescope's focus motor position precisely.¹⁶ The entire procedure is controlled via our self-developed graphical user interface (GUI), which allows an efficient and effective data acquisition and analysis.

Two highly accurate reference sensor systems are utilized to perform validation. On one hand, a LT (Figure 1, middle) with a maximum permissible error of $15 \mu\text{m} + 6 \mu\text{m/m}$ of a 3D point data and measuring rate output of 3000 points per second (3000 Hz)³² was employed. It allows for sub-millimetre range accuracy of the target points, which can be considered as a reference coordinate frame. On the other hand, a PSVC (Figure 1, right) was employed to perform controlled excitation. It consists of a highly accurate reference accelerometer (in our case, a precise PCB ICP quartz reference accelerometer) and two sensitive dials, which allow us to adjust the frequency and amplitude. For a frequency in the ranges of 0.7 Hz–2 kHz and 2 Hz–2 kHz, the acceleration can be read out with accuracies of $\pm 3\%$ and $\pm 10\%$, respectively.³³

Passive target centroid detection

The displacement time series for the captured video frames from the telescope camera of the Leica MS50 can be generated based on the continuous extractions of the point features (i.e. being signalized or non-signalized) at different epochs of time. Omidalizarandi et al.²⁶ proposed an optimal passive target (Figure 3) and its centroid detection approach to tackle this problem. The proposed target constitutes a circular border with line pattern including four intersected lines. It is low-cost and easy to mount. In addition, its target centroid detection approach is accurate, automatic and fast as well as robust and reliable regarding skew angle



Figure 3. Designed passive target.

targets and poor environmental conditions, such as low lighting (i.e. which may be very bright, semi-dark and dark) and dusty situations. However, the detection approach failed in totally dark lighting conditions.

The procedure starts by manual initial pointing of the targets of interest, which is only carried out at the beginning of the measurements. The telescope is then rotated automatically by means of the motorized axes of rotations of the Leica MS50 to the stored positions of the corresponding targets, and images are captured by means of the telescope camera. Subsequently, target centroid detection (see Algorithm 1) is applied, and the telescope is rotated automatically to the detected target centroid to capture images or video frames.

Cropping of the captured images is carried out, taking into account the target object size (in our case 0.06 m), slope distance (here, the maximum slope distance is up to 30 m) and horizontal as well as vertical FOVs of the telescope camera to extract relevant line features of the aforementioned target pattern and to speed up the procedure. Horizontal and vertical FOVs are calculated according to

$$FOV = 2 \cdot \tan^{-1} \left(\frac{D}{2 \cdot S} \right) \text{ (rad)} \quad (1)$$

where D is the target size in the object space and S the slope distance in metres. The calculated FOVs are multiplied by the width and height of the captured image to obtain the width and height of the cropped image. For practical reasons, the width and height of the cropped image are considered three times larger than values calculated to cover the target and its surroundings. This has been found to be beneficial for extracting the target centroid in a significant displacement of the target. We discarded the localising of the target pattern in the captured images by assuming a good initial target pointing at the beginning of the measurement. For further information concerning the localisation of target, please refer to Omidalizarandi et al.²⁶ The median blur and bilateral filtering are applied to reduce the noise and preserve the sharp edges of the images, respectively.

The line segment detector (LSD) algorithm³⁴ is applied with stable threshold parameters to extract the line features:

- The sigma value of the Gaussian filter is set to 0.75;
- The bound of quantization error on the gradient norm is set to 2.0;
- The gradient angle tolerance is set to 22.5° ;
- The minimal density of region points in the rectangle is set to 0.7;
- The number of bins is set to 1024;
- The gradient modulus in the highest bin is set to 255.

Algorithm 1: Target centroid detection using telescope camera of the Leica MS50

Initialisation:

initial pointing to the target

Input: D = target size in object space (m) S = slope distance (m)

captured image

Output:

Detected target centroid (px)

Procedure: w = image width h = image height $FOV = 2 \cdot \tan^{-1} \left(\frac{D}{2S} \right)$ $d_w = 3 \cdot w \cdot FOV$ $d_h = 3 \cdot h \cdot FOV$ crop captured image using d_w and d_h

median blur and bilateral filtering

edge detection using LSD

compute line azimuths

calculate histogram of line azimuths

sort azimuth bin centres in descending order

While (azimuth bin centres array is empty?)

select azimuth bin centre from beginning

select all parallel lines

convert line vectors to raster

RANSAC line fitting

Huber line fitting

discard selected azimuth bin centre

End

compute intersection points of all lines

store intersection points in array

 K -d tree neighbourhood

select neighbouring points within 2 pixels

select cluster with maximum intersection points

mean of selected intersection points

Next, the azimuths of the lines are calculated, and the maximum azimuth is selected based on the histogram of the azimuths. Subsequently, those LSD lines within the angle threshold of 15° from the maximum azimuth direction are selected. A random sample consensus (RANSAC) algorithm is applied to the selected lines to fit the optimal line and to get rid of falsely detected parallel lines. To extract lines more accurately, the Huber-robust line fitting algorithm in Kaehler and Bradski³⁵ with specified buffer width from each side of the fitted RANSAC line is applied. The neighbouring intersection points within 2px from each intersection point are selected by means of the K -d tree neighbourhood algorithm. Finally, the maximum intersection point cluster is selected and their mean yields the final intersection point (Algorithm 1; see Omidalizarandi et al.²⁶ for further information).

Calibration of the optical measurement system

The displacement time series for the captured images of the Leica MS50 is produced by subtracting the

extracted target centroids at different epochs of time. Subsequently, the calculated displacements in the pixel unit are converted to the more meaningful metric unit by means of the calibration parameters. The calibration consists of an internal calibration of the telescope camera of the Leica MS50 (regarding focal length, principal point and radial and tangential distortions) and an internal calibration of the error sources of the Leica MS50 measurements (including the zero offset for distance measurements or horizontal collimation error, vertical index error, tilting axis error and compensator index error of angular measurements). As mentioned previously, the FOV is reduced by $8 \times$ digital zoom to capture a small central portion of the image captured with $1 \times$ zoom (see Figure 2). Subsequently, it has very small impact of the aforementioned camera calibration parameters. However, as described in Ehrhart and Lienhart,¹⁶ these camera calibration parameters can be neglected due to the relative calculation of the displacement for the sequences of the video frames. However, a proper design of the target pattern, as proposed in Omidalizarandi et al.²⁶ (see Figure 3), may eliminate the influences of the aforementioned small distortions using the redundant line features and extract them in the robust and reliable procedure. However, in this research, we treat the remaining systematic errors, such as calibration parameters, as coloured noise and separate them from the white noise based on an AR model of the coloured measurement noise (further discussion about this is in the next section). The displacement time series of the Leica MS50 is compared with the PSVC and the LT datasets to give an impression of the accuracy of the detected target centroid and to visually demonstrate the previous statements concerning the neglecting of the remaining calibration parameters. Since the output of the PSVC is the acceleration, it can be converted to the displacement in metric units based on equation (2)

$$\delta_{z_i} = \frac{a_{z_i} - \bar{a_z}}{(2\pi f)^2} \quad (2)$$

where δ_{z_i} is the calculated displacement in the Z direction (mm), a_{z_i} is the acceleration in the Z direction (m/s^2), $\bar{a_z}$ is the average of the acceleration data within the specified period of time (m/s^2) and f is the frequency (Hz).

As we can see from Figure 4, the differences in the amplitudes for all three sensors are at a sub-millimetre-level accuracy. However, the time synchronization is still a challenge and needs to be performed precisely. In this work, the time synchronization is performed merely for the controlled excitation in the laboratory environment by changing the frequency and amplitude of the PSVC and by fitting the time series of all three sensors at a point of change. Subsequently, as we can also see

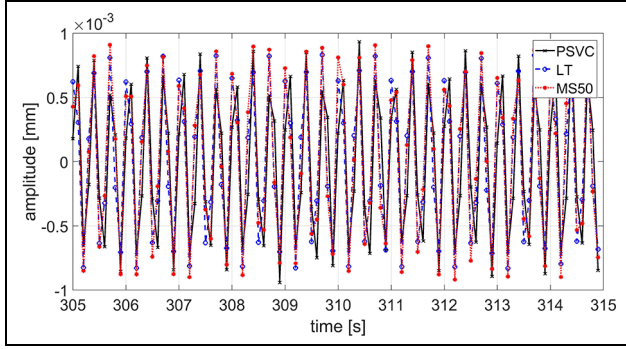


Figure 4. Displacement time series for the PSVC, the LT and the Leica MS50 at 3 Hz and distance of 7.52 m.

in Figure 4, the synchronization was not achieved perfectly. However, time synchronization is not in the focus of this research and will be investigated as part of future research.

The vertical angular conversion factor of the telescope camera of the Leica MS50 is calibrated to convert pixel quantities to metric quantities. The calibration is started by designing a coded target pattern in the software AutoCAD 2016 in the two paper sizes A2 and A4 with fixed coded target distances of 0.09 and 0.0335 m. As previously mentioned, the telescope camera of the Leica MS50 has a small FOV and cannot cover the entire target pattern at different distances (see Figure 5). Subsequently, the coded targets seem to be more advantageous compared to the chessboard pattern, since both the target centroid coordinates and the ID (i.e. target identification number) are obtained simultaneously. The highly accurate 3D object coordinates of the targets are obtained by taking multiple photos with a high-resolution camera from different viewing angles and by solving the space resection bundle adjustment in the iterative procedure.

The next step is to extract the target centroids of the coded target pattern images captured at different distances up to approximately 30 m and to assign them the unique IDs. To extract a target centroid, median blur and bilateral filtering are first applied to reduce the noise and to preserve the sharp edges of the images. The canny edge detector³⁶ is then applied to extract the edges. The inner circular part of the coded target is extracted by means of the Hough circle transform (HCT).³⁵ To find the circles based on the HCT, the circle radius is approximately calculated using equations (1) and (3)–(5)²⁶

$$d_w = \frac{w \cdot FOV}{FOV_h \cdot \left(\frac{\pi}{180}\right)} \text{ (px)} \quad (3)$$

$$d_h = \frac{h \cdot FOV}{FOV_v \cdot \left(\frac{\pi}{180}\right)} \text{ (px)} \quad (4)$$

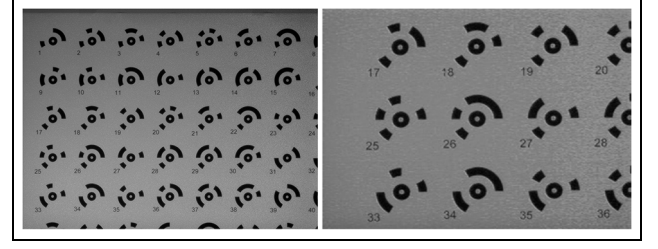


Figure 5. The coded target images captured using the telescope camera of the Leica MS50 at distances of 30.39 m (left) and 14.68 m (right).

$$r_c = \frac{\min(d_w, d_h)}{2} \text{ (px)} \quad (5)$$

where w is the image width (px), h is the image height (px), d_w is the circle diameter in the horizontal direction (px), d_h is the circle diameter in the vertical direction (px), r_c is the circle radius (px) and FOV_h and FOV_v are the horizontal and vertical FOVs, which according to the user manual of the sensor equal 1.3° and 1.0° , respectively.

Next, the ellipse fitting in a least-squares sense is applied to the concentric edge contours with detected Hough circles. In order to assign a unique ID to each target and to detect coded targets, template matching is applied by their comparisons with the designed coded targets. Finally, the vertical angular conversion factor is calculated based on the equations

$$\beta = \cos^{-1} \left(\frac{\delta_y}{\delta_{xy}} \right) \text{ (rad)} \quad (6)$$

$$psy = \frac{\delta_{XYZ} \cdot \cos(\beta)}{\delta_y} \text{ (mm/px)} \quad (7)$$

$$p = \text{polyfit}(psy, S) \quad (8)$$

$$p_v = \text{polyval}(p, S) \quad (9)$$

$$F\hat{O}V_v = \frac{p_v \cdot h}{S} \text{ (rad)} \quad (10)$$

$$\alpha_v = \frac{F\hat{O}V_v}{h} \cdot \frac{180 \cdot 3600}{\pi} \text{ (\"/px)} \quad (11)$$

where δ_y is the difference between the target centroid in y direction (px), δ_{xy} is the difference between the target centroid in both x and y directions (px), δ_{XYZ} is the difference between the target centroid in X , Y and Z directions (m), psy is the pixel size in the y direction, p is the coefficient of the best-fitting polynomial of degree 1 in a least-squares sense, S is the slope distance (m), p_v is the value of the derived polynomial at specified slope distances, $F\hat{O}V_v$ is the calculated vertical FOV (rad), h is the height of the image (px) and α_v is the vertical angular conversion factor (\"/px).

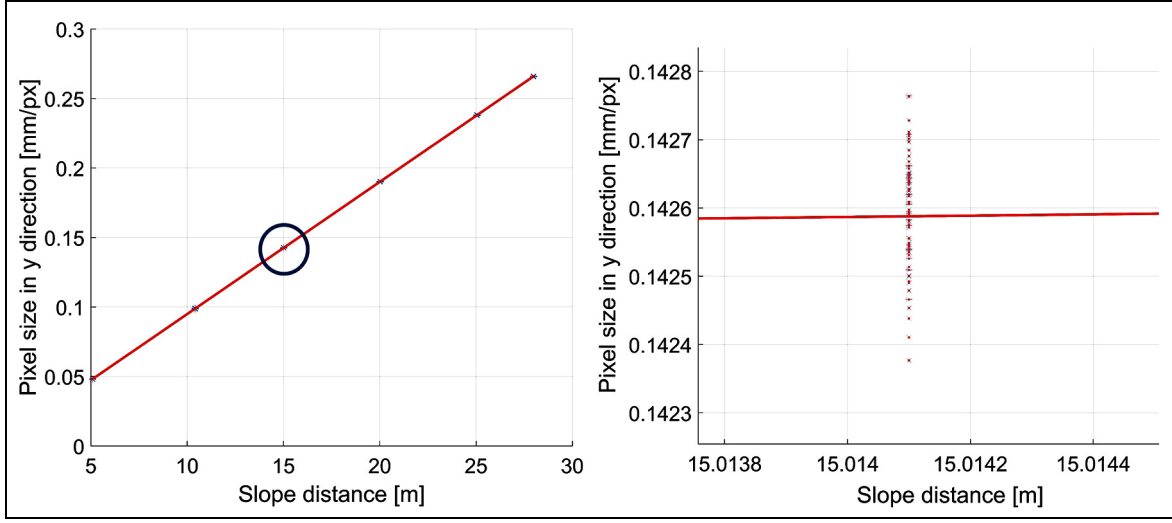


Figure 6. Depiction of the pixel sizes of the captured images in the direction of y axis with respect to the slope distances (left) and the magnification of the area highlighted by the circle (right).

The MATLAB functions *polyfit* and *polyval* are used, respectively, to fit a best line to the psy calculated for different slope distances and to evaluate it at specified distances. Figure 6 (left) depicts the psy values calculated for different slope distances, and Figure 6 (right) zooms in around the slope distance of 15 m.

The value 1.9583 ("/px) is obtained from the evaluation of the previous equations for calculation of the α_v , which is very close to the value 1.9632 ("/px) given in Ehrhart and Lienhart.¹⁶ Furthermore, the calculated FOV_v is approximately 1.04442° , a value which is slightly different from the value given in the user manual of the sensor.

Displacement and vibration analysis

The discrete Fourier transform (DFT) is typically applied to estimate the amplitude and frequency of oscillating objects, such as bridge structures. It might achieve reasonable results while the measurements are less contaminated with the coloured noise. To tackle this problem and to estimate the amplitude and frequency even in the case of high coloured measurement noise, we proposed a robust and consistent procedure which can be extended and used for any type of measurement, particularly the vision-based measurement system, to obtain the highly accurate results. In this research, we utilize the captured video frames from the telescope camera of the Leica MS50 for displacement and vibration analysis of a footbridge structure.

We use a simple harmonic motion to perform the displacement measurements, which means that the acceleration measurement is directly proportional to its displacement from the equilibrium position. In addition, the acceleration is directed towards the

equilibrium position.³⁷ Subsequently, the extracted target centroids from video streams of the Leica MS50 or the 3D coordinates from the LT are always averaged over a specified period of time to define the equilibrium position. We can calculate the displacement and acceleration for Leica MS50 measurements using the equations

$$\delta_{y_i} = \alpha S(y_i - \bar{y}) \quad (12)$$

$$\delta_{a_i} = \alpha S(y_i - \bar{y})(2\pi f)^2 \quad (13)$$

where S is the slope distance (m), α is the vertical angular conversion factor ("/px), y_i is the extracted target centroid at epoch i (px), \bar{y} is the average of the extracted target centroid within the specified period of time (px) and f is the frequency (Hz).

To compare the Leica MS50 and the LT, we can calculate the displacements for the Leica MS50 measurements based on equation (12) and then input the displacements to equation (15) to calculate the amplitude (mm) and the frequency (Hz), respectively. Concerning the comparison of the Leica MS50 and the PSVC, we note that the output of the latter consists of acceleration measurements; we can calculate accelerations for the Leica MS50 measurements based on equation (13) and then use equation (15) to calculate the amplitude (m/s^2) and the frequency (Hz). However, it is also possible to calculate displacements from the acceleration measurements via double integration from equation (15).

To estimate the frequency, merely pixel differences are sufficient to derive reasonable results due to the linearity property

$$F\{cf(t)\} = cF\{f(t)\} \quad (14)$$

of the Fourier transform.^{16,38} Despite this possibility, we performed both displacement and vibration analysis in metric unit measurements.

We modelled the given vibration measurements ℓ_1, \dots, ℓ_n by means of a sum of sinusoids and additive random deviations e_1, \dots, e_n , as proposed by Kargoll et al.,³⁹ that is

$$\ell_t = \frac{a_0}{2} + \sum_{j=1}^M [a_j \cos(2\pi f_j x_t) + b_j \sin(2\pi f_j x_t)] + e_t \quad (15)$$

The frequencies f_1, \dots, f_M and the coefficients a_0, a_1, \dots, a_M and b_1, \dots, b_M are treated as unknown parameters. Collecting these unknowns within the vector ξ , we can write the preceding non-linear observation equations in the form $\ell_t = h_t(\xi) + e_t$. To take coloured measurement noise into account, we assume the random deviations to be autocorrelated through a covariance-stationary AR process

$$e_t = \alpha_1 e_{t-1} + \dots + \alpha_p e_{t-p} + u_t \quad (16)$$

in which the coefficients $\alpha^T = [\alpha_1, \dots, \alpha_p]$ are also considered as unknown parameters. Since we expect numerous outliers of different magnitudes to be present in the data, the white noise components u_1, \dots, u_n are assumed to follow the centred and scaled t -distribution $t_\nu(0, \sigma^2)$ independently with an unknown degree of freedom ν and with unknown scale factor σ^2 . We, thus, have a one-dimensional version of the generic observation model in section ‘Sensor specifications and measurement systems’ in Alkhatib et al.³⁰ Estimation of the model parameters $\theta^T = [\xi^T, \alpha^T, \sigma^2, \nu]^T$ can, thus, be carried out efficiently by means of a one-dimensional version of the GEM algorithm given in section ‘Passive target centroid detection’ in Alkhatib et al.³⁰ To develop this algorithm, the observation and AR equations are inverted into

$$u_t = e_t - \alpha_1 e_{t-1} - \dots - \alpha_p e_{t-p} = \alpha(L)(\ell_t - h_t(\xi)) \quad (17)$$

where the lag operator $L e_t := e_{t-1}$ and the lag polynomial $\alpha(L) = 1 - \alpha_1 L - \dots - \alpha_p L^p$ are used as convenient notations. The required initial values e_0, e_{-1} and so on are set equal to zero for simplicity.

Within iteration step i of this algorithm, the E-step consists of the adjustment of the observation weights

$$w_t^{(i)} = \frac{\nu^{(i)} + 1}{\nu^{(i)} + (u_t^{(i)} / \sigma^{(i)})^2} \quad (18)$$

which depend on currently available initial or estimated parameter values $\xi^{(i)}$, $\alpha^{(i)}$, $\sigma^{(i)}$ and $\nu^{(i)}$. The individual weights then give rise to the diagonal weight matrix $\mathbf{W}^{(i)}$ used within the subsequent M-step. Initially, we

may use the unit weight matrix $\mathbf{W}^{(0)} = \mathbf{I}_n$, the vanishing AR process $\alpha^{(0)} = \mathbf{0}_{[p \times 1]}$, the identity scale factor $\sigma^{(0)} = 1$ and the degree of freedom $\nu^{(0)} = 30$, and these choices correspond to the initial assumption of approximately standard-normal and uncorrelated random deviations.

The M-step can be carried out by solving the four parameter groups individually. First, the parameters ξ are determined by solving the linearised normal equations

$$\Delta \xi^{(i+1)} = \left((\bar{\mathbf{A}}^{(i)})^T \mathbf{W}^{(i)} \bar{\mathbf{A}}^{(i)} \right)^{-1} (\bar{\mathbf{A}}^{(i)})^T \mathbf{W}^{(i)} \Delta \bar{\ell}^{(i)} \quad (19)$$

with reduced observations $\Delta \ell_t^{(i)} = \ell_t - h_t(\xi^{(i)})$, decorrelation filtered reduced observations $\bar{\Delta \ell}_t^{(i)} := \alpha^{(i)}(L) \Delta \ell_t$, Jacobi matrix components $\mathbf{A}_{t,k}^{(i)} = \partial h_t(\xi^{(i)}) / \partial \xi_k$ and decorrelation filtered Jacobi matrix components $\bar{\mathbf{A}}_{t,k}^{(i)} := \alpha^{(i)}(L) \mathbf{A}_{t,k}$. By virtue of the functional relationship (equation (15)), the derivatives occurring read

$$\frac{\partial h_t(\xi^{(i)})}{\partial a_0} = \frac{1}{2}, \quad \frac{\partial h_t(\xi^{(i)})}{\partial a_j} = \cos(2\pi f_j^{(i)} x_t)$$

$$\frac{\partial h_t(\xi^{(i)})}{\partial b_j} = \sin(2\pi f_j^{(i)} x_t)$$

$$\frac{\partial h_t(\xi^{(i)})}{\partial f_j} = 2\pi t [b_j^{(i)} \cos(2\pi f_j^{(i)} x_t) - a_j^{(i)} \sin(2\pi f_j^{(i)} x_t)]$$

A Gauss–Newton step with step size $\gamma \in (0, 1]$ gives

$$\xi^{(i+1)} = \xi^{(i)} + \gamma \Delta \xi^{(i+1)} \quad (20)$$

and this solution yields the estimated coloured noise residuals $e_t^{(i+1)} = \ell_t - h_t(\xi^{(i+1)})$. Based on these residuals, we assemble the matrix

$$\mathbf{E}^{(i+1)} = \begin{bmatrix} e_0^{(i+1)} & \dots & e_{1-p}^{(i+1)} \\ \vdots & & \vdots \\ e_{n-1}^{(i+1)} & \dots & e_{n-p}^{(i+1)} \end{bmatrix} \quad (21)$$

and then compute the solution of the normal equations with respect to the AR coefficients

$$\alpha^{(i+1)} = \left((\mathbf{E}^{(i+1)})^T \mathbf{W}^{(i)} \mathbf{E}^{(i+1)} \right)^{-1} (\mathbf{E}^{(i+1)})^T \mathbf{W}^{(i)} \mathbf{e}^{(i+1)} \quad (22)$$

Here, we need to check whether all roots of $\alpha^{(i+1)}(z) = 0$ are located within the unit circle; if this is not true, we mirror all roots with a magnitude larger than 1 into the unit circle in order for the estimated AR process to be invertible. Applying the inversion (equation (17)) to this process, the white noise residuals

result from the coloured noise residuals through $u_t^{(i+1)} = \alpha_t^{(i+1)}(L)e_t^{(i+1)}$. The scale factor is now computed as the weighted sum of squared white noise residuals divided by the number of observations, that is

$$(\sigma^2)^{(i+1)} = \frac{1}{n} \sum_{t=1}^n w_t^{(i)} \left(u_t^{(i+1)} \right)^2 \quad (23)$$

Finally, to estimate the degree of freedom of the underlying t -distribution, we determine the zero of the equation

$$0 = \log \nu^{(i+1)} + 1 - \psi\left(\frac{\nu^{(i+1)}}{2}\right) + \psi\left(\frac{\nu^{(i+1)}+1}{2}\right) - \log(\nu^{(i+1)} + 1) + \frac{1}{n} \sum_{t=1}^n \left(\log w_t^{(i+1)} - w_t^{(i+1)} \right) \quad (24)$$

where the weights $w_t^{(i+1)}$ are defined as in equation (18) by substituting $u_t^{(i+1)}$, $\sigma^{(i)}$ and the variable $\nu^{(i)}$, and where ψ denotes the digamma function. More details on the derivation and the implementation of this algorithm can be found in Alkhatib et al.³⁰

Experiments and results

We performed accurate displacement and vibration analysis using video streams from the telescope camera of a Leica MS50 with a practical sampling frequency of 10 Hz. Experiments were performed for two case studies under (1) a controlled laboratory environment and (2) an uncontrolled real-world situation observing a footbridge structure using the telescope camera of Leica MS50. Furthermore, an LT and a PSVC were used as two highly accurate reference sensors with a sampling frequency of 200 Hz for the validation purposes. Alternatively, the calculated natural frequencies of the footbridge structure based on the FEM were utilized for a validation.

The primary step to perform a displacement and vibration analysis based on the video frames of the Leica MS50 was to select an optimal passive target pattern and to extract its centroid with high accuracy at different epochs of time. Next, the vertical angular conversion factor of the telescope camera of the Leica MS50 was calibrated, which allows us to convert derived displacements from the pixel unit to the metric unit. In addition, the Fourier series (equation (15)) as a linear regression model and an AR process (equation (16)) as a coloured noise model were employed to estimate amplitudes and frequencies with high accuracy, assuming the white-noise components to follow a scaled t -distribution with an unknown scale factor and unknown degree of freedom. To estimate the model parameters by means of the GEM algorithm described in the preceding section, the number M of Fourier frequencies and the model order p of the AR process were

specified beforehand. We determined the initial values $f_1^{(0)}, \dots, f_M^{(0)}$ for the unknown frequencies based on notable maximum amplitudes within the DFT of the data. In addition, the model order of the AR process was set to 25 throughout the entire procedure. To apply the GEM algorithm, all three datasets were divided to the segments of $n = 1000$ consecutive measurements, spanning approximately 5 s for the LT and PSVC measurements and spanning 100 s for the Leica MS50 measurements.

Example based on the shaker vibration calibrator

The controlled excitations were performed at the laboratory of the Geodetic Institute Hannover (GIH) of the Leibniz Universität Hannover (LUH; see Figure 7, right) by means of the Leica MS50, LT, PSVC and IMU Brick 2.0 (which constitutes a low-cost accelerometer). The analysis of the IMU Brick 2.0 measurements is beyond the scope of this article and will be carried in our future research. As can be seen from Figure 7 (left), the optimal passive target pattern as proposed by Omidalizarandi et al.²⁶ oscillates as part of the PSVC and is simultaneously measured through video streaming by means of the telescope camera of the Leica MS50. The PSVC contains a PCB ICP quartz reference accelerometer, which outputs highly accurate acceleration data. Specifically, the oscillation frequencies of 2, 3 and 4 Hz with an amplitude of 0.3 m/s^2 were adjusted throughout two sensitive dials. Each frequency was measured for a about 7 min by all four sensors. However, since the sampling frequency of the Leica MS50 is only 10 Hz in practice, the frequencies of



Figure 7. Vibration analysis of a controlled excitation based on acceleration measurements from the PSVC 9210D, video streams from the telescope camera of the Leica MS50, 3D coordinates from the LT Leica AT960-LR and acceleration measurements from the IMU Brick 2.0.

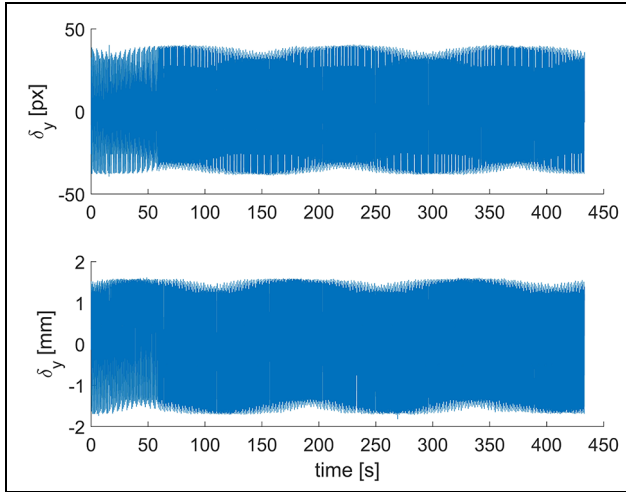


Figure 8. Displacement time series of the extracted target centroid for the telescope camera images of the Leica MS50 at 2 Hz and a distance of 5.3616 m.

higher than 5 Hz could not be captured by the Leica MS50 (in view of the Nyquist sampling theorem). To perform measurements with the LT, a Leica red-ring reflector (RRR) 0.5 in ball with a radius of $6.35 \text{ mm} \pm 0.0025 \text{ mm}$ and an acceptance angle $\leq \pm 30^\circ$ was mounted on the small platform which vibrates simultaneously with aforementioned passive target.

Figure 8 shows the displacement time series of the extracted target centroid with respect to the mean of the extracted centroids throughout time in both millimetre and pixel units at 2 Hz frequency and a slope distance of 5.3616 m. In addition, the first 20 s of the Leica MS50 data and the first 5 s of the LT and PSVC data were discarded as transient oscillations.

Figure 9 depicts the DFT of the video streams from the Leica MS50 at a distance of 5.3616 m, where the frequency induced by the PSVC was 2 Hz. This frequency is clearly associated with the maximum amplitude. Figure 10 shows the target centroid extracted from the Leica MS50 video streams alongside the adjusted Fourier model at 2 Hz for a 5 s time section.

Figure 11 shows the estimated coloured noise residuals and the decorrelated residuals of the Leica MS50 dataset, resulting from the filtering (equation (17)) of the former residuals by means of the inverted estimated AR model. Figure 12 shows the adequacy of the estimated AR coloured noise models in the light of an accepted (periodogram-based) white noise.³⁹

The DFT is shown in Figure 13, which reveals two main amplitudes at 1.25 and 2.5 Hz to shed further light on the impact of the image motion error (see Figure 14) on the estimation of the frequency. In addition, Figure 15 shows a higher coloured noise level in comparison to Figure 11, which proves the existence of

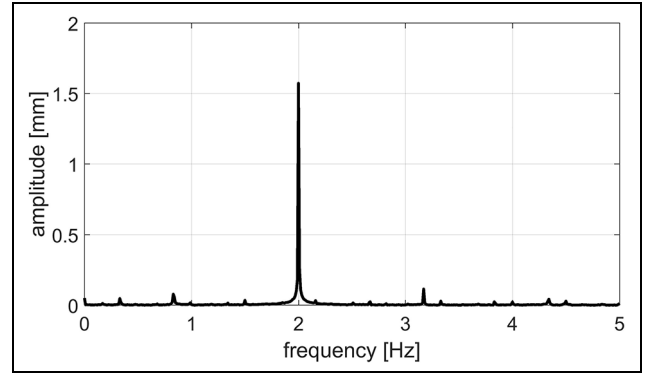


Figure 9. Typical discrete Fourier transform of one segment of the Leica MS50 dataset at distance of 5.3616 m, showing the main amplitude at 2 Hz.

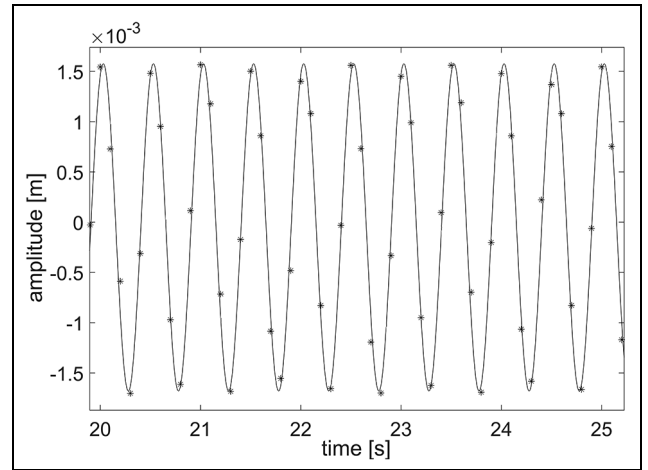


Figure 10. Typical section of the Fourier model (solid line) fitted to the given measurements of the Leica MS50 dataset (stars) at 2 Hz within 5 s.

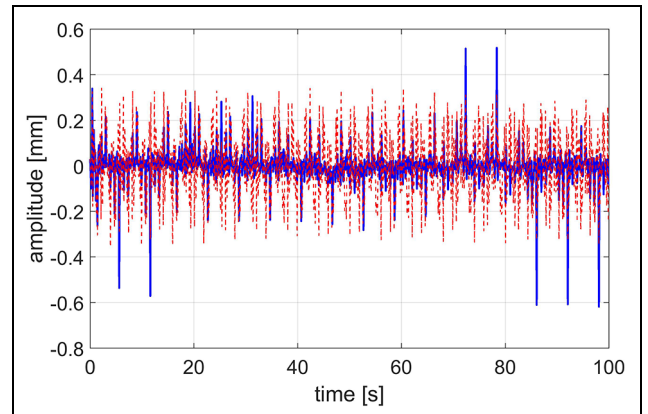


Figure 11. Typical segment showing the estimated coloured noise residuals and the decorrelated residuals of the Leica MS50 dataset at 2 Hz and a distance of 5.3616 m.

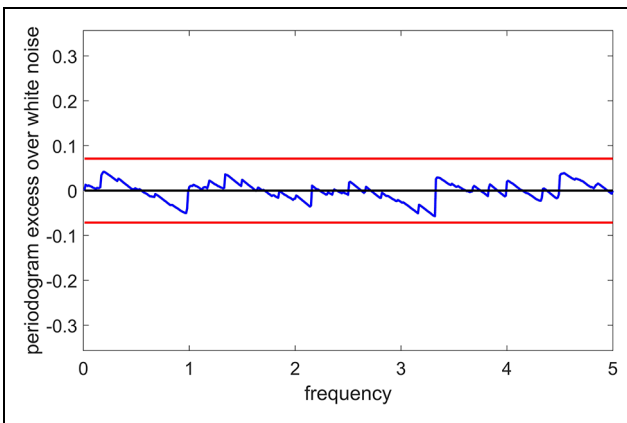


Figure 12. Excess of the estimated periodogram of the decorrelated (i.e. estimated white noise) residuals of the Leica MS50 dataset at 2 Hz and a distance of 5.3616 m for the AR(25) model (jagged line) with respect to the theoretical white noise periodogram (horizontal centred line) and 99% significance bounds (horizontal bounded lines).

the image motion errors throughout this time interval of the experiment.

Table 1 summarizes the statistics of the displacement and vibration analysis for all three sensors. In most cases, the frequencies and amplitudes estimated from the Leica MS50 measurements are very close to those resulting from the two highly accurate reference sensors (LT and PSVC). The estimated degrees of freedom of the t -distribution underlie the white noise components. Concerning the LT and the PSVC measurements, these estimates are roughly between 14 and 60, indicating a rather close approximation of a normal distribution. By contrast, the estimated degrees of freedom regarding the Leica MS50 measurements are in the range of 2–4.5, for which values the t -distribution has substantial tails; we thus found a large number of outliers in the measurement noise of that sensor.

Furthermore, the results show that the highest white noise test acceptance rate (100%) was obtained for the PSVC measurements, for which an AR order of $p = 25$ was chosen. Using the same model order, the LT measurements also produced relatively high acceptance rates in comparison to the PSVC data. However, the acceptance rates regarding the Leica MS50 measurements fluctuate between 25% and 75%, so that the adjusted coloured noise model is clearly inadequate for a number of segments analysed. On one hand, this finding could be related to the image motion error (see Figure 14) derived from a weak PC performance or delay in the data transmission procedure from the Leica MS50 to the PC. On the other hand, it could be related to a minor shaking of the Leica MS50 throughout the measurements, and this phenomenon can be taken into account in our future work by continuously reading the

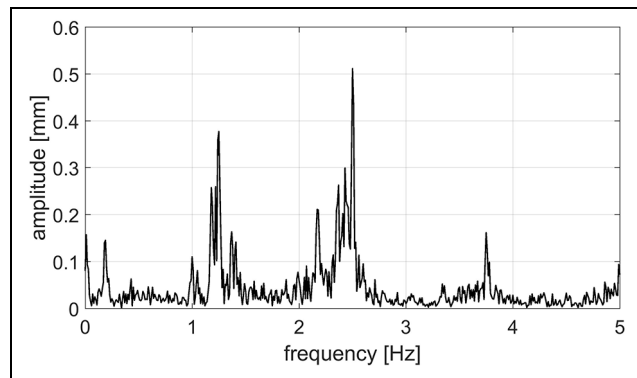


Figure 13. Typical discrete Fourier transform of one segment of the Leica MS50 dataset at a distance of 22.6635 m, showing two main amplitudes at 1.25 and 2.5 Hz.

tilting axis error of the Leica MS50 using the GeoCOM interface as described in Lienhart and colleagues.^{3,16} To improve the coloured noise models and the resulting performance of the white noise test, it might be beneficial in future experiments to increase the measurement time to obtain more redundant data and to be able to increase the AR model order. Moreover, the absolute deviation of the *Mode* of estimated amplitudes of the sensors are listed in Table 1 and compared to those from the PSVC with an AR order of $p = 25$. As we expected, the absolute deviations of the two reference sensors of LT and the PSVC have minor differences, which are significantly smaller than those of the Leica MS50.

Table 2 summarizes the statistics of the displacement and vibration analysis for all three sensors without AR processing to give an impression about strength of the developed algorithm. In addition, the degree of freedom was fixed to 120, which stands for the t -distribution, approximating the normal distribution as described in Abramowitz and Stegun⁴⁰ and Koch.⁴¹ As we expected, the absolute deviations from the PSVC without the AR processing are not significant and has less coloured measurement noise, as the estimated degree of freedoms indicate approximately the normal distribution (see Table 1). In addition, the absolute deviations for the LT measurement without the AR processing are slightly larger than those including AR processing. However, the absolute deviations for the Leica MS50 without the AR processing are mostly and significantly larger than those included in the AR processing. In addition, as the estimated degrees of freedom for the Leica MS50 data are represented by a range of 2–4.5 (see Table 1), it proves the existence of numerous outliers in the dataset. Subsequently, by ignoring the AR processing within the robust estimation procedure developed for the Leica MS50, the results in some cases do not prove to be reliable or accurate enough.

Table 1. Statistics of the displacement and vibration analysis for the Leica MS50, LT and PSVC measurements with an AR order of $p = 25$.

Sensor	Mode (\hat{f} , Hz)	Time (s)	NS	S (m)	Max (\hat{L} , mm)	Mode (\hat{L} , mm)	Min (\hat{L} , mm)	Mode ($\hat{\nu}$)	WNT (%)	Δ_d (mm)
LT	2.000067	5	85	5.3616	1.7476	1.7358	1.7067	28.467	94.11	0.0327
	3.000077	5	83	5.3616	0.8264	0.8203	0.8002	53.229	78.31	0.0011
	4.000103	5	87	5.3616	0.4616	0.4598	0.4567	54.345	66.66	0.0032
	2.000077	5	80	11.9425	1.7708	1.7565	1.7478	59.547	96.25	0.0269
	3.000071	5	104	11.9425	0.8221	0.8186	0.8148	51.202	82.69	0.0008
	4.000105	5	83	11.9425	0.4608	0.4578	0.4545	50.171	75.90	0.0057
	2.000042	5	85	16.8771	1.7378	1.7256	1.7066	50.212	96.47	0.0310
	3.000152	5	82	16.8771	0.8271	0.8151	0.8025	28.257	75.60	0.0044
	4.000112	5	127	16.8771	0.4606	0.4574	0.4497	38.732	82.67	0.0061
	2.000027	5	99	22.6635	1.7455	1.7231	1.7094	26.180	90.90	0.0321
	3.000061	5	86	22.6635	0.8333	0.8246	0.7994	14.272	87.21	0.0044
	4.000070	5	84	22.6635	0.4694	0.4665	0.4518	18.819	29.76	0.0035
PSVC	2.000106	5	95	5.3616	1.7227	1.7031	1.675	44.371	100	0.0
	3.000221	5	99	5.3616	0.8300	0.8192	0.8006	54.612	100	0.0
	4.000146	5	101	5.3616	0.4665	0.4630	0.4595	53.664	100	0.0
	2.000142	5	91	11.9425	1.7514	1.7296	1.7041	47.149	100	0.0
	3.000186	5	93	11.9425	0.8262	0.8194	0.8104	51.829	100	0.0
	4.000299	5	93	11.9425	0.4667	0.4635	0.4569	50.199	100	0.0
	2.000099	5	97	16.8771	1.7166	1.6946	1.6755	40.411	100	0.0
	3.000128	5	97	16.8771	0.8256	0.8195	0.8043	49.681	100	0.0
	4.000220	5	137	16.8771	0.4665	0.4635	0.4593	42.223	100	0.0
	2.000075	5	121	22.6635	1.7111	1.6910	1.6721	45.319	100	0.0
	3.000178	5	113	22.6635	0.8258	0.8202	0.8118	54.992	100	0.0
	4.000215	5	133	22.6635	0.4661	0.4630	0.4602	48.468	100	0.0
MS50	2.001359	100	4	5.3616	1.6256	1.6181	0.4063	3.8933	75	0.0850
	3.002026	100	4	5.3616	0.7496	0.7473	0.7424	4.4704	75	0.0719
	4.002689	100	4	5.3616	0.4849	0.4119	0.4091	3.4502	25	0.0511
	2.001327	100	4	11.9425	1.7250	1.7184	1.7147	4.4514	75	0.0112
	3.003544	100	4	11.9425	0.7888	0.7842	0.6814	4.2560	25	0.0352
	4.002680	100	4	11.9425	0.4339	0.4322	0.4287	1.9757	25	0.0313
	2.002867	100	4	16.8771	1.6986	1.5932	0.2670	4.4179	50	0.1014
	3.002015	100	4	16.8771	0.8293	0.7925	0.7678	3.4979	50	0.0270
	4.002692	100	3	16.8771	0.4352	0.4347	0.4225	3.1020	33.33	0.0288
	2.001887	100	4	22.6635	1.7356	1.4911	0.1650	1.9504	25	0.1999
	3.002021	100	4	22.6635	0.7808	0.7591	0.7536	3.3790	75	0.0611
	4.002694	100	4	22.6635	0.4240	0.4209	0.3817	2.8920	25	0.0421

LT: laser tracker; PSVC: portable shaker vibration calibrator; AR: autoregressive.

\hat{f} is the estimated frequency, NS the number of segments analysed, S the slope distance, \hat{L} the estimated amplitude or displacement, $\hat{\nu}$ the estimated degree of freedom, WNT the acceptance rate of the white noise test applied to the NS segments analysed and Δ_d the absolute deviation of the mode (\hat{L}) of the sensors compared to those from PSVC.

Example based on real application of a footbridge structure

An uncontrolled excitation of a footbridge structure with a length of 27.051 m and a width of 2.72 m close to the GIH (see Figure 16) was measured using the Leica MS50 and LT. The measurements were carried out for the first quarter and the middle of the footbridge structure (marked by the circles in Figure 16). Alternatively, the known natural frequencies of the footbridge structure were utilized for a validation. They were calculated based on the FEM analysis of a design model of the footbridge structure, which was carried out by the Institute of Concrete Construction

of the LUH. According to that, the vertical natural frequencies of the footbridge structure are 3.642 and 13.294 Hz, the longitudinal and the lateral natural frequencies are 2.295 and 7.053 Hz, and the torsional natural frequencies are 3.759 and 11.828 Hz, respectively. As we can see in Figure 16, the Leica MS50 and the LT are located at the footpath close to the side of the footbridge structure. Regarding the natural frequencies, we could only detect the vertical natural frequency of 3.642 Hz and could not detect another one with the value of 13.294 Hz due to the low practical sampling frequency of 10 Hz of the Leica MS50 and in view of Nyquist sampling theorem. On the other hand, it might be necessary to set-up the Leica MS50 in a place, where

Table 2. Statistics of the displacement and vibration analysis for the Leica MS50, LT and PSVC measurements without AR model and $\nu = 120$ the degree of freedom.

Sensor	Mode (\hat{f} , Hz)	Time (s)	NS	S (m)	Max (\hat{L} , mm)	Mode (\hat{L} , mm)	Min (\hat{L} , mm)	Mode ($\hat{\nu}$)	WNT (%)	Δ_d (mm)
LT	2.000060	5	85	5.3616	1.7480	1.7363	1.7076	120	0	0.0332
	3.000081	5	83	5.3616	0.8263	0.8203	0.8003	120	0	0.0011
	4.000134	5	87	5.3616	0.4617	0.4597	0.4568	120	0	0.0033
	2.000075	5	80	11.9425	1.7707	1.7565	1.7481	120	0	0.0269
	3.000089	5	104	11.9425	0.8223	0.8187	0.8148	120	0	0.0007
	4.000113	5	83	11.9425	0.4606	0.4579	0.4546	120	0	0.0056
	2.000072	5	85	16.8771	1.7364	1.7247	1.7063	120	0	0.0301
	3.000158	5	82	16.8771	0.8312	0.8158	0.8014	120	0	0.0037
	4.000096	5	127	16.8771	0.4652	0.4575	0.4525	120	0	0.0060
	2.000060	5	99	22.6635	1.7452	1.7228	1.7097	120	0	0.0318
PSVC	3.000103	5	86	22.6635	0.8394	0.8251	0.8057	120	0	0.0049
	4.000111	5	84	22.6635	0.4732	0.4669	0.4618	120	0	0.0039
	2.000087	5	95	5.3616	1.7231	1.7032	1.6747	120	0	0.0001
	3.000249	5	99	5.3616	0.8298	0.8194	0.8006	120	0	0.0002
	4.000129	5	101	5.3616	0.4665	0.4630	0.4595	120	0	0.0000
	2.000204	5	91	11.9425	1.7503	1.7289	1.7040	120	0	0.0007
	3.000169	5	93	11.9425	0.8262	0.8193	0.8102	120	0	0.0001
	4.000279	5	93	11.9425	0.4667	0.4633	0.4568	120	0	0.0002
	2.000151	5	97	16.8771	1.7176	1.6941	1.6748	120	0	0.0005
	3.000116	5	97	16.8771	0.8253	0.8196	0.8042	120	0	0.0001
MS50	4.000233	5	137	16.8771	0.4666	0.4635	0.4592	120	0	0.0000
	2.000024	5	121	22.6635	1.7115	1.6912	1.6743	120	0	0.0002
	3.000144	5	113	22.6635	0.8258	0.8204	0.8118	120	0	0.0002
	4.000229	5	133	22.6635	0.4662	0.4631	0.4602	120	0	0.0001
	2.001361	100	4	5.3616	1.6205	1.6161	1.0136	120	0	0.0870
	3.002032	100	4	5.3616	0.7492	0.7462	0.7449	120	0	0.0730
	4.002711	100	4	5.3616	0.4067	0.4059	0.3928	120	0	0.0571
	2.001328	100	4	11.9425	1.7182	1.7125	1.7012	120	0	0.0171
	3.002494	100	4	11.9425	0.7857	0.7490	0.3325	120	0	0.0704
	4.002717	100	4	11.9425	0.4276	0.4261	0.4222	120	0	0.0374
	2.001526	100	4	16.8771	1.6960	1.5940	0.8262	120	0	0.1006
	3.002020	100	4	16.8771	0.7934	0.7840	0.7752	120	0	0.0355
	4.002711	100	3	16.8771	0.4325	0.3174	0.1332	120	0	0.1461
	2.001868	100	4	22.6635	1.0612	0.5376	0.4042	120	0	1.1534
	3.002025	100	4	22.6635	0.7619	0.7578	0.7422	120	0	0.0624
	4.002723	100	4	22.6635	0.4212	0.4178	0.4114	120	0	0.0452

LT: laser tracker; PSVC: portable shaker vibration calibrator; AR: autoregressive.

\hat{f} is the estimated frequency, NS the number of segments analysed, S the slope distance, \hat{L} the estimated amplitude or displacement, WNT the acceptance rate of the white noise test applied to the NS segments analysed and Δ_d the absolute deviation of the Mode (\hat{L}) of the sensors compared to those from PSVC in Table 1.

it can measure the passive targets perpendicularly to detect the longitudinal and lateral natural frequencies of the footbridge structure. However, this was not the case in our measurement campaign and we could not detect those natural frequencies either.

Figures 17 and 18 show the DFT results for the Leica MS50 measurement at Points A1 and A2, respectively. In addition, Figure 19 shows the DFT result at point A1 for the LT measurement as well. Since the time synchronization needed to be performed between the Leica MS50 and the LT measurements and was not the case in our measurement campaign, the one-to-one comparison between the results of the aforementioned sensors does not make sense. However, we can rely on

the FEM results of the design model of the footbridge structure for the validation in this case study. As can be seen from Figures 17 and 19, the DFT results at point A1 show the frequency of 4.07 Hz with the maximum amplitude of 0.07 mm, which was captured by the Leica MS50 measurements, whereas the frequency of 4.06 Hz with the maximum amplitude of 0.0497 mm was obtained for the LT measurements. However, the results from the proposed approach show the frequencies of 4.0768 and 4.0631 Hz with the maximum amplitudes of 0.0433 and 0.0462 mm for the Leica MS50 and LT measurements, respectively. However, the DFT result in Figure 18 at point A2 shows the frequencies of 3.65 and 4.1 Hz with the maximum amplitudes of 0.079

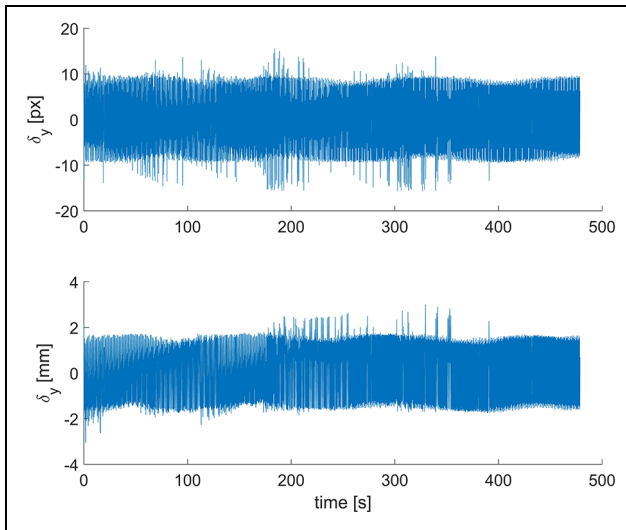


Figure 14. Displacements of the extracted target centroid for telescope camera images of Leica MS50 at 2 Hz and a distance of 22.6635 m.

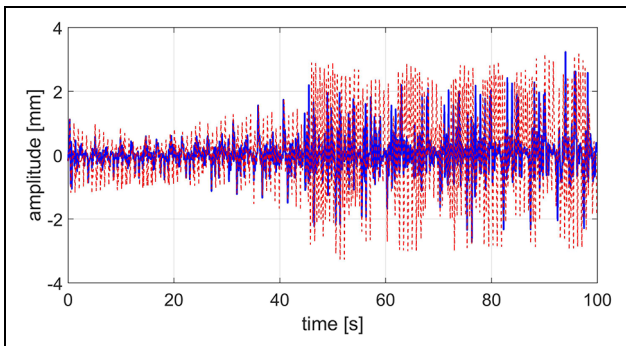


Figure 15. Typical segment showing the estimated coloured noise residuals (dashed line) and the estimated white noise residuals (solid line) of the Leica MS50 dataset at 2 Hz and a distance of 22.6635 m.

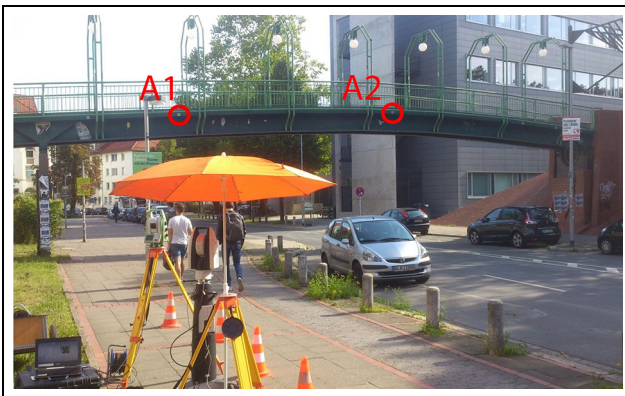


Figure 16. Vibration analysis of the footbridge structure using the telescope camera of the Leica MS50 to measure the passive targets attached to the side of the footbridge (areas highlighted by the circles) and using the LT to measure an attached corner cube reflector close to the aforementioned passive targets.

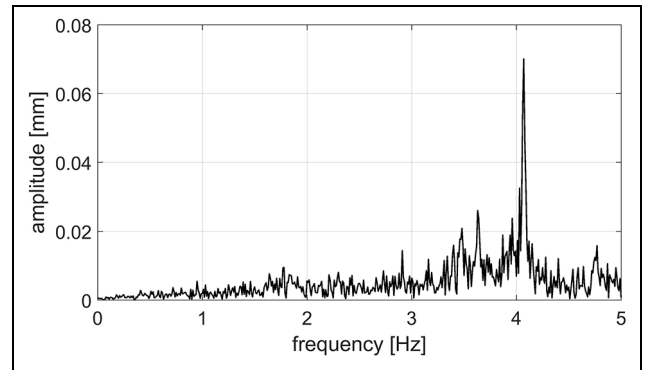


Figure 17. Point A1: Typical discrete Fourier transform of one segment of the Leica MS50 dataset at a distance of 16.5 m from footbridge structure, showing the main amplitude of 0.07 mm at a frequency of 4.07 Hz.

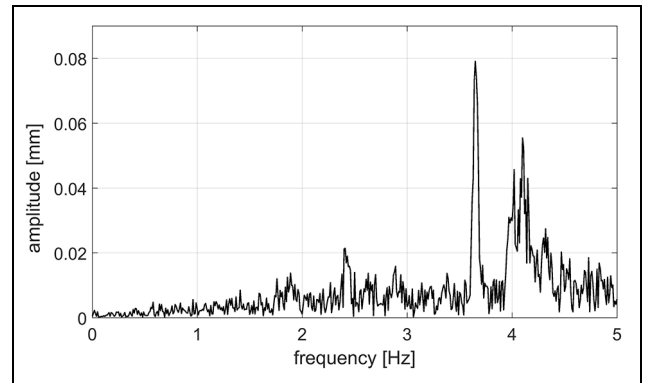


Figure 18. Point A2: Typical discrete Fourier transform of one segment of the Leica MS50 dataset at a distance of 20.01 m from footbridge structure, showing the main amplitudes of 0.079 and 0.055 mm at frequencies of 3.65 and 4.1 Hz, respectively.

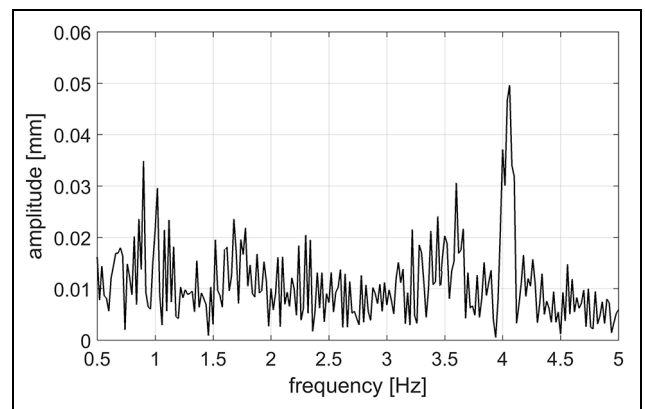


Figure 19. Point A1: Typical discrete Fourier transform of one segment of the LT dataset at a distance of 16.499 m from the footbridge structure, showing the main amplitude of 0.0497 mm at a frequency of 4.06 Hz.

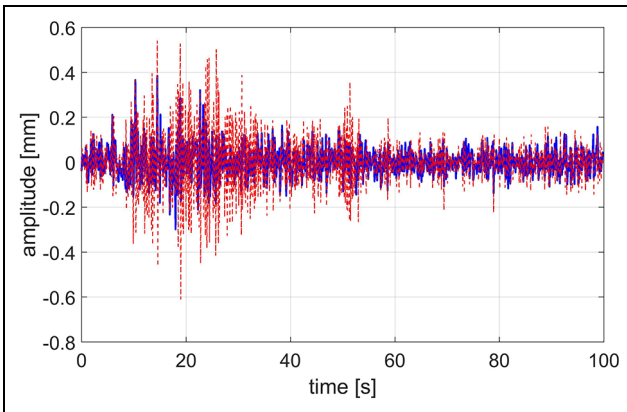


Figure 20. Point A1: Typical segment showing the estimated coloured noise residuals (dashed line) and the estimated white noise residuals (solid line) of the Leica MS50 dataset with the main amplitude at 4.07 Hz for the footbridge structure.

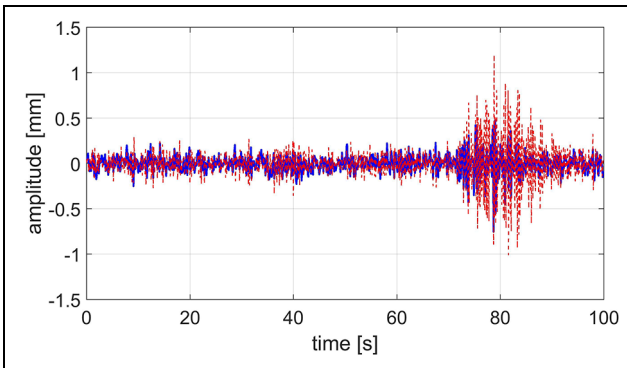


Figure 21. Point A2: Typical segment showing the estimated coloured noise residuals (dashed line) and the estimated white noise residuals (solid line) of the Leica MS50 dataset with the main amplitudes at frequencies of 3.65 and 4.1 Hz for the footbridge structure.

and 0.055 mm, respectively. However, the proposed approach shows the frequencies of 3.6451 and 4.0978 Hz with the maximum amplitudes of 0.051 and 0.0367 mm, respectively, which are comparable to those calculated from the FEM with the frequency of 3.642 Hz, and these findings demonstrate the correctness of our calculations. The higher frequency of approximately 4.07 Hz obtained might be due to either modulating the higher frequency of 13.294 Hz or an additional vibration produced by people passing across the footbridge structure and the latter not reaching a stable situation at the time of measurement.

In addition, Figures 20–22 illustrate the estimated coloured noise residuals and the decorrelated (i.e. estimated white noise) residuals for the Leica MS50 at the two points of A1 and A2 in addition to the LT measurements, respectively. We should mention that the LT

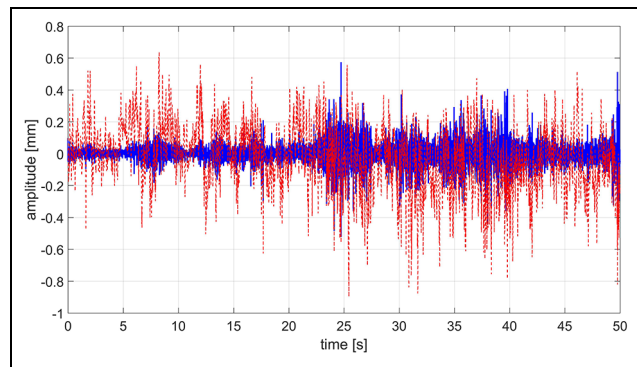


Figure 22. Point A1: Typical segment showing the estimated coloured noise residuals (dashed line) and the estimated white noise residuals (solid line) of the LT dataset with the main amplitude at 4.06 Hz for the footbridge structure.

measurements of the bridge structure were performed with a corner cube reflector of lesser quality than for measurements within the laboratory experiment. Consequently, a high level of noise in the displacements for some segments appears in the results, which we can be improved in our future work by employing a corner cube reflector of a better quality. In addition, we could even improve the Leica MS50 results by taking angular tilt axis errors into account and by avoiding the very minor shaking of the instrument.

Conclusion

A robust and consistent procedure was proposed to perform an accurate displacement and vibration analysis of a footbridge structure using an IATS (here, Leica MS50). The Leica MS50 benefits accurate distance measurements to the object in addition to the captured video streams with a practical sampling frequency of 10 Hz using an embedded on-axis telescope camera. The experiments were carried out for two case studies under a controlled excitation in the laboratory environment and an uncontrolled excitation of a footbridge structure. In a first case study, the results were validated by means of two highly accurate reference measurement systems, namely, the portable shaker vibration calibrator 9210D (with a sampling frequency of 200 Hz) and the Leica AT960-LR LT (with a sampling frequency of 200 Hz). In the second case study, the validation was performed based on the known natural frequencies of the footbridge structure calculated from the FEM analysis. In addition, the LT measurement was also used for a validation.

To extract target centroid from video streams of the Leica MS50, the feasibility of an optimal passive target pattern including four intersected lines and its accurate and reliable detection approach, proposed in Omidalizarandi et al.,²⁶ were investigated at different

epochs of time as a preliminary step. Subsequently, the vertical angular conversion factor was calibrated in the laboratory environment to convert derived displacements from the pixel unit to the metric unit.

To estimate amplitudes and frequencies for all three sensors with high accuracy, vibration measurements either in the length unit or the acceleration unit were input to the Fourier series as a linear regression model comprising a sum of sinusoids and additive random deviations. Furthermore, the coloured measurement noise was decorrelated through a covariance-stationary AR process of an order 25, assuming the white noise components to independently follow a central and scaled t -distribution with an unknown scale factor and unknown degree of freedom. At the end, model parameters were estimated by means of the GEM algorithm as described in Alkhatib et al.³⁰ The unknown frequencies were initiated by means of notable maximum amplitudes within the DFT of the data to perform adjustment of the combined observation model for a footbridge application.

The results indicate that the estimated frequencies and amplitudes from the Leica MS50 measurements were very close to those resulting from the two highly accurate reference sensors (LT and PSVC) in the laboratory environment and to those resulting from the FEM analysis and the LT for the real application of the footbridge structure. It was shown that the DFT results and our proposed approach achieved approximately similar results when estimating the frequencies. However, the results for the amplitudes varied from minor to significant changes depending on the coloured noise behaviour of the measurements. To show the strength of the proposed approach, the estimated results were compared in two cases of the AR model in the order of 25: with an unknown degree of freedom and without the AR process considering a constant degree of freedom of 120, which is close approximation of a normal distribution.

The estimated degrees of freedom of the t -distribution, in the case of considering the AR model order of 25, reveals that the LT and the PSVC measurements are a rather close approximation of a normal distribution, while, by contrast, the estimated degrees of freedom regarding the Leica MS50 measurements with substantial tails show a large number of outliers in the measurement noise of that sensor. Moreover, the results show that the highest white noise test acceptance rate (100%) was obtained for the PSVC measurements. The LT measurements also produced relatively high acceptance rates in comparison to the PSVC data. However, the acceptance rates regarding the Leica MS50 measurements fluctuate between 25% and 75%, so that the adjusted coloured noise model is clearly inadequate for a number of analysed segments. Furthermore, the image motion error for some video frames derived from

a weak PC performance or delay in the data transmission procedure from the Leica MS50 to the PC has a significant influence on the estimated frequencies and amplitudes and shows a higher coloured noise level compared to the good quality video frames captured. In summary, the results show the feasibility of Leica MS50 for an accurate displacement and vibration analysis of the footbridge structure for frequencies less than 5 Hz (in view of the Nyquist sampling theorem).

In our future work, we will measure the minor shaking of the Leica MS50 throughout the measurements by continuously reading the tilting axis error of the Leica MS50 using the GeoCOM interface. It might be beneficial to increase the measurement time to obtain more redundant data and to be able to increase AR model order to improve the coloured noise models and the resulting performance of the white noise test. In addition, the proposed approach can be extended to the time-dependant AR model to characterize the coloured noise behaviour of the measurements over time. Furthermore, the time synchronization for the measurements of the sensors can be performed to have a more realistic comparison of the results at a certain point of time. Moreover, we will improve the LT measurements for a footbridge structure by employing a corner cube reflector of a better quality. The internal calibration of the error sources of the Leica MS50 measurements might improve the results. The possibility of performing experiment with the Leica MS60 with a maximum sampling frequency of 20 Hz could also improve the results. Finally, global optimization can be applied for more accurate and reliable results to estimate model parameters with unknown frequencies.

Acknowledgements

The authors would like to acknowledge the Institute of Concrete Construction (Leibniz Universität Hannover) for providing the portable shaker vibration calibrator instrument used within this experiment and for the calculation of the natural frequencies of the footbridge structure based on the FEM. In addition, the authors would also like to acknowledge Falko Klasen, B. Eng., for his assistance with the experiments as part of his master thesis.

Declaration of conflicting interests

The author(s) declared no potential conflicts of interest with respect to the research, authorship and/or publication of this article.


Funding


The author(s) disclosed receipt of the following financial support for the research, authorship, and/or publication of this article: The publication of this article was funded by the Open Access fund of Leibniz Universität Hannover. The research presented was partly carried out within the scope of the

collaborative project ‘Spatio-temporal monitoring of bridge structures using low cost sensors’ with ALLSAT GmbH, which was supported by the German Federal Ministry for Economic Affairs and Energy (BMWi) and the Central Innovation Programme for SMEs (Grant ZIM Kooperationsprojekt, ZF4081803DB6).

ORCID iD

Mohammad Omidalizarandi  <https://orcid.org/0000-0002-9897-4473>

Boris Kargoll  <https://orcid.org/0000-0003-3496-6391>

Jens-André Paffenholz  <https://orcid.org/0000-0003-1222-5568>

References

- Alvandi A and Cremona C. Assessment of vibration-based damage identification techniques. *J Sound Vib* 2006; 292: 179–202.
- Ehrhart M and Lienhart W. Monitoring of civil engineering structures using a state-of-the-art image assisted total station. *J Appl Geodes* 2015; 9: 174–182.
- Lienhart W, Ehrhart M and Grick M. High frequent total station measurements for the monitoring of bridge vibrations. *J Appl Geodes* 2017; 11: 1–8.
- Leach M and Hyzak M. GPS structural monitoring as applied to a cable-stayed suspension bridge. In: *Proceedings of the International Federation of Surveyors (FIG) XX congress, Commission 6*, Melbourne, VIC, Australia, 1994. [CD-ROM].
- Psimoulis PA and Stiros SC. Measuring deflections of a short-span railway bridge using a robotic total station. *J Bridge Eng* 2013; 18: 182–185.
- Pytharoulis SI and Stiros SC. Spectral analysis of unevenly spaced or discontinuous data using the ‘norm-period’ code. *Comput Struct* 2008; 86: 190–196.
- Roberts GW, Meng X and Dodson AH. Integrating a global positioning system and accelerometers to monitor the deflection of bridges. *J Surv Eng: ASCE* 2004; 130: 65–72.
- Neitzel F, Niemeier W, Weisbrich S, et al. Investigation of low-cost accelerometer, terrestrial laser scanner and ground-based radar interferometer for vibration monitoring of bridges. In: *Proceedings of the 6th European workshop on structural health monitoring*, Dresden, 3–6 July 2012, pp.542–551. Deutsche Gesellschaft für Zerstörungsfreie Prüfung (DGZfP).
- Vosselman G and Maas HG. *Airborne and terrestrial laser scanning*. Boca Raton, FL: CRC Press, 2010.
- Omidalizarandi M and Neumann I. Comparison of target-and mutual information based calibration of terrestrial laser scanner and digital camera for deformation monitoring. *ISPRS Arch* 2015; 40: 559–564.
- Omidalizarandi M, Paffenholz J-A, Stenz U, et al. Highly accurate extrinsic calibration of terrestrial laser scanner and digital camera for structural monitoring applications. In: *Proceedings of the 3rd joint international symposium on deformation monitoring (JISDM)*, Vienna, 30 March–1 April 2016, p.8. [CD-ROM].
- Reiterer A, Lehmann M, Miljanovic M, et al. A 3D optical deformation measurement system supported by knowledge-based and learning techniques. *J Appl Geodes* 2009; 3: 1–13.
- Bürki B, Guillaume S, Sorber P, et al. DAEDALUS: a versatile usable digital clip-on measuring system for total stations. In: *Proceedings of the international conference on indoor positioning and indoor navigation (IPIN)*, Zurich, 15–17 September 2010, pp.1–10. New York: IEEE.
- Wagner A, Wasmeier P, Reith C, et al. Bridge monitoring by means of video-tacheometer – a case study. *Allgem Vermessungs-Nachr* 2013; 120: 283–292.
- Wagner A, Huber B, Wiedemann W, et al. Long-range geo-monitoring using image assisted total stations. *J Appl Geodes* 2014; 8: 223–234.
- Ehrhart M and Lienhart W. Image-based dynamic deformation monitoring of civil engineering structures from long ranges. *Proc SPIE* 2015; 9405: 94050J.
- Guillaume S, Clerc J, Leyder C, et al. Contribution of the image-assisted theodolite system QDaedalus to geodetic static and dynamic deformation monitoring. In: *Proceedings of the 3rd joint international symposium on deformation monitoring (JISDM)*, Vienna, 30 March–1 April 2016. [CD-ROM].
- Wagner A. A new approach for geo-monitoring using modern total stations and RGB + D images. *Measurement* 2016; 82: 64–74.
- Wagner A. *New geodetic monitoring approaches using image assisted total stations*. PhD Thesis, Technische Universität München, München, 2017.
- Leica Geosystems. *Leica Nova MS50 Geocom reference manual* (version 5.50). St. Gallen: Leica Geosystems AG, 2014.
- Gruen A. Least squares matching: a fundamental measurement algorithm. In: Atkinson KB (ed.) *Close range photogrammetry and machine vision*. Dunbeath: Whittles Publishing, 1996, pp.217–255.
- Akca D. Full automatic registration of laser scanner point clouds. In: *Proceedings of the optical 3-D measurement techniques VI*, Zurich, 22–25 September 2003, pp.330–337. Wichmann.
- Gruen A and Akca D. Least squares 3D surface and curve matching. *ISPRS J Photogramm* 2005; 59: 151–174.
- Zhou Y, Wagner A, Wunderlich T, et al. Close range angles deformation monitoring by telescope camera of total station MS50 using automatic detection of coded targets. In: *Proceedings of the 2nd international workshop on civil engineering and architecture*, Istanbul, 12–13 September 2015, pp.153–162.
- Reiterer A and Wagner A. System consideration of an image assisted total station – evaluation and assessment. *Allgem Vermessungs-Nachr* 2012; 119: 83–94.
- Omidalizarandi M, Paffenholz J-A and Neumann I. Automatic and accurate passive target centroid detection for applications in engineering geodesy. *Surv Rev.* 2018; 1–16.
- Walser B. *Development and calibration of an image assisted total station*. PhD Thesis, ETH Zürich, Zürich, 2004.
- Ehrhart M and Lienhart W. Accurate measurements with image-assisted total stations and their prerequisites. *J Surv Eng: ASCE* 2016; 143: 04016024.

29. Zhou Y, Wagner A, Wunderlich T, et al. Calibration method for IATS and application in multi-target monitoring using coded targets. *J Appl Geodes* 2017; 11: 99–106.
30. Alkhatib H, Kargoll B and Paffenholz J-A. Robust multivariate time series analysis in nonlinear models with autoregressive and t-distributed errors. In: *Proceedings of the international work-conference on time series analysis (ITISE)*, Granada, 18–20 September 2017. Godel Impresiones Digitales S.L.
31. Leica Geosystems. *Leica Nova MS50 white paper*. St. Gallen: Leica Geosystems AG, 2013.
32. Leica Geosystems. PCMM system specifications: Leica absolute tracker and Leica T-products, 2010, <http://www.hsands.com/productpdfs/leica.pdf>
33. The Modal Shop. Model 9210D: low frequency portable vibration calibrator (datasheet), 2015, [http://www.modalshop.com/filelibrary/9210D-Low-Frequency-Portable-Vibration-Calibrator\(DS-0140\).pdf](http://www.modalshop.com/filelibrary/9210D-Low-Frequency-Portable-Vibration-Calibrator(DS-0140).pdf)
34. Grompone von Gioi R, Jakubowicz J, Morel JM, et al. LSD: a line segment detector. *Image Process On Line* 2012; 2: 35–55.
35. Kaehler A and Bradski G. *Learning OpenCV 3: computer vision in C++ with the OpenCV library*. Sebastopol, CA: O'Reilly Media, Inc., 2016.
36. Canny J. A computational approach to edge detection. *IEEE T Pattern Anal* 1986; 8: 679–698.
37. PhysicsNet, <http://physicsnet.co.uk> (accessed 1 September 2017).
38. Andrews LC and Phillips RL. *Mathematical techniques for engineers and scientists*. Bellingham, WA: SPIE Press, 2003.
39. Kargoll B, Omidalizarandi M, Loth I, et al. An iteratively reweighted least-squares approach to adaptive robust adjustment of parameters in linear regression models with autoregressive and t-distributed deviations. *J Geodesy* 2018; 92: 271–297.
40. Abramowitz M and Stegun IA. *Handbook of mathematical functions: with formulas, graphs, and mathematical tables*. Gaithersburg, MD: US Department of Commerce, National Institute of Standards and Technology, 1964.
41. Koch KR. Expectation maximization algorithm and its minimal detectable outliers. *Stud Geophys Geod* 2017; 61: 1–18.

Paper 3

Mohammad Omidalizarandi*, Boris Kargoll, Jens-André Paffenholtz, and Ingo Neumann

Robust external calibration of terrestrial laser scanner and digital camera for structural monitoring

<https://doi.org/10.1515/jag-2018-0038>

Received September 5, 2018; accepted January 8, 2019

Abstract: In the last two decades, the integration of a terrestrial laser scanner (TLS) and digital photogrammetry, besides other sensors integration, has received considerable attention for deformation monitoring of natural or man-made structures. Typically, a TLS is used for an area-based deformation analysis. A high-resolution digital camera may be attached on top of the TLS to increase the accuracy and completeness of deformation analysis by optimally combining points or line features extracted both from three-dimensional (3D) point clouds and captured images at different epochs of time. For this purpose, the external calibration parameters between the TLS and digital camera needs to be determined precisely. The camera calibration and internal TLS calibration are commonly carried out in advance in the laboratory environments. The focus of this research is to highly accurately and robustly estimate the external calibration parameters between the fused sensors using signalised target points. The observables are the image measurements, the 3D point clouds, and the horizontal angle reading of a TLS. In addition, laser tracker observations are used for the purpose of validation. The functional models are determined based on the space resection in photogrammetry using the collinearity condition equations, the 3D Helmert transformation and the constraint equation, which are solved in a rigorous bundle adjustment procedure. Three different adjustment procedures are developed and implemented: (1) an expectation maximization (EM) algorithm to solve a Gauss-Helmert model (GHM) with grouped t-distributed random deviations, (2) a novel EM algorithm to solve a corresponding quasi-Gauss-Markov model (qGMM) with t-distributed pseudo-misclosures, and (3) a classical least-

squares procedure to solve the GHM with variance components and outlier removal. The comparison of the results demonstrates the precise, reliable, accurate and robust estimation of the parameters in particular by the second and third procedures in comparison to the first one. In addition, the results show that the second procedure is computationally more efficient than the other two.

Keywords: Terrestrial laser scanner, digital camera, external calibration, Gauss-Helmert model, quasi-Gauss-Markov model, adaptive robust estimation, expectation maximisation algorithm, structural monitoring

1 Introduction

Numerous research studies have been conducted concerning short- and long-term deformation monitoring of natural objects such as landslides, rocks and ice glaciers ([1], [2], [3], [4]), as well as of civil engineering infrastructures such as dams, bridges and towers ([5], [6], [7], [8], [9], [10], [11], [12], [13], [14]). In this context, the integration of a terrestrial laser scanner (TLS) and digital photogrammetry, besides the integration of other sensors, has received considerable attention ([15], [16], [17], [18]). On the one hand, a TLS can typically be used for an area-based deformation analysis by comparing surfaces from scanned point clouds captured at different epochs, as shown for instance in [1], [4], [5], [8], [12], [13] and [19]. A TLS directly provides fast, dense and accurate three-dimensional (3D) coordinates (i. e., unstructured 3D point clouds) of the object's surface in combination with reflectivity values, which represent the energy of backscattered laser light. The accuracy of a single point measurement by a TLS varies depending on the distance to objects and the object properties (e. g., colour and roughness) in the range of sub-millimetre to millimetre. On the other hand, photogrammetric techniques have been widely applied in a variety of deformation monitoring applications, see e. g. [20], [21], [22], [23], [24], [25], [26] and [27]. It is possible to perform a 3D deformation analysis based on photogrammetric techniques using at least two stereo images from different standpoints. To produce the 3D coordinates, signalised

***Corresponding author: Mohammad Omidalizarandi**, Leibniz Universität Hannover, Geodetic Institute, Nienburger Str. 1, 30167 Hannover, Germany, e-mail: zarandi@gih.uni-hannover.de, ORCID: <https://orcid.org/0000-0002-9897-4473>

Boris Kargoll, Jens-André Paffenholtz, Ingo Neumann, Leibniz Universität Hannover, Geodetic Institute, Nienburger Str. 1, 30167 Hannover, Germany, e-mails: kargoll@gih.uni-hannover.de, paffenholtz@gih.uni-hannover.de, neumann@gih.uni-hannover.de, ORCID: <https://orcid.org/0000-0003-1222-5568> (J.-A. Paffenholtz)

or non-signalised points can be extracted from the captured images and solved by means of the stereo intersection bundle adjustment (e. g., [20], [24]).

Both measurement techniques have their own advantages and disadvantages. With both kinds of techniques, the measurements can be performed without any contact to the object. A TLS usually covers a larger area of an object by a single standpoint with a fully horizontal field of view (FOV). However, its coverage for a vertical FOV varies with different types of TLS (e. g., Leica Geosystems Scanstation P40 (270°), RIEGL VZ-400 (100°), Zoller+Fröhlich (Z+F) Imager 5016 (320°) and Faro Focus X330 (300°). By contrast, a digital camera's FOVs are significantly smaller than for a TLS, which fact necessitates multiple standpoints to cover the whole area. For both measurement systems, the internal calibration should be performed in a controlled laboratory environment. The external orientation parameters (EOPs), including three translations and three orientations, must be calculated to transform the measurements into a common coordinate reference frame. This is typically carried out based on at least three known control points or based on surface matching algorithms and their variants such as the iterative closest point (ICP) algorithm [28]. Furthermore, to tackle the scale problem with photogrammetric techniques and to transform the coordinates from the image space into object space, an approximate distance measurement or *a priori* photogrammetric network adjustment is necessary [25].

1.1 Motivation

In this work, a TLS of type Z+F IMAGER 5006 and a high-resolution digital camera Nikon D750 are integrated as a multi-sensor-system (MSS) to benefit from the advantages of both sensors for an accurate structural monitoring. To this end, the digital camera is rigidly attached on top of the TLS using a clamping system (see Fig. 1, right). This integration allows for the usage of digital cameras with different image sizes or focal lengths [29]. Since the 6 EOPs of the MSS vary for each set-up of the camera, an *in-situ* calibration is performed.

To extract meaningful features such as points, lines, or even small cracks from the 3D point clouds, either the scan resolution or the number of scan stations should be sufficiently increased. However, the latter is preferable to former since:

- two low-resolution scans are often performed faster than one high-resolution scan, while approximately

providing the same point spacing distances between the measured 3D point clouds of the object;¹

- better geometry between the scans is obtained, which allows one to solve for the (internal and external) calibration parameters with lower correlations between them;
- the systematic error sources of the TLS, such as incidence angles (i. e., the angle between the TLS and object), are eliminated, which may lead to a more reliable estimation of the calibration parameters.

It should be noted that the systematic error sources of TLS measurements (e. g., incidence angles, range noise, scale factor, zero point error) can also be eliminated by the deterministic and stochastic modelling. For more information in this regard, please refer to [30], [31], [32] and [33].

The high-resolution images captured by the digital camera allow for a simplified extraction of aforementioned features. Subsequently, the high-resolution images provide measurements with a high angular accuracy at the subpixel level and therefore improve the lateral accuracy of the 3D point clouds [34]. Such a high angular accuracy can be obtained by capturing the images either from a free set-up of cameras at closer distances to the object or from a camera attached on top of the TLS at multiple scan stations. Although each captured image covers just a portion of the object and not the entire object, the resolution is thus increased. As a drawback with photogrammetric approaches, those images captured with larger incidence angles to the objects cause a weak geometrical configuration of the cameras, which leads to an inaccurate estimation of the cameras' pose parameters. This, however, can be avoided for the MSS by using the external calibration parameters. Here, the combination of the 3D point clouds with high-resolution images is beneficial due to the increase of redundancy (i. e., including more feature points or lines) in the adjustment procedure. However, in case of a large incidence angle of the TLS, those images captured from the camera mounted on top of the TLS also suffer from a weak geometry. Thus, those feature points or lines located at higher incidence angles need to be considered with lower weights within the adjustment procedure. Consequently, the high-resolution images do not necessarily improve the accuracy of displacement monitoring, but increase the precision. Still, the considered integration may allow for an accurate and precise 3D deformation analysis both in the direction of the laser beam and perpendicular

¹ Depending on the distances of scan stations to an object, the point spacing distances between the 3D point clouds can be varied.

lar to the laser beam. For this MSS, the information from the both sensors are complementary to each other, and the strength of one measurement method overcomes the weakness of the other one.

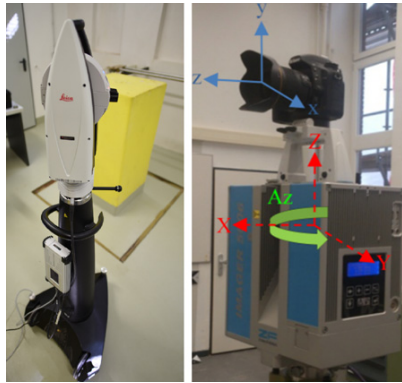


Figure 1: Laser tracker Leica AT960LR (left), a Nikon D750 24.3-megapixel digital camera is rigidly attached on top of the Z+F Imager 5006 TLS (right).

The innovations in this paper are threefold: firstly, at a theoretical level, a novel quasi-Gauss-Markov model (qGMM) is proposed as alternatives to the Gauss-Helmert model (GHM) with t-distributed random deviations (introduced by [35]) and to a classical GHM with variance component estimation (VCE) and outlier detection. For the solution of this qGMM, a tailored expectation maximisation (EM) algorithm is provided. Secondly, these three procedures are applied to compute highly accurate, robust and reliable parameter estimates of the external calibration of the TLS and the digital camera, which task has previously not been achieved to the best knowledge of the authors. However, the previous researchers solved such a problem by the GMM, which would not be an ideal adjustment model due to high non-linearity of the functional models. Thirdly, a laser tracker (LT; see Fig. 1, left) is included as a highly accurate reference sensor for the purpose of validation. Here, the 6 EOPs between the TLS and the camera (i. e., the position and orientation of the digital camera relative to the TLS; see Fig. 1, right), the 7 EOPs between the TLS and the LT (i. e., the scale, position and orientation of the TLS with respect to the LT), and the target coordinates in the object space are considered as unknown parameters. To simplify the approach, it is assumed that there are no correlations between the observables since they are measured independently. Subsequently, the stochastic model is considered as a diagonal matrix.

1.2 Literature review on external calibration between TLS and digital camera

In the last two decades, several approaches were proposed to obtain the EOPs between the digital camera and a 2D or 3D laser scanner. [36] proposed an algorithm to estimate the external calibration parameters between a digital camera and a 2D laser range finder using a planar checkerboard pattern. The laser scan lines are matched on the planar pattern with the pattern plane from the camera image. Subsequently, a global optimisation method is applied to refine the parameters. [37] and [38] extended the work of [36] from a 2D to a 3D laser scanner using the planar checkerboard pattern to be observed from different viewing points. [39] performed a self-calibration of an integrated range camera system using signalised targets. Next, the internal orientation/calibration parameters (IOPs) of the digital camera, in addition to the range finder's systematic error parameters, are estimated simultaneously based on the collinearity equations and range observation equations in a free-network bundle adjustment. Variance component estimation is applied to optimally re-weight observations in an iterative manner. [34] proposed an algorithm to combine the 3D point clouds with central perspective and panoramic images within an integrated bundle adjustment based on a Gauss-Markov model (GMM) with VCE. The 3D object point coordinates as well as the IOPs and EOPs of the sensors are treated as unknown parameters in the adjustment procedure. Subsequently, the evaluation of the estimated parameters is carried out by means of statistical tests. [40] proposed an automatic target-less external calibration of a 3D laser scanner and digital camera based on the mutual information algorithm. The calibration parameters are calculated by maximising the mutual information between the reflectivity values of the 3D point clouds and intensity values of the captured image. Then, the gradient ascent algorithm is applied to consider different 3D point clouds from different scenes in a single optimisation framework. A drawback of this approach is that it requires relatively precise initial values for the 6 EOPs. [41] adopted the work of [40] for an MSS consisting of a TLS and a high-resolution digital camera, for which results were promising. [42] proposed an algorithm for highly accurate estimation of the external calibration parameters between a TLS and a digital camera using the signalised target points. The space resection bundle adjustment, 3D Helmert transformation and a constraint equation were solved in an adjustment model based on the GMM and GHM with VCE and a statistical testing procedure. [43] proposed an algorithm to estimate the IOPs and EOPs of a 3D laser scanner and a

rigidly connected digital camera in two least-squares sub-problems using measurements of a calibration plane under various configurations. [44] fused the 3D point clouds and high-resolution digital images using interest point features extracted from an intensity image generated from the 3D point clouds and an image captured by the digital camera. The point features are extracted using a Harris corner detector and then matched based on the zero mean normalised cross correlation measure. To refine the correspondences, the random sample consensus (RANSAC) algorithm [45] is applied. Subsequently, to calculate the EOPs, the matched points and their corresponding object coordinates are input to the collinearity equations, solved within the bundle adjustment procedure. [46] proposed an approach for the registration of photogrammetric imagery and LiDAR (light detection and ranging) data using linear features in the photogrammetric bundle adjustment. The system of equations include the collinearity equations for the endpoints of each line in both the image and object space. In addition, a coplanarity constraint is defined for an intermediate point of each line in the image space, which is within the plane defined by the perspective centre of the image and two endpoints of that straight line in the object space.

The robust procedure of sensor fusion suggested in this contribution can be extended to other sensor fusion problems with different applications, by identifying a proper mathematical model for the orientation between the used sensors. For example, the work of [47] could be extended by using a high-resolution digital camera (such as a Nikon D750 with a frame rate up to 60 Hz) equipped with a telescopic lens and mounted on top of an image assisted total station (IATS) (e. g., a Leica Nova MS50 MultiStation with a frame rate up to 20 Hz). Thus, the deficiency of the IATS regarding the low sampling rate in vibration analysis of bridge structures could be improved. In addition, the newly developed methodology allows to strictly consider the stochasticity of the observations (i. e. the propagation process from the observations to the parameters of interest (6 EOPs)) and rigorously treats fully populated variance covariance matrix (VCM).

2 Data acquisition, interfacing and pre-processing

The data acquisition step consists of capturing the images, the 3D point clouds, horizontal angle readings of the TLS (A_z) and the LT measurements (optionally).

The 3D point clouds are acquired with a Z+F IMAGER 5006 in “super high” resolution mode with normal quality. The vertical and horizontal resolution and accuracy are 0.0018° and 0.007° rms, respectively [48]. In addition, the signalised target points in the 3D point clouds are extracted using the “Fit target” mode of the software Z+F LaserControl version 8.5.5.12510. For more information regarding the uncertainty of the signalised targets in the 3D point clouds measurements, please refer to [49].

The full-frame digital single-lens reflex (DSLR) camera Nikon D750, is used to capture high-resolution images. The pixel [px] resolution of the captured images in the large mode image size is approximately 0.00597 mm. To capture sharp images, the camera setting is adjusted accordingly: the focus mode is set to “manual”, the white balance to “auto”, the ISO sensitivity (the camera’s sensitivity to light) to “100”, the f-stop to “6.3”, the autofocus to “off” (to avoid changing of the camera calibration parameters) and the focus lens to “infinity”. To prevent a change of focus, the focus ring is fixed with rubber bands. In addition, the aperture needs to be optimised according to the distance to the object. It is desired to set to “manual” to avoid changes of the depth of field, which could lead to focus shift [50]. Moreover, the images are captured remotely on the cell phone using a Nikon wireless mobile utility application to avoid blurring of the captured images in case of a shake of the camera. The most challenging issue in this regard is related to the changes of the camera calibration parameters with respect to the distance to objects in a real monitoring measurement. Subsequently, the camera calibration is performed in a laboratory in advance for the specified focus lens, which can be adjusted from “near infinity” to “far infinity”, depending on the distances of the scan stations to the object of interest.

To perform camera calibration, 12 different images are captured from different viewing directions to the 3D calibration pattern (see Fig. 2). For this purpose, the camera is first set up on a stabilised tripod. Then, the camera is rotated about 45° towards the 3D calibration pattern. Among the 12 captured images, 8 capture the top, bottom, left and right part of the pattern in both landscape and portrait camera positions (rolling the camera around by approximately 0° and 90° , respectively). Subsequently, the captured images are processed in PhotoModeler to calculate the internal calibration parameters based on the bundle adjustment algorithm.

To estimate the external calibration parameters of the MSS, the images are captured by the digital camera mounted on top of TLS. A sequence of images is taken by varying the azimuth (A_z) of the TLS with step sizes approximately between 10 and 15 degrees, thereby covering a

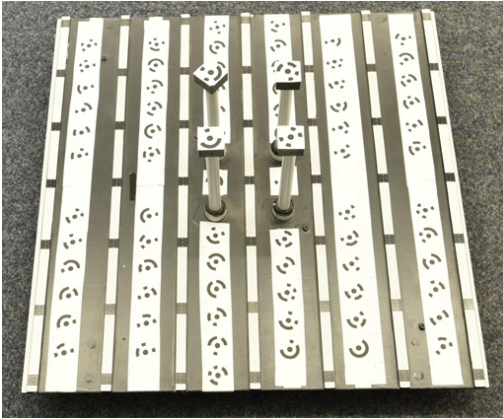


Figure 2: 3D calibration pattern with precisely known target coordinates for the internal camera calibration.

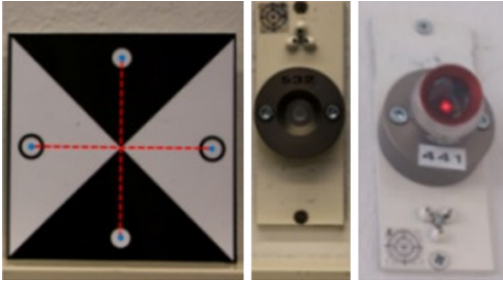


Figure 3: Depiction of detected circle centroids in a signalised target using the PhotoModeler software (left), a magnetic holder (middle), and a corner cube reflector attached to the magnetic holder (right).

360° rotation of the TLS. The Az is read off a side screen of the TLS and stored for each captured image to rotate the 3D point clouds from the TLS coordinate system to the camera coordinate system.

The image measurements are performed for the signalised targets using the sub-pixel target mode of the software PhotoModeler version 5.2.3 by Eos Systems Inc. As can be seen from Figure 3 (left), the four centroids of the circles in each target are measured, and a target centroid is computed by averaging the measured circle centres. The back of the target consists of a hemispherical metal staff that fits precisely to the magnetic holder (Fig. 3, middle). Alternatively, the signalised target points are extracted by an automatic procedure as well as a high accuracy based on the work of [51] in which the results have the same level of accuracy as PhotoModeler measurements.

The LT is used as a reference sensor for validation purposes, which allows sub-millimetre range accuracy of the target points in the object space with a maximum permissible error of $15 \mu\text{m} + 6 \mu\text{m/m}$ [52]. It is pointed to the corner cubes reflector (Fig. 3, right) attached to the magnetic holder (Fig. 3, middle) and measured for each target.

3 Calibration modelling

The focus of this research is to estimate the 6 EOPs between the TLS and digital camera robustly, reliably and with a very high accuracy. In addition, the 7 EOPs between the TLS and LT are determined for validation. The internal camera calibration was carried out in advance in the laboratory environment to avoid their correlation with the external calibration parameters.²

To estimate the 6 EOPs, the image coordinates are first rectified using the calculated IOPs of the digital camera, consisting of the principal point (x_p, y_p) , the focal length (f) , the coefficients of radial distortion (K_1, K_2, K_3) and the coefficients of decentring distortion (P_1, P_2) . According to Brown's equations [53], the image measurements (x, y) are rectified to (x', y') according to

$$x' = x + \bar{x}(K_1 r^2 + K_2 r^4 + K_3 r^6 + \dots) + (P_1(r^2 + 2\bar{x}^2) + 2P_2\bar{x}\bar{y}), \quad (1)$$

$$y' = y + \bar{y}(K_1 r^2 + K_2 r^4 + K_3 r^6 + \dots) + (P_2(r^2 + 2\bar{y}^2) + 2P_1\bar{x}\bar{y}), \quad (2)$$

where

$$\bar{x} = x - x_p, \quad (3)$$

$$\bar{y} = y - y_p, \quad (4)$$

$$r = \sqrt{(x - x_p)^2 + (y - y_p)^2}. \quad (5)$$

Next, a (3×3) rotation matrix based on the measured Az is defined to rotate the 3D point clouds around its Z-axis at the exposure time [54] (see Fig. 4). Therefore, the Az is considered as an additional observable in the adjustment procedure.

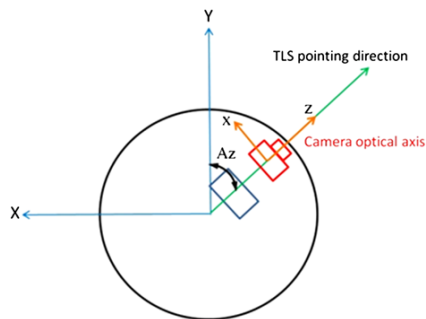


Figure 4: The TLS and camera coordinate systems from top view.

² The TLS internal calibration is assumed to be up to date by regular calibrations performed by the manufacturer.

The mathematical function for computing the 6 EOPs between the TLS and digital camera is based on the space resection in photogrammetry using the collinearity condition equations [54]

$$\mathbf{F}_x = x' - f \frac{p}{q}, \quad (6)$$

$$\mathbf{F}_y = y' - f \frac{s}{q}, \quad (7)$$

where (x', y') are the rectified target coordinates in the image space. Furthermore, the 7 EOPs between the TLS and LT are determined by the 3D Helmert transformation

$$\mathbf{F} = \lambda \mathbf{R}_{\kappa' \varphi' \omega'} \begin{bmatrix} X_{TLS} \\ Y_{TLS} \\ Z_{TLS} \end{bmatrix} + \begin{bmatrix} X'_c \\ Y'_c \\ Z'_c \end{bmatrix} - \begin{bmatrix} X_L \\ Y_L \\ Z_L \end{bmatrix}. \quad (8)$$

Here, (X'_c, Y'_c, Z'_c) are the translations, $(\kappa', \varphi', \omega')$ the rotation angles, λ is the scale factor, $(X_{TLS}, Y_{TLS}, Z_{TLS})$ are the target coordinates in the TLS coordinate system, (X_L, Y_L, Z_L) the target coordinates in the LT coordinate system, and the rotation matrix $\mathbf{R}_{\kappa' \varphi' \omega'}$ is the product of the individual rotation matrices

$$\mathbf{R}_{\omega'} = \begin{bmatrix} 1 & 0 & 0 \\ 0 & \cos \omega' & \sin \omega' \\ 0 & -\sin \omega' & \cos \omega' \end{bmatrix}$$

$$\mathbf{R}_{\varphi'} = \begin{bmatrix} \cos \varphi' & 0 & -\sin \varphi' \\ 0 & 1 & 0 \\ \sin \varphi' & 0 & \cos \varphi' \end{bmatrix}$$

$$\mathbf{R}_{\kappa'} = \begin{bmatrix} \cos \kappa' & \sin \kappa' & 0 \\ -\sin \kappa' & \cos \kappa' & 0 \\ 0 & 0 & 1 \end{bmatrix}$$

In addition, the constraints

$$\mathbf{F} = \begin{bmatrix} X \\ Y \\ Z \end{bmatrix} - \begin{bmatrix} X_{TLS} \\ Y_{TLS} \\ Z_{TLS} \end{bmatrix}, \quad (9)$$

involving the unknown target coordinates (X, Y, Z) in the object space (TLS coordinate system) are defined to estimate the target coordinates as unknown parameters within the adjustment procedure. The four non-linear model equations (6)–(9) are solved by means of three adjustment procedures, which are described in Section 4. The non-linear collinearity equations and the 3D Helmert transformation are linearised based on the Taylor series expansion. The initial values for the collinearity equations are estimated using a direct linear transform (DLT) in combination with a RANSAC algorithm to robustly estimate the

parameters. For further information concerning the DLT algorithm, collinearity equations and rotation matrices, please refer to, e. g., [55]. Furthermore, the initial values for the 3D Helmert transformation are computed via the closed-form solution using unit quaternions [56] to obtain the transformation parameters between the TLS and LT coordinate system. The target coordinates in the 3D point clouds are transformed to the 3D camera coordinate system through

$$\begin{bmatrix} p \\ s \\ q \end{bmatrix} = \mathbf{R}_{\kappa \varphi \omega} \left(\mathbf{R}_{Az} \begin{bmatrix} X_{TLS} \\ Y_{TLS} \\ Z_{TLS} \end{bmatrix} - \begin{bmatrix} X_c \\ Y_c \\ Z_c \end{bmatrix} \right), \quad (10)$$

where (X_c, Y_c, Z_c) are the corresponding translations and $(\kappa, \varphi, \omega)$ the rotation angles; the rotation matrix $\mathbf{R}_{\kappa \varphi \omega}$ is set up in analogy to $\mathbf{R}_{\kappa' \varphi' \omega'}$, and the rotation matrix \mathbf{R}_{Az} of the same type as $\mathbf{R}_{\kappa'}$.

It should be noted that typically in the photogrammetric approaches, the images are captured from a free set-up of the cameras in which one can achieve a good geometric configuration of the camera poses with wide baselines. However, in our current approach, the camera mounted on top of the TLS merely rotates at nearly the same point, which gives a weak geometry due to the narrow baseline. For this reason, the camera poses are not estimated directly from the stereo matching. Instead; the 3D point clouds are rotated about its Z-axis using the measured Az to be transformed to the unique 3D camera coordinate system. In addition, a possible systematic eccentricity error of the TLS is compensated by the measured Az that cover a 360° rotation of the TLS. Subsequently, its influence on the estimation of the camera pose parameters is eliminated accordingly.

4 Adjustment models

The aforementioned three different adjustment models are employed to tackle the problem of estimating the external calibration parameters. The first adjustment model (Section 4.1) represents a GHM with t-distributed random deviations, as introduced by [35]. The model in [35] is extended to allow for observation group-specific scale factors (proposed in [57]) as well as group-specific degrees of freedom (dof). As a further addition, it is demonstrated that the optimisation problem underlying these GHMs consists of a constrained maximum likelihood estimation, so that the

algorithms derived initially in [35, 57] can be established more rigorously as generalised expectations maximisation (GEM) algorithms with additional constraints.

The second adjustment model (Section 4.2) is a novel kind of ('quasi') GMM with t-distributed pseudo-misclosures (defined through a transformation of the GHM's condition equations into observation equations of a substitute GMM). The idea here is to uniformly down-weight all observations causing an extreme value of their associated misclosure, rather than downweighting outlying observations individually. The third adjustment model (Section 4.3) takes the form of a classical GHM (without specification of a probability distribution) and involves a least-squares estimation with VCE and outlier testing.

The deterministic model, which was determined from the aforementioned four non-linear model equations (6)–(9) is the same for all three estimation procedures. In contrast, the distributional assumptions about the random deviations deviate fundamentally from procedure to procedure. Concerning the variance-covariance model, only the information about the precision of the measurements is included, and currently any correlations that might exist between them are numerically ignored. In particular, there might be correlations between the Az angle observables of the TLS and the observed targets in the 3D point clouds. However, we surmise that the impact of such correlations on the computed parameter estimates are not significant.

The uncertainty modelling of the presented adjustment models has a rigorous treatment of the VCMs in the propagation process from the observations to the parameters of interest. Therefore, fully populated VCMs with correlation between the observations are theoretically and correctly treated. From a numerical point of view, these fully populated VCMs are not considered due to the following reasons. Firstly, the numerical consideration of correlation is very complex topic, which has also not been investigated by other researchers to the best knowledge of the authors. Therefore, it can be considered a research topic on its own. Secondly, from our point of view, the correlation between the observations has a lower impact on the results than the occurring mathematical correlation from the functional model. Furthermore, the measurement strategy with different image coordinates for the targets in each image leads to a decorrelation of the observations. Details of the variance-covariance modelling will be provided in the following sub-sections that correspond to the three adjustment procedures. Numerical results for the correlations of the parameters are given in sub-section 5.1.

4.1 EM algorithm for the Gauss-Helmert model with grouped t-distributed random deviations

In this model, it is generally considered that the observables $\mathcal{L}_1, \dots, \mathcal{L}_n$ are stochastically independent and belong to N distinct groups, where each group k consists of n_k observables. It is further assumed that an observable $\mathcal{L}_{k,i}$ with $k \in \{1, \dots, N\}$ and $i \in \{1, \dots, n_k\}$ follows a scaled (Student's) t-distribution with individual unknown location parameter $\mu_{k,i}$ and group-dependent unknown scale factor σ_k^2 as well as unknown dof v_k . Thus, the stochastic observation model reads

$$\mathcal{L}_{k,i} \stackrel{\text{ind.}}{\sim} t_{v_k}(\mu_{k,i}, \sigma_k^2). \quad (11)$$

On the one hand, the t-distribution model makes sense in situations where numerous outliers are expected. In such situations, t-distributions, having generally thicker tails than normal distributions, may be used as outlier distributions within the framework of a robust maximum likelihood (ML) estimation [58, 59]. On the other hand, the usage of t-distributions with a dof between 3 and 4 has been recommended with the application of the Guide to the Expression of Uncertainty in Measurement [60] in situations, where input quantities with statistically determined (i. e., type-A) standard uncertainties affect the output quantities (i. e., the observables to be adjusted) [61]. The set-up of group-dependent dofs thus allows for different outlier characteristics or input quantities having type-A uncertainties within the different, fused observation groups. The variance of a single observable within group k can be computed from the scale factor via the equation $s_k^2 = \frac{v_k}{v_k-2} \cdot \sigma_k^2$.

Alternatively, the t-distribution model can be stated as the Gaussian variance-inflation model (cf. [62])

$$\mathcal{L}_{k,i} | w_{k,i} \stackrel{\text{ind.}}{\sim} N(\mu_{k,i}, \sigma_k^2 / w_{k,i}), \quad w_{k,i} \stackrel{\text{ind.}}{\sim} \frac{\chi_{v_k}^2}{v_k}, \quad (12)$$

where a small value $w_{k,i}$ ("weight") of the so-called latent variable $\mathcal{W}_{k,i}$ arises for an observation located in the tails of the original t-distribution (i. e., for an outlier). A small weight leads then to an enlarged variance of the associated conditionally Gaussian observable ($\mathcal{L}_{k,i} | w_{k,i}$).

In addition, the adjustment problem involves functions h_1, \dots, h_r of the previous location parameters and additional unknown functional parameters ξ_1, \dots, ξ_u . These functions are used to set up the desired constraint or condition equations $h_j(\xi, \mu) = 0$, where ξ is the $(u \times 1)$ -vector of functional parameters and μ the $(n \times 1)$ -vector of expected

values of \mathcal{L} [see also Equations (1) and (2) in [35]]. The latter location parameters are grouped according to

$$\boldsymbol{\mu} = [\boldsymbol{\mu}_1^T, \dots, \boldsymbol{\mu}_N^T]^T = [\mu_{1,1}, \dots, \mu_{1,n_1}, \dots, \mu_{N,1}, \dots, \mu_{N,n_N}]^T.$$

Combining the condition functions to the vector-valued function \mathbf{h} and denoting by $\mathbf{0}_{[r \times 1]}$ the $(r \times 1)$ -vector of zeros, one thus finds

$$\mathbf{h}(\boldsymbol{\xi}, \boldsymbol{\mu}) = \mathbf{0}_{[r \times 1]}. \quad (13)$$

For brevity of expressions, all of the unknown parameters are stacked within the $(u + n + 2N)$ -vector

$$\boldsymbol{\theta} = [\boldsymbol{\xi}^T, \boldsymbol{\mu}^T, \sigma_1^2, \dots, \sigma_N^2, \nu_1, \dots, \nu_N]^T, \quad (14)$$

all given (grouped) observations within the $(n \times 1)$ -vector

$$\boldsymbol{\ell} = [\boldsymbol{\ell}_1^T, \dots, \boldsymbol{\ell}_N^T]^T = [\ell_{1,1}, \dots, \ell_{1,n_1}, \dots, \ell_{N,1}, \dots, \ell_{N,n_N}]^T,$$

and accordingly the unobserved (grouped) weights in

$$\mathbf{w} = [\mathbf{w}_1^T, \dots, \mathbf{w}_N^T]^T = [w_{1,1}, \dots, w_{1,n_1}, \dots, w_{N,1}, \dots, w_{N,n_N}]^T.$$

Since the natural logarithm of the joint probability density function (pdf) for (12) is given by

$$\begin{aligned} \log f(\boldsymbol{\ell}, \mathbf{w}) = & -\frac{n}{2} \log(2\pi) - \frac{1}{2} \sum_{k=1}^N n_k \log(\sigma_k^2) \\ & + \frac{1}{2} \sum_{k=1}^N n_k \nu_k \log\left(\frac{\nu_k}{2}\right) - \sum_{k=1}^N n_k \log \Gamma\left(\frac{\nu_k}{2}\right) \\ & - \sum_{k=1}^N \sum_{i=1}^{n_k} \frac{1}{2} \left[\nu_k + \left(\frac{\ell_{k,i} - \mu_{k,i}}{\sigma_k} \right)^2 \right] w_{k,i} \\ & + \sum_{k=1}^N \sum_{i=1}^{n_k} \frac{1}{2} (\nu_k - 1) \log w_{k,i}, \end{aligned} \quad (15)$$

a corresponding log-likelihood function can be defined by $\log L(\boldsymbol{\theta}; \boldsymbol{\ell}, \mathbf{w}) := \log f(\boldsymbol{\ell}, \mathbf{w})$. Redefining \mathbf{h} as a function of the complete parameter vector $\boldsymbol{\theta}$ and assuming to have approximate parameter values $\boldsymbol{\theta}^{(s)}$ from a previous computational (iteration) step s , a constrained EM algorithm is employed in the sense of [63] by maximising

$$E_{\mathcal{W}|\boldsymbol{\ell}, \boldsymbol{\theta}^{(s)}} \{\log L(\boldsymbol{\theta}; \boldsymbol{\ell}, \mathcal{W})\} \quad \text{subject to} \quad \mathbf{h}(\boldsymbol{\theta}) = \mathbf{0}_{[r \times 1]} \quad (16)$$

to obtain an improved solution $\boldsymbol{\theta}^{(s+1)}$. Note that the random vector \mathcal{W} of grouped latent variables $[\mathcal{W}_{1,1}, \dots, \mathcal{W}_{N,n_N}]^T$ replaces the unavailable data \mathbf{w} within the log-likelihood. As usual, the conditional expectation of the complete-data log-likelihood function is denoted by $Q(\boldsymbol{\theta}|\boldsymbol{\theta}^{(s)})$, which may be maximised with respect to $\boldsymbol{\theta}$ under the given constraints via maximisation of the Lagrangian function

$$F(\boldsymbol{\theta}, \boldsymbol{\lambda}) = Q(\boldsymbol{\theta}|\boldsymbol{\theta}^{(s)}) - \boldsymbol{\lambda}^T \mathbf{h}(\boldsymbol{\theta}) \quad (17)$$

with respect to $\boldsymbol{\theta}$ and the Lagrange multipliers $\boldsymbol{\lambda}$. The Q -function based on (15) can be shown to take the form

$$\begin{aligned} Q(\boldsymbol{\theta}|\boldsymbol{\theta}^{(s)}) = & \text{const.} - \frac{1}{2} \sum_{k=1}^N n_k \log(\sigma_k^2) \\ & - \frac{1}{2} \sum_{k=1}^N \frac{1}{\sigma_k^2} \sum_{i=1}^{n_k} w_{k,i}^{(s)} (\ell_{k,i} - \mu_{k,i})^2 \\ & + \frac{1}{2} \sum_{k=1}^N n_k \nu_k \log \nu_k - \sum_{k=1}^N n_k \log \Gamma\left(\frac{\nu_k}{2}\right) \\ & + \frac{1}{2} \sum_{k=1}^N n_k \nu_k \left[\psi\left(\frac{\nu_k^{(s)} + 1}{2}\right) - \log(\nu_k^{(s)} + 1) \right] \\ & + \frac{1}{n_k} \sum_{i=1}^{n_k} (\log w_{k,i}^{(s)} - w_{k,i}^{(s)}), \end{aligned} \quad (18)$$

where ψ is the digamma function and where each imputed weight $w_{k,i}^{(s)}$, as the conditional expectation of the latent variable $\mathcal{W}_{k,i}$, is determined by

$$w_{k,i}^{(s)} = E_{\mathcal{W}_{k,i}|\ell_{k,i}, \boldsymbol{\theta}^{(s)}} \{\mathcal{W}_{k,i}\} = \frac{\nu_k^{(s)} + 1}{\nu_k^{(s)} + \left(\frac{\ell_{k,i} - \mu_{k,i}^{(s)}}{\sigma_k^{(s)}} \right)^2}. \quad (19)$$

Note that, in comparison to the Lagrangian function for the standard GHM in the context of the method least squares, (18) contains additional terms besides the sum of squared residuals, which are attributed to the assumption of Student instead of Gaussian distributions.

It will be convenient to fuse each of these weights with the inverse scale factor of the corresponding data group via $p_{k,i}^{(s)} = w_{k,i}^{(s)} / \sigma_k^2$, and to assemble the diagonal matrix

$$\mathbf{P}^{(s)} = \begin{bmatrix} \mathbf{P}_1^{(s)} & \dots & \mathbf{0} \\ \vdots & \ddots & \vdots \\ \mathbf{0} & \dots & \mathbf{P}_N^{(s)} \end{bmatrix} \quad (20)$$

with diagonal elements

$$\text{diag}(\mathbf{P}_k^{(s)}) = [p_{k,1}^{(s)}, \dots, p_{k,n_k}^{(s)}]^T.$$

This allows one to write the double summation in the second line of (18) as

$$\begin{aligned} \sum_{k=1}^N \frac{1}{\sigma_k^2} \sum_{i=1}^{n_k} w_{k,i}^{(s)} (\ell_{k,i} - \mu_{k,i})^2 &= \sum_{k=1}^N \sum_{i=1}^{n_k} p_{k,i}^{(s)} (\ell_{k,i} - \mu_{k,i})^2 \\ &= \sum_{k=1}^N (\boldsymbol{\mu}_k - \boldsymbol{\ell}_k)^T \mathbf{P}_k^{(s)} (\boldsymbol{\mu}_k - \boldsymbol{\ell}_k). \end{aligned}$$

As usual, $\mathbf{h}(\boldsymbol{\theta})$ is linearised if necessary. Choosing the initial Taylor point $\boldsymbol{\theta}^{[0]} := \boldsymbol{\theta}^{(s)}$, one obtains

$$\begin{aligned} \mathbf{h}(\boldsymbol{\theta}) &\approx \mathbf{h}(\boldsymbol{\theta}^{[0]}) + \frac{\partial \mathbf{h}(\boldsymbol{\theta}^{[0]})}{\partial \boldsymbol{\theta}} (\boldsymbol{\theta} - \boldsymbol{\theta}^{[0]}) \\ &= \mathbf{m} + \frac{\partial \mathbf{h}(\boldsymbol{\theta}^{[0]})}{\partial \boldsymbol{\xi}} (\boldsymbol{\xi} - \boldsymbol{\xi}^{[0]}) + \sum_{k=1}^N \frac{\partial \mathbf{h}(\boldsymbol{\theta}^{[0]})}{\partial \boldsymbol{\mu}_k} (\boldsymbol{\mu}_k - \boldsymbol{\mu}_k^{[0]}), \end{aligned}$$

where $\mathbf{m} = \mathbf{h}(\boldsymbol{\theta}^{[0]})$ is defined to be the vector of misclosures, $\mathbf{A} = \partial \mathbf{h}(\boldsymbol{\theta}^{[0]}) / \partial \boldsymbol{\xi}$ to be the $(r \times u)$ -matrix of partial derivatives of $\mathbf{h}(\boldsymbol{\theta})$ with respect to $\boldsymbol{\xi}$ evaluated at $\boldsymbol{\theta}^{[0]}$, and $\mathbf{B}_k = \partial \mathbf{h}(\boldsymbol{\theta}^{[0]}) / \partial \boldsymbol{\mu}_k$ the $(r \times n_k)$ -matrix of partial derivatives of $\mathbf{h}(\boldsymbol{\theta})$ with respect to $\boldsymbol{\mu}_k$ (also evaluated at $\boldsymbol{\theta}^{[0]}$). This yields

$$\begin{aligned} \mathbf{h}(\boldsymbol{\theta}) &\approx \mathbf{m} + \mathbf{A}(\boldsymbol{\xi} - \boldsymbol{\xi}^{[0]}) + \sum_{k=1}^N \mathbf{B}_k(\boldsymbol{\mu}_k - \boldsymbol{\ell}_k + \boldsymbol{\ell}_k - \boldsymbol{\mu}_k^{[0]}) \\ &= \mathbf{A}\boldsymbol{\Delta\xi} + \sum_{k=1}^N \mathbf{B}_k(\boldsymbol{\mu}_k - \boldsymbol{\ell}_k) + \mathbf{m} + \sum_{k=1}^N \mathbf{B}_k(\boldsymbol{\ell}_k - \boldsymbol{\mu}_k^{[0]}) \\ &= \mathbf{A}\boldsymbol{\Delta\xi} + \sum_{k=1}^N \mathbf{B}_k(\boldsymbol{\mu}_k - \boldsymbol{\ell}_k) + \mathbf{m}_p \end{aligned} \quad (21)$$

with $\boldsymbol{\Delta\xi} = \boldsymbol{\xi} - \boldsymbol{\xi}^{[0]}$ and pseudo-misclosures

$$\mathbf{m}_p = \mathbf{m} + \sum_{k=1}^N \mathbf{B}_k(\boldsymbol{\ell}_k - \boldsymbol{\mu}_k^{[0]}). \quad (22)$$

Then, the problem of maximising (17) is replaced by the problem of maximising

$$F(\boldsymbol{\theta}, \boldsymbol{\lambda}) = Q(\boldsymbol{\theta} | \boldsymbol{\theta}^{(s)}) - \boldsymbol{\lambda}^T \left(\mathbf{A}\boldsymbol{\Delta\xi} + \sum_{k=1}^N \mathbf{B}_k(\boldsymbol{\mu}_k - \boldsymbol{\ell}_k) + \mathbf{m}_p \right). \quad (23)$$

Within the M-step, the first partial derivatives of this Lagrangian function with respect to all of the parameter groups in $\boldsymbol{\theta}$ are set equal to zero. According to the principle of expectation conditional maximisation (ECM), one parameter group may be optimised at a time while using the most recent estimates of the parameters of other groups when necessary. As part of the first ECM-step, first the parameter group consisting of $\boldsymbol{\Delta\xi}, \boldsymbol{\mu}_1, \dots, \boldsymbol{\mu}_N$ and $\boldsymbol{\lambda}$ is considered, for which one finds

$$\frac{\partial F(\boldsymbol{\theta}, \boldsymbol{\lambda})}{\partial \boldsymbol{\Delta\xi}} = -\mathbf{A}^T \boldsymbol{\lambda} = \mathbf{0}_{[u \times 1]}, \quad (24)$$

$$\frac{\partial F(\boldsymbol{\theta}, \boldsymbol{\lambda})}{\partial \boldsymbol{\mu}_k} = -\mathbf{P}_k^{(t)}(\boldsymbol{\mu}_k - \boldsymbol{\ell}_k) - \mathbf{B}_k^T \boldsymbol{\lambda} = \mathbf{0}_{[n_k \times 1]}, \quad (25)$$

$$\frac{\partial F(\boldsymbol{\theta}, \boldsymbol{\lambda})}{\partial \boldsymbol{\lambda}} = -\left(\mathbf{A}\boldsymbol{\Delta\xi} + \sum_{k=1}^N \mathbf{B}_k(\boldsymbol{\mu}_k - \boldsymbol{\ell}_k) + \mathbf{m}_p \right) = \mathbf{0}_{[r \times 1]}. \quad (26)$$

Here, (25) gives

$$\boldsymbol{\mu}_k - \boldsymbol{\ell}_k = (\mathbf{P}_k^{(s)})^{-1} \mathbf{B}_k^T \boldsymbol{\lambda},$$

which can be substituted into (26), giving

$$\sum_{k=1}^N \mathbf{B}_k (\mathbf{P}_k^{(s)})^{-1} \mathbf{B}_k^T \boldsymbol{\lambda} + \mathbf{A}\boldsymbol{\Delta\xi} + \mathbf{m}_p = \mathbf{0}_{[r \times 1]}.$$

Taking the inverted weight matrix $(\mathbf{P}^{(s)})^{-1}$ as the scaling matrix $\boldsymbol{\Sigma}^{(s)}$, which has the blocks

$$\boldsymbol{\Sigma}^{(s)} = \begin{bmatrix} \boldsymbol{\Sigma}_1^{(s)} & \dots & \mathbf{0} \\ \vdots & \ddots & \vdots \\ \mathbf{0} & \dots & \boldsymbol{\Sigma}_N^{(s)} \end{bmatrix} = \begin{bmatrix} (\mathbf{P}_1^{(s)})^{-1} & \dots & \mathbf{0} \\ \vdots & \ddots & \vdots \\ \mathbf{0} & \dots & (\mathbf{P}_N^{(s)})^{-1} \end{bmatrix}, \quad (27)$$

one arrives at the normal equation system derived in [35, Section 3] for a single observation group. In view of the applications considered in subsequent sections, the matrices \mathbf{A} and $\mathbf{B} = [\mathbf{B}_1 \dots \mathbf{B}_N]$ may be assumed to have full rank. Consequently, the inverses of $\mathbf{B}\boldsymbol{\Sigma}^{(s)}\mathbf{B}^T = \sum_{k=1}^N \mathbf{B}_k \boldsymbol{\Sigma}_k^{(s)} \mathbf{B}_k^T$ and $\mathbf{A}^T (\mathbf{B}\boldsymbol{\Sigma}^{(s)}\mathbf{B}^T)^{-1} \mathbf{A}$ also exist, so that the solution for the current parameter groups can be computed through

$$\begin{aligned} \boldsymbol{\Delta\xi} &= -\left(\mathbf{A}^T \left(\sum_{k=1}^N \mathbf{B}_k \boldsymbol{\Sigma}_k^{(s)} \mathbf{B}_k^T \right)^{-1} \mathbf{A} \right)^{-1} \\ &\quad \mathbf{A}^T \left(\sum_{k=1}^N \mathbf{B}_k \boldsymbol{\Sigma}_k^{(s)} \mathbf{B}_k^T \right)^{-1} \mathbf{m}_p, \end{aligned} \quad (28)$$

$$\boldsymbol{\xi}^{[1]} = \boldsymbol{\xi}^{[0]} + \boldsymbol{\Delta\xi}, \quad (29)$$

$$\boldsymbol{\lambda}^{[1]} = \left(\sum_{k=1}^N \mathbf{B}_k \boldsymbol{\Sigma}_k^{(s)} \mathbf{B}_k^T \right)^{-1} (-\mathbf{A}\boldsymbol{\Delta\xi}^{[1]} - \mathbf{m}_p), \quad (30)$$

$$\boldsymbol{\mu}_k^{[1]} = \boldsymbol{\ell}_k + \boldsymbol{\Sigma}_k^{(s)} \mathbf{B}_k^T \boldsymbol{\lambda}^{[1]}. \quad (31)$$

In these equations, $\boldsymbol{\Sigma}^{(s)}$ contains the scale factors $\sigma_1^2, \dots, \sigma_N^2$ still to be estimated within the current M-step. Applying the aforementioned ECM principle, one may substitute for these the available estimates $(\sigma_1^2)^{(s)}, \dots, (\sigma_N^2)^{(s)}$ from the preceding EM iteration step. Applying the principle of constrained EM described in [63], the estimates $\boldsymbol{\xi}^{[1]}$ and $\boldsymbol{\mu}_k^{[1]}$ should now be used (alongside the available $(\sigma_1^2)^{(s)}, \dots, (\sigma_N^2)^{(s)}$ and $v_1^{(s)}, \dots, v_N^{(s)}$ of the previous Taylor point $\boldsymbol{\theta}^{[0]}$) to repeat the linearisation of $\mathbf{h}(\boldsymbol{\theta})$ with a new Taylor point $\boldsymbol{\theta}^{[1]}$. When the misclosures become small enough (say, at iteration step t , when the maximum absolute misclosure is less than a specified threshold ε), the first ECM-step is complete, providing the estimates $\boldsymbol{\xi}^{(s+1)} := \boldsymbol{\xi}^{[t]}$ and $\boldsymbol{\mu}^{(s+1)} := \boldsymbol{\mu}^{[t]}$.

In the second ECM-step, new estimates of the scale factors associated with the different observation groups are sought. One evidently obtains

$$\frac{\partial F(\boldsymbol{\theta}, \boldsymbol{\lambda})}{\partial \sigma_k^2} = -\frac{n_k}{2\sigma_k^2} - \frac{1}{2\sigma_k^4} \sum_{i=1}^{n_k} w_{k,i}^{(s)} (\ell_{k,i} - \mu_{k,i})^2 = 0, \quad (32)$$

and then, substituting the already available estimates $\boldsymbol{\mu}^{(s+1)}$,

$$(\sigma_k^2)^{(s+1)} = \frac{1}{n_k} \sum_{i=1}^{n_k} w_{k,i}^{(s)} (\ell_{k,i} - \mu_{k,i}^{(s+1)})^2. \quad (33)$$

Therefore, the *a posteriori* variances of the observables are calculated as

$$(s_k^2)^{(s+1)} = (\sigma_k^2)^{(s+1)} \left(\frac{v_k^{(s+1)}}{v_k^{(s+1)} - 2} \right). \quad (34)$$

In case of $v_k^{(s+1)} < 2$, the variance $(s_k^2)^{(s+1)}$ is not well defined, so that this estimate may become extremely small and thus unrealistic. If desired, the preceding estimation step can be extended to a VCE as shown in [57].

Regarding the final parameter group consisting of the dofs v_1, \dots, v_N , an ECM *either* (ECME) step can be employed, in which the log-likelihood function of the original t-distribution model is maximised with respect to these variables. In analogy to Equation (27) in [64], this step requires zero searches of $v_1^{(s+1)}, \dots, v_N^{(s+1)}$ within the N equations

$$\begin{aligned} 0 = & 1 + \log v_k^{(s+1)} - \psi \left(\frac{v_k^{(s+1)}}{2} \right) \\ & + \psi \left(\frac{v_k^{(s+1)} + 1}{2} \right) - \log (v_k^{(s+1)} + 1) \\ & + \sum_{i=1}^{n_k} \frac{1}{n_k} (\log w_{k,i}^{(s+1)} - w_{k,i}^{(s+1)}), \end{aligned} \quad (35)$$

with variables

$$w_{k,i}^{(s+1)} = \frac{v_k^{(s+1)} + 1}{v_k^{(s+1)} + \left(\frac{\ell_{k,i} - \mu_{k,i}^{(s+1)}}{\sigma_k^{(s+1)}} \right)^2}. \quad (36)$$

The zero search is carried out by means of an interval Newton method (Algorithm 6.1 in [65]), which always gave a unique solution within an extremely narrow interval.

4.2 EM algorithm for a quasi-Gauss-Markov model with t-distributed pseudo-misclosures

In this section, a quasi-Gauss-Markov model is introduced, which is adjusted by means of an EM algorithm based on the assumption of t-distributed pseudo-misclosures. The algorithm starts with the linearisation of the condition

Algorithm 1: EM algorithm for the GHM with groups of t-distributed errors.

Input : $\ell_1, \dots, \ell_N; \mathbf{h}(\boldsymbol{\xi}, \boldsymbol{\mu}); \boldsymbol{\xi}^{(0)}$; itermax; $\varepsilon, \varepsilon_v$

Output: $\hat{\boldsymbol{\xi}}; \hat{\boldsymbol{\mu}}; \hat{\sigma}_1^2, \dots, \hat{\sigma}_N^2; \hat{v}_1, \dots, \hat{v}_N$

$\boldsymbol{\mu}_k^{(0)} := \ell_k$

$\mathbf{m} = \mathbf{h}(\boldsymbol{\xi}^{(0)}, \boldsymbol{\mu}^{(0)}), \mathbf{A} = \frac{\partial \mathbf{h}(\boldsymbol{\xi}^{(0)}, \boldsymbol{\mu}^{(0)})}{\partial \boldsymbol{\xi}}, \mathbf{B}_k = \frac{\partial \mathbf{h}(\boldsymbol{\xi}^{(0)}, \boldsymbol{\mu}^{(0)})}{\partial \boldsymbol{\mu}_k}$

$\boldsymbol{\xi}^{(1)} =$

$\boldsymbol{\xi}^{(0)} - \left(\mathbf{A}^T \left(\sum_{k=1}^N \mathbf{B}_k \mathbf{B}_k^T \right)^{-1} \mathbf{A} \right)^{-1} \mathbf{A}^T \left(\sum_{k=1}^N \mathbf{B}_k \mathbf{B}_k^T \right)^{-1} \mathbf{m}$

$\boldsymbol{\mu}_k^{(1)} = \ell_k + \mathbf{B}_k^T \left(\sum_{k=1}^N \mathbf{B}_k \mathbf{B}_k^T \right)^{-1} (-\mathbf{A} \Delta \boldsymbol{\xi}^{(1)} - \mathbf{m})$

$(\sigma_k^2)^{(1)} = \frac{1}{n_k} \sum_{i=1}^{n_k} (\ell_{k,i} - \mu_{k,i}^{(1)})^2$

$v_k^{(1)} := 30$

for $s = 1 \dots \text{itermax}$ **do**

$w_{k,i}^{(s)} = \frac{v_k^{(s)} + 1}{v_k^{(s)} + \left(\frac{\ell_{k,i} - \mu_{k,i}^{(s)}}{\sigma_k^{(s)}} \right)^2},$

$\boldsymbol{\Sigma}_k^{(s)} = \begin{bmatrix} (\sigma_k^2)^{(s)} / w_{k,1}^{(s)} & \dots & 0 \\ \vdots & \ddots & \vdots \\ 0 & \dots & (\sigma_k^2)^{(s)} / w_{k,n_k}^{(s)} \end{bmatrix}$

$\boldsymbol{\xi}^{[0]} := \boldsymbol{\xi}^{(s)}, \boldsymbol{\mu}^{[0]} := \boldsymbol{\mu}^{(s)}$

for $t = 0 \dots \text{itermax}$ **do**

$\mathbf{m}_p = \mathbf{h}(\boldsymbol{\xi}^{[t]}, \boldsymbol{\mu}^{[t]}) + \sum_{k=1}^N \mathbf{B}_k (\ell_k - \mu_k^{[t]}),$

$\mathbf{A} = \frac{\partial \mathbf{h}(\boldsymbol{\xi}^{[t]}, \boldsymbol{\mu}^{[t]})}{\partial \boldsymbol{\xi}}, \mathbf{B}_k = \frac{\partial \mathbf{h}(\boldsymbol{\xi}^{[t]}, \boldsymbol{\mu}^{[t]})}{\partial \boldsymbol{\mu}_k}$

$\boldsymbol{\xi}^{[t+1]} = \boldsymbol{\xi}^{[t]} - \left(\mathbf{A}^T \left(\sum_{k=1}^N \mathbf{B}_k \boldsymbol{\Sigma}_k^{(s)} \mathbf{B}_k^T \right)^{-1} \mathbf{A} \right)^{-1} \mathbf{A}^T \left(\sum_{k=1}^N \mathbf{B}_k \boldsymbol{\Sigma}_k^{(s)} \mathbf{B}_k^T \right)^{-1} \mathbf{m}_p$

$\boldsymbol{\mu}_k^{[t+1]} = \ell_k +$

$\boldsymbol{\Sigma}_k^{(s)} \mathbf{B}_k^T \left(\sum_{k=1}^N \mathbf{B}_k \boldsymbol{\Sigma}_k^{(s)} \mathbf{B}_k^T \right)^{-1} (-\mathbf{A} \Delta \boldsymbol{\xi}^{[t+1]} - \mathbf{m}_p)$

$\boldsymbol{\xi}^{(s+1)} := \boldsymbol{\xi}^{[t+1]}, \boldsymbol{\mu}^{(s+1)} := \boldsymbol{\mu}^{[t+1]}$

$(\sigma_k^2)^{(s+1)} = \frac{1}{n_k} \sum_{i=1}^{n_k} w_{k,i}^{(s)} (\ell_{k,i} - \mu_{k,i}^{[t+1]})^2$

Solve (35) using (36) for $k = 1, \dots, N$

$d = \max(\max |\boldsymbol{\xi}^{(s)} - \boldsymbol{\xi}^{(s+1)}|, |(\sigma_k^2)^{(s)} - (\sigma_k^2)^{(s+1)}|),$

$d_v = |v_k^{(s)} - v_k^{(s+1)}|$

if $s < \text{itermax}$ **and** $d > \varepsilon$ **and** $d_v > \varepsilon_v$ **then**

$s = s + 1$

else

$\hat{\boldsymbol{\xi}} := \boldsymbol{\xi}^{(s+1)}, \hat{\boldsymbol{\mu}} := \boldsymbol{\mu}^{(s+1)}, \hat{\sigma}_k^2 := (\sigma_k^2)^{(s+1)},$

$\hat{v}_k := v_k^{(s+1)}$; **break**

equations at some Taylor point $\boldsymbol{\theta}^{[t]}$ and rewriting (21)–(22), respectively, as

$$\mathbf{h}(\boldsymbol{\theta}) \approx \mathbf{A} \Delta \boldsymbol{\xi} + \mathbf{B}(\boldsymbol{\mu} - \boldsymbol{\ell}) + \mathbf{m}_p \quad (37)$$

and

$$\mathbf{m}_p = \mathbf{m} + \mathbf{B}(\boldsymbol{\ell} - \boldsymbol{\mu}^{(t)}). \quad (38)$$

We do not group the observations $\boldsymbol{\ell}$, location parameters $\boldsymbol{\mu}$ and constraint matrix \mathbf{B} since we do not make distributional assumptions about different groups of observables. Instead, we view

$$\bar{\mathbf{e}} = \mathbf{B}(\boldsymbol{\ell} - \boldsymbol{\mu}) \quad (39)$$

as linearly transformed residuals and as realizations of independently t-distributed random deviations

$$\bar{\varepsilon}_j \stackrel{\text{ind.}}{\sim} t_\nu(0, \sigma^2) \quad (j \in \{1, \dots, r\}). \quad (40)$$

This assumption makes sense if no two of these random deviations share the same (stochastically independent) observables in $\mathcal{L}_1, \dots, \mathcal{L}_n$. To establish an EM algorithm, the preceding t-distribution model is replaced by the equivalent Gaussian variance-inflation model

$$\bar{\varepsilon}_j | w_j \stackrel{\text{ind.}}{\sim} N(0, \sigma^2/w_j), \quad w_j \stackrel{\text{ind.}}{\sim} \frac{\chi_\nu^2}{\nu}. \quad (41)$$

Treating now the pseudo-misclosures as new (transformed) observations $\bar{\boldsymbol{\ell}} = \mathbf{m}_p$ and defining $\bar{\mathbf{A}} = -\mathbf{A}$ as well as $\bar{\boldsymbol{\xi}} = \Delta \boldsymbol{\xi}$, we may rewrite (38) as observation equations

$$\bar{\boldsymbol{\ell}} = \bar{\mathbf{A}} \bar{\boldsymbol{\xi}} + \bar{\mathbf{e}} \quad (42)$$

of a quasi-Gauss-Markov model with t-distributed (transformed) random deviations. The stochastic model (41) is defined by the joint pdf

$$\begin{aligned} \log f(\bar{\mathbf{e}}, \mathbf{w}) = & -\frac{r}{2} \log(2\pi) - \frac{r}{2} \log(\sigma^2) + \frac{r\nu}{2} \log\left(\frac{\nu}{2}\right) \\ & - r \log \Gamma\left(\frac{\nu}{2}\right) - \sum_{j=1}^r \frac{1}{2} \left[\nu + \left(\frac{\bar{\ell}_j - \bar{\mathbf{A}}_j \bar{\boldsymbol{\xi}}}{\sigma} \right)^2 \right] w_j \\ & + \sum_{j=1}^r \frac{1}{2} (\nu - 1) \log w_j. \end{aligned} \quad (43)$$

In this case, the total parameter vector constitutes $\bar{\boldsymbol{\theta}} = [\bar{\boldsymbol{\xi}}^T, \sigma^2, \nu]^T$ and the log-likelihood function $\log L(\bar{\boldsymbol{\theta}}; \boldsymbol{\ell}, \mathbf{w}) := \log f(\bar{\mathbf{e}}, \mathbf{w})$, which depends on the given observations $\boldsymbol{\ell}$ through $\bar{\mathbf{e}}$ via (42). The imputation of the weights

$$w_j^{(0)} = E_{\mathcal{W}_j | \bar{\mathbf{e}}; \bar{\boldsymbol{\theta}}^{(0)}} \{\mathcal{W}_j\} = \frac{\nu^{(0)} + 1}{\nu^{(0)} + \left(\frac{\bar{\ell}_j - \bar{\mathbf{A}}_j \bar{\boldsymbol{\xi}}^{(0)}}{\sigma^{(0)}} \right)^2}, \quad (44)$$

and the maximisation of the Q -function

$$Q(\bar{\boldsymbol{\theta}} | \bar{\boldsymbol{\theta}}^{(0)}) = E_{\mathcal{W} | \bar{\mathbf{e}}; \bar{\boldsymbol{\theta}}^{(0)}} \{\log L(\bar{\boldsymbol{\theta}}; \boldsymbol{\ell}, \mathcal{W})\}$$

$$\begin{aligned} = & \text{const.} - \frac{r}{2} \log(\sigma^2) - \frac{1}{2\sigma^2} \sum_{j=1}^r w_j^{(0)} (\bar{\ell}_j - \bar{\mathbf{A}}_j \bar{\boldsymbol{\xi}})^2 \\ & + \frac{r\nu}{2} \log \nu - r \log \Gamma\left(\frac{\nu}{2}\right) + \frac{r\nu}{2} \left[\psi\left(\frac{\nu^{(0)} + 1}{2}\right) \right. \\ & \left. - \log(\nu^{(0)} + 1) + \frac{1}{r} \sum_{j=1}^r (\log w_j^{(0)} - w_j^{(0)}) \right] \end{aligned} \quad (45)$$

is accomplished by employing the basic EM algorithm described in [62]. Convergence of this iterative algorithm (say, at iteration step s) yields the estimate $\hat{\bar{\boldsymbol{\xi}}} = \hat{\bar{\boldsymbol{\xi}}}^{(s)}$, as an estimate of $\Delta \boldsymbol{\xi}$. Adding the latter to the previous functional parameter solution $\boldsymbol{\xi}^{[t]}$ of the current Taylor point gives us $\boldsymbol{\xi}^{[t+1]}$. To obtain a new location parameter solution $\boldsymbol{\mu}^{[t+1]}$, the estimated residuals $\hat{\bar{\mathbf{e}}} = \bar{\mathbf{e}}^{(s)}$ resulting from the EM algorithm must first be transformed from the vector space \mathbb{R}^r to an element $\hat{\mathbf{e}} = \boldsymbol{\ell} - \hat{\boldsymbol{\mu}}$ of the vector space \mathbb{R}^n . Although the mapping (39) cannot be inverted, one can compute

$$\boldsymbol{\mu}^{[t+1]} = \boldsymbol{\ell} - (\mathbf{B}^T \mathbf{B})^+ \mathbf{B}^T \hat{\bar{\mathbf{e}}} \quad (46)$$

by using the pseudo-inverse $(\mathbf{B}^T \mathbf{B})^+$ of the rank-deficient matrix $\mathbf{B}^T \mathbf{B}$. Alternatively, one may evaluate

$$\boldsymbol{\mu}^{[t+1]} = \boldsymbol{\ell} + \mathbf{B}^T (\mathbf{B} \mathbf{B}^T)^{-1} (-\mathbf{A} \Delta \boldsymbol{\xi} - \mathbf{m}_p) \quad (47)$$

according to (30)–(31), as suggested by [66, Section 6.2] in the context of least-squares adjustment.

Defining then a new Taylor point $\boldsymbol{\theta}^{[t+1]}$ by means of the new estimates, the linearisation can be improved iteratively, as shown in Algorithm 2.

4.3 Classical adjustment model based on Gauss-Helmert model using statistical test and variance component estimation

In this section, we consider stochastically independent observation vectors \mathbf{l}_k (with $k \in \{1, \dots, N\}$) that belong to N distinct groups and each group k consists of n_k observables, which follows a normal distribution. Thus, the stochastic observation vector and its corresponding error vector model read

$$\mathbf{l}_k \sim N(\boldsymbol{\mu}_k, \boldsymbol{\Sigma}_k), \quad \mathbf{e}_k \sim N(\mathbf{0}, \boldsymbol{\Sigma}_k) \quad (48)$$

where $\boldsymbol{\mu}_k$ is the expected values of \mathbf{l}_k , $\boldsymbol{\Sigma}_k$ is the positive definite variance-covariance matrix of \mathbf{l}_k and $E(\mathbf{e}_k) = \mathbf{0}$.

The non-linear GHM is defined based on Equation 13, and is solved by minimising the square sum of the residuals for all the observables n_k . Subsequently, the linearisation is carried out according to (21). Next, the $\boldsymbol{\xi}$ and $\boldsymbol{\mu}$

Algorithm 2: Second variant of QGMM using EM.

Input : $\ell; \mathbf{h}(\xi, \mu); \xi^{(0)}$; itermax; $\varepsilon, \varepsilon_v$
Output: $\hat{\xi}; \hat{\mu}; \hat{\sigma}^2; \hat{v}$
 $\mu^{(0)} := \ell$
for $t = 0 \dots \text{itermax}$ **do**
 $\mathbf{A} = \frac{\partial \mathbf{h}(\xi^{(t)}, \mu^{(t)})}{\partial \xi}$
 $\mathbf{B} = \frac{\partial \mathbf{h}(\xi^{(t)}, \mu^{(t)})}{\partial \mu}$
 $\mathbf{m} = \mathbf{h}(\xi^{(t)}, \mu^{(t)})$
 $\mathbf{m}_p = \mathbf{m} + \mathbf{B}(\ell - \mu^{(t)})$
 $\bar{\ell} := \mathbf{w}_m$
 $\bar{\mathbf{A}} := -\mathbf{A}$
 Compute $\hat{\xi}$ and $\hat{\mathbf{e}}$ by means of Algorithm 1
 $\Delta \xi := \hat{\xi}$
 $\xi^{(t+1)} = \xi^{(t)} + \Delta \xi$
 $\mu^{(t+1)} = \ell - (\mathbf{B}^T \mathbf{B})^{-1} \mathbf{B}^T \hat{\mathbf{e}}$
 $w_{\max} = \max(|\mathbf{h}(\xi^{(t+1)}, \mu^{(t+1)})|)$
 if $w_{\max} > \varepsilon$ **then**
 $t = t + 1$
 else
 break

are estimated based on (29) and (31). For more information concerning the GHM, please refer to [67]. In the entire procedure, the dofs are determined by the difference of the total number of condition equations (i. e., the number m of rows of the \mathbf{B} matrix) and number of unknown parameters (u). In addition, the weight is calculated for each distinct group instead of each individual observables n_k with

$$\mathbf{P}_k = \sigma_0^2 \Sigma_k^{-1} \quad (49)$$

where σ_0^2 is the unknown theoretical variance of unit weight, which can be considered equal to 1.

The adjustment model includes three iterative procedures. In the first iterative procedure, a convergence is fulfilled until the maximum absolute differences of the estimated unknown parameters are less than a specified threshold ε ($\approx 10^{-14}$)

$$d = (\max |\xi^{(s)} - \xi^{(s+1)}|). \quad (50)$$

In the second iterative procedure, VCE is applied to recalculate the covariance matrix of the observations as proposed by [57] (see Algorithm 3). For this purpose, the co-

variance matrix of the observations is calculated as

$$\Sigma_0 = \sum_{k=1}^N \mathbf{V}_k = \begin{bmatrix} V_1 & \dots & 0 \\ \vdots & \ddots & \vdots \\ 0 & \dots & V_N \end{bmatrix} = \begin{bmatrix} s_1^2 \sigma_1^2 & \dots & 0 \\ \vdots & \ddots & \vdots \\ 0 & \dots & s_N^2 \sigma_N^2 \end{bmatrix} \quad (51)$$

where the factors $\{s_1^2, \dots, s_N^2\}$ are chosen based on a priori variances of the observables given by the manufacturer in such a way that variance components $\{\sigma_1^2, \dots, \sigma_N^2\}$ have values close to 1 [57]. Furthermore, the diagonal elements are arranged based on the indices of the observations from the bundle adjustment procedure. Therefore, the symmetric matrix \mathbf{W}_b , vector \mathbf{q} , symmetric matrix \mathbf{S} and $\hat{\sigma}_k$ are calculated, respectively as described by [57] (see Algorithm 3)

$$\mathbf{W}_b = \left(\sum_{k=1}^N \mathbf{B}_k \Sigma_k^{(c)} \mathbf{B}_k^T \right)^{-1} - \left(\sum_{k=1}^N \mathbf{B}_k \Sigma_k^{(c)} \mathbf{B}_k^T \right)^{-1} \mathbf{A} \left(\mathbf{A}^T \left(\sum_{k=1}^N \mathbf{B}_k \Sigma_k^{(c)} \mathbf{B}_k^T \right)^{-1} \mathbf{A} \right)^{-1} \mathbf{A}^T \left(\sum_{k=1}^N \mathbf{B}_k \Sigma_k^{(c)} \mathbf{B}_k^T \right)^{-1} \quad (52)$$

$$\mathbf{q} = (q_i) = \left(\mathbf{m}_p^T \mathbf{W}_b \left(\sum_{k=1}^N \mathbf{B}_k \right) \mathbf{V}_i \left(\sum_{k=1}^N \mathbf{B}_k^T \right) \mathbf{W}_b \mathbf{m}_p \right) \quad \text{for } i \in \{1, \dots, k\} \quad (53)$$

$$\mathbf{S} = \text{tr} \left(\mathbf{W}_b \left(\sum_{k=1}^N \mathbf{B}_k \right) \mathbf{V}_i \left(\sum_{k=1}^N \mathbf{B}_k^T \right) \mathbf{W}_b \left(\sum_{k=1}^N \mathbf{B}_k \right) \mathbf{V}_j \left(\sum_{k=1}^N \mathbf{B}_k^T \right) \right) \quad \text{for } i, j \in \{1, \dots, k\} \quad (54)$$

$$\hat{\sigma}_k = \mathbf{S}^{-1} \mathbf{q}. \quad (55)$$

This procedure proceeds until $\hat{\sigma}_k = [1, \dots, 1]^T$ is obtained with a sufficient estimation accuracy. Then, the estimated factors, which are the posteriori variances of the observables, are calculated as

$$\hat{s}_k^2 = \max(\mathbf{V}_k) \quad \text{for } k \in \{1, \dots, N\} \quad (56)$$

In the third iterative procedure, firstly, a global test is performed to evaluate the correctness of the results due to consideration of all observations, deterministic (functional) and stochastic models into the computation of $\hat{\sigma}_0^2$ [68]. The null and alternative hypotheses are defined as proposed by [69] and [70] with

$$H_0 : \sigma_0^2 = \hat{\sigma}_0^2 \quad \text{vs.} \quad H_1 : \sigma_0^2 \neq \hat{\sigma}_0^2. \quad (57)$$

Next, the test value is defined under the normality of the observation as proposed by [68] and [71] with

$$T_{\chi^2} = \frac{\hat{\sigma}_0^2}{\sigma_0^2} (m - u). \quad (58)$$

If $T_{\chi^2} \leq \chi_{(m-u, 1-\alpha)}^2$ with consideration of $\alpha = 0.003$ or $\alpha = 0.05$, the null hypothesis is accepted otherwise it is rejected, which means observations are not normally distributed.

The local test (Data snooping [72]) is applied for a few observables (e. g. image target observables in both x and y directions, target observables in 3D point clouds in X , Y and Z directions, LT target observables in X , Y and Z directions) or a observable (e. g. Az observable of the TLS) of each group of observations to reject the outliers and large residuals in the adjustment model iteratively and one by one. Consequently, the statistical testing such as χ^2 or t-student tests are beneficial to interpret the adjustment results and to evaluate the uncertainties of the measurements and unknown parameters. However, they are appropriate to identify outliers in the observations and exclude them from the solutions [73]. Therefore, the χ^2 test with 99.7 % and 95 % confidence levels are applied with

$$T_{\chi_g^2} = \frac{\mathbf{e}_g^T \mathbf{P}_g \mathbf{e}_g}{\sigma_0^2} \quad (59)$$

where $T_{\chi_g^2}$ is the χ^2 test value, the \mathbf{e}_g is the residuals of a few observables and \mathbf{P}_g stands for the weight matrix of a few observables.

Alternatively, the t-student test can be applied by a normalised residuum with

$$T_{t_g} = \frac{\mathbf{e}_g}{\hat{s}_k} \quad (60)$$

where T_{t_g} is the t-student test value and \hat{s}_k is standard deviation of the residuals for each group of the observation. Subsequently, the computed normalized residuum is compared with the predetermined limit (here 2.5 to 4.0 as proposed by [71]) whether above it (outlier) or below it (no outlier) to reject or accept the null hypothesis, respectively. This procedure proceeds till no outlier or large residual remains in the set of observations.

5 Experiments and results

As part of two different case studies, six independent experiments were carried out in the 3D laboratory at our institute. The room has a size of 6.2 m (width) \times 8.6 m (length) \times 4.9 m (height), and is covered with randomly placed signalised targets on the walls, ceiling and floor. The 6 EOPs between the TLS and digital camera and the 7 EOPs between the TLS and LT were estimated within the three different adjustment models, and compared regarding the accuracy, reliability, robustness and run time speed

Algorithm 3: GHM based on the statistical test and VCE.

Input : $\ell_1, \dots, \ell_N; \mathbf{h}(\xi, \mu); \xi^{(0)}; s_1^2, \dots, s_N^2; \text{itermax}; \varepsilon$

Output: $\hat{\xi}; \hat{\mu}; \hat{s}_1^2, \dots, \hat{s}_N^2$

$\mu_k^{(0)} := \ell_k$

$\mathbf{m} = \mathbf{h}(\xi^{(0)}, \mu^{(0)}), \mathbf{A} = \frac{\partial \mathbf{h}(\xi^{(0)}, \mu^{(0)})}{\partial \xi}, \mathbf{B}_k = \frac{\partial \mathbf{h}(\xi^{(0)}, \mu^{(0)})}{\partial \mu_k}$

Compute $\xi^{(1)}$ by (29)

$\mu_k^{(1)} = \ell_k + \mathbf{B}_k^T (\sum_{k=1}^N \mathbf{B}_k \mathbf{B}_k^T)^{-1} (-\mathbf{A} \Delta \xi^{(1)} - \mathbf{m})$

for $c = 1 \dots \text{itermax}$ **do**

for $s = 1 \dots \text{itermax}$ **do**

$$\Sigma_k^{(c)} = \begin{bmatrix} (s_1^2 \sigma_1^2)^{(c)} & \dots & 0 \\ \vdots & \ddots & \vdots \\ 0 & \dots & (s_N^2 \sigma_N^2)^{(c)} \end{bmatrix}$$

$\xi^{[0]} := \xi^{(s)}, \mu^{[0]} := \mu^{(s)}$

for $t = 0 \dots \text{itermax}$ **do**

$\mathbf{e}_k = \ell_k - \mu_k^{[t]}$

$\mathbf{m}_p = \mathbf{h}(\xi^{[t]}, \mu^{[t]}) + \sum_{k=1}^N \mathbf{B}_k \mathbf{e}_k$

$\mathbf{A} = \frac{\partial \mathbf{h}(\xi^{[t]}, \mu^{[t]})}{\partial \xi}, \mathbf{B}_k = \frac{\partial \mathbf{h}(\xi^{[t]}, \mu^{[t]})}{\partial \mu_k}$

Compute $\Delta \xi$ by (28)

$\xi^{(s+1)} = \xi^{(s)} + \Delta \xi$

$d = (\max |\xi^{(s)} - \xi^{(s+1)}|),$

if $d > \varepsilon$ **then**

└ $s = s + 1$

else

└ **break**

Compute \mathbf{W}_b by (52)

$(\hat{\sigma}_k)^{(1)} = [1, \dots, 1]^T$

for $r = 1 \dots \text{itermax}$ **do**

$\sum_{k=1}^N \mathbf{V}_k = |(s_k^2)^{(c)} (\hat{\sigma}_k)^{(r)}|$

Compute \mathbf{q} by (53)

Compute \mathbf{S} by (54)

$(\hat{\sigma}_k)^{(r)} = \mathbf{S}^{-1} \mathbf{q}$

if $(\max |(\hat{\sigma}_k)^{(r)} - [1, \dots, 1]^T|) < \varepsilon$ **then**

└ **break**

else

└ $r = r + 1$

$(\hat{s}_k^2)^{(c)} = \max(\mathbf{V}_k) \text{ for } k \in \{1, \dots, N\}$

Global and local tests based on χ^2 test

$d_s = \max(|(\hat{s}_k^2)^{(c)} - (\hat{s}_k^2)^{(c+1)}|)$

if $d_s > \varepsilon$ and \exists (rejected n_k) **then**

└ $c = c + 1$

else

└ **break**

up procedure. For ease of expressions, the first to third adjustment model names were abbreviated to EM-GHM, EM-qGMM and GHM-VCE, respectively.

5.1 Case study I: External calibration between TLS and digital camera

In the first case study, the three different adjustment models of section 4 are applied to achieve the external calibration of the TLS and digital camera. Additionally, due to mounting and demounting the digital camera on top of the TLS by the clamping system, the 6 EOPs between the fused sensors are slightly changing, which their variations are investigated in 6 independent experiments.

The observables consist of 3 groups of the observations, which are the rectified target coordinates in the image space (Image target observations: ℓ_1), the target coordinates in the 3D point clouds coordinate system (TLS target observations: ℓ_2) and the Az angle observables of the TLS (ℓ_3).

The number of observables for each group of the observation are represented in Table 1. The number of image target observations varied with the number of images, the possible number of viewed targets in each image and the overlapping of the images. However, the number of image target observations and their corresponding TLS target observations are equivalent in the adjustment model.

The condition equations (13) are defined based on non-linear model equations (6)–(7) and are given by

$$\mathbf{h}_1 = \tilde{x}_i + e_{\tilde{x}_i} - f \frac{p}{q} = 0, \quad (61)$$

$$\mathbf{h}_2 = \tilde{y} + e_{\tilde{y}_i} - f \frac{s}{q} = 0, \quad (62)$$

Table 1: Statistics of the measurements for all six experiments. The first column is the experiment number, the second column is the number of captured images (i. e. equals to the number of Az angle observables), the third column is the number of signalised targets, and the fourth column is the number of image or TLS target observations.

Experiments No.	Images No.	Signalised targets No.	Image/TLS target observations No.
1	31	33	221
2	27	33	221
3	29	33	205
4	30	33	217
5	32	33	226
6	29	33	211

where

$$\begin{bmatrix} p \\ s \\ q \end{bmatrix} = \mathbf{R}_{\kappa\varphi\omega} \left(\mathbf{R}_{(\tilde{A}z + e_{\tilde{A}z})} \begin{bmatrix} \tilde{X}_{TLSi} + e_{\tilde{X}_{TLSi}} \\ \tilde{Y}_{TLSi} + e_{\tilde{Y}_{TLSi}} \\ \tilde{Z}_{TLSi} + e_{\tilde{Z}_{TLSi}} \end{bmatrix} - \begin{bmatrix} X_c \\ Y_c \\ Z_c \end{bmatrix} \right). \quad (63)$$

The \tilde{x}_i and \tilde{y}_i are the rectified image target observations, \tilde{X}_{TLSi} , \tilde{Y}_{TLSi} and \tilde{Z}_{TLSi} are the TLS target observations with $i \in \{1, \dots, n_k\}$ and $\tilde{A}z$ is the Az angle observation of the TLS. The $e_{\tilde{x}_i}$, $e_{\tilde{y}_i}$, $e_{\tilde{X}_{TLSi}}$, $e_{\tilde{Y}_{TLSi}}$, $e_{\tilde{Z}_{TLSi}}$ and $e_{\tilde{A}z}$ are the errors of the aforementioned observations.

The 6 EOPs (consisting three translations and three rotations) are the unknown parameters (ξ) with (6×1) -vector of functional parameters in the adjustment model, which are estimated jointly with their uncertainties (see Table 12 in the Appendix section 7). The calculated mean values of estimated parameters from the six experiments and based on all adjustment models demonstrate that they achieve approximately similar results and mostly altering at the level of their uncertainties (see Table 2). The estimated φ parameter changes significantly from experiment to experiment, which is due to the minor changes of the zero direction for each new set-up of the TLS. This issue is also clearly visible from calculated maximum deviations and their corresponding standard deviations within all six experiments in Table 2. The estimates of the rotation angles ω and κ as well as three translations differ slightly between the experiments, which can also be explained by the detachment of the clamping system for each set-up of the camera on top of the TLS. In addition, since the aperture priority was set to “automatic” during the capturing the images, subsequently it causes slightly changes of the focal length of camera. Subsequently, the translation parameter in the Z direction changed slightly more compared to two other axes due to its correlation with the focal length of camera. Interestingly, in most cases the estimated 6 EOPs in GHM-VCE algorithm with confidence level of 95 % is between that of with confidence level of 99.7 % and the EM-qGMM algorithm. Furthermore, concerning the run time speed up procedure, the EM-qGMM algorithm is significantly faster than GHM-VCE algorithm with confidence level of 95 %, which may even be much faster specially while the measured data contaminated with greater number of outliers or large residuals (see Tables (12–13) in the Appendix section 7).

The *a priori* and *a posteriori* standard deviations of the observables are given in Table 3. The *a posteriori* standard deviations of the observable in the EM-GHM algorithm estimated more robustly from experiment to experiment except for those observables with low estimated dofs. However, in the GHM-VCE algorithm, the results sometimes

Table 2: Case study I: Statistics of the external calibration/orientation parameters (6 EOPs) between the TLS and digital camera with applied three adjustment models (EM-GHM, EM-qGMM and GHM-VCE algorithms with 99.7 % and 95 % confidence levels) and for all the six experiments. The first column lists the adjustment models, the second column lists the 6 EOPs, the third column is the mean values, the fourth column is the max deviations from the mean values, and the fifth column is the standard deviations.

Adjustment models	6 EOPs	Mean	Max dev.	σ
EM-GHM	ω (°)	90.4762	0.0504	0.0344
	φ (°)	-9.5793	0.2730	0.2030
	κ (°)	-0.2147	0.0166	0.0097
	X_c (m)	-0.0132	0.0006	0.0005
	Y_c (m)	0.2154	0.0029	0.0018
	Z_c (m)	0.0838	0.0054	0.0041
EM-qGMM	ω (°)	90.4599	0.0370	0.0264
	φ (°)	-9.5770	0.2750	0.2055
	κ (°)	-0.2156	0.0130	0.0075
	X_c (m)	-0.0130	0.0007	0.0005
	Y_c (m)	0.2140	0.0005	0.0005
	Z_c (m)	0.0835	0.0041	0.0039
GHM-VCE 99.7 %	ω (°)	90.4615	0.0371	0.0261
	φ (°)	-9.5785	0.2750	0.2044
	κ (°)	-0.2168	0.0128	0.0072
	X_c (m)	-0.0131	0.0007	0.0005
	Y_c (m)	0.2142	0.0006	0.0005
	Z_c (m)	0.0839	0.0042	0.0041
GHM-VCE 95 %	ω (°)	90.4585	0.0361	0.0258
	φ (°)	-9.5759	0.2793	0.2057
	κ (°)	-0.2161	0.0122	0.0070
	X_c (m)	-0.0131	0.0008	0.0006
	Y_c (m)	0.2140	0.0006	0.0005
	Z_c (m)	0.0834	0.0038	0.0039

seems too optimistic or pessimistic for one type of the observable compared to another type, which may arise due to significant fluctuations of the *a posteriori* variance factor of the unit weight ($\hat{\sigma}_0^2$) between 0.72 and 1.0 through all experiments. Therefore, it causes different re-scaling of the *a posteriori* standard deviations of the observables, which leads to different rejection rate of the measurements for each experiment. The *a priori* standard deviation of the 0.006 mm for the image targets equals one pixel, which the *a posteriori* standard deviations of the image targets in most cases indicate the sub-pixel image measurements. It should be noted that within the EM-qGMM algorithm, an estimation of the uncertainties is currently not possible.

As previously mentioned, in the GHM-VCE algorithm, the dof is calculated by subtracting the total number of condition equations and number of unknown parameters, which differs from experiment to experiment due to the different number of rejected outliers or large residuals. Consequently, it fluctuates between 348 to 444 (i. e. consider-

ing the confidence levels of 99.7 % and 95 %), which approximates the normal distribution. The estimated dofs for the image targets or the targets in the 3D point clouds in the EM-GHM algorithm fluctuate in the range of approximately 2.0–5.5, for which values the t-distribution has substantial tails and show large number of outliers in the measurement noise of that sensor. However, those estimated dofs below 2.0 are unstable and unrealistic in which their multiplication with the scale factor (see Equation 34) do not achieve reasonable results. Furthermore, the estimated dofs in the EM-qGMM algorithm for that of below 2.0 are unstable too.

Moreover, Table 4 represents the statistics of the rejected measurements for all the six experiments including the rejection rate of the Az, image and TLS target observations by considering confidence levels of 99.7 % and 95 %. The rejected Az in the adjustment procedure yields rejecting all those relevant observables of that captured image in the GHM-VCE algorithm. Such rejection of the Az observables may also occur while the number of the remaining image or TLS targets (after performing the statistical tests) are less than three in each captured image. In addition, those problematic Az observables resulted in inaccurate estimation of the 6 EOPs in the EM-GHM algorithm, which its evidence reveals in the large estimation of their uncertainties. For instance, the estimated dofs for the Az in experiments 3 and 4, which are below 2.0, may prove the existence of such Az problem.

To investigate the possible correlations between the calculated 6 EOPs, the covariance matrix of the parameters based on the GHM-VCE algorithm with 95 % confidence level is provided in Table 5. Accordingly, the correlation coefficients were calculated between the 6 EOPs (see Table 6). The results represent a high correlation coefficients between the $\varphi-X_c$ as well as $\omega-Y_c$ as we expected. This is mainly due to the mathematical correlations between the observations. In addition, it may also be influenced by the distribution of the targets in our 3D laboratory.

The re-projection errors are calculated by subtracting the back projection of the TLS target observations into the image space from their corresponding image target observations based on Equations (6–7) and using the 6 EOPs calculated based on the proposed three adjustment models. For instance, Figure 5 depicts the absolute deviations of that re-projection errors in the pixel unit resulted from EM-GHM algorithm. It also shows the total number of targets in the experiment 1 since there is no rejection of the outliers in the EM-GHM algorithm. For each image, all the targets with their deviations are considered in one column bar and the number of targets extracted in each captured image is indicated on top of the each column. Therefore,

Table 3: Case study I: A priori and a posteriori standard deviations of the observables, estimated degree of freedom and a posteriori variance factor of unit weight. The first column indicates the experiment number, the second column lists the observables (which are the target coordinates in the images captured, the target coordinates in the 3D point clouds and the Az of the TLS, respectively). The third column is a priori standard deviations of observables (which are equal to nominal or expected standard deviations of the observations). The columns (4–11) give a posteriori standard deviations and the estimated degrees of freedom of the observables obtained by the three adjustment algorithms.

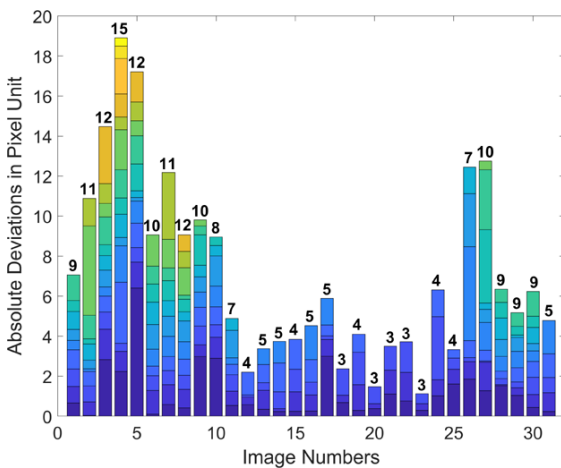
Experiments No.	Observables	σ	$\hat{\sigma}_{EM-GHM}$	\hat{v}_{EM-GHM}	$\hat{\sigma}_{EM-qGMM}$	$\hat{v}_{EM-qGMM}$	$\hat{\sigma}_{GHM-VCE-99.7\%}$	$v_{GHM-VCE-99.7\%}$	$\hat{\sigma}_{GHM-VCE-95\%}$	$v_{GHM-VCE-95\%}$
1	Image	0.006	0.0031	4.564	–	1.901	0.0013	428	0.0007	372
	TLS	1.0	0.2634	2.670	–	1.901	0.8593	428	0.4777	372
	Az	0.007	0.0050	3.956	–	1.901	0.0057	428	0.0055	372
	$\hat{\sigma}_0^2$	1.0	–	–	–	–	0.82208	–	1.00000	–
2	Image	0.006	0.0033	4.237	–	1.952	0.0008	394	0.0008	382
	TLS	1.0	0.2819	2.606	–	1.952	0.7271	394	0.6804	382
	Az	0.007	0.0074	2.871	–	1.952	0.0066	394	0.0043	382
	$\hat{\sigma}_0^2$	1.0	–	–	–	–	0.90576	–	0.87005	–
3	Image	0.006	0.0030	2.897	–	1.598	0.0010	390	0.0010	348
	TLS	1.0	0.4154	1.816	–	1.598	0.8357	390	0.5473	348
	Az	0.007	0.0071	1.833	–	1.598	0.0066	390	0.0060	348
	$\hat{\sigma}_0^2$	1.0	–	–	–	–	0.88184	–	0.99999	–
4	Image	0.006	0.0032	3.085	–	1.808	0.0016	422	0.0017	416
	TLS	1.0	0.4182	1.929	–	1.808	1.1046	422	1.0617	416
	Az	0.007	0.0048	1.274	–	1.808	0.0073	422	0.0060	416
	$\hat{\sigma}_0^2$	1.0	–	–	–	–	0.82158	–	0.79768	–
5	Image	0.006	0.0037	5.241	–	2.581	0.0022	444	0.0013	408
	TLS	1.0	0.3964	2.337	–	2.581	1.1345	444	0.8799	408
	Az	0.007	0.0060	120	–	2.581	0.0069	444	0.0047	408
	$\hat{\sigma}_0^2$	1.0	–	–	–	–	0.71948	–	0.82502	–
6	Image	0.006	0.0037	5.312	–	2.232	0.0020	416	0.0021	406
	TLS	1.0	0.3982	2.225	–	2.232	1.1272	416	1.0516	406
	Az	0.007	0.0050	120	–	2.232	0.0068	416	0.0056	406
	$\hat{\sigma}_0^2$	1.0	–	–	–	–	0.74339	–	0.69059	–

Table 4: Case study I: Statistics of the rejected measurements for all six experiments based on GHM-VCE algorithm with 99.7 % and 95 % confidence levels.

Confidence level	Experiments No.	Rejection rate of Az observations [%]	Rejection rate of image target observations [%]	Rejection rate of TLS target observations [%]
99.7 %	1	0	0	1.81
	2	0	0	4.52
	3	3.45	0	2.44
	4	3.33	0.46	0
	5	0	0	0.44
	6	0	0	0
95 %	1	0	0	14.48
	2	0	0	7.24
	3	6.90	0.48	11.22
	4	3.33	0.46	1.38
	5	3.12	0	7.52
	6	0	0	2.37

Table 5: Case study I: Covariance matrix of the 6 EOPs calculated for the first experiment based on GHM-VCE algorithm with 95 % confidence level.

6 EOPs	ω (rad)	φ (rad)	κ (rad)	X_c (mm)	Y_c (mm)	Z_c (mm)
ω (rad)	6.7884e-10	-3.8852e-11	-1.1456e-10	2.9509e-07	3.0473e-06	-6.4059e-07
φ (rad)	-3.8852e-11	2.0945e-09	-6.584e-11	-7.7556e-06	-1.3073e-07	-1.4797e-06
κ (rad)	-1.1456e-10	-6.584e-11	4.0677e-10	2.1049e-07	-5.67e-07	1.9822e-07
X_c (mm)	2.9509e-07	-7.7556e-06	2.1049e-07	0.035906	0.001067	0.004912
Y_c (mm)	3.0473e-06	-1.3073e-07	-5.67e-07	0.001067	0.015135	-0.002501
Z_c (mm)	-6.4059e-07	-1.4797e-06	1.9822e-07	0.004912	-0.002501	0.010834

**Figure 5:** Case study I: Absolute deviations between the re-projected TLS data and measured image targets using 6 EOPs calculated from EM-GHM algorithm in pixel unit (Experiment 1). The X-axis corresponds to the image numbers and Y-axis corresponds to the absolute deviations in pixel unit.**Table 6:** Case study I: Correlation coefficients matrix calculated between the 6 EOPs 2 by 2 for the first experiment based on GHM-VCE algorithm with 95 % confidence level.

6 EOPs	ω	φ	κ	X_c	Y_c	Z_c
ω		-0.03258	-0.21801	0.05977	0.95069	-0.23621
φ			-0.07133	-0.89432	-0.02322	-0.31063
κ				0.05508	-0.22852	0.09442
X_c					0.04578	0.24905
Y_c						-0.19527
Z_c						

the first column represents that the image 1 contains 9 targets, which derives 9 colourful blocks obtained from the norm of absolute deviations in both x and y directions. Additionally, it shows subpixel accuracy for most of blocks of that image. As we expected, the subpixel re-projection errors obtained except of that targets with large incidence angles. The Figures (13–15) in the Appendix section 7 show the results of the re-projection errors in the EM-qGMM and

GHM-VCE algorithms with 99.7 % and 95 % confidence levels in which the outliers or large residuals were rejected in the GHM-VCE algorithms and no targets with large residuals are visible.

The Figures (6–8) show the residuals for three groups of the observables in the first experiment, which each of them includes the results from the EM-GHM and GHM-VCE algorithms with 99.7 % and 95 % confidence levels and there are no systematic trends visible. The residuals from the EM-GHM algorithm are at the level of the uncertainty of measurements, which demonstrate the reliability of the estimation procedure. However, the residuals from the GHM-VCE algorithms with 99.7 % and 95 % confidence levels represent that more optimistic results obtained for the image target observations whereas more pessimistic results obtained for the TLS target observations. In addition, the obtained residuals from the GHM-VCE algorithms with 95 % confidence levels depicts more smoother results compared to other adjustment models due to rejecting more large residuals.

5.2 Case study II: External calibration between TLS, digital camera and LT – Validation

In the second case study, the LT target coordinates, which have been calculated and obtained from a network adjustment for all the targets in the 3D laboratory, are utilized as an additional observation group in the adjustment procedure to validate the accuracy of the calibration results.

The observables consist of 4 groups of the observations, which are the rectified target coordinates in the image space (Image target observations: ℓ_1), the target coordinates in the 3D point clouds coordinate system (TLS target observations: ℓ_2), the target coordinates in the LT coordinate system (LT target observations: ℓ_3) and the Az angle observables of the TLS (ℓ_4). The number of LT target obser-

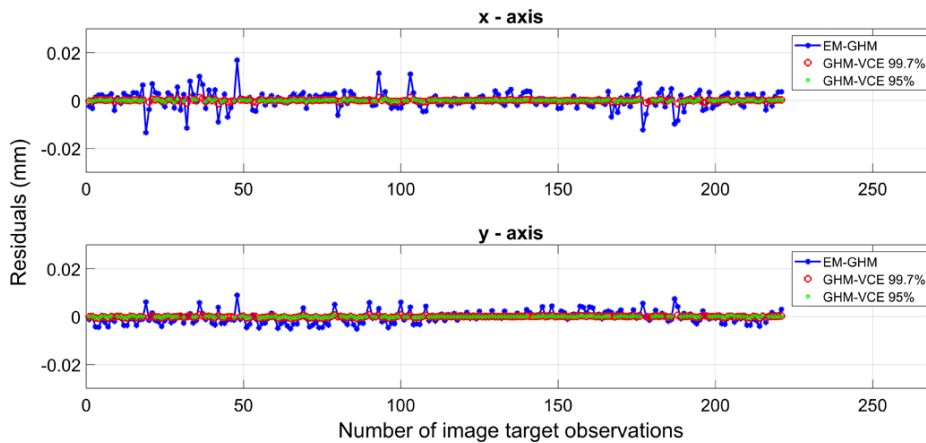


Figure 6: Case study I: Residuals of the image target observations based on EM-GHM algorithm, GHM-VCE algorithm with 99.7 % confidence level and GHM-VCE algorithm with 95 % confidence level (Experiment 1). From top, the graphs (1–2) are the image measurements residuals in x and y directions, respectively.

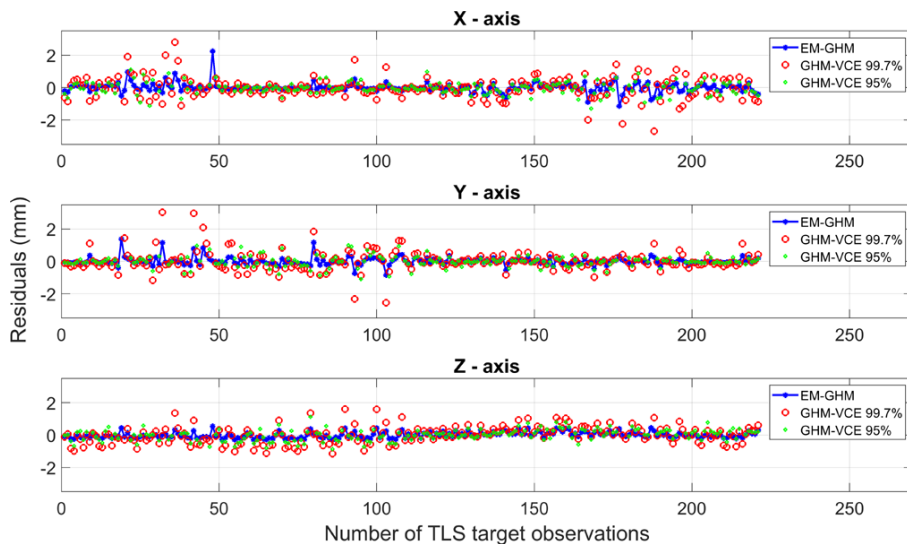


Figure 7: Case study I: Residuals of the TLS target observations based on EM-GHM algorithm, GHM-VCE algorithm with 99.7 % confidence level and GHM-VCE algorithm with 95 % confidence level (Experiment 1). From top, the graphs (1–3) are the TLS observation in X, Y and Z directions, respectively.

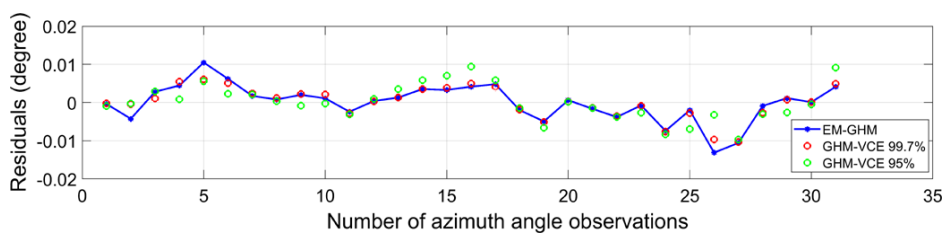


Figure 8: Case study I: Residuals of the Az angle observations based on EM-GHM algorithm, GHM-VCE algorithm with 99.7 % confidence level and GHM-VCE algorithm with 95 % confidence level (Experiment 1).

variations are the same as image and TLS target observations in the adjustment models.

The condition equations (13) are defined based on non-linear model equations (6)–(9) and are given by

$$\mathbf{h}_1 = \tilde{x}_i + e_{\tilde{x}_i} - f \frac{p}{q} = 0, \quad (64)$$

$$\mathbf{h}_2 = \tilde{y} + e_{\tilde{y}_i} - f \frac{s}{q} = 0, \quad (65)$$

$$\mathbf{h}_3 = \lambda \mathbf{R}_{k' \varphi' \omega'} \begin{bmatrix} \widetilde{X}_{TLSi} + e_{\widetilde{X}_{TLSi}} \\ \widetilde{Y}_{TLSi} + e_{\widetilde{Y}_{TLSi}} \\ \widetilde{Z}_{TLSi} + e_{\widetilde{Z}_{TLSi}} \end{bmatrix} + \begin{bmatrix} X'_c \\ Y'_c \\ Z'_c \end{bmatrix} - \begin{bmatrix} \widetilde{X}_{LTi} + e_{\widetilde{X}_{LTi}} \\ \widetilde{Y}_{LTi} + e_{\widetilde{Y}_{LTi}} \\ \widetilde{Z}_{LTi} + e_{\widetilde{Z}_{LTi}} \end{bmatrix} = 0, \quad (66)$$

$$\mathbf{h}_4 = \begin{bmatrix} X \\ Y \\ Z \end{bmatrix} - \begin{bmatrix} \widetilde{X}_{LTi} + e_{\widetilde{X}_{LTi}} \\ \widetilde{Y}_{LTi} + e_{\widetilde{Y}_{LTi}} \\ \widetilde{Z}_{LTi} + e_{\widetilde{Z}_{LTi}} \end{bmatrix} = 0, \quad (67)$$

where \widetilde{X}_{LTi} , \widetilde{Y}_{LTi} and \widetilde{Z}_{LTi} are the LT target observations with $i \in \{1, \dots, n_k\}$ and $e_{\widetilde{X}_{LTi}}$, $e_{\widetilde{Y}_{LTi}}$, $e_{\widetilde{Z}_{LTi}}$ are their corresponding errors.

The 6 EOPs (consisting three translations and three rotations) between the TLS and digital camera, the 7 EOPs (consisting three translations, three rotations and scale) between the TLS and LT and the target point coordinates in the TLS coordinate system are the unknown parameters with $((6 + 7 + 3P) \times 1)$ -vector of functional parameters, where P is the number of targets. The aforementioned unknown parameters are estimated jointly with their uncertainties in the adjustment models (see Tables (13–14) in the Appendix section 7). As we expected, the estimated parameters are comparable to those of estimated from previous case study, and in most cases the differences are at the level of their uncertainties. In addition, the mean values of the estimated 6 EOPs and 7 EOPs as well as their maximum deviations and standard deviations were calculated based on the proposed adjustment models and for all the six experiments (see Tables (7–8)). The obtained results in Table 8 demonstrates the highly accurate, precise and reliable estimation of the 7 EOPs between the TLS and LT.

The *a priori* and *a posteriori* standard deviations of the observables are given in Table 9. Furthermore, a *a posteriori* variance factor of the unit weight ($\hat{\sigma}_0^2$) was computed for each experiment in the GHM-VCE algorithm with confidence levels of 99.7 % and 95 % and their values in entire experiments are approximately equal to 0.66. The estimated dofs for the image targets, the targets in the 3D point clouds or LT targets measurements in the EM-GHM algorithm fluctuate in the range of approximately 2.0–7.30. This may be due to the existence of systematic errors in TLS data, some remaining minor errors in internal camera calibration parameters or possibly a correlation between the

Table 7: Case study II: Statistics of the external calibration/orientation parameters (6 EOPs) between the TLS and digital camera with applied three adjustment models (EM-GHM, EM-qGMM and GHM-VCE algorithms with 99.7 % and 95 % confidence levels) – Validation. The first column lists the adjustment models, the second column lists the 6 EOPs, the third column is the mean values, the fourth column is the max deviations from the mean values, and the fifth column is the standard deviations.

Adjustment models	6 EOPs	Mean	Max dev.	σ
EM-GHM	ω (°)	90.4918	0.0655	0.0495
	φ (°)	−9.5981	0.2865	0.2011
	κ (°)	−0.2069	0.0242	0.0182
	X_c (m)	−0.0120	0.0025	0.0016
	Y_c (m)	0.2163	0.0050	0.0031
	Z_c (m)	0.0827	0.0074	0.0048
EM-qGMM	ω (°)	90.4617	0.0355	0.0251
	φ (°)	−9.5745	0.2792	0.2076
	κ (°)	−0.2161	0.0135	0.0077
	X_c (m)	−0.0132	0.0009	0.0007
	Y_c (m)	0.2141	0.0005	0.0004
	Z_c (m)	0.0831	0.0041	0.0041
GHM-VCE 99.7 %	ω (°)	90.4631	0.0358	0.0253
	φ (°)	−9.5788	0.2704	0.2022
	κ (°)	−0.2161	0.0146	0.0080
	X_c (m)	−0.0131	0.0006	0.0005
	Y_c (m)	0.2142	0.0005	0.0004
	Z_c (m)	0.0841	0.0037	0.0036
GHM-VCE 95 %	ω (°)	90.4593	0.0381	0.0273
	φ (°)	−9.5790	0.2759	0.2046
	κ (°)	−0.2157	0.0148	0.0085
	X_c (m)	−0.0127	0.0008	0.0006
	Y_c (m)	0.2140	0.0007	0.0005
	Z_c (m)	0.0829	0.0041	0.0039

measurements. Moreover, the estimated dofs for the Az in experiments 1 and 6, which are equal to 120 are approximating the normal distribution. However, its estimation in experiments 3 and 4, which are below 2.0, may depicts the Az data problem as shown in previous case study. On the other hand, better results obtained for the *a posteriori* standard deviations of the observables in the GHM-VCE algorithm by including the LT measurements as a reference measurements and by solving the scale problem. This is clearly visible from nearly close estimation of the $\hat{\sigma}_0^2$ for the entire experiments. However, in the EM-GHM algorithm, more optimistic results obtained for the LT target observations whereas more pessimistic results obtained for the image target observations, which may also due to the correlation between the measurements.

Table 10 represents the statistics of the rejected measurements based on the GHM-VCE algorithm with 99.7 % and 95 % confidence levels. Subsequently, the rejection rate of about 25 % for image target measurements in GHM-

Table 8: Case study II: Statistics of the external calibration/orientation parameters (7 EOPs) between the TLS and LT with applied three adjustment models (EM-GHM, EM-qGMM and GHM-VCE algorithms with 99.7 % and 95 % confidence levels) – Validation. The first column lists the adjustment models, the second column lists the 7 EOPs, the third column is the mean values, the fourth column is the max deviations from the mean values, and the fifth column is the standard deviations.

Adjustment models	7 EOPs	Mean	Max dev.	σ
EM-GHM	ω' (°)	0.1023	0.0026	0.0021
	φ' (°)	−0.0670	0.0032	0.0020
	κ' (°)	43.2167	0.0052	0.0033
	X'_c (m)	12.8018	0.0001	0.0001
	Y'_c (m)	15.7212	0.0001	0.0001
	Z'_c (m)	1.7022	0.0001	0.0001
	λ	0.99988	0.00002	0.00002
EM-qGMM	ω' (°)	0.1023	0.0026	0.0021
	φ' (°)	−0.0677	0.0043	0.0026
	κ' (°)	43.2165	0.0053	0.0033
	X'_c (m)	12.8018	0.0001	0.0001
	Y'_c (m)	15.7211	0.0001	0.0001
	Z'_c (m)	1.7022	0.0001	0.0001
	λ	0.99987	0.00002	0.00001
GHM-VCE 99.7 %	ω' (°)	0.1013	0.0036	0.0027
	φ' (°)	−0.0670	0.0035	0.0024
	κ' (°)	43.2173	0.0052	0.0034
	X'_c (m)	12.8018	0.0001	0.0001
	Y'_c (m)	15.7212	0.0001	0.0001
	Z'_c (m)	1.7022	0.0001	0.0001
	λ	0.99989	0.00002	0.00002
GHM-VCE 95 %	ω' (°)	0.0998	0.0027	0.0020
	φ' (°)	−0.0675	0.0035	0.0023
	κ' (°)	43.2180	0.0055	0.0034
	X'_c (m)	12.8018	0.0001	0.0001
	Y'_c (m)	15.7213	0.0001	0.0001
	Z'_c (m)	1.7021	0.0001	0.0001
	λ	0.99989	0.00002	0.00002

VCE algorithm with 95 % confidence level, may show that sometimes VCE components were estimated so optimistic that yields such a high rejection rate of the observations. However, as previously mentioned, the larger number of rejected image and TLS measurements compared to the previous case study may be related to remaining internal errors in TLS or images data, which their influences become more visible by considering the LT data as a reference and additional observable in the adjustment model. Table 11 depicts the RMSE calculated between the estimated target point coordinates and their corresponding measurements in the 3D point clouds for all the six experiments based on GHM-VCE algorithm with 99.7 % and 95 % confidence levels. It depicts that the RMSE results in X, Y and Z axes are gradually and slightly increasing, which might be due to increase of the φ values in all experiments

and the existence of the correlation between the TLS measurements and the Az measurements of the TLS.

The Figures (9–12) illustrate the residuals for four groups of the observables. As we expected, there are no systematic trends visible and again more smoother results obtained for the GHM-VCE algorithm with 95 % confidence level.

6 Conclusion

This research work aims to propose a robust procedure of sensor fusion, which can be extended to other sensor fusion problems with different applications by identifying a proper mathematical model for the orientation between the used sensors.

A high resolution digital camera may be attached on top of a TLS to increase the accuracy and completeness of the deformation analysis. This integration is beneficial since the strength and weakness of both sensors are complementary to each other. For this purpose, the EOPs between the MSS (here TLS, digital camera and LT for validation) needs to be determined robustly, reliably and with a high accuracy. Therefore, four non-linear mathematical functions were determined based on the space resection by collinearity condition equations, the 3D Helmert transformation and the constraint equation, which were solved in a rigorous bundle adjustment procedure using the signalised target points. Next, the three different adjustment models such as the EM algorithm to solve the GHM with grouped t-distributed random deviations (EM-GHM), a novel EM algorithm to solve a corresponding quasi-GMM with t-distributed pseudo-misclosures (EM-qGMM) and a classical least square procedure to solve the GHM with VCE and outlier removal (GHM-VCE) were developed and implemented. They compute highly accurate, robust and reliable parameter estimates of the external calibration of the TLS and the digital camera, which has previously not been achieved to the best knowledge of the authors. Additionally, the LT was included as a highly accurate reference sensor for the purpose of validation.

As part of two different case studies, six independent experiments were carried out in the 3D laboratory. In the first case study, the 6 EOPs (consisting of three translations and three rotations) between the TLS and the digital camera were estimated based on 3 groups of the observations such as the image target observations, the TLS target observations and the Az angle observables of the TLS. The condition equations were defined based on the space resection by collinearity condition equations. Due

Table 9: Case study II: A priori and a posteriori standard deviations of the observables, estimated degree of freedom and a posteriori variance factor of unit weight – Validation.

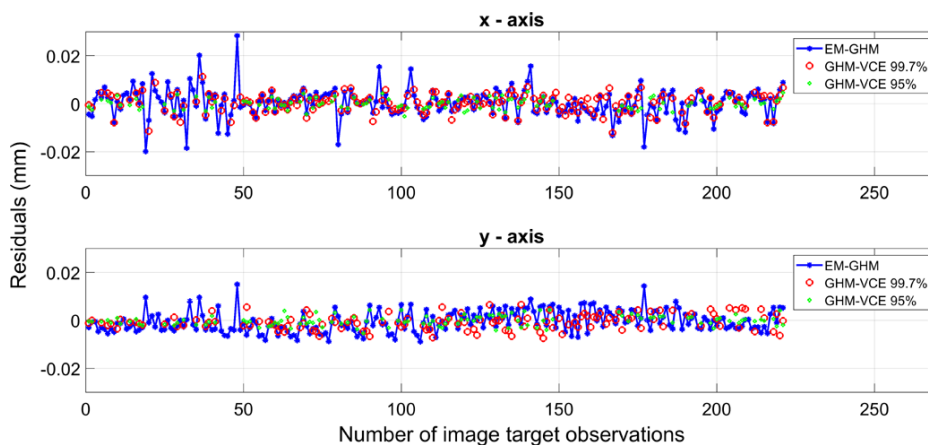
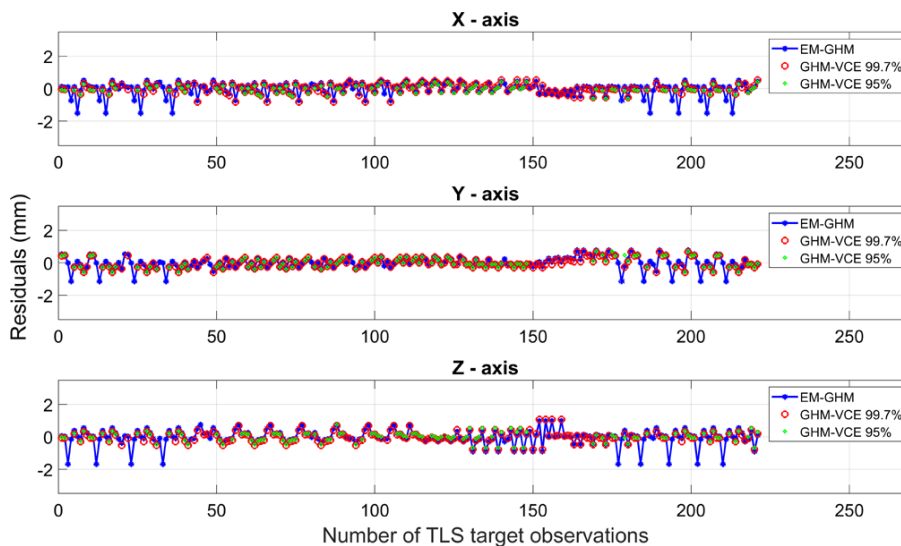
Experiments No.	Observables	σ	$\hat{\sigma}_{EM-GHM}$	\hat{V}_{EM-GHM}	$\hat{\sigma}_{EM-qGMM}$	$\hat{V}_{EM-qGMM}$	$\hat{\sigma}_{GHM-VCE-99.7\%}$	$V_{GHM-VCE-99.7\%}$	$\hat{\sigma}_{GHM-VCE-95\%}$	$V_{GHM-VCE-95\%}$
1	Image	0.006	0.0052	6.491	–	0.139	0.0037	1378	0.0022	862
	TLS	1.0	0.5047	2.762	–	0.139	0.3228	1378	0.2910	862
	LT	0.01	0.0003	3.143	–	0.139	0.0071	1378	0.0002	862
	Az	0.007	0.0053	120	–	0.139	0.0072	1378	0.0036	862
	$\hat{\sigma}_0^2$	1.0	–	–	–	–	0.65839	–	0.66936	–
2	Image	0.006	0.0054	5.657	–	0.141	0.0038	1383	0.0031	1163
	TLS	1.0	0.4285	3.572	–	0.141	0.3423	1383	0.3145	1163
	LT	0.01	0.0003	3.589	–	0.141	0.0072	1383	0.0072	1163
	Az	0.007	0.0064	6.389	–	0.141	0.0073	1383	0.0051	1163
	$\hat{\sigma}_0^2$	1.0	–	–	–	–	0.65961	–	0.65971	–
3	Image	0.006	0.0108	1.929	–	0.141	0.0043	1367	0.0026	825
	TLS	1.0	0.4266	3.332	–	0.141	0.3363	1367	0.3363	825
	LT	0.01	0.0007	3.543	–	0.141	0.0026	1367	0.0026	825
	Az	0.007	0.0299	1.813	–	0.141	0.0074	1367	0.0074	825
	$\hat{\sigma}_0^2$	1.0	–	–	–	–	0.65986	–	0.66912	–
4	Image	0.006	0.0091	2.058	–	0.142	0.0055	1540	0.0032	987
	TLS	1.0	0.4352	4.614	–	0.142	0.3990	1540	0.3500	987
	LT	0.01	0.0008	3.412	–	0.142	0.0011	1540	0.0011	987
	Az	0.007	0.0186	1.571	–	0.142	0.0099	1540	0.0078	987
	$\hat{\sigma}_0^2$	1.0	–	–	–	–	0.65715	–	0.66566	–
5	Image	0.006	0.0061	5.436	–	0.142	0.0050	1625	0.0029	947
	TLS	1.0	0.4435	4.298	–	0.142	0.4364	1625	0.3372	947
	LT	0.01	0.0002	3.817	–	0.142	0.0065	1625	0.0065	947
	Az	0.007	0.0069	25.575	–	0.142	0.0102	1625	0.0068	947
	$\hat{\sigma}_0^2$	1.0	–	–	–	–	0.65670	–	0.66750	–
6	Image	0.006	0.0057	7.270	–	0.140	0.0055	1577	0.0030	963
	TLS	1.0	0.4849	3.707	–	0.140	0.4660	1577	0.3727	963
	LT	0.01	0.0002	3.644	–	0.140	0.0066	1577	0.0066	963
	Az	0.007	0.0055	120	–	0.140	0.0109	1577	0.0077	963
	$\hat{\sigma}_0^2$	1.0	–	–	–	–	0.65766	–	0.66678	–

Table 10: Case study II: Statistics of the rejected measurements for all six experiments based on GHM-VCE algorithm with 99.7 % and 95 % confidence levels – Validation.

Confidence level	Experiments No.	Rejection rate of Az observations [%]	Rejection rate of image target observations [%]	Rejection rate of TLS target observations [%]	Rejection rate of LT target observations [%]
99.7 %	1	0	6.33	10.41	0
	2	0	6.33	4.97	0
	3	3.45	4.88	4.88	0
	4	3.33	1.38	3.23	0
	5	3.12	3.54	0	0
	6	0	0.47	0	0
95 %	1	19.35	28.05	13.12	0
	2	11.11	14.93	6.79	0
	3	20.69	26.34	12.68	0
	4	20.00	23.50	9.22	0
	5	25	26.10	9.73	0
	6	17.24	24.17	9.00	0

Table 11: Case study II: The RMSE calculated between the estimated target point coordinates and the TLS measurements for all six experiments based on GHM-VCE algorithm.

Experiments No.	$RMSE_x$ (mm)	$RMSE_y$ (mm)	$RMSE_z$ (mm)	$RMSE_{xyz}$ (mm)	$RMSE_x$ (mm)	$RMSE_y$ (mm)	$RMSE_z$ (mm)	$RMSE_{xyz}$ (mm)
	Confidence level 99.7 %				Confidence level 95 %			
1	0.2998	0.3024	0.3570	0.5557	0.2429	0.3178	0.2991	0.4994
2	0.3498	0.3288	0.3419	0.5894	0.3354	0.2960	0.3038	0.5408
3	0.3250	0.3553	0.3214	0.5790	0.2393	0.2819	0.2562	0.4499
4	0.3445	0.3868	0.4516	0.6872	0.3373	0.3527	0.3512	0.6013
5	0.4235	0.4182	0.4596	0.7520	0.3131	0.3665	0.3209	0.5791
6	0.4612	0.4385	0.4894	0.8028	0.3493	0.4043	0.3524	0.6401

**Figure 9:** Case study II: Residuals of the image target observations based on EM-GHM algorithm, GHM-VCE algorithm with 99.7 % confidence level and GHM-VCE algorithm with 95 % confidence level (Experiment 1). From top, the graphs (1–2) are the image measurements residuals in x and y directions, respectively.**Figure 10:** Case study II: Residuals of the TLS observation based on EM-GHM algorithm, GHM-VCE algorithm with 99.7 % confidence level and GHM-VCE algorithm with 95 % confidence level (Experiment 1). From top, the graphs (1–3) are the TLS observation in X, Y and Z directions, respectively.

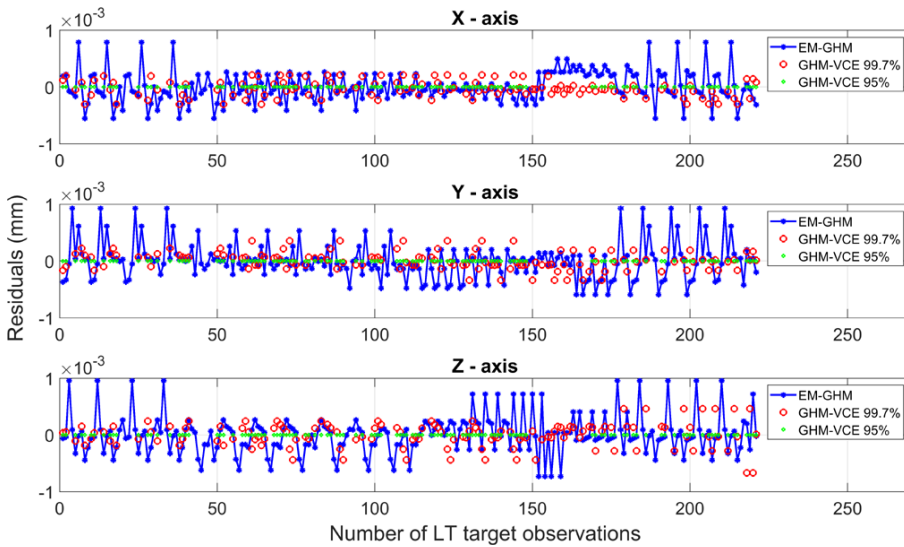


Figure 11: Case study II: Residuals of the LT observation based on EM-GHM algorithm, GHM-VCE algorithm with 99.7 % confidence level and GHM-VCE algorithm with 95 % confidence level (Experiment 1). From top, the graphs (1–3) are the LT observation in X, Y and Z directions, respectively.

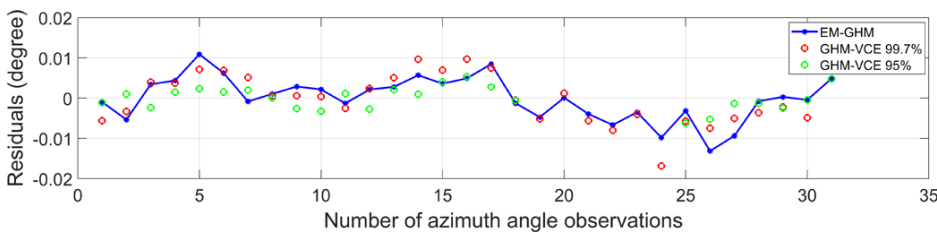


Figure 12: Case study II: Residuals of the Az angle observation based on EM-GHM algorithm, GHM-VCE algorithm with 99.7 % confidence level and GHM-VCE algorithm with 95 % confidence level (Experiment 1).

to mounting and demounting the digital camera on top of the TLS by the clamping system, the calculated 6 EOPs varied slightly from experiment to experiment, i. e. for the rotation angles. The significant difference was related to the estimated φ , which was due to the minor changes of the zero direction for each new set-up of the TLS. However, the estimation of the rotation angles ω and κ as well as of the three translations slightly differed, which can also be related to the usage of that clamping system.

The estimated 6 EOPs in GHM-VCE algorithm with confidence level of 95 % were approximately in between the results of the GHM-VCE algorithm with confidence level of 99.7 % and EM-qGMM algorithm. Moreover, a *posteriori* variance factor of the unit weight ($\hat{\sigma}_0^2$) calculated for each experiment in the GHM-VCE algorithm with confidence levels of 99.7 % and 95 %, which their values fluctuate approximately between 0.72 and 1.0 for the entire experiments. Subsequently, it causes different re-scaling of the *a posteriori* standard deviations of the observables, which influences the rejection rates of the measurements.

The estimated dofs for the image target observation or the TLS target observations in the EM-GHM algorithm fluctuated in the range of approximately 2.0–5.5, which illustrated a substantial tails in the t-distribution and consequently large number of outliers in the measurement noise of that sensor. In addition, it was shown that in case of Az data problem, the EM-GHM was not accurate and reliable as two other algorithms.

In the second case study, the accuracy of the calibration results are evaluated, compared and validated by considering the LT observations as additional observable in the adjustment model. The 6 EOPs between the TLS and the digital camera, the 7 EOPs (consisting of three translations, three rotations and scale) between the TLS and the LT and the target point coordinates in the TLS coordinate system were the unknown parameters, which were estimated jointly with their uncertainties by the aforementioned three adjustment models. The observables consisted of 4 group of observations, which were image target observations, the TLS target observations, the LT tar-

get observations and Az angle observables of the TLS. The mathematical functions were determined based on the space resection by collinearity condition equations, the 3D Helmert transformation and the constraint equation. The $\hat{\sigma}_0^2$ estimates for all the experiments in the GHM-VCE algorithm with confidence levels of 99.7 % and 95 % were approximately equal to 0.66. The estimated dofs for the image targets, TLS or LT targets measurements in the EM-GHM algorithm fluctuated in the range of approximately 2.0–7.30. This may be due to the existence of systematic errors in TLS data, some remaining minor errors in the internal camera calibration parameters or possibly a correlation between the measurements. On the other hand, the rejection rate of 25 % for image target measurements in GHM-VCE algorithm with 95 % confidence level may show that sometimes VCE components were estimated too optimistic yielding to such high rejection rates of the observations.

At the end, the comparison of the results from proposed three adjustment models in estimation of the EOPs between the MSS show the precise, reliable, accurate and robust estimation of the parameters in all the proposed adjustment models. However, in case of Az data problem, the EM-GHM algorithm was not able to properly reweight the observations, which leads to inaccurate estimation of the parameters. Considering the run time speed-up procedure, the EM-qGMM algorithm was computationally efficient comparing to other two.

In the future work, an effect of the incidence angle for the targets in the 3D point clouds can be considered in the stochastic model. Moreover, the correlation between the Az angle of the TLS and the TLS target observations as well as a correlation between the internal camera calibration and estimated parameters need to be investigated. Possi-

bly the proposed robust estimation procedure is extended by considering a fully populated stochastic model instead of the diagonal stochastic model to tackle the correlation between the measurements. In addition, the zero direction problem regarding the TLS measurements can be improved by sending a command to the TLS via a software developer's kit (SDK) to start the measurements at the same zero direction. Furthermore, the points or line features can be considered in addition to the signalled targets in the rigorous adjustment procedure to improve the results.

7 Appendix

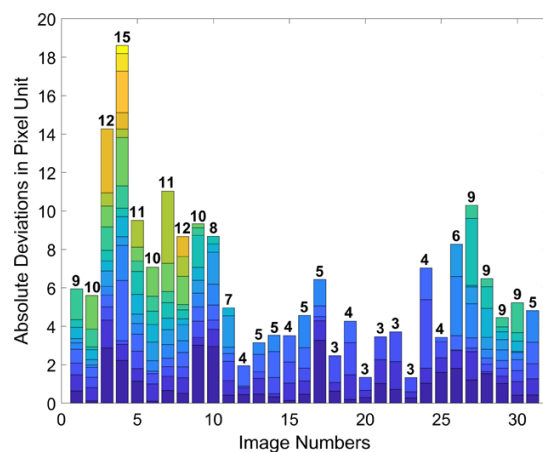


Figure 14: Case study I: Absolute deviations between the re-projected TLS data and measured image targets using 6 EOPs calculated from GHM-VCE algorithm with 99.7 % confidence level in pixel unit (Experiment 1).

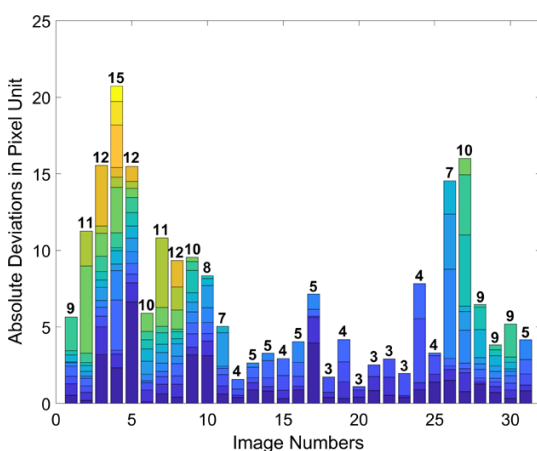


Figure 13: Case study I: Absolute deviations between the re-projected TLS data and measured image targets using 6 EOPs calculated from EM-qGMM algorithm in pixel unit (Experiment 1).

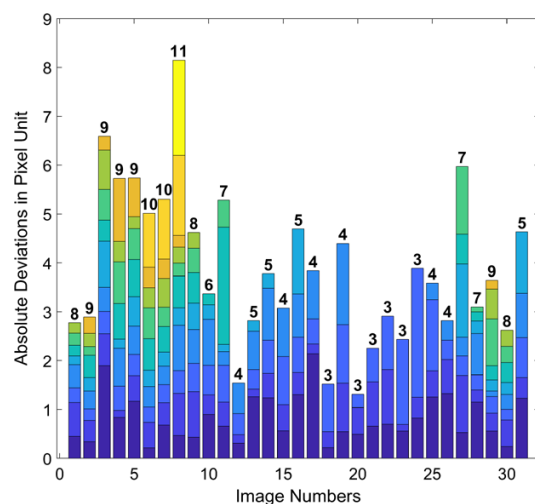


Figure 15: Absolute deviations between the re-projected TLS data and measured image targets using 6 EOPs calculated from GHM-VCE algorithm with 95 % confidence level in pixel unit (Experiment 1).

Table 12: Case study I: External calibration/orientation parameters (6 EOPs) between the TLS and digital camera with applied three adjustment models. The first column is the experiment number, the second column lists the 6 EOPs, the third column is the initial values, the columns (4–11) are the estimated 6 EOPs and their uncertainties calculated from the EM-GHM, EM-qGMM and GHM-VCE algorithms with 99.7 % and 95 % confidence levels, respectively.

Experi- ments No.	6 EOPs	Initial values	EM-GHM	σ	EM-qGMM	σ	GHM-VCE– 99.7 %	σ	GHM-VCE– 95 %	σ
1	ω (°)	88.00	90.4894	0.0035	90.4824	0.0016	90.4845	0.0023	90.4791	0.0015
	φ (°)	–11.00	–9.3096	0.0045	–9.3020	0.0104	–9.3052	0.0032	–9.2966	0.0026
	κ (°)	–0.23	–0.2313	0.0025	–0.2286	0.0021	–0.2296	0.0015	–0.2283	0.0012
	X_c (m)	–0.02	–0.0129	0.0003	–0.0131	0.0006	–0.0131	0.0003	–0.0135	0.0002
	Y_c (m)	0.22	0.2148	0.0003	0.2143	0.0001	0.2146	0.0002	0.2142	0.0001
	Z_c (m)	0.09	0.0881	0.0002	0.0872	0.0002	0.0879	0.0001	0.0869	0.0001
	Elapsed time (s)		247		368		779		2617	
2	ω (°)	88.00	90.5013	0.0035	90.4934	0.0006	90.4933	0.0021	90.4921	0.0019
	φ (°)	–11.00	–9.4399	0.0045	–9.4371	0.0002	–9.4402	0.0031	–9.4357	0.0027
	κ (°)	–0.23	–0.2201	0.0025	–0.2175	0.0003	–0.2182	0.0014	–0.2178	0.0013
	X_c (m)	–0.02	–0.0138	0.0003	–0.0137	0.0022	–0.0137	0.0002	–0.0140	0.0002
	Y_c (m)	0.22	0.2151	0.0003	0.2145	0.0097	0.2147	0.0002	0.2146	0.0002
	Z_c (m)	0.09	0.0880	0.0002	0.0871	0.0021	0.0875	0.0001	0.0872	0.0001
	Elapsed time (s)		246		350		1146		1632	
3	ω (°)	88.00	90.5085	0.0675	90.4654	0.0007	90.4679	0.0024	90.4635	0.0018
	φ (°)	–11.00	–9.4934	0.1037	–9.4890	0.0003	–9.4915	0.0035	–9.4944	0.0031
	κ (°)	–0.23	–0.2075	0.0459	–0.2151	0.0004	–0.2161	0.0016	–0.2158	0.0013
	X_c (m)	–0.02	–0.0138	0.0075	–0.0137	0.0032	–0.0137	0.0003	–0.0133	0.0002
	Y_c (m)	0.22	0.2183	0.0054	0.2144	0.0111	0.2148	0.0002	0.2144	0.0002
	Z_c (m)	0.09	0.0860	0.0043	0.0869	0.0014	0.0874	0.0002	0.0868	0.0001
	Elapsed time (s)		177		292		834		1847	
4	ω (°)	88.00	90.4917	0.0644	90.4561	0.0008	90.4583	0.0030	90.4564	0.0029
	φ (°)	–11.00	–9.6299	0.0997	–9.6323	0.0005	–9.6309	0.0040	–9.6317	0.0037
	κ (°)	–0.23	–0.2064	0.0426	–0.2128	0.0004	–0.2146	0.0019	–0.2140	0.0018
	X_c (m)	–0.02	–0.0128	0.0072	–0.0123	0.0068	–0.0124	0.0003	–0.0123	0.0003
	Y_c (m)	0.22	0.2168	0.0052	0.2135	0.0101	0.2138	0.0003	0.2137	0.0002
	Z_c (m)	0.09	0.0784	0.0041	0.0794	0.0040	0.0797	0.0002	0.0796	0.0002
	Elapsed time (s)		207		320		660		863	
5	ω (°)	88.00	90.4258	0.0025	90.4229	0.0006	90.4244	0.0028	90.4224	0.0024
	φ (°)	–11.00	–9.7507	0.0033	–9.7511	0.0002	–9.7495	0.0037	–9.7482	0.0031
	κ (°)	–0.23	–0.2082	0.0018	–0.2057	0.0002	–0.2076	0.0019	–0.2067	0.0016
	X_c (m)	–0.02	–0.0127	0.0002	–0.0125	0.0020	–0.0127	0.0003	–0.0126	0.0003
	Y_c (m)	0.22	0.2136	0.0002	0.2134	0.0129	0.2136	0.0002	0.2135	0.0002
	Z_c (m)	0.09	0.0812	0.0001	0.0806	0.0020	0.0806	0.0002	0.0798	0.0002
	Elapsed time (s)		3275		460		479		2021	
6	ω (°)	88.00	90.4402	0.0025	90.4390	0.0008	90.4408	0.0030	90.4376	0.0027
	φ (°)	–11.00	–9.8523	0.0031	–9.8506	0.0002	–9.8534	0.0038	–9.8489	0.0034
	κ (°)	–0.23	–0.2148	0.0018	–0.2138	0.0004	–0.2147	0.0019	–0.2142	0.0018
	X_c (m)	–0.02	–0.0130	0.0002	–0.0129	0.0024	–0.0128	0.0003	–0.0131	0.0003
	Y_c (m)	0.22	0.2137	0.0002	0.2136	0.0114	0.2138	0.0003	0.2136	0.0002
	Z_c (m)	0.09	0.0808	0.0001	0.0798	0.0021	0.0802	0.0002	0.0800	0.0002
	Elapsed time (s)		5879		458		299		746	

Table 13: Case study II: External calibration/orientation parameters (6 EOPs) between the TLS and digital camera with applied three adjustment models – Validation. The first column is the experiment number, the second column lists the 6 EOPs, the third column is the initial values, the columns (4–11) are the estimated 6 EOPs and their uncertainties calculated from the EM-GHM, EM-qGMM and GHM-VCE algorithms with 99.7 % and 95 % confidence levels, respectively.

Experi- ments No.	6 EOPs	Initial values	EM-GHM	σ	EM-qGMM	σ	GHM-VCE– 99.7 %	σ	GHM-VCE– 95 %	σ
1	ω (°)	88.00	90.4919	0.0056	90.4827	0.0049	90.4849	0.0019	90.4825	0.0016
	φ (°)	–11.00	–9.3116	0.0071	–9.2953	0.0195	–9.3084	0.0027	–9.3031	0.0021
	κ (°)	–0.23	–0.2311	0.0041	–0.2296	0.0029	–0.2307	0.0013	–0.2305	0.0012
	X_c (m)	–0.02	–0.0128	0.0005	–0.0136	0.0009	–0.0128	0.0002	–0.0128	0.0001
	Y_c (m)	0.22	0.2149	0.0004	0.2144	0.0004	0.2145	0.0001	0.2143	0.0001
	Z_c (m)	0.09	0.0882	0.0003	0.0872	0.0003	0.0875	0.0001	0.0862	0.0001
	Elapsed time (s)		6682		915		6814		11777	
2	ω (°)	88.00	90.5038	0.0056	90.4938	0.0036	90.4949	0.0019	90.4942	0.0018
	φ (°)	–11.00	–9.4407	0.0069	–9.4340	0.0171	–9.4417	0.0026	–9.4393	0.0023
	κ (°)	–0.23	–0.2181	0.0041	–0.2174	0.0026	–0.2166	0.0014	–0.2182	0.0013
	X_c (m)	–0.02	–0.0138	0.0005	–0.0139	0.0012	–0.0136	0.0002	–0.0135	0.0002
	Y_c (m)	0.22	0.2152	0.0004	0.2146	0.0004	0.2147	0.0001	0.2147	0.0001
	Z_c (m)	0.09	0.0880	0.0003	0.0865	0.0005	0.0873	0.0001	0.0870	0.0001
	Elapsed time (s)		569		746		3999		7123	
3	ω (°)	88.00	90.5573	0.1512	90.4659	0.0050	90.4685	0.0021	90.4653	0.0018
	φ (°)	–11.00	–9.5637	0.2425	–9.4845	0.0124	–9.4922	0.0029	–9.4959	0.0024
	κ (°)	–0.23	–0.1849	0.1099	–0.2157	0.0045	–0.2160	0.0015	–0.2159	0.0014
	X_c (m)	–0.02	–0.0095	0.0159	–0.0139	0.0009	–0.0136	0.0002	–0.0130	0.0002
	Y_c (m)	0.22	0.2213	0.0109	0.2145	0.0004	0.2146	0.0002	0.2145	0.0001
	Z_c (m)	0.09	0.0815	0.0082	0.0867	0.0005	0.0874	0.0001	0.0862	0.0001
	Elapsed time (s)		353		930		3408		7627	
4	ω (°)	88.00	90.5278	0.1390	90.4597	0.0035	90.4599	0.0025	90.4551	0.0022
	φ (°)	–11.00	–9.6655	0.2262	–9.6351	0.0123	–9.6308	0.0037	–9.6330	0.0029
	κ (°)	–0.23	–0.1867	0.1004	–0.2114	0.0022	–0.2139	0.0018	–0.2120	0.0016
	X_c (m)	–0.02	–0.0106	0.0152	–0.0122	0.0008	–0.0125	0.0003	–0.0120	0.0002
	Y_c (m)	0.22	0.2191	0.0101	0.2138	0.0003	0.2138	0.0002	0.2136	0.0002
	Z_c (m)	0.09	0.0753	0.0079	0.0791	0.0003	0.0804	0.0002	0.0789	0.0001
	Elapsed time (s)		324		921		2005		7992	
5	ω (°)	88.00	90.4282	0.0041	90.4262	0.0047	90.4273	0.0023	90.4212	0.0021
	φ (°)	–11.00	–9.7527	0.0050	–9.7483	0.0815	–9.7510	0.0033	–9.7513	0.0027
	κ (°)	–0.23	–0.2071	0.0030	–0.2066	0.0015	–0.2064	0.0016	–0.2051	0.0015
	X_c (m)	–0.02	–0.0127	0.0004	–0.0125	0.0007	–0.0126	0.0002	–0.0121	0.0002
	Y_c (m)	0.22	0.2137	0.0003	0.2136	0.0002	0.2137	0.0002	0.2134	0.0002
	Z_c (m)	0.09	0.0817	0.0002	0.0800	0.0004	0.0810	0.0001	0.0795	0.0001
	Elapsed time (s)		983		921		2028		10146	
6	ω (°)	88.00	90.4420	0.0040	90.4420	0.0012	90.4432	0.0025	90.4375	0.0021
	φ (°)	–11.00	–9.8543	0.0047	–9.8498	0.0114	–9.8485	0.0038	–9.8514	0.0027
	κ (°)	–0.23	–0.2136	0.0029	–0.2159	0.0009	–0.2131	0.0018	–0.2127	0.0015
	X_c (m)	–0.02	–0.0129	0.0004	–0.0129	0.0024	–0.0133	0.0003	–0.0127	0.0002
	Y_c (m)	0.22	0.2138	0.0003	0.2138	0.0001	0.2139	0.0002	0.2136	0.0002
	Z_c (m)	0.09	0.0813	0.0002	0.0791	0.0002	0.0809	0.0001	0.0795	0.0001
	Elapsed time (s)		3689		876		448		7740	

Table 14: Case study II: External calibration/orientation parameters (7 EOPs) between the TLS and LT with applied three adjustment models – Validation. The first column is the experiment number, the second column lists the 7 EOPs, the third column is the initial values, the columns (4–11) are the estimated 7 EOPs and their uncertainties calculated from the EM-GHM, EM-qGMM and GHM-VCE algorithms with 99.7 % and 95 % confidence levels, respectively.

Experi- ments No.	7 EOPs	Initial values	EM-GHM	σ	EM-qGMM	σ	GHM-VCE– 99.7 %	σ	GHM-VCE– 95 %	σ
1	ω' (°)	0.10	0.1013	0.0005	0.1017	0.0001	0.0995	0.0003	0.0992	0.0004
	ϕ' (°)	−0.07	−0.0673	0.0006	−0.0688	0.0001	−0.0681	0.0003	−0.0686	0.0004
	κ' (°)	43.20	43.2115	0.0004	43.2112	0.0001	43.2129	0.0003	43.2125	0.0003
	X'_c (m)	12.80	12.8019	0.0001	12.8019	0.0001	12.8018	0.0001	12.8019	0.0001
	Y'_c (m)	15.70	15.7212	0.0001	15.7212	0.0001	15.7213	0.0001	15.7213	0.0001
	Z'_c (m)	1.70	1.7021	0.0001	1.7021	0.0001	1.7021	0.0001	1.7021	0.0001
	λ	1.0	0.99987	0.00001	0.99987	0.00001	0.99987	0.00002	0.99987	0.00001
	Elapsed time (s)		6682		915		6814		11777	
2	ω' (°)	0.10	0.0997	0.0005	0.0998	0.0001	0.0984	0.0004	0.0971	0.0004
	ϕ' (°)	−0.07	−0.0693	0.0006	−0.0696	0.0001	−0.0696	0.0004	−0.0696	0.0004
	κ' (°)	43.20	43.2214	0.0004	43.2212	0.0001	43.2225	0.0003	43.2228	0.0003
	X'_c (m)	12.80	12.8019	0.0001	12.8018	0.0001	12.8019	0.0001	12.8019	0.0001
	Y'_c (m)	15.70	15.7212	0.0001	15.7211	0.0001	15.7213	0.0001	15.7213	0.0001
	Z'_c (m)	1.70	1.7022	0.0001	1.7022	0.0001	1.7022	0.0001	1.7021	0.0001
	λ	1.0	0.99987	0.00001	0.99986	0.00001	0.99988	0.00001	0.99989	0.00001
	Elapsed time (s)		569		746		3999		7123	
3	ω' (°)	0.10	0.1006	0.0073	0.1002	0.0001	0.0987	0.0003	0.0982	0.0003
	ϕ' (°)	−0.07	−0.0690	0.0080	−0.0703	0.0001	−0.0695	0.0004	−0.0698	0.0004
	κ' (°)	43.20	43.2189	0.0060	43.2182	0.0001	43.2196	0.0003	43.2194	0.0003
	X'_c (m)	12.80	12.8018	0.0005	12.8019	0.0001	12.8019	0.0001	12.8019	0.0001
	Y'_c (m)	15.70	15.7212	0.0005	15.7213	0.0001	15.7213	0.0001	15.7214	0.0001
	Z'_c (m)	1.70	1.7023	0.0006	1.7022	0.0001	1.7022	0.0001	1.7021	0.0001
	λ	1.0	0.99987	0.0002	0.99986	0.00001	0.99989	0.00001	0.99987	0.00001
	Elapsed time (s)		353		930		3408		7627	
4	ω' (°)	0.10	0.1043	0.0065	0.1034	0.0001	0.1030	0.0004	0.1015	0.0004
	ϕ' (°)	−0.07	−0.0668	0.0069	−0.0682	0.0001	−0.0660	0.0004	−0.0667	0.0004
	κ' (°)	43.20	43.2172	0.0053	43.2171	0.0001	43.2179	0.0003	43.2190	0.0004
	X'_c (m)	12.80	12.8018	0.0005	12.8017	0.0001	12.8018	0.0001	12.8017	0.0001
	Y'_c (m)	15.70	15.7212	0.0005	15.7211	0.0001	15.7212	0.0001	15.7213	0.0001
	Z'_c (m)	1.70	1.7023	0.0005	1.7022	0.0001	1.7022	0.0001	1.7021	0.0001
	λ	1.0	0.99990	0.0001	0.99989	0.00001	0.99992	0.00001	0.99992	0.00001
	Elapsed time (s)		324		921		2005		7992	
5	ω' (°)	0.10	0.1031	0.0005	0.1038	0.0001	0.1030	0.0004	0.1004	0.0004
	ϕ' (°)	−0.07	−0.0659	0.0005	−0.0661	0.0001	−0.0655	0.0004	−0.0661	0.0004
	κ' (°)	43.20	43.2159	0.0004	43.2158	0.0001	43.2158	0.0003	43.2171	0.0004
	X'_c (m)	12.80	12.8017	0.0001	12.8018	0.0001	12.8017	0.0001	12.8018	0.0001
	Y'_c (m)	15.70	15.7212	0.0001	15.7211	0.0001	15.7212	0.0001	15.7213	0.0001
	Z'_c (m)	1.70	1.7022	0.0001	1.7023	0.0001	1.7022	0.0001	1.7021	0.0001
	λ	1.0	0.99991	0.00001	0.99989	0.00001	0.99991	0.00001	0.99992	0.00001
	Elapsed time (s)		983		921		2028		10146	
6	ω' (°)	0.10	0.1049	0.0006	0.1049	0.0001	0.1049	0.0004	0.1025	0.0005
	ϕ' (°)	−0.07	−0.0638	0.0006	−0.0634	0.0001	−0.0635	0.0005	−0.0640	0.0004
	κ' (°)	43.20	43.2156	0.0004	43.2153	0.0001	43.2154	0.0004	43.2171	0.0004
	X'_c (m)	12.80	12.8018	0.0001	12.8017	0.0001	12.8018	0.0001	12.8018	0.0001
	Y'_c (m)	15.70	15.7212	0.0001	15.7211	0.0001	15.7212	0.0001	15.7213	0.0001
	Z'_c (m)	1.70	1.7022	0.0001	1.7022	0.0001	1.7022	0.0001	1.7022	0.0001
	λ	1.0	0.99991	0.00001	0.99986	0.00001	0.99990	0.00001	0.99991	0.00001
	Elapsed time (s)		3689		876		448		7740	

Acknowledgment: The authors would like to acknowledge Dr.-Ing. Manfred Wiggenghagen from the Institute of Photogrammetry and Geoinformation of Leibniz Universität Hannover for his invaluable advice and kind supports concerning the camera settings and calibration.

Funding: The research presented was partly carried out within the scope of the collaborative project “Spatio-temporal monitoring of bridge structures using low cost sensors” with ALLSAT GmbH, which was supported by the German Federal Ministry for Economic Affairs and Energy (BMWi) and the Central Innovation Programme for SMEs (Grant ZIM Kooperationsprojekt, ZF4081803DB6).

References

- [1] A. Abellán, M. Jaboyedoff, T. Oppikofer, and J. M. Vilaplana (2009). Detection of millimetric deformation using a terrestrial laser scanner: experiment and application to a rockfall event. *Natural Hazards and Earth System Sciences*, 9(2), 365–372.
- [2] F. Buill, M. A. Núñez-Andrés, N. Lantada, and A. Prades (2016). Comparison of photogrammetric techniques for rockfalls monitoring. In *IOP Conference Series: Earth and Environmental Science*, 44(4), 042023, IOP Publishing.
- [3] A. Ebeling (2014). Ground-based deformation monitoring. Ph. D. thesis, University of Calgary.
- [4] D. Wujanz (2016). Terrestrial laser scanning for geodetic deformation monitoring. Ph. D. thesis, Technischen Universität Berlin.
- [5] M. Alba, L. Fregonese, F. Prandi, M. Scaioni, and P. Valgoi (2006). Structural monitoring of a large dam by terrestrial laser scanning. *International Archives of Photogrammetry, Remote Sensing and Spatial Information Sciences*, 36(5), 6.
- [6] S. Gamse (2018). Dynamic modelling of displacements on an embankment dam using the Kalman filter. *Journal of Spatial Science*, 63(1), 3–21.
- [7] W. Li and C. Wang (2011). GPS in the tailings dam deformation monitoring. *Procedia Engineering*, 26, 1648–1657.
- [8] H. Löhmus, A. Ellmann, S. Märdla, and S. Idnurm (2017). Terrestrial laser scanning for the monitoring of bridge load tests—two case studies. *Survey Review*, 1–15.
- [9] J. W. Lovse, W. F. Teskey, G. Lachapelle, and M. E. Cannon (1995). Dynamic deformation monitoring of tall structure using GPS technology. *Journal of Surveying Engineering*, 121(1), 35–40.
- [10] D. Reagan, A. Sabato, and C. Niezrecki (2017). Feasibility of using digital image correlation for unmanned aerial vehicle structural health monitoring of bridges. *Structural Health Monitoring*, 1475921717735326.
- [11] M. Scaioni and J. Wang (2016). Technologies for Dam Deformation Measurement: Recent Trends and Future Challenges. In *3rd Joint Int. Symp. on Deformation Monitoring (IJSDM 2016)*, 1–8.
- [12] D. Schneider (2006). Terrestrial laser scanning for area based deformation analysis of towers and water dams. In *Proc. of 3rd IAG/12th FIG Symp.*, Baden, Austria, 22–24.
- [13] L. Truong-Hong, H. Falter, D. Lennon, and D. F. Laefer (2016). Framework for bridge inspection with laser scanning. In *EASEC-14 Structural Engineering and Construction*, Ho Chi Minh City, Vietnam, 6–8.
- [14] J.-A. Paffenholz, J. Hüge, and U. Stenz (2018). Integration von Lasertracking und Laserscanning zur optimalen Bestimmung von lastinduzierten Gewölbeverformungen. *Allgemeine Vermessungs-Nachrichten (avn)*, 125(4), 73–88.
- [15] N. Haala, R. Reulke, M. Thies, and T. Aschoff (2004). Combination of terrestrial laser scanning with high resolution panoramic images for investigations in forest applications and tree species recognition. *International Archives of Photogrammetry, Remote Sensing and Spatial Information Sciences*, 34(5/W16).
- [16] J. A. Beraldin (2004). Integration of laser scanning and close-range photogrammetry—The last decade and beyond. In *Proceedings of the XXth ISPRS Congress, Commission VII*, Istanbul, Turkey, 972–983.
- [17] H. J. Przybilla (2006). Fusion of terrestrial laser scanning and digital photogrammetry. *International Archives of Photogrammetry, Remote Sensing and Spatial Information Sciences*, 36, 5.
- [18] M. N. S. Sayyad (2016). Joint use and mutual control of terrestrial laser scans and digital images for accurate 3D measurements. Ph. D. thesis, Fachrichtung Geodäsie und Geoinformatik, Univ.
- [19] H. Yang, M. Omidalizarandi, X. Xu, and I. Neumann (2017). Terrestrial laser scanning technology for deformation monitoring and surface modeling of arch structures. *Composite Structures*, 169, 173–179.
- [20] J. Albert, H. G. Maas, A. Schade, and W. Schwarz (2002). Pilot studies on photogrammetric bridge deformation measurement. In *Proceedings of the 2nd IAG Commission IV Symposium on Geodesy for Geotechnical and Structural Engineering*, 21–24.
- [21] Ö. Avsar, D. Akca, and O. Altan (2014). Photogrammetric deformation monitoring of the second Bosphorus Bridge in Istanbul. *The International Archives of Photogrammetry, Remote Sensing and Spatial Information Sciences*, 40(5), 71.
- [22] I. Datchev, A. Habib, and M. El-Badry (2011). Case study of beam deformation monitoring using conventional close range photogrammetry. In *ASPRS 2011 Annual Conference, ASPRS*, Milwaukee, Wisconsin, USA.
- [23] U. Hampel and H. G. Maas (2003). Application of digital photogrammetry for measuring deformation and cracks during load tests in civil engineering material testing. *Optical 3-D Measurement Techniques VI*, 2, 80–88.
- [24] H. G. Maas (1998). Photogrammetric techniques for deformation measurements on reservoir walls. In *The Proceedings Of The IAG Symposium On Geodesy For Geotechnical And Structural Engineering*, Eisenstadt, Austria, 319–324.
- [25] H. G. Maas and U. Hampel (2006). Photogrammetric techniques in civil engineering material testing and structure monitoring. *Photogrammetric Engineering & Remote Sensing*, 72(1), 39–45.

- [26] W. Niemeier, B. Riedel, C. Fraser, H. Neuss, R. Stratmann, and E. Ziem (2008). New digital crack monitoring system for measuring and documentation of width of cracks in concrete structures. In *Proc. of 13th FIG Symp. on Deformation Measurement and Analysis and 14th IAG Symp. on Geodesy for Geotechnical and Structural Engineering*, Lisbon, 12–15.
- [27] T. Whiteman, D. D. Lichti, and I. Chandler (2002). Measurement of deflections in concrete beams by close-range digital photogrammetry. In *Proceedings of the Symposium on Geospatial Theory, Processing and Applications*, 9–12.
- [28] P. J. Besl and N. D. McKay (1992). Method for registration of 3-D shapes. In *Sensor Fusion IV: Control Paradigms and Data Structures*, 1611, 586–607, International Society for Optics and Photonics.
- [29] A. Wendt and C. Dold (2005). Estimation of interior orientation and eccentricity parameters of a hybrid imaging and laser scanning sensor. *Proceedings of the ISPRS Working Group*, 5, 1682–1750.
- [30] D. D. Lichti, S. J. Gordon, and T. Tipdecho (2005). Error models and propagation in directly georeferenced terrestrial laser scanner networks. *Journal of Surveying Engineering*, 131(4), 135–142.
- [31] M. Zámečníková, H. Neuner, S. Pegritz, and R. Sonleitner (2015). Investigation on the influence of the incidence angle on the reflectorless distance measurement of a terrestrial laser scanner. *Vermessung & Geoinformation*, 2(3), 208–218.
- [32] D. Wujanz, M. Burger, M. Mettenleiter, and F. Neitzel (2017). An intensity-based stochastic model for terrestrial laser scanners. *ISPRS Journal of Photogrammetry and Remote Sensing*, 125, 146–155.
- [33] X. Zhao, H. Alkhatib, B. Kargoll, and I. Neumann (2017). Statistical evaluation of the influence of the uncertainty budget on B-spline curve approximation. *Journal of Applied Geodesy*, 11(4), 215–230.
- [34] D. Schneider and H. G. Maas (2007). Integrated bundle adjustment of terrestrial laser scanner data and image data with variance component estimation. *The Photogrammetric Journal of Finland*, 20, 5–15.
- [35] K. R. Koch (2014). Robust estimations for the nonlinear Gauss Helmert model by the expectation maximization algorithm. *Journal of Geodesy*, 88(3), 263–271.
- [36] Q. Zhang and R. Pless (2004). Extrinsic calibration of a camera and laser range finder (improves camera calibration). In *Intelligent Robots and Systems, 2004 (IROS 2004)*. *Proceedings. 2004 IEEE/RSJ International Conference on IEEE*, 3, 2301–2306.
- [37] G. Pandey, J. McBride, S. Savarese, and R. Eustice (2010). Extrinsic calibration of a 3d laser scanner and an omnidirectional camera. *IFAC Proceedings Volumes*, 43(16), 336–341.
- [38] R. Unnikrishnan and M. Hebert (2005). Fast extrinsic calibration of a laser rangefinder to a camera. *Carnegie Mellon University*.
- [39] D. D. Lichti, C. Kim, and S. Jamtsho (2010). An integrated bundle adjustment approach to range camera geometric self-calibration. *ISPRS Journal of Photogrammetry and Remote Sensing*, 65(4), 360–368.
- [40] G. Pandey, J. R. McBride, S. Savarese, and R. M. Eustice (2012). Automatic Targetless Extrinsic Calibration of a 3D Lidar and Camera by Maximizing Mutual Information. In *Proceedings of the AAAI National Conference on Artificial Intelligence*, 2054–2056.
- [41] M. Omidalizarandi and I. Neumann (2015). Comparison of target-and mutual information based calibration of terrestrial laser scanner and digital camera for deformation monitoring. *The International Archives of Photogrammetry, Remote Sensing and Spatial Information Sciences*, 40(1), 559–564.
- [42] M. Omidalizarandi, J.-A. Paffenholz, U. Stenz, and I. Neumann (2016). Highly accurate extrinsic calibration of terrestrial laser scanner and digital camera for structural monitoring applications. In: *Proceedings of the 3rd Joint International Symposium on Deformation Monitoring (JISDM)*, Vienna, 30 March–1 April, 2016, p. 8, CD Proceedings.
- [43] F. M. Mirzaei, D. G. Kottas, and S. I. Roumeliotis (2012). 3D LIDAR—camera intrinsic and extrinsic calibration: Identifiability and analytical least-squares-based initialization. *The International Journal of Robotics Research*, 31(4), 452–467.
- [44] E. K. Forkuo and B. King (2004). Automatic fusion of photogrammetric imagery and laser scanner point clouds. *International Archives of Photogrammetry and Remote Sensing*, 35(2004), 921–926.
- [45] M. A. Fischler and R. C. Bolles (1987). Random sample consensus: a paradigm for model fitting with applications to image analysis and automated cartography. *Readings in Computer Vision*, 726–740.
- [46] A. Habib, M. Ghanma, M. Morgan, and R. Al-Ruzouq (2005). Photogrammetric and LiDAR data registration using linear features. *Photogrammetric Engineering & Remote Sensing*, 71(6), 699–707.
- [47] M. Omidalizarandi, B. Kargoll, J.-A. Paffenholz, and I. Neumann (2018). Accurate vision-based displacement and vibration analysis of bridge structures by means of an image-assisted total station. *Advances in Mechanical Engineering*, 10(6), 1687814018780052.
- [48] Zoller+Fröhlich GmbH (2007). Technical Data IMAGER 5006; Version 1.0.5; Zoller+Fröhlich GmbH: Wangen im Allgäu, Germany (in German).
- [49] U. Stenz, J. Hartmann, J.-A. Paffenholz, and I. Neumann (2017). A framework based on reference data with superordinate accuracy for the quality analysis of terrestrial laser scanning-based multi-sensor-systems. *Sensors*, 17(8), 1886.
- [50] PhotographyLife. <https://photographylife.com> (Accessed 27 November 2018)..
- [51] M. Omidalizarandi, J.-A. Paffenholz, and I. Neumann. Automatic and accurate passive target centroid detection for applications in engineering geodesy. *Survey Review*, 1–16.
- [52] Hexagon Metrology (2015). Leica Absolute Tracker AT960 Brochure. Available online: <http://www.hexagonmi.com/products/laser-tracker-systems/leica-absolute-tracker-at960#loren> (Accessed on 2015).
- [53] C. B. Duane (1971). Close-range camera calibration. *Photogram. Eng. Remote Sens.*, 37, 855–866.
- [54] K. Al-Manasir and C. S. Fraser (2006). Registration of terrestrial laser scanner data using imagery. *The Photogrammetric Record*, 21(115), 255–268.
- [55] T. Luhmann, S. Robson, S. Kyle, and J. Boehm (2015). *Close-Range Photogrammetry and 3D Imaging*. 2nd ed. de Gruyter, Berlin.
- [56] B. K. Horn (1987). Closed-form solution of absolute orientation using unit quaternions. *JOSA A*, 4(4), 629–642.

- [57] K. R. Koch (2014). Outlier detection for the nonlinear Gauss Helmert model with variance components by the expectation maximization algorithm. *Journal of Applied Geodesy*, 8(3), 185–194.
- [58] E. Parzen (1979). A density-quantile function perspective on robust estimation. In: L. Launer, G. N. Wilkinson (eds.) *Robustness in Statistics*, pp. 237–258, Academic Press.
- [59] Z. Wiśniewski (2014). M-estimation with probabilistic models of geodetic observations. *Journal of Geodesy*, 88(10), 941–957.
- [60] ISO/IEC (2008). JCGM 100:2008 Evaluation of measurement data — Guide to the expression of uncertainty in measurement. First edition 2008, corrected version 2010. International Organization for Standardization (ISO), Geneva.
- [61] K. D. Sommer, B. R. L. Siebert (2004). Praxisgerechtes Bestimmen der Messunsicherheit nach GUM. *Technisches Messen*, 71, 52–66.
- [62] K. R. Koch and B. Kargoll (2013). Expectation maximization algorithm for the variance-inflation model by applying the t-distribution. *Journal of Applied Geodesy*, 7(3), 217–225.
- [63] K. Takai (2012). Constrained EM algorithm with projection method. *Computational Statistics*, 27, 701–714.
- [64] H. Alkhatib, B. Kargoll, and J.-A. Paffenholz (2017). Robust multivariate time series analysis in nonlinear models with autoregressive and t-distributed errors. In O. Valenzuela, F. Rojas, H. Pomares, I. Rojas (eds.), *Proceedings ITISE 2017 – International work-conference on Time Series*, 1, 23–36.
- [65] G. I. Hargreaves (2002). Interval Analysis in MATLAB. Numerical Analysis Report, No. 416, Manchester Centre for Computational Mathematics, The University of Manchester, ISSN 1360-1725.
- [66] E. M. Mikhail and F. E. Ackermann (1976). *Observations and least squares*. Dun-Donnelly, New York.
- [67] W. Niemeier (2008). *Ausgleichsrechnung: eine Einführung für Studierende und Praktiker des Vermessungs- und Geoinformationswesens*, 2nd ed. Walter de Gruyter, Berlin (in German).
- [68] A. R. Amiri-Simkooei and S. Jazaeri (2013). Data-snooping procedure applied to errors-in-variables models. *Studia Geophysica et Geodaetica*, 57(3), 426–441.
- [69] P. J. G. Teunissen (2006). *Testing Theory: an Introduction*. Series on Mathematical Geodesy and Positioning. Delft University Press, Delft University of Technology, Delft, The Netherlands.
- [70] K. R. Koch (2013). *Parameter estimation and hypothesis testing in linear models*. 2nd ed. Springer Science and Business Media, Berlin, Germany.
- [71] F. Neitzel (2010). *Ausgleichsrechnung–Modellbildung, Auswertung, Qualitätsbeurteilung*. Qualitätsmanagement geodätischer Mess- und Auswerteverfahren, Beiträge zum, 93, 95–127 (in German).
- [72] W. Baarda (1968). A testing procedure for use in geodetic networks. Delft, Kanaalweg 4, Rijkscommissie voor Geodesie, 1968, 1.
- [73] D. Schneider (2008). *Geometrische und stochastische Modelle für die integrierte Auswertung terrestrischer Laserscannerdaten und photogrammetrischer Bilddaten*. Ph. D. thesis, Deutsche Geodätische Kommission, Reihe C, Nr. 642, Technische Universität Dresden, Dresden, Germany. Available from: <http://dgk.badw.de/fileadmin/docs/c-642.pdf>.

Paper 4

Mohammad Omidalizarandi*, Ralf Herrmann, Boris Kargoll, Steffen Marx,
Jens-André Paffenholz, and Ingo Neumann

A validated robust and automatic procedure for vibration analysis of bridge structures using MEMS accelerometers

<https://doi.org/10.1515/jag-2020-0010>

Received February 19, 2020; accepted May 28, 2020

Abstract: Today, short- and long-term structural health monitoring (SHM) of bridge infrastructures and their safe, reliable and cost-effective maintenance has received considerable attention. From a surveying or civil engineer's point of view, vibration-based SHM can be conducted by inspecting the changes in the global dynamic behaviour of a structure, such as natural frequencies (i. e. eigenfrequencies), mode shapes (i. e. eigenforms) and modal damping, which are known as modal parameters. This research work aims to propose a robust and automatic vibration analysis procedure that is so-called robust time domain modal parameter identification (RT-MPI) technique. It is novel in the sense of automatic and reliable identification of initial eigenfrequencies even closely spaced ones as well as robustly and accurately estimating the modal parameters of a bridge structure using low numbers of cost-effective micro-electro-mechanical systems (MEMS) accelerometers. To estimate amplitude, frequency, phase shift and damping ratio coefficients, an observation model consisting of: (1) a damped harmonic oscillation model, (2) an autoregressive model of coloured measurement noise and (3) a stochastic model in the form of the heavy-tailed family of scaled t-distributions is employed and

jointly adjusted by means of a generalised expectation maximisation algorithm. Multiple MEMS as part of a geo-sensor network were mounted at different positions of a bridge structure which is precalculated by means of a finite element model (FEM) analysis. At the end, the estimated eigenfrequencies and eigenforms are compared and validated by the estimated parameters obtained from acceleration measurements of high-end accelerometers of type PCB ICP quartz, velocity measurements from a geophone and the FEM analysis. Additionally, the estimated eigenfrequencies and modal damping are compared with a well-known covariance driven stochastic subspace identification approach, which reveals the superiority of our proposed approach. We performed an experiment in two case studies with simulated data and real applications of a footbridge structure and a synthetic bridge. The results show that MEMS accelerometers are suitable for detecting all occurring eigenfrequencies depending on a sampling frequency specified. Moreover, the vibration analysis procedure demonstrates that amplitudes can be estimated in submillimetre range accuracy, frequencies with an accuracy better than 0.1 Hz and damping ratio coefficients with an accuracy better than 0.1 and 0.2 % for modal and system damping, respectively.

Keywords: Vibration analysis, Automatic modal parameters identification, MEMS accelerometer, Robust parameter estimation, EM algorithm, Double integration, FEM analysis, Bridge monitoring

*Corresponding author: **Mohammad Omidalizarandi**, Geodetic Institute, Leibniz University Hannover, Hannover, Germany, e-mail: zarandi@gih.uni-hannover.de, ORCID: <https://orcid.org/0000-0002-9897-4473>

Ralf Herrmann, Bundesanstalt für Materialforschung und -prüfung (BAM), Berlin, Germany, e-mail: ralf.herrmann@bam.de

Boris Kargoll, Institut für Geoinformation und Vermessung Dessau, Hochschule Anhalt, Dessau-Roßlau, Germany, e-mail: boris.kargoll@hs-anhalt.de, ORCID: <https://orcid.org/0000-0003-3496-6391>

Steffen Marx, Institute of Concrete Construction, Leibniz University Hannover, Hannover, Germany, e-mail: marx@ifma.uni-hannover.de

Jens-André Paffenholz, Institute of Geotechnical Engineering and Mine Surveying, Clausthal University of Technology, Clausthal-Zellerfeld, Germany, e-mail: jens-andre.paffenholz@tu-clausthal.de, ORCID: <https://orcid.org/0000-0003-1222-5568>

Ingo Neumann, Geodetic Institute, Leibniz University Hannover, Hannover, Germany, e-mail: neumann@gih.uni-hannover.de

1 Introduction

Short- and long-term structural health monitoring (SHM) of bridge infrastructures and their safe, reliable and cost-effective maintenance has received increasing attention in the last three decades. The SHM process involves regular measurements of the structure over time using an array of sensors to detect unsafe conditions, unexpected behaviour or structural damage, which allows us to realise the current state of the health of a structure [1]. The SHM is commonly carried out based on visual observation, the

properties of the material of the structures and the interpretation of the structural dynamic characteristics by inspecting the changes in the global dynamic behaviour of the structure, such as natural frequencies (i. e. eigenfrequencies), mode shapes (i. e. eigenforms) and modal damping [2], which are known as modal parameters.

As reported by the US Federal Highway Agency in 2005, 28 % of the US bridges, 10 % of the European bridges and an average of 10 % of the Asian bridges are deficient [3], which illustrates the important role of frequent diagnosis, improvement and monitoring. Thus, it is crucial to develop a hardware measurement system as well as implementing a software, which enable us to perform a cost-effective, automatic, timely, continuous, robust, reliable, accurate and precise vibration-based SHM of the bridge structures.

The vibration-based SHM can be accomplished either in near real-time by estimating the modal parameters or in a post-processing step, by interpretation of the parameters calculated by statistical testing, which are usually the time-consuming tasks. However, such interpretation can also vary depending on the material and geometry of the structure case by case. Additionally, applied excitations and temperature changes also have an influence on the modal parameters, which make it more challenging to recognise the degradation of the structure [4]. As described by Rohrmann et al. [5], such physical phenomena (i. e. temperature variations) can lead to frequency changes up to 10 % over the year. Inspecting the influence of the temperature on the modal parameters requires a large-scale data acquisition over a year, which was out of scope of this study. Therefore, we mainly focus on the estimation procedure for a specific temperature to simplify the task.

Different contact-based or non-contact-based measurement techniques can be utilised to monitor the long-term movement of bridge structures, induced, for example, by foundation settlement, or the short-term movements, induced, for example, by wind and traffic [6]. Roberts et al. [7], for example, performed bridge deflection monitoring using a GPS with a sampling frequency of 10 Hz and a triaxial accelerometer with a sampling frequency of 200 Hz. The GPS measurements were utilised to suppress the accumulation drift of the acceleration data over time through zero velocity update and coordinate updates. Neitzel et al. [8] performed vibration analysis of a bridge using a sensor network of low-cost accelerometers with a sampling frequency of 600 Hz, a terrestrial laser scanner (TLS; Zoller+Fröhlich Imager 5003) in a single-point measurement mode with a sampling frequency of 7812 Hz and a terrestrial interferometric synthetic aperture radar with

a sampling frequency of 200 Hz as a reference sensor for the validation purpose. The modal parameters, such as first natural frequency and damping coefficients, were calculated based on a damped harmonic oscillation (DHO) model and were solved in the sense of the least square adjustment. Psimoulis and Stiros [9] performed vibration monitoring of a short span railway bridge using a robotic total station (RTS) with non-constant sampling rate measurements in a range of 5–7 Hz. The spectral analysis was carried out based on the least squares spectrum analysis [10] and the Norm-Period code [11] to deal with non-equidistant data. Ehrhart and Lienhart [12] carried out displacement and vibration analysis of a footbridge structure using an image-assisted total station (IATS) of type Leica MS50 with a sampling frequency of 10 Hz, an accelerometer of type HBM B12/200 with a sampling frequency of 200 Hz and a RTS of type Leica TS15 with a sampling frequency of 20 Hz. A displacement time series was generated using captured video frames from the telescope camera of the IATS for a circular target marking attached to the footbridge structure and structural features, such as bolts.

As a preliminary step, on the one hand, a suitable sensor with an adequate measurement rate (in the light of Nyquist sampling theorem) must be selected which allows us to identify all eigenfrequencies occurred at the bridge structures. On the other hand, an opportunity must be provided to set up cost-effective sensors at the bridge structures which will perform regular measurements for a long period of time. Preferably, it is also advantageous when the measurement system does not require frequent recalibration.

The modal identification techniques can be categorised into three groups: 1) the experimental modal analysis (EMA) [13] using input data (e. g. measured forces) and output data (e. g. acceleration data), 2) the operational modal analysis (OMA), relying on the output-only data and 3) the combined experimental OMA with exogenous inputs (OMAX) [14], using an artificial force. The induced forces for the excitation of a structure in EMA methods need to be measured and considered in an estimation procedure, such as the frequency response function (FRF) [15] technique. However, such an experiment is not practically suitable to be carried out for the large structures, such as bridges, and too expensive to generate excitation [16]. On the other hand, the OMA has two disadvantages, as described by Parloo [17]: 1) it often records poor data quality due to a low ambient excitation level or lower signal to noise ratio (SNR) compared to data recorded from a forced excitation, and 2) the incorrectly scaled estimates of the mode shapes, which vary depending on the ambient excitation level. The main difference between OMAX and EMA

approaches is that the induced forces are considered as useful excitation and not as a noise in a modal identification process with excitation amplitudes (i. e. due to the artificial forces) at the level of amplitudes of the operational forces or lower [18]. In vibration-based SHM of a bridge structure, the ambient excitation is of utmost interest, since it reflects the true excitation due to traffic, wind, wave and micro-earthquakes over its lifetime [4].

The OMA can be performed in either the frequency domain or the time domain. The spectra or the half-spectra are typically estimated from the measurements in a pre-processing step in frequency domain OMA methods and used as input (e. g. Peeters et al. [19], Peeters and Van der Auweraer [20]). However, the measurement or their cross covariance in time domain OMA methods are being used directly as input. Previous researchers performed OMA based on the natural excitation technique [21], stochastic subspace identification (SSI) [22, 23, 24, 25, 26, 27, 28], frequency domain decomposition (FDD) [29], random decrement technique [30], wavelet [31] and the polyreference [19, 20] version of least squares complex frequency-domain (LSCF) [32] estimates.

In order to identify the modal parameters based on the OMA method, for example, Van Overschee and De Moor [22] proposed the SSI algorithm to determine state space matrices using QR-factorisation, singular value decomposition (SVD) and least squares adjustment. The SSI method can be performed using either the raw measurements that is so-called data driven stochastic subspace identification (SSI-DATA) or covariance matrices of the measurements that is so-called covariance driven stochastic subspace identification method (SSI-COV). The SSI-COV is memory efficient and fast compared to the SSI-DATA due to using the covariance matrices instead of the raw measurements [27]. More details comparison of the aforementioned methods is presented in Peeters [24]. The disadvantages of the SSI approach are threefold [16]: 1) is not computationally efficient to process a large dataset due to the QR-factorisation of a high-dimensional matrix [33], 2) the system order of an identified model needs to be identified, and 3) there is no estimate of amplitudes. Bendat and Piersol [34] proposed a basic FDD using a discrete Fourier transform (DFT) and estimates the well-separated modes directly from the power spectral density (PSD) matrix. Brincker et al. [29] extended the work of Bendat and Piersol [34] to detect the closely spaced frequencies. It is performed by calculating the SVD of the spectral matrix into a set of auto spectral density functions. Three assumptions to achieve precise results were made by considering the impact of loading as a white noise, slight damping of a structure and geometrical orthogonality between closely

spaced modes. Otherwise, its results are an approximation of the true modal parameters. Considering the white measurements noise of 10 and 20 %, it yields nearly precise results for the frequencies with a maximum deviation of 0.037 Hz. Peeters et al. [19] and Peeters and Van der Auweraer [20] proposed the polyreference version of the LSCF estimates using FRF that is called PolyMAX. The spectra or half spectra are determined based on the Fourier transform of the correlation sequences of positive time lags, which are used as input instead of raw measurements. Unmeasured ambient forces are considered as white noise with zero mean. The LSCF is applied to find initial values for iterative maximum likelihood estimation. In most of the aforementioned approaches, a separation of physical modes from spurious ones is a challenging issue. Peeters and Van der Auweraer [20] characterises the eigenforms by selecting stable poles from a clear stabilisation diagram based on user interaction. Magalhaes et al. [27] performed automatic identification of the modal parameters based on the SSI-COV method and applying a Fuzzy C-means clustering to the stabilisation algorithm to select the stable poles. However, a large number of tuning parameters such as time lag for calculating the cross covariance functions, minimum and maximum numbers of modal orders, eigenfrequency variation, modal damping coefficient variation, minimum modal assurance criterion (MAC) variation between eigenforms and a distance between two modes are needed to be defined in advance. Particularly, the time lag and the distance between two modes are the most important parameters, which are significantly influencing on the accuracy of the estimated parameters as well as the number of modes identified.

The system identification of the structure, where the vibration analysis is a detailed investigation of the dynamic behaviour, is also used to develop a mathematical model. The latter can be an analytical expression of a set of parameters or a numerical finite element model (FEM). The numerical modelling with the FEM has been extensively developed and applied in many experiments. The static deflection of a high-speed railway track under high-compression loads has been simulated [35] to identify the bending shape and ultimate load limit with imperfections. The FEM is applied to investigate processes that develop over time, such as redistribution of bending strains in prestressed concrete beams under fatigue loading [36] or the analysis of offshore wind turbine foundations under general transient loading, such as wind and waves [37]. For very short impulse excitations, the impact damage and crack development of reinforced concrete plates are modelled numerically [38] and were validated within experiments.

We propose a novel robust and automatic procedure to perform displacement and vibration analysis of bridge structures using low numbers of cost-effective micro-electro-mechanical (MEMS) accelerometers. The proposed approach is so-called robust time domain modal parameter identification (RT-MPI) technique. It is superior to the previous approaches, since it allows to estimate the modal parameters including eigenfrequencies, amplitudes, phase shifts and damping ratio coefficients robustly, reliably, accurately and in an automatic manner with less need for defining tuning parameters.

For this purpose, a proper excitation window including either ambient or forced vibration measurements is selected in an automatic manner. Initial eigenfrequencies used within the adjustment procedure are identified reliably using a novel cost function. Additionally, it allows one to tackle the difficulties in extraction of closely spaced frequencies. To perform robust estimation of the modal parameters, an observation model is defined based on the DHO model, an autoregressive (AR) model of coloured measurement noise and a stochastic model in the form of the heavy-tailed family of scaled t-distributions, which are jointly adjusted by means of a generalised expectation maximisation (GEM) algorithm.

In contrast to the standard least squares techniques, our proposed algorithm is not sensitive to the initialisation values as the simulation results shown in Kargoll et al. [39]. The proposed approach allows to overcome a highly coloured measurement noise contaminated in the measurements recorded from the MEMS accelerometers. The eigenforms are identified robustly and accurately for the eigenfrequencies occurred at the bridge structures. Furthermore, a double integration of the DHO model allows one to estimate amplitudes in a metric unit with a high accuracy. Subsequently it enables us to characterise deflection mode shapes with a true scale for the excitation window selected within a short time interval.

In this study, the vibration-based SHM is performed by defining an excitation as a function of time and not modelling an influence of loads, which is so-called kinematic deformation monitoring. Different types of excitation, such as the ambient excitation imposed by pedestrians and the wind and the forced excitation imposed by a modal hammer, are investigated for two types of bridge: a footbridge and a synthetic outdoor laboratory bridge and the analyses are compared and validated with high-end reference measurements, the FEM analysis as well as the well known SSI-COV approach. In addition, a simulation experiment is performed to compare the estimated modal parameters with their known values.

2 Data acquisition and measurements set-up

A geo-sensor network of the cost-effective MEMS accelerometers of type BNO055 from Bosch are mounted at specific positions, which is precalculated by means of the FEM analysis. The FEM analysis is carried out based on a 3D CAD model obtained from 3D point clouds measured by a TLS. Based on the FEM analysis, the position of the MEMS and the measurement directions are defined (see Section 5). The MEMS are connected via wires and the data transmission is conducted via USB to a PC. The time synchronisation between sensors is carried out based on the GPS time and by triggering the slave sensors (i. e. MEMS accelerometers) from a master sensor. The aforementioned measurement system is protected by a plastic housing against temperature and humidity changes, wind, rain and so on.

A data acquisition of the MEMS accelerometer is accomplished with specified sampling frequency of 100 Hz, which may be adequate to identify all eigenfrequencies of road bridge structures in the range of 0.1 to 50 Hz (in the view of Nyquist sampling theorem). However, the relevant eigenfrequencies of some bridge structures such as a railway bridge may reach 50 Hz [7] or even higher, which requires higher sampling rate to be defined. The data acquisition is carried out with a record length of 10 minutes and for a certain number of times per a day, which possibly allows one to acquire the vibration measurements with less influences of imposed external forces.

A side-by-side vibration measurement have been accomplished using the cost-effective MEMS sensor network and reference sensors to get a reliable evaluation of a cost-effective vibration measurement system for civil structures. For this purpose, the PCB ICP quartz piezoelectric accelerometers [40] have been used. A piezoelectric accelerometer generally covers a frequency range of 1 Hz to 10 kHz. To perform data acquisition of the piezoelectric sensors, a 24-bit analog-to-digital converter (ADC) with 16 measurement channels has been used. Each channel is measured with an independent ADC which is controlled with an internal hardware circuit, a so-called field programmable gate array. This ensures very accurate time synchronisation for all channels and a constant sampling rate. The time variations not visible between the time stamp in the measurement data and the real-time of the measurement are called jitter. A low jitter $< 10 \mu\text{s}$ is especially relevant for identifying eigenforms. The readers are referred to the [40] for further technical information about the PCB piezoelectric accelerometer.

3 Suitability analysis in selecting optimal MEMS accelerometers

A selection of an optimal and cost-effective MEMS accelerometer is a crucial and preliminary step to perform timely long-term measurements of the bridge structures. Therefore, Omidalizarandi et al. [41] proposed two scenarios. In the first scenario, the MEMS accelerometers are calibrated to compensate for the systematic errors, including three biases, three scale factors and three non-orthogonality angles between axes. A functional model of the calibration procedure is defined similar to the work of Shin and El-Sheimy [42]. To automatically perform calibration for fixed positions and for certain time interval, a KUKA youBot is utilised. It is an omnidirectional mobile robot with an arm consists of 5 axes and 4 wheels [43]. The MEMS accelerometer is rigidly attach to the arm of the KUKA youBot, which ensures the stability of the acceleration measurements through the calibration procedure.

The calibration experiment is conducted in a climate chamber and over certain temperature ranging between 10 and 30 °C to have a proper realisation of the changes of the calibration parameters. It should be noted that higher or lower temperature ranges were not possible due to the restrictions of the climate chamber and youBot. Subsequently, in situ acceleration data can be corrected by estimating the calibration parameters based on a linear interpolation at a measured temperature. Further detailed discussion of the calibration procedure developed is outside the focus of this study.

The second scenario is performed to estimate the harmonic oscillation parameters, such as frequency, amplitude, damping ratio coefficient and phase shift, in a controlled excitation experiment in a laboratory environment using a shaker (Fig. 1). The benefit of using such a shaker is twofold: 1) it includes a highly accurate reference accelerometer recording the acceleration measurements with a sampling rate of 1024 Hz, which is used for the purpose of the validation, and 2) the time synchronisation between MEMS accelerometers can be compared together based on the estimated phase shifts.

According to the analysis in Omidalizarandi et al. [41], the phase shifts between MEMS accelerometers varied between 2 and 5°. Additionally, it was shown that the time synchronisation has a significant impact at higher frequencies compared to lower ones. As an example, there is about 0.01 Hz frequency difference between its estimated and nominal value for the frequency of 20 Hz, which is approximately 0.003 Hz for the frequency of 5 Hz.

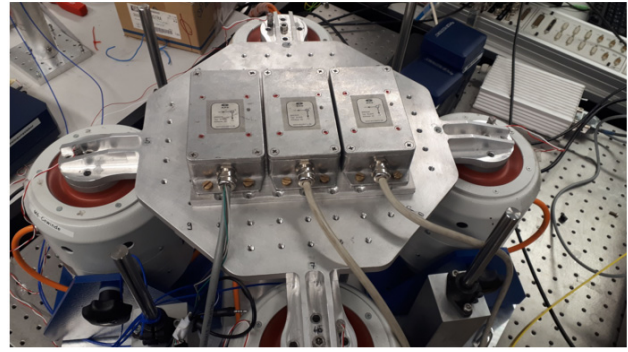


Figure 1: A controlled excitation experiment at the Institute of Dynamics and Vibration Research, Leibniz University Hannover, to validate the time synchronisation between all three MEMS accelerometers.

4 Robust vibration analysis based on time series analysis

This section starts by selecting a proper excitation window, possibly including a free vibration decay of measurements, which is introduced in subsection 4.1. Eigenfrequencies are identified in subsection 4.2, which are used as initial frequency values within the adjustment procedure. Next, a robust estimation procedure is explained in subsection 4.3. Finally, the displacement analysis in a metric unit is described in subsection 4.4.

4.1 Ambient window selection

To characterise the dynamic behaviour of the structure including eigenfrequencies, amplitudes, phase shifts and damping ratio coefficient, a proper excitation window, possibly including ambient vibration measurements is selected as a preliminary step. In this study, aforementioned excitation window is so called ambient window. The estimation of the damping ratio coefficients depends on the amplitudes and the energy content of the signal [3]. Therefore, such an ambient window selection is even more challenging when the structure is under the continued imposition of the forces due to moving vehicles or wind.

The imposition of the forces due to passing trains or electrical sources are represented by extremely sharp rises, whose magnitudes are significantly greater than a normal signal [3]. As described by Wenzel [3], pattern recognition methodologies might be helpful to detect unwanted signals, since the noise measurement characteristics are quite unique. In our case, such a sharp rises appear in the acceleration measurements by means of the

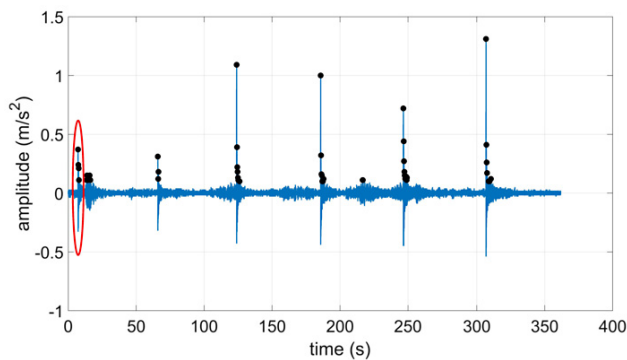


Figure 2: Time series of the acceleration data (m/s^2) recorded by the cost-effective MEMS accelerometer for a footbridge (blue line) and selected positive peaks (black dots).

modal (impulse) hammer. Figure 2 depicts the time series of the acceleration measurements under different loads for a footbridge structure. As we can see in this figure, despite the imposition of the loads by the modal hammer, the acceleration measurements recorded under influence of a traffic, which is mainly due to pedestrian passage over the bridge, which in turn, does not allow a perfect free vibration decay of the acceleration data.

To begin with the selection of the ambient window, the peaks of the acceleration data are identified based on MATLAB¹ routine *findpeaks*. It is parameterised by defining the minimum peak height value based on three times the standard deviations of the acceleration measurements, which can be interpreted as outliers (see Fig. 2). Next, the nearest neighbouring search algorithm in a range of 10–15 s based on the MATLAB routine *knnsearch* is applied to cluster the peaks selected. The selection of the aforementioned time interval relies on the fact that the energy contents of external forces are decreased in a few seconds. The peak with maximum value in each cluster is selected as a starting point. Next, the ambient window size is enlarged incrementally by a step size of 10 s to meet the next significant peak of a new cluster (see **Algorithm 1**).

In near real-time processing of our proposed algorithm, it is not necessary to omit the sharply rising peaks. For each ambient window selected, the modal parameters are initialised as explained in subsection 4.2 and then input into the estimation procedure described in subsection 4.3. A post-processing step is carried out to increase the reliability and accuracy of the estimated modal param-

Algorithm 1: Robust and automatic modal parameter identification in near real-time processing.

Input : Time series of measurements; step size=10

Output: Array of estimated modal parameters ($\hat{\theta}$)

find dominant peaks

cluster the peaks based on *knnsearch*

find the peaks with maximum amplitudes in each cluster

st = starting time of the peaks

C = length(clusters)

$k = 1$

NextPeak = 'not visited'

for $i = 1 \dots C$ **do**

while NextPeak = 'not visited' **do**

$st(i) = st(i) + \text{step size}$

$\hat{\theta}^{(k)}$ = identify modal parameters based on

Algorithms 2 & 3

$k = k + 1$

if $st(i) < st(i + 1)$ **then**

 step size = step size + 10

else

 step size = 10

 NextPeak = 'visited'

eters by moving forward through the peaks within each cluster and repeating the estimation procedure. This procedure continues till the higher frequencies imposed, i. e. mainly due to the external forces, have less impact on the estimation procedure, which can be realised via an acceptance of white noise test (WNT) criterion described by Kargoll et al. [44]. The aforementioned test statistic is accepted while the maximum cumulated periodogram excess over a cumulated white noise periodogram is smaller than a critical value based on a predefined significance level (i. e. $1 - \alpha = 0.95$).

4.2 Identification of initial modal frequency

An identification of eigenfrequencies plays an important role in our proposed robust vibration analysis procedure, since they are considered as initial values. This is even more challenging either in the case of measurements contaminated with high coloured measurement noise or closely spaced modal frequencies.

The determination of initial values for the eigenfrequencies is carried out in two steps and with different parameterization of the signal subspace dimension and noise power threshold (see **Algorithms 2; Steps 1 and 2**).

¹ The MATLAB software R2018b – Academic version licensed by the Leibniz University Hannover – has been used in our proposed algorithm. The MATLAB toolboxes include Signal Processing Toolbox and the Statistics and Machine Learning Toolbox.

The first step allows one to determine well-separated and dominant eigenfrequencies, while the second step enables us to extract the closely spaced frequencies or frequencies with lower amplitudes. For this purpose, first, a pseudospectrum is applied, which is based on the eigenspace analysis of correlation matrix of the measurements (ℓ) [45]. As described by Jiang and Adeli [46], the use of pseudospectrum for estimation of eigenvalues of a non-normal matrix achieves a reliable result. For this purpose, the pseudospectrum is applied using the multiple signal classification (MUSIC) as proposed by Jiang and Adeli [46] and Amezcua-Sanchez and Adeli [47]. It is used to extract high-resolution frequencies, even in case of a low SNR or having the measurements contaminated with high coloured noise [47]. Thus, the MATLAB routine *pmusic* is applied for both steps with different parameterization of signal subspace dimension by defining it to the integer values of half of a sampling frequency ($F_s/2$) and ($3 \cdot F_s/2$), respectively. In addition, in the parametrisation of the *pmusic* function, an integer length of the FFT (*nfft*) is defined to 1024 and 4096, respectively, for the first and the second parameterization of the MUSIC algorithm.

The MUSIC algorithm yields so many spurious frequencies with aforementioned parameterization. In addition, the extracted frequencies and their corresponding powers do not correspond to their true values with such parameterization. To overcome these problems, firstly, the boundaries around the frequencies are defined based on the MATLAB routine *isocalmin*. Figure 3 depicts the pseudospectrum estimation based on the MUSIC algorithm, which represents the frequencies bounded with their corresponding boundaries. Thus, the frequencies identified from the pseudospectrum are replaced with frequencies with maximum amplitudes obtained from the DFT (Fig. 4) within the boundaries determined. Secondly, two noise power thresholds are determined to reject spurious frequencies obtained from the first and the second parameterizations of the MUSIC algorithm, which have less power compared to it. To determine the noise power threshold for the first step, firstly, the power spectral density (PSD) is estimated based on the MATLAB routine *periodogram*. Next, the noise power is obtained based on the MATLAB routine *snr* and by considering the estimated PSD as input (set PSD estimate as one-sided). However, there is still a risk of missing some important frequencies with less power. Therefore, the M-estimator Sample and Consensus (MSAC) algorithm [48] is applied to fit a line to the PSD. The fitted line is shifted by 2.5σ error towards the SNR line. Thus, the average of the SNR line and the shifted MSAC line values yields the determination of the noise power threshold, which is considered for the first step of the initiali-

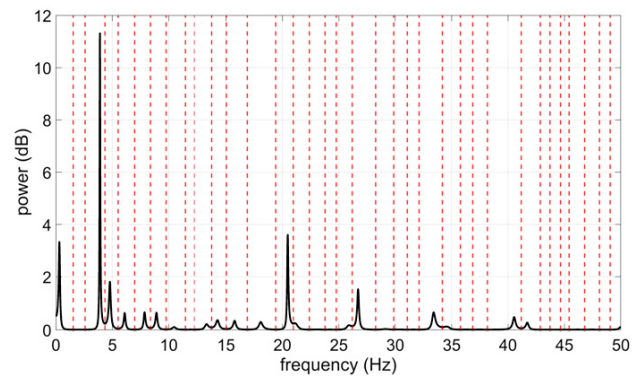


Figure 3: Pseudospectrum estimation based on the MUSIC algorithm (black solid line), which frequencies bounded with their corresponding boundaries (red dashed line).

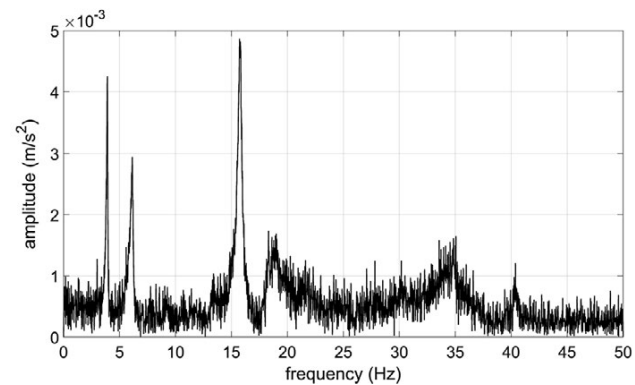


Figure 4: The DFT of the MEMS measurements obtained from BAM synthetic bridge experiment.

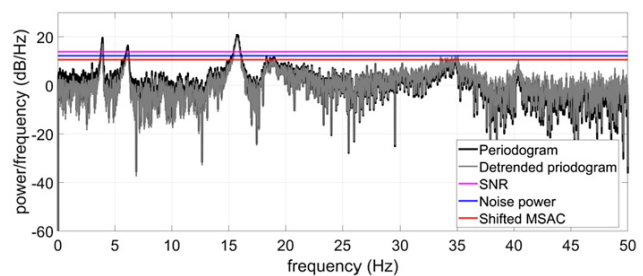


Figure 5: Periodogram of the MEMS measurements obtained from the BAM synthetic bridge experiment (black line), determined noise power based on SNR (magenta line), determined noise power based on 2.5σ error of the fitted line to the periodogram using the M-estimator Sample and Consensus (MSAC) algorithm (red line) and final determined noise power (blue line).

sation of eigenfrequencies. The noise power threshold for the second step is determined based on the minimum of the SNR line and the shifted MSAC line values. However, a priori knowledge about the SNR of the measurements

Algorithm 2: Robust modal parameter estimation procedure – initialisation step.**Input** : $\ell; F_s; SNR_{apriori}$ (Optional)**Output:** $\mathbf{f}^0; [\mathbf{freq}]$ **Step 1:**

Calculate pseudospectrum using MUSIC algorithm as:

 $[\mathbf{P}_{MUSIC}^1, \mathbf{f}_{MUSIC}^1] = pmusic(\ell, F_s/2, 'half', 1024, F_s);$ Define boundaries for \mathbf{f}_{MUSIC}^1 Calculate **frequency** & **power** using Periodogram SNR_{PSD} = Calculate SNR based on Periodogram SNR_{MSAC} = Calculate SNR using shifted MSAC line fitting on the Periodogram $SNR_{Mean} = \text{Mean}(SNR_{apriori}, SNR_{PSD}, SNR_{MSAC})$ Select \mathbf{f}_{MUSIC}^1 with **power** higher than SNR_{Mean} Assign corresponding **frequency**¹ with maximum **power** within boundaries for each selected \mathbf{f}_{MUSIC}^1
 $\mathbf{f}^0 = \mathbf{frequencies}^1$ **Step 2:** $[\mathbf{P}_{MUSIC}^2, \mathbf{f}_{MUSIC}^2] := pmusic(\ell, 3 \cdot F_s/2, 'half', 4096, F_s);$ Define boundaries for \mathbf{f}_{MUSIC}^2 $SNR_{Min} = \text{Min}(SNR_{apriori}, SNR_{PSD}, SNR_{MSAC})$ Select \mathbf{f}_{MUSIC}^2 with **power** higher than SNR_{Min} Assign corresponding **frequency**² with maximum **power** within boundaries for each selected \mathbf{f}_{MUSIC}^2
 $\mathbf{f}^{00} = \mathbf{frequencies}^2 \setminus \mathbf{frequencies}^1$ $[\mathbf{freq}] = \text{all possible combination of } \mathbf{f}^{00}$

($SNR_{apriori}$) recorded either from controlled or ambient excitation without external forces may assist us to increase the reliability of the estimated noise power thresholds.

With the completion of the aforementioned two initialisation steps, we are now ready to estimate the modal parameters using the proposed robust estimation procedure described in subsection 4.3. To this end, the frequencies identified from the first step of the initialisation step (\mathbf{f}^0) (see **Algorithms 2; Step 1**) are input to the estimation step (see **Algorithms 3**). Alternative to the first step of the **Algorithms 2**, other eigenfrequency identification approaches, for example, the SSI-COV algorithm implemented in MATLAB by Cheynet [49] may be used. However, multiple measurements recorded from different sensors are required in the SSI-COV algorithm to calculate the cross covariance of the measurements, which is not demanded in our proposed algorithm.

Next, the frequencies identified from the first and second steps are subtracted to form a new vector of frequencies (\mathbf{f}^{00}), which have not been selected before (see **Algo-**

Algorithm 3: Robust modal parameter estimation procedure – estimation step.**Input** : $\ell; F_s; \mathbf{f}^0; [\mathbf{freq}]; \text{itermax}; p_{\max} = 10$ **Output:** $\hat{\boldsymbol{\theta}}$ $\mathbf{f}^0 = \mathbf{F}^0$ $N = \text{length}([\mathbf{freq}])$ **for** $n = 1 \dots N + 1$ **do** $wnt^{(n)} = \text{false}$ **if** $n > 1$ **then**└ Add $\mathbf{freq}(k)$ to \mathbf{f}^0 $M = \text{length}(\mathbf{f}^0)$ $\boldsymbol{\xi}^0 = \mathbf{0}$ **for** $p = 1 \dots p_{\max}$ **do**└ $[\hat{\boldsymbol{\theta}}^{(n)}, \hat{\boldsymbol{\Sigma}}_{\theta}^{(n)}, \mathbf{a}^{(n)}, \mathbf{v}^{(n)}, \mathbf{e}^{(n)}, \mathbf{u}^{(n)}, wnt^{(n)}] \leftarrow \text{GEM algorithm}(\ell, F_s, \mathbf{f}^0, \boldsymbol{\xi}^0, p, \text{itermax})$ $\hat{\mathbf{f}}, \hat{\boldsymbol{\xi}} \leftarrow \hat{\boldsymbol{\theta}}^{(n)}$ $T_f^{(n)} = \frac{\hat{\mathbf{f}}^T \hat{\boldsymbol{\Sigma}}_f \hat{\mathbf{f}}}{M}$ $T_{\xi}^{(n)} = \frac{\hat{\boldsymbol{\xi}}^T \hat{\boldsymbol{\Sigma}}_{\xi} \hat{\boldsymbol{\xi}}}{M}$ **if** $wnt^{(n)} = \text{true}$ **then**└ $p^{(n)} = p$ └ $wnt_c = 0$ └ **break;****else**└ $p^{(n)} = p_{\max}$ └ $wnt_c = 1$ $\text{cost}^{(n)} = e^{T_f^{(n)}} + e^{T_{\xi}^{(n)}} + \log_{10}(p^{(n)}) + wnt_c + \epsilon_A$ $\mathbf{f}^0 = \mathbf{F}^0$ $j = \text{Min}(\text{cost})$ $\hat{\boldsymbol{\theta}} = \hat{\boldsymbol{\theta}}^{(j)}$

gorithms 2; Step 2). Then, all possible combination of the new vectors of frequencies are added to the vector of the initial frequencies identified from the first step at each iteration (see **Algorithm 3**).

A cost value is calculated for each vector of initial eigenfrequencies based on

$$\text{cost}^{(n)} = e^{T_f^{(n)}} + e^{T_{\xi}^{(n)}} + \log_{10}(p^{(n)}) + wnt_c + \epsilon_A. \quad (1)$$

where p is the AR model order, wnt_c the cost value for the WNT criterion (i. e. being 0 in case of the acceptance of the WNT criterion or otherwise being 1), ϵ_A the root mean square error of amplitudes of the frequencies identified from the first step of the **Algorithms 2**, which is calculated between the amplitude spectrum of the raw measurements and the estimated measurements, and $T_f^{(n)}$ and $T_{\xi}^{(n)}$ are test statistics at iteration (n) calculated based on

the weighted square sum of estimates of the eigenfrequencies and the damping ratio coefficients (see subsection 4.3) as follows:

$$\begin{aligned} T_f^{(n)} &= \frac{\hat{\mathbf{f}}^T \hat{\Sigma}_f \hat{\mathbf{f}}}{M}, \\ T_\xi^{(n)} &= \frac{\hat{\xi}^T \hat{\Sigma}_\xi \hat{\xi}}{M}. \end{aligned} \quad (2)$$

where $\hat{\mathbf{f}}$ is the estimated eigenfrequencies, $\hat{\xi}$ the estimated damping ratio coefficients, $\hat{\Sigma}_f$ and $\hat{\Sigma}_\xi$ are the joint a posteriori covariance matrices of the estimated frequencies and damping ratio coefficients, respectively, and M the number of identified eigenfrequencies.

A choice of \log_{10} function in the aforementioned cost function is due to the fact that the less autoregressive (AR) model order is desired, since a higher AR model order may absorb those undefined eigenfrequencies as coloured measurement noise. It should be noted that other monotonic functions with a same behaviour of the \log_{10} function can also be used for this purpose. Such a repetitive procedure is terminated when no more vector of eigenfrequencies remaining from the second step for inclusion. At the end, the vector of the initial frequencies with minimum estimates of the cost value is selected as the final initial eigenfrequencies and input into the adjustment procedure again to obtain the final estimates of the modal parameters (see **Algorithm 3**).

4.3 Robust modal parameter identification

A proper functional model is defined to robustly and accurately estimate the modal parameters in the time domain. It can be considered based on either an undamped harmonic oscillation or DHO model. Omidalizarandi et al. [50] proposed a robust vibration analysis procedure based on a linear regression model in terms of the undamped harmonic oscillation model, the AR model of the coloured measurement noise and stochastic model, which were jointly adjusted by means of the GEM algorithm described by Alkhatib et al. [51]. However, on the one hand, the proposed approach had a deficiency in the initialisation of the eigenfrequencies, particularly for those closely spaced frequencies. On the other hand, it was not complete enough to characterise the damping ratio coefficients. To overcome these problems, the deterministic model is extended to the DHO model introduced in Amezcua-Sanchez and Adeli [47] to estimate frequency, amplitude, phase shift and damping ratio coefficient. Therefore, we modelled the given vibration measurements ℓ_1, \dots, ℓ_n (recorded either

from the accelerometers or from the geodetic sensors) for the specified time instance x_t in which $t = 1, \dots, n$ (i.e., corresponding to the measurement time through the ambient window selected) based on

$$\begin{aligned} \ell_t &= h_t(\boldsymbol{\theta}) + e_t \\ &= \frac{a_0}{2} + \sum_{j=1}^M [a_j \cos(2\pi f_j \sqrt{1 - \xi_j^2} x_t) + \dots \\ &\quad b_j \sin(2\pi f_j \sqrt{1 - \xi_j^2} x_t)] \cdot \exp(-2\pi \xi_j f_j x_t) + e_t. \end{aligned} \quad (3)$$

where the undamped frequencies f_1, \dots, f_M , the coefficients a_0, a_1, \dots, a_M , and b_1, \dots, b_M and damping ratio coefficients ξ_1, \dots, ξ_M constitute the unknown parameter vector $(\boldsymbol{\theta})$. It should be noted that $f_{jd} = f_j \sqrt{1 - \xi_j^2}$ corresponds to the damped frequency. The vibration measurements (ℓ_t) are subtracted from their mean value throughout the entire ambient window. The full observation model here consists of a parametric DHO model, a parametric autocorrelation model in terms of the AR process and a parametric stochastic model in the form of the heavy-tailed scaled t-distribution.

Nassar et al. [52] benefit the AR process to describe the stochastic behaviour of inertial sensors (i.e. gyroscope) measurements due to relatively high measurement noise. Thus, to tackle highly coloured measurement noise contaminated with the MEMS acceleration data, we assume that the random deviations (e_t) are autocorrelated through a covariance-stationary AR process by

$$e_t = \alpha_1 e_{t-1} + \dots + \alpha_p e_{t-p} + u_t. \quad (4)$$

As proposed by Kargoll et al. [44], the AR coefficients $\boldsymbol{\alpha}^T = [\alpha_1, \dots, \alpha_p]$ are considered as unknown parameters to handle the autocorrelation. To account for the outliers of unknown frequencies and amplitudes, heavy-tailed white noise components and setting the level of precision [39], the white noise components u_1, \dots, u_n are assumed to independently follow the centred and scaled t-distribution $t_\nu(0, \sigma^2)$ with an unknown degree of freedom ν and with an unknown scale factor σ^2 , that is,

$$u_t \stackrel{\text{ind.}}{\sim} t_\nu(0, \sigma^2). \quad (5)$$

The aforementioned three parametric models are combined in the joint log-likelihood function (See Kargoll et al. [44] for details) based on the

$$\begin{aligned} \log L(\boldsymbol{\theta}, \sigma^2, \boldsymbol{\alpha}, \nu | \boldsymbol{\ell}) &= n \log \left[\frac{\Gamma(\frac{\nu+1}{2})}{\sqrt{\nu\pi}\sigma\Gamma(\frac{\nu}{2})} \right] - \dots \\ &\quad \frac{\nu+1}{2} \cdot \sum_{t=1}^n \log \left[1 + \frac{1}{\nu} \left(\frac{\alpha(L)(\ell_t - h_t(\boldsymbol{\theta}))}{\sigma} \right)^2 \right]. \end{aligned} \quad (6)$$

The maximisation of such a joint log-likelihood function allows for a self-tuning, robust, maximum likelihood estimation of the parameters [39]. To reliably estimate v of the t -distribution, a zero search based on the interval Newton method (see Algorithm 6.1 in Hargreaves [53] for details) is applied [54] by using *INTLAB* library [55].² However, the zero search based on the interval Newton method is not computationally efficient and is merely applied in post-processing of our proposed algorithm. In order to speed up the procedure in near real-time processing, the v is estimated based on the standard MATLAB routine *fzero*.

Next, the GEM algorithm is employed to estimate the model parameters. The initial frequencies are estimated based on our proposed algorithm described in the subsection 4.2. The model order of the AR process is initially set to 1 and progressively increases by 1 to reach its maximum predefined value. In addition, the initial damping ratio coefficients are set to 0.

Consequently, our proposed algorithm allows one to estimate all eigenfrequencies occurred without losing important information. In addition, the well-defined determination of the eigenfrequencies based on our proposed algorithm speed up the process by fast convergence within the adjustment procedure with lower AR model order. It should be noted that a higher AR model order (e. g. higher than 10) may absorb those undefined (might be important!) eigenfrequencies with low amplitudes as coloured measurement noise. According to our exhaustive experimental study, the reliable identification of the initial frequencies play an important role to avoid the aforementioned problem. In this study, the maximum AR model order is set to 10, which also guarantees the fast convergence of the algorithm.

4.4 Displacement analysis based on double integration

The amplitudes in the metric unit (e. g. millimetre) is calculated by double integrating the DHO model (see Eq. 3) without considering the term of the offset as

$$\begin{aligned} d_t &= H_t(\theta) + e_t \\ &= \sum_{j=1}^M \left[\exp(-2\pi f_j x_t \xi_j) \cdot \cos(2\pi f_j x_t \sqrt{1 - \xi_j^2}) \cdot \dots \right. \\ &\quad \left. (2a_j \xi_j^2 - a_j + 2b_j \xi_j \sqrt{1 - \xi_j^2}) / (4f_j^2 \pi^2) - \dots \right] \end{aligned}$$

$$\begin{aligned} &[\exp(-2\pi f_j x_t \xi_j) \cdot \sin(2\pi f_j x_t \sqrt{1 - \xi_j^2}) \cdot \dots \\ &(b_j - 2b_j \xi_j^2 + 2a_j \xi_j \sqrt{1 - \xi_j^2}) / (4f_j^2 \pi^2)] + e_t. \end{aligned} \quad (7)$$

where the coefficients a_1, \dots, a_M , and b_1, \dots, b_M , the eigenfrequencies f_1, \dots, f_M and the damping ratio coefficients ξ_1, \dots, ξ_M are the estimates of the modal parameters obtained from the estimation procedure (see subsection 4.3). Next, the DHO model is fitted to the calculated displacements ($\mathbf{d} = \sum_{t=1}^n d_t$) to estimate the amplitudes for each of the eigenfrequencies.

Alternatively, the double integration can be carried out for the adjusted acceleration data based on the numerical integration of the equations of motion using the trapezoidal rule. However, such double integration is a challenging issue since the absolute displacement changes derived from the adjusted acceleration data are drifting very fast in a few seconds. To tackle this problem, the displacements calculated from the double integration are detrended based on a piece-wise spline approximation within the ambient window selected. Another critical issue is the proper choice of the number of breaks and order, which are here set to $(\text{length}(\mathbf{d})/50)$ and 3, respectively. Next, the DHO model is fitted to the displacements (\mathbf{d}) calculated using the estimated eigenfrequencies.

To make sure of the correctness of the estimated amplitudes in the metric unit, as proposed by Omidalizarandi et al. [50], the amplitude is calculated based on

$$Am_j = \frac{A_j}{(2 \cdot \pi \cdot f_j)^2} \cdot 1000. \quad (8)$$

where f_j is the estimated eigenfrequency in the unit of [Hz], A_j is the estimated amplitude in the unit of [m/s^2] and Am_j is the amplitude in the unit of [mm].

To avoid the drifting of the displacements over a longer period of time, Omidalizarandi et al. [41] used a generated 1D displacement time series using video frames of a passive target (attached in the vicinity of one of the MEMS accelerometers, whose centroid was extracted based on the work of Omidalizarandi et al. [56]) captured from the embedded on-axis telescope camera of an IATS of type Leica Nova MS50 MultiStation with a practical sampling frequency of 10 Hz. Subsequently, 1D coordinate updates were performed using the MEMS acceleration data in the vertical direction together with the 1D displacement measurements from the IATS within a Kalman filter approach. The double integration for a longer period of time, by just using the acceleration data without use of additional displacement measurements is a very complex problem and is out of the scope of this study.

² The *INTLAB* library version 10 has been used.

5 Vibration analysis based on finite element model analysis

The FEM can be used for a dynamic analysis of a structure modelled as a linear and a non-linear system. In simple systems, such as beams, frames and trusses, which consist of individual members or elements that are connected at joints (called nodal nodes), the behaviour of each element can be regarded independently. This is realised by the calculation of the element stiffness matrix and the element mass matrix. The matrices of all elements are then assembled into the system stiffness matrix and the system mass matrix so that the equilibrium of force and the compatibility of displacements are satisfied at each nodal node. This is called matrix structural analysis. The FEM method for dynamic analysis is used for complex structures by means of geometry, material properties and loading conditions, although it does not differ much from the matrix structural analysis. Only the mapping of the nodal nodes to the finite elements is not naturally established by the geometry, such as for the skeletal structures, and the displacements at internal points of an element are expressed by appropriate interpolating functions and not by the exact analytical relationship. The loads at each element in all directions are called degrees of freedom and can be combined by a vector \mathbf{F} and the displacements at the corresponding points are noted by \mathbf{x} . The relation between the load and the displacement is linked by the stiffness matrix \mathbf{K} in Equation (9) for the static behaviour.

$$\mathbf{K} \cdot \mathbf{x} = \mathbf{F}. \quad (9)$$

The inertia of the masses and the damping in the dynamic formulation must be considered by the introduction of a mass matrix \mathbf{M} and the damping matrix \mathbf{C} . The general equation of motion (10), as an ordinary differential equation, describes the movement of the nodal nodes (degrees of freedom) and their first and second derivatives, $\dot{\mathbf{x}}$ and $\ddot{\mathbf{x}}$.

$$\mathbf{M} \cdot \ddot{\mathbf{x}} + \mathbf{C} \cdot \dot{\mathbf{x}} + \mathbf{K} \cdot \mathbf{x} = \mathbf{F}. \quad (10)$$

For the modal analysis, the vector \mathbf{F} is considered a function of time of a harmonic excitation of the structure in a selected frequency range. Simultaneously, the same load is applied to all degrees of freedom of the entire FEM. This ideal excitation cannot be achieved exactly for real structures. Common finite element software package can usually support the calculation of the eigenfrequencies and eigenforms of a complex structure for dynamic FE analysis. The modelling is usually simplified for real structures to realise such an analysis, for example, as a girder grid model.

6 Experiments and results

6.1 Case study I: Robust vibration analysis based on time series analysis using simulated data

In this section, a simulated acceleration data was generated and then employed and solved by our proposed algorithm (RT-MPI) and the SSI-COV algorithm to compare and validate the entire estimation procedure. For this propose, firstly, a true observation vector was defined based on the DHO model with a sampling frequency of 100 Hz, which spanned 100 s of the acceleration data using the parameter values $a_0 = 0$, $a_j = (4.0, 2.0, 2.0, 8.0)$, $b_j = (-3.0, 3.0, 3.0, 7.0)$, $f_j = (5.0, 5.3, 15.0, 35.0)$ [Hz] and the damping ratio coefficients $\xi_j = (0.5, 0.8, 0.8, 0.5)$ [%] (for $j \in [1, 2, 3, 4]$). In order to calculate the amplitudes and phase shifts, we consider a cosine form of the sum of cosine and sine terms in Equation (3) without considering the damping ratio coefficient as follows

$$a_j \cos(2\pi f_j x_t) + b_j \sin(2\pi f_j x_t) = A_j \cos(2\pi f_j x_t + \phi_j). \quad (11)$$

Thus, the amplitudes and the phase shifts³ were calculated by

$$\begin{aligned} A_j &= \sqrt{a_j^2 + b_j^2}, \\ \phi_j &= \tan^{-1}\left(\frac{-b_j}{a_j}\right). \end{aligned} \quad (12)$$

The white noise vector was generated with the same length of the acceleration data and under the t-distribution assumption (see Equation (5)) with parameter values $\sigma^2 = 0.04$ and $\nu = 4.0$. Next, the white noise vector was turned into the autocorrelated coloured noise vector considering AR(1) process and the parameter value $\alpha_1 = 0.4$. The generated coloured noise vector was then added to the true observation vector to generate the noisy acceleration data (see Fig. 6). In the case of the SSI-COV algorithm, two slightly different time series were generated based on two different white noise vectors, which were generated with the same parameterisation as before.

In order to apply the SSI-COV algorithm [49], the tuning parameters are defined as follows: the time lag of the correlation function is set to 6.4 cycles of a lower frequency as proposed by Magalhaes et al. [27] (i. e. here $6.4 \cdot 5 = 32$), the minimum and maximum numbers of modal orders are

³ To estimate the phase shifts, the MATLAB routine *atan2* was used to calculate a four-quadrant inverse tangent using the estimated Fourier coefficients.

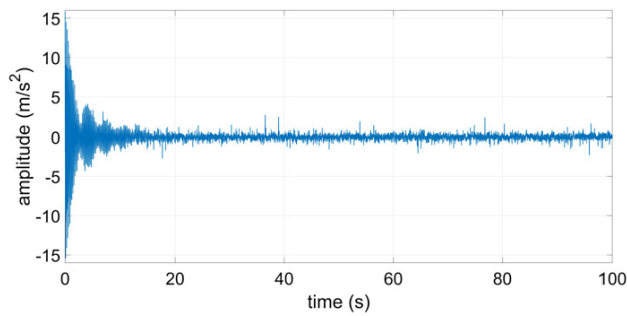


Figure 6: Simulated acceleration data based on the DHO model contaminated with coloured noise.

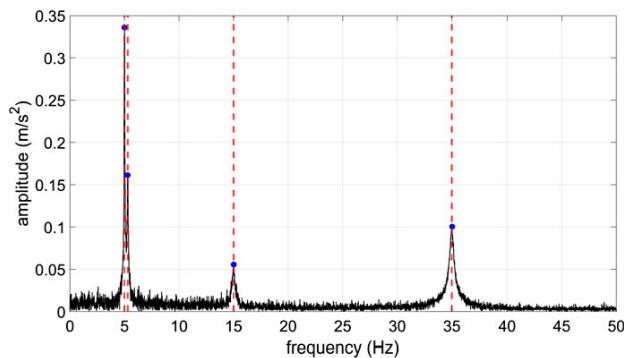


Figure 7: The DFT of the simulated acceleration data in the amplitude spectrum (black solid line) and initialised and extracted frequencies (blue dots and red dashed lines), respectively.

set to 2 and 30, respectively, the eigenfrequency variation is set to $1 \cdot 10^{-2}$, the modal damping coefficient variation is set to $3 \cdot 10^{-2}$, the minimum MAC variation between eigenforms is set to $5 \cdot 10^{-3}$ and the distance between two modes is set to $2 \cdot 10^{-2}$ similar to the tuning parameters used by Cheynet et al. [57].

The unknown parameters of the functional model (Equation (3)) consist of Fourier coefficients, frequencies, amplitudes, phase shifts and damping ratio coefficients. The unknown parameters of the correlation model (Equation (4)) consist of the AR model coefficients. The unknown parameters of the stochastic model (Equation (5)) consist of the unknown degree of freedom and the unknown scale factor. All aforementioned unknown parameters were estimated together by the maximisation of the joint log-likelihood function (Equation (6)) using the GEM algorithm. The initial frequencies were identified based on our proposed algorithm described in the subsection 4.2.

Figure 7 illustrates the DFT of the acceleration data in the amplitude spectrum. As can be seen, two closely spaced frequencies of 5.0 and 5.3 Hz were intentionally defined very close together for the validation purpose. In ad-

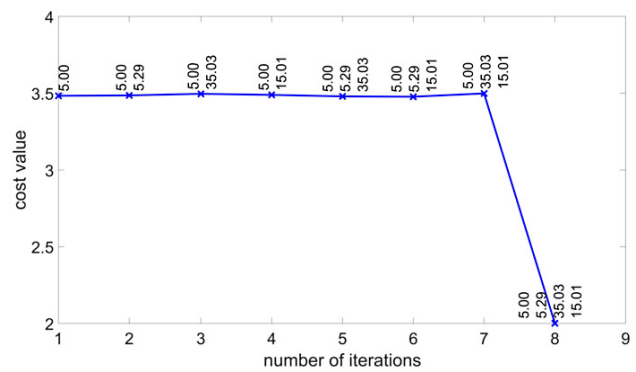


Figure 8: The cost values calculated at each iteration for the simulated acceleration data.

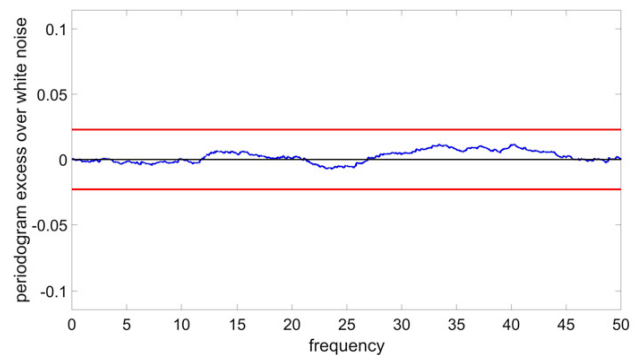


Figure 9: Excess of the estimated periodogram of the decorrelated (i. e. estimated white noise) residuals of the simulated acceleration data the AR(1) model (jagged blue line) with respect to the theoretical white noise periodogram (horizontal centred black line) and 95 % significance bounds (horizontal bounded red lines).

dition, their corresponding phase shifts are approximately orthogonal (see Table 1), which causes less influence of the possible correlation between them on the estimation of the modal parameters. The SNR value calculated from the RT-MPI algorithm was equal to 17.85, which enables us to identify the frequencies of 5.0, 15.0 and 35.0 [Hz] at the first step of the **Algorithms 2**. However, we intentionally increased the SNR value to 25 to decrease the number of frequencies identified from the first step and to observe their influences on the introduced cost function (see Equation (1)).

Figure 8 shows the cost values calculated at each iteration. The first iteration stands for those frequencies identified from the first step. As we can see from this figure, the combination of four frequencies achieves a lower cost value due to the acceptance of the WNT criterion. Figure 9 depicts the adequacy of the estimated AR coloured noise models in the light of an accepted WNT criterion.

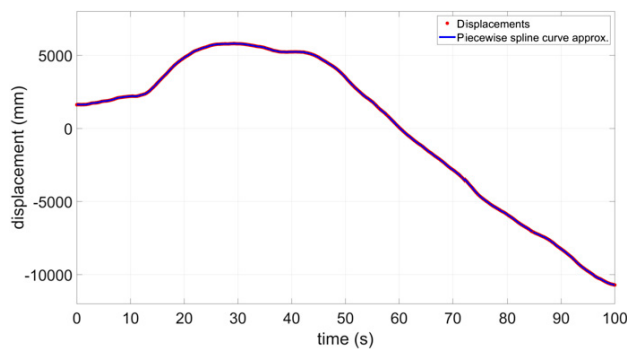


Figure 10: Detrending simulated acceleration data based on the piece-wise spline curve approximation.

As we previously mentioned in the subsection 4.4, the amplitudes in the metric unit (mm) are calculated based on two different methods of the double integration using the DHO model and the equations of motion, respectively. Figure 10 shows the detrended acceleration data based on the piece-wise spline curve approximation used for the second method of double integration. Figure 11 depicts the displacement time series obtained by applying the double integration for the detrended acceleration data and the detrended adjusted acceleration data.

Table 1 represents the statistics of the estimated unknown parameters calculated by the RT-MPI and the SSI-COV algorithms. In the RT-MPI algorithm, the unknown parameters of the DHO model, the correlation model and the stochastic model are computed for two cases where

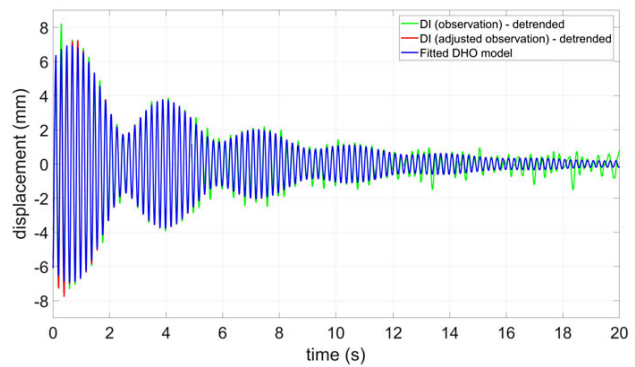


Figure 11: The displacement time series calculated for the simulated acceleration data: based on the double integration using the detrended acceleration data (green) and the adjusted acceleration data (red) as well as fitting the DHO model to the detrended adjusted acceleration data (blue).

the ν was estimated by applying *INTLAB* and *fzero*. As we can see, the differences between the estimated frequencies in both approaches are at the level of third or fourth decimals. Regarding the estimated amplitudes in the unit of $[m/s^2]$ in the RT-MPI algorithm, as we have previously shown in Omidalizarandi et al. [41], such small variations from the reference or true values at such frequencies have less quantity differences in the metric unit [mm] at the level of the first to second decimals that can be neglected. However, the SSI-COV algorithm does not allow us to calculate the amplitudes. The damping ratio coefficients estimated from two aforementioned different cases

Table 1: Statistics of the estimated unknown parameters in the functional model based on the DHO model, the correlation model based on AR process and the stochastic model based on the centred and scaled t-distribution with an unknown degree of freedom and unknown scale factor from the RT-MPI algorithm compared and validated with the SSI-COV algorithm for the simulated acceleration data.

Parameters	f [Hz]	A [m/s^2]	A_{DHO} [mm]	A_{MOTION} [mm]	ξ [%]	ϕ [°]	α_1 [-]	ν [-]	σ^2 [-]
Simulated data	5.0000	5.0000	5.0661	5.0661	0.5000	36.8699	0.5000	4.0000	0.0400
	5.3000	3.6056	3.2514	3.2514	0.8000	-56.3099			
	15.0000	3.6056	0.4059	0.4059	0.8000	-56.3099			
	35.0000	10.6301	0.2198	0.2198	0.5000	-41.1859			
Estimated by RT-MPI (ν determined by <i>INTLAB</i>)	4.9996	5.1110	5.1792	5.1539	0.5141	37.7709	0.4939	4.3662	0.0411
	5.3016	3.6282	3.2697	3.2494	0.7976	-58.1599			
	15.0001	3.5848	0.4036	0.3798	0.8053	-56.8767			
	34.9999	10.6103	0.2194	0.1452	0.5015	-41.2764			
Estimated by RT-MPI (ν determined by <i>fzero</i>)	4.9999	5.1322	5.2003	5.1745	0.5153	37.2764	0.4991	10000	0.0757
	5.3029	3.5597	3.2064	3.1862	0.7731	-59.4356			
	14.9978	3.5773	0.4028	0.3789	0.7942	-56.1857			
	34.9992	10.6376	0.2199	0.1452	0.5016	-41.3963			
Estimated by SSI-COV	5.0010	—	—	—	0.4900	36.8331	—	—	—
	5.3010	—	—	—	0.8100	55.7620			
	15.0012	—	—	—	0.7800	56.5484			
	34.9991	—	—	—	0.5000	56.9214			

of the RT-MPI algorithm show the average levels of 0.005 % and 0.015 % differences from their nominal values, respectively, which its corresponding estimates from the SSI-COV algorithm is 0.01 %. The phase shifts estimated from two aforementioned different cases of the RT-MPI algorithm represents the average levels of 0.95° and 1.1° differences from their nominal values, respectively, while the SSI-COV algorithm achieves significantly different results (i. e. different signs or values) that is not comparable with the RT-MPI algorithm and their nominal values. The differences of the estimated AR(1) model coefficient (α_1) for both cases of the RT-MPI algorithm are very small. The stochastic model parameters (ν and σ^2) obtained from the former case of the RT-MPI algorithm shows a very precise estimation of the parameters. By contrast, the latter case of the RT-MPI algorithm shows significant differences from their nominal values. However, the SSI-COV algorithm does not allow to calculate the AR and stochastic model parameters.

The analysis based on the former case of the RT-MPI algorithm is computationally very expensive compared to the latter case of the RT-MPI algorithm, whereas the estimated modal parameters do not show significant differences from their nominal values. The frequencies and damping ratio coefficients were estimated very precisely with a high accuracy in the both algorithms. However, the RT-MPI algorithm does not need any tuning parameters and achieves robust results, which is not the case in the SSI-COV algorithm. Additionally, the SSI-COV algorithm does not achieve a reasonable results for the phase shifts and also could not provide the estimates of the amplitudes. At the end, a comparison of the estimated amplitudes in the RT-MPI algorithm and in the metric unit reveals a very close and reliable estimation for the first method of the double integration using the DHO model. Consequently, the analysis of the simulation study demonstrates and validates the reliability, robustness, high accuracy and precision of the RT-MPI algorithm.

6.2 Case study II: Robust vibration analysis based on time series analysis using experimental data validated with FEM analysis

6.2.1 Example based on a footbridge

A vibration analysis of a footbridge structure that is a so-called Mensa footbridge (located in Hannover, Germany; see Fig. 12) with a length of 27.05 m (23.22 m main span and 3.83 m side span) and a width of 2.42 m (see Fig. 13) was carried out using the MEMS and high-end (refer-



Figure 12: A scheme of the Mensa footbridge, which was measured by the MEMS and high-end (reference) accelerometers, the laser tracker Leica AT960-LR and the terrestrial laser scanner Z+F IMAGER 5016.

ence) accelerometers with sampling frequencies of 100 and 2000 Hz, respectively. The reference acceleration data was downsampled to 100 Hz in order to increase the run time speed-up of the processing. It was additionally measured by means of a laser tracker of type Leica AT960-LR (reference sensor), in a pointwise mode and a TLS of type Z+F IMAGER 5016, in profile mode. However, the TLS measurements analysis is out of the scope of this study.

Moreover, the Mensa footbridge has been dynamically analysed using the FE program ‘Sofistik’ for the purpose of validation. The FEM is generated by means of two main girders. The cross-section of the main girders is a wide-flange beam of two IPBL (HEA) girders with a material thickness of 10 mm. The lateral stiffness of the superstructure is considered with 20 cross-beams (see Fig. 14). The cross-beams are rectangular tubes 200 by 120 mm and a material thickness of 10 mm. The total system is a girder grid model. The expansion in width at one end of the bridge that faces towards the Mensa is modelled with four additional nodes. The stiffening sheets at the bearings and the reduced beam height in this section is neglected. The stiffness of the cover plates must be considered by an additional steel thickness of 10 mm on top of the cross beams.

The four bearings of the bridge are modelled as loose-jointed connection nodes, but the displacements are limited in the longitudinal and lateral directions. The horizontal stiffness results mainly from the pile stiffness of these directions. The bearings in the vertical direction are considered fixed. The software converts the dead weight of the constructions to point masses for the dynamic calculation for the application of the loads.

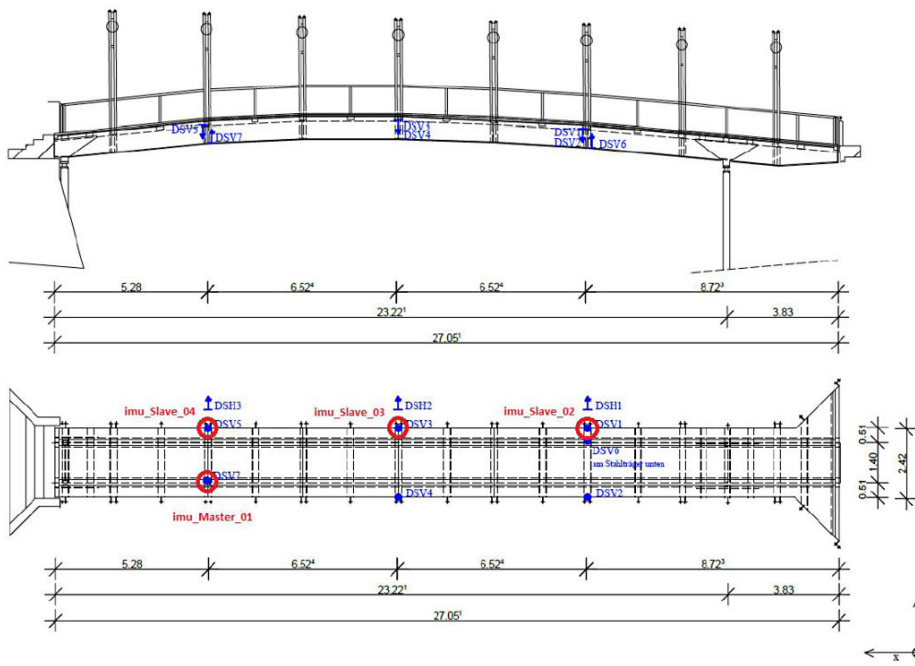


Figure 13: Measurement set-up in the Mensa bridge experiment: The locations of the MEMS and PCB piezoelectric accelerometers are depicted by red and blue coloured circles, respectively. All metric values are in meter [58].

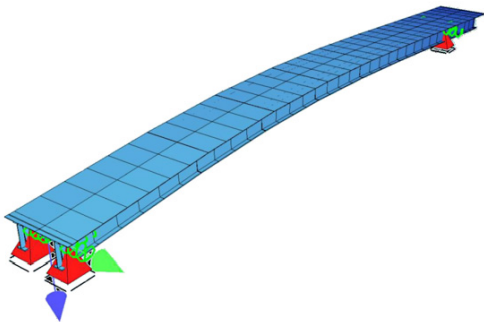


Figure 14: Girder grid model of the main girders.

To identify eigenforms of the Mensa footbridge, a geosensor network of the MEMS accelerometers are located at certain positions, which their positions were precalculated from the FEM analysis. As we can see in Figure 13, the locations of the MEMS accelerometers (i. e. provided by Allsat GmbH) and the reference accelerometers (i. e. provided by the Institute of Concrete Construction – Leibniz University Hannover) are illustrated. The MEMS accelerometer is a three axis accelerometer which can perform measurements in the longitudinal (x-axis), lateral (y-axis) and vertical (z-axis) directions of the bridge. By contrast, the reference accelerometer is a one axis accelerometer, which needs multiple set-ups for recording acceleration data in all three directions. The eigenforms are

only characterised in the vertical direction, which is due to the usage of only three MEMS slave sensors, namely, *IMU_Slave_02*, *IMU_Slave_03* and *IMU_Slave_04*, respectively, (see Fig. 13). To reach this goal, the acceleration data are recorded for the duration of a maximum of 6 minutes and in the direction of the x-axes of the MEMS accelerometers (see Figure 15; left). The PSD estimates of the MEMS acceleration data are provided in Figure 15 (right). For the purpose of the validation, three reference sensors, namely, DSV1, DSV3 and DSV5 located close to the aforementioned MEMS slave sensors, respectively. Figure 16 depicts the time series of the acceleration data recorded from the DSV3 sensor close to the *IMU_Slave_03* and located nearly at the centre of the bridge.

Typically, such a footbridge structure is under ambient excitations by pedestrians (mainly in the vertical direction) or wind (mainly in the lateral direction). In this study, additional excitations were also imposed by impulses from a modal hammer. The ambient windows were selected incrementally with a step size of 10 s starting from a peak with high amplitude. The modal parameters, such as the eigenfrequencies and the damping ratio coefficients were estimated and represented for the vertical and torsion modes. Figures 17–19 represent the estimated modal parameters for the aforementioned modes at different step sizes of the ambient windows and for the entire time series of the acceleration data recorded from the aforementioned

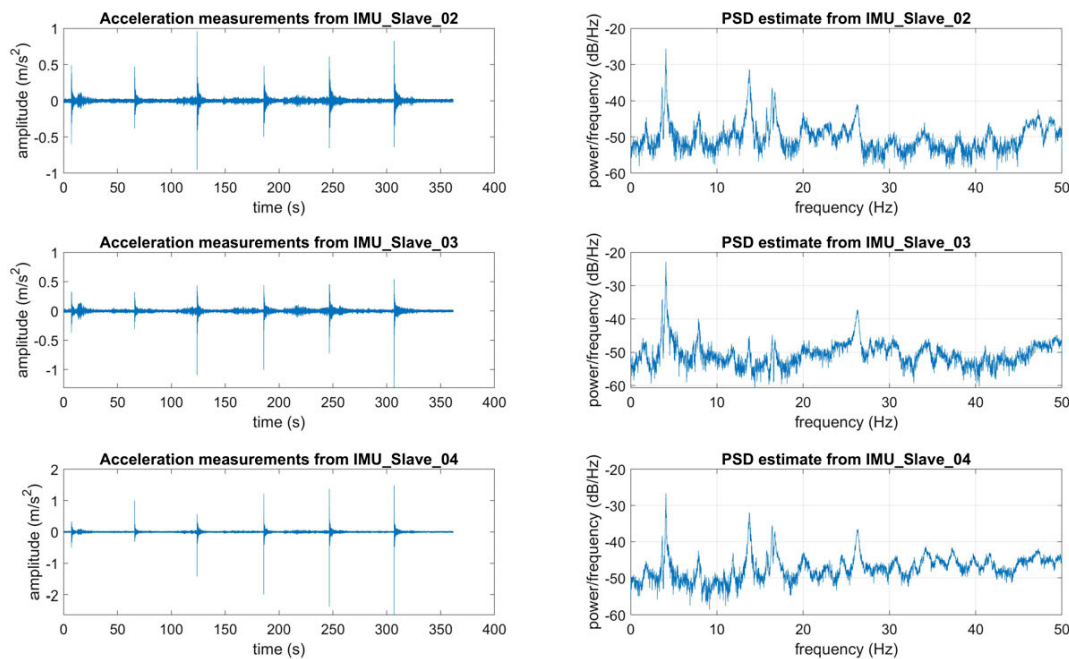


Figure 15: The MEMS accelerometer measurements – Mensa footbridge: time series of the acceleration measurements (m/s^2) recorded from three different sensors (left) and the PSD estimates of the acceleration measurements (right).

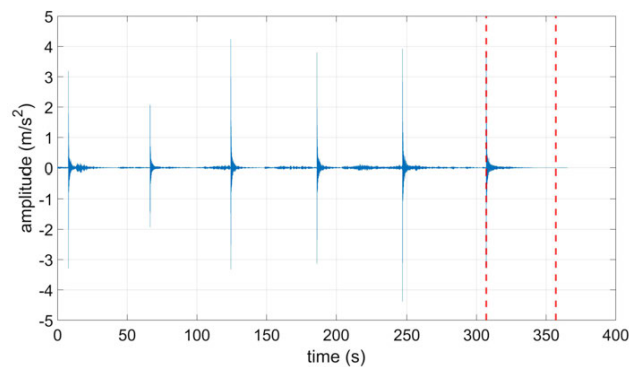


Figure 16: The reference accelerometer (DSV3) measurement – Mensa footbridge: time series of the acceleration measurements (m/s^2) (blue line) and the selected (ambient) window with a maximum duration of 50 s (red dashed lines).

three MEMS slave sensors (see **Algorithm 1**). They clearly show how the estimated damping ratio coefficients fluctuate depending on the loads. As we can see in the first 60 s of the measurements and for the estimated eigenfrequency associated with the first vertical mode, the damping ratio coefficients have minus values, which is due to short decay and a sudden rise of the amplitudes for the selected ambient window within the 10 s. Since the energy of the external force decreased throughout the time, the estimated damping ratio coefficients approximately reach an equilibrium, which allows us to identify them more reliably. One

can calculate the weighted average or the median of the estimated values to determine a unique damping ratio coefficient for each eigenfrequency for the entire measurements. It is also valid for the eigenfrequencies.

Table 2 represents the statistics of the estimates of the eigenfrequencies (Hz) and the damping ratio coefficients (%) calculated by means of the RT-MPI algorithm (see Figs. 17–19). The vertical and torsion modes are indexed by V and T, respectively. For example, the first vertical and torsion modes are indexed by V1 and T1, respectively. The analyses were performed by calculating the median of the parameters calculated at each time interval. Additionally, the aforementioned parameters were also calculated by means of the SSI-COV algorithm. It should be noted that two other vertical modes of 16.4 and 16.7 Hz were also detected from both approaches, which were not included in the aforementioned table. Their corresponding eigenfrequencies and the damping ratio coefficients estimated from the RT-MPI and the SSI-COV algorithms and with consideration of the entire time series are as follows: $\hat{f}_{V3} = 16.4088$ (Hz) with $\tilde{\xi}_{V3} = 0.2753$ (%) and $\hat{f}_{V4} = 16.6807$ (Hz) with $\tilde{\xi}_{V4} = 0.4848$ (%), which are the median values of their corresponding estimated parameters obtained from the RT-MPI algorithm and $f_{V3} = 16.4080$ (Hz) with $\xi_{V3} = 0.28$ (%) and $f_{V4} = 16.6856$ (Hz) with $\xi_{V4} = 0.43$ (%) are obtained from the SSI-COV algorithm.

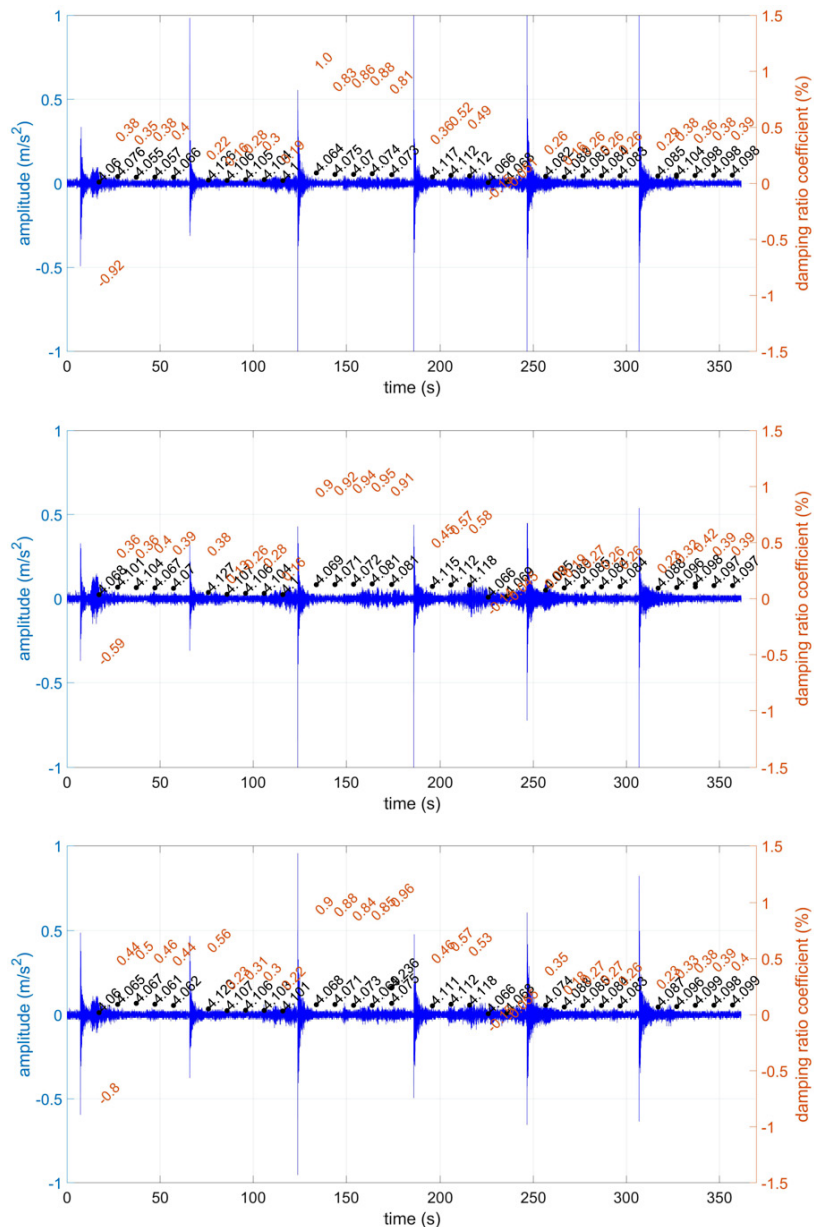


Figure 17: The MEMS accelerometer measurements for all three MEMS sensors – Mensa footbridge: time series of the acceleration measurements [m/s^2] recorded from the IMU_Slave_02, the IMU_Slave_03 and the IMU_Slave_04 are depicted from top to bottom (blue line). The black and orange coloured texts stand for the estimated frequencies [Hz] and damping ratio coefficients [%], respectively, for the first vertical mode ($f_{V1} = 4.1$ Hz) at the specified positions with the incremental step size of 10 s starting from the peaks with high amplitudes.

The comparison of the both aforementioned algorithms demonstrates that the RT-MPI algorithm enables us to possibly decrease the influence of the loads on the estimated parameters by means of the median of the estimates. As we expected, the SSI-COV algorithm does not achieve reasonable results for the damping ratio coefficients for the first and second vertical modes as well as the first torsion mode while considering the entire time series at once. For the shorter time interval, which are cor-

responding to the ambient windows 1–6 selected, both approaches achieve very close estimates of the eigenfrequencies and the damping ratio coefficients for the first, third and fourth vertical modes as well as the fourth torsion mode. However, the SSI-COV algorithm does not achieve stable results for the damping ratio coefficients of the second vertical mode as well as the first torsion mode. The estimates of the eigenfrequencies obtained from the both approaches have a maximum deviation of approximately

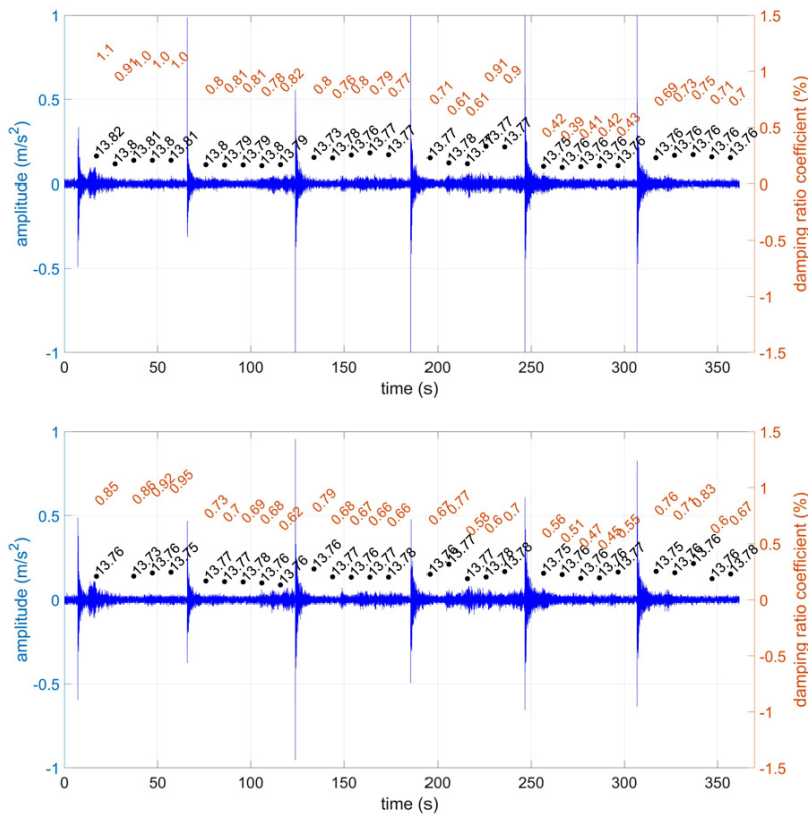


Figure 18: The MEMS accelerometer measurements for two of MEMS sensors – Mensa footbridge: time series of the acceleration measurements [m/s^2] recorded from the IMU_Slave_02 (top) and the IMU_Slave_04 (bottom) (blue line). The black and orange coloured texts stand for the estimated frequencies [Hz] and damping ratio coefficients [%], respectively, for the second vertical mode ($f_{v2} = 13.76$ Hz) at the specified positions with the incremental step size of 10 s starting from the peaks with high amplitudes.

Table 2: Statistic of the frequencies (Hz) and the damping ratio coefficients (%) estimated from all three MEMS acceleration data based on the RT-MPI and SSI-COV algorithms for the Mensa footbridge.

Sensor	Time [s]	Method	f_{v1} [Hz]	ξ_{v1} [%]	f_{v2} [Hz]	ξ_{v2} [%]	f_{T1} [Hz]	ξ_{T1} [%]	f_{T4} [Hz]	ξ_{T4} [%]
MEMS	7.22–357.05	RT-MPI	4.0853	0.3618	13.7645	0.7150	3.6697	0.2226	26.3233	0.6653
		SSI-COV	4.0838	0.8100	13.7337	0.4700	3.6635	0.7300	26.2943	0.6500
	7.22–57.22	RT-MPI	4.0656	0.3827	13.8010	0.9528	3.6678	0.1533	26.3529	0.7229
		SSI-COV	4.0725	0.3200	13.7418	0.7300	3.6570	0.4300	26.3351	0.5400
	65.95–115.95	RT-MPI	4.1059	0.2642	13.7813	0.7777	3.6705	0.1384	26.3140	0.5828
		SSI-COV	4.1002	0.2000	13.8678	0.1900	3.6572	0.3600	26.3019	0.5500
	123.95–173.95	RT-MPI	4.0724	0.9005	13.7659	0.7642	3.6694	0.2428	26.3443	0.6549
		SSI-COV	4.0715	1.1000	13.7697	0.6000	3.6541	0.4000	26.3197	0.5700
	185.79–235.79	RT-MPI	4.1116	0.4510	13.7693	0.7045	3.6751	0.5035	26.2930	0.6211
		SSI-COV	4.0877	0.4000	13.7763	0.5100	–	–	26.2853	0.6300
	246.62–296.62	RT-MPI	4.0841	0.2605	13.7627	0.4392	3.6692	0.3407	26.2837	0.6720
		SSI-COV	4.0873	0.2800	13.7738	0.3200	–	–	26.2821	0.6500
	307.05–357.05	RT-MPI	4.0976	0.3843	13.7621	0.7123	3.6719	0.3127	26.3241	0.6863
		SSI-COV	4.0946	0.4000	13.7644	0.4900	–	–	26.3121	0.5700
TLS		FEM	3.6420	–	13.2940	–	3.7590	–	–	–

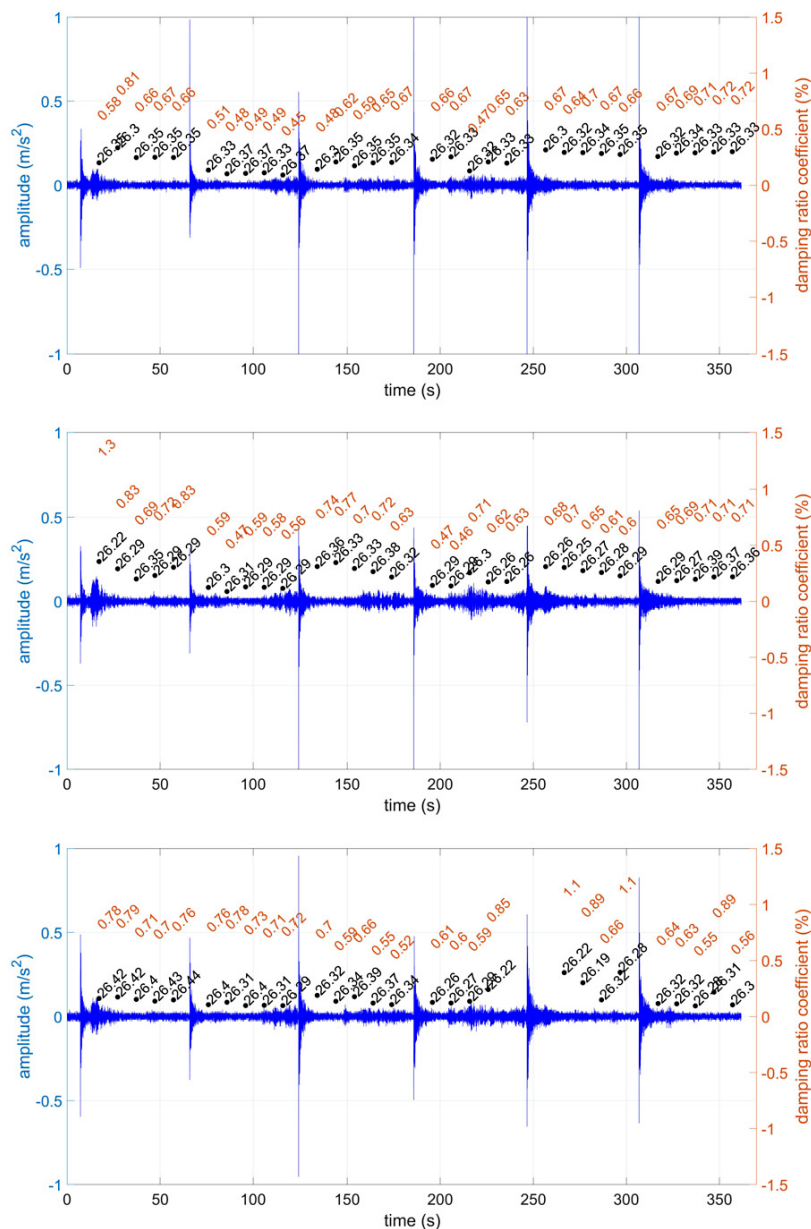


Figure 19: The MEMS accelerometer measurements for all three MEMS sensors – Mensa footbridge: time series of the acceleration measurements $[m/s^2]$ recorded from the IMU_Slave_02, the IMU_Slave_03 and the IMU_Slave_04 are depicted from top to bottom (blue line). The black and orange coloured texts stand for the estimated frequencies $[Hz]$ and damping ratio coefficients $[\%]$, respectively, for the fourth torsion mode ($f_{T4} = 26.30$ Hz) at the specified positions with the incremental step size of 10 s starting from the peaks with high amplitudes.

0.03 $[Hz]$. Moreover, the SSI-COV algorithm were not able to estimate the first torsion mode in the ambient windows 4–6.

In addition, the result of the FE simulations calculated from the CAD model obtained from the TLS measurements are illustrated in Figures 20–24 associating to the correlated eigenforms for the vertical f_V , the horizontal bending f_H and the torsion f_T . The comparison of the FEM analysis and the RT-MPI algorithm shows that

the frequencies of 3.642, 13.294 and 3.759 Hz from the FEM analysis are equivalent to the frequencies of 4.1, 13.75 and 3.67 Hz, respectively. Subsequently, it demonstrates that the FEM analysis can only provide us with the approximate estimates of the eigenfrequencies and there is no estimates of the damping ratio coefficients. However, to obtain more accurate and precise results, it needs to be calibrated, which is out of the scope of this study.

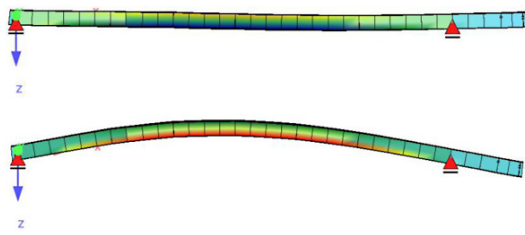


Figure 20: $f_{V1} = 3.642 \text{ Hz}$ (first vertical mode).

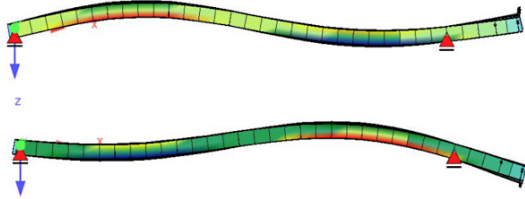


Figure 21: $f_{V2} = 13.294 \text{ Hz}$ (second vertical mode).

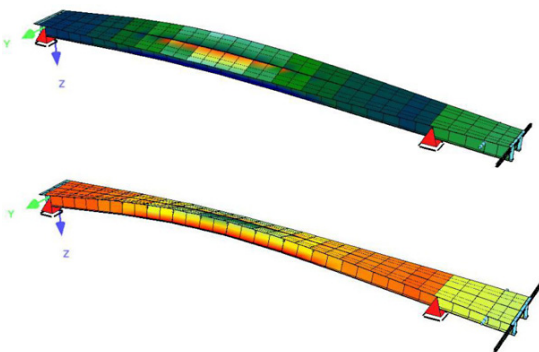


Figure 22: $f_{H1-T1} = 3.759 \text{ Hz}$ (first horizontal and torsion mode).

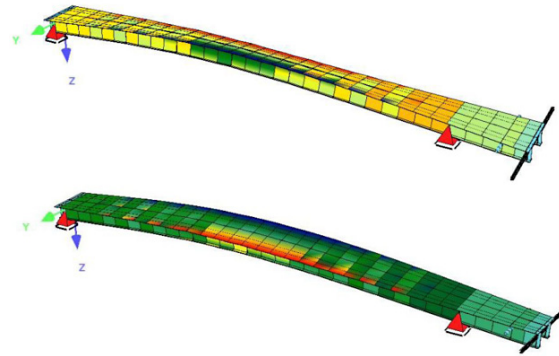


Figure 23: $f_{H2-T2} = 7.053 \text{ Hz}$ (second horizontal and torsion mode).

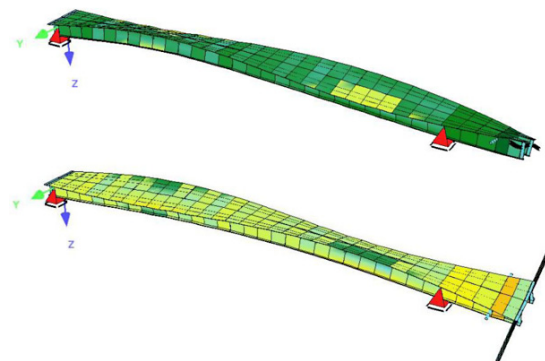


Figure 24: $f_{T3} = 11.828 \text{ Hz}$ (third torsion mode).

The eigenfrequencies (Hz) and the damping ratio coefficients (%) were also estimated for the last 60 s of the measurements with an incremental step size of 5 s (see Table 3), since the analysis from the previous step depicts more stable results at this part. Furthermore, we performed its validation by comparing the analysis from the MEMS and the reference acceleration measurements.

The analysis prove that all eigenfrequencies occurred were detected very precisely, and are validated with the analysis from the reference acceleration data. Due to the imposition of the load by the modal hammer, the higher frequencies, such as 100 Hz (visible from the DFT of the reference acceleration data; see Fig. 25), could not be detected in the MEMS acceleration data in the light of the Nyquist sampling theorem. Subsequently, it directly influences the estimated amplitudes and damping ratio coefficients of the frequency of 26.30 Hz. As we can see in

Table 3, there is a significant difference between the amplitudes calculated from the MEMS and the reference accelerometers for the first 20 s, which could be due to the superimposition of the higher frequencies about 100 Hz to 200 Hz derived from additional impulses imposed by the modal hammer that would not be detectable at all by the MEMS accelerometers (in the light of the Nyquist sampling theorem). As described in Wenzel [3], the modal and system damping can vary between 0–0.1 and 0–0.2, respectively. According to the aforementioned damping ranges, the median of all estimated damping ratio coefficients for the entire selected ambient window is within the range and is acceptable.

Figures 26 and 27 illustrate the DFT of the reference and the MEMS acceleration data for the duration of 30 s within the selected ambient window and Figures 28 and 29 show the fitted DHO model to the given acceleration data for the duration of 30 s within the selected ambient window using our proposed algorithm.

To characterise the eigenforms, the amplitudes, the eigenfrequencies and the phase shifts were calculated based on undamped harmonic oscillation model described by Kargoll et al. [44] and Omidalizarandi et al. [50].

Table 3: Statistic of the eigenfrequencies (Hz) and the damping ratio coefficients (%) estimated from the last ambient window of the MEMS and the reference acceleration data for the Mensa footbridge.

Time [s]		317.05	322.05	327.05	332.05	337.05	342.05	347.05	352.05	357.05
MEMS	f_{V1} [Hz]	4.088	4.101	4.096	4.095	4.097	4.097	4.097	4.098	4.097
	ξ_{V1} [%]	0.226	0.363	0.319	0.327	0.419	0.369	0.385	0.382	0.386
	A_{V1} [m/s^2]	0.062	0.076	0.066	0.066	0.087	0.074	0.077	0.076	0.077
	f_{T4} [Hz]	26.291	26.290	26.271	26.272	26.387	26.388	26.367	26.403	26.364
	ξ_{T4} [%]	0.649	0.650	0.686	0.654	0.711	0.716	0.712	0.743	0.709
	A_{T4} [m/s^2]	0.118	0.118	0.123	0.117	0.131	0.136	0.144	0.130	0.146
Reference Accel.	f_{V1} [Hz]	4.094	4.101	4.102	4.098	4.100	4.099	4.099	4.097	4.101
	ξ_{V1} [%]	0.202	0.286	0.293	0.390	0.428	0.434	0.449	0.449	0.458
	A_{V1} [m/s^2]	0.057	0.058	0.058	0.077	0.089	0.084	0.081	0.086	0.086
	f_{T4} [Hz]	26.354	26.356	26.355	26.347	26.359	26.334	26.346	26.370	26.358
	ξ_{T4} [%]	0.649	0.649	0.649	0.541	0.615	0.635	0.580	0.583	0.541
	A_{T4} [m/s^2]	0.231	0.231	0.231	0.181	0.230	0.217	0.184	0.185	0.161

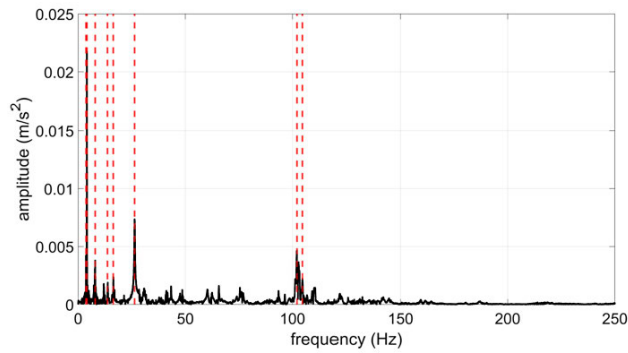


Figure 25: The DFT of the reference acceleration data (recorded from DSV3) downsampled to 500 Hz in the Mensa footbridge experiment (black solid line) for the duration of 30 s within the selected ambient window.

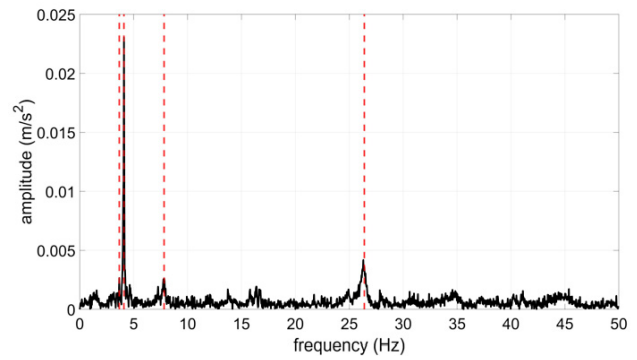


Figure 27: The DFT of the MEMS acceleration data (recorded from IMU_Slave_03) in the Mensa footbridge experiment (black solid line), and extracted frequencies (red dashed lines) for the duration of 30 s within the selected ambient window.

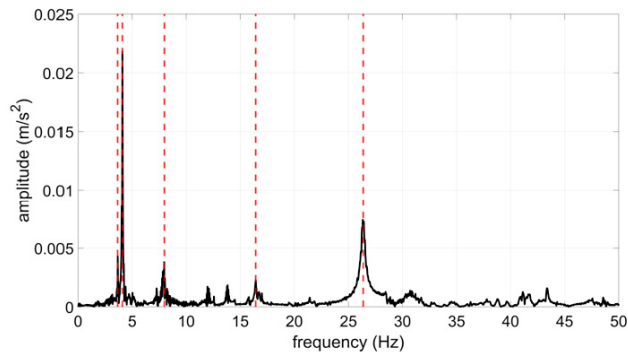


Figure 26: The DFT of the reference acceleration data (recorded from DSV3) downsampled to 100 Hz in the Mensa footbridge experiment (black solid line), and extracted frequencies (red dashed lines) for the duration of 30 s within the selected ambient window.

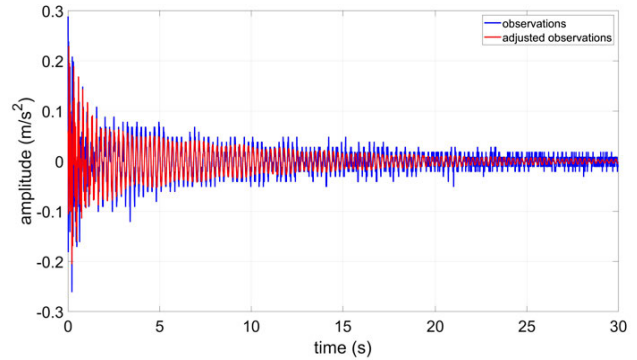


Figure 28: The MEMS acceleration data (recorded from IMU_Slave_03) in the Mensa footbridge experiment (blue solid line) for the duration of 30 s within the selected ambient window, and the DHO model fitted to the given acceleration data (red solid line).

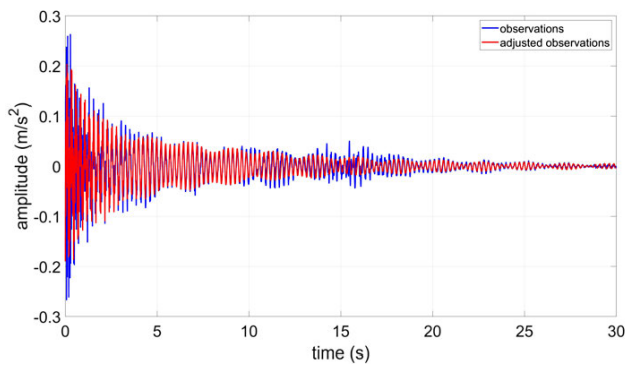


Figure 29: The reference acceleration data (recorded from DSV3) in the Mensa footbridge experiment (blue solid line) for the duration of 30 s within the selected ambient window, and the DHO model fitted to the given acceleration data (red solid line).

Therefore, the estimation was carried out using the acceleration measurements of each sensor and for the entire time series (see Figs. 30 and 32). This yields the estimates of the modal parameters without considering the damping ratio coefficients. By considering the damping ratio coefficients for the selected ambient window, it is also possible to characterise deflection eigenforms at different time intervals. Since the estimated amplitudes always have positive values, the estimated phase shift can identify the sign of its corresponding amplitude. As an example (see Figure 32), for the frequency of 13.75 Hz, the differences between the estimated phase shifts from the acceleration measurements of the sensors DSV5 and DSV1

are above 180° , which change the sign of the corresponding amplitude. The comparison of the estimated eigenforms between the MEMS and the reference accelerometers demonstrates the high accuracy, robustness and reliability of our estimation procedure.

6.2.2 Example based on a synthetic bridge

A vibration analysis of a synthetic bridge structure from the BAM, located approximately 80 km from Berlin, Germany, with a length of 24.0 m, a width of 0.8 m and a height of 0.3 m (see Fig. 33), is investigated. The measurements were carried out using the MEMS accelerometers, a geophone, the laser tracker of type Leica AT960-LR and the IATS of type Leica MS50 with sampling frequencies of 100 Hz, 1000 Hz, 1000 Hz and 10 Hz, respectively. However, in this study, we will focus on the analysis of the measurements from the MEMS and the geophone.

To estimate the modal parameters, the acceleration and the velocity data recorded from the MEMS and the geophone, respectively, which were placed at a first quarter of the BAM synthetic bridge. The modal hammer was utilised to generate the artificial oscillation, since the aforementioned bridge was a rigid platform without any natural frequencies.

Figures 34 and 35 depict the acceleration and the velocity data acquired from the aforementioned sensors in the Z direction. The ambient windows were selected by a

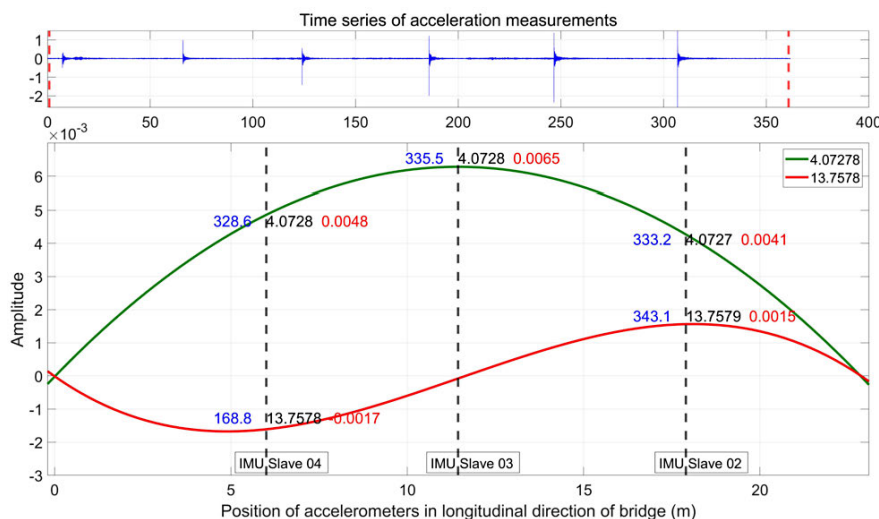


Figure 30: MEMS accelerometer: time series of the acceleration measurements (top) (selected ambient window highlighted between red dashed lines) in which the X-axis and Y-axis represent a time (s) and amplitude (m/s^2), respectively; vertical eigenforms calculated for different eigenfrequencies (bottom). The texts for each eigenform represent estimated phase shifts (blue), eigenfrequencies (black) and amplitudes (red) at specified positions.

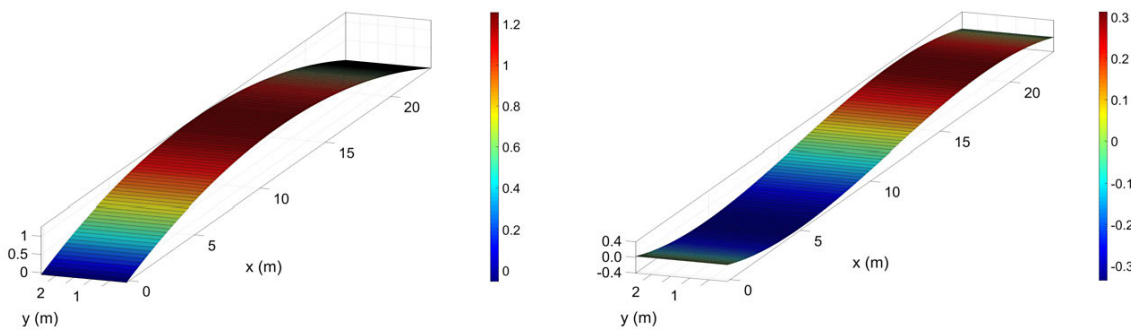


Figure 31: 3D Vertical eigenforms represented for different eigenfrequencies: the first vertical eigenform (4.07 Hz; left) and the second vertical eigenform (13.75 Hz; right). Amplitudes scaled by 200 in Z-axes.

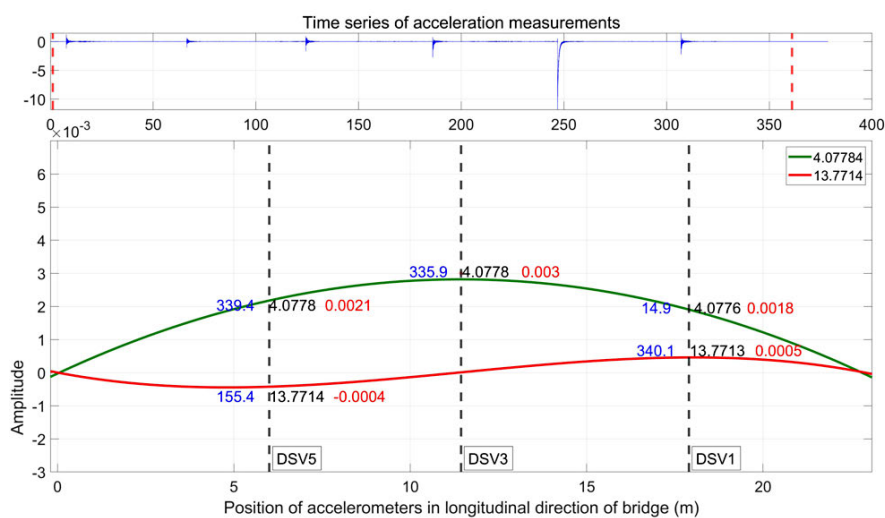


Figure 32: Reference accelerometer: time series of the acceleration measurements (top) (selected ambient window highlighted between red dashed lines) in which the X-axis and Y-axis represent a time (s) and amplitude (m/s^2), respectively; vertical eigenforms calculated for different eigenfrequencies (bottom). The texts for each eigenform represent estimated phase shifts (blue), eigenfrequencies (black) and amplitudes (red) at specified positions.

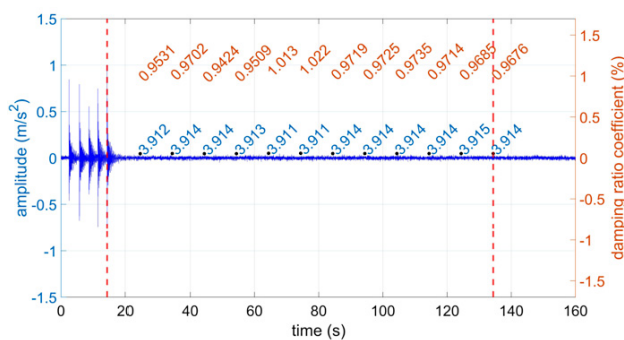
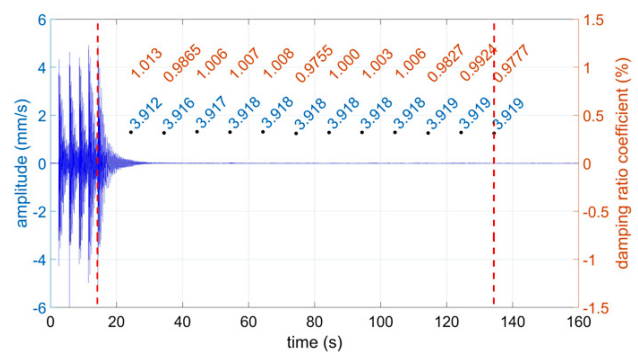


Figure 33: A scheme of the BAM synthetic bridge, which was measured by the MEMS accelerometers, the geophone, the laser tracker Leica AT960-LR and the IATS Leica MS50.

step size of 10 s starting from the last peak with high amplitude and for the maximum duration of 120 s. The estimates of the first eigenfrequency and its corresponding damping ratio coefficient for different ambient window sizes were shown in the aforementioned figures. Table 4 represents the eigenfrequencies [Hz] and damping ratio coefficients [%] estimated for the different ambient windows using the RT-MPI algorithm, which are compared with the analysis obtained using the SSI-COV algorithm and for the MEMS acceleration data within the selected ambient window shown in Figure 34. The frequencies of 3.91, 6.13 and 15.77 Hz correspond to the 1st–3rd modes. The analysis proves that the eigenfrequencies and the damping ratio coefficients of the MEMS acceleration data were estimated robustly, reliably and with high accuracy in the RT-MPI algorithm, as they are compared and evaluated with the anal-

Table 4: Statistic of the frequencies (Hz) and the damping ratio coefficients (%) estimated from the MEMS acceleration data and the geophone velocity data using the RT-MPI and SSI-COV algorithms for the BAM synthetic bridge.

Time [s]		24.4	34.4	44.4	54.4	64.4	74.4	84.4	94.4	104.4	114.4	Median
MEMS RT-MPI	f_1 [Hz]	3.911	3.914	3.914	3.913	3.911	3.911	3.914	3.914	3.914	3.914	3.914
	ξ_1 [%]	0.953	0.970	0.942	0.951	1.013	1.022	0.972	0.973	0.974	0.971	0.971
	f_2 [Hz]	6.132	6.131	6.129	6.137	6.119	6.121	6.134	6.135	6.136	6.136	6.132
	ξ_2 [%]	1.554	1.543	1.625	1.626	1.590	1.559	1.528	1.527	1.518	1.502	1.543
	f_3 [Hz]	15.774	15.772	15.775	15.771	15.760	15.757	15.783	15.783	15.781	15.781	15.775
	ξ_3 [%]	0.926	0.917	0.895	0.922	0.928	0.949	0.910	0.913	0.916	0.926	0.920
Geophone RT-MPI	f_1 [Hz]	3.912	3.916	3.917	3.918	3.918	3.918	3.918	3.918	3.918	3.919	3.918
	ξ_1 [%]	1.013	0.987	1.006	1.007	1.008	0.976	1.000	1.003	1.006	0.983	1.000
	f_2 [Hz]	6.135	6.141	6.139	6.140	6.141	6.143	6.136	6.135	6.136	6.148	6.141
	ξ_2 [%]	1.520	1.484	1.521	1.534	1.526	1.526	1.519	1.527	1.537	1.541	1.526
	f_3 [Hz]	15.764	15.769	15.773	15.772	15.777	15.775	15.769	15.769	15.770	15.780	15.772
	ξ_3 [%]	0.954	0.928	0.923	0.944	0.910	0.899	0.922	0.924	0.917	0.874	0.920
MEMS SSI-COV	f_1 [Hz]					3.920						
	ξ_1 [%]					0.90						
	f_2 [Hz]					6.131						
	ξ_2 [%]					1.48						
	f_3 [Hz]					15.734						
	ξ_3 [%]					0.97						

**Figure 34:** The MEMS accelerometer (IMU_Slave_02) measurement – BAM synthetic bridge: time series of the acceleration measurements (m/s^2) (blue line); selected ambient window within the red dashed lines for the duration of 120 s. The blue and orange coloured texts stand for the estimated eigenfrequencies (Hz) and damping ratio coefficients (%), respectively, for the first mode at the specified positions.**Figure 35:** The geophone measurement – BAM synthetic bridge: time series of the velocity measurements (mm/s) (blue line); selected ambient window within the red dashed lines for the duration of 120 s. The blue and orange coloured texts stand for the estimated frequencies (Hz) and damping ratio coefficients (%), respectively, for the first mode at the specified positions.

ysis obtained from the geophone measurements and the SSI-COV algorithm. The estimated eigenfrequencies deviate about a maximum of 0.01 and 0.04 Hz in comparison to the analysis obtained from the geophone measurements and the SSI-COV algorithm. As we can see, the deviation of the estimates of the damping ratio coefficients estimated from the both aforementioned approaches is below 0.1 %, which is within the range and is acceptable.

Figure 36 shows the nice overlaying of the DFT results for the MEMS acceleration data and its corresponding adjusted data. Figure 37 illustrates the fitted DHO model to

the given acceleration data for the duration of 20 s within the selected ambient window using our proposed algorithm. The eigenfrequencies are clearly visible from the peaks at the frequencies with the maximum amplitudes. There are also three other frequencies of 18.30, 18.80 and 34.65 Hz, so-called system frequencies, which have higher amplitudes directly after imposition of the load and their amplitudes damped very fast to the lower amplitudes in a few seconds. This can be seen from Figure 38, which represents all the extracted frequencies for the duration of 20 s within the selected ambient window.

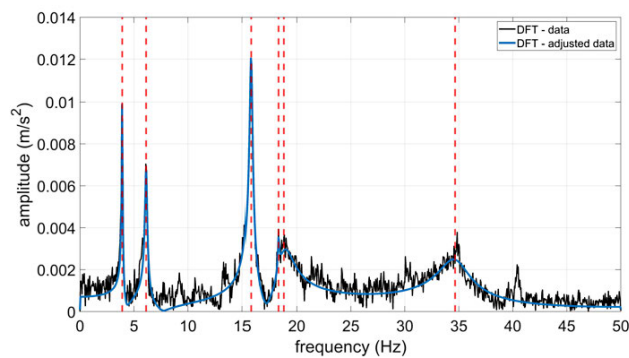


Figure 36: The DFT of the MEMS acceleration data (recorded from IMU_Slave_02) in the BAM synthetic bridge experiment and its corresponding adjusted data (black and blue solid lines, respectively) and extracted frequencies (red dashed lines) for the duration of 20 s within the selected ambient window.

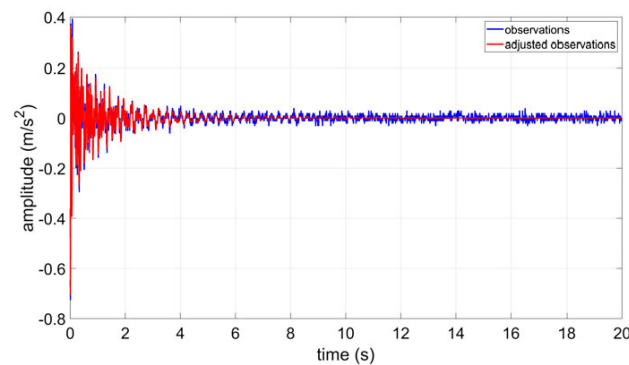


Figure 37: The MEMS acceleration data (recorded from IMU_Slave_02) in the BAM synthetic bridge experiment (blue solid line) for the duration of 20 s within the selected ambient window, and the DHO model fitted to the given acceleration data (red solid line).

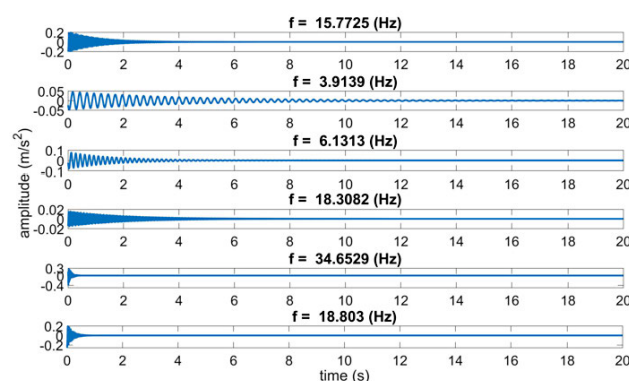


Figure 38: Representation of the extracted frequencies for the MEMS acceleration data (recorded from IMU_Slave_02) for the duration of 20 s within the selected ambient window.

7 Conclusion

In this study, a robust and automatic time domain vibration analysis procedure was proposed that is so-called RT-MPI technique. It allows one to estimate the modal parameters such as eigenfrequencies, eigenforms, damping ratio coefficients as well as amplitudes robustly, reliably and high accurately. Additionally, it allows to characterise the deflection eigenforms at the specified time intervals with a high accuracy. Furthermore, a good feasibility of the cost-effective MEMS accelerometers for deformation monitoring of bridge structures is demonstrated.

Two scenarios were proposed in the preprocessing step, to guarantee a precise and reliable vibration analysis using the MEMS accelerometers. Firstly, the MEMS accelerometers were calibrated in an automatic manner using a KUKA youbot in a climate chamber. Thus, such calibration procedure allows one to obtain the calibration parameters over different temperature ranges. According to our extensive experimental studies, the calibration parameters obtained has a minor influence on the estimated modal parameters, particularly on the frequencies for short time intervals, for example, in the range of a few minutes. Subsequently, it might not be necessary to perform a calibration for the estimation of a deflection eigenform at such short time intervals. However, to characterise a eigenform for a longer period of time (e. g. 10 minutes or more), the MEMS calibration procedure is beneficial, since it allows one to refine the acceleration data by compensating for the systematic errors, such as biases, scales and non-orthogonality angles between the axes. The second scenario was conducted in a controlled excitation environment using a shaker, which includes high-end reference accelerometers. Therefore, it allows one to check for time synchronisation between the slave MEMS accelerometers used. According to our analysis, the estimated phase shifts between the MEMS accelerometers fluctuate up to 5° in the controlled excitation experiment, which is sufficient to characterise the eigenforms. To this end, both scenarios assist us to select a proper and optimal MEMS accelerometer for our purpose of bridge monitoring. This is carried out by selecting the MEMS accelerometers, which their measurements have been less influenced by the systematic errors such as biases. In addition, their measurements have a reasonable time delay compared to the measurements of other MEMS accelerometers used.

A novel vibration analysis procedure was proposed in the processing step, which is new regarding the automatic ambient window selection, automatic identification of initial eigenfrequencies, robust, reliable and accurate estimation of the modal parameters and a double integration.

To initialise the frequencies used in the estimation procedure and to avoid direct frequency peak picking from a noisy DFT, the identification was performed in two steps and with different parameterization of the noise power threshold and the signal subspace dimension. In the first step, the well-separated initial eigenfrequencies above noise power threshold calculated are extracted. Next, all possible combination of those frequencies identified from the second step, which have not been selected in the first step, are added to the vector of the initial frequencies identified from the first step, which form a new vector of initial frequencies at each iteration.

To estimate the modal parameters, the observation model was determined based on the DHO model, the AR model of the coloured measurement noise and a stochastic model in the form of heavy tailed family of scaled t-distributions with an unknown degree of freedom and with unknown scale factor. The aforementioned observation model was combined in a joint log-likelihood function and adjusted by means of the GEM algorithm. Therefore, it allows for a self-tuning, robust and maximum likelihood estimation of the modal parameters. A novel cost function is introduced, which allows to calculate a cost value for each vector of initial eigenfrequencies at each iteration. The estimation procedure is terminated while no more vector of initial eigenfrequencies remains to be included. Thus, a reliable, robust and accurate estimates of the modal parameters are obtained using the optimal vector of initial frequencies caused the minimum value of the defined cost function. The well-defined initial eigenfrequencies speed up the process by fast convergence within the adjustment procedure.

The overall analysis demonstrates that the MEMS accelerometers used within our experimental studies allows the identification of all possible eigenfrequencies and eigenforms of the bridge structures with a submillimetre accuracy level for amplitudes, much better than 0.1 Hz for the eigenfrequencies and damping ratio coefficients estimates better than 0.1 and 0.2% for modal and system damping, respectively. The validation was carried out based on the analyses of the reference sensors measurements, the FEM analysis as well as the well-known SSI-COV algorithm.

The analysis proves the superiority of the RT-MPI algorithm compared to the SSI-COV algorithm, since the RT-MPI algorithm derives the estimates of the eigenfrequencies and the damping ratio coefficients based on the median values of the estimated parameters at different step sizes of the ambient windows selected. However, the SSI-COV algorithm can only achieve an accurate estimates of the damping ratio coefficients, while there is a perfect free

vibration decay of the measurements. Moreover, the estimates of the eigenfrequencies for both aforementioned approaches are very close together and their deviations can be neglected.

A global optimisation can be applied to fit the DHO model to the entire time series in future work. In addition, the determination of initial eigenfrequencies will be improved based on either a model selection problem or a significant test. Furthermore, a correlation between closely spaced frequencies will be taken into account. Moreover, a pattern recognition technique can also be applied to improve the ambient window selection.

Acknowledgment: The authors would like to acknowledge ALLSAT GmbH for providing the low-cost sensors used in the experiments. In addition, the authors would also like to acknowledge Eva Kemkes, M.Sc. (ALLSAT GmbH) and Dmitri Diener, M.Sc. (GIH) for their assistance in data acquisition within the experiments.

Funding: The research presented was carried out within the scope of the collaborative project “Spatio-temporal monitoring of bridge structures using low cost sensors” with ALLSAT GmbH, which was supported by the German Federal Ministry for Economic Affairs and Energy (BMWi) and the Central Innovation Programme for SMEs (Grant ZIM Kooperationsprojekt, ZF4081803DB6).

References

- [1] Dawson B. Vibration condition monitoring techniques for rotating machinery. *Shock Vib Dig* 1976; 8(12): 3.
- [2] Alvandi A, Cremona C. Assessment of vibration-based damage identification techniques. *J Sound Vib* 2006; 292(1): 179–202.
- [3] Wenzel H. *Health monitoring of bridges*. United Kingdom: John Wiley and Sons Ltd., 2009.
- [4] Peeters B, Maeck J, De Roeck G. Vibration-based damage detection in civil engineering: excitation sources and temperature effects. *Smart Mater Struct* 2001; 10(3): 518–27.
- [5] Rohrmann RG, Baessler M, Said S, Schmid W, Ruecker WF. Structural causes of temperature affected modal data of civil structures obtained by long time monitoring. *Proc. 18th Int. Modal Analytical Conf. IMAC 18*, San Antonio, Tex., 1–7, 2000.
- [6] Duff K, Hyzak M. Structural monitoring with GPS. https://www.fhwa.dot.gov/publications/publicroads/97spring/_gps.cfm (Accessed 2 November 2018).
- [7] Roberts GW, Meng X, Dodson AH. Integrating a global positioning system and accelerometers to monitor the deflection of bridges. *J Surv Eng* 2004; 130(2): 65–72.
- [8] Neitzel F, Niemeier W, Weisbrich S, et al. Investigation of low-cost accelerometer, terrestrial laser scanner and ground-based radar interferometer for vibration monitoring of bridges. *Proc of the 6th European Workshop on Structural Health Monitoring*, 542–51, 2012.

- [9] Psimoulis PA, Stiros SC. Measuring deflections of a short-span railway bridge using a robotic total station. *J Bridge Eng* 2013; 18(2): 182–5.
- [10] Pagiatakis SD. Stochastic significance of peaks in the least-squares spectrum. *J Geodesy* 1999; 73(2): 67–78.
- [11] Pytharoulis SI, Stiros SC. Spectral analysis of unevenly spaced or discontinuous data using the Normperiod code. *Comput Struct* 2008; 86(1–2): 190–6.
- [12] Ehrhart M, Lienhart W. Monitoring of civil engineering structures using a state-of-the-art image assisted total station. *J Appl Geodesy* 2015; 9(3): 174–82.
- [13] Heylen W, Lammens S, Sas P. *Modal analysis theory and testing*. Leuven, Belgium: Katholieke Universiteit Leuven, 1997.
- [14] Guillaume P, De Troyer T, Devriendt C, De Sitter G. OMAX—a combined experimental-operational modal analysis approach. *Proc of ISMA2006 international conference on noise and vibration engineering*, Leuven, Belgium, 2985–96, September 2006.
- [15] Brandt A. *Noise and vibration analysis: signal analysis and experimental procedures*. Chichester, UK: John Wiley and Sons Ltd., 2011.
- [16] Zhang G, Tang B, Tang G. An improved stochastic subspace identification for operational modal analysis. *Measurement* 2012; 45(5): 1246–56.
- [17] Parloo E. Application of frequency-domain system identification techniques in the field of operational modal analysis. *PhD thesis*, Belgium: Department of Mechanical Engineering, Vrije Universiteit Brussel, 2003.
- [18] Reynders E. System identification methods for (operational) modal analysis: review and comparison. *Arch Comput Method Eng* 2012; 19(1): 51–124.
- [19] Peeters B, Vanhollenbeke F, Van der Auweraer H. Operational PolyMAX for estimating the dynamic properties of a stadium structure during a football game. *Proc of the IMAC*, Vol. 23, Orlando, FL, USA, January 2005.
- [20] Peeters B, Van der Auweraer H. PolyMAX: a revolution in operational modal analysis. *1st International Operational Modal Analysis Conference*, Copenhagen, Denmark, April 2005.
- [21] James GH, Carne TG, Lauffer JP. The natural excitation technique (NExT) for modal parameter extraction from operating structures. *Modal Anal* 1995; 10(4): 260–77.
- [22] Van Overschee P, De Moor B. Subspace algorithms for the stochastic identification problem. *Automatica* 1993; 29(3): 649–60.
- [23] Hermans L, Van der Auweraer H. Modal testing and analysis of structures under operational conditions: industrial applications. *Mech Sys Signal Process* 1999; 13(2): 193–216.
- [24] Peeters B. System identification and damage detection in civil engineering, *PhD thesis*, Belgium: Department of Civil Engineering, K. U. Leuven, 2000.
- [25] Fan J, Zhang Z, Hua H. Data processing in subspace identification and modal parameter identification of an arch bridge. *Mech Sys Signal Process* 2007; 21(4): 1674–89.
- [26] Reynders E, Pintelon R, De Roeck G. Uncertainty bounds on modal parameters obtained from stochastic subspace identification. *Mech Sys Signal Process* 2008; 22(4): 948–69.
- [27] Magalhaes F, Cunha A, Caetano E. Online automatic identification of the modal parameters of a long span arch bridge. *Mech Sys Signal Process* 2009; 23(2): 316–29.
- [28] Boonyapinyo V, Janesupasaeree T. Data-driven stochastic subspace identification of flutter derivatives of bridge decks. *J Wind Eng Ind Aerod* 2010; 98(12): 784–99.
- [29] Brincker R, Zhang L, Andersen P. Modal identification of output-only systems using frequency domain decomposition. *Smart Mater Struct* 2001; 10(3): 441–5.
- [30] Ibrahim SR. Efficient random decrement computation for identification of ambient responses. *Proc of the International Modal Analysis Conference – IMAC*, Orlando, FL, 2001, 698–703.
- [31] Lardies J, Gouttebroze S. Identification of modal parameters using the wavelet transform. *Int J Mech Sci* 2002; 44(11): 2263–83.
- [32] Guillaume P, Verboven P, Vanlanduit S. Frequency-domain maximum likelihood identification of modal parameters with confidence intervals. *Proc of ISMA 23, Noise and Vibration Engineering*, Belgium: K. U. Leuven, 1998.
- [33] Golub GE, Van Loan CF. *Matrix computations*. The Johns Hopkins University Press, 2013.
- [34] Bendat JS, Piersol AG. *Engineering applications of correlation and spectral analysis*. New York: Wiley-Interscience, 1980.
- [35] Kang C, Bode M, Wenner M, Marx S. Experimental and numerical investigations of rail behaviour under compressive force on ballastless track systems. *Eng Struct* 2019; 197: 1–13. DOI:10.1016/j.engstruct.2019.109413.
- [36] Diederley J, Herrmann R, Marx S. Ermüdungsversuche an großformatigen Betonprobekörpern mit dem Resonanzprüfverfahren. *Beton- Stahlbetonbau* 2018; 113(8): 589–97. DOI:10.1002/best.201800010.
- [37] Cuéllar P, Mira P, Pastor M, Fernández Merodo JA, Baeßler M, Rücker W. A numerical model for the transient analysis of offshore foundations under cyclic loading. *Comput Geotech* 2014; 59: 75–86.
- [38] Nerger D, Hille F, Moosavi R, Grunwald M, Redmer B, Kühn T, Hering M, Bracklow F. Improved tomographic investigation for impact damage characterization. *Proc of the 25th SMiRT conference (SMiRT 25)*, Charlotte, 4–9 August 2019.
- [39] Kargoll B, Omidalizarandi M, Paffenholz JA, Neumann I, Kermarrec G, Alkhatib H. Bootstrap tests for model selection in robust vibration analysis of oscillating structures. *Proc of the 4th Joint International Symposium on Deformation Monitoring (JISDM)*, Athens, 15–17 May 2019.
- [40] PCB piezoelectric accelerometer. PCB piezotronics MTS systems corporation, <https://www.pcb.com/resources/technical-information/introduction-to-accelerometers> (accessed 17 September 2019).
- [41] Omidalizarandi M, Neumann I, Kemkes E, Kargoll B, Diener D, Rüffer J, Paffenholz JA. MEMS based bridge monitoring supported by image-assisted total station. *Int. Arch. Photogramm. Remote Sens. Spatial Inf. Sci.*, XLII-4/W18, 833–42, Karaj, 12–14 October 2019.
- [42] Shin EH, El-Sheimy N. A new calibration method for strapdown inertial navigation systems. *Z Vermess* 2002; 127: 1–10.
- [43] KUKA youBot. KUKA youBot User Manual. Document revision 1.01. ftp://ftp.youbot-store.com/manuals/KUKA-youBot_UserManual.pdf (25 November 2019).
- [44] Kargoll B, Omidalizarandi M, Loth I, Paffenholz JA, Alkhatib H. An iteratively reweighted least-squares approach to adaptive robust adjustment of parameters in linear regression models with autoregressive and t-distributed deviations. *J Geodesy*

- 2018; 92(3): 271–97.
- [45] Marple SL. *Digital Spectral Analysis*. Englewood Cliffs, NJ: Prentice-Hall, 1987, pp. 373–8.
- [46] Jiang X, Adeli H. Pseudospectra, MUSIC and dynamic wavelet neural network for damage detection of highrise buildings. *Int J Numer Meth Eng* 2007; 71(5): 606–29.
- [47] Amezcua-Sanchez JP, Adeli H. A new music-empirical wavelet transform methodology for time–frequency analysis of noisy nonlinear and non-stationary signals. *Digit Signal Process* 2015; 45: 55–68.
- [48] Torr PH, Zisserman A. MLESAC: A new robust estimator with application to estimating image geometry. *Comput Vis Image Und* 2000; 18(1): 138–56.
- [49] Cheynet E. Operational modal analysis with automated SSI-COV algorithm (<https://www.mathworks.com/matlabcentral/fileexchange/69030-operational-modal-analysis-with-automated-ssi-cov-algorithm>), MATLAB Central File Exchange. Retrieved February 7, 2020.
- [50] Omidalizarandi M, Kargoll B, Paffenholz JA, Neumann I. Accurate vision-based displacement and vibration analysis of bridge structures by means of an image-assisted total station. *Adv Mech Eng* 2018; 10(6): 1687814018780052.
- [51] Alkhatib H, Kargoll B, Paffenholz JA. Further results on a robust multivariate time series analysis in nonlinear models with autoregressive and t-distributed errors, *Time Series Analysis and Forecasting*. ITISE 2017. Rojas I, Pomares H, Valenzuela O (eds.). Contributions to statistics, Cham: Springer, 25–38, 2018.
- [52] Nassar S, Schwarz KP, EL-Sheimy N, Noureldin A. Modeling inertial sensor errors using autoregressive (AR) models. *Navigation* 2004; 51(4): 259–68.
- [53] Hargreaves GI. Interval analysis in MATLAB. *Numerical Analysis Report No. 416*, Manchester Centre for Computational Mathematics, The University of Manchester, ISSN 1360-725, 2002.
- [54] Kargoll B, Omidalizarandi M, Alkhatib H, Schuh WD. Further results on a modified EM algorithm for parameter estimation in linear models with time-dependent autoregressive and t-distributed errors. *International Work-Conference on Time Series Analysis*, 323–37, Cham: Springer, 2017.
- [55] Rump SM. INTLAB—interval laboratory. *Tibor Csendes, editor, developments in reliable computing*, Dordrecht: Kluwer Academic Publishers, 77–104, 1999.
- [56] Omidalizarandi M, Paffenholz JA, Neumann I. Automatic and accurate passive target centroid detection for applications in engineering geodesy. *Surv Rev* 2019; 51(367): 318–33.
- [57] Cheynet E, Jakobsen JB, Snæbjörnsson J. Damping estimation of large wind-sensitive structures. *Procedia engineering* 2017; 199: 2047–53.
- [58] Herrmann R. Dataset: Reference Vibration Measurement of Mensa Bridge Hannover. DOI:<https://doi.org/10.25835/0081614>.

Paper 5

MEMS BASED BRIDGE MONITORING SUPPORTED BY IMAGE-ASSISTED TOTAL STATION

M. Omidalizarandi ^{1,*}, I. Neumann ¹, E. Kemkes ², B. Kargoll ³, D. Diener ¹, J. Rüffer ², J.-A. Paffenholz ¹

¹ Geodetic Institute, Leibniz University Hannover, Nienburger Str.1, 30167 Hannover, Germany - (zarandi, neumann, diener, paffenholz)@gih.uni-hannover.de

² Allsat GmbH, 30165 Sokelant Str.5, Hannover, Germany - (eva.kemkes, juergen.rueffer@allsat.de)

³ Institut für Geoinformation und Vermessung Dessau, Hochschule Anhalt, Bauhaus Str. 8, 06846 Dessau-Roßlau, Germany - (boris.kargoll@hs-anhalt.de)

KEY WORDS: Displacement and vibration analysis, MEMS accelerometer, Image-assisted total station, Modal parameter identification, Robust parameter estimation, Kalman filter, Bridge monitoring

ABSTRACT:

In this study, the feasibility of Micro-Electro-Mechanical System (MEMS) accelerometers and an image-assisted total station (IATS) for short- and long-term deformation monitoring of bridge structures is investigated. The MEMS sensors of type BNO055 from Bosch as part of a geo-sensor network are mounted at different positions of the bridge structure. In order to degrade the impact of systematic errors on the acceleration measurements, the deterministic calibration parameters are determined for fixed positions using a KUKA youBot in a climate chamber over certain temperature ranges. The measured acceleration data, with a sampling frequency of 100 Hz, yields accurate estimates of the modal parameters over short time intervals but suffer from accuracy degradation for absolute position estimates with time. To overcome this problem, video frames of a passive target, attached in the vicinity of one of the MEMS sensors, are captured from an embedded on-axis telescope camera of the IATS of type Leica Nova MS50 MultiStation with a practical sampling frequency of 10 Hz. To identify the modal parameters such as eigenfrequencies and modal damping for both acceleration and displacement time series, a damped harmonic oscillation model is employed together with an autoregressive (AR) model of coloured measurement noise. The AR model is solved by means of a generalized expectation maximization (GEM) algorithm. Subsequently, the estimated model parameters from the IATS are used for coordinate updates of the MEMS sensor within a Kalman filter approach. The experiment was performed for a synthetic bridge and the analysis shows an accuracy level of sub-millimetre for amplitudes and much better than 0.1 Hz for the frequencies.

1. INTRODUCTION

1.1 Motivation

For more than 10 years now, the damage to road bridges from the 60s and 70s, which has been increasingly noticed, has been attracting more and more attention from the media. Besides this, the monitoring of bridges with different tasks and methods came into the focus of attention. These questions require an interdisciplinary cooperation between geodesists, civil engineers and geotechnical engineers.

Over the last decade of bridge monitoring, the authors and most likely other researchers as well as infrastructure operators have made different experiences. Initially, the scepticism towards permanent monitoring with geodetic sensors and methods was particularly high, but this methodology has gained an increasing reputation due to positive practical examples on selected bridges and other structures such as locks and dams. The impressive demonstration of geodetic methods soon led to the use of this technology in several cases: (1) for extensive rehabilitation measures on existing bridges, (2) to prevent early decommissioning, and (3) to ensure sufficient safety for people and the structure itself during operation. In combination with geotechnical monitoring procedures, this leads to undeniable economic advantages for the operators and for the society.

However, the infrastructure operators, in particular the road construction authorities in Germany, were soon confronted with the demand for a massive expansion of the geomonitoring of

bridges. Not only in the case of extensive rehabilitation measures, but also for the preventive monitoring of bridges with condition grades 3 according to DIN 1076. In particular, a high percentage of 21% of all bridges built before 1980 in Germany was affected.

In particular, the high initial investment in the permanent use of geodetic methods caused the initial interest of the operators to drop considerably. The reason was seen in an economically unacceptable permanent monitoring of dilapidated, severely damaged or endangered bridges. And as long as nothing serious happened, the existing methodology for bridge monitoring seemed to be sufficient and in particular economically justifiable.

The increasing number of critical bridge structures with a simultaneous rehabilitation backlog and a lack of experienced experts for the inspection and assessment of bridges suggests the question of whether there are not effective and inexpensive methods that only initiate a visual inspection or precise geodetic monitoring of bridges when verifiable indications are available through efficient and cost-effective monitoring procedures. Then the targeted and detailed inspection and monitoring of structures classified as critical could be initiated as required.

The authors' goals are the self-sufficient use of a larger number of cost-effective and redundantly arranged sensors (here: Micro-Electro-Mechanical System (MEMS) technology from the automotive industry) and the intelligent and continuous evaluation of data permanently obtained from potentially critical bridge structures based on frequency- and time-domain analysis methods. The following partial goals are in focus: (1) early and

timely detection of variations of the modal parameters relevant for the structural condition of the bridge (e.g. natural frequencies and eigenforms), (2) permanent control and long-term statements for structural deformations and (3) allocation of deformations to the relevant influencing variables on the building deformation.

Therefore, this paper is organized as follows: The ongoing section gives a brief literature overview. Section 2 introduces the sensor specifications, the measurement set-up and the data acquisition. In Section 3 the suitability analysis of triaxial MEMS accelerometers for the purpose of bridge monitoring is discussed. The robust and automatic identification of modal parameters is introduced in Section 4. Section 5 presents the fusion of MEMS and image-assisted total station (IATS) data for a displacement analysis based on Kalman filtering. The realised experiment in Section 6 is sketched for a synthetic bridge, which is constructed by the Bundesanstalt für Materialforschung und -prüfung (BAM). The results of the experiment for the BAM synthetic bridge using the MEMS and the IATS are discussed in Section 7. The conclusion and the outlook on future work is given in Section 8.

1.2 Literature review

For the monitoring of long-term movements of bridges (induced by foundation settlement, creep, and stress relaxation) or short-term movements (caused by wind and traffic) (Duff and Hyzak, 1997), different contact-based or non-contact-based measurement methods can be utilised. As a surveying engineer's point of view, typically geodetic measurement systems, such as the global navigation satellite system (GNSS), robotic total stations (RTS), IATS, terrestrial laser scanner (TLS), laser tracker and/or other sensors such as accelerometers or digital cameras, can be used in the context of vibration monitoring of bridge structures. In the following, a brief and exemplarily overview of the state of the art based on a literature review is given. Roberts et al. (2004) utilised the hybrid measurement system consisting of a GNSS with a sampling frequency of 10 Hz and a triaxial accelerometer with sampling frequency of 200 Hz for a bridge deflection monitoring. Both measurement systems were complementary to each other since the GNSS measurements were used to suppress the accumulation drift of the acceleration data over time through zero velocity updates (ZUPT) and coordinate updates (CUPT). In order to filter out the high frequency noise, static test measurements with the accelerometers were carried out to identify those spurious frequencies induced by the sensor noise. Subsequently, the designed low-pass or band-pass filters were defined to suppress those frequencies with respect to the structural specifications and the results of the aforementioned static test. This is a challenging issue while the natural frequencies of bridges are located in the same band as those spurious frequencies. In addition, the hybrid measurement suffers from the drawback that the accuracy of the GNSS measurements are degraded due to multipath and cycle slips errors or poor satellite coverage. On the other hand, the state-of-the-art GNSS measurements cannot detect submillimetre displacement changes induced by higher natural frequencies. Neitzel et al. (2012) performed a vibration analysis of a bridge for a single point located along the bridge using a sensor network of accelerometers with a sampling frequency of 600 Hz, a TLS (Zoller+Fröhlich Imager 5003) with a sampling frequency of 7812 Hz in single-point measurement mode and a terrestrial interferometric synthetic aperture radar (t-InSAR) with a sampling frequency of 200 Hz for a validation. In order to overcome the deficiency of the TLS in detecting such small displacements in the submillimetre range, an averaging over 100 measurements was carried out to reach a practical sampling

frequency of 78.12 Hz. Psimoulis and Stiros (2013) used the RTS with non-constant sampling rate measurements in a range of 5–7 Hz for vibration monitoring of a short span railway bridge. Ehrhart and Lienhart (2015a) performed displacement and vibration monitoring of a footbridge structure by capturing video frames from the telescope camera of an IATS for a circular target marking rigidly attached to the structure. Ehrhart and Lienhart (2015b) and Lienhart et al. (2017) were carried out vibration analysis of a footbridge structure using an IATS of type Leica MS50 with a sampling frequency of 10 Hz, an RTS of type Leica TS15 with a sampling frequency of 20 Hz and an accelerometer of type HBM B12/200 with a sampling frequency of 200 Hz based on measurements of the circular target markings and structural features such as bolts of the bridge structure. Omidiazarandi et al. (2018) used an IATS of type Leica MS50 with sampling frequency of 10 Hz for displacement and vibration analysis of a footbridge structure. Schill and Eichhorn (2019) employed a phase-based profile scanner of type Zoller+Fröhlich Profiler 9012 with a sampling frequency of 50 Hz for deformation monitoring of the bridge structures.

2. SENSOR SPECIFICATIONS, MEASUREMENT SET-UP AND DATA ACQUISITION

The MEMS sensors of type BNO055 from the Bosch company have been used in this study. It includes a triaxial 14-bit accelerometer, a triaxial 16-bit gyroscope and a triaxial magnetometer, which allows to acquire acceleration, rotation and magnetic field strength, respectively (see manufacturer's data sheet for details in Bosch (2016)). However, we merely benefit its accelerometer sensor to record the acceleration data in three main directions of a bridge structure (i.e. longitudinal, lateral and vertical directions). Its maximum sampling frequency is 200 Hz. But, we set it to 100 Hz by considering typical eigenfrequency ranges of the bridge structures between 0.1 up to minimum 25 Hz, which is sufficient in the light of Nyquist–Shannon sampling theorem. Acceleration ranges can be defined in the ranges of $\pm 2g/\pm 4g/\pm 8g/\pm 16g$, which is here set to $\pm 2g$. At the moment, a geo-sensor network of the MEMS accelerometers includes a master node and three measuring nodes that are so called master and slaves, respectively.

The measurement starts by triggering the slave sensors from the master sensor via cable. The acceleration measurements are recorded into the SD memory card in blocks. Each memory block has a time stamp transmitted by the master, which is provided by an integrated low-cost GNSS equipment. Both, the master and the slaves contain a Bosch BNO055 accelerometer and a control/storage unit. The components are mounted in an aluminium housing, which protects the electronics against temperature and humidity changes, wind and rain by means of a suitable design.

To perform evaluation and validation of the estimated modal parameters from the MEMS accelerometers, a highly accurate reference sensor is employed. We have used a laser tracker of type Leica AT960-LR with a maximum permissible error of $15\mu\text{m} + 6\mu\text{m}/\text{m}$ for a 3D point with a sampling frequency of 1000 Hz (Hexagon Metrology, 2015). Therefore, the use of the laser tracker as a reference sensor allows high measuring accuracy with a high and precise measuring frequency.

An IATS of type Leica Nova MS50 MultiStation is utilized to perform 1D CUPT of the acceleration data acquired by the MEMS accelerometers in the vertical direction. The angular accuracy is 1" according to ISO 17123-3. The outputs of the IATS are polar measurements, which can be used to calculate

Cartesian coordinates. Such 3D coordinates of the measured object are not practically suitable to perform displacement analysis in a sub-millimetre range. To overcome this problem, a 1D displacement time series is generated based on continuous extraction of the passive target centroids from the video frames captured from the embedded on-axis telescope camera of the IATS with practical sampling frequency of 10 Hz. The conversion of the 1D displacement changes from the pixel unit to the metric unit is carried out based on a vertical angular conversion factor, target object size as well as a slope distance measured to the aforementioned passive target. For more information regarding the calibration procedure of the vertical angular conversion factor, please refer to cf. Ehrhart and Lienhart (2015a) or Omidalzarandi et al. (2018). It should be noted that merely 1D displacement time series has been generated using the aforementioned video frames due to availability of only one IATS at time of the measurements, which subsequently allows to perform just 1D CUPT in this study.

The passive target centroids are extracted based on the work of Omidalzarandi et al. (2019a). The used target pattern comprises a circular border with four intersected line patterns (Figure 1). The procedure starts by manual initial sighting to the target at the beginning of the measurements and measuring its corresponding slope distance. Next, the images obtained from captured video frames are cropped based on a target object size as well as the slope distance. The median blur and bilateral filtering are applied for the purpose of noise reduction and sharp edge preservation. The line segment detector (LSD) (Grompone von Gioi et al., 2012) is applied to extract line features. A histogram of azimuth of the extracted lines is calculated to select the lines with maximum azimuth bin values in an iterative procedure. Afterwards, the RANSAC algorithm is applied to those LSD lines with maximum deviation less than 15° from the selected lines from the previous step. A Huber-robust line fitting (Kaehler and Bradski, 2016) is then applied to those LSD lines within a predefined buffer width around the RANSAC lines to increase the robustness and reliability of the extracted lines. To this end, the extracted lines are intersected and then clustered based on their proximity by considering a threshold of 2 pixels. At the end, the maximum cluster is selected and its weighted average value results in the final intersection point. For further details the reader is referred to Omidalzarandi et al. (2019a).

Figure 1 depicts the passive target attached to a frontal side of the BAM synthetic bridge in the vicinity of one the MEMS accelerometers, which is mounted at the bottom of the aforementioned synthetic bridge. In addition, a corner cube reflector is mounted to be measured by the laser tracker.

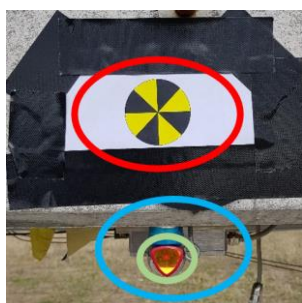


Figure 1. A passive target (located inside the red ellipse) attached to the BAM synthetic bridge, which is close to the MEMS (located inside the cyan ellipse) and corner cube reflector (located inside the green ellipse).

3. SUITABILITY ANALYSIS OF TRIAXIAL MEMS ACCELEROMETERS

The acceleration measurements recorded from the MEMS accelerometer yields accurate results over short time intervals but may suffer from accuracy degradation with time in particular for absolute position estimates calculated from the double integration. Therefore, due to combined effects of MEMS related systematic and random errors such as noises, biases, drifts and scale factor instabilities on its long-term measurements, a calibration procedure is carried out to compensate the systematic errors and to provide reliable measurement results.

To select a proper and optimal MEMS sensor despite of considering purchase price of the sensor and their sampling frequency, two scenarios are proposed. Firstly, a robust and reliable calibration procedure is developed and implemented to estimate the calibration parameters including three biases, three scale factors and three non-orthogonality angles between the axes in an automated manner. For this purpose, the calibration functions are defined based on common six-position static acceleration tests (cf. Shin and El-Sheimy, 2002) using a KUKA youBot (Figure 2). The used youBot enables us to perform calibration automatically for fixed positions and for certain time intervals. To have a better realisation of changes of the calibration parameters, the calibration procedure is carried out in a climate chamber over different temperature ranges between 10°C to 30°C . Higher or lower temperatures were not possible due to climate chamber and youBot restrictions. To this end, such a calibration procedure allows to avoid in-situ calibration by estimating the calibration parameters based on the interpolation of the parameters estimated at different temperatures in the controlled environmental experiment. Due to the use of only 1D acceleration data in this study, the calibration of the non-orthogonality angles between the three axes may not play an important role. However, in our future research the 3D acceleration data in all three directions can be considered. Further explanation regarding the developed robust calibration procedure is also part of our future publication and it is out of scope of this study.

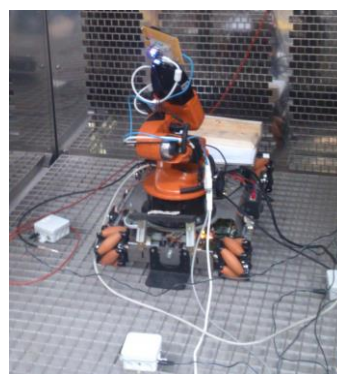


Figure 2. A calibration experiment using a KUKA youBot inside the climate chamber at the Institute of Thermodynamics, Leibniz University Hannover.

Secondly, controlled excitation experiments are conducted at the laboratory environment using a high-precision shaker (Figure 3). The advantages of such experiment are twofold: (1) it allows us to estimate harmonic oscillation parameters such as frequency, amplitude, damping ratio coefficient as well as phase shift and to compare them with those estimated parameters either from other slave MEMS accelerometers or from the reference sensors such as reference accelerometers or laser tracker. (2) The time

synchronisation between MEMS accelerometers can be compared together based on the estimated phase shifts.

The measurements were performed at frequencies of 5, 10 and 20 Hz. The shaker includes a highly accurate reference accelerometer recording the acceleration measurements with a sampling rate of 1024 Hz for the duration of 5 minutes.

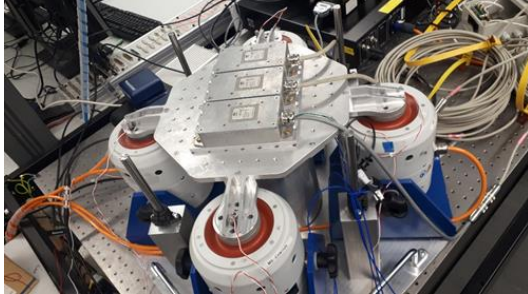


Figure 3. A controlled excitation experiment at the Institute of Dynamics and Vibration Research, Leibniz University Hannover to validate the time synchronisation between all three slave MEMS accelerometers.

f (Hz)	A (m/s ²)	A (mm)	φ (°)	g (m/s ²)	p
5.0027	0.3449	0.3491	5.7263	9.82	71
10.0054	1.5612	0.3950	153.204	9.82	88
20.0109	5.8159	0.3679	101.052	9.88	81

f (Hz)	A (m/s ²)	A (mm)	φ (°)	g (m/s ²)	p
5.0027	0.3512	0.3555	5.6675	10.42	71
10.0054	1.5909	0.4025	153.147	10.42	88
20.0109	5.9290	0.3751	100.859	10.53	81

Table 1. Statistics of the controlled excitation experiment for a MEMS (IMU_slave_03) measurements **with** (top) and **without** (bottom) applying calibration parameters.

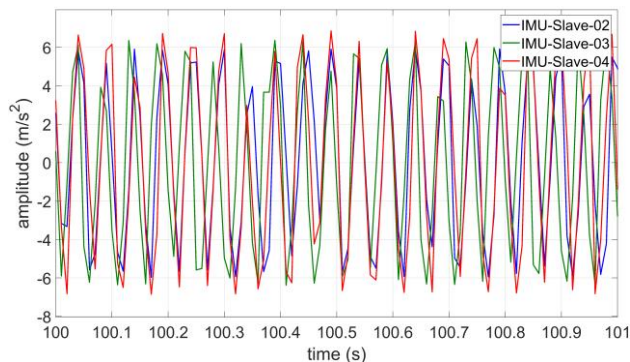


Figure 4. Overlaying of time series of the acceleration data recorded from all three slave MEMS sensors for a duration of 1 s and at the frequency of 20 Hz within the controlled excitation experiment.

Figure 4 shows the overlaying of time series of the acceleration data recorded from all three slave MEMS sensors for a duration of 1 s and at the frequency of 20 Hz. As we can see from this figure, the peaks of the measurements obtained from the two of the MEMS sensors (IMU_slave_02 and IMU_slave_04) have been better matched compared to another one (IMU_slave_03). However, the time delay between their measurements is

approximately 0.01 s, which is still acceptable for our application in this study.

The analysis of the second scenario is exemplarily provided in Table 1 for one slave MEMS accelerometer, namely, IMU_slave_03 in two cases: (1) with and (2) without applying the calibration parameters. The estimated parameters include the frequency (Hz), the amplitudes in both units of (m/s²) and (mm), the phase shift (°), the calculated absolute gravity value based on the calibration parameters (m/s²) and an autoregressive (AR) model order, for which the estimation procedure is described in Section 4. Further analyses show that the phase shifts between sensors vary between 2 to 5 degrees. Moreover, the differences of approximately 0.003 Hz for the frequency of 5 Hz and 0.01 Hz for the frequency of 20 Hz in comparison with the nominal frequency values are realised. Such differences prove that the time synchronisation has greater influence at higher frequencies. Additionally, the analyses prove a very less influence of the calibration parameters on the estimated modal parameters for a short period of time.

4. ROBUST AND AUTOMATIC IDENTIFICATION OF MODAL PARAMETERS

To inspect the changes in the global dynamic behaviour of the structure such as natural frequencies, mode shapes (i.e. eigenforms) and modal damping, a proper functional model should be identified. To tackle this problem and to estimate amplitudes as well as frequencies for displacement and vibration analysis, a linear regression model in terms of a sum of sinusoids and the AR model of the coloured measurement noise were previously employed and solved by means of the generalized expectation maximization (GEM) algorithm (Omidiazarandi et al. 2018). However, the estimated amplitude might be influenced by the damping characteristics of the structure, which the previous undamped model does not capture. Therefore, the deterministic model is extended to a damped harmonic oscillation (DHO) introduced in Amezcua-Sanchez and Adeli (2015) and applied by Kargoll et al. (2019) to estimate frequency, amplitude, phase shift as well as damping ratio coefficient.

We modelled the given acceleration measurements l_1, \dots, l_n according to the DHO model

$$l_t = \frac{a_0}{2} + \sum_{j=1}^M \left[a_j \cos(2\pi f_j \sqrt{1 - \xi_j^2} x_t) + b_j \sin(2\pi f_j \sqrt{1 - \xi_j^2} x_t) \right] \times \exp(-2\pi \xi_j f_j x_t) + e_t \quad (1)$$

where the time instances x_1, \dots, x_n correspond to the ambient window of the acceleration time series and where the undamped frequencies f_1, \dots, f_M , the coefficients a_0, a_1, \dots, a_M , and b_1, \dots, b_M as well as damping ratio coefficients ξ_1, \dots, ξ_M are treated as unknown parameters. Subsequently, the damped frequencies are calculated by $f_{jd} = f_j \sqrt{1 - \xi_j^2}$. It should be noted that the acceleration measurements are subtracted from their mean value for each selected ambient window.

To deal with the strong coloured measurement noise in the acceleration measurements, we assume the random deviations (e_t) are autocorrelated through a covariance-stationary AR process as proposed by Kargoll et al. (2018)

$$e_t = \alpha_1 e_{t-1} + \dots + \alpha_p e_{t-p} + u_t \quad (2)$$

in which the coefficients $\alpha^T = [\alpha_1, \dots, \alpha_p]$ are also considered as unknown parameters. Since we expect numerous outliers of different magnitudes to be present in the data, the white noise components u_1, \dots, u_n of that AR noise model are assumed to follow the centred and scaled t-distribution $t_\nu(0, \sigma^2)$, where the degree of freedom ν and scale factor σ^2 are treated as further parameters to be estimated, as suggested by Kargoll et al. (2018).

Equation (1) only achieves reasonable results while the measurements do not have a significant drift. Therefore, acceleration measurements should be detrended by means of the calibration parameters to compensate a linear bias drift. However, this method is not applicable to the displacement time series obtained by using the IATS. Alternatively, the offset $\frac{a_0}{2}$ in Equation (1) can be replaced by $c_0 + c_1 x_t$ to account for the linear drift either of the acceleration or displacement measurements. This model can be made more complex for displacement time series with higher orders, which extensions are, however, beyond the scope of this study.

To estimate the model parameters by means of the aforementioned GEM algorithm, the number M of Fourier frequencies and the model order p of the AR process are specified beforehand. The required initial frequency values $f_1^{(0)}, \dots, f_M^{(0)}$ and the AR model order are defined as explained in Omidizarandi et al. (2019b). In addition, the initial damping ratio coefficients are set to 0.

5. FUSION OF MEMS AND IATS FOR DISPLACEMENT ANALYSIS BASED ON KALMAN-FILTERING

Typically, the 3D coordinate measurements of a state of the art IATS are at the level of 1 mm accuracy or above depending on the distance to the object, which are not sufficiently accurate to characterise such small displacements at the level of sub-millimetre ranges for the application of bridge displacement monitoring. To achieve this goal in this study, the 1D displacement time series generated from the passive target centroid detection are fused with the acceleration measurements recorded from one of the MEMS accelerometers. Such a data fusion is also beneficial to overcome the 1D displacement drift of the MEMS accelerometer over time. For this purpose, the 1D CUPT is performed based on an iterative extended Kalman filter (iEKF). The Kalman filter is a recursive optimal filter which is carried out in three steps of initialisation, prediction and filtering. For more information in this regard, please refer to Kalman (1961).

The state vector $\mathbf{y}^{(k)}$ at epoch k is described as

$$\mathbf{y}^k = [d^k, v^k, a^k] \quad (3)$$

here d^k, v^k, a^k are the displacements, the velocities and the accelerations at the epoch k in the vertical direction. Since the acceleration and displacement are acquired with different sampling frequencies of 100 Hz and 10 Hz, respectively, the prediction step allows to compensate the displacement gaps. Alternatively, the displacement time series can be reconstructed from the estimated DHO model parameters to fill out those displacement gaps with resampling. The predicted state vector ($\hat{\mathbf{y}}^{k+1}$) at epoch $k+1$ is calculated based on the linear system equation as

$$\hat{\mathbf{y}}^{k+1} = \Phi^k \cdot \hat{\mathbf{y}}^k + \mathbf{G}^k \cdot \mathbf{w}^k + \mathbf{L}^k \cdot \mathbf{u}^k \quad (4)$$

where Φ^k is the transition matrix calculated from the dynamic model of the system (i.e. equations of motion) with respect to the state vector parameters, $\hat{\mathbf{y}}^k$ is the updated state vector at epoch k , \mathbf{G}^k and \mathbf{w}^k are the matrix and vector of disturbing variables or noises, \mathbf{L}^k and \mathbf{u}^k are the matrix and vector of acting forces. It should be noted that the influence of acting forces is neglected to simplify the problem.

The observation model is determined as

$$\begin{aligned} \mathbf{l}^{k+1} &= \mathbf{A}^{k+1} \cdot \hat{\mathbf{y}}^{k+1} + \mathbf{v}^{k+1}, \\ \begin{bmatrix} d^{k+1} \\ a^{k+1} \end{bmatrix} &= \begin{bmatrix} 1 & 0 & 0 \\ 0 & 0 & 1 \end{bmatrix} \begin{bmatrix} d^{k+1} \\ v^{k+1} \\ a^{k+1} \end{bmatrix} + \mathbf{v}^{k+1} \end{aligned} \quad (5)$$

where \mathbf{l} is the observation vector, \mathbf{A} is the design matrix and \mathbf{v} is the vector of residuals. The transition matrix is then given by integration with respect to the state vector parameters as

$$\Phi^k = \begin{bmatrix} 1 & \Delta t & \frac{1}{2} \Delta t^2 \\ 0 & 1 & \Delta t \\ 0 & 0 & 1 \end{bmatrix} \quad (6)$$

where Δt is the sampling period. The covariance matrix of the process noise is defined based on Wiener-sequence acceleration as described by Bar-Shalom et al. (2001)

$$\Sigma_{ww} = \begin{bmatrix} \frac{1}{20} \Delta t^5 & \frac{1}{8} \Delta t^4 & \frac{1}{6} \Delta t^3 \\ \frac{1}{8} \Delta t^4 & \frac{1}{3} \Delta t^3 & \frac{1}{2} \Delta t^2 \\ \frac{1}{6} \Delta t^3 & \frac{1}{2} \Delta t^2 & \Delta t \end{bmatrix} \tilde{q} \quad (7)$$

where \tilde{q} is the ratio between the system noise and observation noise. The covariance matrix of the observations is given by

$$\Sigma_{ll} = \begin{bmatrix} \sigma_d^2 & 0 \\ 0 & \sigma_a^2 \end{bmatrix} \quad (8)$$

where σ_d and σ_a are the a-priori standard deviations of the displacements and the accelerations. It should be noted that the noise behaviour of the MEMS acceleration data at rest and for its 3-axes (i.e. X, Y and Z) are approximately about 0.016, 0.018 and 0.045 m/s², respectively. However, the uncertainty for its Z axis at motion (i.e. under oscillation imposed by the modal hammer) is about 0.013 m/s² according to the analysis performed for the synthetic bridge described in Section 6. Subsequently, the a-priori standard deviations are set to 0.0001 m and 0.013 m/s², respectively. For further details concerning the iEKF steps, please refer to cf. Omidizarandi and Zhou (2013).

6. EXPERIMENTAL SET-UP

A kinematic deformation analysis of the BAM synthetic bridge structure, located in approximately 80 km distance from Berlin, Germany, with a length of 24.0 m, a width of 0.8 m and a height of 0.3 m (Figure 5) is investigated. The measurements were carried out using the MEMS accelerometers, the laser tracker Leica AT960-LR and the IATS (Leica MS50) with sampling frequencies of 100 Hz, 1000 Hz and 10 Hz, respectively.

To identify all possible mode shapes of the aforementioned BAM synthetic bridge, the three slave and one master MEMS

accelerometers were attached at certain positions and at the first half of the synthetic bridge due to the symmetric behaviour of the mode shapes. Therefore, the three slave MEMS accelerometers are placed at the first, second and third quarters of the synthetic bridge. The master MEMS accelerometer is placed at the first quarter.



Figure 5. The BAM synthetic bridge measured by the MEMS accelerometers, the laser tracker and the IATS.

Since the BAM synthetic bridge is a rigid platform without any natural frequencies, therefore an artificial oscillation was generated using a modal hammer.

As mentioned before, the acceleration measurements were acquired from all three slave MEMS accelerometers in three directions. However, only the acceleration measurements in the Z direction were considered.

7. RESULTS FOR THE MEMS ACCELEROMETERS AND THE IATS

Figure 6 depicts the displacement time series obtained from the video frames captured by the telescope camera of the IATS at a centre position of the BAM synthetic bridge for a duration of 10 minutes. The large peaks illustrate the time instances while the external forces were imposed by the modal hammer. A steep rise at approximately 310 s is due to the bridge movement as it was visible from displacement time series obtained from the IATS and the laser tracker as well.

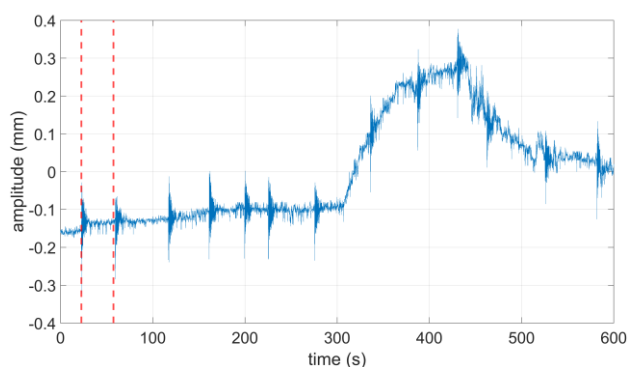


Figure 6. Displacement time series at the centre position of the BAM synthetic bridge, which was obtained from the video frames captured by the telescope camera of the IATS (blue solid), and selected ambient window of 35 s (red dashed lines).

Figure 7 shows the discrete Fourier transform (DFT) of the MEMS acceleration data. As we can see in this figure, it is very challenging to directly extract dominant eigenfrequencies from the DFT due to numerous spurious frequencies.

Figure 8 illustrates the time series of the 1D displacements from the IATS and its adjusted data within the selected ambient window. Figures (9-10) depict the eigenfrequencies estimated for the acceleration data from the MEMS and for the displacement data from the IATS. As we can see in Figure 9, there might be a correlation between closely spaced frequencies of 5.73 and 5.33 Hz, which have amplitudes approximately close to the noise level of the acceleration data.

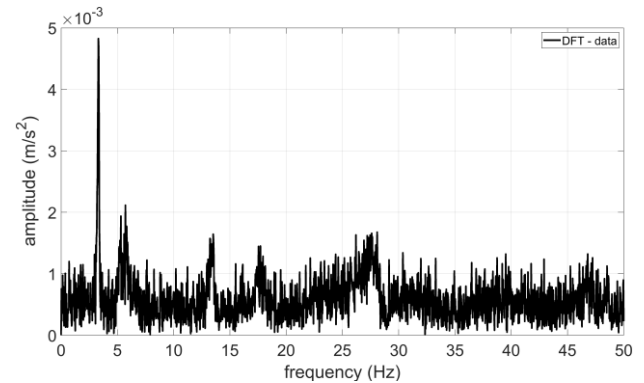


Figure 7. The DFT of the MEMS accelerations for the selected ambient window of 35 s shown in Figure 6.

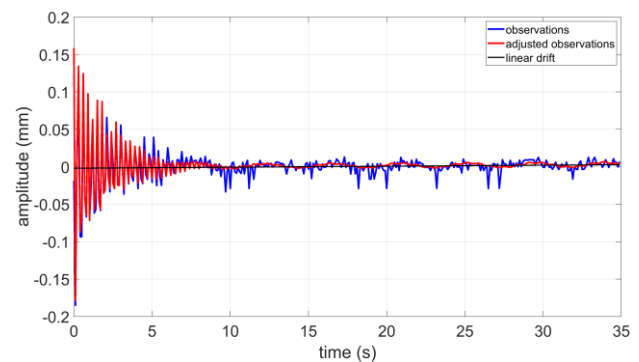


Figure 8. The time series of the displacements from the IATS within the selected ambient window (blue) and their adjusted observations (red).

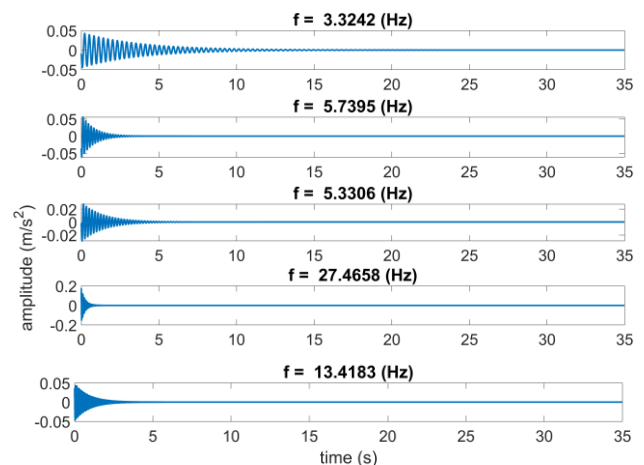


Figure 9. Identified frequencies from the MEMS acceleration data within the selected ambient window.

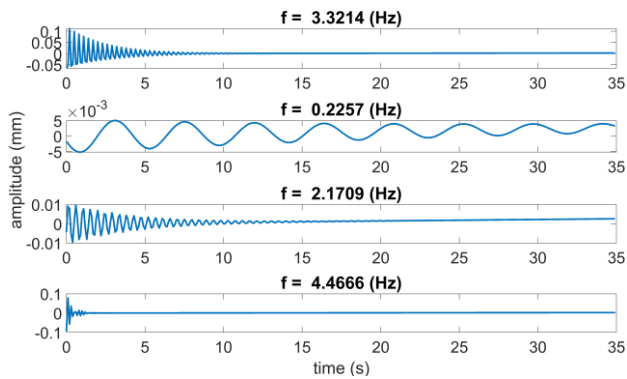


Figure 10. Identified frequencies for the displacement data from the IATS within the selected ambient window by considering the linear drift of the offset.

In real applications of bridge structures, the natural frequencies might be changed but may not be diminished, which can be seen for the frequency of 3.3 Hz. In contrast, a system frequency caused by the imposition of the load will be diminished in a few seconds such as for the frequency of 27.46 Hz extracted from the acceleration data. The impact of the linear drift offset for the displacement data obtained from the IATS is visible for the lower frequency of 0.22 Hz. The frequency of 4.46 Hz for the displacement data from the IATS shows a superimposition of higher frequencies than 5 Hz, which is related to the deficiency of the IATS and its low sampling frequency.

In order to obtain the acceleration measurements at the metric unit, a double integration is performed within the selected ambient window based on the work of Omidalizarandi et al. (2019b). Subsequently, the displacements are estimated for each identified eigenfrequency by fitting the DHO model to the double integrated adjusted acceleration data (Figure 11).

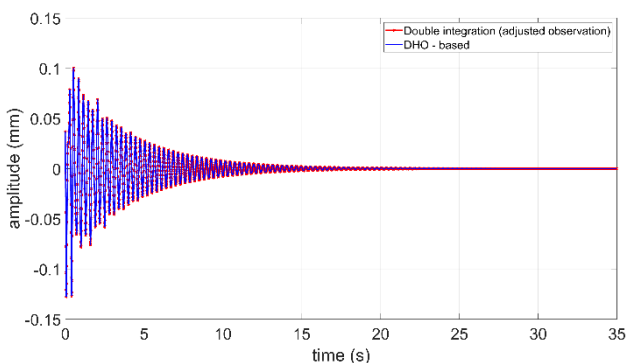


Figure 11. The calculated displacements for the adjusted MEMS acceleration data within the selected ambient window based on: double integration (red) and fitted DHO model (blue).

An eigenfrequency of 3.3 Hz is detected precisely from the measurements of the MEMS, the IATS and the laser tracker as we can see in Table 2. The double integration accuracy might be degraded for the calculated displacements obtained from the MEMS acceleration data for a duration of 10 s or less in case of high load impact on the structure. This is due to the fact that the modal parameters might not be identified reliably for such short time interval. Furthermore, the analysis shows that the estimated damping ratio coefficients from the IATS and the laser tracker are not as accurate as from the MEMS due to superimposition of those higher frequencies with small amplitudes. The reason lies

in the uncertainty of the measurements, which are higher than the amplitudes of the oscillations.

Time: 15 s	f (Hz)	A (mm)	ξ (%)
MEMS	3.3278	0.1064	1.30
IATS	3.2968	0.1357	2.27
Laser tracker	3.3190	0.1263	1.61

Time: 35 s	f (Hz)	A (mm)	ξ (%)
MEMS	3.3242	0.0977	1.20
IATS	3.3214	0.1217	1.97
Laser tracker	3.3181	0.1282	1.64

Table 2. Statistics of estimated modal parameters for the MEMS accelerometer, the IATS and the laser tracker measurements for a duration of 15 s (top) and 35 s (bottom) within the selected ambient window and at the centre position of the BAM synthetic bridge.

In order to perform a data fusion of different measurements obtained from different sensors, a time synchronisation between the sensors plays an important role. In an ideal case, the time synchronisation should be performed at the hardware level. However, in this study, as described in Ferrari et al. (2016), to obtain better synchronisation between the measurements and to calculate a time delay between them, a cross-correlation is carried out. But, this is a challenging issue since the outputs of the sensor measurements are in different units. To tackle this problem, the adjusted MEMS acceleration data are converted to a displacement vector at the metric unit based on a double integration for a duration of 35 s within the selected ambient window. Next, the adjusted MEMS acceleration data and the IATS displacement data are resampled to the sampling frequency of the laser tracker. Then the cross-correlation between the IATS and MEMS with respect to the laser tracker is calculated. The analysis shows that a maximum cross-correlation between the MEMS and the laser tracker (10.909) is slightly higher than the maximum cross-correlation between the IATS and the laser tracker (10.631) (see Fig. 12). This makes sense due to extraction of higher eigenfrequencies from the MEMS compared to the IATS.

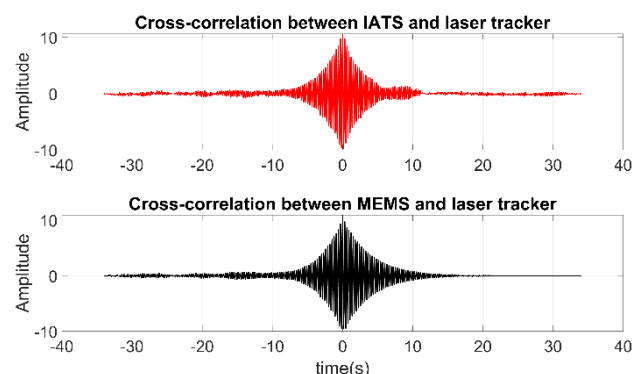


Figure 12. Cross-correlation between the displacement time series obtained from the IATS data, the double integration of the adjusted MEMS acceleration data and the laser tracker data for a duration of 35 s within the selected ambient window.

Figure 13 depicts an overlay of the displacement time series from aforementioned sensors after performing the time synchronisation. It shows how the peaks nicely fit together. Additionally, as we can also see from this figure, the amplitudes

of the peaks in the laser tracker and the MEMS are slightly higher than the IATS, which is due to the extracting the higher eigenfrequencies.

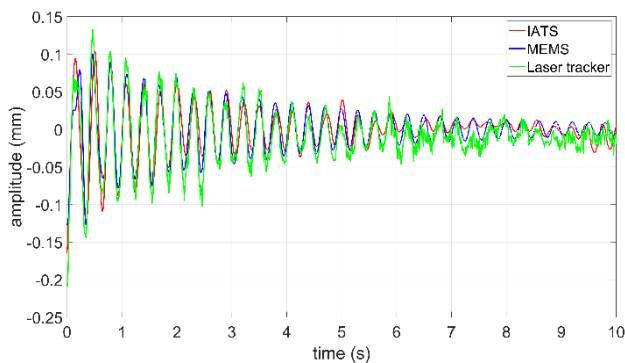


Figure 13. Overlaying of displacement time series obtained from the IATS data, the double integration of the adjusted MEMS acceleration data and the laser tracker data within the selected ambient window.

The iEKF is conducted by data fusion of the 1D displacements and 1D acceleration measurements with practical sampling frequencies of 10 Hz and 100 Hz, respectively. The 1D displacements obtained by the IATS are considered for a 1D CUPT in the filtering step of the iEKF to minimize the displacement drift resulting from the double integration of the 1D accelerations. In order to perform iEKF, two alternative solutions were investigated. Firstly, the raw measurements from the 1D displacement and 1D acceleration datasets are included into the iEKF with different sampling frequencies by performing a multi-rate configuration similar to the work of Smyth and Wu (2006) and Ferrari et al. (2016). In this case, innovation and design matrices are adaptively updated to be compatible with the raw measurement sampling frequencies (Figure 14).

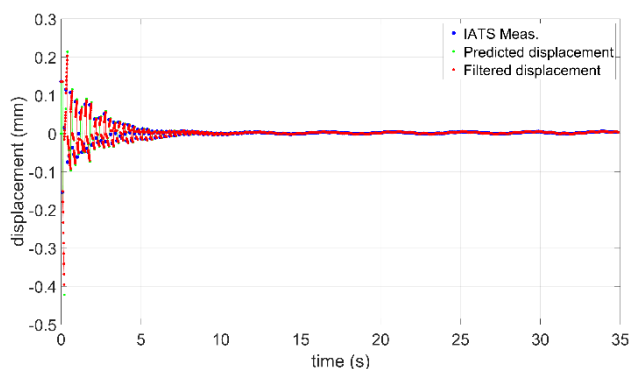


Figure 14. The displacements analysis based on iEKF and the multi-rate configuration using the displacement and acceleration measurements: the displacements obtained from the IATS (blue), the predicted displacements (green) and the filtered displacements (red).

In the second solution, the resampled displacement data from the IATS as well as the raw acceleration data are included into the iEKF. In this case, more displacement observations than the raw displacement observations are considered (Figure 15).

However, the prior knowledge about a-posteriori standard deviations of the displacement and acceleration data obtained from the estimation procedure allows to have more reliable estimation within the iEKF procedure. Consequently, such

filtering procedure enables us to avoid the drift of the displacements estimates derived from the MEMS acceleration data over a longer period of time (few minutes or higher) by means of the displacement data from the IATS. In our future work, the linear drift of the offset in the DHO model can be extended to higher order polynomials to enhance the generality of the proposed algorithm.

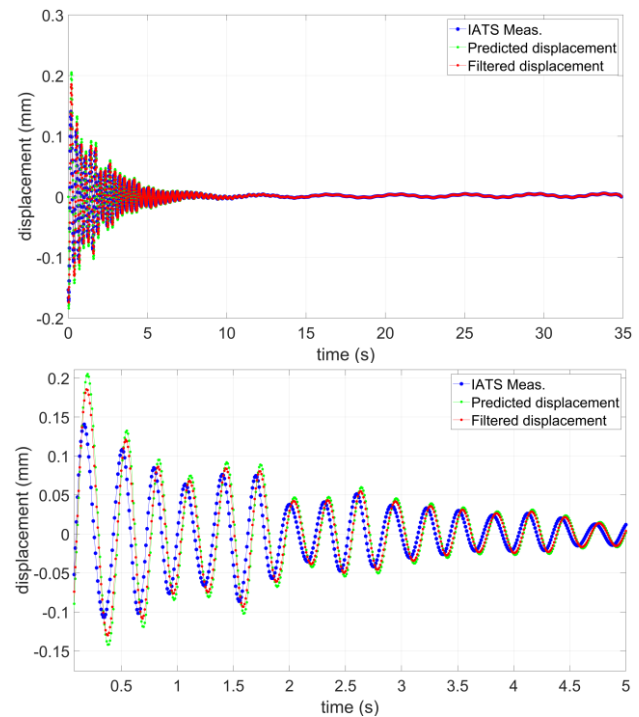


Figure 15. The displacements analysis based on iEKF and performing the resampling using the displacement and acceleration measurements (top) and its magnification (bottom): the displacements obtained from the IATS (blue), the predicted displacements (green) and the filtered displacements (red).

8. CONCLUSIONS

In this study the good feasibility of MEMS accelerometers supported by an IATS for short- and long-term deformation monitoring of bridge structure is shown.

To allow for a precise and reliable deformation monitoring of oscillating structures with less accuracy degradation over time, two scenarios are proposed. Firstly, a calibration procedure for MEMS accelerations is conducted to obtain calibration parameters, which enables us to later refine the measurements in a real monitoring of bridge structures. It is carried out using a KUKA youbot for fixed positions in a climate chamber and over different temperature ranges. However, the analysis reveals a minor influence of the calibration parameters on the estimated parameters for the short time interval (few minutes). The second scenario is performed to estimate the modal parameters in a controlled excitation experiment using a shaker. In addition, it enables us to observe the time synchronisation between the three used MEMS accelerometers. To this end, both scenarios support the selection process of finding the proper and optimal MEMS accelerometers.

To perform a vibration analysis, the observation model is determined based on a DHO model, an auto-correlation model in the form of an AR process as well as a stochastic model in the

form of heavy tailed family of scaled t-distributions with an unknown degree of freedom and with unknown scale factor. The analyses prove that such a combination allows for robust, reliable and accurate estimation of the modal parameters.

The overall analysis shows that the MEMS used within the experiment are capable to identify all possible eigenfrequencies of the synthetic bridge structure with an accuracy level of sub-millimetre for amplitudes and much better than 0.1 Hz for the frequencies.

A precise and reliable double integration of the acceleration measurements is carried out for a short time (i.e. 15 - 35 s) to obtain displacement changes within the selected ambient window.

To overcome a displacement drift of the MEMS accelerometers in the vertical direction, the 1D CUPT is performed based on an iEKF by involving displacement time series generated from the video frames of the IATS. The resampling of the displacement data based on their estimated modal parameters significantly improves the results.

In the future work, a possible correlation between closely spaced frequencies will be investigated. The estimation procedure for the displacement data is improved by extending the offset in the DHO model to higher order polynomials. Furthermore, a global optimization is applied to estimate the modal parameters for a longer period of time. Additionally, the influence of the calibration parameters on the estimated modal parameters within the long-term interval is investigated.

ACKNOWLEDGEMENTS

The authors would like to acknowledge the Bundesanstalt für Materialforschung und -prüfung (BAM) for providing the synthetic bridge used within this experiment. The research presented was carried out within the scope of the collaborative project 'Spatio-temporal monitoring of bridge structures using low cost sensors' with ALLSAT GmbH, which was supported by the German Federal Ministry for Economic Affairs and Energy (BMWi) and the Central Innovation Programme for SMEs (Grant ZIM Kooperationsprojekt, ZF4081803DB6).

REFERENCES

- Amezquita-Sanchez, J.P. and Adeli, H., 2015. A new music-empirical wavelet transform methodology for time-frequency analysis of noisy nonlinear and non-stationary signals. *Digital Signal Processing*, 45, 55–68.
- Bar-Shalom, Y., Li, X.-R. and Kirubarajan, T., 2001. *Estimation with applications to tracking and navigation*. Wiley, New York NY.
- Bosch, 2016. Data sheet BNO055 Intelligent 9-axis absolute orientation sensor. Document revision 1.4. https://ae-bst.resource.bosch.com/media/_tech/media/datasheets/BST-BNO055-DS000.pdf (10 January 2019).
- Duff, K., and Hyzak, M., 1997. *Structural monitoring with GPS*. <https://www.fhwa.dot.gov/publications/publicroads/97spring/gps.cfm> (2 November 2018).
- Ehrhart, M. and Lienhart, W., 2015a. Image-based dynamic deformation monitoring of civil engineering structures from long ranges. *Proc SPIE* 2015; 9405: 94050J.
- Ehrhart, M. and Lienhart, W., 2015b. Monitoring of civil engineering structures using a state-of-the-art image assisted total station. *Journal of applied geodesy*, 9(3), 174–182.
- Ferrari, R., Pioldi, F., Rizzi, E., Gentile, C., Chatzi, E. N., Serantoni, E. and Wieser, A., 2016. Fusion of wireless and non-contact technologies for the dynamic testing of a historic RC bridge. *Measurement Science and Technology*, 27(12), 124014.
- Grompone von Gioi R, Jakubowicz J, Morel JM, Randall, G., 2012. LSD: a line segment detector. *Image Process On Line*, 2, 35–55.
- Hexagon Metrology, 2015. Leica absolute Tracker AT960: Product Brochure (2 July 2019).
- Kaehler A and Bradski G., 2016. *Learning OpenCV 3: computer vision in C++ with the OpenCV library*. Sebastopol, CA: O'Reilly Media, Inc.
- Kalman, R. E., 1961. New methods and results in linear prediction and filtering theory. *Research Institute for Advanced Study*, Baltimore, Md., Tech. Rep. 61–1.
- Kargoll, B., Omidalizarandi, M., Loth, I., Paffenzholz, J. A., and Alkhatib, H., 2018. An iteratively reweighted least-squares approach to adaptive robust adjustment of parameters in linear regression models with autoregressive and t-distributed deviations. *Journal of Geodesy*, 92(3), 271–297.
- Kargoll, B., Omidalizarandi, M., Paffenzholz, J.-A., Neumann, I., Kermarrec, G., Alkhatib, H., 2019. Bootstrap tests for model selection in robust vibration analysis of oscillating structures, In: *Proceedings of the 4th Joint International Symposium on Deformation Monitoring (JISDM)*, Athens.
- Lienhart, W., Ehrhart, M. and Grick, M., 2017. High frequent total station measurements for the monitoring of bridge vibrations. *Journal of applied geodesy*, 11(1), 1–8.
- Neitzel, F., Niemeier, W., Weisbrich, S., and Lehmann, M., 2012. Investigation of low-cost accelerometer, terrestrial laser scanner and ground-based radar interferometer for vibration monitoring of bridges. In *Proceedings of the 6th European Workshop on Structural Health Monitoring*, Dresden, Germany (pp. 542–551).
- Omidalizarandi, M. and Zhou, C., 2013. Positioning based on integration of multi-sensor systems using Kalman filter and least square adjustment. *International Archives of the Photogrammetry, Remote Sensing and Spatial Information Sciences*, 1, W3.
- Omidalizarandi, M., Kargoll, B., Paffenzholz, J.-A. and Neumann, I., 2018. Accurate vision-based displacement and vibration analysis of bridge structures by means of an image-assisted total station. *Advances in Mechanical Engineering*, 10(6), 1687814018780052.
- Omidalizarandi, M., Paffenzholz, J.-A. and Neumann I., 2019a. Automatic and accurate passive target centroid detection for applications in engineering geodesy. *Survey Review*, 51(367), 318–333.
- Omidalizarandi, M., Herrmann, R., Marx, S., Kargoll, B., Paffenzholz, J.-A. and Neumann I., 2019b. A validated robust and automatic procedure for vibration analysis of bridge structures using MEMS accelerometers (Under preparation).

Psimoulis, P. A. and Stiros, S.C., 2013. Measuring deflections of a short-span railway bridge using a robotic total station. *Journal of Bridge Engineering*, 18(2), 182–185.

Roberts, G. W., Meng, X., and Dodson, A. H., 2004. Integrating a global positioning system and accelerometers to monitor the deflection of bridges. *Journal of Surveying Engineering*, 130(2), 65–72.

Schill, F., Eichhorn, A., 2019. Deformation Monitoring of Railway Bridges with a Profile Laser Scanner. In: *zfv* 144 (2), S. 109–118. DOI: 10.12902/zfv-0248-2018.

Shin, E. H. and El-Sheimy, N., 2002. A new calibration method for strapdown inertial navigation systems. *Z. Vermess*, 127, 1–10.

Smyth, A., & Wu, M., 2006. Multirate Kalman filtering for the data fusion of displacement and acceleration measurements. In *Smart Structures and Materials 2006: Sensors and Smart Structures Technologies for Civil, Mechanical, and Aerospace Systems* (Vol. 6174, p. 61741G). International Society for Optics and Photonics.

Paper 6

Bootstrap tests for model selection in robust vibration analysis of oscillating structures

Boris Kargoll, Mohammad Omidalizarandi, Jens-André Paffenholtz, Ingo Neumann, Gaël Kermarrec, Hamza Alkhatib

Geodetic Institute, Leibniz University Hannover, Nienburger Str. 1, 30167 Hannover, Germany,
{[kargoll](mailto:kargoll@gih.uni-hannover.de),[zarandi](mailto:zarandi@gih.uni-hannover.de),[paffenholtz](mailto:paffenholtz@gih.uni-hannover.de),[neumann](mailto:neumann@gih.uni-hannover.de),[kermarrec](mailto:kermarrec@gih.uni-hannover.de),[alkhatib](mailto:alkhatib@gih.uni-hannover.de)}@gih.uni-hannover.de

Key words: structural health monitoring; low-cost accelerometer; vibration analysis; damped harmonic oscillation; robust parameter estimation; model selection; bootstrap test

ABSTRACT

In this contribution, a procedure for deciding, whether the oscillation of a surveyed structure is damped or not, is proposed. For this purpose, two bootstrap tests under fairly general assumptions regarding auto-correlation and outlier-affliction of the random deviations (“measurement errors”) are suggested. These tests are derived from an observation model consisting of (1) a parametric oscillation model based on trigonometric functions, (2) a parametric auto-correlation model in the form of an autoregressive process, and (3) a parametric stochastic model in terms of the heavy-tailed family of scaled t-distributions. These three levels, which generalize current observation models for oscillating structures, are jointly expressed as a likelihood function and jointly adjusted by means of a generalized expectation maximization algorithm. Closed-loop Monte Carlo simulations are performed to validate the bootstrap tests. Visual inspection of models fitted by standard least-squares techniques are shown to be insufficient to detect a small significant damped oscillation. Furthermore, the tests are applied to a controlled experiment in a laboratory environment. The oscillation was generated by means of a portable shaker vibration calibrator and measured by a reference accelerometer and a low-cost accelerometer.

1. INTRODUCTION

Models for periodic phenomena based on trigonometric functions have played an important role in geodesy for decades (Vanicek, 1969; Wells *et al.*, 1985; Craymer, 1998; Pagiatakis, 1999; Mautz and Petrovic, 2005; Kaschenz and Petrovic, 2005; Psimoulis *et al.*, 2008; Neitzel *et al.*, 2011; Neitzel *et al.*, 2012; Lehmann, 2014; Bogusz and Klos, 2016). Oscillations may be accurately measured in various ways, for instance, by means of a global navigation satellite system (GNSS) receiver, a ground based synthetic aperture radar (GBSAR), a terrestrial laser scanner (TLS), a laser tracker, an accelerometer and an image-assisted total station (cf. Neitzel and Schwarz, 2017; Omidalizarandi *et al.*, 2018). The stochastic model employed for the inference of oscillation models greatly depends on the kind of observable.

Besides the variances of the random deviations, auto-correlations play a large role for such electronic instruments measuring at a high sampling rate and should therefore be taken into account in deformation analysis in general (cf. Kuhlmann, 2003). While covariance functions and covariance matrices have been traditionally employed for this purpose, autoregressive (AR) processes have become increasingly popular since the early 2000s in diverse fields of geodetic science (e.g., Schuh, 2003; Nassar *et al.*, 2004; Park and Gao, 2008; Li, 2011; Luo *et al.*, 2012). These studies demonstrated that AR models can be easily fitted to geodetic data in connection with least-

squares estimation (LSE) or Kalman filtering techniques. While constituting a parsimonious time-domain model that can easily be combined with a functional observation model, AR processes can be transformed into and interpreted through a covariance function/matrix and a spectral density function. Therefore, the specification and fitting of an AR correlation model are adopted also in the current contribution.

Outliers constitute another phenomenon often found in geodetic data. A common approach to dealing with outliers consists of a robust (i.e., outlier-resistant) method of iteratively reweighted least squares (IRLS) based on an error law whose defining probability density function (pdf) has “longer tails” than a Gaussian bell curve (e.g., the L1-norm estimator and Huber estimator). Thus, when outliers are defined to be errors larger than three times the standard deviation of a random deviation (see Lehmann, 2013), they obtain substantially more probability mass via IRLS (reflected by lower weights) than with (uniformly weighted) LSE. To obtain estimation results that are as realistic as possible, it is desirable to match the shape of the pdf or the error law with the actual distribution of the residuals/outliers (cf. Wisniewski, 2014). To enable this, it makes sense to use a flexible family of error laws having suitable mathematical properties and having - besides a scale parameter that accounts for the variance of a random deviation - at least one shape parameter that controls the thickness of the tails. To foster automatization of the adjustment procedure, the

heavy-tailed family of scaled t-distributions is employed in this contribution. Its shape parameter/tuning constant is the degree of freedom, which can be estimated as part of an IRLS procedure (cf. Koch and Kargoll, 2013), so that this robust estimator has been called *self-tuning* (Parzen, 1979). Standard LSE corresponds to the special case, where the degree of freedom takes a large value.

Parameter estimation is an intermediate step that reduces the observations to sufficient statistics, which are then used to express the test statistic (cf. Kargoll, 2012). Under the standard assumptions of linear observation equations involving normally distributed random deviations and a given covariance or weight matrix, optimal (*uniformly most powerful invariant*) parameter tests are readily available (cf. Teunissen, 2003). As these assumptions do not hold under the given model, we make use of bootstrap tests (cf. McKinnon, 2007), which can be tailored to such nonstandard model assumptions. In combination with Monte Carlo (MC) simulation (cf. Koch, 2018), such tests do not require knowledge of the distribution of the test statistic employed. In Section II, we develop various bootstrap tests for deciding, whether an observed oscillation is damped or not. This methodology extends recent developments of bootstrapping techniques in geodesy for confidence intervals (Neuner et al., 2014), parameter estimation (e.g., Angrisano et al., 2018) and uncertainty quantification (Lösler et al., 2018), to the domain of hypothesis testing. In Section III, it is shown how MC simulations are carried out to estimate the type-I error probabilities and power functions of the bootstrap tests. The performance of these tests is assessed and contrasted with the standard F-Test. The limits of standard least-squares fitting and visual inspection of resulting model plots for the purpose of detecting a damped oscillation are also explored. Subsequently, the proposed tests are applied to measurements of an oscillation generated by a portable shaker vibration calibrator and recorded both by the associated reference accelerometer and a low-cost accelerometer. Section IV draws some conclusions and gives an outlook to potential applications of the tests.

II. METHODOLOGY

A. Observation Model

When observations describe a time-dependent undamped oscillation, one may use the model

$$h_t(\boldsymbol{\beta}) = \frac{a_0}{2} + \sum_{j=1}^M a_j \cos(2\pi f_j x_t) + b_j \sin(2\pi f_j x_t) \quad (1)$$

consisting of an unknown offset $\frac{a_0}{2}$ and a sum of sinusoids, which involve unknown coefficients a_j and b_j , unknown frequencies f_j , and specified equidistant time instances x_t for $t = 1, \dots, n$. The unknowns a_j, b_j, f_j ($j = 1, \dots, M$) form the vector $\boldsymbol{\beta}$ of functional

model parameters. In the case of a damped oscillation, the deterministic model (1) is extended to

$$h_t(\boldsymbol{\beta}, \boldsymbol{\xi}) = \frac{a_0}{2} + \sum_{j=1}^M \left[a_j \cos\left(2\pi f_j \sqrt{1 - \xi_j^2} x_t\right) + b_j \sin\left(2\pi f_j \sqrt{1 - \xi_j^2} x_t\right) \right] \times \exp(-2\pi \xi_j f_j x_t) \quad (2)$$

where ξ_j is the so-called damping ratio coefficient and $f_{jd} = f_j \sqrt{1 - \xi_j^2}$ the corresponding damped frequency (cf. Amezcua-Sanchez and Adeli, 2015). Clearly, the undamped oscillation model (1) is nested inside the damped oscillation model (2) since the former results from the latter by setting all damping ratio coefficients equal to zero.

For both kinds of deterministic model, the observations l_t are considered to be subject to auto-correlated random deviations

$$e_t = \sum_{j=1}^p \alpha_j e_{t-j} + u_t \quad (3)$$

The coefficients $\boldsymbol{\alpha} = [\alpha_1 \dots \alpha_p]^T$ of this AR(p) model are treated as unknown parameters to take unknown forms of auto-correlation into account. The boundary conditions are simply fixed by setting $e_0 = e_{-1} = \dots = e_{1-p} = 0$. The AR model order p has to be specified based on prior information or through a statistical model selection procedure. To set the level of precision and to model outliers of unknown absolute frequency and magnitudes, the white noise components u_1, \dots, u_n are assumed to be stochastically independent and to follow a scaled, centred t-distribution with unknown scale factor σ^2 and degree of freedom ν , symbolically

$$u_t \sim t_\nu(0, \sigma^2). \quad (4)$$

This combined parametric auto-correlation and error model allows for a self-tuning, robust, maximum likelihood estimation of the parameters. This estimation is based on the log-likelihood function

$$\log L(\boldsymbol{\beta}, \boldsymbol{\xi}, \boldsymbol{\alpha}, \sigma^2, \nu; \mathbf{l}) = n \log \left[\frac{\Gamma(\frac{\nu+1}{2})}{\sqrt{\nu\pi\sigma^2} \Gamma(\frac{\nu}{2})} \right] - \frac{\nu+1}{2} \times \sum_{t=1}^n \log \left[1 + \frac{1}{\nu} \left(\frac{u_t}{\sigma} \right)^2 \right] \quad (5)$$

where u_t is expressed through (3) and the observations equations as functions of $\boldsymbol{\beta}$, possibly $\boldsymbol{\xi}$, and $\boldsymbol{\alpha}$. The maximization of this log-likelihood function constitutes an alternative to a least-squares approach based on outlier-elimination and noise reduction through filtering. One advantage of the former approach is that a single algorithm and adjustment routine can be devised while avoiding some pre-processing steps. Furthermore, (5) allows for likelihood ratio (LR) tests about the model parameters or

constraints thereof, as the deterministic and stochastic model assumptions are included.

B. Hypotheses

Besides estimating model parameters, we wish to identify an adequate oscillation model from (1) and (2). Since parsimonious observation models are preferred over models that include unnecessary parameters, it is desirable to test the null hypothesis H_0 that the damping ratio coefficients ξ are equal to zero. The alternative hypothesis can simply be specified to be the negation of H_0 , so that the problem is to test

$$H_0: \xi = \mathbf{0} \quad \text{versus} \quad H_1: \xi \neq \mathbf{0}. \quad (6)$$

A simple case is given by testing the damping ratio coefficient ξ associated with a single natural frequency of the oscillating structure (the vector ξ thus reduces to a scalar quantity).

One possibility of measuring the deviation from H_0 is to compute the weighted square sum $T = \hat{\xi}^T \hat{\Sigma}_{\xi\xi}^{-1} \hat{\xi} / M$, based on estimates $\hat{\xi}$ and their joint *a posteriori* covariance matrix $\hat{\Sigma}_{\xi\xi}$. In the special case of uncorrelated and normally distributed random deviations (corresponding to $p = 0$ and $\nu \rightarrow \infty$), the kind of Wald (W) test statistic T would approximately follow Fisher's $F_{M,n-u}$ -distribution, where $u = 4M + 1$ is the total number of functional parameters β, ξ in model (2). However, due to the stochastic model based on the family of scaled t-distributions, the test statistic T might not follow any standard distribution to a sufficient level of approximation. This hindrance, however, does not prevent the solution of the testing problem (6) since simulation-based bootstrap tests do not require the specification of a test distribution. A second natural test statistic is based on the difference

$$LR = \log L(\tilde{\beta}, \mathbf{0}, \tilde{\alpha}, \tilde{\sigma}^2, \tilde{\nu}; \mathbf{l}) - \log L(\hat{\beta}, \hat{\xi}, \hat{\alpha}, \hat{\sigma}^2, \hat{\nu}; \mathbf{l})$$

of the log-likelihoods at the constraint and unconstraint maximum likelihood estimates. Like the test statistic T , the LR test statistic $T_{LR} = -2 LR$ (cf. Section 2.5.6 in Kargoll, 2012) generally does not have a standard distribution, so that it will also be carried out by means of bootstrapping.

C. The Bootstrap Tests

The idea of a bootstrap test is to generate a large number B of observation vectors under the true H_0 , to compute the B values that the test statistic takes for these generated measurement series, and to check whether the value of the test statistic obtained for the actual measurement results is extremely large in comparison to the test values obtained under H_0 . These comparisons replace the comparison with a critical value derived from a fully specified test distribution (which is unknown in the present situation). As with a classical hypothesis test, the significance level α may be

fixed in advance. Then, given a vector \mathbf{l} of measurement results, the order M of the oscillation model (1)/(2) and the order p of the AR model (3), the following steps can be carried out in order to arrive at the test decision (see also Fig. 1).

1. Estimation step: The generalized expectation maximization (GEM) algorithm described in Alkhatib *et al.* (2018) is used to compute:
 - a) Parameter estimates $\hat{\beta}, \hat{\xi}, \hat{\alpha}, \hat{\sigma}^2, \hat{\nu}$, covariance matrix $\hat{\Sigma}_{\xi\xi}$ and white noise components $\hat{u}_1, \dots, \hat{u}_n$ in the damped harmonic oscillation model (2). The nonlinear model is linearized within each GEM iteration (see the Appendix for the derivation of the Jacobi matrix);
 - b) Parameter estimates $\tilde{\beta}, \tilde{\alpha}, \tilde{\sigma}^2, \tilde{\nu}$ and white noise components $\tilde{u}_1, \dots, \tilde{u}_n$ in the undamped harmonic oscillation model (1). The Jacobi matrix of this nonlinear model is obtained from the Jacobi matrix used in a) by setting $\xi = \mathbf{0}$.
2. Testing step: The test statistic $T = \hat{\xi}^T \hat{\Sigma}_{\xi\xi}^{-1} \hat{\xi} / M$ or $T_{LR} = -2 LR$ is computed.
3. Simulation step: Firstly, B white noise vectors

$$\begin{aligned} \mathbf{u}^{(1)} &= [u_1^{(1)} \dots u_n^{(1)}]^T \\ &\vdots \\ \mathbf{u}^{(B)} &= [u_1^{(B)} \dots u_n^{(B)}]^T \end{aligned}$$

are generated in one of the following two variants:

- a) *Parametric bootstrapping*: each white noise component $u_t^{(k)}$ ($t = 1, \dots, n; k = 1, \dots, B$) is generated randomly from the fitted t-distribution $t_{\hat{\nu}}(0, \hat{\sigma}^2)$.
- b) *Nonparametric bootstrapping*: each $u_t^{(k)}$ is "randomly drawn" from the fitted white noise series $\hat{u}_1, \dots, \hat{u}_n$ "with replacement" by generating random numbers $\tau_t^{(k)}$ from the discrete uniform distribution $U(1, n)$. Each number $\tau_t^{(k)}$ defines an index, and the associated value $\hat{u}_{\tau_t^{(k)}}$ of the fitted white noise series defines the newly generated white noise component $u_t^{(k)} = \hat{u}_{\tau_t^{(k)}}$.

Secondly, the white noise series are inserted into the fitted AR models to generate the coloured noise components $e_t^{(k)} = \sum_{j=1}^p \hat{\alpha}_j e_{t-j}^{(k)} + u_t^{(k)}$ based on the initial values $e_0^{(k)} = \dots = e_{1-p}^{(k)} = 0$, resulting in the vectors

$$\begin{aligned} \mathbf{e}^{(1)} &= [e_1^{(1)} \dots e_n^{(1)}]^T \\ &\vdots \\ \mathbf{e}^{(B)} &= [e_1^{(B)} \dots e_n^{(B)}]^T \end{aligned}$$

Thirdly, these realizations of the random deviations are added to the deterministic model

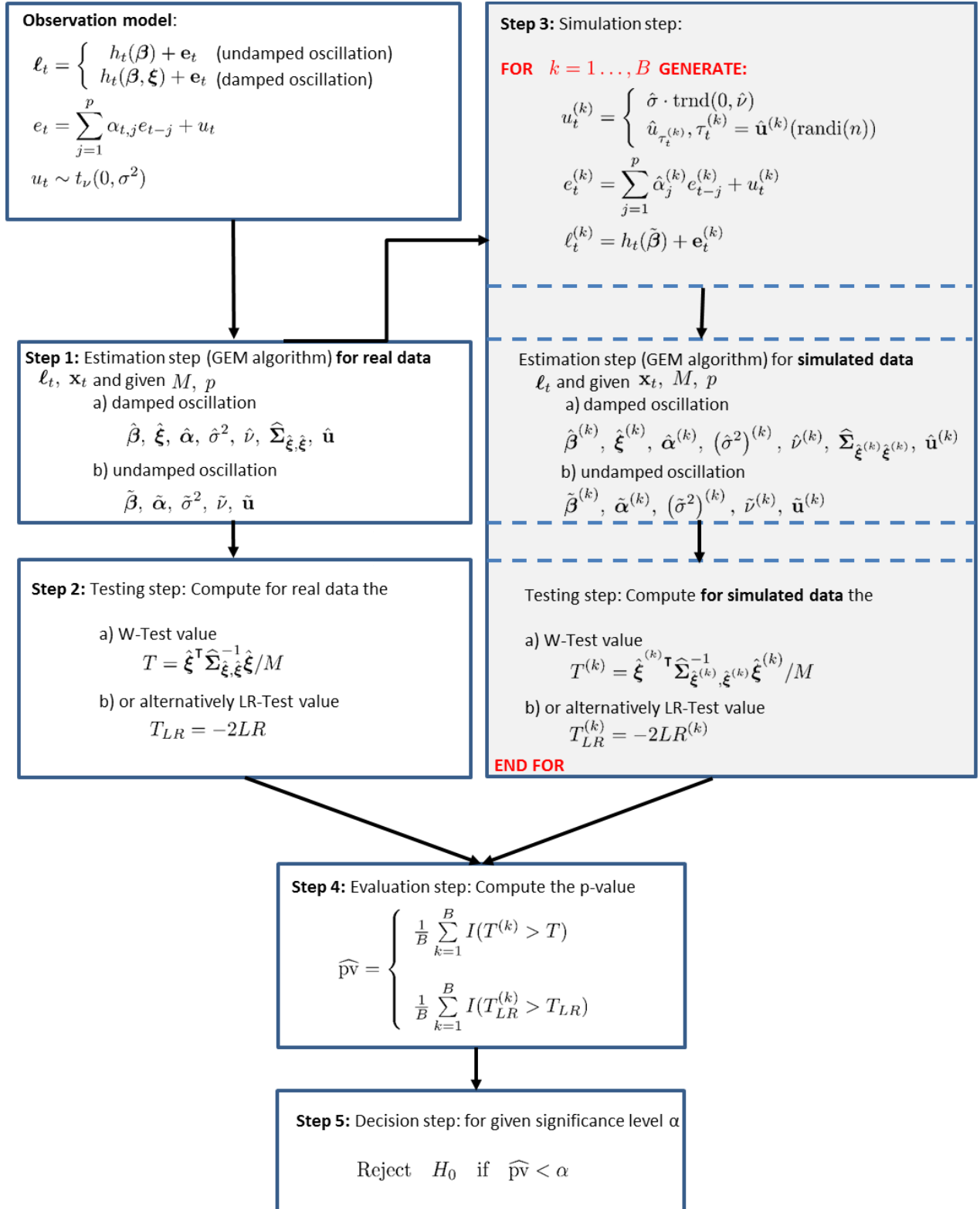


Figure 1. Flowchart of the computational steps of the bootstrap tests described in Section II.C. The random number generation within the simulation step is shown here by employing the MATLAB routines *trnd* (t-distribution) and *randi* (discrete uniform distribution).

fitted under H_0 , that is, $l_t^{(k)} = h_t(\tilde{\beta}) + e_t^{(k)}$, thereby producing the observation vectors

$$\begin{aligned} \mathbf{l}^{(1)} &= [l_1^{(1)} \dots l_n^{(1)}]^T \\ &\vdots \\ \mathbf{l}^{(B)} &= [l_1^{(B)} \dots l_n^{(B)}]^T \end{aligned}$$

The aforementioned GEM algorithm is then used to compute, for every $\mathbf{l}^{(k)}$, the parameter estimates $\hat{\xi}^{(k)}$ and covariance matrix $\hat{\Sigma}_{\hat{\xi}^{(k)}\hat{\xi}^{(k)}}$ required for evaluating the test statistic via $T^{(k)} = \hat{\xi}^{(k)T} \hat{\Sigma}_{\hat{\xi}^{(k)}\hat{\xi}^{(k)}}^{-1} \hat{\xi}^{(k)}$. The algorithm also outputs $\log L(\tilde{\beta}^{(k)}, \mathbf{0}, \tilde{\alpha}^{(k)}, \tilde{\sigma}^{2(k)}, \tilde{v}^{(k)}; \mathbf{l})$ and $\log L(\hat{\beta}^{(k)}, \hat{\xi}^{(k)}, \hat{\alpha}^{(k)}, \hat{\sigma}^{2(k)}, \hat{v}^{(k)}; \mathbf{l})$ with respect to the adjusted constraint and unconstraint model, necessary for the determination of $T_{LR}^{(k)}$.

4. Evaluation step: The p-value is estimated by computing (cf. McKinnon, 2007, Section 2)

$$\widehat{pV} = \frac{1}{B} \sum_{k=1}^B I(T^{(k)} > T),$$

or

$$\widehat{pV} = \frac{1}{B} \sum_{k=1}^B I(T_{LR}^{(k)} > T_{LR}),$$

where the indicator function $I(\cdot)$ takes the value 1 if the argument is true and the value 0 if the argument is false. Note that in case H_0 is false, the test value T tends to be large. As the test values generated under the true H_0 tend to be small, the indicator function tends to take the value 0, so that the p-value tends to be small in this case.

5. Decision step: H_0 is rejected if $\widehat{pV} < \alpha$.

III. RESULTS

A. Simulation of the Bootstrap Tests

Every statistical test is characterized by the complementary type-I and type-II error rates, which constitute its primary quality measures. On the one hand, it is important to know if the specified significance level α is truly reflected by the actual type-I error rate for the described bootstrap test. On the other hand, it is useful to study the power function of that test in order to obtain an impression of its sensitivity. Both measures can be estimated via Monte Carlo simulation.

To analyse the empirical type-I and type-II error rates for the bootstrap tests developed in Section II, Monte Carlo simulations based on $R = 500$ and $R = 1,000$ samples of $n = 1,000$ observations were carried out. For this purpose, firstly white noise samples

$$\begin{aligned} \mathbf{u}^{(1)} &= [u_1^{(1)} \dots u_{10,000}^{(1)}]^T \\ &\vdots \\ \mathbf{u}^{(R)} &= [u_1^{(R)} \dots u_{10,000}^{(R)}]^T \end{aligned}$$

were generated, on the one hand, using the t-distribution (4) with parameter values $\sigma = 0.001$ and $\nu = 3$, on the other hand using the centred normal distribution $N(0, \sigma^2)$ with the same scaling. Note that the vectors are 10 times longer than the actual number of observations. The reason for this is to eliminate the so-called warm-up effect created by the initial conditions (i.e., the zero values for time index values $t = 0, -1, \dots$) in the recursive computation of the coloured noise samples by means of (3). The last 1,000 values of the generated coloured noise vectors thus truly reflect the characteristics of the AR process. The indexes 9,001...10,000 of these 1,000 values are shifted by -9,000 in order to obtain the indexing $t = 1, \dots, n$ as defined for the models (1) – (4). Thus, the generated coloured noise vectors are denoted by

$$\begin{aligned} \mathbf{e}^{(1)} &= [e_1^{(1)} \dots e_{1,000}^{(1)}]^T \\ &\vdots \\ \mathbf{e}^{(R)} &= [e_1^{(R)} \dots e_{1,000}^{(R)}]^T \end{aligned}$$

In this simulation study, an AR(1) process with parameter value $\alpha_1 = 0.6828$ was applied. A set of true deterministic models was defined to consist of the oscillation model (2) with the parameter values $a_0 = 0.0016$, $a_1 = 0.0572$, $b_1 = -0.0950$, $f_1 = 16$ [Hz] and $\xi_1 = i \cdot 10^{-9}$ ($i \in \{0, \dots, 51\}$) for the time instances $x_t = 67.6813$ [s] + $(t - 1) \cdot 0.00512$ [s]. Adding the resulting true observations to the previously generated coloured noise vectors gave the observation samples

$$\begin{aligned} \mathbf{l}^{(1)} &= [l_1^{(1)} \dots l_{1,000}^{(1)}]^T \\ &\vdots \\ \mathbf{l}^{(R)} &= [l_1^{(R)} \dots l_{1,000}^{(R)}]^T \end{aligned}$$

under

- the two MC sample sizes $R = 500$ and $R = 1,000$,
- the two sample distributions $t_3(0, 0.001^2)$ and $N(0, 0.001^2)$, and
- the various damping ratio coefficient values ξ_1 listed before.

Note that the case $\xi_1 = 0$ ($i = 0$) corresponds to the simulation of a true H_0 , whereas the other non-zero values for ξ_1 (when $i \in \{1, \dots, 51\}$) are associated with a true H_1 .

Three tests were applied to all these observation samples at a significance level of $\alpha = 0.05$ under various settings:

1. both the parametric and the nonparametric bootstrap test based on the LR statistic $T_{LR}^{(k)}$ ("BS LR-Test") sampled $B = 99$ and $B = 999$ times,

- both the parametric and the nonparametric bootstrap test based on the W statistic $T^{(k)}$ ("BS W-Test") for $B = 99$ and $B = 999$ times, and
- the standard "F-Test" based on the previous W statistic with the distributional assumption $T \sim F_{1,995}$. With this test, the presence of the AR process and the non-normality of the white noise are ignored, so that the assumed redundancy is $n - (4M + 1) = 995$ with $M = 1$.

The odd choice of 99 or 999 bootstrap samples is motivated by the requirement of a Monte Carlo test that $\alpha(B + 1)$ is an integer (cf. McKinnon, 2007). To keep the computational burden of the Monte Carlo simulations manageable, the parameter ν was fixed at the true value 3 within the GEM algorithm. This yields a robust (though not self-tuning) estimator. The choice of the low degree of freedom $\nu = 3$ is also in line with certain applications of the Guide to the Expression of Uncertainty in Measurement (ISO/IEC, 2008), when the observables are explained by input quantities having type-A (i.e., statistically determined) standard uncertainties (cf. Sommer and Siebert, 2004). For the samples generated by means of the normal distribution, the GEM algorithm was run with the fixed degree of freedom $\nu = 120$, as this value leads to a close approximation of the sampling normal distribution $N(0, 0.001^2)$ by the t-distribution $t_{120}(0, 0.001^2)$ (cf. Koch, 2017).

Now, counting for each application of a test throughout the R MC runs the number of times that H_0 is rejected and dividing that number by R yields an estimate of the test's

- type-I error rate if H_0 is true (i.e., if the MC simulation was carried out with $\xi_1 = 0$).
- power if H_1 is true (i.e., if the MC simulation was carried out with $\xi_1 > 0$).

Table 1 shows that the empirical type-I error rate of the F-Test greatly differs from the specified significance level $\alpha = 0.05$ in case of Student white noise correlated by the AR(1) model. In contrast, the significance level is reproduced by the two bootstrap tests rather well already for $B = 99$ bootstrap samples. Increasing to $B = 999$ samples results in a correct second digit of type-I error rate. This confirms the finding of McKinnon (2007, p.3) that "it might be dangerous to use a value of B less than 999." Evidently, increasing in addition the number of MC runs does not further improve the approximation. Furthermore, the results for parametric and nonparametric bootstrapping are surprisingly similar, in view of their fundamentally different ways of generating the white noise series. The former leads to slightly closer approximations of α than the latter.

Table 1. Bold numbers: Average rejections of H_0 as estimates of the respective test's type-I error rate. Regarding the bootstrap (BS) Wald (W-) and likelihood ratio (LR-) Test, the numbers of the first row correspond to nonparametric (np), of the second row to parametric (p) bootstrapping.

R	500		1000	
F-Test	0.006		0.007	
B	99	999	99	999
BS W-Test: np	0.044	0.052	0.061	0.053
p	0.048	0.052	0.042	0.051
BS LR-Test: np	0.044	0.052	0.061	0.054
p	0.046	0.052	0.043	0.051

Generating Gaussian white noise without auto-correlations leads to the power functions shown in Fig. 1. As the graphs for the parametric and the nonparametric bootstrap tests coincide, only the latter are displayed. Figure 2 (top) demonstrates that all three tests correctly reproduce $\alpha = 0.05$ when H_0 is true (i.e., for the vanishing damping ratio coefficient $\xi_1 = 0$). For most $\xi_1 > 0$ the F-Test has slightly larger power than the bootstrap tests. As the F-Test is known to be *uniformly most powerful invariant* for linear models, the bootstrap tests could be expected to outperform the F-Test as the distribution of the F-Test statistic is not exact for a nonlinear model, as given by the damped harmonic oscillation model (2). Increasing the number of Monte Carlo runs or bootstrap samples might improve the performance of the bootstrap tests in this regard. More importantly, the bootstrap tests clearly outperform the F-Test in power when the Student distribution and the AR(1) model are used to generate the random deviations (see Fig. 2, bottom). The bootstrap W- and LR-Test again produce very similar results, which is not obvious since the standard Wald and likelihood ratio test are known to be equivalent mainly for linear models with Gaussian errors.

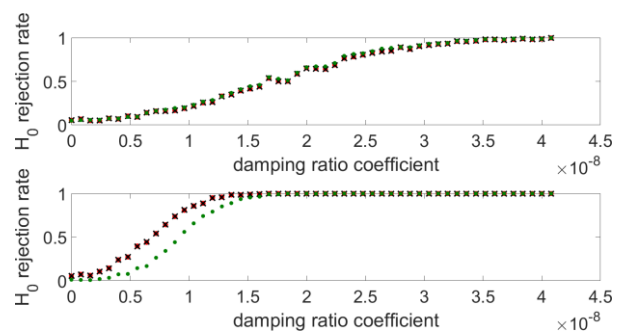


Figure 2. Average rejections of H_0 as estimates of the type-I error rate (for damping ratio coefficient $\xi_1 = 0$) and power (for $\xi_1 > 0$) for the F-Test (green dots), the bootstrap W-Test (dark crosses) and the bootstrap LR-Test (red dots). Top subplot: The bootstrap samples are generated with Gaussian white noise and without AR model (top subplot), alternatively with Student white noise and an AR(1) model (bottom subplot).

B. Failure of Least Squares Curve Fitting and Visual Inspection of Model Plots

Taking the bootstrap tests as the reference methods for detecting a damped oscillation, the performance of a simpler testing procedure based on LSE and visual inspection of the fitted oscillation model is now explored. For this purpose, two different damped oscillation models (2) were defined for 100 s of data with a sampling rate of 100 Hz using the parameter values $a_0 = 0$, $a_1 = 4.0$, $b_1 = -3.0$, $f_1 = 5$ [Hz] as well as the two alternative damping ratio coefficients (i) $\xi_1 = 1 \cdot 10^{-6}$ and (ii) $\xi_1 = 1 \cdot 10^{-5}$. Such small values were selected because the focus of the current study is on the reliable detection of a significant damping. In real applications, these levels could be larger, and the purpose of the test procedure would then be to test whether the damping ratio coefficient differs significantly from the permissible level available, e.g., from existing ISO standards. Note that the choice of the coefficient values a_1 and b_1 corresponds to the amplitude $A = \sqrt{a_1^2 + b_1^2} = 5.0$ and the phase angle $\varphi = \text{atan2}\left(\frac{-b_1}{a_1}\right) \cdot \frac{180}{\pi} = 36.87$ [degree]. The true observations resulting from this model were added to a white noise path generated from a scaled t-distribution with parameter values $\sigma = 0.2$ and $\nu = 4$.

In order for the LSE based on the linearization of the highly non-linear functional model (2) to converge, a precise initial value in particular of the frequency should be given. It is well known that the determination of oscillations with unknown frequencies is a challenging task requiring generally global optimization (cf. Mautz, 2001; Mautz and Petrovic, 2005). In Tables 2 and 3 it can be seen that LSE converges for the initial frequency value 5.005 [Hz] but diverges for the initial values 5.2 [Hz] and 5.3 [Hz]. MATLAB's curve fitting routine *fit*, which was applied using the robust fitting option since the simulated t-distribution gives rise to outliers, yields estimates similar to LSE for the initial frequency value 5.005 [Hz]; the estimates of the amplitude, phase angle and damping ratio coefficients differ greatly from the true values for the two larger initial frequency values. The unreliable LSE can be improved to some extent by decreasing the step size in the computation of the parameter update. This Gauss-Newton method is also employed within the aforementioned GEM algorithm (applied in the estimation step of the bootstrap tests); see Alkhatib *et al.* (2018). The results in Tables 2 – 3 show that LSE with decreased step size converges for the initial frequency values 5.005 [Hz] and 5.2 [Hz], but produces strongly distorted estimates for the initial value 5.3 [Hz]. In contrast, the GEM algorithm, which includes the fitting of an AR error process and of a scaled t-distribution, approximates the true solution precisely for all three initial values. Although the generated observations contain only white noise, AR model orders of 1 or 2 were identified through the application of the white noise test described in Kargoll *et al.* (2018a). Thus, the parameter estimates by the

GEM algorithm are not distorted by the additional low-order AR model estimation. Applying the bootstrap tests to the reference solution produced by the GEM algorithm results yields the results that the damping ratio coefficient $\xi_1 = 1 \cdot 10^{-6}$ is not significant (i.e., H_0 is accepted) whereas $\xi_1 = 1 \cdot 10^{-5}$ is significant (i.e., H_0 is rejected). In the cases where the LSE and the Gauss-Newton method both converge they produce identical oscillation models (shown in Fig. 3). Clearly, the significant damping by $\xi_1 = 1 \cdot 10^{-5}$ cannot be detected by visual inspection of the corresponding model plot (Fig. 3, bottom). It would not help either to zoom into a smaller time window since it needs to be analysed whether the entire segment analysed is damped or not. It may therefore be concluded that the employed curve fitting tool and the least squares methods, in connection with model plots, are inferior to a rigorous hypothesis test for damping such as the proposed bootstrap tests.

Table 2. Estimated parameters of the damped oscillation model with $\xi_1 = 1 \cdot 10^{-6}$ by three methods for three different initial frequency values. 'NaN' indicates divergence of the iterations.

Parameters	f_1 [Hz]	A [-]	φ [degree]	ξ_1 [%]
True values	5.0	5.0	36.87	0.0001
Initial values	5.005	-	-	0.0000
MATLAB-fit	5.0029	5.0029	36.92	0.00012
LSE	4.9999	5.0008	36.95	0.00008
Gauss-Newton	4.9999	5.0008	36.95	0.00008
GEM alg.	4.9999	5.0043	36.92	0.00013

Parameters	f_1 [Hz]	A [-]	φ [degree]	ξ_1 [%]
True values	5.0	5.0	36.87	0.0001
Initial values	5.2	-	-	0.0000
MATLAB-fit	5.009	3.9039	-30.80	0.1357
LSE	NaN	NaN	NaN	NaN
Gauss-Newton	4.9999	5.0008	36.95	0.00008
GEM alg.	4.9999	5.0043	36.92	0.00013

Parameters	f_1 [Hz]	A [-]	φ [degree]	ξ_1 [%]
True values	5.0	5.0	36.87	0.0001
Initial values	5.3	-	-	0.0000
MATLAB-fit	5.028	2.8375	-37.95	0.2623
LSE	NaN	NaN	NaN	NaN
Gauss-Newton	5.1074	0.0000	-137.27	-1.5645
GEM alg.	4.9999	5.0043	36.92	0.00013

Table 3. Estimated parameters of the damped oscillation model with $\xi_1 = 1 \cdot 10^{-5}$ by three methods for three different initial frequency values. 'NaN' indicates divergence of the iterations.

Parameters	f_1 [Hz]	A [-]	φ [degree]	ξ_1 [%]
True values	5.0	5.0	36.87	0.001
Initial values	5.005	-	-	0.0000
MATLAB-fit	5.0000	5.0022	36.90	0.00102
LSE	4.9999	4.9986	36.91	0.00099
Gauss-Newton	4.9999	4.9986	36.91	0.00099
GEM alg.	4.9999	5.0022	36.90	0.0010

Parameters	f_1 [Hz]	A [-]	φ [degree]	ξ_1 [%]
True values	5.0	5.0	36.87	0.001
Initial values	5.2	-	-	0.0000
MATLAB-fit	5.013	3.5886	-32.52	0.1412
LSE	NaN	NaN	NaN	NaN
Gauss-Newton	4.9999	4.9986	36.91	0.00099
GEM alg.	4.9999	5.0022	36.90	0.0010

Parameters	f_1 [Hz]	A [-]	φ [degree]	ξ_1 [%]
True values	5.0	5.0	36.87	0.001
Initial values	5.3	-	-	0.0000
MATLAB-fit	5.028	2.8496	-37.58	0.2608
LSE	NaN	NaN	NaN	NaN
Gauss-Newton	5.1255	0.0000	-61.15	-1.6032
GEM alg.	4.9999	5.0022	36.90	0.0010

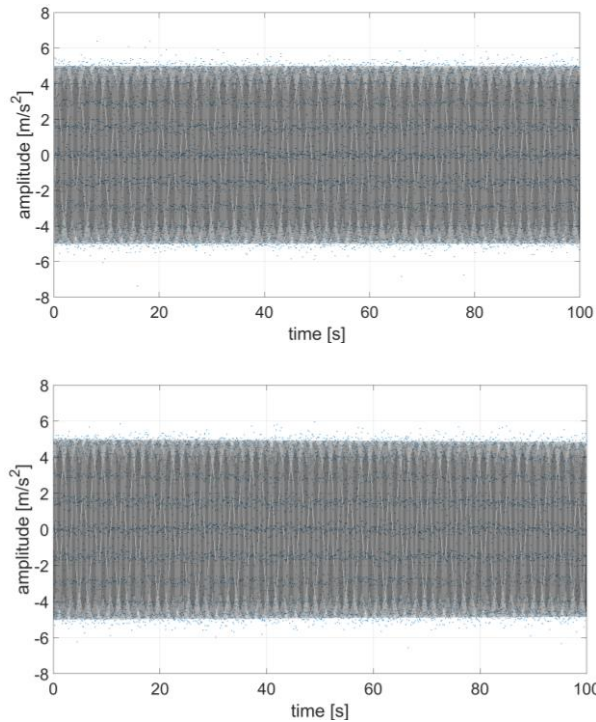


Figure 3. Oscillation time series of simulated acceleration data (blue dots) with damping ratio coefficient $\xi = 1 \cdot 10^{-6}$ (top) and $\xi = 1 \cdot 10^{-5}$ (bottom) and the model computed by converged LSE/Gauss-Newton method using the initial frequency value 5.005 [Hz].

C. Controlled Excitation Experiment

In the context of short-term deformation analysis of oscillating structures such as bridges, a geo-sensor network of low-cost accelerometers can be utilised for an accurate and robust vibration analysis of the structure (cf. Neitzel *et al.*, 2012). For this purpose, a proper deterministic model needs to be identified to truly characterise the global behaviour of a bridge structure such as natural frequencies, mode shapes and modal damping. Therefore, the time-dependent undamped oscillation model (1) considered by Kargoll *et al.* (2018a,b) and Omidalizarandi *et al.* (2018) is extended to the time-dependent damped harmonic oscillation model (2). In these previous studies, it was demonstrated in particular that the frequencies and amplitudes can be estimated robustly and accurately. Concerning the amplitudes, which are of great importance for a subsequent mode shape analysis, it should be noted that their estimation is directly influenced by the choice of the deterministic model. In the context of structural health monitoring, it is desirable to test whether the damping of a structure has a certain level or not, since deviations from that level would indicate a deterioration of the structure's intactness. As this level is usually non-zero, the hypotheses (6) and the test statistics should be adapted accordingly.

As a preparation for such more general testing problems, we consider in this contribution the simpler case of testing whether an oscillation with a single natural frequency is damped or not. For this purpose, a controlled excitation experiment was performed at the Institute of Concrete Construction of Leibniz University Hannover, using a portable shaker vibration calibrator (PSVC) 9210D and a low-cost accelerometer. The PSVC comes along with a highly accurate reference accelerometer of type PCB ICP quartz, which is used for the validation. The acceleration data are acquired by the low-cost accelerometer of type BNO055 (Bosch Sensortec) and reference accelerometer with an oscillation frequency of 4 Hz and sampling rates of 100 Hz and 200 Hz, respectively. For further information concerning the experimental setup and the used sensors, the reader is referred to Omidalizarandi *et al.* (2018).

In this section, the hypotheses are one-dimensional cases of (6). To analyse damping behaviour throughout the measured time series, the low-cost and reference acceleration datasets were firstly divided into 45 segments of consecutive 1000 and 2000 observations, respectively (each spanning 10 s). The auto-correlations of the accelerometer measurements are modelled by means of AR processes, which have previously been found to be an adequate class of models for this purpose (see, Nassar *et al.*, 2014; Park and Gao, 2008). The order of the AR process was assumed to be $p = 15$, based on the experience with previous analyses of the

datasets (see Kargoll *et al.*, 2018a). Two tests were applied to all these observation samples at a significance level of $\alpha = 0.05$, based on the LR statistic $T_{LR}^{(k)}$ ("BS LR-Test") and the W statistic $T^{(k)}$ ("BS W-Test"). For both tests, nonparametric bootstrapping based on $B = 99$ and $B = 999$ times was performed. The parameter ν was fixed at the value 4 within the GEM algorithm, reflecting the expectation of a moderate number of outliers in the data.

In view of the setup of the controlled experiment, we expected to find no significant damping of the oscillation. To verify this, the p-values of both tests applied to all segments of the low-cost and reference accelerometer sensor data were calculated. The results for 99 bootstrap samples were found to be similar to those for 999 samples, so that only the former are shown in Figs. 4 and 5. It can be seen that all p-values are greater than the significance level, so that the rejection rate is 0, i.e., H_0 is always accepted, so that there is no evidence for significant damping ratio coefficients. This finding demonstrates that the PSVC device including the reference accelerometer produces an oscillation at the specified frequency with no significant damping.

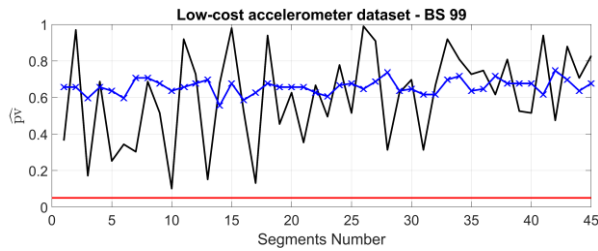


Figure 4. Low-cost accelerometer: The estimated p-value based on the bootstrap W-Test (black solid line) and the bootstrap LR-Test (blue cross line) corresponding to nonparametric bootstrapping with $B = 99$ samples. The red horizontal line shows the significance level of $\alpha = 0.05$.

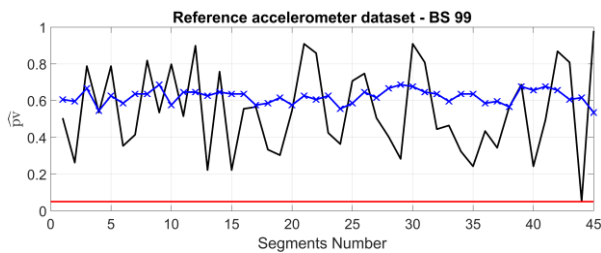


Figure 5. Reference accelerometer: The estimated p-value based on the bootstrap W-Test (black solid line) and the bootstrap LR-Test (blue cross line) corresponding to nonparametric bootstrapping with $B = 99$ samples. The red horizontal line shows the significance level of $\alpha = 0.05$.

IV. CONCLUSIONS AND OUTLOOK

A comprehensive observation model for a damped harmonic oscillation involving multiple frequencies, autoregressive random deviations and t-distributed white noise components can be adjusted by means of a GEM algorithm, which acts as a self-tuning robust estimator of all model parameters. Due to the intricacy

of the model, test statistics in general do not have an exact standard distribution. Reasons for this are the non-linearity of the functional model (cf. Lehmann and Lösler, 2018), the non-normality of the estimator, and the non-normality of the random deviations. To test in particular whether the damping of an observed oscillation is significant or not, two bootstrap tests based on the well-known W and LR statistics were proposed since small significant damping is generally not visible to the eye in a plot of the oscillation model fitted by means of standard least-squares estimation or MATLAB's curve fitting tool. The bootstrap tests are carried out by means of randomly generated bootstrap samples, without resorting to critical values from a test distribution. The number of bootstrap samples is crucial. To reproduce the significance level of $\alpha = 0.05$ precisely by the empirical type-I error rate, it is recommended to generate at least 999 bootstrap samples. Both bootstrap tests have almost identical power functions, and it is also irrelevant whether parametric or nonparametric bootstrapping is carried out. The standard F-Test is slightly more powerful than the bootstrap tests when the random deviations are normally distributed and uncorrelated. In cases of Student and AR errors, however, the F-Test has an erratic type-I error rate and visibly reduced power, so that the bootstrap tests are clearly preferable in such situations. In the future, it is intended to extend the model selection procedure to determine whether certain sinusoids of within the damped harmonic oscillation model are significant or not. Furthermore, the test decisions could be contrasted with standard information criteria such as the AIC and BIC. The bootstrap tests confirmed that oscillations induced by a portable shaker vibration calibrator within a controlled experiment and observed by means of the reference and a low-cost accelerometer are practically undamped. The next step will be to adapt the procedure such that the damping ratio coefficient(s) can be tested against specified values in order to verify the structural health of an oscillating structure such as a bridge. Such a bootstrap testing procedure can be extended and used for a factory calibration of a portable shaker vibration calibrator measuring the accelerations by means of a reference accelerometer. In that case it is desirable to detect changes of all the parameters of the damped harmonic oscillation model, that is, possibly multiple frequencies, amplitudes and damping ratio coefficients simultaneously. In addition, the measurements of a low-cost accelerometer oscillating in combination with such a shaker can be investigated over a long period of time regarding aforementioned parameter changes.

V. ACKNOWLEDGEMENTS

The research was funded partly by the Deutsche Forschungsgemeinschaft (DFG, German Research Foundation) – 386369985. In addition, the research was

partly funded and carried out within the scope of the collaborative project "Spatio-Temporal Monitoring of Bridge Structures Using Low Cost Sensors" with ALLSAT GmbH, which was supported by the German Federal Ministry for Economic Affairs and Energy (BMWi) and the Central Innovation Programme for SMEs (Grant ZIM Kooperationsprojekt, ZF4081803DB6). The authors acknowledge the Institute of Concrete Construction (Leibniz University Hannover) for providing the shaker table and the reference accelerometer used within the experiment.

References

- Alkhatib, H., Kargoll, B., and Paffenholz, J.-A. (2018). Further Results on a Robust Multivariate Time Series Analysis in Nonlinear Models with Autoregressive and t-Distributed Errors. In: *Time Series Analysis and Forecasting. ITISE 2017*. Rojas, I., Pomares, H., and Valenzuela, O. (eds.) Contributions to Statistics, Springer, Cham, pp. 25-38.
- Amezquita-Sanchez, J.P. and Adeli, H. (2015). A New Music-Empirical Wavelet Transform Methodology for Time-Frequency Analysis of Noisy Nonlinear and Non-Stationary Signals. *Digital Signal Processing*, Vol. 45, pp. 55-68.
- Angrisano, A., Maratea, A., and Gaglione, S. (2018). A Resampling Strategy Based on Bootstrap to Reduce the Effect of Large Blunders in GPS Absolute Positioning. *Journal of Geodesy*, Vol. 92, pp. 81-92.
- Bogusz, J. and Klos, A. (2016). On the Significance of Periodic Signals in Noise Analysis of GPS Station Coordinates Time Series. *GPS Solutions*, Vol. 20, pp. 655-664.
- Craymer, M.R. (1998). The Least Squares Spectrum, Its Inverse Transform and Autocorrelation Function: Theory and Some Applications in Geodesy. PhD thesis, Graduate Department of Civil Engineering, University of Toronto, Canada.
- ISO/IEC (2008). Uncertainty of measurement – Part 3: Guide to the expression of uncertainty in measurement (GUM:1995 with minor corrections). Geneva.
- Kargoll, B. (2012). On the Theory and Application of Model Misspecification Tests in Geodesy. Deutsche Geodätische Kommission, Series C (Dissertations), No. 674, Munich.
- Kargoll, B., Omidalizarandi, M., Loth, I., Paffenholz, J.-A., and Alkhatib, H. (2018a). An Iteratively Reweighted Least Squares Approach to Adaptive Robust Adjustment of Parameters in Linear Regression Models with Autoregressive and t-Distributed Deviations. *Journal of Geodesy*, Vol. 92, No. 3, pp. 271-297.
- Kargoll B., Omidalizarandi, M., Alkhatib, H., and Schuh, W.-D. (2018b). Further Results on a Modified EM Algorithm for Parameter Estimation in Linear Models with Time-Dependent Autoregressive and t-Distributed Errors. In: *Time Series Analysis and Forecasting. ITISE 2017*. Rojas, I., Pomares, H., and Valenzuela, O. (eds.) Contributions to Statistics, Springer, Cham, pp. 323-337.
- Kaschenz, J. and Petrovic, S. (2005). A Methodology for the Identification of Periodicities in Two-Dimensional Time Series. *Zeitschrift für Geodäsie, Geoinformation und Landmanagement*, Vol. 134, pp. 105-112.
- Koch, K.R. (2017). Expectation Maximization Algorithm and its Minimal Detectable Outliers. *Studia Geophysica et Geodaetica*, Vol. 61, pp. 1-18.
- Koch, K.R. (2018). Bayesian Statistics and Monte Carlo Methods. *Journal of Geodetic Science*, Vol. 8, pp. 18-29.
- Koch, K.R. and Kargoll, B. (2013). Expectation-maximization algorithm for the variance-inflation model by applying the t distribution. *Journal of Applied Geodesy*, Vol. 7, pp. 217-225.
- Kuhlmann, H. (2003). Kalman-Filtering with Coloured Measurement Noise for Deformation Analysis. In: *Proceedings of the 11th FIG International Symposium on Deformation Measurements*, FIG.
- Lehmann, R. (2013). 3 σ -Rule for Outlier Detection from the Viewpoint of Geodetic Adjustment. *Journal of Surveying Engineering*, Vol. 139, pp. 157-165.
- Lehmann, R. (2014). Detection of a Sinusoidal Oscillation of Unknown Frequency in a Time Series - a Geodetic Approach. *Journal of Geodetic Science*, Vol. 4, pp. 136-149.
- Lehmann, R. and Lösler, M. (2018). Hypothesis Testing in Non-Linear Models Exemplified by the Planar Coordinate Transformations. *Journal of Geodetic Science*, Vol. 8, pp. 98-114.
- Li, L. (2011). Separability of Deformations and Measurement Noises of GPS Time Series with Modified Kalman Filter for Landslide Monitoring in Real-Time. Ph.D. thesis, Institute of Geodesy and Geoinformation, University of Bonn.
- Lösler, M., Eschelbach, C., and Haas, R. (2018). Bestimmung von Messunsicherheiten mittels Bootstrapping in der Formanalyse. *Zeitschrift für Geodäsie, Geoinformatik und Landmanagement zfv*, Vol. 143, pp. 224-232.
- Luo, X., Mayer, M., and Heck, B. (2012). Analysing Time Series of Residuals by Means of AR(I)MA Processes. In: *Proceedings of the VII Hotine-Marussi Symposium of Mathematical Geodesy*. Sneeuw, N., Novák, P., Crespi, M., and Sansó, F. (eds.) International Association of Geodesy Symposia, Vol. 137, pp. 129-134, Springer, Berlin.
- Mautz R. (2001). Zur Lösung nichtlinearer Ausgleichungsprobleme bei der Bestimmung von Frequenzen in Zeitreihen. Deutsche Geodätische Kommission C 532, München.
- Mautz, R. and Petrovic, S. (2005). Erkennung von physikalisch vorhandenen Periodizitäten in Zeitreihen. *Zeitschrift für Geodäsie, Geoinformation und Landmanagement*, Vol. 130, pp. 156-165.
- McKinnon, J. (2007). Bootstrap Hypothesis Testing. Queen's Economics Department Working Paper, No. 1127, Queen's University, Kingston, Ontario, Canada.
- Nassar, S., Schwarz, K.-P., El-Sheimy, N., and Noureldin, A. (2004). Modeling Inertial Sensor Errors Using Autoregressive (AR) Models. *Navigation*, Vol. 51, No. 4, pp. 259-268.
- Neitzel, F., Resnik, B., Weisbrich, S., and Friedrich, A. (2011). Vibration Monitoring of Bridges. *Reports on Geodesy* Vol. 1/90, pp. 331-340.
- Neitzel, F., Niemeier, W., Weisbrich, S., and Lehmann, M. (2012). Investigation of Low-Cost Accelerometer, Terrestrial Laser Scanner and Ground-Based Radar Interferometer for Vibration Monitoring of Bridges. 6th European Workshop on Structural Health Monitoring, <http://www.ndt.net/search/docs.php3?showForm=off&id=14063>.
- Neitzel, F. and Schwarz, W. (2017). Schwingungsuntersuchungen – Ein Beitrag zum Monitoring im Bauwesen. In:

- Ingenieurgeodäsie*. Freeden, W. and Rummel, R. (eds.) Handbuch der Geodäsie, Springer Spektrum.
- Neuner, H., Wieser, A., and Krähenbühl, N. (2014). Bootstrapping: Moderne Werkzeuge für die Erstellung von Konfidenzintervallen. In: *Zeitabhängige Messgrößen - Ihre Daten haben (Mehr-)Wert*. Neuner, H. (ed.) Schriftenreihe des DVW, Vol. 74, pp. 151-170.
- Omidalizarandi, M., Kargoll, B., Paffenholz, J.-A., and Neumann, I. (2018). Accurate Vision-Based Displacement and Vibration Analysis of Bridge Structures by Means of an Image-Assisted Total Station. *Advances in Mechanical Engineering*, Vol. 10, pp. 1-19.
- Pagiatakis, S.D. (1999). Stochastic Significance of Peaks in the Least-Squares Spectrum. *Journal of Geodesy*, Vol. 73, pp. 67-78.
- Park, M. and Gao, Y. (2008). Error and Performance Analysis of MEMS-based Inertial Sensors with a Low-Cost GPS Receiver. *Sensors*, Vol. 8, pp. 2240-2261.
- Parzen, E. (1979). A Density-Quantile Function Perspective on Robust Estimation. In: *Robustness in Statistics*. Launer, L. and Wilkinson, G.N. (eds.) pp. 237-258, Academic Press, New York.
- Psimoulis, P., Pytharouli, S., Karambalis, D., and Stiros, S. (2008). Potential of Global Positioning System (GPS) to Measure Frequencies of Oscillations of Engineering Structures. *Journal of Sound and Vibration*, Vol. 318, pp. 606-623.
- Schuh, W.-D. (2003). The Processing of Band-Limited Measurements; Filtering Techniques in the Least Squares Context and in the Presence of Data Gaps. *Space Science Reviews*, Vol. 108, No. 1, pp. 67-78.
- Sommer, K.D. and Siebert, B.R.L. (2004). Praxisgerechtes Bestimmen der Messunsicherheit nach GUM. *Technisches Messen*, Vol. 71, pp. 52-66.
- Teunissen, P.J.G. (2003). *Testing Theory; an Introduction*. Delft University Press, Delft.
- Vaniček, P. (1969). Approximate Spectral Analysis by Least-Squares Fit. *Astrophysics and Space Science*, Vol. 4, pp. 387-391.
- Wells, D., Vaniček, P., and Pagiatakis, S.D. (1985). Least-Squares Spectral Analysis Revisited. Technical Report No. 84, Department of Geodesy and Geomatics Engineering, University of New Brunswick, Canada.
- Wiśniewski, Z. (2014). *M*-estimation with probabilistic models of geodetic observations. *Journal of Geodesy*, Vol. 88, pp. 941-957.

APPENDIX

The Jacobi matrix \mathbf{A} with respect to the damped harmonic oscillation model (2) is based on the partial derivatives $\frac{\partial h_t(\boldsymbol{\beta}, \boldsymbol{\xi})}{\partial a_0} = 0.5$ as well as

$$\frac{\partial h_t(\boldsymbol{\beta}, \boldsymbol{\xi})}{\partial a_j} = \cos\left(2\pi f_j \sqrt{1 - \xi_j^2} x_t\right),$$

$$\frac{\partial h_t(\boldsymbol{\beta}, \boldsymbol{\xi})}{\partial b_j} = \sin\left(2\pi f_j \sqrt{1 - \xi_j^2} x_t\right),$$

$$\begin{aligned} \frac{\partial h_t(\boldsymbol{\beta}, \boldsymbol{\xi})}{\partial \xi_j} = & \left[-a_j \sin\left(2\pi f_j [1 - \xi_j^2]^{-\frac{1}{2}} x_t\right) \right. \\ & \left. + b_j \cos\left(2\pi f_j [1 - \xi_j^2]^{-\frac{1}{2}} x_t\right) \right] \\ & \times \left(-2\pi f_j \xi_j [1 - \xi_j^2]^{-\frac{1}{2}} x_t \right) \exp(-2\pi f_j \xi_j x_t) \\ & + \left[a_j \cos\left(2\pi f_j [1 - \xi_j^2]^{-\frac{1}{2}} x_t\right) \right. \\ & \left. + b_j \sin\left(2\pi f_j [1 - \xi_j^2]^{-\frac{1}{2}} x_t\right) \right] \\ & \times \exp(-2\pi f_j \xi_j x_t) (-2\pi f_j x_t) \end{aligned}$$

$$\begin{aligned} \frac{\partial h_t(\boldsymbol{\beta}, \boldsymbol{\xi})}{\partial f_j} = & \left[-a_j \sin\left(2\pi f_j [1 - \xi_j^2]^{-\frac{1}{2}} x_t\right) \right. \\ & \left. + b_j \cos\left(2\pi f_j [1 - \xi_j^2]^{-\frac{1}{2}} x_t\right) \right] \\ & \times \left(2\pi [1 - \xi_j^2]^{-\frac{1}{2}} x_t \right) \exp(-2\pi f_j \xi_j x_t) \\ & + \left[a_j \cos\left(2\pi f_j [1 - \xi_j^2]^{-\frac{1}{2}} x_t\right) \right. \\ & \left. + b_j \sin\left(2\pi f_j [1 - \xi_j^2]^{-\frac{1}{2}} x_t\right) \right] \\ & \times \exp(-2\pi f_j \xi_j x_t) (-2\pi \xi_j x_t) \end{aligned}$$

Bibliography

- Alkhatib, H., Kargoll, B. and Paffenholz, J.-A. (2017). Robust multivariate time series analysis in nonlinear models with autoregressive and t-distributed errors. In: Proceedings of the international work-conference on time series analysis (ITISE), 23–36, Granada. Godel Impresiones Digitales S.L.
- Alvandi, A. and Cremona, C. (2006). Assessment of vibration-based damage identification techniques. *Journal of sound and vibration*, 292(1–2), 179–202.
- Amezquita-Sanchez, J. P. and Adeli, H. (2015). A new music-empirical wavelet transform methodology for time-frequency analysis of noisy nonlinear and non-stationary signals. *Digital Signal Processing*, 45, 55–68.
- Amiri-Simkooei, A. R. and Jazaeri, S. (2013). Data-snooping procedure applied to errors-in-variables models. *Studia Geophysica et Geodaetica*, 57(3), 426–441.
- Baarda, W. (1968). A testing procedure for use in geodetic networks. Delft, Kanaalweg 4, Rijkscommissie voor Geodesie, 1968., 1.
- Bar-Shalom, Y., Li, X.-R. and Kirubarajan, T. (2004). Estimation with applications to tracking and navigation: theory algorithms and software. John Wiley & Sons, New York NY.
- Boonyapinyo, V. and Janesupasaeree, T. (2010). Data-driven stochastic subspace identification of flutter derivatives of bridge decks. *Journal of Wind Engineering and Industrial Aerodynamics*, 98(12), 784–799.
- Brandt, A. (2011). Noise and vibration analysis: signal analysis and experimental procedures. Chichester, UK, John Wiley & Sons.
- Brincker, R., Zhang, L. and Andersen, P. (2001). Modal identification of output-only systems using frequency domain decomposition. *Smart materials and structures*, 10(3): 441–445.
- Bürki, B., Guillaume, S., Sorber, P. and Oesch, H. P. (2010). DAEDALUS: a versatile usable digital clip-on measuring system for total stations. In: R. Mautz, M. Kunz, and H. Ingensand, eds. Proceedings of the 2010 International Conference on Indoor Positioning and Indoor Navigation (IPIN). IEEE, 1–10.
- Bureick, J., Alkhatib, H., Neumann, I. (2016). Robust spatial approximation of laser scanner point clouds by means of free-form curve approaches in deformation analysis. *Journal of Applied Geodesy*, 10(1), 27–35.
- Canny, J. (1986). A computational approach to edge detection. *IEEE Transactions on Pattern Analysis and Machine Intelligence*, 8(6), 679–698.
- Cantiemi, R. (1984). Dynamic load testing of highway bridges. *Transportation Research Record* 950, National Research Council, Washington, DC.
- Caspary, W. F. (2000). Concepts of Network and Deformation Analysis. School of Surveying, The University of New South Wales, Kensington.

- Cheyne, E., Jakobsen, J. B. and Snaebjörnsson J. (2017). Damping estimation of large wind-sensitive structures. *Procedia engineering*, 199, 2047–2053.
- Cheyne, E. (2020). Operational modal analysis with automated SSI-COV algorithm (<https://www.mathworks.com/matlabcentral/fileexchange/69030-operational-modal-analysis-with-automated-ssi-cov-algorithm>), MATLAB Central File Exchange. Retrieved February 7, 2020.
- Datasheet ADXL345. 3-Axis, $\pm 2\text{ g}/\pm 4\text{ g}/\pm 8\text{ g}/\pm 16\text{ g}$ Digital Accelerometer. Analog Devices. Available at: <http://www.analog.com/media/en/technical-documentation/datasheets/ADXL345.pdf>.
- Datasheet BNO055 (2016). Data sheet BNO055 Intelligent 9-axis absolute orientation sensor. Bosch Sensortec. Document revision 1.4. Available at: https://ae-bst.resource.bosch.com/media/_tech/media/datasheets/BST-BNO055-DS000.pdf (last accessed 28 May 2020).
- Dawson, B. (1976). Vibration condition monitoring techniques for rotating machinery. *The shock and vibration digest*, 8(12), 3.
- Dempster, A. P., Laird, N. M. and Rubin, D. B. (1977). Maximum likelihood from incomplete data via the EM algorithm. *Journal of the Royal Statistical Society: Series B (Methodological)*, 39(1), 1–22.
- Doebling, S. W., Farrar, C. R., and Prime, M. B. (1998). A summary review of vibration-based damage identification methods. *Shock and vibration digest*, 30(2), 91–105.
- Duane, C. B. (1971). Close-range camera calibration. *Photogramm. Eng.*, 37(8), 855–866.
- Ehrhart, M. and Lienhart, W. (2015a). Image-based dynamic deformation monitoring of civil engineering structures from long ranges. In *Image Processing: Machine Vision Applications VIII* (Vol. 9405, p. 94050J). International Society for Optics and Photonics.
- Ehrhart, M. and Lienhart, W. (2015b). Monitoring of civil engineering structures using a state-of-the-art image assisted total station. *Journal of applied geodesy*, 9(3), 174–182.
- Ehrhart, M. and Lienhart, W. (2017a). Accurate measurements with image-assisted total stations and their prerequisites. *Journal of surveying engineering*, 143(2), 04016024.
- Ehrhart, M. (2017b). Applications of image-assisted total stations: Concepts, experiments, results and calibration. PhD dissertation, Graz University of Technology, Graz, Austria.
- Eibl, J. (1988) Baudynamik. In *Betonkalender 1988, Band II*, Ernst & Sohn, Berlin.
- Fan, J., Zhang, Z. and Hua, H. (2007). Data processing in subspace identification and modal parameter identification of an arch bridge. *Mechanical Systems and Signal Processing*, 21(4), 1674–1689.
- Ferrari, R., Pioldi, F., Rizzi, E., Gentile, C., Chatzi, E. N., Serantoni, E. and Wieser, A. (2016). Fusion of wireless and non-contact technologies for the dynamic testing of a historic RC bridge. *Measurement Science and Technology*, 27(12), 124014.
- Fischler, M. A. and Bolles, R. C. (1981). Random sample consensus: a paradigm for model fitting with applications to image analysis and automated cartography. *Communications of the ACM*, 24 (6), 381–395.
- Frýba, L. (1996). *Dynamics of Railway Bridges*. Thomas Telford, London.

- Gelb, A. (1974). *Applied Optimal Estimation*. MIT Press, Cambridge, MA.
- Guillaume, P., Verboven, P. and Vanlanduit, S. (1998). Frequency-domain maximum likelihood identification of modal parameters with confidence intervals. In *Proceedings of ISMA 23, Noise and Vibration Engineering*, Vol. 1, 359–366, K.U.Leuven, Belgium.
- Guillaume, P., De Troyer, T., Devriendt, C. and De Sitter, G. (2006). OMAX—a combined experimental-operational modal analysis approach. In *Proceedings of ISMA2006 international conference on noise and vibration engineering*, Leuven, Belgium, pp. 2985–2996, September 2006.
- Grompone von Gioi, R., Jakubowicz, J., Morel, J. M. and Randall, G. (2012). LSD: a line segment detector. *Image Processing On Line*, 2, 35–55.
- Hamm, P. (2003). *Ein Beitrag zum Schwingungs-und Dämpfungsverhalten von Fußgängerbrücken aus Holz*. PhD dissertation, Technische Universität München.
- Hargreaves, G. I. (2002). *Interval Analysis in MATLAB*. Numerical Analysis Report No. 416, Manchester Centre for Computational Mathematics, The University of Manchester, ISSN 1360–1725.
- Hermans, L. and Van der Auweraer, H. (1999). Modal testing and analysis of structures under operational conditions: industrial applications. *Mechanical systems and signal processing*, 13(2), 193–216.
- Herrmann, R. (2018). Dataset: Reference Vibration Measurement of Mensa Bridge Hannover. DOI: <https://doi.org/10.25835/0081614>
- Heunecke, O., Kuhlmann, H., Welsch, W., Eichhorn, A., and Neuner, H. (2013). *Auswertung geodätischer Überwachungsmessungen*. 2. Aufl. Handbuch Ingenieurgeodäsie.
- Heylen, W., Lammens, S. and Sas, P. (1997). *Modal analysis theory and testing* (Vol. 200, No. 7). Leuven, Belgium: Katholieke Universiteit Leuven.
- Hexagon Metrology (2015). *Leica Absolute Tracker AT960 Brochure*. Hexagon Metrology: Unterentfelden, Switzerland.
- Hong, Y. H., Lee, S. G. and Lee, H. S. (2013). Design of the FEM-FIR filter for displacement reconstruction using accelerations and displacements measured at different sampling rates. *Mechanical Systems and Signal Processing*, 38(2), 460–481.
- Horn, B. K. (1987). Closed-form solution of absolute orientation using unit quaternions. *JOSA A*, 4(4), 629–642.
- Ibrahim, S. R. (2001). Efficient random decrement computation for identification of ambient responses. In *Proceedings of the International Modal Analysis Conference - IMAC*, Orlando, FL, 698–703.
- ISO/IEC (2008). *JCGM 100:2008 Evaluation of measurement data – Guide to the expression of uncertainty in measurement*. First edition 2008, corrected version 2010. International Organization for Standardization (ISO), Geneva.
- James, G. H., Carne, T. G. and Laufer, J. P. (1995). The natural excitation technique (NExT) for modal parameter extraction from operating structures. *Modal Analysis-the International Journal of Analytical and Experimental Modal Analysis*, 10(4), 260–277.
- Jiang, X. and Adeli, H. (2007). Pseudospectra, MUSIC, and dynamic wavelet neural network for damage detection of highrise buildings. *International Journal for Numerical Methods in Engineering*, 71(5), 606–629.

- Kaehler, A., and Bradski, G. (2016). *Learning OpenCV 3: Computer vision in C++ with the OpenCV library*. Sebastopol, CA: O'Reilly Media, Inc.
- Kalman, R. E. (1961). New methods and results in linear prediction and filtering theory. Research Institute for Advanced Study, Baltimore, Md., Tech. Rep. 61–1.
- Kargoll, B., Omidalizarandi, M., Alkhatib, H. and Schuh, W. D. (2017). Further Results on a Modified EM Algorithm for Parameter Estimation in Linear Models with Time-Dependent Autoregressive and t-Distributed Errors. In *International Work-Conference on Time Series Analysis*, 323–337, Springer, Cham.
- Kargoll, B., Omidalizarandi, M., Loth, I., Paffenzholz, J.-A. and Alkhatib, H. (2018). An iteratively reweighted least-squares approach to adaptive robust adjustment of parameters in linear regression models with autoregressive and t-distributed deviations. *Journal of Geodesy*, 92(3), 271–297.
- Kargoll, B., Omidalizarandi, M., Paffenzholz, J.-A., Neumann, I., Kermarrec, G., Alkhatib, H. (2019). Bootstrap tests for model selection in robust vibration analysis of oscillating structures. In: *Proceedings of the 4th Joint International Symposium on Deformation Monitoring (JISDM)*, Athens.
- Kargoll, B., Kermarrec, G., Korte J. and Alkhatib H. (2020a). Self-tuning robust adjustment within multivariate regression time series models with vector-autoregressive random errors. *Journal of Geodesy*, 94, 51. DOI: <https://doi.org/10.1007/s00190-020-01376-6>
- Kargoll, B., Dorndorf, A., Omidalizarandi, M., Paffenzholz, J.-A. and Alkhatib H. (2020b). Modeling and estimation of auto- and cross-Correlations in multivariate geodetic times series using vector-autoregressive models. Under preparation.
- Kemkes, E. (2016). Suitability testing of micro-electro-mechanical-systems (MEMS) for integration into a geosensor network for the automated monitoring of the swing structures. Master thesis, Geodetic Institute, Leibniz Universität Hannover.
- Kemkes, E., Rüffer, J., Omidalizarandi, M., Diener, D., Paffenzholz, J.-A., Neumann, I. (2019). Ein neues Verfahren zum MEMS-basierten Brückenmonitoring-Zielsetzung und Statusbericht. In: *Tagungsband Geomonitoring 2019*, 215–226. DOI: <https://doi.org/10.15488/4524>
- Koch, K. R. (2013a). *Parameter estimation and hypothesis testing in linear models*. 2nd Edition, Springer Science and Business Media, Berlin, Germany.
- Koch, K. R. and Kargoll, B. (2013b). Expectation maximization algorithm for the variance-inflation model by applying the t-distribution. *Journal of Applied Geodesy*, 7(3), 217–225.
- Koch, K. R. (2014a). Outlier detection for the nonlinear Gauss Helmert model with variance components by the expectation maximization algorithm. *Journal of Applied Geodesy*, 8(3), 185–194.
- Koch, K. R. (2014b). Robust estimations for the nonlinear Gauss Helmert model by the expectation maximization algorithm. *Journal of Geodesy*, 88(3), 263–271.
- Kuhlmann, H. (2003). Kalman-filtering with coloured measurement noise for deformation analysis. In *Proceedings, 11th FIG Symposium on Deformation Measurements*, Santorini, Greece.
- KUKA youBot (2012). *KUKA youBot User Manual*. Document revision 1.01. ftp://ftp.youbot-store.com/manuals/KUKA-youBot_UserManual.pdf. (25 November 2019).
- Lämmle, S. (2002). *Schwingungen von Fußgängerbrücken*. Master thesis, Technische Universität München.

- Lardies, J. and Gouttebroze, S. (2002). Identification of modal parameters using the wavelet transform. *International Journal of Mechanical Sciences*, 44(11), 2263–2283.
- Leica Geosystems (2013). Leica NovaMS50 white paper. St. Gallen: Leica Geosystems AG, 2013.
- Leica Geosystems (2014). Leica Nova MS50 GeoCOM Reference Manual (version 5.50). St. Gallen: Leica Geosystems AG, 2014.
- Liebig, J. P., Grünberg, J., Paffenholz, J.-A., and Vennegeerts, H. (2011). Taktile und laserbasierte Messverfahren für die messtechnische Überwachung einer Autobahnbrücke. *Bautechnik*, 88(11), 749–756.
- Lienhart, W., Ehrhart, M. and Grick, M. (2017). High frequent total station measurements for the monitoring of bridge vibrations. *Journal of applied geodesy*, 11(1), 1–8.
- Magalhaes, F., Cunha, A., Caetano, E. (2009). Online automatic identification of the modal parameters of a long span arch bridge. *Mechanical Systems and Signal Processing*, 23(2): 316–329.
- Maia, N. M. M. and Silva, J. M. M. (2001). Modal analysis identification techniques. *Philosophical Transactions of the Royal Society of London. Series A: Mathematical, Physical and Engineering Sciences*, 359(1778), 29–40.
- Marple, S. L. (1987). *Digital Spectral Analysis*. Englewood Cliffs, NJ: Prentice-Hall, 373–378.
- Mautz, R. (2001). Zur Lösung nichtlinearer Ausgleichungs-probleme bei der Bestimmung von Frequenzen in Zeitreihen. *Deutsche Geodätische Kommission C 532*, München.
- Medić, T., Holst, C., Janßen, J. and Kuhlmann, H. (2019). Empirical stochastic model of detected target centroids: Influence on registration and calibration of terrestrial laser scanners. *Journal of Applied Geodesy*, 13(3), 179–197.
- Meng, X. (2002). Real-time deformation monitoring of bridges using GPS/accelerometers. PhD dissertation, University of Nottingham, England.
- Nassar, S., Schwarz, K. P., EL-sheimy, N., Noureldin, A. (2004). Modeling inertial sensor errors using autoregressive (AR) models. *Navigation*, 51(4), 259–268.
- Neitzel, F. (2010). Ausgleichungsrechnung-Modellbildung, Auswertung, Qualitätsbeurteilung. Qualitätsmanagement geodätischer Mess-und Auswerteverfahren, Beiträge zum, 93, 95–127. (In German)
- Neitzel, F., Resnik, B., Weisbrich, S. and Friedrich, A. (2011). Vibration monitoring of bridges. *Reports on Geodesy*.
- Neitzel, F., Niemeier, W., Weisbrich, S. and Lehmann, M. (2012). Investigation of low-cost accelerometer, terrestrial laser scanner and ground-based radar interferometer for vibration monitoring of bridges. In: *Proceedings of the 6th European Workshop on Structural Health Monitoring*, 542–551, Dresden, Germany.
- Niemeier, W. (2008). *Ausgleichungsrechnung: eine Einführung für Studierende und Praktiker des Vermessungs-und Geoinformationswesens*. 2. ed. Walter de Gruyter, Berlin. (In German)
- Omidalizarandi, M. and Zhou, C. (2013). Positioning based on integration of multi-sensor systems using Kalman filter and least square adjustment. *International Archives of the Photogrammetry, Remote Sensing and Spatial Information Sciences*, 1, W3.

- Omidalizarandi, M. and Neumann, I. (2015). Comparison of target- and mutual information based calibration of terrestrial laser scanner and digital camera for deformation monitoring. *The International Archives of Photogrammetry, Remote Sensing and Spatial Information Sciences*, 40(1), 559–564.
- Omidalizarandi, M., Paffenholz, J.-A., Stenz, U. and Neumann, I. (2016). Highly accurate extrinsic calibration of terrestrial laser scanner and digital camera for structural monitoring applications. In: *Proceedings of the 3rd Joint International Symposium on Deformation Monitoring (JISDM)*, Vienna [CD-ROM].
- Omidalizarandi, M., Kargoll, B., Paffenholz, J.-A. and Neumann, I. (2018). Accurate vision-based displacement and vibration analysis of bridge structures by means of an image-assisted total station. *Advances in Mechanical Engineering*, 10(6). DOI: <https://doi.org/10.1177/1687814018780052>
- Omidalizarandi, M., Paffenholz, J.-A., Neumann, I. (2019a). Automatic and accurate passive target centroid detection for applications in engineering geodesy. *Survey Review*, 51(367), 318–333.
- Omidalizarandi, M., Kargoll, B., Paffenholz, J.-A. and Neumann, I. (2019b). Robust external calibration of terrestrial laser scanner and digital camera for structural monitoring. *Journal of Applied Geodesy*, 13(2), 105–134. DOI: <https://doi.org/10.1515/jag-2018-0038>
- Omidalizarandi, M., Neumann, I., Kemkes, E., Kargoll, B., Diener, D., Rüffer, J., Paffenholz, J.-A. (2019c). MEMS based bridge monitoring supported by image-assisted total station. *The International Archives of Photogrammetry, Remote Sensing and Spatial Information Sciences*, XLII-4/W18, 833–842. DOI: <https://doi.org/10.5194/isprs-archives-XLII-4-W18-833-2019>
- Omidalizarandi, M., Herrmann, R., Marx, S., Kargoll, B., Paffenholz, J.-A. and Neumann, I. (2020). A validated robust and automatic procedure for vibration analysis of bridge structures using MEMS accelerometers. *Journal of Applied Geodesy*, 14(3), 327–354. DOI: <https://doi.org/10.1515/jag-2020-0010>
- Pagiatakis, S. D. (1999). Stochastic significance of peaks in the least-squares spectrum. *Journal of Geodesy*, 73(2): 67–78.
- Pakzad, S. N., Fennes, G. L., Kim, S. and Culler, D. E. (2008). Design and implementation of scalable wireless sensor network for structural monitoring. *Journal of infrastructure systems*, 14(1), 89–101.
- Park, J. W., Moon, D. S., Yoon, H., Gomez, F., B.F.Spencer, J. r., and Kim, J. R. (2018). Visual-inertial displacement sensing using data fusion of vision-based displacement with acceleration. *Structural Control and Health Monitoring*. 25(3), e2122.
- Parloo, E. (2003). Application of frequency-domain system identification techniques in the field of operational modal analysis. PhD dissertation, Department of Mechanical Engineering, Vrije Universiteit Brussel, Belgium.
- Parzen, E. (1979). A Density–Quantile Function Perspective on Robust Estimation. In *Robustness in Statistics* (pp. 237–258). Academic Press.
- PCB piezoelectric accelerometer (2019). PCB piezotronics MTS systems corporation, <https://www.pcb.com/resources/technical-information/introduction-to-accelerometers> (accessed 17 September 2019).
- Peeters, B. (2000). System identification and damage detection in civil engineering. PhD dissertation, Department of Civil Engineering, K.U.Leuven, Belgium.

- Peeters, B., Maeck, J., De Roeck, G. (2001). Vibration-based damage detection in civil engineering: excitation sources and temperature effects. *Smart materials and Structures*, 10(3), 518–527.
- Peeters, B., Vanhollenbeke, F. and Van der Auweraer, H. (2005a). Operational PolyMAX for estimating the dynamic properties of a stadium structure during a football game. In *Proceedings of the IMAC*, Vol. 23, Orlando, FL, USA.
- Peeters, B. and Van der Auweraer, H. (2005b). PolyMAX: a revolution in operational modal analysis. 1st International Operational Modal Analysis Conference, Copenhagen, Denmark.
- Porat, B. (1994) *Digital processing of random signals*. Dover Publications, Mineola, New York.
- Psimoulis, P. A. and Stiros, S. C. (2013). Measuring deflections of a short-span railway bridge using a robotic total station. *Journal of Bridge engineering*, 18(2), 182–185.
- Pytharouli, S. I. and Stiros, S. C. (2008). Spectral analysis of unevenly spaced or discontinuous data using the Normperiod code. *Computers & structures*, 86(1–2): 190–196.
- Reiterer, A. and Wagner, A. (2012). System consideration of an image assisted total station – evaluation and assessment. *Allgemeine Vermessungsnachrichten (avn)*, 119 (3), 83–94. Available from: <https://mediatum.ub.tum.de/doc/1099092/1099092.pdf>.
- Reynders, E., Pintelon, R. and De Roeck, G. (2008). Uncertainty bounds on modal parameters obtained from stochastic subspace identification. *Mechanical systems and signal processing*, 22(4): 948–969.
- Reynders, E. (2012). System identification methods for (operational) modal analysis: review and comparison. *Archives of Computational Methods in Engineering*, 19(1), 51–124.
- Roberts, G. W., Meng, X. and Dodson, A. H. (2004). Integrating a global positioning system and accelerometers to monitor the deflection of bridges. *Journal of Surveying Engineering*, 130(2), 65–72.
- Rohrmann, R. G., Baessler, M., Said, S., Schmid, W. and Ruecker, W. F. (2000). Structural causes of temperature affected modal data of civil structures obtained by long time monitoring. *Proc. 18th Int. Modal Analytical Conf. IMAC 18*, San Antonio, Tex., 1–7.
- Rump, S. M. (1999). INTLAB–interval laboratory. In Tibor Csendes, editor, *Developments in Reliable Computing*, Kluwer Academic Publishers, Dordrecht, 77–104.
- Schill F. and Eichhorn A. (2019). Deformation Monitoring of Railway Bridges with a Profile Laser Scanner. In: *zfv* 144 (2), 109–118. DOI: <https://doi.org/10.12902/zfv-0248-2018>
- Schmitt, C., Neuner, H., and Neumann, I. (2013). Strain detection on bridge constructions with kinematic laser scanning. In *Proceedings of the 2nd Joint international Symposium on Deformation Monitoring*. Nottingham, England.
- Schneider, D. (2008). Geometrische und stochastische Modelle für die integrierte Auswertung terrestrischer Laserscannerdaten und photogrammetrischer Bilddaten. PhD dissertation, Deutsche Geodätische Kommission, Reihe C, Nr.642, Technische Universität Dresden, Dresden, Germany. Available from: https://dgk.badw.de/fileadmin/user_upload/Files/DGK/docs/c-642.pdf.
- Shin, E. H. and El-Sheimy, N. (2002). A new calibration method for strapdown inertial navigation systems. *Z. Vermess*, 127, 1–10.
- Smyth, A. and Wu, M. (2007). Multi-rate Kalman filtering for the data fusion of displacement and acceleration response measurements in dynamic system monitoring. *Mechanical Systems and Signal Processing*, 21(2), 706–723.

- Teunissen, P. J. G. (2006). *Testing Theory: an Introduction*. Series on Mathematical Geodesy and Positioning. Delft University Press, Delft University of Technology, Delft, The Netherlands.
- TIRA Schwingtechnik (2019). Data sheet Vibration Test System TV 51110. Document vision 09. https://www.tira-gmbh.de/fileadmin/inhalte/download/schwingprueftechnik/schwingpruefanlagen/standard/EN/9N_bis_400N/data_sheet_system_tv_51110_eng_V09.pdf (accessed 20 November 2019).
- Titterton, D. H. and Weston, J. L. (1997). *Strapdown Inertial Navigation Technology*. Peter Peregrinus Ltd., London.
- von der Haar, C. (2017). *Eigenfrequenzuntersuchungen an der Fußgängerbrücke am Schneiderberg*. Report No. 1721/1 from 20.09.2017. Leibniz University Hannover, Institute of Concrete Construction.
- Wagner, A., Wasmeier, P., Reith, C. and Wunderlich T. (2013). Bridge monitoring by means of video-tacheometer—a case study. *avn-Allgemeine Vermessungs-Nachrichten*, 120(8–9), 283–292.
- Wagner, A., Wasmeier, P., Wunderlich, T. and Ingensand, H. (2014). Vom selbstzielenden Theodolit zur Image Assisted Total Station. *avn-Allgemeine Vermessungs-Nachrichten*, 121(5), 171–180. (In German)
- Walser, B. H. (2004). *Development and calibration of an image assisted total station*. PhD dissertation, ETH Zürich, Zürich, Switzerland.
- Wenzel, H., Pichler, D. and Schedler, R. (1999). Ambiente Schwingungsmessungen zur System- und Schadenserkennung an Tragwerken. *Bauingenieur* 74, Heft 3, 115–123.
- Wenzel, H. (2009a). *Health monitoring of bridges*. United Kingdom: John Wiley & Sons, Ltd.
- Wenzel, H. (2009b). *Ambient vibration monitoring*. United Kingdom: John Wiley & Sons, Ltd.
- Wiśniewski, Z. (2014). M-estimation with probabilistic models of geodetic observations. *Journal of Geodesy*, 88(10), 941–957.
- Xu, Y., Brownjohn, J., M. W., Hester, D. and Koo, K. Y. (2017). Long-span bridges: Enhanced data fusion of GPS displacement and deck accelerations. *Engineering Structures*, 147, 639–651.
- Xu, Y., Brownjohn, J. M. W. and Huseynov, F. (2019). Accurate deformation monitoring on bridge structures using a cost-effective sensing system combined with a camera and accelerometers: Case study. *Journal of Bridge Engineering*, 24(1), 05018014.
- Zhang, G., Tang, B. and Tang, G. (2012). An improved stochastic subspace identification for operational modal analysis. *Measurement*, 45(5), 1246–1256.
- Zhou, Y., Wagner, A., Wunderlich, T. and Wasmeier, P. (2017). Calibration method for IATS and application in multi-target monitoring using coded targets. *Journal of Applied Geodesy*, 11(2), 99–106.

Curriculum Vitae

Personal Information

Name: Mohammad Omidalizarandi
Date of birth: 03.06.1981
Place of birth: Tehran, Iran
Nationality: Iranian

Education

09.2009 – 05.2011 Master of Science, Geomatics Engineering (GEOENGINE),
Universiy of Stuttgart, Stuttgart, Germany
09.2000 – 09.2004 Bachelor of Science, Surveying Engineering, Iran University of
Science and Technology-Arak Branch, Iran
09.1998 – 06.1999 Pre-university Studies, Mathematics, Shahid Motahhari, Tehran,
Iran
09.1995 – 06.1998 High School, Physics and Mathematics, Shahid Hassan Ghadami,
Tehran, Iran

Working experience

06.2014 – now Research Assistant, Geodetic Institute, Leibniz University Hannover,
Hannover, Germany
11.2013 – 12.2013 Chief Surveyor, Prospectiuni Seismic Company, Tbilisi, Georgia
09.2012 – 06.2013 Head of Surveying, Stratus Construction Company, Between
Sanandaj and Marivan, Iran
01.2012 – 07.2012 Senior Surveyor, Oil Exploration Operations Company (OEOC),
Lali, Iran
2006 – 2009 Junior Surveyor, Miaad Andisheh Saz Research and Development
Company, Tehran, Iran
2004 – 2006 Junior Surveyor, Fire Fighting Organization and Safety Services,
Tehran, Iran

Acknowledgement

The presented research was carried out within the scope of the collaborative project “Spatio-temporal monitoring of bridge structures using low cost sensors” with ALLSAT GmbH, which was supported by the German Federal Ministry for Economic Affairs and Energy (BMWi) and the Central Innovation Programme for SMEs (Grant ZIM Kooperationsprojekt, ZF4081803DB6). In addition, it was partly supported by the Deutsche Forschungsgemeinschaft (DFG, German Research Foundation) – project number 386369985. I greatly acknowledge both aforementioned project funding organisations.

My sincere appreciation is conveyed to my supervisor, Prof. Dr.-Ing. Ingo Neumann, who gave me the opportunity to work, research, and explore my own ideas in Geodätisches Institut Hannover (GIH). His continuous guidance, discussions and helpful advice have been invaluable, which played a key role in reaching the goal of this dissertation.

I would also like to thank my dissertation reviewers, Prof. Dr.-Ing. habil. Jürgen Müller, Univ.-Prof. Dipl.-Ing. Dr.techn. Werner Lienhart and Prof. Dr.-Ing. Mohammad Ali Sharifi for their willingness to appraise this dissertation and to give valuable comments. Many appreciation to Prof. Dr.-Ing. habil. Christian Heipke for taking the time and being the chairman of my dissertation defense.

I wish to greatly acknowledge Prof. Dr.-Ing. Jens-André Paffenholz, Prof. Dr.-Ing. Boris Kargoll and Dr.-Ing. Hamza Alkhatib for their continuous supports, regular meetings, fruitful discussions and advice over the years at the GIH as postdoctoral researchers.

I would like to thank the project partners in ALLSAT GmbH, especially M.Sc. Eva Kemkes and Dipl.-Ing. Jürgen Rüffer. Their cooperation has significantly contributed to the success of the project and this dissertation.

Many thanks to Dr.-Ing. Ralf Herrmann from Bundesanstalt für Materialforschung und -prüfung (BAM) for his great support and advice.

Special thanks go to my colleagues at GIH for many fruitful discussions, and for always being supportive about work and research-related topics. Special thanks go to M.Sc. Dmitri Diener for his kind support during the experiments. In addition, I wish to deeply gratitude M.Sc. Rozhin Moftizadeh for English proofreading of my dissertation.

I would like to express my deep and sincere gratitude to my family. Especially to my parents for their encouragement, support and advice to achieve this stage of my life. And my sincerest gratitude goes to my wife, Tahmineh Partovi, for her endless support, encouragement, patience and understanding, which words cannot express my gratitude and appreciation to her.

Last, but not least, I would like to thank all those, who helped me throughout this research either directly or even indirectly. I hereby would like to extend my gratitude to all of them.

